

Automatic quantitative digital analysis of concrete microstructures by 64-bit imageJ analysis software

Author:

Rider, Myca Irene

Publication Date:

2010

DOI:

<https://doi.org/10.26190/unsworks/15770>

License:

<https://creativecommons.org/licenses/by-nc-nd/3.0/au/>

Link to license to see what you are allowed to do with this resource.

Downloaded from <http://hdl.handle.net/1959.4/52211> in <https://unsworks.unsw.edu.au> on 2024-04-28

Automatic Quantitative Digital Analysis of Concrete Microstructures

by
64-bit ImageJ Analysis Software

A Thesis
by
Myca Irene Rider

Submitted in Partial Fulfilment of the
Requirements for the Degree
of
Master of Engineering
in
Ceramic Engineering

School of Materials Science and Engineering

Faculty of Science

University of New South Wales

August 2010

THE UNIVERSITY OF NEW SOUTH WALES
Thesis/Dissertation Sheet

Surname or Family name: Rider

First name: Myca

Other name/s: Irene

Abbreviation for degree as given in the University calendar: ME

School: Materials Science and Engineering

Faculty: Science

Title: Automatic Quantitative Digital Analysis of Concrete
Microstructures by 64-bit ImageJ Analysis Software

Abstract

This is the first reporting in Materials Science and Engineering at UNSW of accurate quantitative digital micro-structural analyses of 95-100mm diameter concrete cores utilising 64-bit image acquisition, and 64-bit image analysis software.

The results of these newly developed, highly accurate automated quantitative analysis techniques to forensically compare micro-structural variations between hardened concrete core samples are presented.

Quantitative micro-structural digital analysis of large image data files (>3 GB), have only recently been able to be studied outside the proprietary concrete laboratories with the release of 64-bit Image J, 64-bit Windows 7 operating system and 64-bit Office 2010.

This thesis will demonstrate that only three simple procedures need to be followed to attain accurate quantitative digital analysis of large hardened concrete micro-structures:

1. The samples must be prepared by slow and careful fine diamond lapping with surface cooling to prevent any underlying damage to concrete micro-structure from overheating, thus preventing pull-outs of fine aggregate and sand particles within the fine cement paste matrix. This also ensures that accurately sized sharp pore perimeters remain and very fine air voids and hairline shrinkage micro-cracks are revealed.
2. The digital image needs to be obtained by a highly accurate white cold cathode fluorescent lamp IR LED light sourced digital scanner, such as a flat bed Epson Perfection V700 Photo scanner with true optical resolution of at least 6400ppi x 6400ppi ($\sim 4\mu^2$). It will be preferable in the near future to use a much higher resolution, as for example 50800ppi x 50800ppi ($0.5\mu^2$), comparable to the best current proprietary photo scanners and saved in uncompressed TIFF file in 128-bit software, as soon as 128-bit Windows 8 becomes available.
3. **All digital image files must not be altered or enhanced in any way.** Any enhancement of the digital image file changes forever its ability to be used for accurate quantitative digital analysis. All image analysis software calculations thereafter can only be then roughly qualitative.

Hundreds of digital image files ranging from 72ppi to 6400ppi in 32-bit and 64-bit digital analysis software were required to be able to say that the calibrated, guaranteed, and highly accurate quantitative analyses of complex microstructures from a variety of hardened concrete mixes were correct.

The 64-bit Image Analysis and Processing Software enabled me to develop automated, highly accurate, forensic comparative methods to study the macro-structures and micro-structures of commercial sized concrete core samples.

Declaration relating to disposition of project thesis/dissertation

I hereby grant to the University of New South Wales or its agents the right to archive and to make available my thesis or dissertation in whole or in part in the University libraries in all forms of media, now or here after known, subject to the provisions of the Copyright Act 1968. I retain all property rights, such as patent rights. I also retain the right to use in future works (such as articles or books) all or part of this thesis or dissertation.

I also authorise University Microfilms to use the 350 word abstract of my thesis in Dissertation Abstracts International (this is applicable to doctoral theses only).

.....
Signature

.....
Witness

.....
Date

The University recognises that there may be exceptional circumstances requiring restrictions on copying or conditions on use. Requests for restriction for a period of up to 2 years must be made in writing. Requests for a longer period of restriction may be considered in exceptional circumstances and require the approval of the Dean of Graduate Research.

FOR OFFICE USE ONLY

Date of completion of requirements for Award:

THIS SHEET IS TO BE GLUED TO THE INSIDE FRONT COVER OF THE THESIS

ORIGINALITY STATEMENT

I hereby declare that this submission is my own work and to the best of my knowledge it contains no materials previously published or written by another person, or substantial proportions of material which have been accepted for the award of any other degree or diploma at UNSW or any other educational institution, except where due acknowledgement is made in the thesis. Any contribution made to the research by others, with whom I have worked at UNSW or elsewhere, is explicitly acknowledged in the thesis. I also declare that the intellectual content of this thesis is the product of my own work, except to the extent that assistance from others in the project's design and conception or in style, presentation and linguistic expression is acknowledged.

Signed

Date

Acknowledgments

My heartfelt thanks go first to Professor Chris Sorrell who gave me the opportunity to work on this research and consequently on this thesis. Only thanks to Dr. Sorrell, his input and his encouragement I finally completed the research.

Thank you to Professor Sri Bandyopadhyay for his constructive comments at my presentation to make me aware of the most important issue in this study - size of the pixels in each image and what it meant in relation to real measurements. Due to Dr. Bandyopadhyay's input I carried out the work entirely differently and the results then were always related to the true resolution of the digital images.

Big thank you to Dr. Rui Ping Hoo who was most helpful introducing me to the original 32-bit ImageJ and its use in my study.

I also wish to thank the other members of the staff of the School of Materials Science and Engineering of UNSW for their assistance in many ways.

The biggest thank you to my husband John and consequently to my daughter Irene and son-in-law Craig, who tirelessly helped and encouraged me when I was almost giving up on the whole study and the immense amount of work associated with it.

To my dear Mum and Dad, Marie Grodl - Přeučilová and Jan Grodl, who taught me all

I know and shaped me into the person I am. Thank you.

Mým drahým rodičům, kterým jsem vděčná za to, kdo jsem a za vše, co znám. Děkuji.

ABSTRACT

This is the first reporting in Materials Science and Engineering at UNSW of accurate quantitative digital micro structural analyses of 95-100mm diameter concrete cores utilising 64-bit image acquisition, and 64-bit image analysis software.

The results and procedures of these newly developed and highly accurate automated quantitative analysis techniques to forensically study micro structural variations between hardened concrete core samples are presented.

Quantitative micro structural digital analysis of large image data files (>3 GB), have only recently been able to be studied outside the proprietary concrete laboratories with the release of 64-bit ImageJ, 64-bit Windows 7 operating system and 64-bit Office 2010.

This thesis will demonstrate that only three simple procedures need to be followed to attain accurate quantitative digital analysis of large hardened concrete micro structures:

1. The samples must be prepared slowly and carefully by fine diamond lapping with surface cooling to prevent any underlying damage to concrete micro-structure from overheating, thus preventing pull-outs of fine aggregate and sand particles within the fine cement paste matrix. This also ensures that accurately sized sharp pore perimeters remain and very fine air voids and hairline shrinkage micro cracks are revealed.
2. The digital image needs to be obtained by a highly accurate white cold cathode fluorescent lamp IR LED light sourced digital scanner, such as a flat bed Epson Perfection V700 Photo scanner with true optical resolution of at least 6400ppi x 6400ppi ($\sim 4\mu^2$). It will be preferable in the near future to use a much higher resolution, as for example 50800ppi x 50800ppi ($0.5\mu^2$), comparable to the best

current proprietary photo scanners and saved in uncompressed TIFF file in 128-bit software, as soon as 128-bit Windows 8 becomes available.

3. **All digital image files must not be altered or enhanced in any way.** Any enhancement of the digital image file changes forever its ability to be used for accurate quantitative digital analysis. All image analysis software calculations thereafter can only be then roughly qualitative.

Hundreds of digital image files ranging from 72ppi to 6400ppi in 32-bit and 64-bit digital analysis software were required to be able to say that the calibrated, guaranteed, and highly accurate quantitative analyses of complex microstructures from a variety of hardened concrete mixes were correct.

The 64-bit Image Analysis and Processing Software enabled me to develop automated, highly accurate, forensic comparative methods to study the macro structures and micro structures of commercial sized concrete core samples.

Table of Contents

Section	Page
Certificate of Originality	ii
Acknowledgements	iii
Dedication	iv
Abstract	v
Table of Contents	vii
List of Figures	xi
List of Tables	xxix
Thesis Outline	xxxii
1 Introduction	1
2 Literature Review	6
2.1 Skyscan	32
2.1.1 Microtomography	37
2.2 Digital Analysis	39
2.2.1 Automated Digital Analysis	44
2.2.2 Hardened Concrete Air-Void Analysis with a Flatbed Scanner	62
2.2.3 RapidAir 457 Automatic System for Analysis Air Void	
Content of Hardened Concrete	63
2.3 Vickers	67
3 Experimental Procedures	69
3.1 Bulk Density and Apparent Porosity	76
3.2 Skyscan X-Ray Microtomograph Examination	77

Section	Page
3.2.1 Variable (Random) Cuts	78
3.2.2 Perpendicular Cuts	79
3.3 Digital Analysis	84
3.3.1 Study 1 - 72 ppi Digital Analysis with 32-Bit ImageJ	96
3.3.1.1 Study 1 - A Procedure for Calculations of Porosity Using 32-bit ImageJ	107
3.3.1.2 Study 1 - A Procedure for Calculations of Coarse Aggregate Using 32-bit ImageJ	112
3.3.2 Study 2 - 2400 ppi Digital Analysis with 64-bit ImageJ	116
3.3.2.1 Study 2 - A Procedure for Calculations of Porosity Using 64-bit ImageJ	127
3.3.2.2 Study 2 - A Procedure for Calculations of Coarse Aggregate Using 64-bit ImageJ	127
3.3.3 Study 3 - High Optical Resolution (4800 ppi and 6400 ppi) Digital Analysis with 64-bit ImageJ	128
3.3.3.1 Study 3 - A Procedure for Calculations of Porosity Using 64-bit Adobe PhotoShop Elements 7.0, SilverFast Epson SE, 64-bit ImageJ and Microsoft Excel in 64-bit Windows	139
3.3.3.2 Study 3 - A Procedure for 100% Quantitative Calculations of Coarse Aggregate Using 64-bit Adobe PhotoShop Elements 7.0, SilverFast Epson SE, 64-bit ImageJ and Microsoft Excel in 64-bit Windows	158
3.3.3.3 Study 3 - A Procedure for Auto Calculations of Coarse Aggregate Using 64-bit Adobe PhotoShop Elements 7.0,	

Section	Page
SilverFast Epson SE, 64-bit ImageJ and Microsoft Excel in 64-bit Windows	174
3.3.3.4 Study 3 - Calibration of Micro-Porosity in Cement Matrix	180
3.4 Optical Microscopy of Cement Paste Microstructure	183
3.5 Vickers Micro Hardness of Cement Matrix	185
4 Experimental Results	188
4.1 Bulk Density and Apparent Porosity Results	189
4.1.1 Discussion of Results	193
4.2 Skyscan X-Ray Microtomograph Results	194
4.2.1 Variable (Random) Cuts	194
4.2.2 Samples Cut Perpendicular to the Notch	207
4.2.3 Discussion of Results	235
4.3 Digital Analysis Results	243
4.3.1.1 Study 1 - Results for Calculations of Porosity 72 ppi Digital Images	243
4.3.1.2 Study 1 - Results for 100% Quantitative Calculations of Coarse Aggregate Percentage 72 ppi in 32-bit ImageJ ..	253
4.3.2.1 Study 2 - Results for Calculations of Porosity 2400 ppi Digital Images	263
4.3.2.2 Study 2 - Results for Auto Calculations of Coarse Aggregate Percentage 2400 ppi in 64-bit ImageJ	273
4.3.3.1 Study 3 - Results for Calculations of Porosity 6400 ppi Digital Images	283
4.3.3.2 Study 3 - Results for 100% Quantitative Calculations of	

Section	Page
Coarse Aggregate Percentage 4800 ppi in 64-bit ImageJ	293
4.3.3.3 Study 3 - Results for Automatic Calculations of	
Coarse Aggregate Percentage 4800 ppi in 64-bit ImageJ	303
4.3.3.4 Study 3 - Results For Calibration of Micro-Porosity in	
Cement Matrix Calculated in 64-bit ImageJ	318
4.4 Optical Microscopy of Cement Paste Microstructure Results	329
4.4.1 Discussion of Results	338
4.5 Vickers Micro Hardness of Cement Matrix Results	339
4.5.1 Discussion of Results	341
5 Conclusion	342
References	345
Appendix A	351
Appendix B	no paging
Appendix C	no paging

List of Figures

Figure	Title	Page
2.1	Four stages in the setting and hardening of Portland cement ..	9
2.2	Hydration stages	10
2.3	Classification of tobermorites	10
2.4	Space relationships for paste components at various stages of hydration	11
2.5	Composition of concrete	12
2.6	Range in proportions of materials used in concrete (by absolute volume)	13
2.7	Modulus of elasticity of concrete	20
2.8	Automated calculation of air voids from a scanned image, right, is accurate and less time-consuming than microscopic evaluation of the same sample on the left	24
2.9	Image of microstructure from the Optical Microscope	27
2.10	Image from SkyScan X-Ray Microtomograph, Model 1072 Micro CT	28
2.11	Digital analysis for porosity and aggregate	29
2.12	Relationship between the microhardness and porosity	30
2.1.1	SkyScan 1172	33
2.1.2	Carbon foam sample	34
2.1.3	SkyScan 2011	36
2.2.1	Original scan of the Sample 5B at 200 ppi (the scale is in cm/mm)	39

Figure	Title	Page
2.2.2	200 ppi image of Sample 5B magnified 16 times to show the coarse perimeters which resulted in higher calculations of the air voids	40
2.2.3	Original scan of the Sample 5B at 2400 ppi (the scale is in cm/mm)	40
2.2.4	2400 ppi image magnified 16 times to show smooth perimeters of calculated air voids	41
2.3.1	Relation between compressive strength and number of blows to 'no-rebound' for concretes made with different aggregates ..	68
3.1	Original Concrete Core 1	71
3.2.	Original Concrete Core 2	71
3.3	Original Concrete Core 3	72
3.4	Original Concrete Core 4	72
3.5	Original Concrete Core 5	73
3.6	Original Concrete Core Rm	73
3.7	Original Concrete Core Dar	74
3.8	Original Concrete Core FI	75
3.9	Original Concrete Core FII	75
3.2.1	Digital Image of concrete sample and associated X-Ray micro CT scans	79
3.2.2	Detail of Perpendicular cut sample from Concrete Core Sample 1-1 with its X-Ray Micro CT image	80
3.2.3	Skyscan X-Ray Microtomograph 1072 Micro CT (sample loaded)	81
3.2.4	Close up of sample 2-3 loaded and held in static mode for 2D analysis	81

Figure	Title	Page
3.2.5	Sample 2-6 under X-Ray CT Scan (note: red light on: X-Rays ON)	83
3.2.6	Detail of sample 2-6 scanned (displayed on the computer screen)	83
3.3.1	Original 24-bit colour picture taken by a digital camera and its greyscale conversion	87
3.3.2	Pixels are normally arranged in a regular 2-dimensional grid, and are often represented using squares (as shown), dots, or rectangles	88
3.3.3	2400ppi image with a detail of pixels showing here in a format of squares after a large magnification	88
3.3.4	64-bit ImageJ programme	89
3.3.5	ImageJ memory adjustment	89
3.3.6	72 ppi true optical resolution	90
3.3.7	2400 ppi true optical resolution	91
3.3.8	4800 ppi true optical resolution	92
3.3.9	6400 ppi true optical resolution	93
3.3.10	Position of the selected area in Figures 3.3.6.to 3.3.9	94
3.3.11	Image 5B with grid and ruler	95
3.3.1.1	Canon EOS 20D camera	96
3.3.1.2	Sample 1A	97
3.3.1.3	Sample 1B	97
3.3.1.4	Sample 1C	98
3.3.1.5	Sample 1D	98
3.3.1.6	Sample 2A	99

Figure	Title	Page
3.3.1.7	Sample 2B	99
3.3.1.8	Sample 3A	100
3.3.1.9	Sample 3B	100
3.3.1.10	Sample 4A.....	101
3.3.1.11	Sample 4B	101
3.3.1.12	Sample 5A.....	102
3.3.1.13	Sample 5B	102
3.3.1.14	Sample RmA	103
3.3.1.15	Sample RmB	103
3.3.1.16	Sample DarA	104
3.3.1.17	Sample DarB	104
3.3.1.18	Sample FIA	105
3.3.1.19	Sample FIB	105
3.3.1.20	Sample FIIA	106
3.3.1.21	Sample FIIB	106
3.3.1.1.1	Select the circumference of the object in ImageJ	107
3.3.1.1.2	Find the area of a selected object and paste into the spreadsheet	108
3.3.1.1.3	Threshold tool masks the white pores in the selected range red	109
3.3.1.1.4	Histogram and a list of values	110
3.3.1.1.5	Final calculated result for the percentage of porosity in the selected object in the spreadsheet	111
3.3.1.2.1	Original Image and masked greyscale image	112
3.3.1.2.2	The detail of the aggregate masking required	113

Figure	Title	Page
3.3.1.2.3	Select the circumference of the object in ImageJ	114
3.3.1.2.4	Result of the calculation of a percentage of the coarse aggregate	115
3.3.2.1	HP ScanJet 5400C	116
3.3.2.2	Sample 1A	117
3.3.2.3	Sample 1B	117
3.3.2.4	Sample 1C	118
3.3.2.5	Sample 1D	118
3.3.2.6	Sample 2A	119
3.3.2.7	Sample 2B	119
3.3.2.8	Sample 3A	120
3.3.2.9	Sample 3B	120
3.3.2.10	Sample 4A	121
3.3.2.11	Sample 4B	121
3.3.2.13	Sample 5A	122
3.3.2.14	Sample 5B	122
3.3.2.15	Sample RmA	123
3.3.2.16	Sample RmB	123
3.3.2.17	Sample DarA	124
3.3.2.18	Sample DarB	124
3.3.2.19	Sample FIA	125
3.3.2.20	Sample FIB	125
3.3.2.21	Sample FIIA	126
3.3.2.22	Sample FIIB	126

Figure	Title	Page
3.3.3.1	Epson Perfection V700	128
3.3.3.2	Sample 1A	129
3.3.3.3	Sample 1B	129
3.3.3.4	Sample 1C	130
3.3.3.5	Sample 1D	130
3.3.3.6	Sample 2A	131
3.3.3.7	Sample 2B	131
3.3.3.8	Sample 3A	132
3.3.3.9	Sample 3B	132
3.3.3.10	Sample 4A	133
3.3.3.11	Sample 4B	133
3.3.3.12	Sample 5A	134
3.3.3.13	Sample 5B	134
3.3.3.14	Sample RmA	135
3.3.3.15	Sample RmB	135
3.3.3.16	Sample DarA	136
3.3.3.17	Sample DarB	136
3.3.3.18	Sample FIA	137
3.3.3.19	Sample FIB	137
3.3.3.20	Sample FIIA	138
3.3.3.21	Sample FIIB	138
3.3.3.1.1	Original colour picture scanned at true optical resolution 6400x6400 ppi 48-bit colour (Reference Sample 5)	139

Figure	Title	Page
3.3.3.1.2	Porous aggregate ready to be masked	140
3.3.3.1.3	Magnetic Lasso tool selected the inside of the aggregate to be filled	141
3.3.3.1.4	Fully filled porous aggregate ready for a calculation of porosity	141
3.3.3.1.5	Careful selection, and masking inside of the circumference of a large porous aggregate (on the left), removes its porosity from digital analysis, but retains surface cracking on the outside surface of the aggregate; the lasso on a small aggregate (on the right) selects the area inside of the aggregate required to be masked in black	142
3.3.3.1.6	Fully filled Reference Sample 5b, ready for automatic digital analysis, and calculation of the percentage porosity	142
3.3.3.1.7	Open the image in ImageJ (pixels 25142 x 25292, size 606 MB, 8-bit greyscale, scanned 6400 dpi in true optical resolution)	143
3.3.3.1.8	Select carefully the circumference of the Sample with Elliptical tool on the menu bar	144
3.3.3.1.9	Type of the image is changed to 8-bit for the calculation	145
3.3.3.1.10	Select Image, Adjust and Threshold to start the calculation	146
3.3.3.1.11	Automatic selection of the threshold by the software that needs to be manually adjusted in the following steps	147
3.3.3.1.12	The bottom button in the threshold gets adjusted to 255 (full red fill)	147
3.3.3.1.13	Red coloured entrained micro-pores on the original colour scanned image	148

Figure	Title	Page
3.3.3.1.14	Porosity (originally in white) is now covered in red for the calculation	149
3.3.3.1.15	Select the Histogram under the Analyze on the Menu bar to calculate the values of the selected area to calculate	150
3.3.3.1.16	List of values is displayed from bits 0 to 255 where the first selection will be in this case the value at the bit 180, after that slide down to the value of 255 and copy the whole selection (between 180 to 255) into the Clipboard	151
3.3.3.1.17	Values of selected bits from the List in the Histogram are pasted into the spreadsheet	152
3.3.3.1.18	Formula for the sum of values is selected on the Menu bar	153
3.3.3.1.19	Sum is inserted underneath	154
3.3.3.1.20	Copy the value for total Count underneath	155
3.3.3.1.21	Formula for the calculation of the percentage of the porosity is manually inputted	156
3.3.3.1.22	Formula gets formatted, the final value of 5.05% for Reference Sample 5B	157
3.3.3.2.1	Magnetic lasso tool selects the circumference of the aggregate	158
3.3.3.2.2	The bucket tool gradually fills the object with black colour	159
3.3.3.2.3	Fully filled aggregate	159
3.3.3.2.4	Fully filled Reference Sample 5b 4800 ppi , 48-24 bit colour, 1GB, 18856 x 18968 pi xels (ready for a calculation in ImageJ)	160
3.3.3.2.5	Original Reference Sample 5b 4800 ppi , 48-24 bit colour, 1.78 GB, 25142 x 25292 pixels	160
3.3.3.2.6	Open the image in ImageJ (pixels 18856 x 18968, 4800 ppi, size 1.3 GB, 24-bit colour depth)	161

Figure	Title	Page
3.3.3.2.7	Select carefully the circumference of the Sample with Elliptical tool on the menu bar	162
3.3.3.2.8	Type of the image is changed to 8-bit for the calculation	163
3.3.3.2.9	Select Image, Adjust and Threshold to start the calculation	164
3.3.3.2.10	Automatic selection of the threshold by the software that needs to be manually adjusted in the following steps	165
3.3.3.2.11	The bottom button in the threshold gets adjusted to 255 (full red fill)	165
3.3.3.2.12	Aggregate in black and the rest is in red ready for the calculation	166
3.3.3.2.13	Select the Histogram under the Analyze on the menu bar to calculate the values of the selected area	167
3.3.3.2.14	Histogram is displayed on the screen	167-168
3.3.3.2.15	List of values is displayed from bits 0 to 255 where the first selection will be in this case the value at the bit 0, after that slide down to the value of 72 and copy the whole selection (between 0 to 72) into the Clipboard as shown in detail in Figure 3.3.3.2.16 bottom part	168
3.3.3.2.16	Selection of values in the range of 0 to 72 bits is copied and pasted into the Microsoft Excel for calculations	169
3.3.3.2.17	Values are copied onto the spreadsheet	170
3.3.3.2.18	The Sum formula gets inserted	170
3.3.3.2.19	The Sum gets calculated	171
3.3.3.2.20	Total sum of pixels is copied manually into the spreadsheet as shown in detail on the following page in Figure 3.3.3.2.21	171
3.3.3.2.21	The value of the sum of all pixels in the selected object is copied into the spreadsheet manually	172

Figure	Title	Page
3.3.3.2.22	Formula is inserted to calculate the percentage of the aggregate	172
3.3.3.2.23	The resulting calculation gets formatted	173
3.3.3.3.1	Open the image	174
3.3.3.3.2	Select the circumference	175
3.3.3.3.3	Select the Type	175
3.3.3.3.4	Select Image, Adjust, Threshold	176
3.3.3.3.5	Calibration masking of the "invisible" aggregate for an automatic calculation is shown here on Sample FIIB	177
3.3.3.3.6	Select Analyze, Histogram and List in the Histogram, then select the values in the List of values to copy into the Clipboard	178
3.3.3.3.7	Calculate the automatic percentage of Coarse Aggregate	179
3.3.3.4.1	Small section 10x10 mm on Sample 5B	181
3.3.3.4.2	6400 ppi 48 bit HDR colour scanned image of the section 10 mm ²	181
3.3.3.4.3	Screen dump of the quantitative calculation of percentage micro-porosity for sample 6400 ppi	182
3.3.3.4.4	Blue circle highlights the 10 μ diameter pores used for quantitative calibration and calculation of percentage air void porosity	182
3.4.1	Nikon Epiphot 2000 Microscope	182
3.4.2	Detail of Sample 5B microstructure showing micro pores ~ 500 μ m in diameter	184
3.5.1	Diagram of the indenter	185
3.5.2	Indent shape	186

Figure	Title	Page
3.5.3	Vickers micro indenter used	187
4.1.1	Bulk Density Variations in Core Samples	190
4.1.2	Apparent Porosity Variations in Core Samples	191
4.1.3	Average Bulk Density	192
4.1.4	Average Apparent Porosity	192
4.2.1.1	Sample 1-1 (in detail) Random cut 1-1 from Concrete Core Sample 1 with its 2 X-Ray images 1-1B and 1-1A on the right	194-195
4.2.1.2	Sample 1-2	195
4.2.1.3	Sample 1-3	195
4.2.1.4	Sample 1-4	195
4.2.1.5	Sample 1-5	196
4.2.1.6	Sample 1-6	196
4.2.1.7	Sample 2-1	196
4.2.1.8	Sample 2-2	196
4.2.1.9	Sample 2-3	197
4.2.1.10	Sample 2-4	197
4.2.1.11	Sample 2-5	197
4.2.1.12	Sample 2-6	197
4.2.1.13	Sample 3-1	198
4.2.1.14	Sample 3-2	198
4.2.1.15	Sample 3-3	198
4.2.1.16	Sample 3-4	198
4.2.1.17	Sample 3-5	199
4.2.1.18	Sample 3-6	199

Figure	Title	Page
4.2.1.19	Sample 4-1	199
4.2.1.20	Sample 4-2	199
4.2.1.21	Sample 4-3	200
4.2.1.22	Sample 4-4	200
4.2.1.23	Sample 4-5	200
4.2.1.24	Sample 4-6	200
4.2.1.25	Sample 5-1	201
4.2.1.26	Sample 5-2	201
4.2.1.27	Sample 5-3	201
4.2.1.28	Sample 5-4	201
4.2.1.29	Sample 5-5	202
4.2.1.30	Sample 5-6	202
4.2.1.31	Sample 5-7	202
4.2.1.32	Sample 5-8	202
4.2.1.33	Sample 5-9	203
4.2.1.34	Sample 5-10	203
4.2.1.35	Sample Rm-1	203
4.2.1.36	Sample Rm-2	203
4.2.1.37	Sample Rm-3	204
4.2.1.38	Sample Rm-4	204
4.2.1.39	Sample Rm-5	204
4.2.1.40	Sample Rm-6	204
4.2.1.41	Sample Dar-1	205
4.2.1.42	Sample Dar-2	205

Figure	Title	Page
4.2.1.43	Sample Dar-3	205
4.2.1.44	Sample Dar-4	205
4.2.1.45	Sample Dar-5	206
4.2.1.46	Sample Dar-6	206
4.2.2.1	X-Ray Detail of Sample 1-1 (in detail) Perpendicular cut from Concrete Core Sample 1-1 with its X-Ray image	207-208
4.2.2.2	X-Ray Detail of Sample 1-2	209
4.2.2.3	X-Ray Detail of Sample 1-3	210
4.2.2.4	X-Ray Detail of Sample 1-4	211
4.2.2.5	X-Ray Detail of Sample 2-1	212
4.2.2.6	X-Ray Detail of Sample 2-2	213
4.2.2.7	X-Ray Detail of Sample 2-3	214
4.2.2.8	X-Ray Detail of Sample 2-4	215
4.2.2.9	X-Ray Detail of Sample 2-5	216
4.2.2.10	X-Ray Detail of Sample 2-6	217
4.2.2.11	X-Ray Detail of Sample 3-1	218
4.2.2.12	X-Ray Detail of Sample 3-2	219
4.2.2.13	X-Ray Detail of Sample 4-1	220
4.2.2.14	X-Ray Detail of Sample 4-2	221
4.2.2.15	X-Ray Detail of Sample 5-1	222
4.2.2.16	X-Ray Detail of Sample 5-2	223
4.2.2.17	X-Ray Detail of Sample Rm-1	224
4.2.2.18	X-Ray Detail of Sample Rm-2	225
4.2.2.19	X-Ray Detail of Sample Rm-3	226

Figure	Title	Page
4.2.2.20	X-Ray Detail of Sample Dar-1	227
4.2.2.21	X-Ray Detail of Sample Dar-2	228
4.2.2.22	X-Ray Detail of Sample FI-1	229
4.2.2.23	X-Ray Detail of Sample FI-2	230
4.2.2.24	X-Ray Detail of Sample FI-3	231
4.2.2.25	X-Ray Detail of Sample FII-1	232
4.2.2.26	X-Ray Detail of Sample FII -2	233
4.2.2.27	X-Ray Detail of Sample FII-3.....	234
4.3.1.1.1	Porosity images 1A to 2B from ImageJ	244
4.3.1.1.2	Porosity images 3A to 5B from ImageJ	246
4.3.1.1.3	Porosity images RmA to DarB from ImageJ	248
4.3.1.1.4	Porosity images FIA to FIIB from ImageJ	250
4.3.1.1.5	Percentage of Porosity in all samples	251
4.3.1.1.6	Average Percentage of Porosity in each core sample	251
4.3.1.2.1	Coarse Aggregate Images 1A to 2B from ImageJ	254
4.3.1.2.2	Coarse Aggregate Images 3A to 5B from ImageJ	256
4.3.1.2.3	Coarse Aggregate Images RmA to DarB from ImageJ	258
4.3.1.2.4	Coarse Aggregate Images FIA to FIIB from ImageJ	260
4.3.1.2.5	Percentage of Coarse Aggregate of all samples	261
4.3.1.2.6	Average Percentage of Coarse Aggregate of each core sample	261
4.3.2.1.1	Porosity images 1A to 2B from ImageJ	264
4.3.2.1.2	Porosity images 3A to 5B from ImageJ	266
4.3.2.1.3	Porosity images DarA to DarB from ImageJ	268
4.3.2.1.4	Porosity images FIA to FIIB from ImageJ	270

Figure	Title	Page
4.3.2.1.5	Percentage of Porosity of all samples	271
4.3.2.1.6	Average Percentage of Porosity of each core sample	271
4.3.2.1.7	Comparison % Porosity for 72 ppi and 2400 ppi	272
4.3.2.1.8	Comparison % Porosity for 72 ppi, 2400 ppi and 6400 ppi	272
4.3.2.2.1	Coarse Aggregate Images 1A to 2B from ImageJ	274
4.3.2.2.2	Percentage of Coarse Aggregate Samples 3A to 5B	276
4.3.2.2.3	Coarse Aggregate Images RmA to DarB from ImageJ	278
4.3.2.2.4	Coarse Aggregate Images FIA to FIIB from ImageJ	280
4.3.2.2.5	Percentage of auto calculations Coarse Aggregate of all samples	281
4.3.2.2.6	Average percentage of auto calculations Coarse Aggregate of each core sample	281
4.3.2.2.7	Comparison % Coarse Aggregate 72 ppi and 2400 ppi	282
4.3.3.1.1.	Porosity images 1A to 2B from ImageJ	284
4.3.3.1.2	Porosity images 3A to 5B from ImageJ	286
4.3.3.1.3	Porosity images RmA to DarB from ImageJ	288
4.3.3.1.4	Porosity images FIA to FIIB from ImageJ	290
4.3.3.1.5	Percentage of Porosity of all samples	291
4.3.3.1.6	Average Percentage of Porosity of each core sample	291
4.3.3.1.7	Comparison % Porosity 2400 ppi and 6400 ppi 64-bit ImageJ	292
4.3.3.1.8	Comparison % Porosity 2400 ppi and 6400 ppi 64-bit ImageJ	292
4.3.3.2.1	Coarse Aggregate Images 1A to 2B from ImageJ	294
4.3.3.2.2.	Coarse Aggregate Images 3A to 5B from ImageJ	296
4.3.3.2.3	Coarse Aggregate Images RmA to DarB from ImageJ	298

Figure	Title	Page
4.3.3.2.4	Coarse Aggregate Images FIA to FIIB from ImageJ	300
4.3.3.2.5	Percentage of Coarse Aggregate of all samples	301
4.3.3.2.6	Average Percentage of Coarse Aggregate of each core sample	301
4.3.3.2.7	Comparison Auto 2400 ppi and 100% Quantitative 4800 ppi .	302
4.3.3.3.1	Coarse Aggregate Images 1A to 2B from ImageJ	304
4.3.3.3.2	Coarse Aggregate Images 3A to 5B from ImageJ	306
4.3.3.3.3	Coarse Aggregate Images RmA to DarB from ImageJ	308
4.3.3.3.4	Coarse Aggregate Images FIA to FIIB from ImageJ	310
4.3.3.3.5	Percentage of Coarse Aggregate of all samples	311
4.3.3.3.6	Average Percentage of Coarse Aggregate of each core sample	311
4.3.3.3.7	Comparison coarse aggregate 100% auto and 100% quantitative methods	312
4.3.3.3.8	Comparison Average coarse aggregate Auto and 100% Quantitative	313
4.3.3.3.9	Percentage error auto calibrated from 100% quantitative method	314
4.3.3.3.10	Coarse aggregate average comparison between quantitative method and auto calibrated values in Samples 1 to 5 and Rm .	314
4.3.3.3.11	Comparison of Samples from the damaged Warehouse floor .	316
4.3.3.3.12	Comparison coarse aggregate between auto calibrated and quantitative	317
4.3.3.3.13	Variance between auto calibrated and quantitative values	317
4.3.3.4.1	Original image in 6400 ppi of the selected section	319
4.3.3.4.2	72 ppi resolution micro porosity calculated	319
4.3.3.4.3	Original image in 6400 ppi of the selected section	320

Figure	Title	Page
4.3.3.4.4	200 ppi resolution micro porosity calculated	320
4.3.3.4.5	Original image in 6400 ppi of the selected section	321
4.3.3.4.6	1200 ppi resolution micro porosity calculated	321
4.3.3.4.7	Original image in 6400 ppi of the selected section	322
4.3.3.4.8	2400 ppi resolution micro porosity calculated	322
4.3.3.4.9	Original image in 6400 ppi of the selected section	323
4.3.3.4.10	4800 ppi resolution micro porosity calculated	323
4.3.3.4.11	Original image in 6400 ppi of the selected section	324
4.3.3.4.12	6400 ppi resolution micro porosity calculated	324
4.3.3.4.13	6400 ppi resolution micro porosity in B&W	325
4.3.3.4.14	Quantitative calibration for % porosity from 72 ppi to 6400 ppi	326
4.4.1	Core Sample 1 section 1	329
4.4.2	Core Sample 1 section 2	329
4.4.3	Core Sample 2 section 1	330
4.4.4	Core Sample 2 section 2	330
4.4.5	Core Sample 3 section 1	331
4.4.6	Core Sample 3 section 2	331
4.4.7	Core Sample 4 section 1	332
4.4.8	Core Sample 4 section 2	332
4.4.9	Core Sample 5 section 1	333
4.4.10	Core Sample 5 section 2	333
4.4.11	Core Sample Rm section 1	334
4.4.12	Core Sample Rm section 2	334

Figure	Title	Page
4.4.13	Core Sample Dar section 1	335
4.4.14	Core Sample Dar section 2	335
4.4.15	Core Sample FI section 1	336
4.4.16	Core Sample FI section 2	336
4.4.17	Core Sample FII section 1	337
4.4.18	Core Sample FII section 2	337
4.5.1	Vickers Micro Hardness Comparison of all Samples	339
4.5.2	Average Vickers Micro Hardness of all samples	340
4.5.3	Relationship of Vickers Micro Hardness to Apparent Porosity	340
4.5.1.1	Example of an area in the matrix and Vickers micro hardness indent	341

List of Tables

Table	Title	Page
2.1	Properties of standard concrete grades	20
2.2	Range of basic shrinkage strains for major cities in Australia	21
3.2.1	Operating Parameters of Skyscan X-Ray Microtomograph	82
3.3.1	72 ppi data 24-bit colour	85
3.3.2	2400 ppi data 24-bit colour	85
3.3.3	4800 ppi data 24-bit colour	86
3.3.4	6400 ppi data 8-bit greyscale	86
3.3.5	6400 ppi data 24-bit colour	86
3.3.6	6400 ppi data 48-bit colour	86
3.3.1.1	72 ppi data 24-bit colour	96
3.3.2.1	2400ppi data 24-bit colour	116
3.3.3.1	6400 ppi data 48-bit colour	128
3.3.3.2	6400 ppi data 8-bit greyscale	128
3.3.3.3	4800 ppi and 6400 ppi data 24-bit colour	128
4.1.1	Bulk Density and Apparent Porosity	189
4.3.1.1.1	Percentage of Porosity Samples 1A to 2B	243
4.3.1.1.2	Percentage of Porosity Samples 3A to 5B	245
4.3.1.1.3	Percentage of Porosity Samples RmA to DarB	247
4.3.1.1.4	Percentage of Porosity Samples FIA to FIIB	249
4.3.1.2.1	Percentage of Coarse Aggregate Samples 1A to 2B	253
4.3.1.2.2	Percentage of Coarse Aggregate Samples 3A to 5B	255
4.3.1.2.3	Percentage of Coarse Aggregate Samples RmA to DarB	257
4.3.1.2.4	Percentage of Coarse Aggregate Samples FIA to FIIB	259

Table	Title	Page
4.3.2.1.1	Percentage of Porosity Samples 1A to 2B	263
4.3.2.1.2	Percentage of Porosity Samples 3A to 5B	265
4.3.2.1.3	Percentage of Porosity Samples RmA to DarB	267
4.3.2.1.4	Percentage of Porosity Samples FIA to FIIB	269
4.3.2.2.1	Percentage of Coarse Aggregate Samples 1A to 2B	273
4.3.2.2.2	Percentage of Coarse Aggregate Samples 3A to 5B	275
4.3.2.2.3	Percentage of Coarse Aggregate Samples RmA to DarB	277
4.3.2.2.4	Percentage of Coarse Aggregate Samples FIA to FIIB	279
4.3.3.1.1	Percentage of Porosity Samples 1A to 2B	283
4.3.3.1.2	Percentage of Porosity Samples 3A to 5B	285
4.3.3.1.3	Percentage of Porosity Samples RmA to DarB	287
4.3.3.1.4	Percentage of Porosity Samples FIA to FIIB	289
4.3.3.2.1	Percentage of Coarse Aggregate Samples 1A to 2B	293
4.3.3.2.2	Percentage of Coarse Aggregate Samples 3A to 5B	295
4.3.3.2.3	Percentage of Coarse Aggregate Samples RmA to DarB	297
4.3.3.2.4	Percentage of Coarse Aggregate Samples FIA to FIIB	299
4.3.3.3.1	Percentage of Coarse Aggregate Samples 1A to 2B	303
4.3.3.3.2	Percentage of Coarse Aggregate Samples 3A to 5B	305
4.3.3.3.3	Percentage of Coarse Aggregate Samples RmA to DarB	307
4.3.3.3.4	Percentage of Coarse Aggregate Samples FIA to FIIB	309
4.3.3.3.5	Difference between 100% Auto and 100% Quantitative calculations	312
4.3.3.3.6	Auto calibrated average values in Samples 1 to 5 and Rm	313
4.3.3.3.7	Samples 1A to 5B auto calibrated	315

Table	Title	Page
4.3.3.4.1	Percentage of micro porosity from Sample 5B in various resolutions	318
4.3.3.4.2	Data for the small section image 10 x 10 mm	326
4.5.1	Vickers Micro Hardness table	339

THESIS OUTLINE

What my thesis is about

The project started 18 months ago as an investigation of 7 unknown concrete cores (later extended to 9 cores).

The request presented with 7 unknown concrete cores created the purpose of this study:

Find the differences in composition and microstructure to establish the cause of the damage on the new concrete floor.

Professor Sorrell suggested that the following specific tests would find the answer:

- Image analysis of the pores and coarse aggregate;
- High resolution X-Ray general imaging of the microstructure;
- High resolution X-Ray specific imaging for micro-cracking;
- Optical microscopy;
- Micro-hardness.

The decision then came to study relationship between microstructure, micro-cracking and durability in service.

The study of full cross section of a concrete core by computer digital analysis enabled a lot of these questions to be answered.

Hundreds of individual digital and X-Ray images unlocked a lot of mysteries.

Durability of concrete

- Durability is the ability to last a long time without significant deterioration;
- Concrete is characterised by the type of aggregate or cement used, by the specific qualities it manifests, or by the methods used to produce it;
- In ordinary structural concrete, the character of the concrete is largely determined by a water-cement ratio. The lower the water content, all else being equal, the stronger is the concrete;
- Another durability factor is the amount of cement in relation to the aggregate (expressed as a three part ratio – cement to fine aggregate to coarse aggregate);
- Durability of concrete is based on its ability to resist weathering action, chemical attack, and abrasion while maintaining its desired engineering properties.

Concrete durability is related to:

- The design process;
- Specification of materials;
- Workmanship;
- Environmental effects;
- Accidents;
- Repairs.

Why does concrete crack?

- Concrete, like most materials, will shrink slightly when it dries out;
- Common shrinkage is about 0.5mm per meter of concrete;
- The reason contractors place joints in concrete pavements and floors is to allow the concrete to crack in a neat, straight line at the joint, where concrete cracks due to shrinkage are expected to occur.

The Microstructure of Concrete

- Concrete is a continuously changing system – starting from its mixing to its placement;
- Even after hardening, concrete gains strength for long periods and interacts with the environment to which it is exposed;
- Strength, durability, and dimensional stability have long been recognised as the three fundamental parameters for a good concrete;
- The microstructure of concrete is the detailed anatomy of it;
- Strength and durability are two sides of the same coin – the concrete microstructure;
- Until recent years, the overwhelming focus has been on concrete's compressive strength, which has been mainly related to the overall porosity of the cement paste matrix and the amount and structure of the aggregates;
- Mechanical strength depends on defects and not on any overall average property, and so is very difficult to relate to microstructure;
- This has caused relatively little attention to be paid to the details of the pore space, micro cracking and laminations around the aggregate.

Traditionally a study of the reasons behind damage to concrete would have been undertaken in a totally different manner. This study was specifically undertaken to solve other questions.

- Can hardened concrete microstructures be forensically compared by only digital analysis techniques?
- If so, can fully automated digital analysis method be developed to quantitatively calculate percentage porosity and percentage coarse aggregate?

1 INTRODUCTION

Forensic investigations of hardened concrete can take many paths, and analyses are usually very specific to the causes of damage.

This thesis came about as the result of many forensic micro-structural examinations of concrete cores taken from a new commercial/industrial warehouse concrete slab flooring, and no further details were supplied with the concrete cores, making this an unbiased examination.

The detailed study of full cross sectioned concrete cores aimed to achieve the development of automated highly accurate quantitative digital analysis techniques utilising new 64-bit software development.

This became possible only recently by the release of the newest Java 64-bit ImageJ Digital Analysis Package, and latest 64-bit Windows 7 Operating System, and 64-bit Office 2010.

Micro-structural detail was only limited by the optical resolution of the original digital image.

It must be emphasised however, that scanned micro-structural images 100mm x100mm in 6400ppi true optical resolution 48-bit deep colour (digital image file around 4GB) have to date, not been able to be opened in 64-bit ImageJ.

This is despite having dedicated 10 GB of high speed DDR3 RAM allocated to the software package, and the fastest Intel i7 microprocessor. These images take 6 minutes

to open in proprietary 64-bit image processing software. It should become easier when I can afford to upgrade the DD3 RAM to at least 48GB or more.

Most of the time, my purpose built \$7500 computer froze, trying to open these extremely large digital graphic files, however, 100% guaranteed quantitative digital analysis required these hurdles to be overcome, and it was achieved by reducing the colour depth, and converting the digital image files to greyscale, thus still retaining the true optical pixel resolution (4 microns) for high resolution digital image analysis.

Specific, high optical resolution macro and micro-structural digital analysis techniques, developed over the last year, will be used for the first time, to study large sectioned complex fired ceramics, within my approved PhD study, which has begun.

The literature review is intended to give the reader a very brief overview of concrete properties and digital test procedures to understand and correlate micro-structural material properties to durability.

It will also discuss the latest high resolution digital analysis methods and techniques, but unfortunately most of these are proprietary in confidence developed within private concrete micro-structural analysis laboratories.

No comparable 64-bit micro-structural digital study of hardened concrete could be found in the literature as the ability to analyse large data files is only just becoming available to materials science students who now operate computers running 64-bit Windows 7, 64-bit Office 2010, and can analyse large digital image files in 64-bit ImageJ.

The anticipated release of 128-bit Windows 8, hopefully by 2013, will really speed up the quantitative analyses of complex ceramic micro-structures.

The properties and performance of cement based materials are directly related to their microstructure, and the analysis of this can be very complex. For example, processes occurring at the nanometre sized gel pores will ultimately govern the structural performance of the concrete at the millimetre to metre level.

Researchers throughout the world have developed countless models, consisting of individual digital image based structural models for the calcium silicate hydrate gel at the nanometre level, the hydrated cement paste at the micrometre level, and the multi-phase concrete at the millimetre to metre level. Garboczi et al (1990) demonstrated this methodology for the property of ionic diffusivity in saturated concrete, and the ideas of percolation theory were shown to unify microstructure to larger scale physical phenomenon.

Computations performed at one level provide input properties to be used in simulations of performance at the next higher level. Each level of micro-structural analysis has provided quantitative data for product improvement, with the publishing of thousands of technical reports, PhD and Masters' theses, and industrial proprietary knowledge.

Concrete being the largest building product used worldwide, has generated the largest amount of research, and hopefully the greatest amount of understanding, of any ceramic building product.

The vast complexity of ceramic reactions, that currently are known to occur within concrete microstructure, are still however, yet to be well understood.

Exacting standards are applied to mix, batching, and laying design, so that performance and durability of concrete can be accurately specified, and realised in practice. If concrete design parameters are exceeded in practice however, damage may occur.

When the cause of damage is unknown, and only some parts of a concrete structure are affected, fast and highly accurate quantitative forensic investigations of microstructure become necessary.

This thesis forensically compares microstructures between concrete core samples by very high resolution digital analysis, to find liability, avoid court action, to recover costs, compensation and rectification, rather than quantifying all the underlying microstructures.

Durability of concrete can be one of the most difficult parameters to specify, when cost benefit analyses suggest a certain grade as being adequate for service life, but may fail due to unforeseen circumstances.

I can remember my grandfather's concrete path that he laid across the dirt driveway. It was full of blue metal, and the cement matrix was so strong, he could drive a fully loaded truck over it. We thought as children, "it was as strong as blue metal", and it never ever cracked. This was a high strength concrete mix design.

Commercial slab floors these days use adequate, but lower strength mixes, batched with softer river gravels, use less cement in the paste, purely for economic affordability. They are adequate for ordinary service, but not extraordinary service, as this study will demonstrate.

My thesis presents a forensic comparative micro-structural digital analysis between concrete core samples of unknown composition or compressive strength.

The quantitative results presented are not directly related to the concrete chemistry, as this was totally unknown, rather the individual concrete core samples micro-structural differences were revealed.

The 64-bit automated quantitative digital image analysis techniques developed during this very specific forensic study of damaged, and quite different concrete micro-structures, can be applied to the analysis of any complex material micro-structure.

The quantitative digital analysis principles revealed from high resolution digital photo scanner technology and 64-bit image acquisition software, together with 64-bit ImageJ analysis are universally applicable to all larger scale micro-structural analyses.

2 LITERATURE REVIEW

Performance of cement pastes and concretes is controlled by their microstructure; in particular the pore network plays a critical role in determining mechanical properties and interactions with the environment, which determine durability.

The determination of durability in service is the focus of considerable research effort, and is the subject of this forensic examination.

To predict the performance of concrete over the lifetime of a building, which is a minimum of several decades and increasingly over a century for the most important structures, is the major challenge.

Connectivity of the capillary pore structure is the most important. The porosity of cement extends over a broad range of measurement; classically this is divided into gel-pores which are inherent to the Calcium-Silicate-Hydrate (C-S-H) product. This porosity lies in the range of a few nanometres and due to this small size plays only a minor role in transport processes affecting durability and other aspects of performance. Capillary pores corresponding to the originally water filled spaces not filled by hydration products, varying in size from a few nanometres to tens of micrometers.

Air voids range from tens of micro-millimetres (μm) to millimetres (mm) in size and are a part of the original mix. They are a small fraction of the whole porosity and as they are isolated have a minor role on overall transport processes. The voids in hollow shells or the gaps between un-reacted grains and C-S-H shells that are observed in cement pastes may also be considered as porosity although it is not clear to what extent these voids are connected to the capillary pore network. Hence capillary porosity of cement pastes is the main factor affecting the performance of most cementitious materials.

In this study the percentage air-voids ranging in size from 10 microns to millimetres in diameter may be one of the major contributing factors to the reduction in durability and resultant damage to the new commercial concrete slab floor.

Composition of Concrete

Concrete is a mixture of two main components: aggregate and paste. The paste binds the aggregates (usually sand and gravel or crushed stone) into a rocklike mass as the paste hardens through the chemical reaction of the cement and water.

The paste is composed of water and entrapped air or purposely entrained air, and sometimes chemical admixtures. The paste constitutes about 25 to 40% of the total volume of concrete.

Aggregates are generally designed as either fine (ranging in size from 0.025 to 4.5 mm), coarse (from 4.5 to 38 mm) or larger. All aggregate materials must be clean and free from admixture with soft particles or vegetable matter, because even small quantities of organic soil compounds result in chemical reactions that seriously affect the strength of the concrete.

Cement

Cement is a finely ground hydraulic binder for concrete which consists mainly of compounds of calcium oxide with silica, alumina, and iron oxide which has been produced by sintering or melting. When cement is mixed with water it hardens both in air and under water. Its volume must remain constant and must reach a compressive strength after 28 days of at least 25 Mega Pascals (MPa).

When water is mixed with Portland cement, the chemical reaction brings about a change in the structure of the slurry by which the fluid mass becomes rigid and hard. The term setting and hardening denote such reactions. The setting process includes the selective hydration of the cement components, the formation of crystalline hydration products, the development of films around the cement grains, and joint coagulation of components. Setting forms a solid product of low compressive strength. Hardening leads to a strong material. There is a continuous transformation from setting to hardening.

Various processes take place simultaneously during hydration. The essential processes are:

1. Chemical reactions (particularly hydration and hydrolysis reactions);
2. Solution processes and crystallisation (compounds containing chemically bound water are produced from supersaturated solutions and involves reversible and irreversible processes);
3. Grain boundary processes (agglomeration by surface tension forces).

The hydration reactions are exothermic. According to adiabatic tests, the production of heat by hardening, cement reaches a maximum after 1 to 3 days. The added water causing hydration is bound chemically as hydroxide, is also absorbed on the large surfaces of the hydrate phases, and is also found in the capillaries of the solid body. The result of the hydration reaction is a hard product of great strength.

The principal sources of heat of hydration of cement are the heats of solution of some of the anhydrous components and the heat of precipitation of several hydrates from solution. Portland cements continue to evolve heat during hardening for a period of days and months.

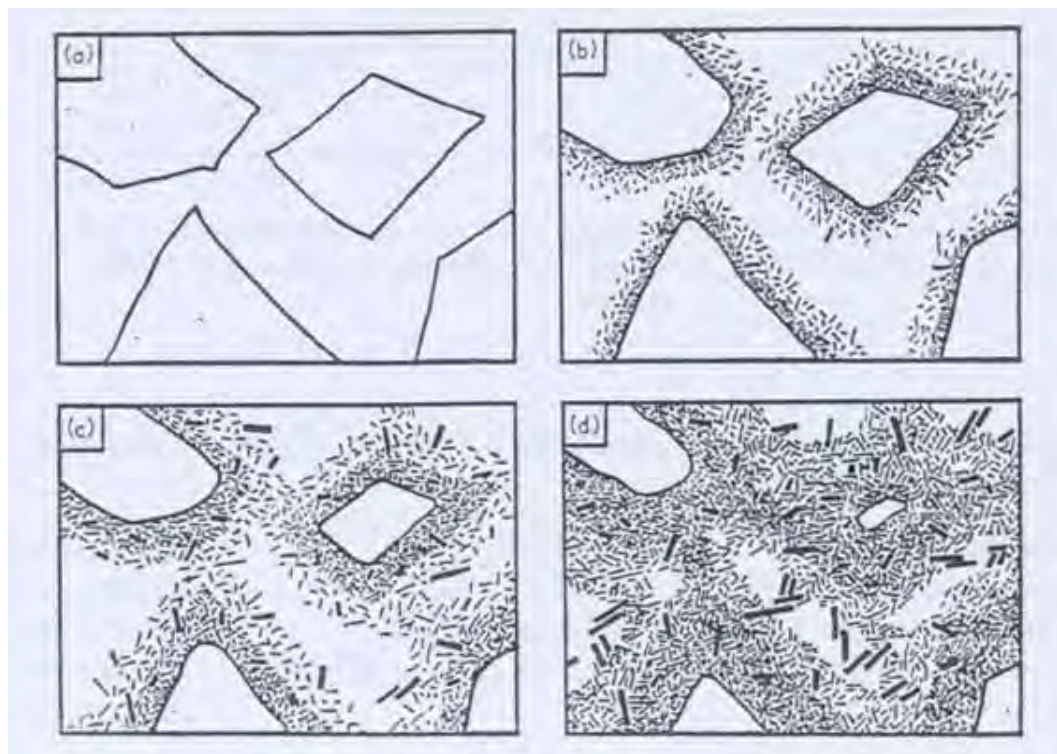


Figure 2.1 Four stages in the setting and hardening of Portland cement:

- a) Dispersion of un-reacted clinker, grains in water;
 - b) After a few minutes hydration products eat into, and grow out from the surface of each grain;
 - c) After a few hours the coatings of different clinker grains have begun to join up, the gel thus becoming continuous (setting);
 - d) After a few days further development of the gel has occurred (hardening).
- (Courtesy of Professor Sorrell)

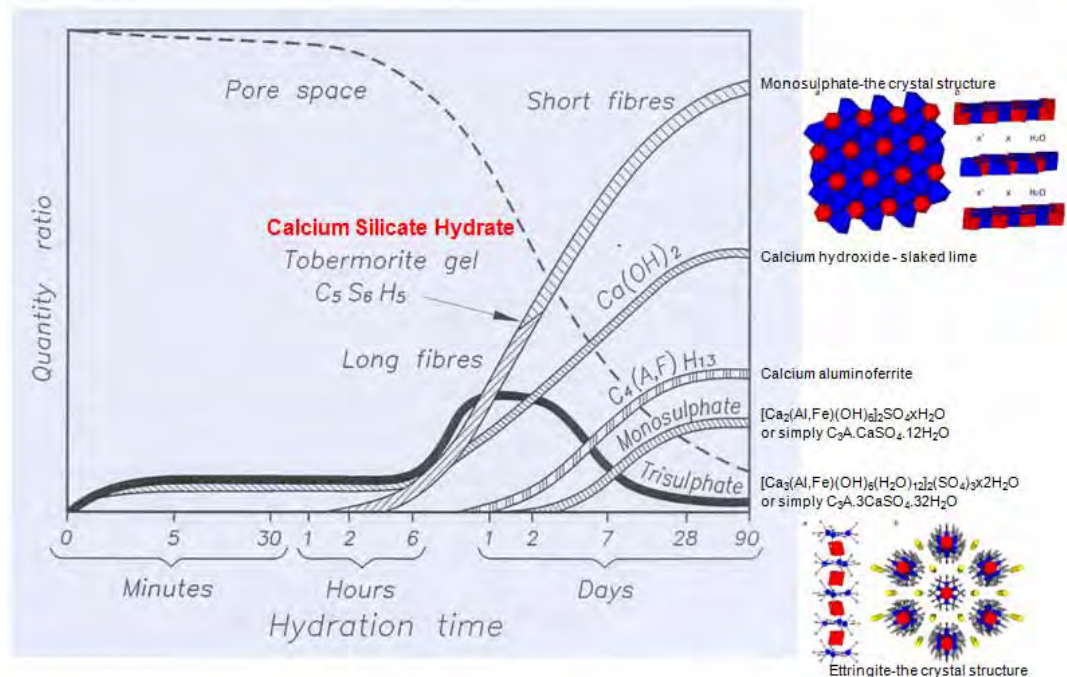


Figure 2.2 Hydration stages (Courtesy of Professor Sorrell)

In Figure 2.2 **Calcium Silicate Hydrate** is the main product of the hydration of Portland cement and is primarily responsible for the strength in cement based materials.

The crystal structure of C-S-H in cement paste has not been fully resolved yet and there is still ongoing debate over its nanostructure.

The SEM micrographs of C-S-H do not show any specific crystalline form. They usually manifest as flakes.

Classification of the tobermorites				
Primary subdivisions	Type of X-ray powder pattern	Secondary subdivisions	Composition	Appearance in electron microscope
Crystalline tobermorites	Full pattern showing many hkl reflections; often 40-50 lines given adequate experimental technique	14 Å Tobermorite 11-3 Å Tobermorite 9-3 Å Tobermorite 12-6 Å Tobermorite 10 Å Tobermorite	$C_2S_6H_8$ $C_3S_6H_8$ $C_4S_6H_{8-2}$ (I) (I)	Flat plates or laths, usually subhedral; rarely fibres
Semi-crystalline tobermorites	Patterns of about 6-12 lines, including mainly hk or $hk0$ reflections and usually a basal reflection at 9-14 Å	C-S-H(I) C-S-H(II)	$Ca/Si < 1.5$ $Ca/Si \geq 1.5$	Crumpled foils Usually fibres
Near-amorphous tobermorites	Weak patterns of 1-3 hk lines or bands (3.05, 2.8, and 1.8 Å approx.)	Tobermorite gel (predominant constituent(s)), etc.	Ca/Si probably usually ≥ 1.5	Irregular platelets or foils, fibres (I)

The initials C-S-H denote "calcium silicate hydrate"; hyphens are used to show that the composition $CaO \cdot SiO_2 \cdot H_2O$ is not necessarily indicated.

Figure 2.3 Classification of tobermorites (Courtesy of Professor Sorrell)

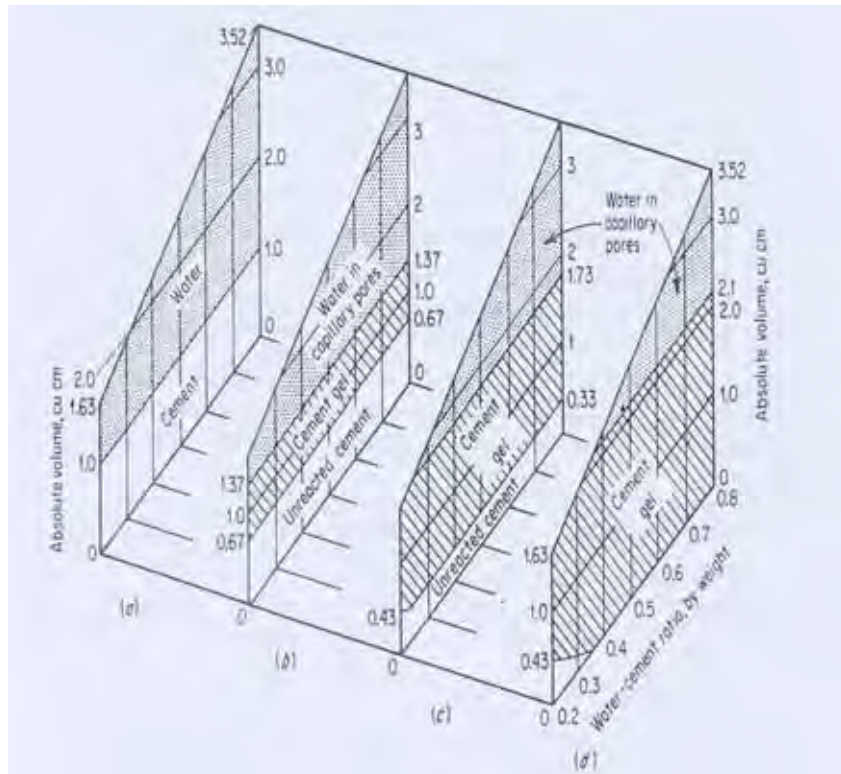


Figure 2.4 Space relationships for paste components at various stages of hydration (Courtesy of Professor Sorrell)

Figure 2.4 shows space relationships for paste components at various stages of hydration:

- a) Fresh paste
- b) Reaction 1/3 complete
- c) Reaction 2/3 complete
- d) Reaction completed

Assumptions: specific gravity of cement = 3.15

When completely hydrated 1 cm³ of cement produces 2.1 cm³ of cement gel.

Note: Specific gravity is defined as the ratio of the density of a given solid or liquid substance to the density of water at a specific temperature and pressure, typically at 4°C (39°F) and 1 atm. Synonymous with **Relative Density** which is a more modern term.

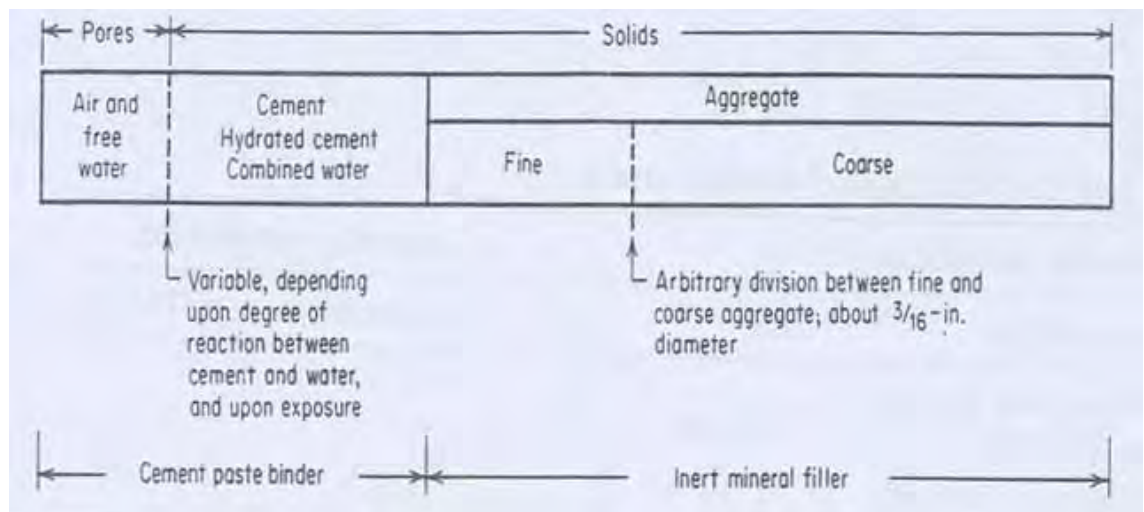


Figure 2.5 Composition of concrete (Courtesy of Professor Sorrell)

Durability of Concrete

Durability is the ability to last a long time without significant deterioration.

Concrete is characterised by the type of aggregate or cement used, by the specific qualities it manifests, or by the methods used to produce it. In ordinary structural concrete, the character of the concrete is largely determined by a water-cement ratio. The lower the water content, all else being equal, the stronger is the concrete.

The mixture must have just enough water to ensure that each aggregate particle is completely surrounded by the cement paste, that the spaces between the aggregate are filled, and that the concrete is liquid enough to be poured and spread effectively.

Another durability factor is the amount of cement in relation to the aggregate (expressed as a three part ratio – cement to fine aggregate to coarse aggregate). Where especially strong concrete is needed, there will be relatively less aggregate.

The strength of concrete is measured in MPa of force needed to crush a sample of a given age or hardness. Strength is affected by environmental factors, especially temperature and moisture. If it is allowed to dry prematurely, it can experience unequal tensile stresses that in an imperfectly hardened state cannot be resisted.

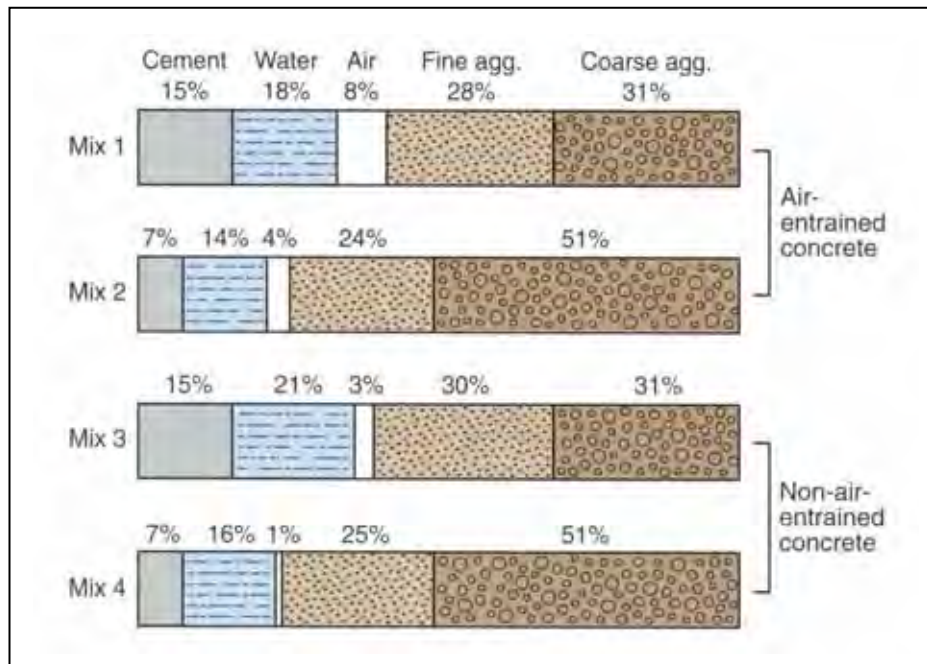


Figure 2.6. Range in proportions of materials used in concrete (by absolute volume); Mixes 1 and 3 represent rich mixes with small-size aggregates; Mixes 2 and 4 represent lean mixes with large-size aggregates (Kosmatka, S.H., Kerkhoff, Beatrix, Panarese, W.C., Design and Control of Concrete Mixtures, 14th edition, USA, 2002-6)

Because aggregates make up about 60 to 75% of the total volume of concrete, their selection is very important. Aggregates must consist of particles with adequate strength and resistance to environmental conditions and should not contain materials that will cause deterioration of the concrete. A continuous gradation of aggregate particle sizes is desirable for efficient use of the paste. The quality of any concrete depends on the quality of the paste and aggregate and the bond between the two. In properly made concrete, each particle of aggregate is coated completely with paste, and all of the spaces between aggregate particles are filled completely with paste.

Durability of concrete is based on its ability to resist weathering action, chemical attack, and abrasion while maintaining its desired engineering properties. The ingredients, proportioning of those ingredients, interactions between the ingredients, placing and curing practices, and the severity of the environment determine the durability and useful life of the concrete.

In the process known as curing, the concrete is kept damp for some time after pouring to slow the shrinkage that occurs as it hardens.

Low temperatures also adversely affect its strength. To compensate for this, an additive such as calcium chloride is mixed in with the cement. This accelerates the setting process, which in turn generates heat sufficient to counteract moderately low temperatures.

Concrete durability is one of the most important considerations in the design of new structures and when assessing the condition of existing structures. Concrete construction is becoming increasingly complex and the importance of producing structures that are both cost effective and durable has never been higher.

An understanding of concrete durability is fundamental to establishing the service life of new or existing structures.

Whether the concrete is within a severe environment such as highway bridges or marine structures or whether it contains uncommon materials such as high alumina cement or re-cycled aggregates, knowledge of the concrete durability potential is a key to the long term performance.

Although all concrete is likely to deteriorate to some extent, ensuring good durability is about minimising the rate of deterioration.

Concrete durability is therefore related to: the design process, specification of materials, workmanship, environmental effects, accidents, and repairs.

Specialist advice at the design stage can prevent many problems occurring during construction.

New specifications can be prepared or existing ones reviewed, to optimise both durability and constructability.

Concrete durability assessments for new structures require interpretation of standards and codes of practice, advice on performance testing for concrete and its constituent materials, production of materials and concrete specifications, advice on all aspects of concrete performance, based on the most recent developments in technology, and construction support.

Consultants offer a range of services to contractors to assist them in achieving their objectives. Whilst based on the latest technology, their approach is focussed on the practical application of technology during construction.

Advice on achieving performance requirements, materials selection, concrete mix design development, advice on appropriate construction techniques, site monitoring, and investigation can help avoid costly litigation.

Should problems occur either during construction or at some subsequent time, forensic investigation can help. Extensive experience in diagnosing and solving concrete related problems are required including; pour fresh concrete characteristics, testing fresh concrete, low strength concrete/failure to meet performance specifications, hardened concrete, load testing, concrete deterioration and damage, concrete durability carbonation and chloride induced corrosion, sulphate attack, alkali aggregate reactivity, high alumina cement concrete, fire and explosion, and failure in service.

The Specifier's Guide to Durable Concrete Item Code: EB221, 2005, is an instruction guide and basic reference for those responsible for writing and implementing concrete specifications. This reference covers the basic concepts of concrete technology as it relates to durability, and is intended to be a companion and supplement to Design and Control of Concrete Mixtures. It provides sufficient information to allow the practitioner to select materials and mix design parameters to achieve durable concrete in a variety of environments. It also warns the user when expert help is recommended.

This study attempts to quantify some of the variables that determine concrete durability, the micro-structure of the hardened concrete by auto quantitative digital analytical methods.

Hooton et al, 2006, states in this full text, that better durability test methods are needed for performance specifications, and although prescriptive specifications for concrete served us reasonably well in the past, when the industry as a whole was much less sophisticated than it is now. They tend, however, to inhibit the most efficient use of the materials currently available for use in concrete, and meeting such specifications is far from a guarantee of concrete durability. The current efforts in moving from prescriptive to performance-based specifications could enable concrete producers to be more imaginative and innovative in their use of materials such as supplementary cementitious materials, admixtures, blended cements, polymers, fibres, and mineral fillers.

Properly devised performance-based specifications would also provide a means for introducing durability concerns more explicitly into the proportioning and testing of concrete mixtures. The ability of the concrete to perform satisfactorily with minimal maintenance over the anticipated service life of the structure should be a major goal of any performance based specification. We cannot accurately predict the life of the concrete in a structure with results from current test methods. Instead, we rely almost entirely on meeting prescriptive requirements such as maximum water cementitious material ratios (w/cm), minimum cement contents, specific cement types, and limitations on the types and amounts of chemical and mineral admixtures in the hope of producing durable concrete.

While compressive strength is a good indicator of load resistance, it is not a major indicator of concrete durability. The lack of adequate performance-related durability test methods is one of the main factors inhibiting the move from prescriptive to performance based specifications. There is therefore a need for quick, reliable tests for concrete durability that would have to go far beyond reliance on such standard performance measures as 28-day compressive strength.

Most deterioration processes have two stages. Initially, aggressive fluids (water, solutions, or gases) penetrate or are transported through the capillary pore structure of the concrete to reaction sites. Examples include chlorides that penetrate to the level of the reinforcement or sulphates that are transported into areas of the concrete matrix containing aluminates. This penetration is followed by the actual chemical or physical deterioration reactions. To assess the concrete's ability to perform well during the first stage, we need tests that measure transport rates, resistance to penetration of aggressive fluids, or both. A related rapid-index test would be a highly desirable development fundamental to the implementation of performance-based durability specifications.

Many codes and specifications contain durability requirements based on currently available test methods. Unfortunately, test methods do not exist for all of the relevant durability or performance concerns, and existing test methods are not always rapid, accurate, and repeatable. Some do not have a good scientific basis, and some do not adequately represent any or all of the exposure conditions.

Microstructure of Concrete

Concrete is a continuously changing system, starting from its mixing to its placement. Even after hardening, concrete gains strength for long periods and interacts with the environment to which it is exposed. Strength, durability, and dimensional stability have long been recognised as the three fundamental parameters for a good concrete.

Less attention, however, is paid to the microstructure of concrete, which is the detailed anatomy of concrete not only controlling these three parameters but also the overall behaviour and performance of concrete. There have been incidences where concrete showed satisfactory project specified strength and workability during the construction, but failed to provide similar satisfaction in performance or long-term durability. The question remains: Strength or Durability – Which is more important?

Actually, strength and durability are two sides of the same coin; the concrete microstructure. The microstructure of concrete is its entire world seen by using a variety of microscopes, which is indistinct to the unaided human eye. It is the microscopically magnified portion(s) within a macrostructure, which reveals the essential details and locates the source and extent of the problem, if any.

Until recent years, the overwhelming focus has been on concrete's compressive strength, which has been mainly related to the overall porosity of the cement paste matrix and the amount and structure of the aggregates. Mechanical strength depends on defects and not on any overall average property, and so is very difficult to relate to microstructure. This has caused relatively little attention to be paid to the details of the pore space.

Unfortunately, it has perhaps led to the idea that concrete is simply a commodity material, with nothing needed to be understood about the microstructure. However, more recently, it has been recognised that much of the concrete in the infrastructure in Australia, USA and Europe and elsewhere has been deteriorating faster than expected, with much of this deterioration due to the corrosion of reinforcing steel coming from the ingress of chloride and other ions from road salts, marine environments, and ground soils. Hence close attention is now being paid to the transport properties of concrete (diffusivity, permeability, etc.) which, although still difficult to relate to the pore structure and microstructure, are easier to study in a fundamental way than is compressive strength (Young, J. F. A Review of the Pore Structure of Cement Paste and Concrete and Its Influence on Permeability, in *Permeability of Concrete*, ed. by D. Whiting, D. and Walitt, A. ACI SP-108 American Concrete Institute, Detroit, 1988).

This has led to new attention being paid to the microstructure of concrete; with the realisation that concrete is a complex composite, whose improvement and control require the usual materials science approach of processing, microstructure, and properties.

Compressive Strength

AS 3600 specifies standard strength grades of 20, 25, 32, 40, 50 and 65 MPa. In this series, the strength of each grade is 25% greater than that of the preceding grade. In practice, the choice of strength grade will frequently be determined by durability and serviceability considerations rather than the structural requirements for the member (load-carrying capacity).

Tensile Strength

The tensile strength of concrete is determined by two different methods:

- a) The **flexural tensile strength** is obtained by testing plain concrete beam specimens and calculating the extreme fibre stress at failure. Alternatively, a conservative or lower bound strength may be taken as $0.6\sqrt{f_c}$. Flexural strength is used in designing plain concrete members such as pavements or in calculations to control flexural cracking.
- b) The **principal tensile strength** is obtained directly by the split-cylinder test method. Alternatively, a conservative value of the characteristic principal tensile strength is used in calculations limiting cracking of concrete such as web shear cracking in prestressed beams.

Modulus of Elasticity

E_c , the modulus of elasticity of concrete, is taken as the secant modulus of the non-linear stress-strain relationship as shown in Figure 2.7 and is used in the calculation of deformations.

Properties of standard concrete grades are given in Table 2.1.

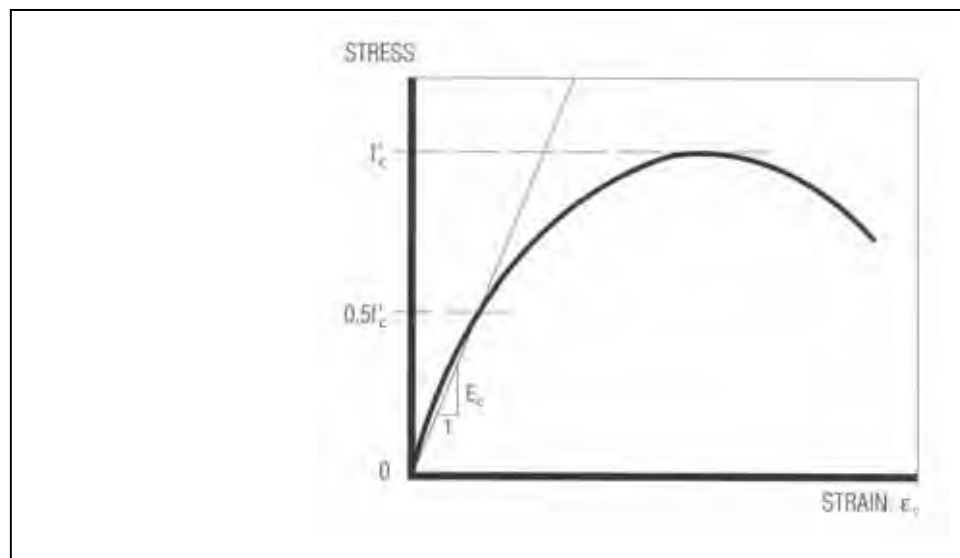


Figure 2.7 Modulus of elasticity of concrete (Handbook of Reinforced Concrete, 2002)

Grade or Characteristic compressive strength, f'_c (MPa)	Flexural tensile strength, $0.6\sqrt{f'_c}$ (MPa)	Principal tensile strength, $0.4\sqrt{f'_c}$ (MPa)	Typical mean compressive strength, $f_{cm,28}$ (MPa)	Modulus of elasticity, $E_{c=28}$ (MPa)
20	2.7	1.8	24.0	25 000
25	3.0	2.0	29.5	27 500
32	3.4	2.3	37.5	31 000
40	3.8	2.5	46.0	34 500
50	4.2	2.8	56.5	38 000
65	4.8	3.2	73.0	42 500

Table 2.1 Properties of standard concrete grades (Handbook of Reinforced Concrete, 2002)

Density

AS 3600 is restricted to concrete with saturated surface-dry density in the range of 1800 to 2800 kg/m³. The density of plain concrete depends on the density of the coarse aggregate and the water-cement ratio. For reinforced concrete, an allowance should be made also for the reinforcement. For most structures a conservative value of 2500 kg/m³ for the unit weight of reinforced or prestressed concrete is satisfactory.

Shrinkage

Shrinkage is the decrease in the volume of hardened concrete caused mainly by the loss of moisture from it as a result of drying, and also by chemical changes in the cement hydration products. It is independent of the load applied to the concrete and depends mainly on the relative humidity and temperature of the environment, the size of the member and the constituent materials of the concrete.

The basic shrinkage strain is measured by taking standard test specimens wet-cured for 28 days and then stored in air at 23°C and a relative humidity of 50% for 56 days. Tests have shown that the aggregate type has a significant influence on the shrinkage of concrete. The range of shrinkage values for normal concrete in major cities of Australia is shown in Table 2.2.

Source of aggregate	Range of basic shrinkage strains (mm/mm x 10 ⁻⁶)
Brisbane	500 to 900
Sydney	500 to 900
Melbourne	600 to 1000
Adelaide	700 to 1100
Perth	600 to 1200

Table 2.2 Range of basic shrinkage strains for major cities in Australia (after AS 1379) (Handbook of Reinforced Concrete, 2002)

Creep of Concrete

Creep of concrete is defined as the time-dependent increase in strain under sustained loading. The basic creep factor is expressed as the ratio of the ultimate creep strain to the elastic strain of a standard specimen initially loaded at 28 days and maintained under a constant stress of $0.4 f_c^l$ (Figure 2.7). For the practical calculation of the creep of a member, the basic creep factor is modified for the effects of member size, exposure environment and the maturity of the concrete at the time of loading.

In absence of specific data for local concrete, the average values for the basic creep and modification factors given in the tables and graphs in the Standard may be used. The suggested order of accuracy of creep calculations based on this average data is $\pm 30\%$.

The creep under constant stress as determined above is known as pure creep. Practical examples of pure creep include creep due to prestressed and sustained or dead load on uncracked concrete. Where stresses are induced by movements such as settlement or shrinkage, the initial stress caused by the induced strain is reduced by creep. This loss of stress is known as relaxation. (Handbook of Reinforced Concrete, 2002)

Concrete Testing

Portland concrete is a mixture of coarse and fine aggregates, Portland cement, and water with or without incorporation of one or more other materials which are called admixtures.

Scientists who specialise in concrete aggregate technology are often called to examine concrete:

- a) To determine the types, amounts, and distribution of the coarse and fine aggregates, and the cement paste including the air-void systems;

- b) To determine the cause of concrete deterioration by examining specimens removed from the structures.

Analysis of Concrete Microstructure and Micro-Properties

The durability and performance of Portland cement concrete varies with the volume of cement, sand, aggregate and water used in a mixture, as well as its air content. For optimal durability, air must be distributed in properly sized bubbles spaced fairly evenly throughout the mixture

Bulk Density (Standard Method)

Cement cores are tested according to *Australian Standard AS 1774.5 – 2001, Refractories and Refractory Materials, Physical Test Methods, Method 5, The Determination of Density, Porosity and Water Absorption.*

Apparent Porosity (Standard Method)

The standard testing for apparent porosity is performed under the same standard as for Bulk Density. Concrete or mortar strength is not only influenced by the initial mix proportions and especially by the water/cement ratio, but also by other factors prevailing during the first hours or days after casting, such as temperature and humidity. Porosity is the characteristic property that is influenced by all these factors and, consequently, acts as a detailed record of these influences. It is therefore potentially an ideal parameter for estimating strength in existing concrete structures. Besides, porosity is a very important factor for estimating concrete durability.

Air-Void Porosity

Two emerging technologies appear promising for assessing parameters in hardened concrete. In one, investigators collect high-resolution images of cross sections from concrete cores with a flatbed scanner and use software to identify each image pixel as aggregate, cement paste or air void. In the other, investigators use a CT X-ray scanner to measure a sample's air-void system parameters in three dimensions, showing the spatial distribution of aggregate, cement paste and air voids. The scanner method is more feasible to implement and more cost-effective than CT X-ray scanning. (Sutter, L. Research Brief, No. 0092-03-16, September 2007)

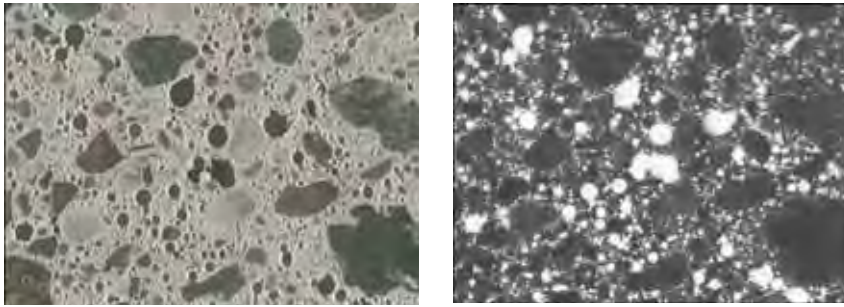


Figure 2.8 Automated calculation of air voids from a scanned image, right, is accurate and less time-consuming than microscopic evaluation of the same sample on the left (Sutter et al, 2007)

Acoustic Emission (Rapid Porosity Measurement)

To assess the deterioration of concrete a method to analyse acoustic emission activity of core samples under uni-axial compression provides information on the amount of potentially critical micro cracks in concrete.

It demonstrates that high strength concrete generates few acoustic emission events in a low stress level. The relation between micro cracks contained in concrete is confirmed by ultrasonic spectroscopy and other test methods.

Although this method is critical for determining fine micro cracks there is a relationship between micro cracking and porosity.

Permeability (Pore Network Continuity)

The over-all permeability is a function of the paste permeability, the permeability of the aggregate particles, and the relative proportions of the two. Fissures under the aggregate particles formed during the period of bleeding, and cracks caused by volume-change restraint also play a part. The permeability of paste has also an important bearing on the vulnerability of concrete to frost action. It determines the relative ease with which the cement paste and the aggregate may become re-saturated after drying, and it is a principal factor determining the destructiveness of freezing—once the paste becomes water-soaked.

The established traditional method uses hydrostatic pressure injection of mercury into the structure.

Modern imaging methods provide an increasing number of continuously improving three-dimensional images of microstructures. 3D Image analysis and modelling of microstructures (permeability) is now possible. Modern image acquisition techniques such as tomography with synchrotron radiation or nanotomography even allow images of materials with a low contrast or an extremely delicate structure. The three-dimensional image data represent new challenges for image processing, image analysis, and visualisation.

Optical Microscopy (Polished Surfaces)

The most common types of concrete specimens observed in an optical microscope are broken pieces, polished slabs, picked grains, and thin sections. Broken pieces require no sample preparation if examined by stereo Optical Microscopy. This is often very useful

for examining fractures, aggregates, and filled voids. Also, reaction products can sometimes be detected and sampled, or picked, for analysis by petrographic Optical Microscopy or scanning electron microscope (SEM). A polished slab is commonly more useful than a broken piece because the cross section of a whole core can be examined.

All constituents of the concrete can be seen and examined in detail. Often, staining is applied to the polished slab to reveal specific types of features. Aggregate type and abundance can be readily determined from a polished slab and cracks are easily seen and traced through the concrete. Reaction rims and products are clearly observed in polished slabs. Picked grains are minute pieces of concrete extracted from a specimen, usually while observing it in the stereo microscope.

These grains may be analysed on the petrographic microscope using refractive index liquids or on the SEM. Thin sections are 20-micron-thick pieces of concrete bonded to a glass slide commonly using fluorescent dyed epoxy. These are useful for transmitted light observation on the petrographic Optical Microscopy and backscattered imaging in the SEM.

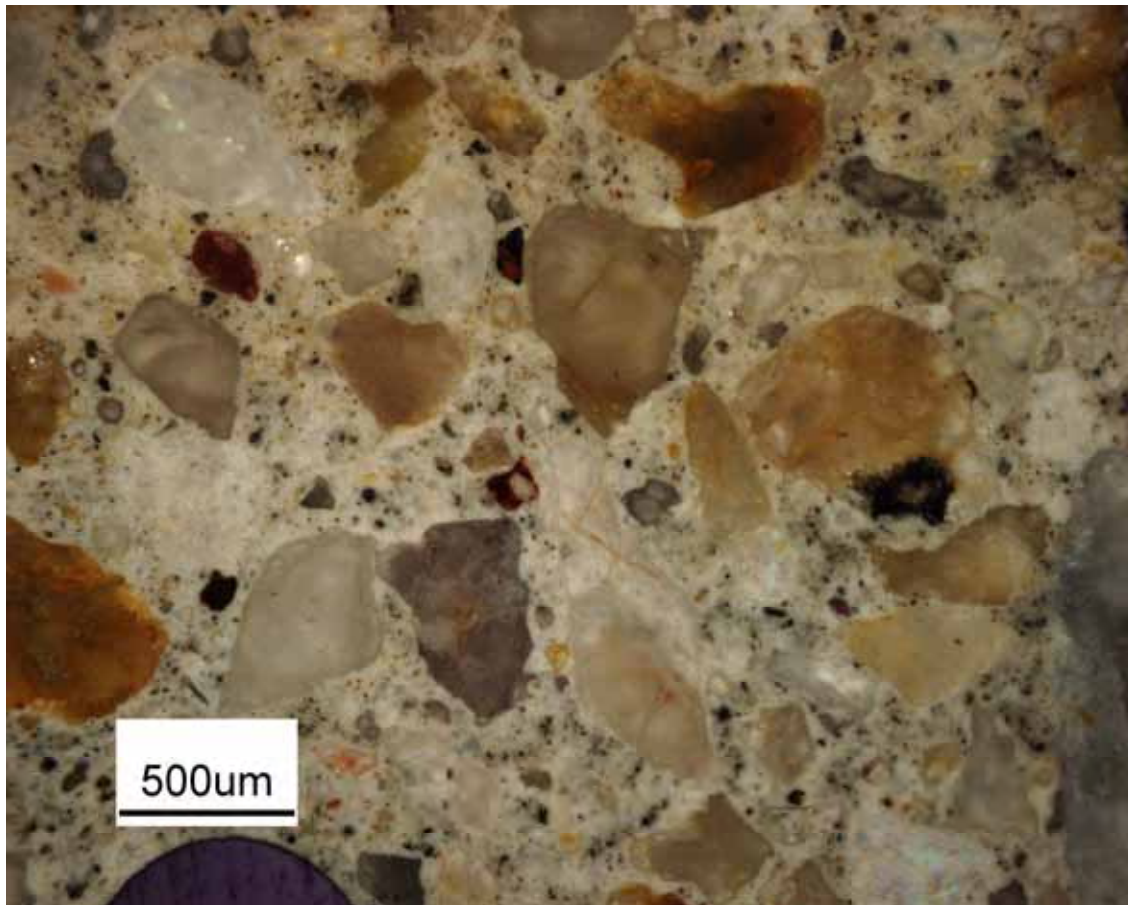


Figure 2.9 Image of microstructure from the Optical Microscope (Rider, M., 2009)

Australian fine and coarse aggregate is multi coloured (as seen in Figure 2.9) and the usual 32-bit digital analysis software could not be used.

Now with the 64-bit ImageJ these nanostructures should be able to be quantitatively resolved in a further study.

X-Ray Tomography (Through Microstructure)

The conventional X-Ray CT is not accurate enough in spatial resolution to separate individual particles and associated voids, but yields only a vague image of an X-Ray attenuation profile. Good progress has been achieved during the past decade in micro-

focus X-Ray CT such that each particle can be clearly distinguished from others even if it is only tens of micrometers in size (e.g. Takahashi et al., 2002).

Recently the researchers throughout the world have recognised that the high resolution X-Ray Micro-tomograph is able to differentiate micro-cracking within the concrete.

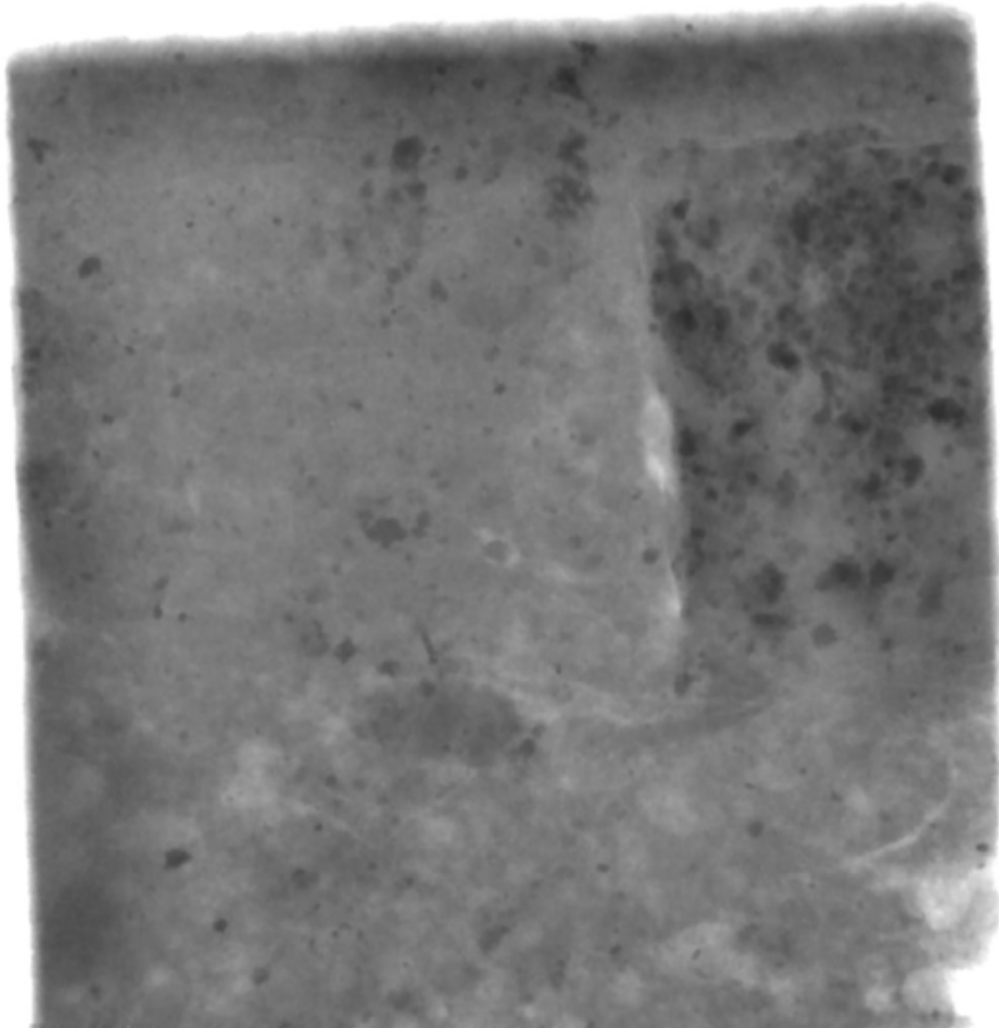


Figure 2.10 Image from SkyScan X-Ray Micro-tomograph, Model 1072 Micro CT (Rider, M., 2009)

High Resolution Image Analysis (Microstructure Quantification)

The microstructure of concrete is digitally photographed or scanned and with appropriate software analysed for porosity and aggregate.

One of these methods involves impregnating concrete materials with a polymeric material that contains fluorescent particles. This allows researchers to easily locate air void spaces in concrete when an ultraviolet light source is shone on a specimen, providing excellent information. Unfortunately, this method does not allow aggregate materials to be distinguished from cement paste materials in the concrete. Without this capability, a practical determination of concrete air void parameters is not possible unless an expert researcher is used. Other methods such as acoustic microscopy, profilometry, and infrared imaging can be explored in an attempt to distinguish the material constituents in concrete. These methods offer some possibilities, but none of them consistently display contrast between the cement paste, aggregate, and void constituents of concrete.

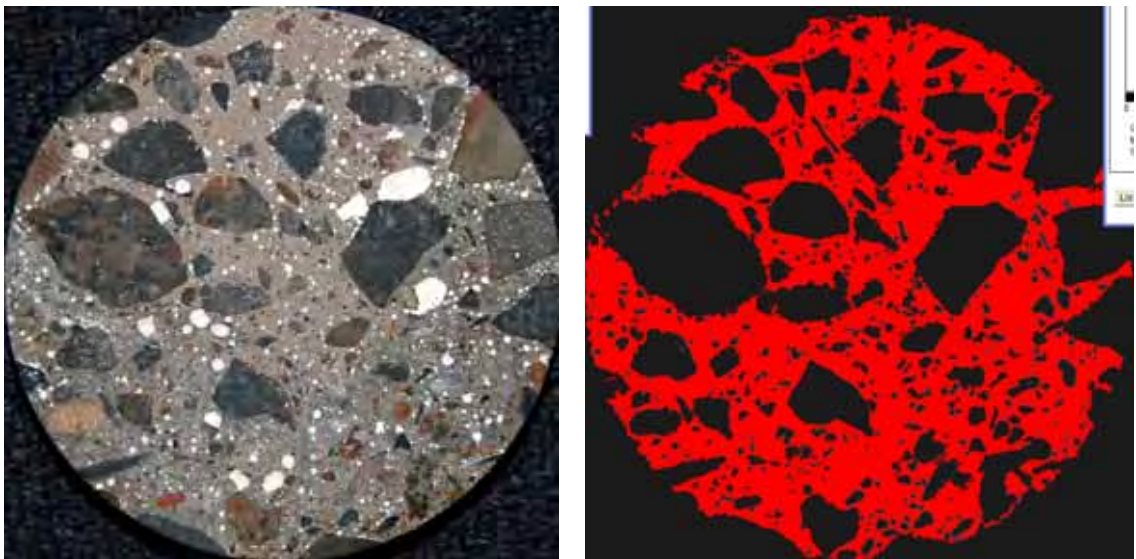


Figure 2.11 Digital analysis for porosity and aggregate (Rider, M., 2009)

In Figure 2.11 the digital image on the left is a picture of a prepared sample for a calculation of the percentage air-void porosity. Digital image on the right has been computer manipulated and masked for the accurate calculation of the multicoloured (as seen on the left) aggregate.

Microhardness of Matrix

Micromechanical properties of cement matrices in cementitious composites are investigated throughout the world by means of the micro indentation method. There is a correlation between micromechanical properties such as modulus of elasticity and creep, and distance of the indentation from the aggregate-matrix interface. The sub-micron accuracy of the positioning system of the micro indentation apparatus provides means for a meaningful investigation of cement matrix in close vicinity to the aggregate-matrix interface.

The microhardness value can be related to the compressive strength of the concrete. It is then related to the porosity in the structure.

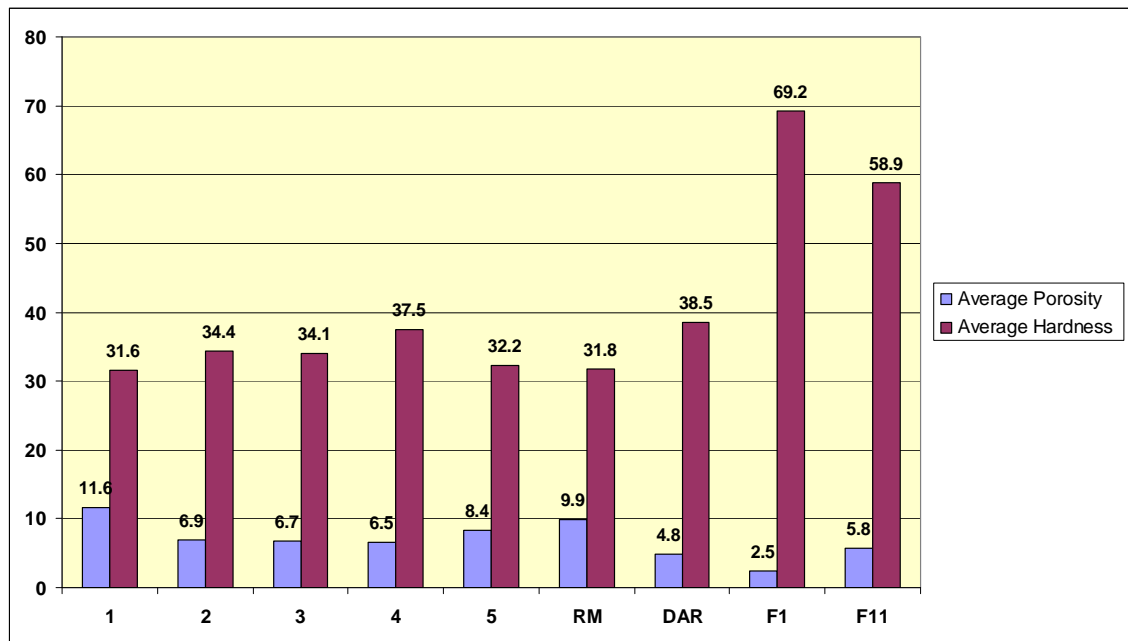


Figure 2.12 Relationship between the microhardness and porosity (Rider, M., 2009)

Core specimen preparation and image processing/analysis techniques are being continually developed for use in automated quantitative micro-structural investigation of concrete, focusing on concrete micro cracks and voids.

Different specimen preparation techniques are developing for use in fluorescent and scanning electron microscopy (SEM) of concrete; those techniques produce a sharp contrast between micro cracks/voids and the body of concrete.

The image processing/analysis techniques that are evolving specifically for use with concrete address the following usages: automatic threshold; development of intersecting micro cracks/voids and connected voids; distinction of micro cracks from voids based on geometric attributes.

2.1 Skyscan X-Ray Micro/Nano-tomography

These latest SkyScan desk-top micro/nano-tomography systems open a unique possibility to image and measure 2D and 3D micro/nano-morphology throughout the entire sample volume, and create realistic visual models for virtual travel within the object.

These new very high resolution units will revolutionise sharp digital analysis of the concrete microstructure that I have studied with the 1072 unit with a 15.19 μ .

SkyScan 1172 High resolution desktop Micro-CT

World's first 11 Megapixel micro-CT

- fully distortion corrected 11Mp X-ray camera,
- up to 8000x8000 pixels in every slice,
- down to 0.7 μ m isotropic detail,
- dynamically variable acquisition geometry for shortest scan at any magnification,
- single computer or cluster 3D reconstruction,
- software for 2D/3D image analysis, bone morphometry and realistic visualisation

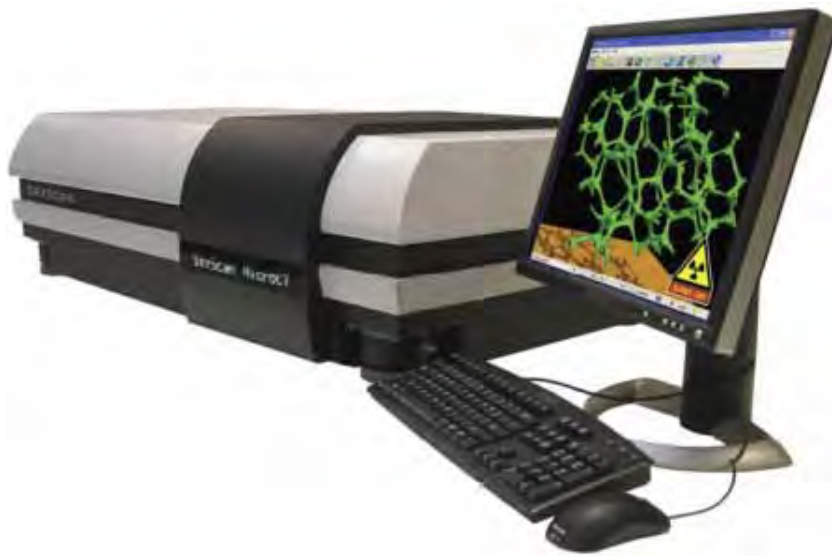


Figure 2.1.1 SkyScan 1172 (SGX Sensortech)

Object Size: up to 68mm

11 mega pixel Camera

Resolution: 5 μ m

Specifications:

X-ray source 20-100kV, 10W, <5 μ m spot size or 20-80kV, 8W, <8 μ m spot size

X-ray detector 11Mp, 12-bit cooled CCD fibre-optically coupled to scintillator

Maximum object size... 27mm in diameter (single scan) or 50mm in diameter (offset scan)

Detail detected <0.8 μ m at highest resolution

Reconstruction single PC or cluster volumetric reconstruction

Optional stages micro positioning, cooling, compression/tension

Radiation safety <1 μ Sv/h at any point on the instrument surface

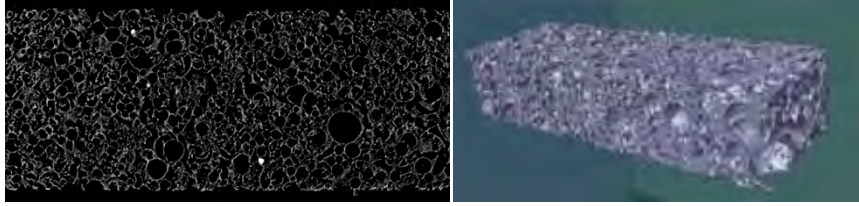


Figure 2.1.2 Carbon foam sample (Katholieke Universiteit Leuven)

Object: carbon foam sample (Katholieke Universiteit Leuven)

Scanner: SkyScan1172 / 100kV / 10Mp

Image: one of reconstructed slices, 1.5um pixel size

Image: 3D rendering of the small internal volume of the sample (CTan+CTvol programs)

The innovative flexible geometry of the SkyScan 1172 scanner is particularly advantageous over intermediate resolution levels, where scans are several times faster (to obtain the same or better image quality) compared to micro-CT systems with a fixed source-detector design. The new large format cooled x-ray digital camera achieves high spatial resolution without compromising sample size.

Fast scan and reconstruction throughput is supported by a computer cluster option, which reconstructs scan datasets in less time than the scan duration in most cases, using several PCs in parallel. Cross section images are generated in a wide range of formats up to 8k x 8k pixels. The full range of SkyScan software for 2D/3D quantitative analysis and for realistic 3D visualisation supplied with all scanners.

All SkyScan Micro-CT scanners include a powerful software suite for 3D modelling and analysis. New software for the calculation of Bone Mineral Density and other morphological parameters is included.

Skyscan 2011 Nano-Tomograph

World's first X-ray nano-tomograph

- compact laboratory system,
- detail detected down to 200nm,
- integrated anti-vibration platform,
- no x-ray optics: all parts of object always in focus,
- single computer or cluster 3D reconstruction,
- software for 2D/3D image analysis, and realistic visualization.

The SkyScan 2011 is a revolutionary laboratory nano-CT scanner with spatial resolution in the range of hundreds of nanometres. This spatial resolution in volume terms is equal to or better than that of synchrotron tomography. For the first time true sub-micron tomographic imaging is available in a laboratory instrument. The 2011 nano-CT employs an open-type x-ray source with a LaB6 cathode which achieves the unprecedented focal spot size of <400nm. At this small spot size, small-angle scattering enhances object details down to 150-200nm.

A sophisticated object manipulator allows object positioning and rotation with an accuracy of better than 100nm. The x-ray detector is based on an intensified CCD with single photon sensitivity. The object is scanned under normal environmental conditions, without any coating, vacuum treatment or other preparation. The full range of SkyScan software is supplied, including fast volumetric reconstruction, software for 2D/3D quantitative analysis and for realistic 3D visualisation.

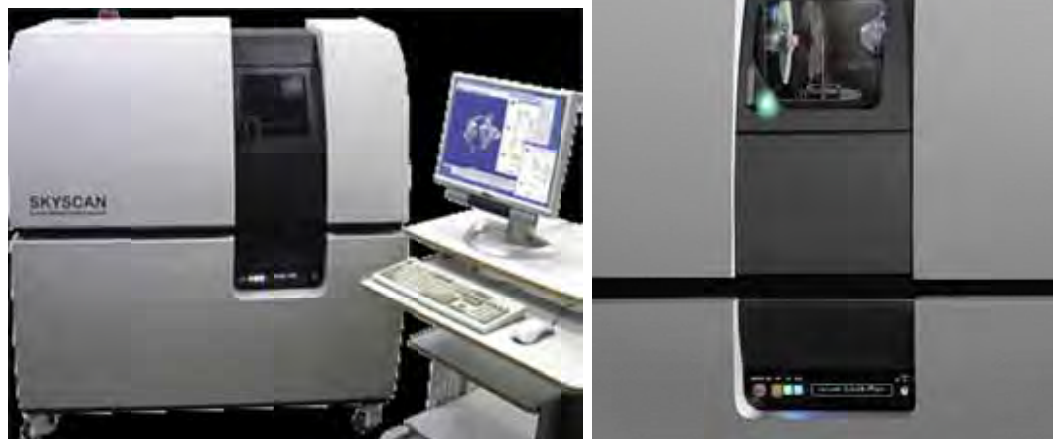


Figure 2.1.3 SkyScan 2011 (SGX Sensortech)

Object Size: 9mm

Resolution: 400 nanometres

Specifications:

X-ray source open (pumped) type 20-80kV, LaB6 filament, W target

X-ray detector intensified 1280x1024 pixels, 12bit CCD with FireWire output

Positioning accuracy <100nm for rotation during scanning, <200nm overall stability

Spatial resolution <150nm pixel size (isotropic), 400nm low-contrast (10%MTF)

Object size 0.2-1mm for max. resolution, 11mm max. diameter (9 μ m pixels)

Typical scanning time15-90min for entire object volume (1280x1280x900 pixels)

Radiation safety<1 μ Sv / h at any point on the instrument surface

2.1.1 Micro-tomography

Using synchrotron micro-tomography, the 3D micro-geometry of hardened cement paste of different ages (2, 7, 28 days) was examined by Promentilla et al 2009 from images of very high spatial resolution ($0.5\text{ }\mu\text{m/voxel}$) obtained at Spring-8, Japan. Diffusion tortuosities in the largest percolating pore cluster was then quantified using 3D-image analysis and random walk simulation.

As the age of hardened cement paste increases, results indicate that the tortuosities increase while the percolating effective porosity decreases as the pores that can be resolved at the given resolution becomes fewer and fewer, and more disconnected. Although the resolution may still be insufficient to resolve the finer pores, the non-invasive 3D imaging of the pore space allows us to investigate the pore connectivity and twisted pathways which is difficult if not impossible to obtain using 2D microscopic imaging alone or other indirect techniques.

This is one of the most important advantages of using 3D micro-geometry technique since it provides information that could complement with the other experimental analyses as regard to pore structure characterization of hardened cement pastes. Furthermore, the synchrotron micro-tomography is expected to be a powerful tool in the study of pore structure-transport property of hardened cement paste as the X-ray CT system continues to improve for higher spatial resolution. Future research would therefore involve investigations on the robustness of the method particularly in its application to predict the transport properties of cement-based material on the basis of the measured pore structure parameters from the micro-tomography images.

In the discussion above, some open issues may still remain on whether the scale at the current resolution of synchrotron micro-tomography could measure the pore structure parameters relevant to the transport properties of hardened cement pastes. If one would argue that Microscope Image Processing (MIP) is adequate enough to characterise pore structure in hardened cement pastes, then the critical pore diameter is said to be the

length scale that plays an important role in the transport properties. This parameter corresponds to the diameter of the smallest pore of the set of largest pores that percolate through the material. In mature cement pastes, this critical pore size obtained from MIP could range between 20 nm and 100 nm, and such length scale may not be resolved properly from the current spatial resolution of the method.

Nevertheless, the diffusion of twisted pathways derived from the digitised images seems to reflect the pore morphology that mainly controls the transport properties in young cement pastes; thus, explaining the rough agreement with the computer model or experimental evidence. Moreover, it has also been shown that water vapour diffusivity and water permeability through hardened cement pastes can be reasonably estimated from a pore network model extracted from micro-tomography images because of the self-similarity of the capillary pore space.

Due to such pore space fragmentation, it is assumed that the images could provide the same pore space morphology with that of the actual transport-relevant part of hardened cement pastes. Thus, synchrotron micro-tomography can be a valuable technique to provide qualitative and quantitative information of the 3D micro-geometry and morphology of pore structure without resorting to any assumption of pore geometry. As the X-ray imaging system continues to improve for higher spatial resolution, this technique can therefore contribute significantly to the investigation of microstructure-property relationship in concrete materials.

2.2 Digital Analysis

Image analysis is the extraction of meaningful information from digital images by means of digital image processing techniques. The accuracy of digital analysis techniques depends on obtaining the highest resolution digital image possible before analysis begins, and the best method found to obtain a perfect digital image for analysis, was to use a high resolution flat bed scanner.

The two digital images below (Figures 2.2.1 to 2.2.4) were obtained in 24-bit colour at 200 pixels per inch (ppi) resolution and 2400 ppi resolution.

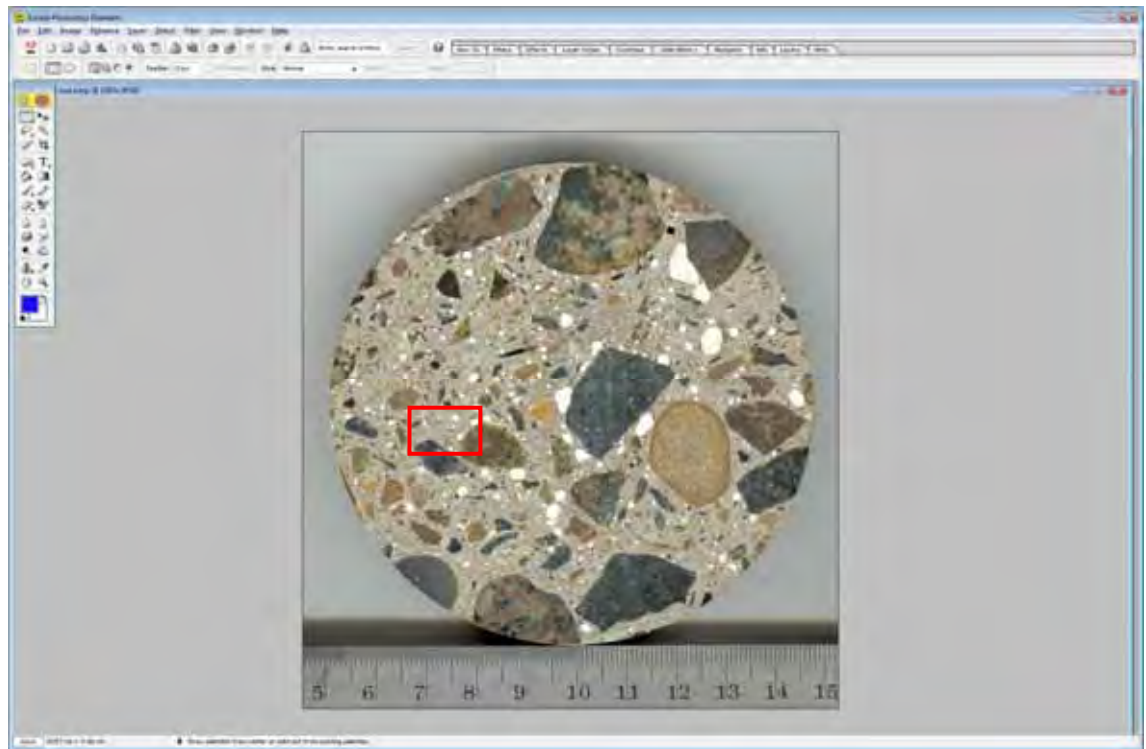


Figure 2.2.1 Original scan of the Sample 5B at 200 ppi (the scale is in cm/mm, the smallest division on the left is 0.5 mm) (Rider, Myca, 2009)

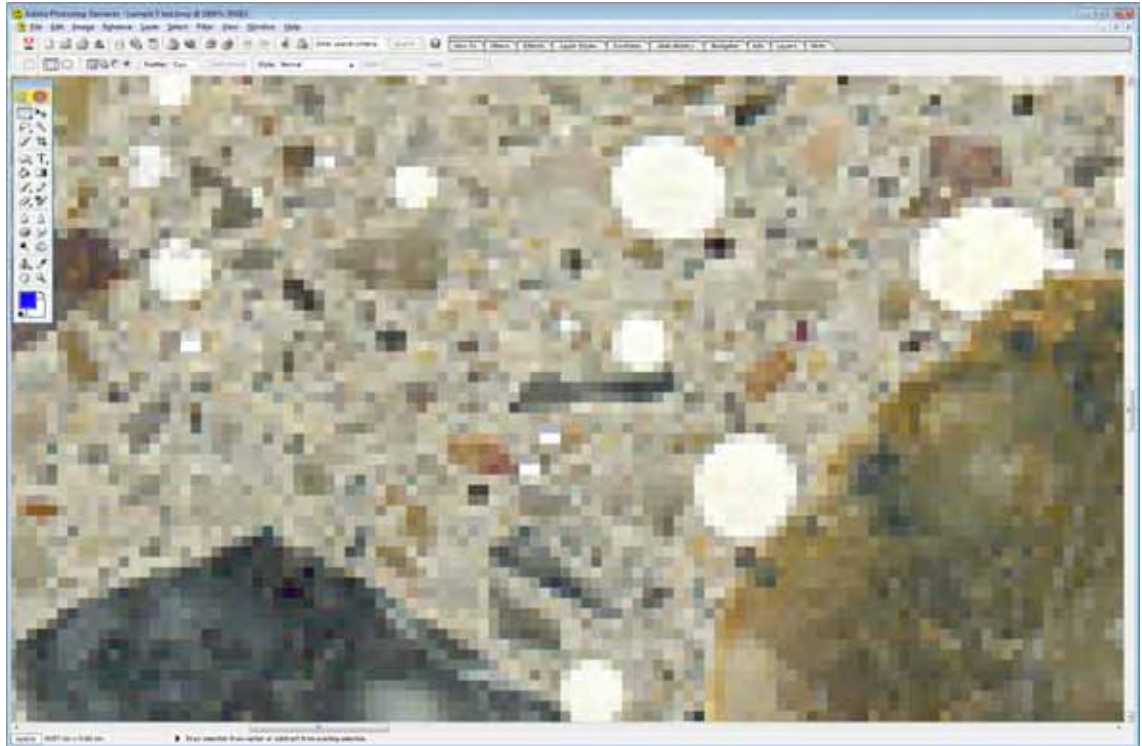


Figure 2.2.2 200 ppi image of Sample 5B magnified 16 times to show the coarse perimeters which resulted in higher calculations of the air voids (Rider, Myca, 2009)

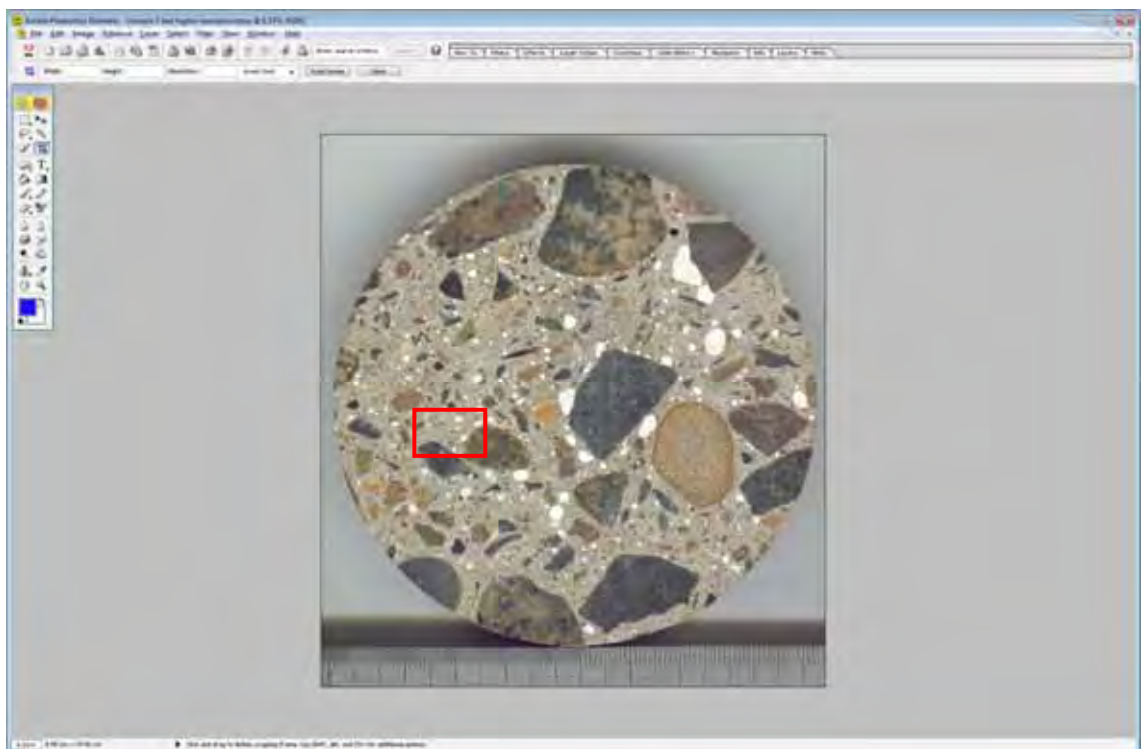


Figure 2.2.3 Original scan of the Sample 5B at 2400 ppi (the scale is in cm/mm) (Rider, Myca, 2009)

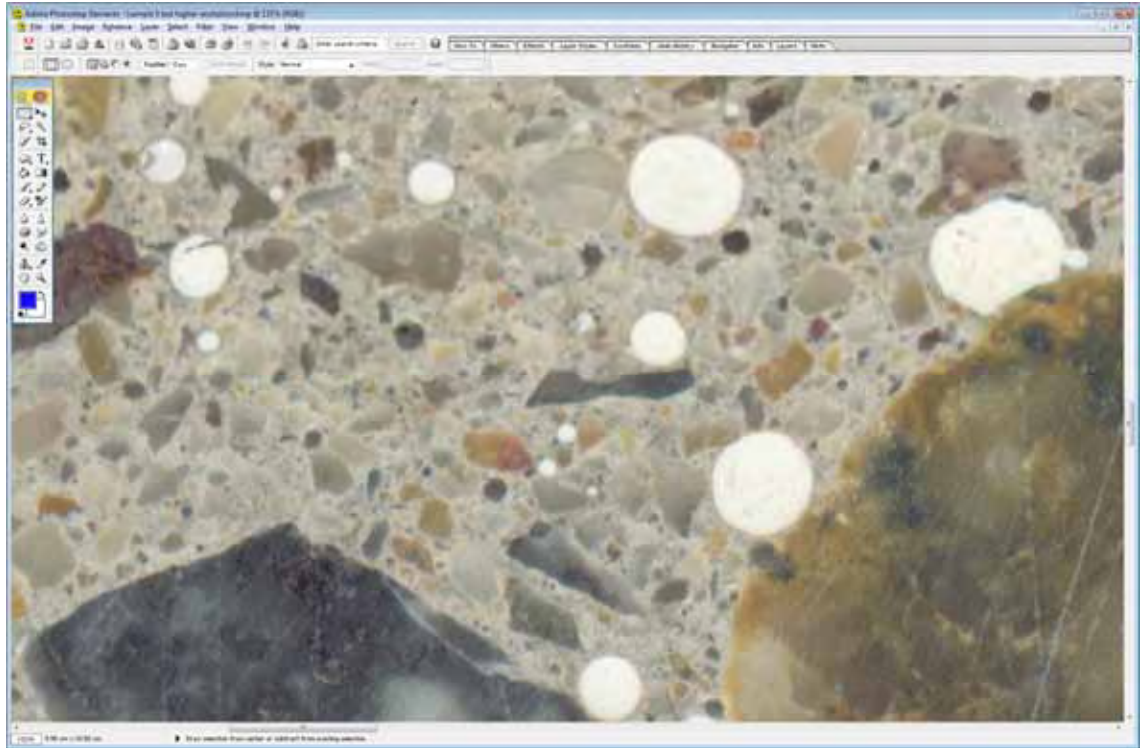


Figure 2.2.4 2400 ppi image magnified 16 times to show smooth perimeters of calculated air voids (Rider, Myca, 2009)

The 200 ppi image requires 2.13 MB of memory and has an image dimension of 832x899 pixels ie. 747,968 pixel elements for analysis.

The 2400 ppi image requires 277MB of memory and has an image dimension of 9400x10320 pixels ie. 97 million pixel elements for analysis.

An older \$25,000 proprietary digital analysis software programme, operating in Windows Vista 32-bit was unable to differentiate or accurately determine the volumes of coloured aggregate microstructure present in the concrete samples under analysis with river gravels and sands. It could not even open the small (277 MB) image data file; the file had to be manipulated to open it successfully in that programme for an analysis.

Higher resolution scanners of 4800 ppi supply an image dimension of 18800 x 20640 pixels ie. 388 million pixel elements for analysis or one of 9600 ppi will supply an image dimension of 37600 x 41280 pixels ie. 1.5 billion pixel elements for analysis.

One can appreciate that to analyse high resolution digital images rapidly require the use of minimum 64-bit Windows operating system with 12 GB and/or more of DDR3 RAM.

ImageJ now operates in the 64-bit format and the restrictions to further Java analysis software development have been removed from the 2.0 GB restriction under the 32-bit operating system.

Terabyte ultra high resolution micro-structural images will be able to be routinely digitally analysed in Materials Science in the near future.

Luckily most 64-bit operating system digital analysis software is able to convert the GB masses of digital colour image data back to 8-bit greyscale for ultimate accuracy analyses.

In the first image 747,968 pixels are counted and assembled into 256 shades of grey from black (0) to white (255). In the second image 97,008,000 pixels are similarly counted and assembled into 256 shades of grey with far greater accuracy to resolve the image elements for digital analysis.

As the scanned image optical resolution (ppi) increases the pixel area decreases and the image resolution increases. Note the small air bubble sizes 100-500 micron cannot be accurately resolved at 200 ppi but are OK at 2400 ppi. At 4800 ppi the accuracy improves further and microstructure can be quantitatively digitally analysed from the optical digital scan.

If the voids were just pure white the digital analysis program would simply count the number of white (255) pixels; however within the white are shades of greyish white thus the threshold must be manually adjusted until the finest resin filled air voids appear filled and sharp on their perimeters.

When the threshold is set so that the outline edge of a fine air-pore is clearly differentiated from the paste background of the high resolution image the pore area is accurately calculated. The lower quality image gives a higher value to the pore area due to the coarse jagged and fuzzy perimeter.

The higher the optical resolution of the scanner, the higher the accuracy of the digital analysis. (Note the calculated % air void at 200 ppi resolution (6.7%) compared to the % air void at 6400 ppi resolution (5.6%) in Figure 4.3.3.4.14 in the same specimen the size of 10 x 10 mm).

A large polished specimen of A4 size scanned at 75 ppi requires an image data file 1.6 MB however the fine detailed microstructure cannot be resolved by digital analysis software, whereas the same specimen scanned at 9600 ppi requires an image data file of 27.2 GB. A normal personal computer with 100 GB hard drive is able to only save 3 images. Fortunately these very high resolution image data files can now be analysed on personal computers using 64-bit Windows and 64-bit image analysis software and multiple (4) hard disc drives (ie. of 2 TB each) giving a working memory of 8 TB. It is worth commenting upon the fact that this immense colour image file of 27.2 GB can be reduced to 560 MB for analysis in greyscale. Imagine the sharpness and accuracy of perimeter identification of aggregate, porosity, cracking and concrete paste components when the threshold setting of 27,000,000,000 pixels are converted to 256 shades of grey for total micro-structural quantitative analysis of macro samples.

64-bit ImageJ is still unable to analyse such large files, and my computer requires 10 GB of DD3 ram allocated to ImageJ for quantitatively analysing 3.6 GB 48-bit TIFF

coloured images at 6400 ppi x 6400 ppi, reduced to <1GB 8 bit TIFF greyscale images at the same true optical resolution of 6400 ppi x 6400 ppi.

Reducing for analysis, the digital image file size from 48-24 bit colour, to 8 bit greyscale, retains the original ultra fine, true optical resolution. The ultra fine pixels are able to accurately define perimeters of fine pores, cracks, aggregates etc., and correctly calculate areas.

What this study will prove beyond doubt is that the higher the original digital image recorded, that is the higher the true optical resolution, the smaller the pixel unit, the higher the accuracy of quantitative digital analysis of microstructure obtained.

2.2.1 Automated Digital Analysis

Often the goal of automated image analysis is simply to replicate humans' observations with much less labour or cost. There are many substantial scientific benefits however, and automated image analysis can yield objective and quantitative measurements, thereby enabling the capture of minute differences among samples, as well as statistical analysis on the data.

This discussion is limited to digital image files from microscopes cameras and flat bed scanners only, although the concept of automated image analysis can be equally applied to images from X-Ray, SEM, TEM, etc. In fact any digital image from any analytical instrumental analyses is able to be subjected to automated image analysis.

A digital camera whether attached to a microscope or not, divides the field of view into a grid of pixels. The intensity of the light absorbed by a pixel is recorded as that pixel's numerical value. The digital image that the computer has to work with for image

analysis, then, is a grid of numbers, each of which indicates the intensity of light in a small part of the field of view. The role of image analysis is to transform these grids of numbers into measurements.

The most challenging part of image analysis is usually determining which pixels in the image belong to each micro-structural component. This task is known as segmentation. The first step toward segmentation is to distinguish foreground (objects of interest) from background. Thresholding methods classify a pixel as foreground if it is brighter than a certain "threshold" intensity value. White porcelain epoxy filled air voids appear as bright objects on a darker background in scanned digital micro-structural images of polished sections of hardened concrete. Other image types can use the same techniques by first inverting the image, turning dark regions into bright regions and vice versa. Because of variations in diamond lapping, polishing, staining and illumination, choosing a single threshold for all locations in all images is not always effective, thus the challenge is to determine appropriate threshold(s) automatically for each channel in each image.

Global thresholding algorithms compute a single threshold for each image. One method for global thresholding is by mixture models, which fit a mixture of two probability density functions (one for the foreground, one for the background) to the intensity histogram of the image. Mixture models work well when the histogram is clearly bimodal or when the mixture probability (the percentage of pixels that belong to the foreground) is known. Working with the logarithm of the intensities is often helpful threshold that minimizes the weighted sum of the intensity variance within each of the pixel classes (foreground and background). This method is often superior when the percentage of pixels belonging to the foreground varies substantially from image to image. This is the case when images are taken with digital cameras at varying times and light illumination.

Adaptive threshold methods use different thresholds in different parts of each image. The threshold for a pixel is based on the intensity statistics of a local neighbourhood

rather than the entire image. Such methods are useful when the intensity of the background varies across the image due to uneven illumination or sample preparation.

A danger with this approach is that if a part of the image contains tightly clustered objects (all foreground) or no objects (all background), the intensity statistics of the local area reflects only one class. One can detect that this condition occurs for a local neighbourhood and instead interpolate from the thresholds of nearby pixels.

Adaptive threshold must not be applied to quantitative digital image analysis because the image file must contain even illumination across the entire microstructure.

An alternative to local thresholding is to use global thresholding on images that have first been corrected for intensity variations in a separate pre-processing step known as illumination correction. A smooth illumination function is fitted to the image. The intensity of each pixel is then adjusted by dividing by the value of the illumination function at that position. This adjustment improves segmentation and a slight decrease in lamp intensity at the edges of images barely noticeable by eye causes detail there to be overlooked by automated algorithms.

Illumination correction, followed by global thresholding, yields a result similar to that of local thresholding, but at a lower computational cost. The illumination function can be calculated by median filtering or by fitting a polynomial or spline surface. The function can be adjusted by placing more weight on pixels that are likely to be background. If the illumination variations are consistent between images in the set, fitting the illumination function to an average of several images, perhaps even the entire set, increases robustness. These light intensity variation problems are virtually eliminated when using calibrated professional flat bed photo scanners, as used in this thesis study.

Alternatives to thresholding are needed when the intensity inside the objects of interest is not markedly different from that of the background, as in many bright field images

from microscope images. In these cases it is sometimes possible to classify pixels as foreground and background based on other features, such as local intensity variation or texture. It can be extremely difficult to choose features that can identify the foreground; a more fruitful strategy has been to extract a large number of image features, hand-select some areas inside and outside the objects of interest, and use machine learning to find combinations of features that distinguish foreground from background.

This technique was employed to accurately quantify multi coloured coarse river gravel aggregate.

Noisy or low-contrast images can sometimes be handled more easily if assumptions can be made about the objects' shapes. For instance, the circular Hough and Radon transforms can identify circular objects such as entrapped air voids, and spatial filters fit to a set of example objects can help identify similarly shaped objects by improving contrast.

Despite the successes in this field, researchers often have images that are not readily tackled by applying algorithms in existing software. This was certainly the case with complex coloured and transparent quartz river gravel aggregates, encountered in this quantitative digital analysis study. Selecting algorithms and adjusting their parameters for a particular experiment can be daunting and time-consuming, and the expertise of an experienced image analyst is often essential. Even with this assistance, many images remain intractable with ready-to-use software. Projects involving time-lapse or three-dimensional image sets, large complex micro and nano structures, or bright field images can be particularly difficult. Still, researchers have several options if existing software struggles to accurately identify and measure the objects of interest.

The first strategy is to adjust sample-preparation, particularly fine diamond slow lapping techniques and image-acquisition techniques to make the images more tractable with existing software. Aside from the obvious good practice of consistent sample preparation and imaging (using automation where possible), a fix might involve

changing staining concentrations, wash steps, or exposure times to improve the signal-to-noise ratio in the images. Using different staining or imaging techniques may also ease image analysis, for it must be emphasised that binary digital analysis only differentiates between two data sets either side of the established threshold at each analysis step.

As the reader can appreciate, it is extremely easy not to know whether you are properly correcting images for accurate digital analysis or not. This is why from this research it is advocated that images not be corrected at all, and original quantitative data is retained for accurate automatic digital analysis.

I am very fortunate that the recently released 64-bit ImageJ is such an extremely powerful package, and excellent for accurate quantitative calculation, provided the original image is of high true optical resolution, and extremely even light intensity across the area of analysis.

Some general principles for optimising imaging experiments are discussed.

Research Scientists often find they are unable to rely on their eyes to decide upon the most suitable sample preparation, image acquisition, or image storage file techniques best suited for quantitative image analysis. The choices made can have very serious implications on data quality, even though the effects of changing these protocols may not be noticeable by eye.

Projects for quantitative image analysis must follow standards of good experimental design: positive and negative control samples need to be included, and all samples should be prepared and imaged in parallel under identical conditions. While this would seem obvious, it is not unusual for research scientists to think it appropriate to gather images from different experimental sources over the course of months, or even years, hoping to obtain quantitative relative measurements between them. Quantitative comparative analysis between images cannot be attained, only qualitative at best

Very high resolution images for quantitative comparison from experimental samples obtained over the course of months, must be undertaken in sequences of highly controlled digital image acquisition sessions, each of several hours maximum.

The image acquisition parameters need to be kept as constant as possible. Parameters such as, lens magnification, auto-focus, exposure times, and filters need to be tested for their effects on subsequent image analyses. A common error is having the microscope, digital scanner, or camera use an auto exposure setting, thus changing the exposure time from one digital image to another. This eliminates any quantitative comparisons.

Also, variations in lamp, or light spectral intensity, or filter settings between samples cause problems. Poor quantitative analysis measurements can often be obtained due to fluctuations in power supply, that cause lamps to change their intensity, or failure to wait for a lamp to warm and stabilise its intensity, before collecting images. Even the gradual loss of lamp brightness over time, and unusually brighter images due to more fluorescent lights being turned on partway through an image acquisition session.

The exposure time needs to be set so that the resulting images utilise the full dynamic range of the camera or CCD chip without saturating or overexposing images.

Most microscope and other digital controlled software, allow viewing a histogram of pixel intensities, and this histogram should fill most of the available pixel intensities. A spike at the highest intensity is to be avoided as this indicates image saturation.

Rescaling options that stretch each images histogram, even though it utilises the full dynamic range, because this action will preclude comparing intensities between different digital images of similar microstructures, for instance.

Choosing a higher magnification lens in general produces a higher resolution image (more pixels per unit area), and this yields better quality image analysis. But this comes at a high cost of imaging smaller fields of view, affecting the statistical significance of

observing the sand grain, however missing the immense variability of the micro and macro-structure. The optimal magnification is thus an empirical question.

Binning combines light received by several adjacent pixels, and combines it into a single pixel. This dramatically reduces the resolution of the images, but increases the signal to noise ratio, and speed of image acquisition, but the optimal choice is again empirical. This should not be contemplated.

For accurate quantitative digital analysis, there is no substitute to very high resolution digital image capture.

Using a 300x digital image from a microscope is able to resolve an optical resolution from 0.3-1.0 microns but the area of micro-structural analysis is limited to 1mm x 1mm.

Each 100mm x 100mm digital image analysed in this thesis is equivalent to 10,000 digital images from such a microscope. The 100 concrete core images analysed in this thesis are equivalent to the digital analysis of 1 million microscope images.

The ultimate optical analysis digital scanner, for digital analysis of hardened concrete core micro-structures, would be zero magnification, with a true optical resolution to 0.25 microns. These are not available. Proprietary scanners with true optical resolutions down to 0.5-1 microns exist now, but cost several hundred thousand dollars.

A professional 6400 ppi true optical resolution scanner was used in this study with a pixel resolution of 4 microns, and was purchased for about one thousand dollars.

A lot of digital image capture microscopes have an option to correct for uneven lighting in the field of view by white referencing or white shading. A blank field of view, called a white-reference image, is collected at the time of the image capture, and the pattern

seen in that image is subtracted from each image that is collected. This may improve the data quality, but only if carried out precisely.

Some image analysis processing software has options for retrospective illumination correction, when a white-reference image is not available.

It is a good idea to choose the number of images to acquire for each sample, based on the statistics of the micro-structures of interest. Large effects can be detected in a very high resolution 2D image of each material, whereas quantitative volumetric 3D images per material sample, could require 10 to 20 2D images per material to obtain statistically valid results.

To obtain full 3D volumetric quantitative analysis, would be obtained by doing 20 x 2D analyses of a 10 mm thick 100 mm diameter core section, that could be diamond lapped in 0.5 mm increments progressively thinner and thinner. This would have been done, had there been an additional 6 months available for the additional 200 core cross sectioned surfaces required. This data would have converted the 2D quantitative micro-structural analysis to real 3D quantitative micro-structural analysis. Such a study may be contemplated by another researcher.

When purchasing a microscope, digital camera, or high resolution digital scanner, preference is not always given to the parameters that save images into standard format, that can be easily readable by standard image analysis software.

Fortunately there is a certain degree of standardisation of image file formats and metadata settings, and conversion software, and now very powerful open source software such as 64-bit Image J that can handle most large TIFF and BMP digital image file formats.

There are some file formats such as JPEG that compress the digital images in a “lossy” manner, and the image quality is dramatically sacrificed to reduce the file size. Lossy compression algorithms take advantage of the inherent limitations of the human eye and discard information invisible to the eye. Most compression algorithms allow for variable quality levels (compression) and as these levels are increased, file size is reduced. At the highest compression levels, image deterioration becomes noticeable as a compression artefact.

File formats such as JPEG compress the digital images in this “lossy” manner, and the image quality is dramatically sacrificed.

It was not until towards the end of this study, that I found that JPEG image files should be avoided, as they are unable to be quantitatively analysed. The original digital camera images saved automatically into JPEG image files, Study 1 in this thesis, thus becoming useless for quantitative image analysis. As the raw digital image file had not been retained, the image analysis was compromised and could not be quantitatively assessed although qualitative trends between different sample micro-structures were noted early in the forensic comparative study.

Not all compression is detrimental, and some image-compression data files retain the original image information exactly, while still reducing the size of the file. These formats such as PNG and most TIFF are perfectly acceptable for image analysis.

Uncompressed file formats, such as TIFF or BMP, are the best for quantitative image analysis; however the file size may be much larger. This complete guide to file formats was found in Wikipedia.

Image file formats are standardised means of organising and storing images, and the image files are composed of either pixel or vector (geometric) data that are converted to pixels when displayed (with few exceptions) in a vector graphic display. The pixels that

constitute an image are ordered as a grid (columns and rows) with each pixel consisting of numbers representing magnitudes of brightness and colour.

Image file size is expressed as the number of bytes and increases with the number of pixels composing an image, and the colour depth of the pixels.

Very high resolution flat bed scanners currently save images in 64-bit image files.

Bit depth describes the number of data bits used to represent the intensity value of a single pixel, and is also known as bits per pixel. A files bit depth indicates the number of separate greyscale intensity values that are allowed by the file format.

- 8-bit images have 28 available pixel intensities, with a range of 0–255;
- 16-bit images have 216 available pixel intensities, with a range of 0–65,535.

Some microscope cameras capture 8-bit images and store them in 8-bit files, which all older 32-bit image-viewing software can display. Many other microscope cameras capture 16-bit images, which contain finer detail (in terms of grey levels) than 8-bit images. A 16-bit format is thus preferable. As cameras and scanners improve, 32-bit 48-bit, 64-bit, and soon 96-bit, and 128-bit images will allow immense greater accuracy with almost nil distortional error for absolute 100% quantitative digital analysis. Super personal computers are now required for micro-structural data storage and image analysis, and multiple conversions for thesis compilation.

Images are fairly large (compared to typical text or numerical data) and can be acquired rapidly; therefore data storage presents some issues to overcome, including procuring sufficient raw storage space and organising the images with enough annotation to allow them to be readily retrieved later. If, despite these efforts, images are still hard to cope with by automated analysis but objects are readily visible by eye, it will be worth the investment to team up with computer scientists to develop new algorithms.

Once validated, the algorithms can be added to existing open-source projects to give them a friendly user interface. ImageJ offers this potential should you become familiar with programming in Java.

All image analysis modelling plug-ins must always be calibrated to real experimentally-obtained highly accurate quantitative data.

For many images, accurate identification and measurement of individual objects is impossible even by eye; for example, objects sometimes overlap, or the borders between them are not visible. This is often the case in digital images of very fine aggregate and transparent silica sand grains in the cement paste microstructure.

Another approach to images where accurate object identification cannot be achieved is to use machine learning, which can operate on measurements acquired from images without first identifying objects. For example, a multi-purpose image classifier, such as the wnd-charm algorithm can distinguish positive and negative control images based on arbitrary tiles of the images rather than identified objects. As in the machine-learning methods described above for foreground-background determination and object segmentation, the measurements used do not have to be specifically designed to target a particular material property, but rather can be a general set of image measurements. Of course, results can sometimes be improved by adding measurements that are customized to the specific material property.

Statistical analysis is usually necessary in order to draw conclusions from the mass of measurements in high-throughput imaging experiments. The end goal in this example is to identify which samples from the top and bottom of this list are statistically significantly different from controls. This step should include identification and elimination of systematic spatial artefacts. Spreadsheets, such as Microsoft Excel, are widely used because of their familiarity, although they are unable to handle large screening datasets and lack sophisticated analysis methods.

The recent release of Microsoft Office 2010 utilising 64-bit Excel has removed a lot of the restrictions associated with 32-bit Excel. High-throughput microscope vendors often bundle some data-analysis functionality with their instruments and image-analysis software. Investigators with knowledge of computer programming often write custom scripts, e.g., in Python, Matlab, or R. High-throughput screening software and general tools for multivariate analysis and visualization (e.g., GeneData Screener, SciTegic Pipeline Pilot, and SpotFire) have proven useful for image-based measurements, as have tools designed for flow cytometry or microarray informatics.

However, such tools are often unable to display images linked to data, handle the huge datasets generated from images, or effectively handle the hierarchical structure of image-based measurements (since each image contains many objects). These features are gradually being added to commercial and open-source software, and tools specific to high-throughput image analysis data have also started to emerge. The 6400 ppi flat bed scanner that could save 4 GB digital image files in 48-bit colour TIFF required proprietary 64-bit German software for image capture, and 64 bit ImageJ for greyscale image analysis. The field of image analysis continues to advance steadily, as material scientists attempt to quantify ever more complex microstructure in ever more challenging image types.

Historically, many of the techniques that are useful for image analysis were first developed for other purposes such as face recognition, satellite surveillance, and manufacturing quality control. This trend will likely continue, as the field transitions to rely more heavily on machine-learning techniques.

A more practical but very welcome development in the field has been the increasing compatibility among various image-acquisition and image-processing software packages. As this software becomes more modular and operation between systems improves, materials scientists will benefit by spending less time converting data from one package to another and more time designing and interpreting their experiments.

We have only seen the tip of the iceberg in terms of extracting detailed knowledge from material micro-structural images. Excellent opportunities exist for using quantitative image-derived data in systems-materials research to gain a global view of the relationships between properties and structure. This immense data source has so far been largely untapped.

The continuing demand for highly accurate quantitative image analysis of microstructures within materials science and engineering research continues to grow. Given the prevalence of automated microscopes, laser scanners, etc large-scale experiments are becoming more routine, and even small-scale experiments are producing more digital data than before: time-lapse images, for example, can be readily captured and lend a rich source of dynamic information about material systems. Automatic image analysis benefits micro-structural analysis by enabling quantitative digital image files from instruments, expressed as the number of bytes—increases with the number of pixels composing an image, and the colour depth of the pixels.

The greater the number of rows and columns, and the greater the image resolution, the larger the image file. Also, each pixel of an image increases in size when its colour depth increases—an 8-bit pixel (1 byte) stores 256 colours, a 24-bit pixel (3 bytes) stores 16 million colours, the latter known as true colour.

My thesis studied digital colour image files of 1 GB uncompressed 4800 ppi TIFF in 48-24 bit colour depth and images 660 MB uncompressed 6400 ppi TIFF in 16 -8 bit greyscale where the limitations were due to the scanner options. The Epson Perfection V700 Photo scanner was unable to scan images in 32-bit colour depth which is the maximum the 64-bit ImageJ can process.

High precision deep colour in 48 bit integer RGB colour representation is stored in three 16-bit channels, resulting in 48 bits of colour data per pixel. This makes it possible to represent 65,536 of each colour tone component instead of the usual 256, hence resulting in a total of 2^{48} (281 Trillion) colours. **(Note: the colour depth and detail**

revealed in the digital image files of concrete micro-structures quantitatively analysed within this thesis.)

Adobe Photoshop supports creating and editing of images up to 32 bits per channel (96 bits per pixel), thus maintaining greater precision when a sequence of more than one image filtering algorithm is used on the image. With only 8 bits per component, rounding errors accumulate more quickly with each filtering algorithm that is employed, degrading the end result.

Image compression uses algorithms to decrease the size of a file. High resolution cameras produce large image files, ranging from hundreds of kilobytes to megabytes, per the camera's resolution and the image-storage format capacity.

High resolution digital cameras record 18 megapixel images, or more, in true colour. For example, an image recorded by a 18 megapixel camera; since each pixel uses 3 bytes to record true colour, the uncompressed image would occupy 54 Megabytes of memory - a great amount of digital storage for one image, given that cameras must record and store many images to be practical. Faced with large file sizes, both within the camera and a storage disc, image file formats were developed to store such large images. An overview of the major graphic file formats follows below.

The discussion on formats equally applies to the huge image files now possible from high resolution scanning technology and 64-bit operating systems.

Single image digital data files now begin in the tens of Gigabytes and are heading for Terabytes and beyond as the optical resolutions are improving and large sections of materials are analysed for macro-structural, micro-structural, and nano-structural (restricted by optical resolution to 0.25 microns) information.

There are two types of image file compression algorithms: lossless and lossy.

Lossless compression algorithms reduce file size without losing image quality, though they are not compressed into as small a file as a lossy compression file. When image quality is valued above file size, lossless algorithms are typically chosen.

For all quantitative digital analysis research only lossless compression can ever be contemplated, but preferably never used as this thesis will show.

There are hundreds of lossy image file types including the proprietary PNG, JPEG, GIF, etc. formats that are most often used to display images on the Internet. At the highest compression levels, image deterioration becomes noticeable as a "compression artefact". These procedures are OK for manipulating photographs for transmission or storage, but can never be applied for accurate quantification of micro-structure from high resolution digital images.

In addition to straight image formats, Metafile formats are portable formats which can include both raster and vector information. Examples are application-independent formats such as WMF and EMEMF. The metafile format is an intermediate format. Most Windows applications open metafiles and then save them in their own native language.

The page description language refers to formats used to describe the layout of a printed page containing text, objects and images. Three examples are PostScript, PDF and PCL. Raster formats store images as bitmaps (BMP image Files).

JPEG (Joint Photographic Experts Group) is a compression method; JPEG-compressed images are usually stored in the JFIF (JPEG File Interchange Format) file format. JPEG compression is (in most cases) lossy compression. The JPEG/JFIF filename extension in DOS is JPG (other operating systems may use JPEG).

Nearly every digital camera can save images in the JPEG/JFIF format, which supports 8 bits per colour (red, green, blue) for a 24-bit total, producing relatively small files. When not too great, the compression does not noticeably detract from the image's quality, but JPEG files suffer generational degradation when repeatedly edited and saved.

Photographic images may be better stored in a lossless non-JPEG format such as a proprietary RAW image, if they will be re-edited, or if small "artefacts" (blemishes caused by the JPEG's compression algorithm) are unacceptable. The JPEG/JFIF format also is used as the image compression algorithm in many Adobe PDF files.

The TIFF (Tagged Image File Format) format is a flexible format that normally saves 8 bits or 16 bits per colour (red, green, blue) for 24-bit and 48-bit totals, respectively, usually using either the TIFF or .tif filename extension. TIFF's flexibility is both a blessing and curse, because no single reader reads every type of TIFF file. TIFFs are lossy and lossless; some offer relatively good lossless compression for bi-level (black & white) images.

Some digital cameras can save in TIFF format, using the LZW compression algorithm for lossless storage. TIFF image format is not widely supported by web browsers. TIFF remains widely accepted as a photograph file standard in the printing business. TIFF can handle device-specific colour spaces, such as the CMYK defined by a particular set of printing press inks. OCR (Optical Character Recognition) software packages commonly generate some (often monochromatic) form of TIFF image for scanned text pages.

All high resolution scanned images for automatic quantitative digital analysis of concrete micro-structures presented in this thesis are 48-24 bit Colour Uncompressed TIFF.

Raw refers to a family of raw image formats that are options available on some digital cameras. These formats usually use a lossless or nearly-lossless compression, and produce file sizes much smaller than the TIFF formats of full-size processed images from the same cameras. Although there is a standard raw image format, (ISO 12234-2, TIFF/EP), the raw formats used by most cameras are not standardised or documented, and differ among camera manufacturers, Adobe's Digital Negative (DNG) specification is an attempt at standardising a raw image format to be used by cameras, or for archival storage of image data converted from undocumented raw image formats, and is used by several niche and minority camera manufacturers including Pentax, and Leica, but not Canon.

The raw image formats of more than 230 camera models, including those from manufacturers with the largest market shares such as Canon, Nikon, Sony, and Olympus, can be converted to DNG. This format was based on ISO 12234-2, TIFF/EP also.

The BMP file format (Windows bitmap) handles graphics files within the 32-bit and 64-bit Microsoft Windows Operating Systems. Typically, BMP files are uncompressed, hence they are large; the advantage is their simplicity and wide acceptance in Windows programs. They are also ideal for quantitative digital image analysis, and Study 2 in this thesis uses 24-bit scanned colour BMP image data files, the portable pixmap (pixel map) file format (PPM).

Vector file formats can contain bitmap data as well. 3D graphic file formats are technically vector formats with pixel data texture mapping on the surface of a vector virtual object, warped to match the angle of the viewing perspective.

At some point all vector graphics must be converted in order to be able to be displayed on high resolution digital monitors. Vector images can be with analogue CRT technology used in some electronic test equipment, medical monitors, radar displays,

laser shows and older video games. Plotters are printers that use vector data rather than pixel data to draw graphics.

Image file bit depth describes the number of data bits used to represent the intensity value of a single pixel and is also known as *bits per pixel*. In other words, a file's bit depth indicates the number of separate greyscale intensity values that are allowable by the file format.

2.2.2 Hardened Concrete Air-Void Analysis with a Flatbed Scanner

Digital images have been collected from polished concrete surfaces by flat bed scanner for more than two years.

Peterson et al in 2001 reported methods to quantify air void characteristics. The surface was scanned three times. Between the first and second scans, the surface was stained with phenolphthalein to colour the cement paste pink. Then between the second and third scans, the surface was painted black, and white powder pressed into depressions left by air voids.

These images collected from the three scans were aligned and classified to yield an output image. Each pixel in the output image was categorized as air void, cement paste, or aggregate. By digitally applying a grid of points and a series of lines to the output image, a modified point count was automatically performed according to ASTM C457, the standard test method for microscopic determination of parameters of the air void system in hardened concrete.

A comparison was made by the results obtained by the automatic analysis and results obtained by a manual analysis of the surface with an optical microscope.

Peterson et al 2009 also reported several automated procedures for the characterisation of the air-void system of hardened concrete rely on a contrast enhancement step to make air-voids appear white and aggregates and paste appear black. Pixels in the digital image darker than a selected threshold level are classified as non-air and pixels brighter are classified as air. Laboratories that perform air-void testing typically have a large number of samples with corresponding results from manual operators. Supporters of automated methods often take advantage of this fact by analysing the same samples and then comparing results. A similar approach is described where scanned images

collected from a significant number of samples are analysed and the threshold optimised to best approximate the results of the manual operator.

Errors of up to 20% were commonly reported. This thesis will attempt to explain why.

The first source of error was the optical resolution of the image, and the second was the limitations of 32-bit image analysis software to accurately resolve perimeters of fine air voids, and particles, and thus overestimating volumes and percentages.

64-bit ImageJ analysis software operating in 64-bit Windows has greatly removed the 2 GB image file limitations to high resolution quantitative analysis, unable to be resolved in 32-bit image analysis software.

2.2.3 RapidAir 457 Automatic System for Analysing Air Void Content of Hardened Concrete

Ramezaniapour 2010 reported the air-void analysis of hardened concrete is typically performed according to ASTM C457–09 [“Standard Test Method for Microscopical Determination of Parameters of Air-Void System in Hardened Concrete, “ *Annual Book of ASTM Standards*, Vol. 4.2, ASTM International, West Conshohocken, PA], which can be tedious to perform and is operator subjective. Several alternative automated methods have been proposed, two of which are the Rapid Air 457 and the scanner method developed at Michigan Technological University (details in Appendix).

In each of these methods, images are collected from contrast enhanced surfaces of polished concrete, and image analysis is performed to calculate air-void system parameters. In this research, 22 concrete samples were examined using these two methods, the air-void system parameters were compared to those obtained from the

ASTM C457 standard, and the precision of the results was compared to the recommendations of ASTM standard. It was concluded that the total air content and the spacing factor of the air voids measured by Rapid Air 457 and the scanner method were comparable to the air content and the spacing factor measured according to the standard manual method.

Considering the fact that the automated image systems could detect air voids smaller in diameter than those typically seen by an operator, it was found that if these small air voids are counted, calculated spacing factors are smaller than those calculated by the manual method. If small diameter air voids are removed from the analysis, then spacing factors agree fairly well with those calculated by ASTM C457 from stereo-optical microscope.

Jakobsen et al 2005 reported the RapidAir is an automatic system for analysing the air void content of hardened concrete. The analysis requires polishing of the concrete surface as described in ASTM C 457 as well as a contrast enhancement of the surface. The system can automatically analyse the air void system according to the ASTM C 457 and EN 480-11 standards.

The sample preparation includes contrast enhancement steps ensuring white air voids in black concrete (aggregate and paste). For a well-lapped sample of good quality concrete the contrast enhancement procedure requires approximately 5–10 min to perform. The air content can be analysed in less than 15 min traversing 241.3 mm (9.5 in.) — a significant improvement compared to several hours normally required to perform a manual linear traverse analysis.

This paper describes the method and technique required for automatic analysis using the RapidAir system as well as data from a Round Robin study. Three samples were circulated to seven different laboratories for automatic air void analysis. Prior to the automatic analysis the samples were analysed manually using linear traverse and point counting methods. The results of the Round Robin study showed very good

repeatability and reproducibility of the RapidAir system but large variations when using manually performed analysis.

A prototype RapidAir system was already developed in the early 1990s. This system, which was DOS software based, was at that time used at three laboratories. Technically much advancement has been made since the early 1990s and in 2002 new and updated Windows software based RapidAir system was developed with new hardware. Today RapidAir systems are present at companies and universities across the world. Of these places seven laboratories agreed to be part of the present Round Robin air void analysis study.

Three samples were lapped by one laboratory and send out for air void analysis following ASTM C 457. The first 2 laboratories did modify point count and linear traverse analysis directly on the lapped concrete surface. After finishing linear traverse at the second laboratory the samples were coloured black (ink) and white powder (BaSO_4) was filled into the voids. The samples were then analysed using the automatic system and shipped to the other laboratories participating in the test.

This test was initiated mainly to test the repeatability and reproducibility of automatic air void analysis using the automatic system as well as to compare these data to manually obtained results. Lately the manual test methods, modified point count and linear traverse according to ASTM C 457 have been the subject to many discussions. The manual methods are very time consuming and judgement calls are involved. There is a need for new methods to perform these analyses and therefore the commercially available RapidAir system was chosen for this Round Robin study of automatic analysis.

The RapidAir system has been validated in an international Round Robin study. Seven laboratories used their RapidAir system for automatic analysis of the air void system in hardened concrete according to ASTM C 457 on the same samples. Prior to the automatic analysis the samples were analysed manually by two of the laboratories.

The results showed a very good reproducibility and repeatability of the automatic system. Even though not many manually performed analyses were performed during this test it is clear that the data shows a much higher variation than when compared to the automatic analysis performed using the RapidAir system. The automatic analysis is much faster than the manual analysis and takes 15 min or less to perform.

The original RapidAir system, as described by Peterson, Karl W., scanned in 3175 ppi image 8-bit greyscale and collected with a Microtech Scan Maker S400 flatbed scanner connected to a PC (1.73 GHz, 2 GB Ram, 32-bit Windows XP). The automatic image correction and filtering options in the Microtech Scan Wizard 5 software were deactivated. The scan time was 10 minutes per sample.

System used for this thesis was as follows:

Purpose built PC - Intel(R) Quad Core i7 CPU, 3.33 GHz, 12 GB DD3 RAM,
64-bit operation system Windows Vista Ultimate, 4x2 TB HDD.

2.3 Vickers Micro Hardness

Glinicki et al 2004 described an application of a depth-sensing indentation (DSI) system to characterise properties of hardened cement paste. The test method developed, based on the microhardness testing concept, was implemented on a universal testing frame. Preliminary experiments were dedicated to evaluate efficiency of mineral additives in cement paste from Vickers hardness data.

A suitable method of specimen preparation for microhardness tests was elaborated and successfully applied. The investigation revealed a clearly linear correlation between Vickers hardness and water-to-cement (w/c) ratio. An evaluation of the efficiency of mineral additives in cement paste was possible assuming a criterion of equal Vickers hardness.

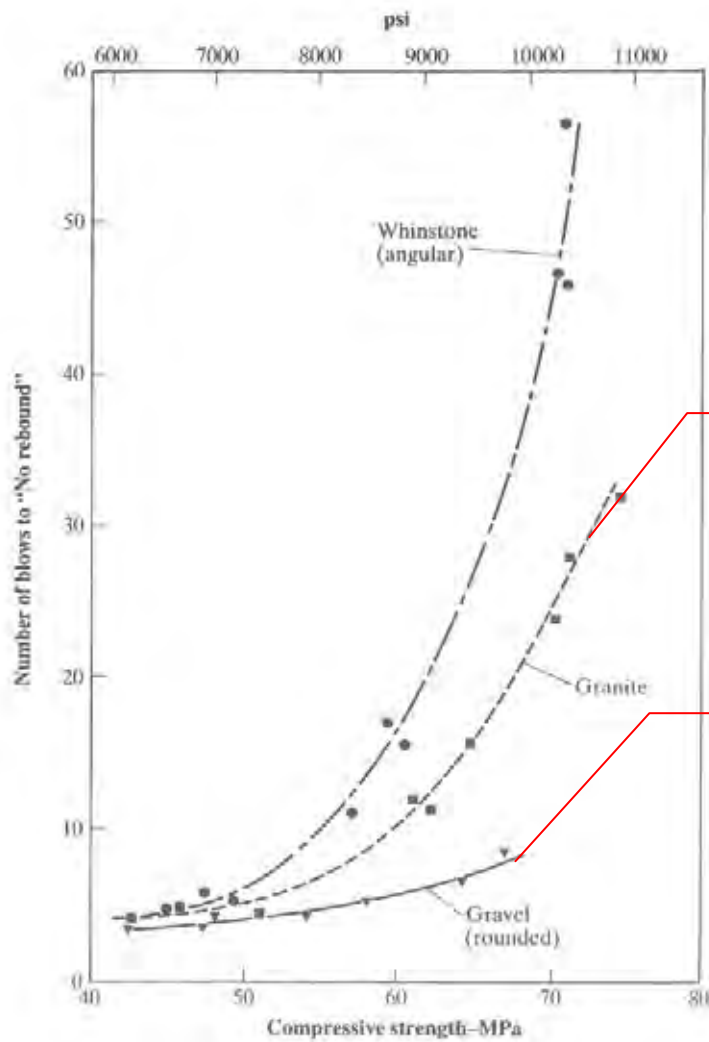
The DSI test method seems to be a valuable method for studying the bulk properties of cementitious composites (concretes). This means there is a linear relationship between micro-hardness in the cement matrix and compressive strength of the concrete mix, and this helped quantify differences in microstructure and hardness and durability.

Other researchers including Kim et al 1987, reported from experimental studies of the influence of mixing and casting techniques and of curing time upon the compressive strength and hardness of methyl methacrylate based polymer concrete.

The Rockwell K and F scales were found to be suitable for the hardness determinations. Over a wide range of hardness and strength values, the average compressive strength (f_c) varied linearly with the average hardness (R_K) according to the relation $f_c \text{ (psi)} = 560 R_K - 12000$, irrespective of casting and curing variables. The weaker materials exhibited greater variations in hardness. Hardness testing was found to provide a meaningful and convenient method for evaluating the quality of polymer concrete.

These researchers have confirmed my observation of a direct relationship between Vickers micro-hardness and the strength in cement paste within concrete samples under test. Hardness, however, cannot be considered to be a fundamental material property, instead, it represents an arbitrary quantity used to provide a relative idea of material properties, Meyers et al 1999. This however still can be related to the perceived compressive strength of the mix, and related directly to the unknown water/cement ratio.

Figure 2.3.1 on the following page shows that the relation between impact strength and compressive strength depends upon the type of coarse aggregate.



Note: related to comparative core sample Dar (blue metal aggregate).

Note: related to my forensic study core samples 1 to 4 (rounded river aggregate).

Figure 2.3.1 Relation between compressive strength and number of blows to 'no-rebound' from concrete made with different aggregates and ordinary Portland (Type I) cement (H. Green, 1964)

For the same compressive strength, impact strength is greater for concrete made with coarse aggregate of greater angularity and surface roughness, a feature which suggests that impact strength of concrete is more closely related to its flexural strength than to the compressive strength. Concrete made with a river gravel coarse aggregate has low impact strength owing to the weaker bond between mortar and coarse aggregate. A smaller maximum size of aggregate significantly improves the impact strength; so does the use of aggregate with a low modulus of elasticity and low Poisson's ratio.

3 EXPERIMENTAL PROCEDURES

Introduction

Seven concrete cores samples of ~ 95 mm diameter and 155 - 200 mm length were provided by Mr. Jim Griffiths of James Griffiths Consulting Structural Engineer Pty. Ltd. These original concrete core samples were labelled:

1 (Figure 3.1)

2 (Figure 3.2)

3 (Figure 3.3)

4 (Figure 3.4)

5 (Figure 3.5)

RM (Figure 3.6)

DAR (Figure 3.7)

It was requested that the samples be examined for the presence of cracks, porosity, aggregate, bulk density etc, in the vicinity of the (cut) notch on the top surface of the cores. Core 5 was a reference sample that did not have a notch, and therefore was not core drilled from across a controlled shrinkage joint.

No other information was provided.

The cores had been cut from the control cracking joints, from different areas of a new warehouse concrete floor. All the cores were initially visually observed for variations in consistency and quality.

Six months into the study, two more samples of concrete cores were supplied for additional testing and interest. These were higher in strength, and of differing micro-structures.

The additional two concrete cores were labelled:

FI (Figure 3.8)

FII (Figure 3.9)

It was decided quite early by my supervising Professor Chris Sorrell to forensically test all the cores for:

- Bulk density and apparent porosity;
- Micro-structural examination and micro-cracking (X- ray micro-tomography);
- Macro-structural percentage of aggregate and air-voids (32-bit digital analysis software);
- Quantitative micro-structural percentage of aggregate and air voids (64-bit digital analysis software);
- Develop an automated quantitative digital analysis of all received concrete micro-structures;
- To forensically compare quantitative test results from cores 1-5;
- Optical microscopy;
- Micro Vickers hardness of the cement bond;
- Arrive at likely causes of concrete damage from quantitative test evidence, establish liability, avoid court litigation, and repair estimated \$200,000 of degraded new concrete warehouse floor surface;
- The experimental forensic procedures remained flexible, and continued, until sufficient evidence was obtained from experimental and digital analysis data, quantitatively and unconditionally differentiated, all sample micro-structures under examination.

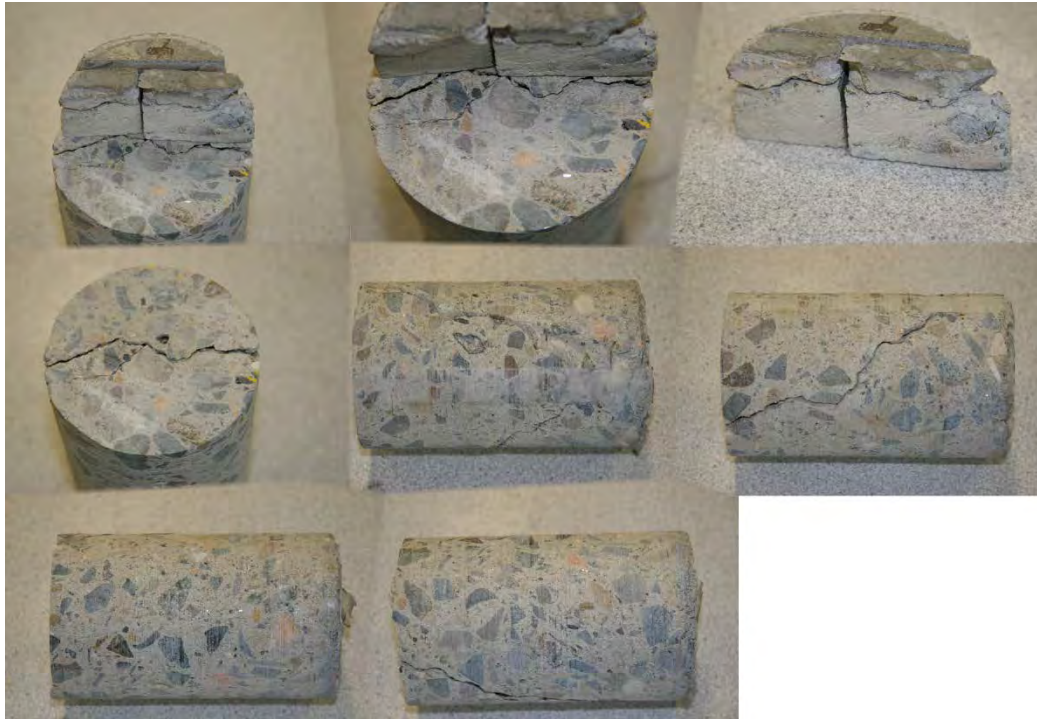


Figure 3.1 Original Concrete Core 1



Figure 3.2 Original Concrete Core 2



Figure 3.3 Original Concrete Core 3



Figure 3.4 Original Concrete Core 4



Figure 3.5 Original Concrete Core 5

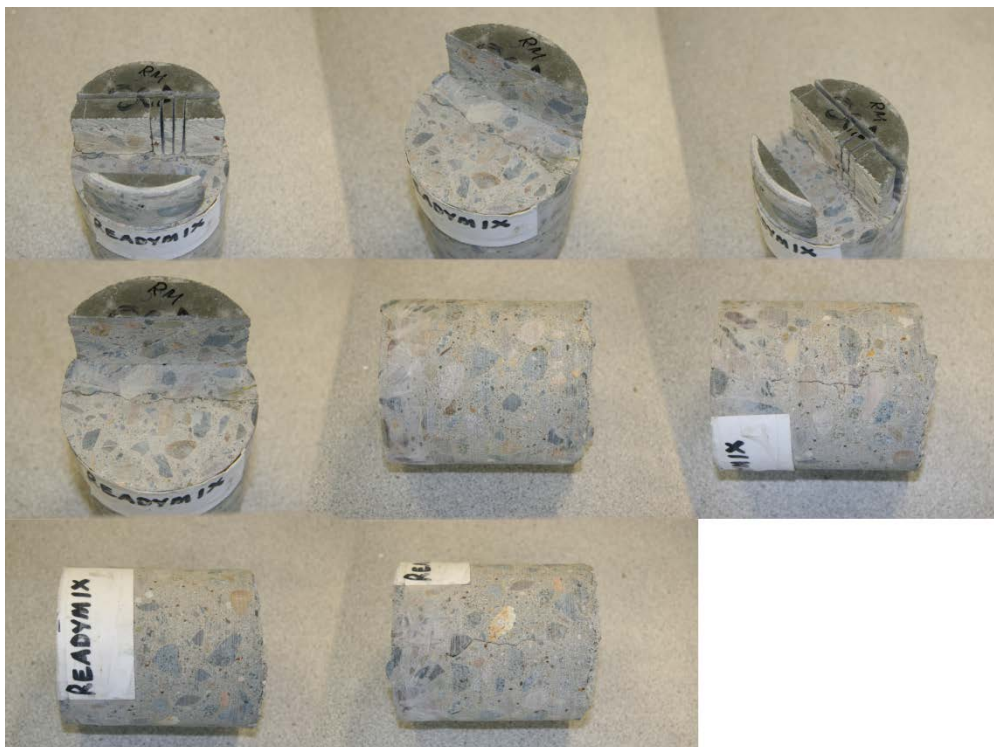


Figure 3.6 Original Concrete Core Rm (Readymix)



Figure 3.7 Original Concrete Core Dar (Western Suburbs)



Figure 3.8 Concrete Core FI (Freedom I)



Figure 3.9 Concrete Core FII (Freedom II)

3.1 Bulk Density and Apparent Porosity

Preparation

The cores were carefully sectioned by hand using a diamond saw. The samples were cut into 6 to 10 blocks of approximate dimensions 35 mm x 15 mm x 5 mm.

Testing

All cut blocks of the seven original samples were tested according to *Australian Standard AS 1774.5 - 2001. Refractories and Refractory Materials - Physical Test Methods. Method 5: The Determination of Density; Porosity and Water Absorption.*

The boiling water method was used.

3.2 Skyscan X-Ray Microtomograph Examination

Introduction

It became vital to X-Ray examine the internal structure of the hardened concrete core samples, associated with the slab surface and the notch, to find out, amongst other things, the degree of damage, the apparent integrity of the mix, the air void structures, micro-cracking and paste aggregate laminations. Cavities in the hardened cement paste can be produced by either the physical mixing process, or air entraining mixtures. When these air voids are produced by physical mixing they are termed entrapped, while voids created by admixtures are termed entrained.

Because entrained air voids tend to be spherical in shape, and almost always less than one millimetre, while entrapped air voids have very irregular shapes, and larger than one millimetre, vital comparative forensic micro-structural information between samples could be determined.

The samples were examined using a Skyscan X-Ray Microtomograph, Model 1072 Micro CT (Figure 3.2.3). This unit was operated at 83 kV and 106 μ A (list of operating parameters in Table 3.2.1), and the total exposure time, involved four exposures of 10 seconds length. This unit produces detailed 2D X-radiograph images, when the samples are examined in the static condition. The maximum sample height that could be accommodated in the unit was 35 mm.

The images were saved in 16-bit TIFF and digital resolution of 1670 ppi and the pixel size (precision) of the result images was 15.19 μ m.

The cores were carefully sectioned held in a jig using a diamond saw. The samples were cut into blocks of approximate dimensions 35 mm x 15 mm x 5 mm. Almost all

samples were cut in such a way that the large face was parallel to the notch direction. In a few cases, the cut was perpendicular to the notch owing to the fragility of the concrete. These samples of variable cut orientation were not initially differentiated, as the initial analysis was to look at general micro-structure and micro-cracking, and not specifically at the cross-section, perpendicular to suspected impact stresses.

All samples, dimensions approximately of 35mm x 15mm faces, were wet diamond lapped.

3.2.1 Variable (Random) Cuts

Six blocks were cut from all samples with the exception of reference sample 5, of which there were ten blocks cut.

A full second set of new sample testing was carried out using the Skyscan X-Ray Microtomograph, Model 1072 Micro CT, setup to the same operating parameters as previously, for quantitative comparison of images.

The digital X-Ray images were processed three times using Corel Paint Shop Pro 9 software to achieve optimal phase contrast between solid matrix and cracks.

Figure 3.2.1 shows the whole sample cut 1-1. The 1-1A is an X-Ray image of the bottom section of 1-1. The 1-1B is an X-Ray image of the top section of 1-1.

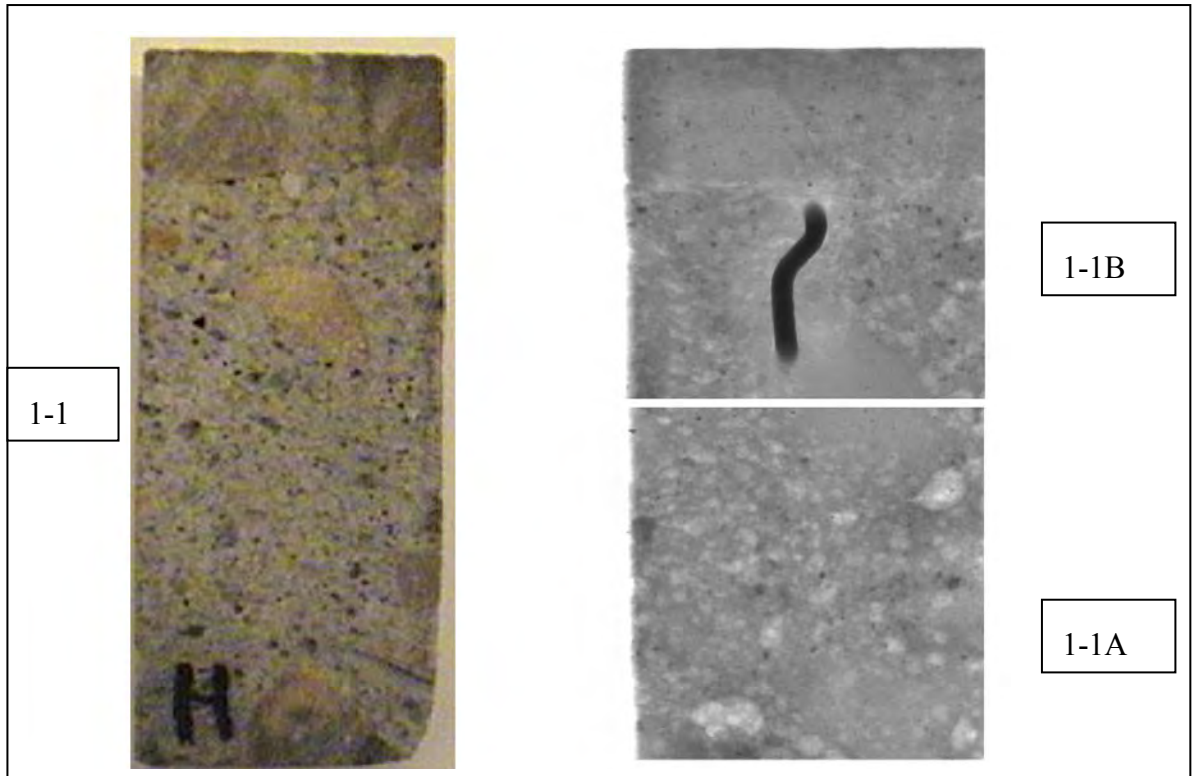


Figure 3.2.1 Digital Image of concrete sample and associated X-Ray micro CT scans

3.2.2 Perpendicular Cuts

Following the initial success of the analysis of random cut micro-structures, it was decided that a further detailed examination of the cut blocks perpendicular to the groove should reveal or not, evidence of stress and fracture damage from the most informative orientation. Consequently, between two to six blocks were cut from each sample in this orientation. The number of cuts (two to six) and size (35 mm x 12 mm x 5 mm) were limited by the amount of core material left, associated with the damaged surface and groove.

The digital images were processed, as previously, three times using Corel Paint Shop Pro 9 software in order to enhance and achieve the optimal phase contrast between the solid matrix and cracks. Even so, the, X-ray scan resolution of 15.2 microns still

produced a rather fuzzy image of the micro-structural detail through the 5mm sample thickness.

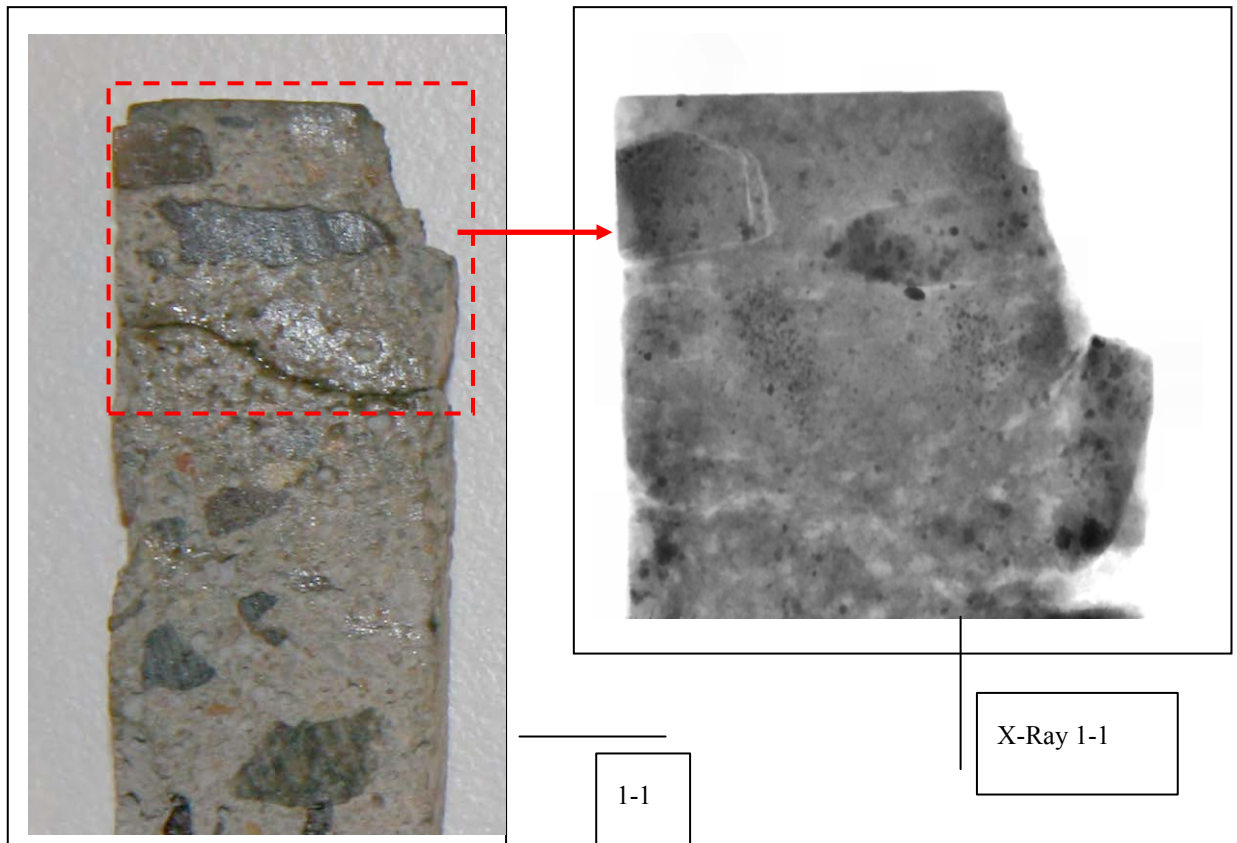


Figure 3.2.2 Detail of Perpendicular cut sample from Concrete Core Sample 1-1 with its X-Ray Micro CT image

Figure 3.2.2 is shown with an explanation where 1-1 is a perpendicular cut Sample 1 from Concrete Core 1, and the right hand side of the image shows the damaged groove.

(In fact, all x-ray images show the top as the floor surface of the concrete slab, and the right hand side is always the cut and or damaged groove).

Perpendicular cuts of all samples 1 to 5, Rm, Dar and FI and FII with their X-Ray images will be presented in this format, with larger x-ray images, for more detailed examination, and explanation, in the experimental results.



Figure 3.2.3 Skyscan X-Ray Microtomograph 1072 Micro CT (sample loaded)



Figure 3.2.4 Close up of sample 2-3 loaded and held in static mode for 2D analysis

SKYSCAN X-Ray MICROTOMOGRAPH

1072 Micro CT

Operating Parameters

X-Ray:	83 kV, 106 μ A
Magnification:	18x
Pixel:	15.19 μ
Rotation:	360 ° (not used)
Rotation Step:	0.45 ° (not used)
Exposure:	10sec
Gain:	1.0
Averaging:	by 4 frames
Random movement:	20
Filter:	A1 1mm

Table 3.2.1 Operating Parameters of Skyscan X-Ray Microtomograph



Figure 3.2.5 Sample 2-6 under X-Ray CT Scan (note: red light on: X-Rays ON)

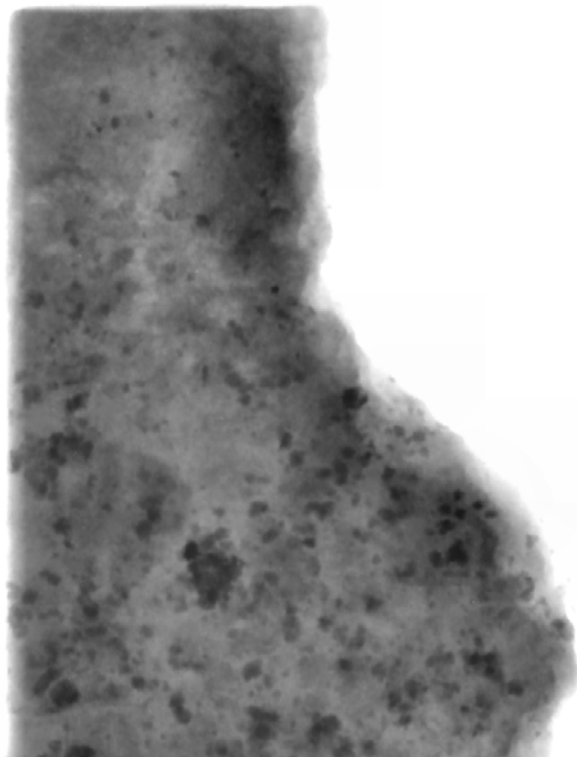


Figure 3.2.6 Detail of sample 2-6 scanned (displayed on the computer screen)

3.3 Digital Analysis

Introduction

The ultimate goal of the following digital analyses studies was to create an accurate and fast procedure for automated 100% quantitative 2D calculations of air-void porosity and coarse aggregate.

The digital analysis was completed for this project in three extensive studies in four different true optical resolutions which amounted to more than 200 completed digital analyses. Each one of them was repeated many times to guarantee the correct and accurate quantitative results (amounting to over 1000 image analyses calculations).

What is presented here is a summary of this vast amount of work. It was done to guarantee my quantitative results for the concrete core Samples analysed.

The reason why this project extended into three studies was the fact, that in the beginning the images were in an unsuitable format for quantitative analyses (images were digital photographs only in JPEG format taken with the digital camera Canon EOS 20D, 8.2 Megapixels).

In the first study (**3.3.1 Study 1**) JPEG images were processed in Adobe Photoshop Elements 2.0, then analysed in ImageJ 32-bit version and the PC ran the Windows Operating system XP 32-bit and Microsoft Excel version 2007.

Details of the pictures taken by the camera were:

Resolution	72 ppi (352.7 μ pixel size)
Dimensions	3504 x 2336 pixels
Bit depth	24-bit colour
Format	compressed in JPEG (no other format available in the camera software)
Size	varied between 5.16 MB to 6.06 MB.

Table 3.3.1 72 ppi data 24-bit colour

In the second study (**3.3.2 Study 2**) the Samples were scanned on a typical office type scanner, the Hewlett Packard ScanJet 5400C with maximum of 2400 ppi true optical resolution with HP precision scan Pro 3.1 software and then transferred to the PC which ran a 64-bit Windows Vista operating system. Images were processed in Adobe Photoshop Elements 2.0, then analysed in ImageJ 32-bit version and Microsoft Excel version 2007.

Details of the images taken by the scanner Hewlett Packard were:

Resolution	2400 ppi (10.58 μ pixel size)
Dimensions	9328 x 9800 pixels
Bit depth	24-bit colour
Format	bitmap in BMP
Size	varied between 250MB to 271 MB

Table 3.3.2 2400 ppi data 24-bit colour

In the third study (**3.3.3 Study 3**) the Samples were scanned on a specialised and highly accurate scanner, the Epson Perfection V700 Photo scanner with 6400 ppi true optical resolution, 48-bit colour depth, with the help of the programme SilverFast 6.6 1r2b. Images were then transferred to a PC running Windows Vista 64-bit operating system. Images were processed in 64-bit Adobe Photoshop Elements 7.0, then analysed in 64-bit ImageJ version 1.44c, and calculated in Microsoft Excel 2007 version and 64-bit Microsoft Excel 2010.

Details of the images taken by the scanner Epson Perfection V700 were:

Resolution	4800 ppi (5.29 μ pixel size)
Dimensions	18856 x 18968 pixels (4800 ppi colour)
Bit depth	24 bit colour
Format	uncompressed in TIFF
Size	1 GB

Table 3.3.3 4800 ppi data 24-bit colour

Resolution	6400 ppi (3.97 μ pixel size)
Dimensions	25142 x 25292 pixels (6400 ppi greyscale)
Bit depth	8 bit greyscale
Format	uncompressed in TIFF
Size	< 1 GB

Table 3.3.4 6400 ppi data 8-bit greyscale

Resolution	6400 ppi (3.97 μ pixel size)
Dimensions	25142 x 25292 pixels (6400 ppi colour)
Bit depth	24 bit colour
Format	uncompressed in TIFF
Size	1.78 GB

Table 3.3.5 6400 ppi data 24-bit colour

Resolution	6400 ppi (3.97 μ pixel size)
Dimensions	25142 x 25292 pixels (6400 ppi colour)
Bit depth	48 bit colour
Format	uncompressed in TIFF
Size	3.48 GB

Table 3.3.6 6400 ppi data 48-bit colour

Most flat bed scanners can computer extrapolate apparent increases in scanner resolution, however this operation only increases the image size, but does nothing to the original pixel size resolution for analysis.

ImageJ programme is a public domain shareware, inspired by NIH Image public domain for Macintosh, was used for all digital analyses. The ImageJ shareware is a powerful image processing programme, originally in 32-bit version and now available in 64-bit version.

Image analysis software typically uses 8 bits per component which gives 256 possible values. In a black and white image there is one component per pixel which is the **brightness**. Number 0 indicates black, number 255 indicates white and all in between values represent different shades of grey. To convert a colour pixel to black and white pixel involves a simple process of computing the average value of the red, green and blue components.

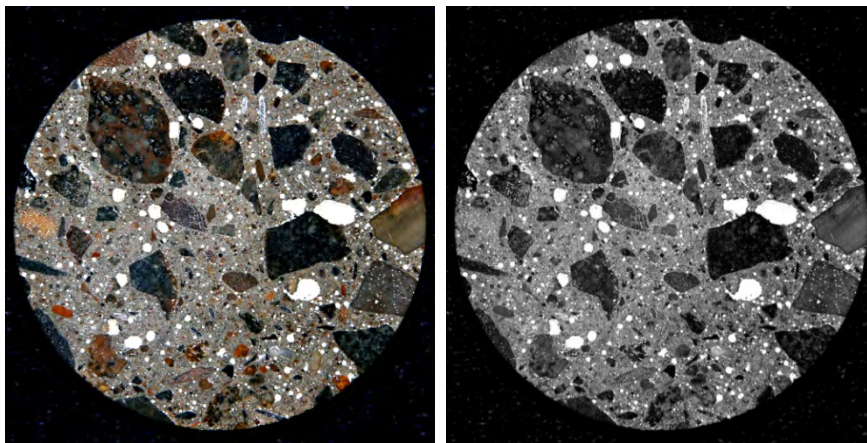


Figure 3.3.1 Original 24-bit colour picture taken by a digital camera and its greyscale conversion

Computerised images are made up of pixels, which are small squares of digital information with a colour value. A pixel is generally thought of as the smallest single component of a digital image.

The word pixel is an abbreviation of the expression 'picture element'. The images in image-editing programmes are known as bitmap images (or raster images).



Figure 3.3.2 Pixels are normally arranged in a regular 2-dimensional grid, and are often represented using **squares** (as shown), dots, or rectangles

In a colour image each pixel has 3 components which are the amount of Red, Green and Blue (RGB = **R**ed, **B**lue and **G**reen) light. Pixels have no inherent size because their sizes will depend on the resolution of the image. (For example UGA screen in high-resolution mode consists of 1600 x 1200 which equals 1,920,000 pixels.)

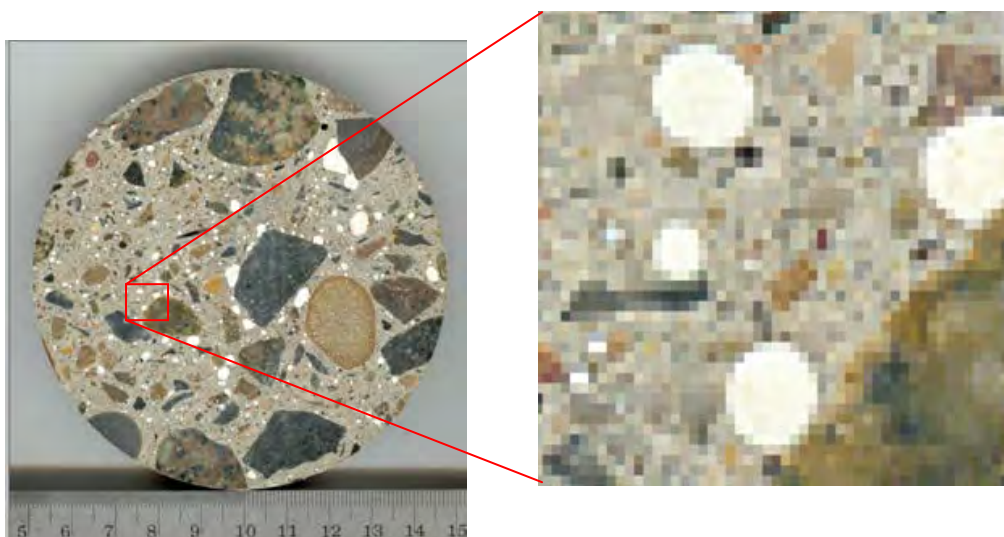


Figure 3.3.3 2400ppi image with a detail of pixels showing here in a format of squares after a large magnification

Image analysis software typically uses 8 bits per component which gives 256 possible values. In a black and white image there is one component per pixel which is the **brightness**. Number 0 indicates black, number 255 indicates white and all in between values represent different shades of grey. To convert a colour pixel to a black and white pixel the average value of the red, green and blue components is calculated.

ImageJ is a public domain shareware, inspired by NIH Image public domain for Macintosh. The ImageJ shareware is a very powerful image processing programme.

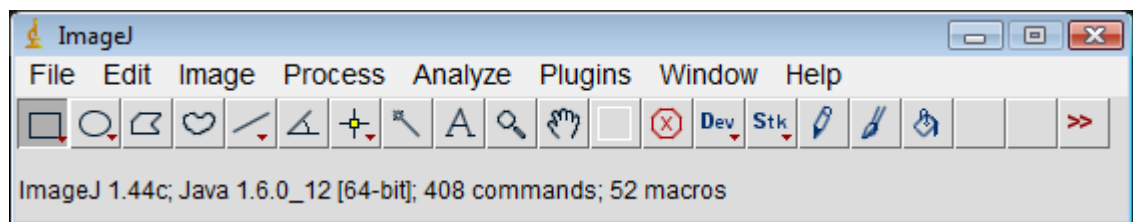


Figure 3.3.4 64-bit ImageJ programme

The 64-bit ImageJ programme required 10 GB of DDR3 RAM which was the minimum memory needed for analysis of large images (1GB).

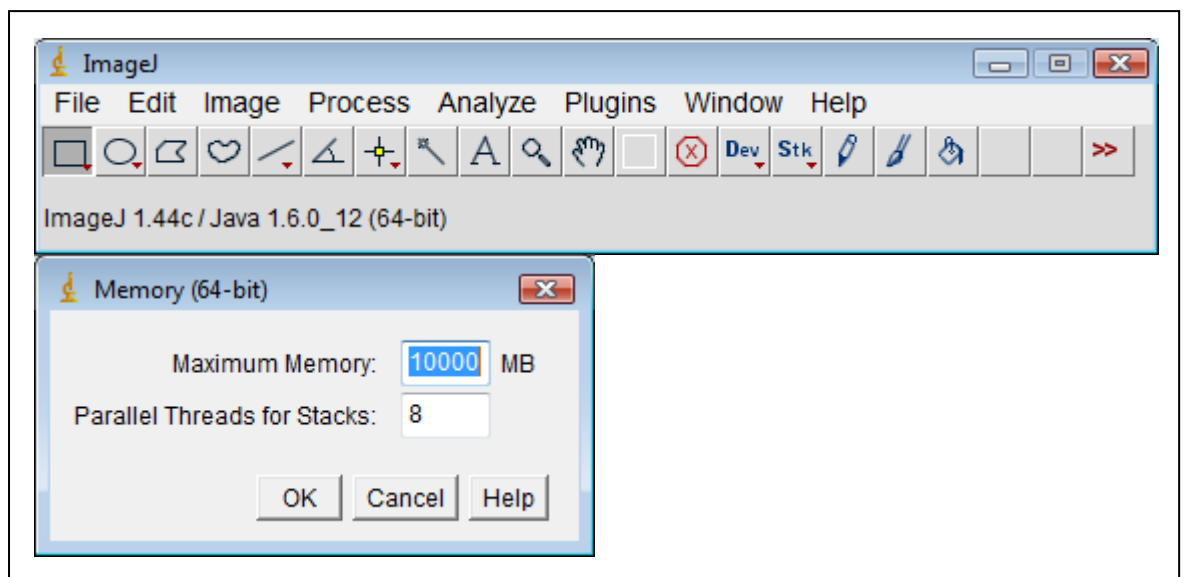
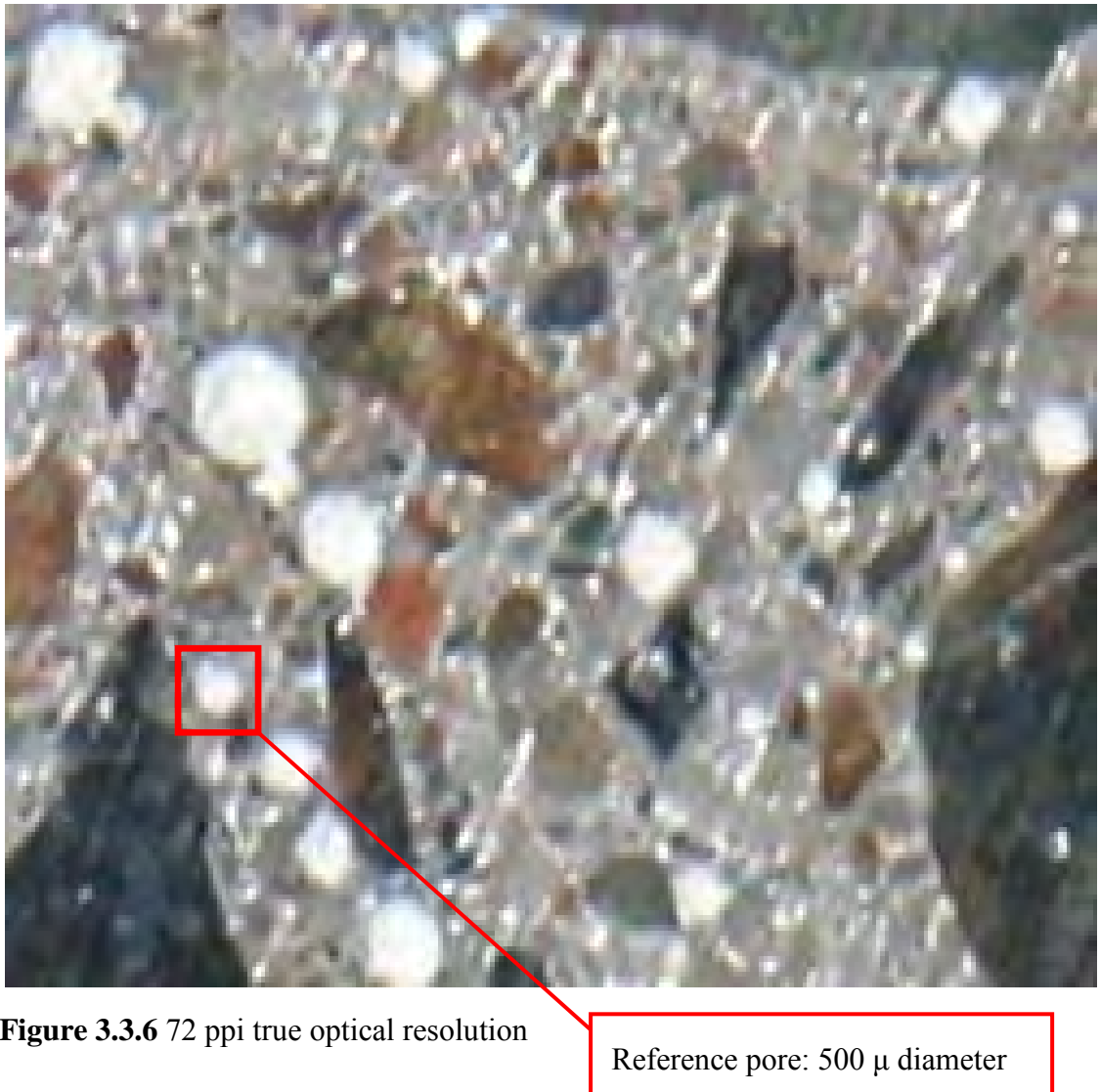


Figure 3.3.5 ImageJ memory adjustment

Surface Micro Finish - Study 1



160 μ coarse diamond surface ground - magnified to 300% 72 ppi true optical resolution in 24-bit colour JPEG format (displaying $\sim 100 \text{ mm}^2$).

Coarse diamond surface grinding produced micro grooves and fine aggregate and sand pullouts. These filled with porcelain epoxy resin and were counted as pores in Study 1.

This is one of the reasons why such high percentage porosities were obtained.

Surface Micro Finish - Study 2



Figure 3.3.7 2400 ppi true optical resolution

Reference pore: 500 μ diameter

Coarse/fine diamond surface ground - magnified to 100% 2400 ppi true optical resolution in 24-bit colour BMP format (displaying $\sim 100 \text{ mm}^2$).

Surface Micro Finish - Study 3



Figure 3.3.8 4800 ppi true optical resolution

Reference pore: 500 μ diameter

Fine diamond surface ground - magnified to 50% 4800 ppi true optical resolution in 24-bit colour TIFF format (displaying $\sim 100 \text{ mm}^2$).

Surface Micro Finish



Figure 3.3.9 6400 ppi true optical resolution

Reference pore: 500 μ diameter

Fine diamond surface ground and fine diamond lapped - magnified to 25% 6400 ppi true optical resolution in 48-bit HDR colour TIFF format (note the perfect image for 100% auto quantitative digital analysis) (displaying $\sim 100 \text{ mm}^2$).

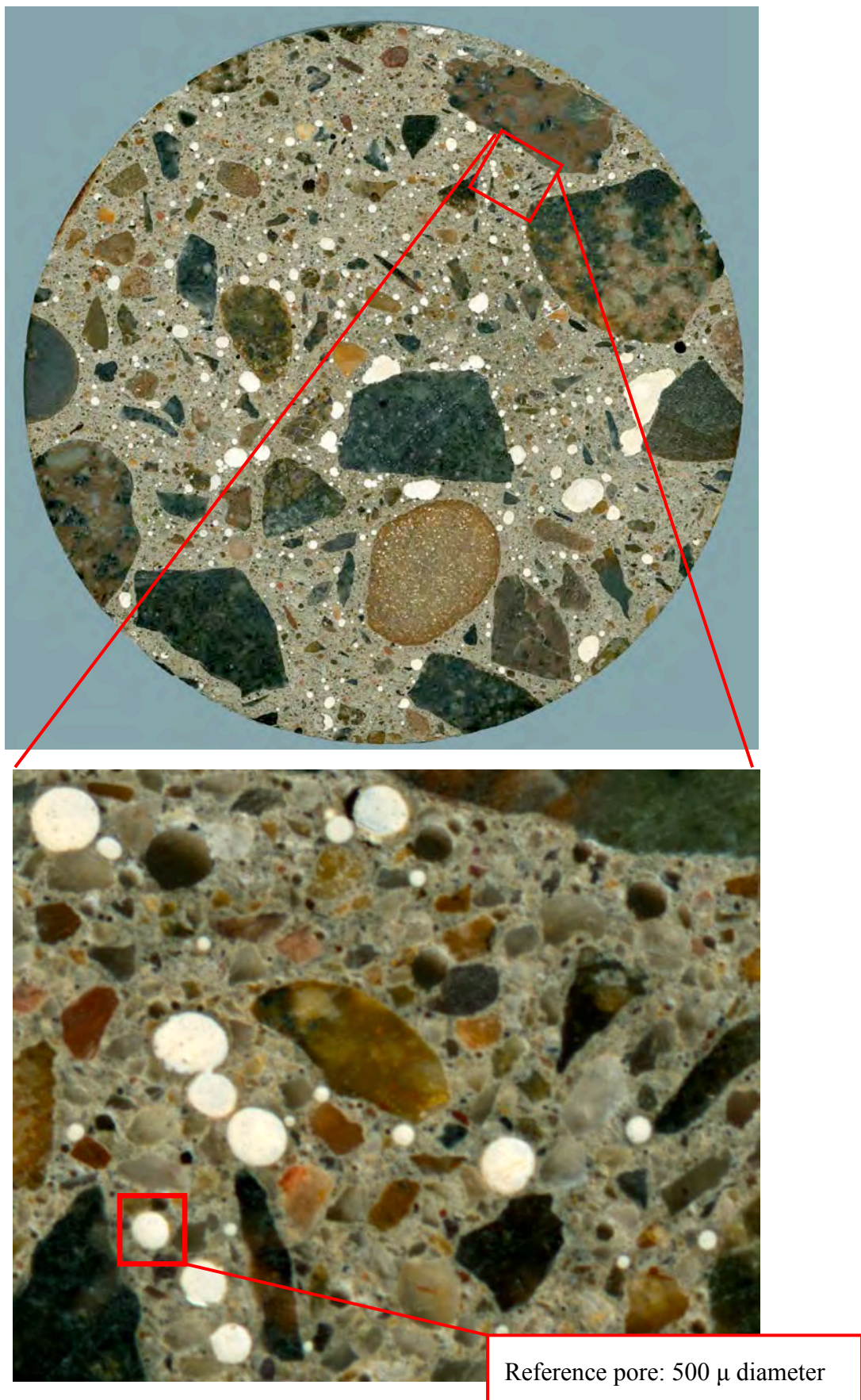


Figure 3.3.10 Position of the selected area in Figures 3.3.6.to 3.3.9

Figure 3.3.11 shows Sample 5B real size of 9.55 cm x 9.53 cm with grid and ruler in 64-bit PhotoShop Elements 7.0, each square on the grid is 5 mm x 5 mm.



Figure 3.3.11 Image 5B with grid and ruler

3.3.1 Study 1 - 72ppi Digital Analysis with 32-Bit ImageJ

The Samples were coarsely diamond ground and then filled with white porcelain epoxy. Then the Samples were diamond ground again.

The digital photographs of all the Samples were taken with the digital camera Canon EOS 20D, 8.2 Megapixels and then transferred to the PC for the analysis.



Figure 3.3.1.1 Canon EOS 20D camera

Resolution	72 ppi (352.7μ) true optical pixel resolution of the image
Dimensions	2336 x 2336 pixels = 5.46 Megapixels
Bit depth	24-bit colour
Format	compressed in JPEG (no other format available in the camera software)
Size	varied between 5.16 MB to 6.06 MB.

Table 3.3.1.1 72 ppi data 24-bit colour

In the first study images were processed in Adobe Photoshop Elements 2.0, then analysed in ImageJ 32-bit version and a PC ran the Windows Operating system XP 32-bit and Microsoft Excel version 2007.

Data Files Prepared For Image Analysis



Figure 3.3.1.2 Sample 1A



Figure 3.3.1.3 Sample 1B

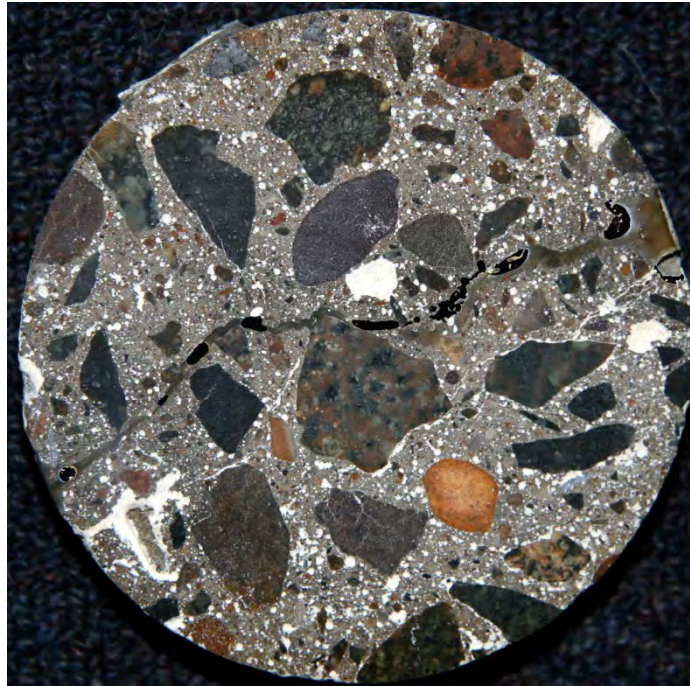


Figure 3.3.1.4 Sample 1C



Figure 3.3.1.5 Sample 1D



Figure 3.3.1.6 Sample 2A



Figure 3.3.1.7 Sample 2B



Figure 3.3.1.8 Sample 3A

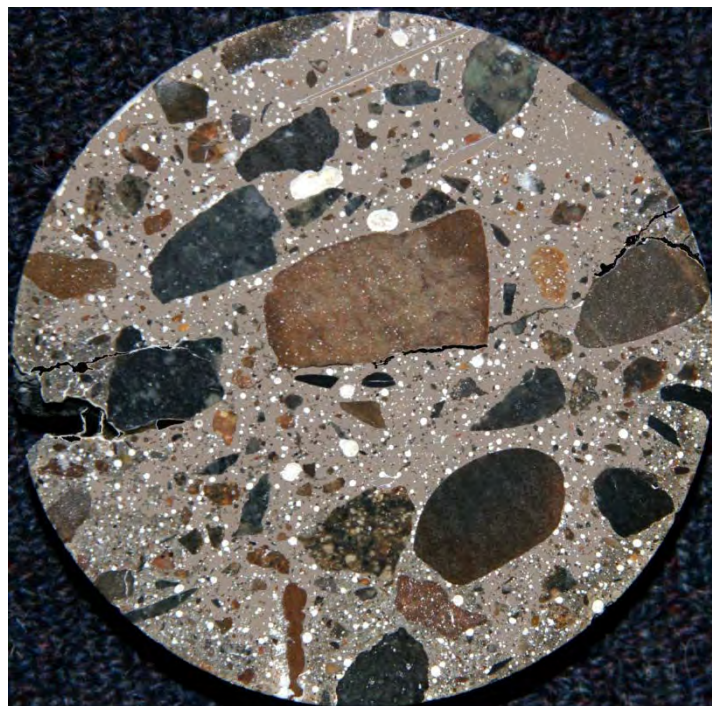


Figure 3.3.1.9 Sample 3B



Figure 3.3.1.10 Sample 4A



Figure 3.3.1.11 Sample 4B

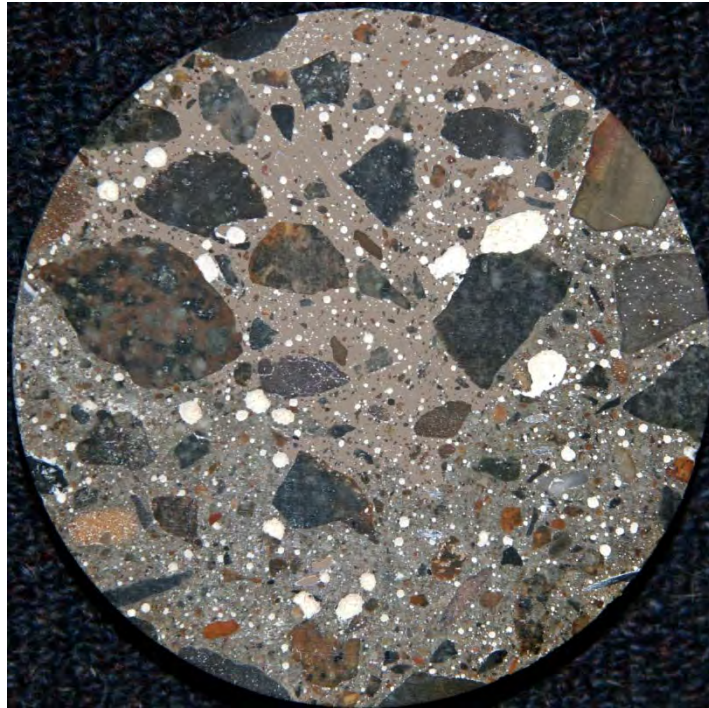


Figure 3.3.1.12 Sample 5A



Figure 3.3.1.13 Sample 5B



Figure 3.3.1.14 Sample RmA



Figure 3.3.1.15 Sample RmB

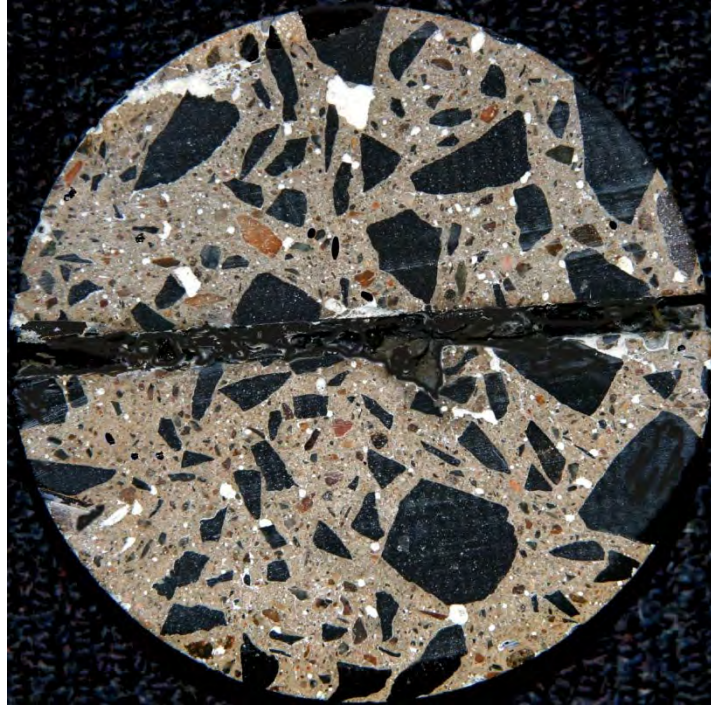


Figure 3.3.1.16 Sample DarA (note the notch for control cracking)



Figure 3.3.1.17 Sample DarB

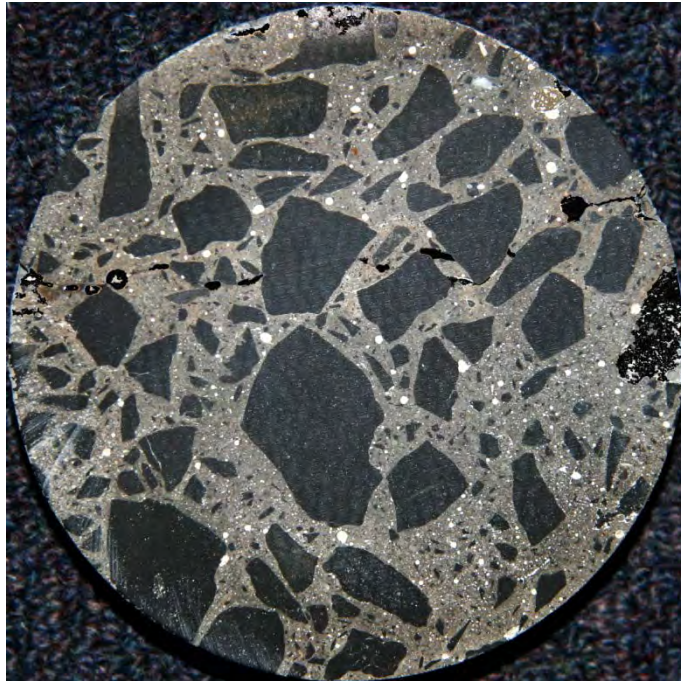


Figure 3.3.1.18 Sample FIA

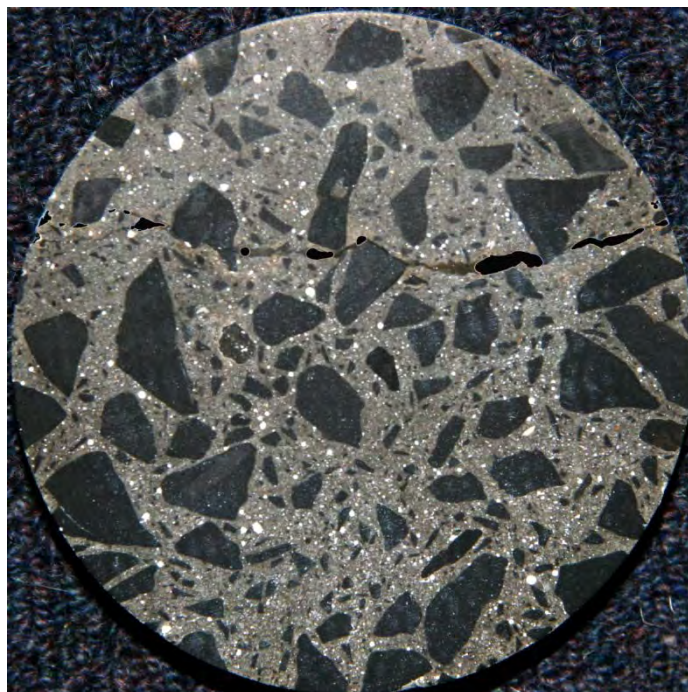


Figure 3.3.1.19 Sample FIB



Figure 3.3.1.20 Sample FIHA

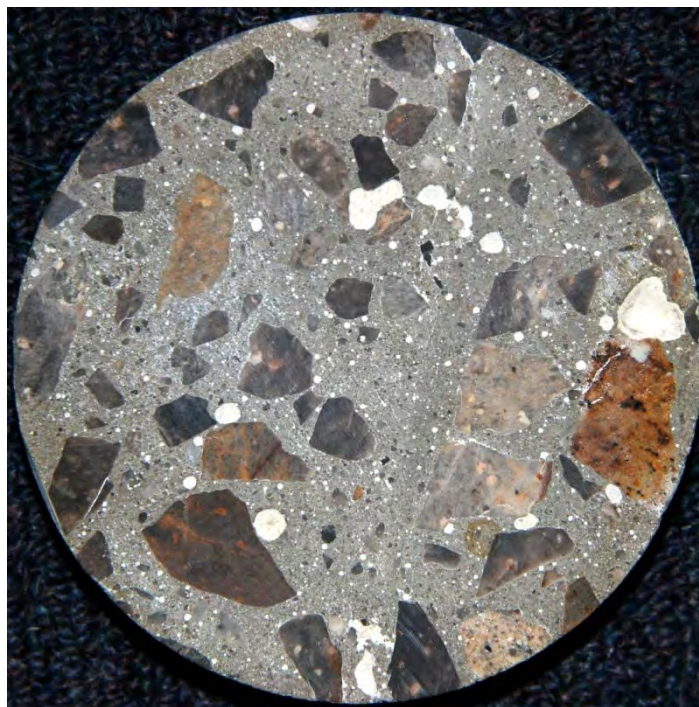


Figure 3.3.1.21 Sample FIIB

3.3.1.1 Study 1 - A Procedure for Calculations of Porosity Using 32-bit ImageJ

To determine the number of pixels and therefore the area of the core section, it must be indicated to the software with the circle selection tool (example shown - Sample 5a);

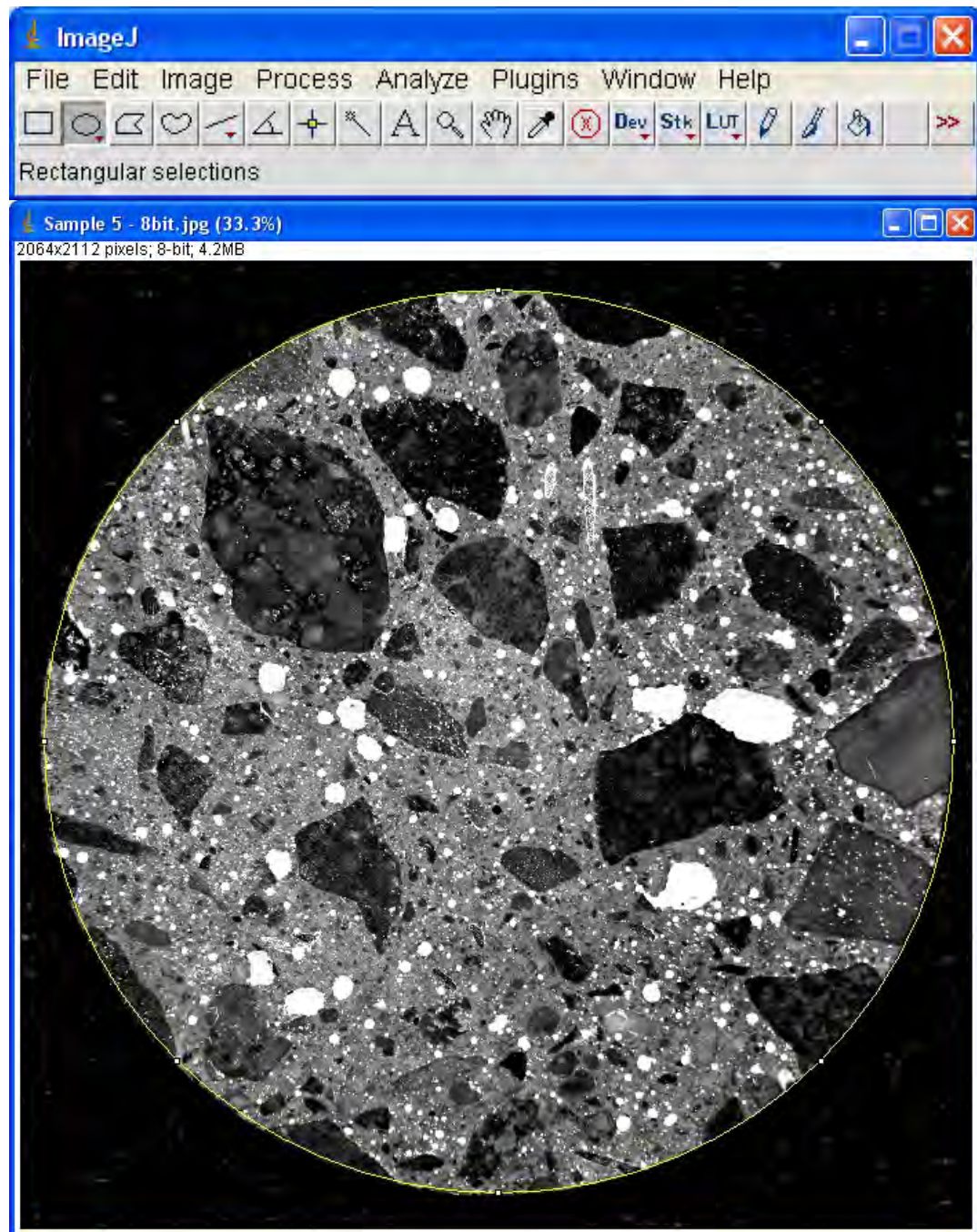


Figure 3.3.1.1.1 Select the circumference of the object in ImageJ

The area of the selected circle is found in the Analyze, Measure and copied into the spreadsheet.

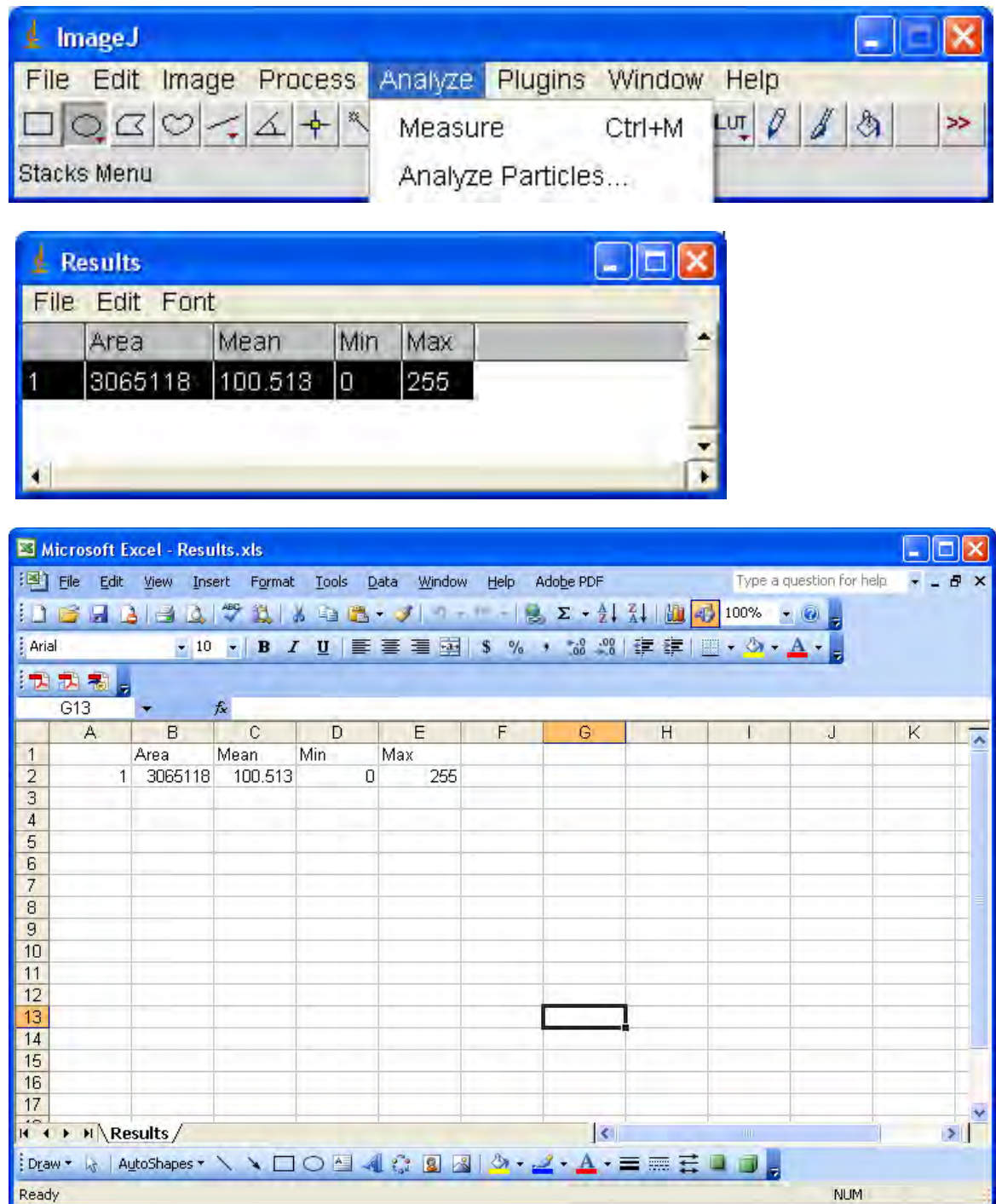


Figure 3.3.1.1.2 Find the area of a selected object and paste into the spreadsheet

To get the area of pores, which are on the picture white, the **threshold** tool is used.

This tool masks in red all the pixels values of which fall within a range specified.

In order to mask the white pixels the upper range is set to 255 (represents white), the lower range is chosen so all (white = now red) pores are included and all the others excluded.

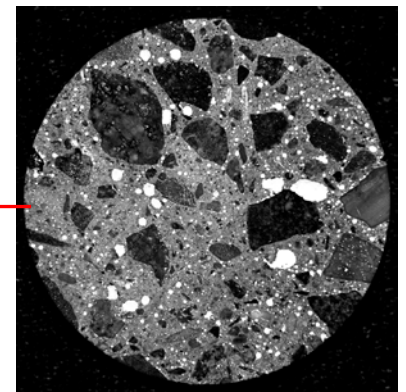
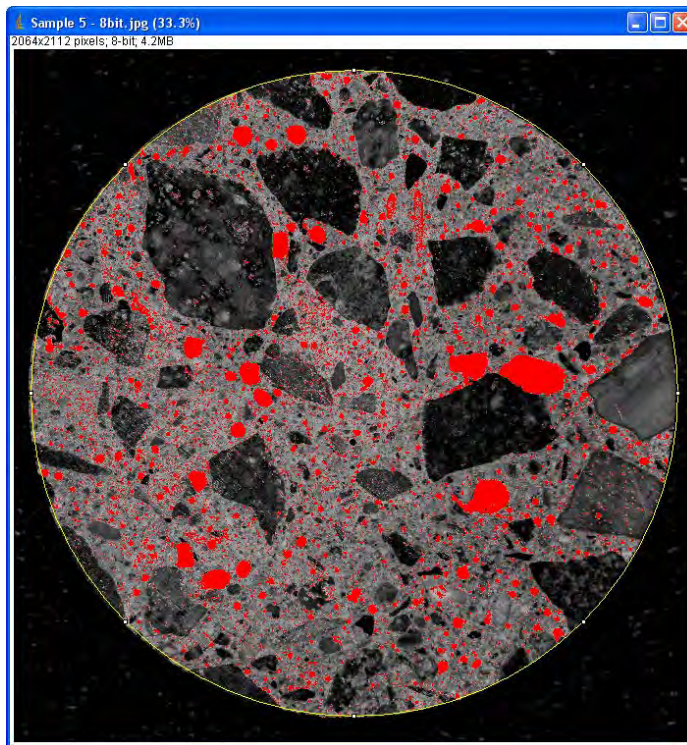


Figure 3.3.1.1.3 Threshold tool masks the white pores in the selected range red

In order to determine the total number of pixels within this range the **Histogram** tool is used.

This tool lists every possible value from 0 to 255 together with the total number of pixels with that value.

The Threshold in Figure 3.3.1.3 displays the range from 183 to 255 the same as is apparent in the Histogram below in the Figure 3.3.1.4.

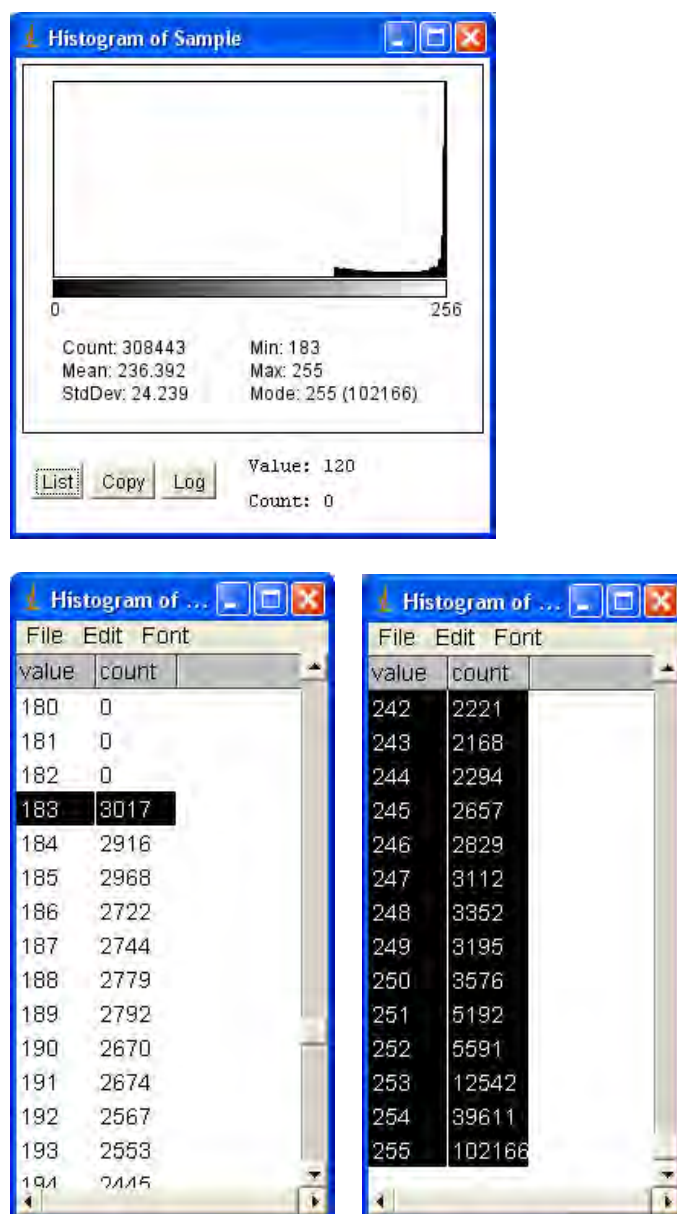


Figure 3.3.1.1.4 Histogram and a list of values

The values from the lowest range to the highest are copied to the spreadsheet. Then they are summed, which gives the total number of white pixels (area). The formula for finding the percentage of white pixels in the full circle is entered into the spreadsheet and calculated.

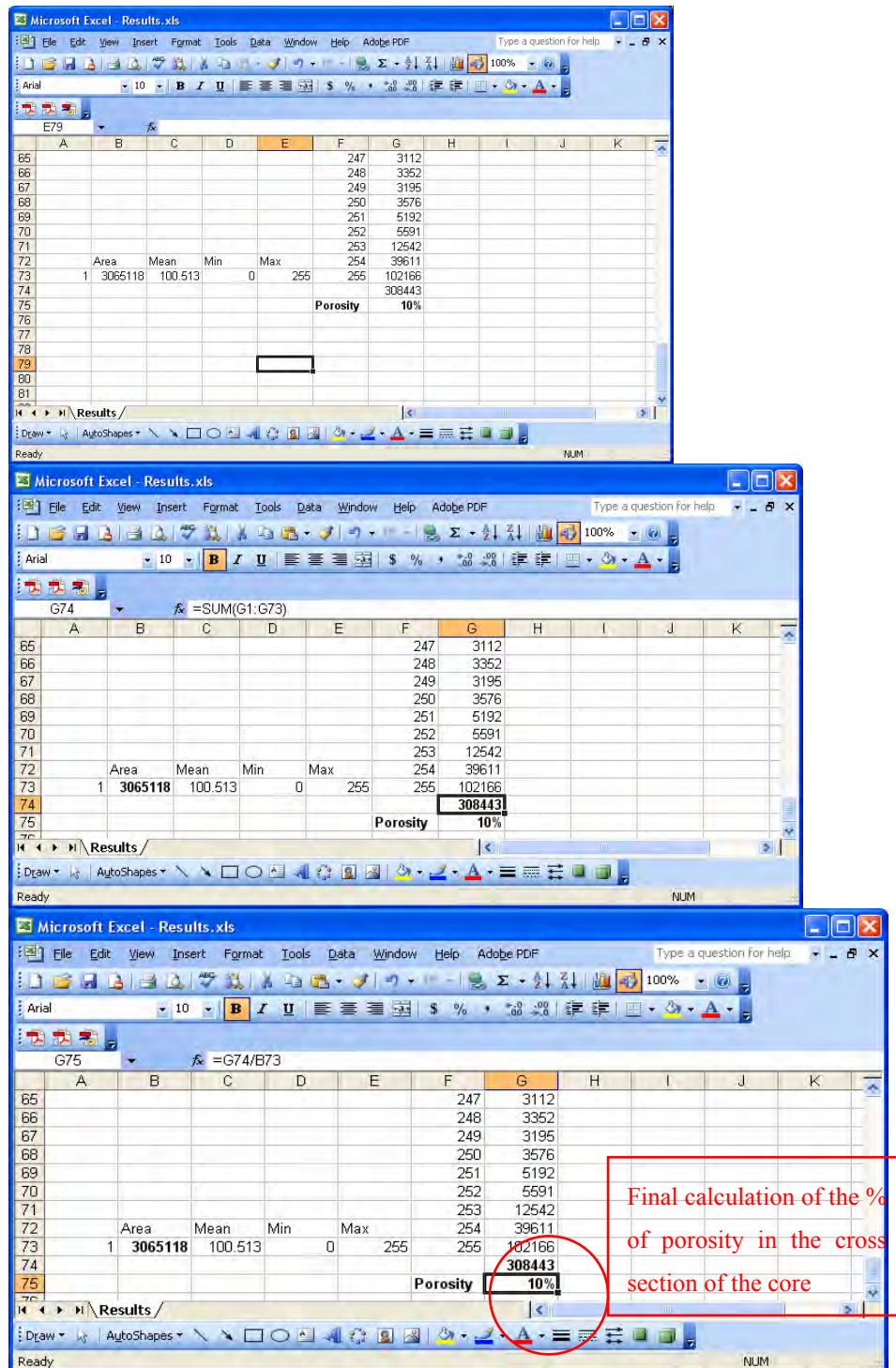


Figure 3.3.1.5 Final calculated result for the percentage of porosity in the selected object in the spreadsheet

3.3.1.2 Study 1 - A Procedure for Calculations of Coarse Aggregate Using 32-bit ImageJ

Calculations of the percentage of coarse aggregate were done in a similar way as the calculations of Porosity using the ImageJ software.

The only difference was in the digital preparation of the image.

The coarse aggregate was masked black using Intuos 3 Graphics Tablet System for Professionals and Adobe Photoshop Elements 2.0.

Masking of each image took on average 3 hours to obtain accurate quantitative results.

The reason for doing this was that the multi-coloured aggregate could not be digitally analysed using any graphics analysis software package available.

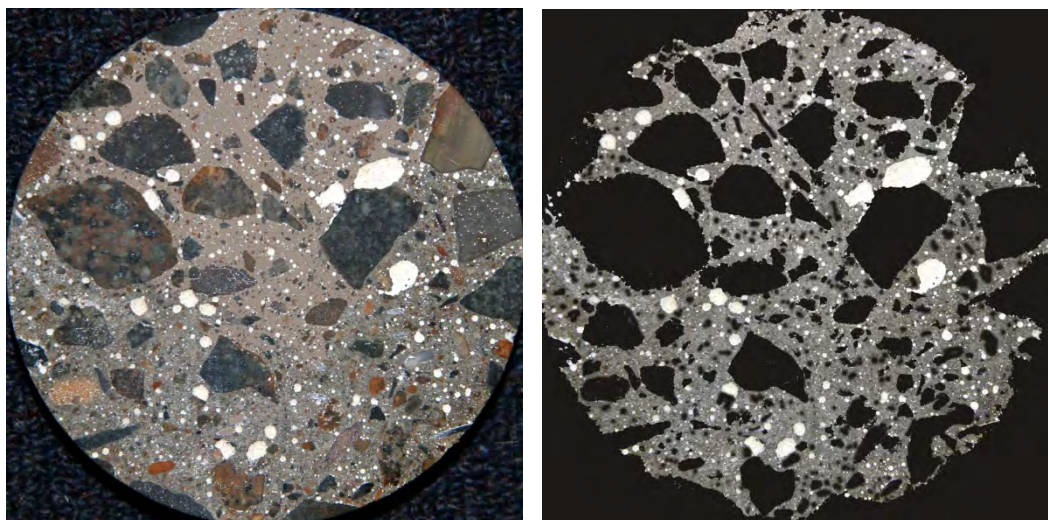


Figure 3.3.1.2.1 Original Image and masked greyscale image

Figure 3.3.1.2.2 shows a fully prepared image for digital analysis.

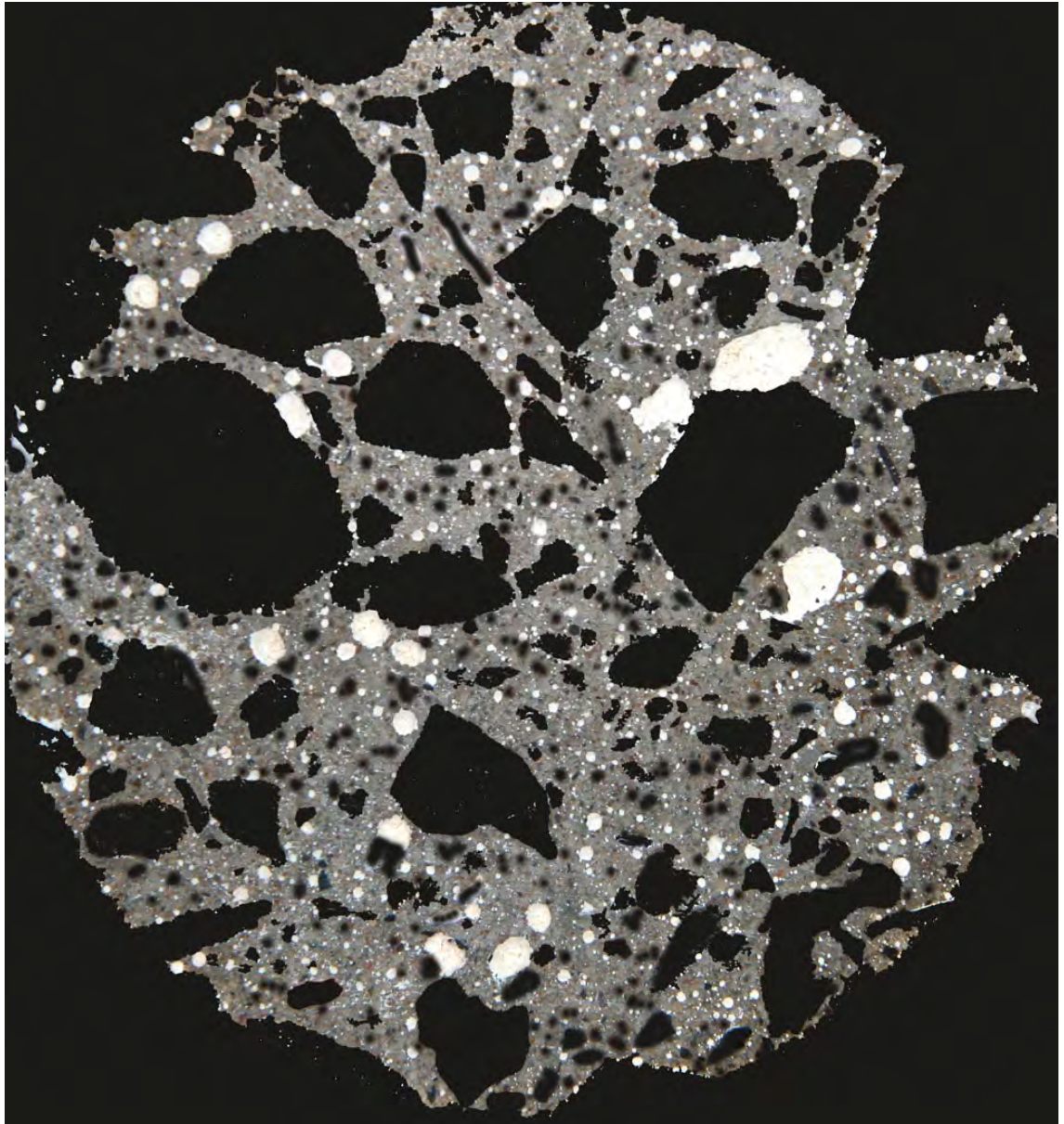


Figure 3.3.1.2.2 The detail of the aggregate masking required

In ImageJ for the analysis the masked picture was changed into an 8-bit image and selected.

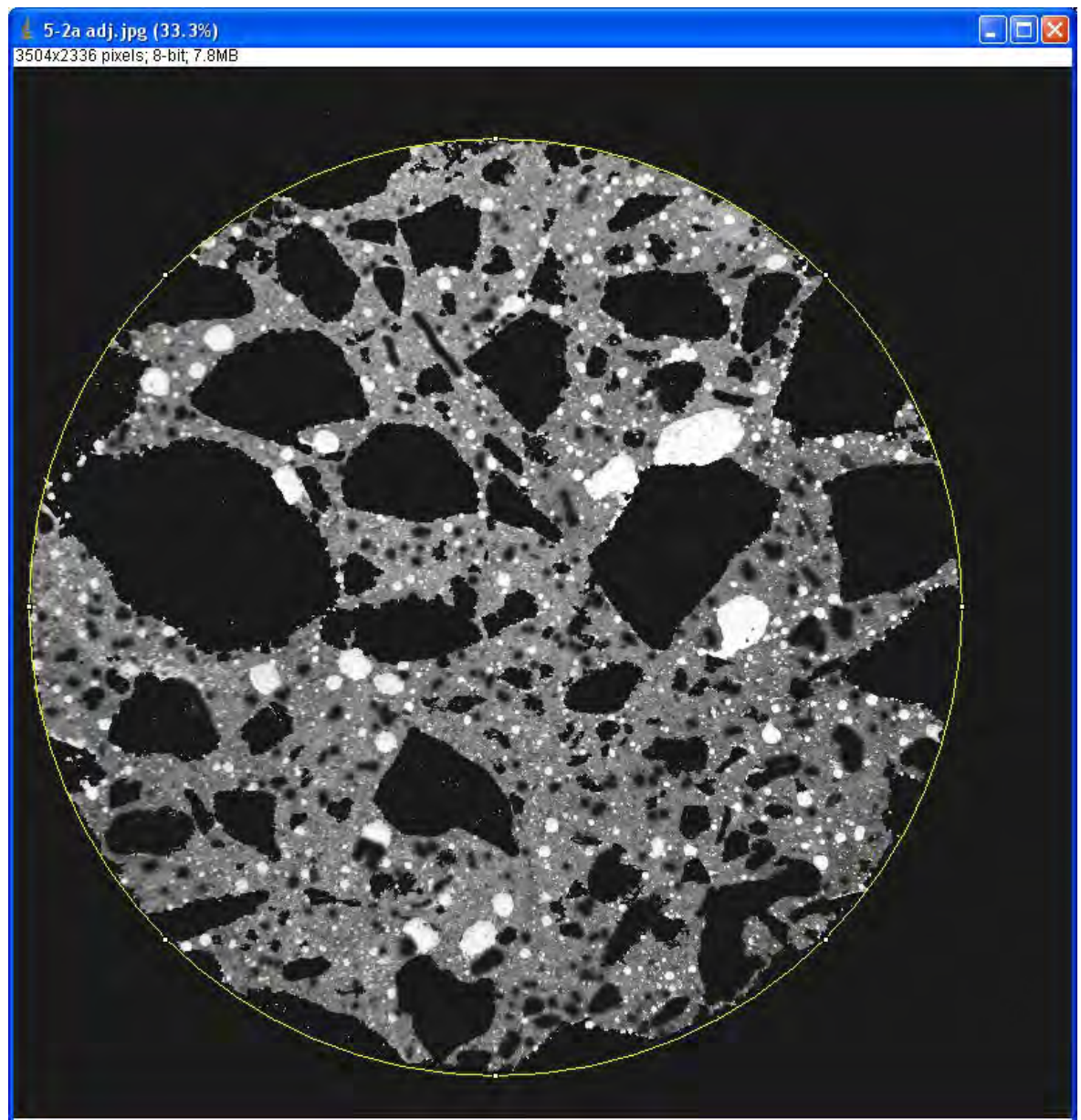


Figure 3.3.1.2.3 Select the circumference of the object in ImageJ

Calculation of the full area of the circle was copied into the spreadsheet.

Values of the selected range from the Histogram were copied into the spreadsheet.

Calculations were completed for the Aggregate (inside the circle) against the full area of the circle (red).

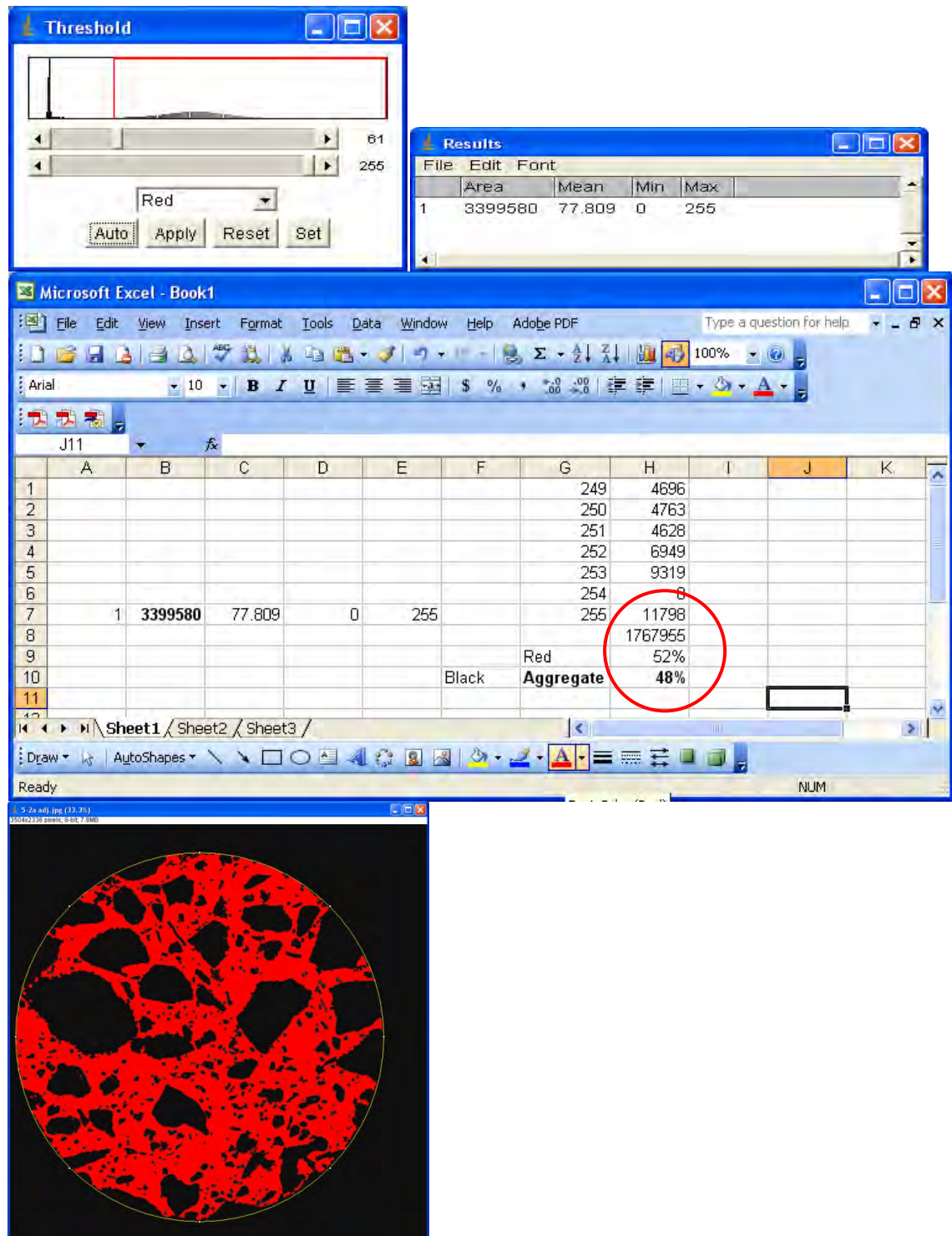


Figure 3.3.1.2.4 Result of the calculation of a percentage of the coarse aggregate

3.3.2 Study 2 - 2400ppi Digital Analysis with 64-bit ImageJ

An A4 24-bit true colour (16.7 million colours), image sized material scanned at 2400 ppi would require 1.7GB of computer memory, per image. Fortunately, concrete micro-structure images, 100mm x 100mm at 2400 ppi digitally analysed in this initial study, required only about 300MB per image.

Samples were scanned on the Hewlett Packard Scanjet 5400C with maximum of 2400 ppi true optical resolution with HP precision scan Pro 3.1 software.



Figure 3.3.2.1 HP ScanJet 5400C

Resolution	2400 ppi (10.58 μ) true optical pixel resolution of the image
Dimensions	9328 x 9800 pixels = 91.4 Megapixels
Bit depth	24-bit colour
Format	bitmap in BMP
Size	varied between 250MB to 271 MB

Table 3.3.2.1 2400ppi data 24-bit colour

Images were then transferred to a PC running Windows Vista 64-bit operating system. Images were processed in 64-bit Adobe Photoshop Elements 7.0, then analysed in 64-bit ImageJ, and calculated in Microsoft Excel 2007.

Image files for analysis in Figures 3.3.2.2. to 3.3.2.21 contain scale bar in the bottom of the image. Smallest divisions are 1 mm.

Data Files Prepared For Image Analysis

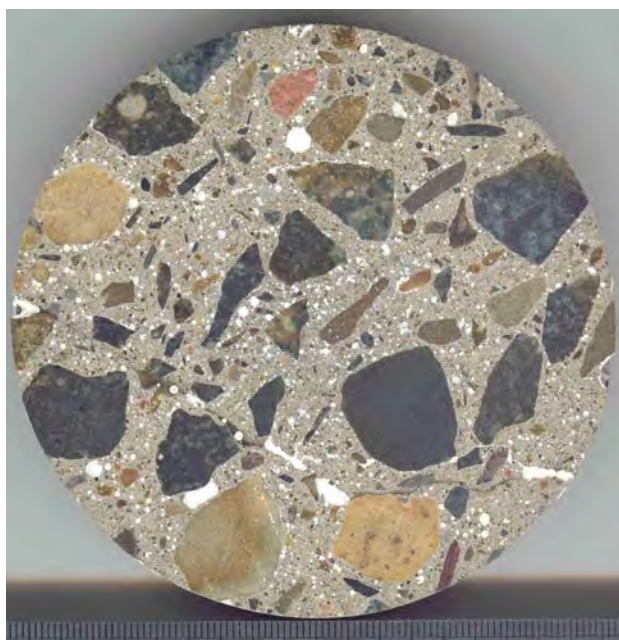


Figure 3.3.2.2 Sample 1A

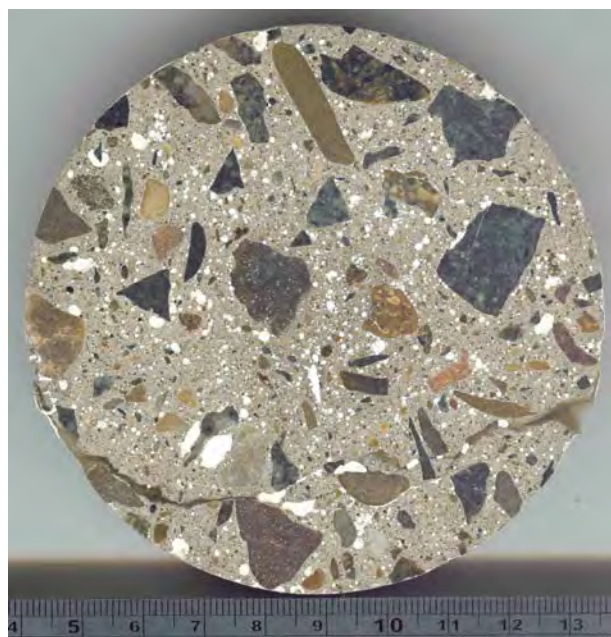


Figure 3.3.2.3 Sample 1B

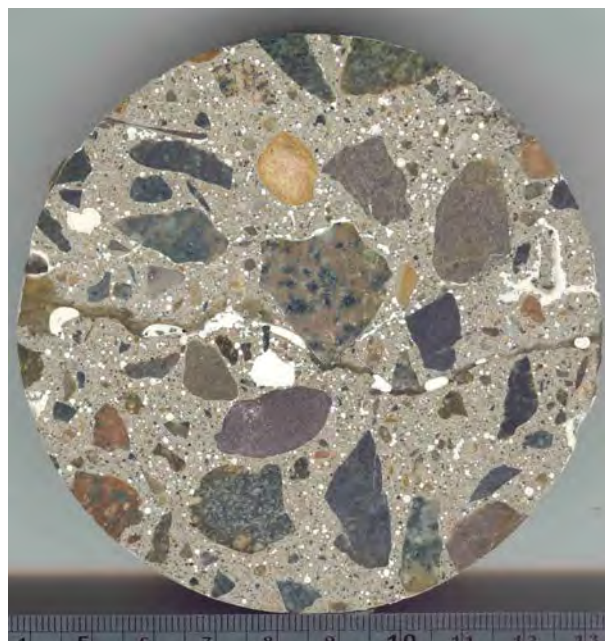


Figure 3.3.2.4 Sample 1C

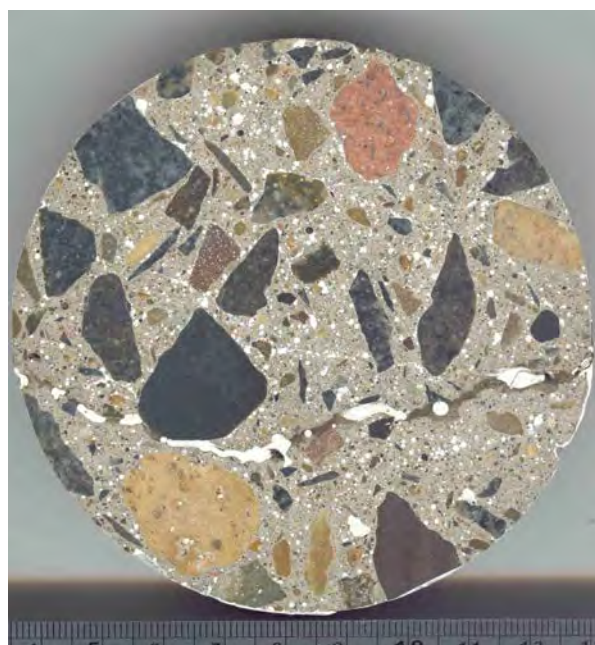


Figure 3.3.2.5 Sample 1D

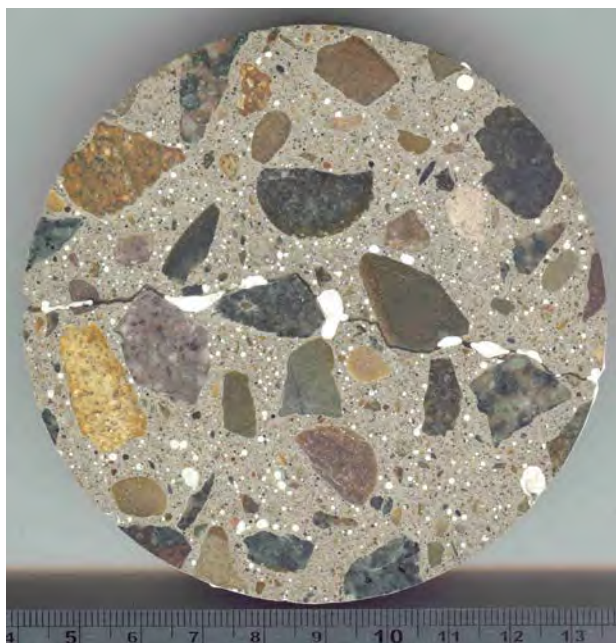


Figure 3.3.2.6 Sample 2A



Figure 3.3.2.7 Sample 2B



Figure 3.3.2.8 Sample 3A

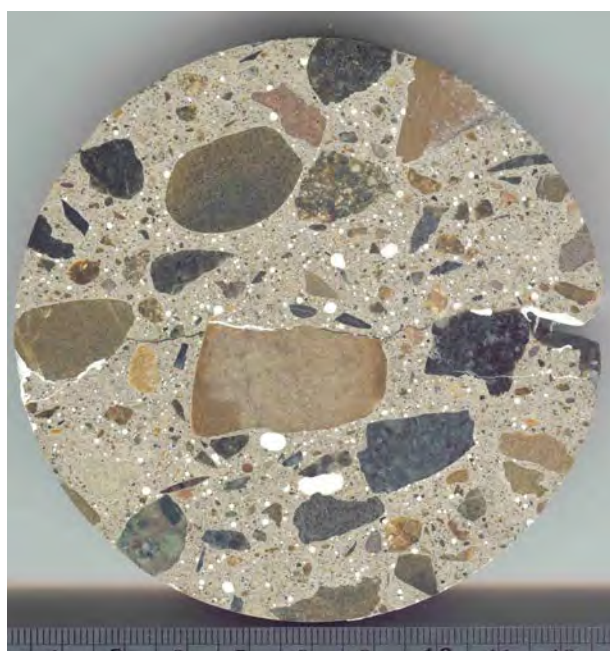


Figure 3.3.2.9 Sample 3B

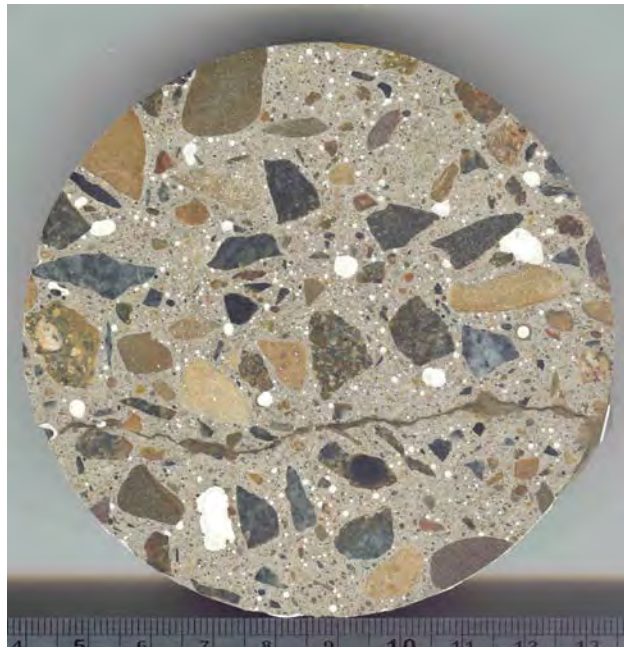


Figure 3.3.2.10 Sample 4A

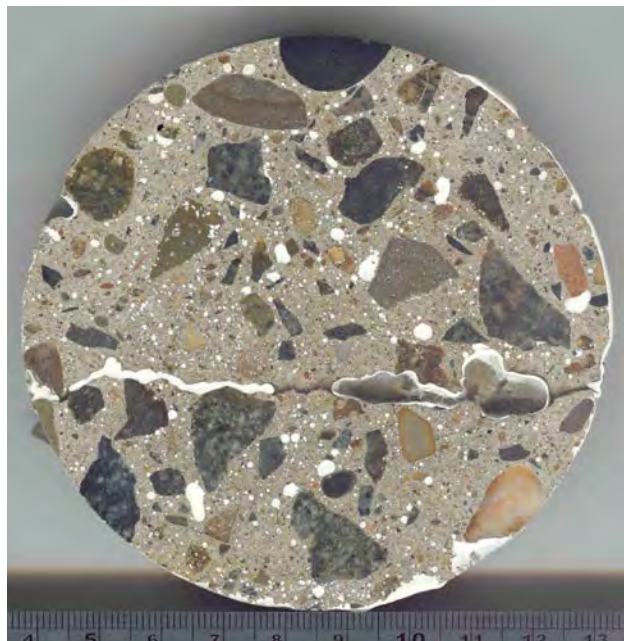


Figure 3.3.2.11 Sample 4B

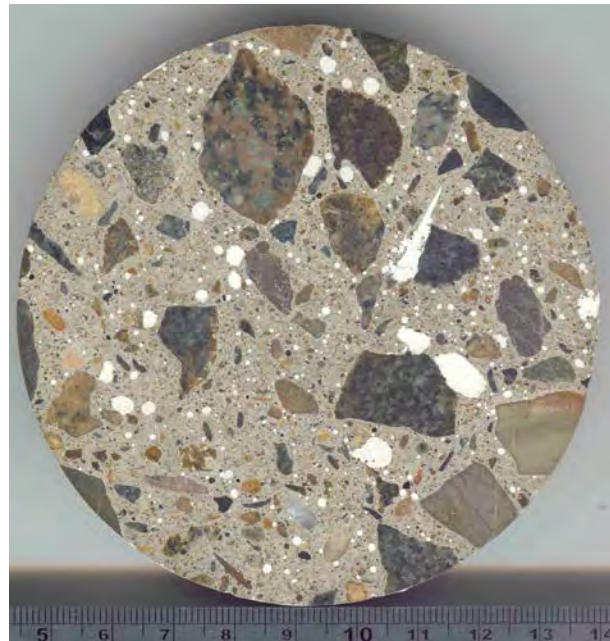


Figure 3.3.2.12 Sample 5A

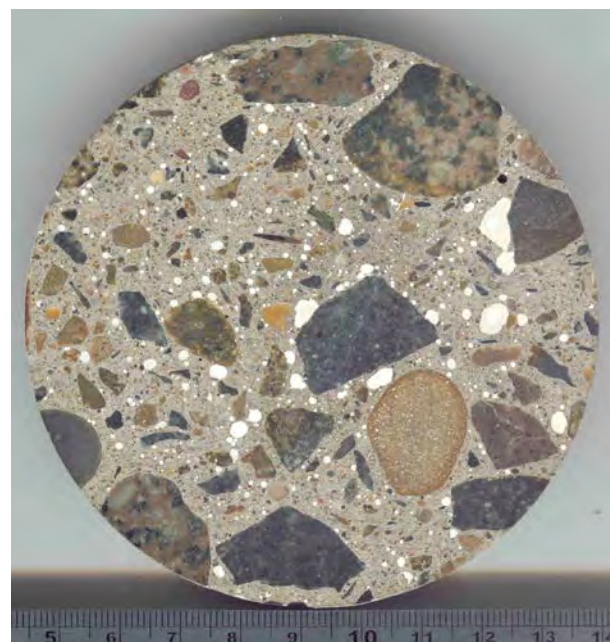


Figure 3.3.2.13 Sample 5B

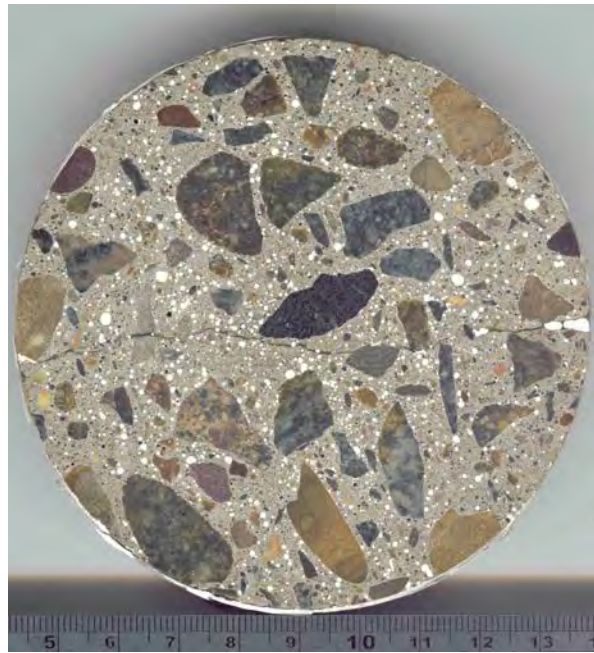


Figure 3.3.2.14 Sample RmA

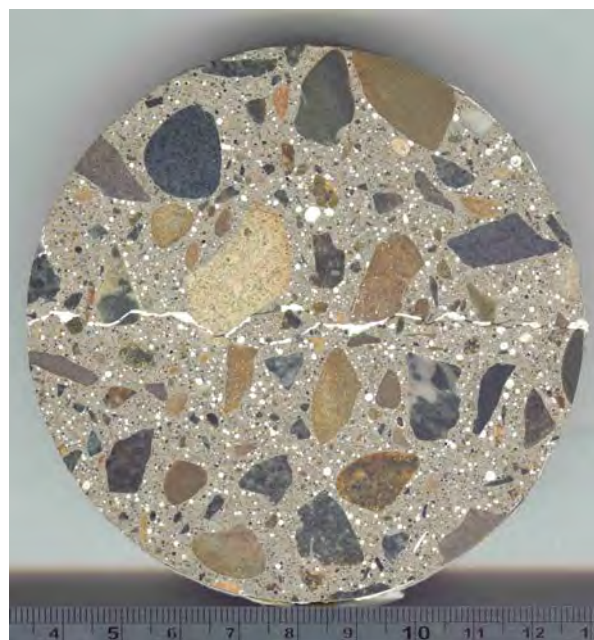


Figure 3.3.2.15 Sample RmB

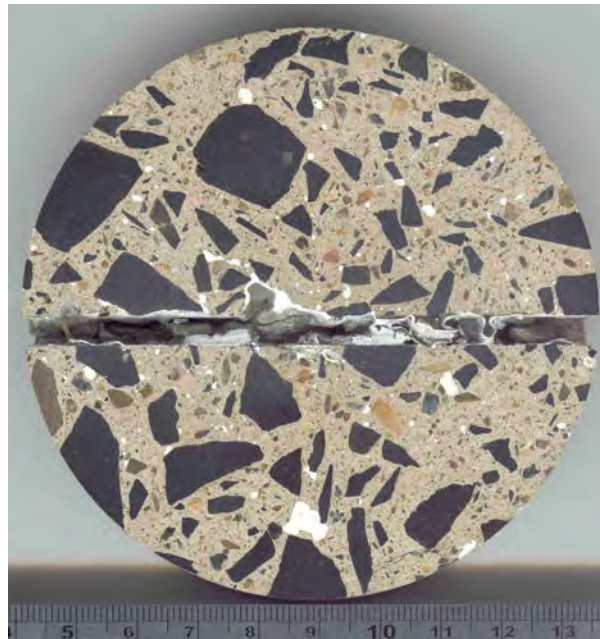


Figure 3.3.2.16 Sample DarA

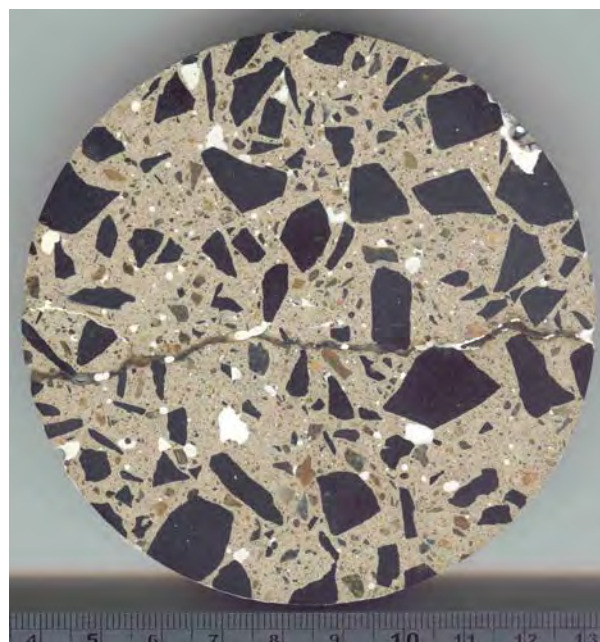


Figure 3.3.2.17 Sample DarB

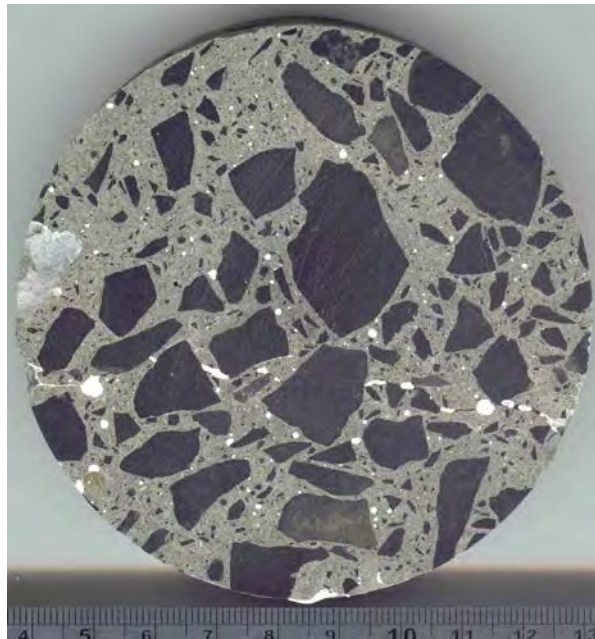


Figure 3.3.2.18 Sample FIA

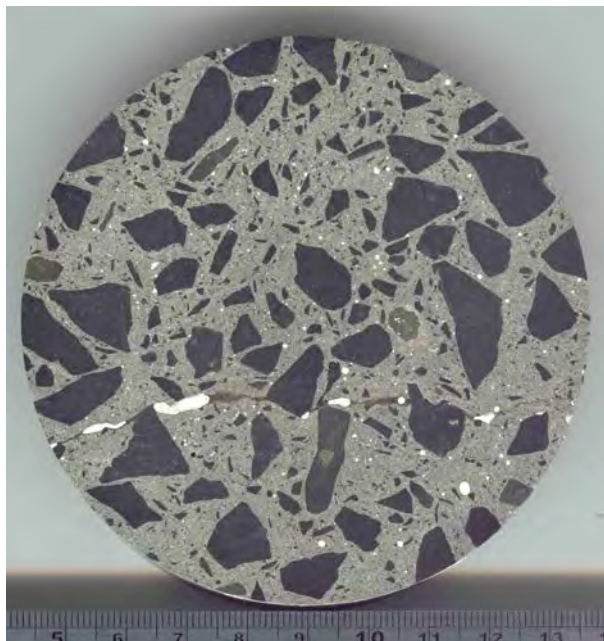


Figure 3.3.2.19 Sample FIB

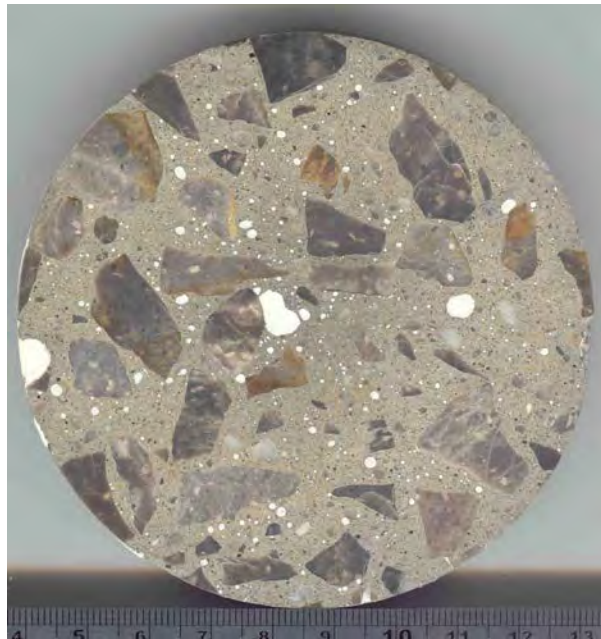


Figure 3.3.2.20 Sample FI1A

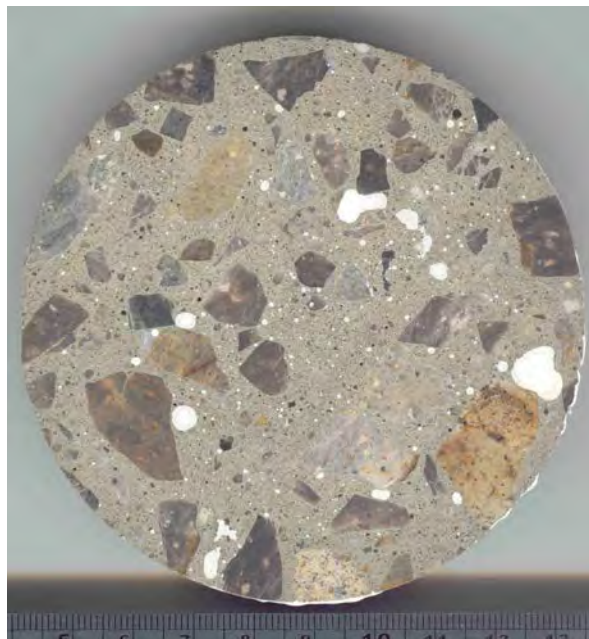


Figure 3.3.2.21 Sample FI1B

3.3.2.1 Study 2 - A Procedure for Calculations of Porosity Using 64-bit ImageJ

Procedures for this study are not documented because they were done in 64-bit ImageJ as the Study 3. (See 3.3.3.1 Study 3 detailed procedures.)

3.3.2.2 Study 2 - A Procedure for Calculations of Coarse Aggregate Using 64-bit ImageJ

Procedures for this study are not documented because they were done in 64-bit ImageJ as the Study 3. (See 3.3.3.2 Study 3 detailed procedures.)

3.3.3 Study 3 - High Optical Resolution (4800 ppi and 6400 ppi) Digital Analysis with 64-bit ImageJ

Samples were scanned on the Epson Perfection V700 Photo scanner with maximum true optical resolution of 4800 ppi colour and 6400 ppi colour and greyscale using SilverFast 6.6 1r2b **with all auto functions for image and colour adjustments disabled**. Images were then transferred to a PC running Windows Vista 64-bit operating system. Images were processed in 64-bit Adobe Photoshop Elements 7.0, then analysed in 64-bit ImageJ, and calculated in Microsoft Excel 2007 version and 64-bit Microsoft Excel 2010.



Figure 3.3.3.1 Epson Perfection V700

Resolution	6400 ppi (3.97 μ) true optical pixel resolution of the image
Dimensions	25142 x 25292 pixels (6400 ppi colour) = 635.9 Megapixels
Bit depth	48 bit colour
Format	uncompressed in TIFF
Size	3.48 GB

Table 3.3.3.1 6400 ppi data 48-bit colour

Resolution	6400 ppi (3.97 μ) true optical pixel resolution of the image
Dimensions	25142 x 25292 pixels (6400 ppi colour) = 635.9 Megapixels
Bit depth	8 bit greyscale
Format	uncompressed in TIFF
Size	< 1 GB

Table 3.3.3.2 6400 ppi data 8-bit greyscale

Resolution	4800 ppi and 6400 ppi (5.29 μ and 3.97 μ) true optical pixel resolution of the image
Dimensions	18856 x 18968 (4800 ppi colour) = 357.7 Megapixels; 25142 x 25292 pixels (6400 ppi colour) = 635.9 Megapixels
Bit depth	24 bit colour
Format	uncompressed in TIFF
Size	1GB and 1.78 GB

Table 3.3.3.3 4800 ppi and 6400 ppi data 24-bit colour

Data Files Prepared For Image Analysis

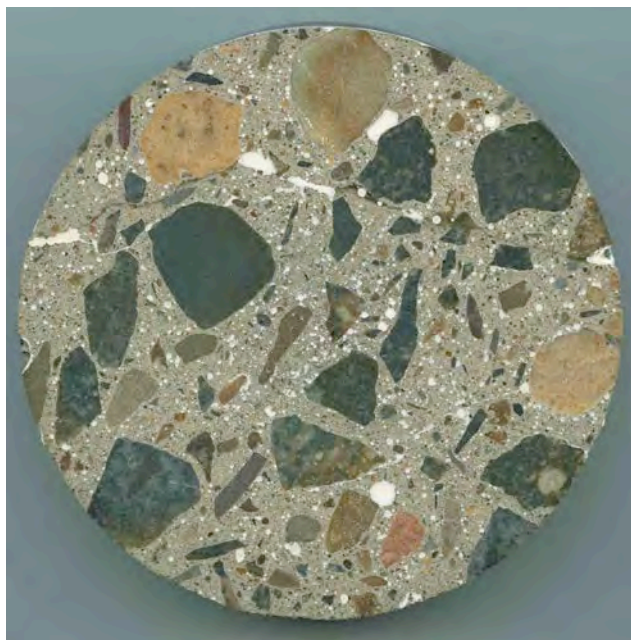


Figure 3.3.3.2 Sample 1A



Figure 3.3.3.3 Sample 1B



Figure 3.3.3.4 Sample 1C

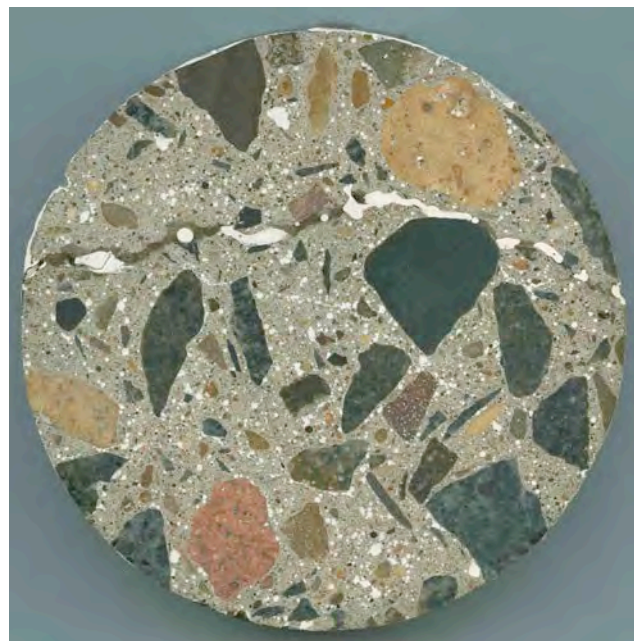


Figure 3.3.3.5 Sample 1D



Figure 3.3.3.6 Sample 2A



Figure 3.3.3.7 Sample 2B



Figure 3.3.3.8 Sample 3A

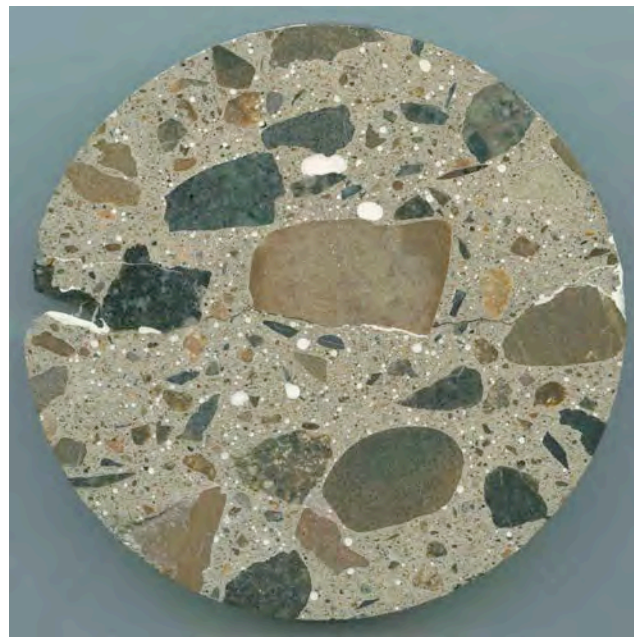


Figure 3.3.3.9 Sample 3B

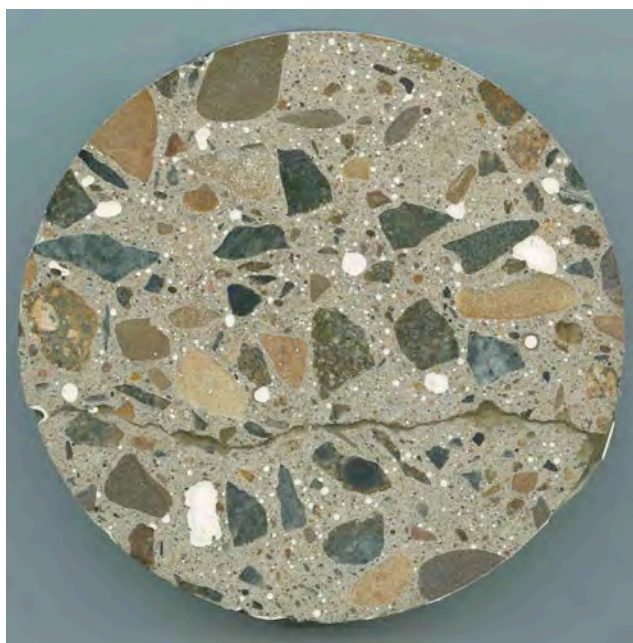


Figure 3.3.3.10 Sample 4A

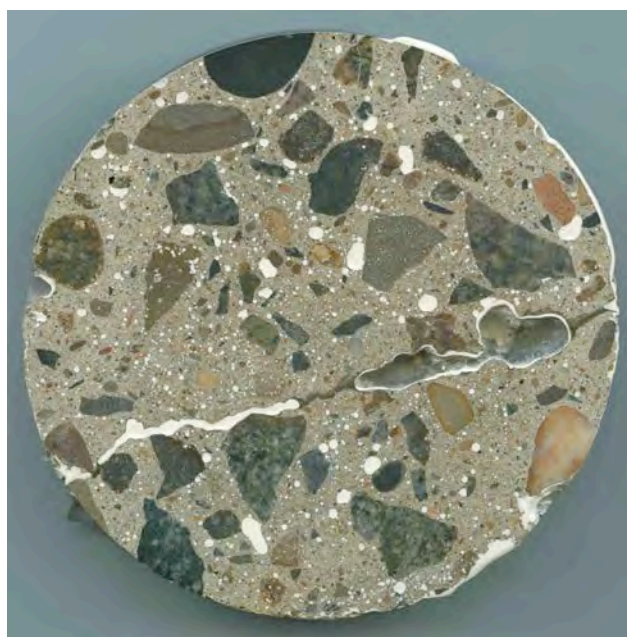


Figure 3.3.3.11 Sample 4B



Figure 3.3.3.12 Sample 5A



Figure 3.3.3.13 Sample 5B

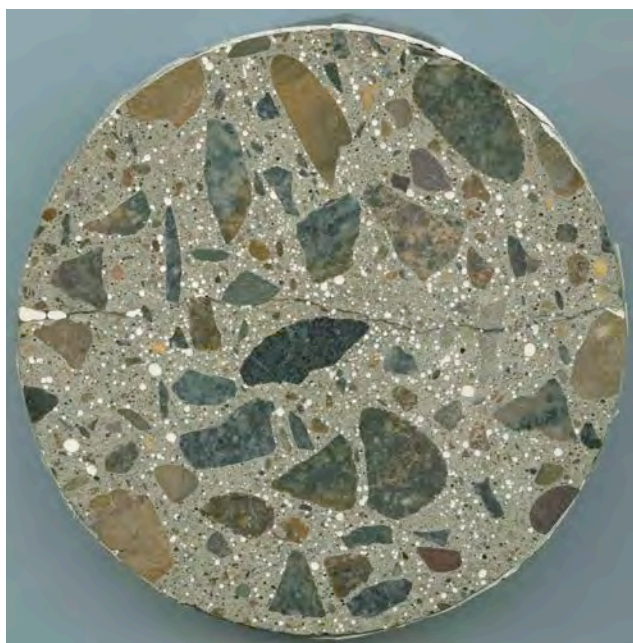


Figure 3.3.3.14 Sample RmA



Figure 3.3.3.15 Sample RmB

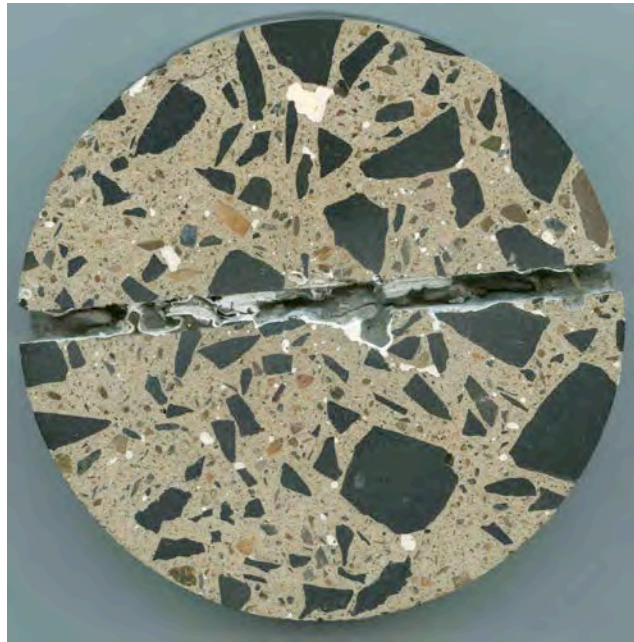


Figure 3.3.3.16 Sample DarA

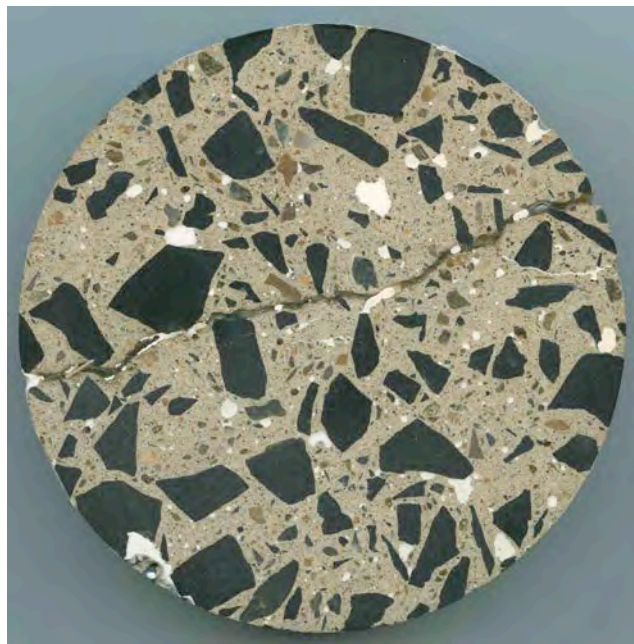


Figure 3.3.3.17 Sample DarB



Figure 3.3.3.18 Sample FIA

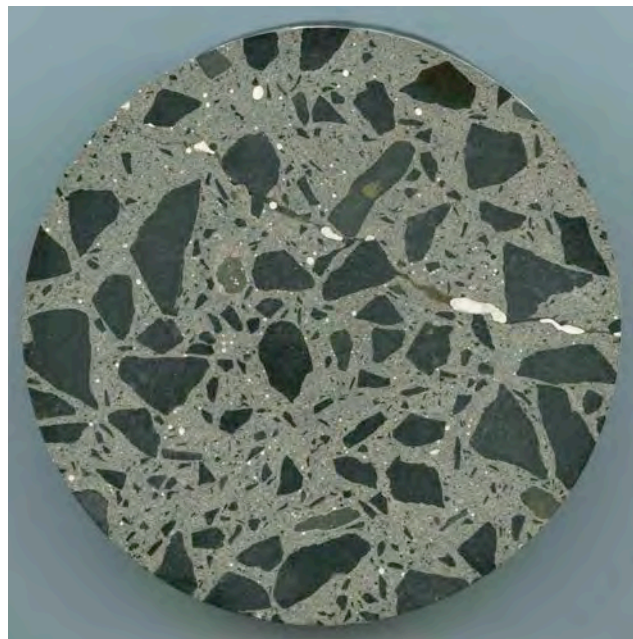


Figure 3.3.3.19 Sample FIB

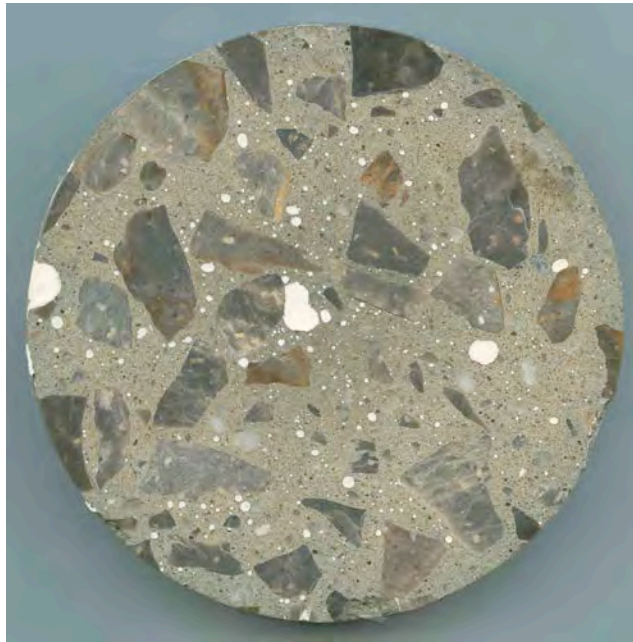


Figure 3.3.3.20 Sample FIIA

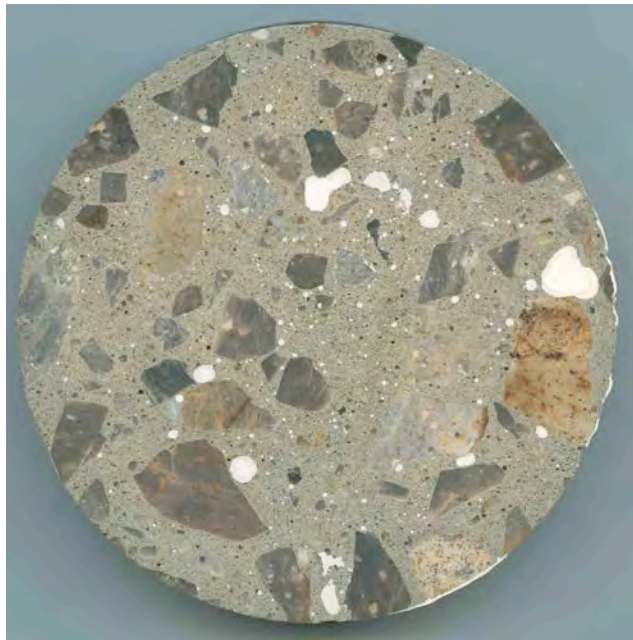


Figure 3.3.3.21 Sample FIIB

3.3.3.1 Study 3 - A Procedure for Calculations of Porosity Using 64-bit Adobe PhotoShop Elements 7.0, SilverFast Epson SE, 64-bit ImageJ and Microsoft Excel in 64-bit Windows

Prior to starting to do any calculations, the Samples had to be prepared first. The Samples were originally cut horizontally across, filled with a white porcelain two part epoxy impregnation and diamond polished (~ 5 microns) for digital calculations.

Dimensions of cut Samples were about 95 to 100 mm in diameter and a thickness of about 16-18 mm. As these cuts are across the aggregate that were quite porous, those porous aggregates had to be masked in the software 64-bit Adobe PhotoShop Elements 7.0 in such manner that the inside of the aggregates the pores would be covered and the circumference of the aggregates would stay uncovered to be available for the porosity calculations. The reason for it was that the pores on the outside of the aggregate/aggregates were a part of the porosity calculation.

The original picture of a porous aggregate needed to be filled for the purpose of calculations:

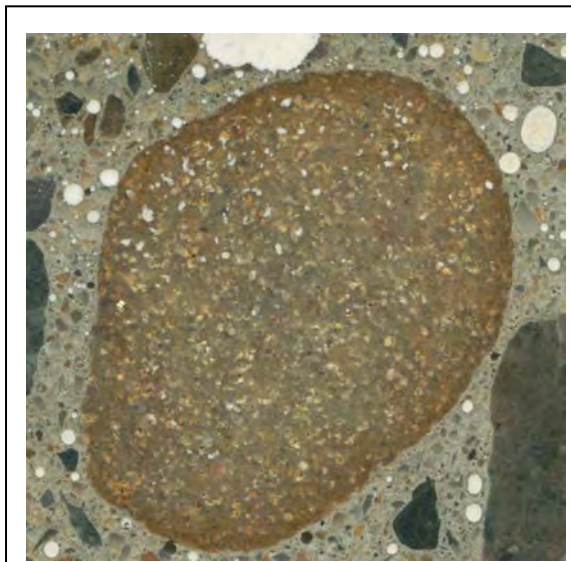


Figure 3.3.3.1.1 Original colour picture scanned at true optical resolution 6400x6400 ppi 48-bit colour (Reference Sample 5)

The steps needed were as follows:

1. The porous aggregate was selected with a magnetic lasso tool in the Adobe PhotoShop Elements 7.0 very carefully inside of the circumference to leave the circumference fully opened to the calculation of porosity in the region of interfacial zone of the aggregate and cement matrix;
2. After the careful selection the aggregate got filled with a bucket tool to black colour;
3. Then gradually filled until fully done as the Figures 3.3.3.1.2 to 3.3.3.1.4 are showing.
4. All porous aggregates on one Sample were completed the same way and then the Sample was opened in the image processing programme ImageJ for the calculation.

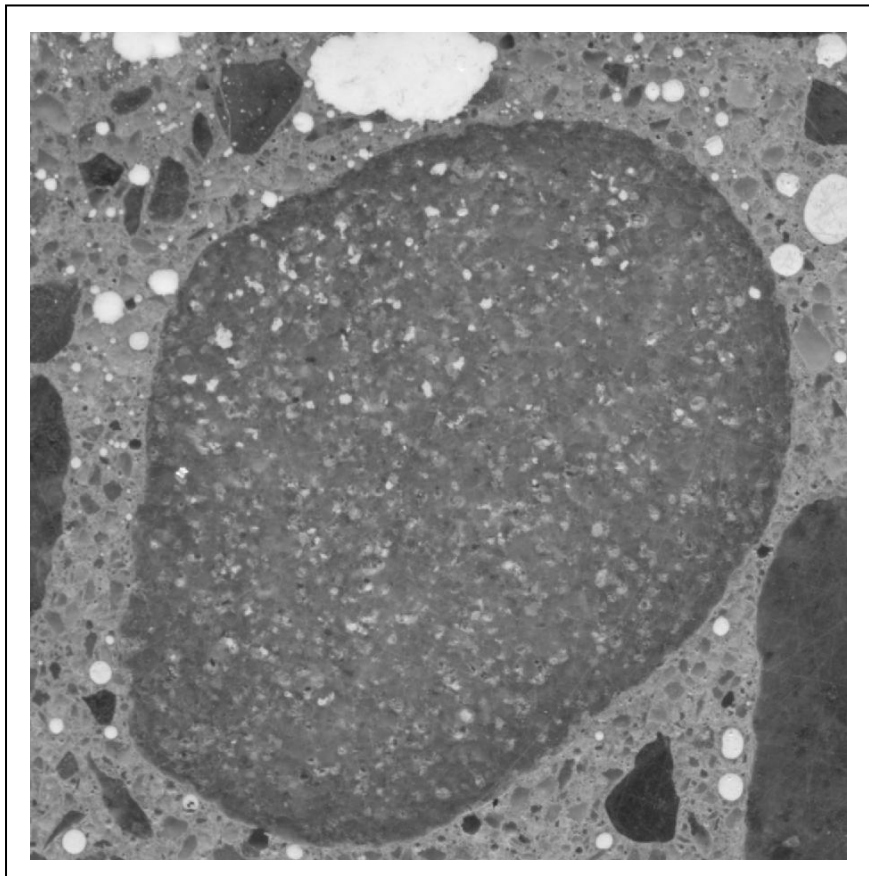


Figure 3.3.3.1.2 Porous aggregate ready to be masked

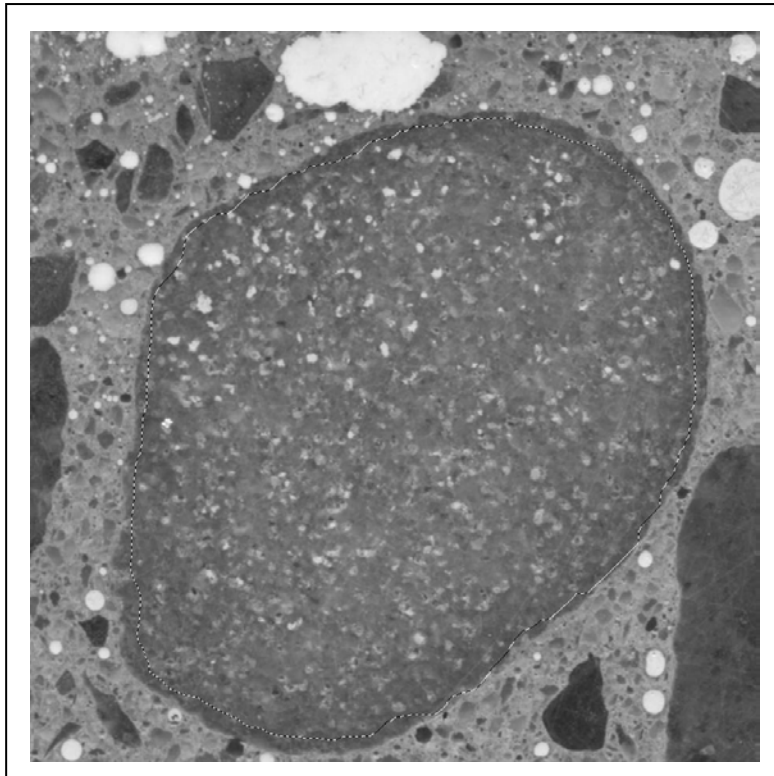


Figure 3.3.3.1.3 Magnetic Lasso tool selected the inside of the aggregate to be filled

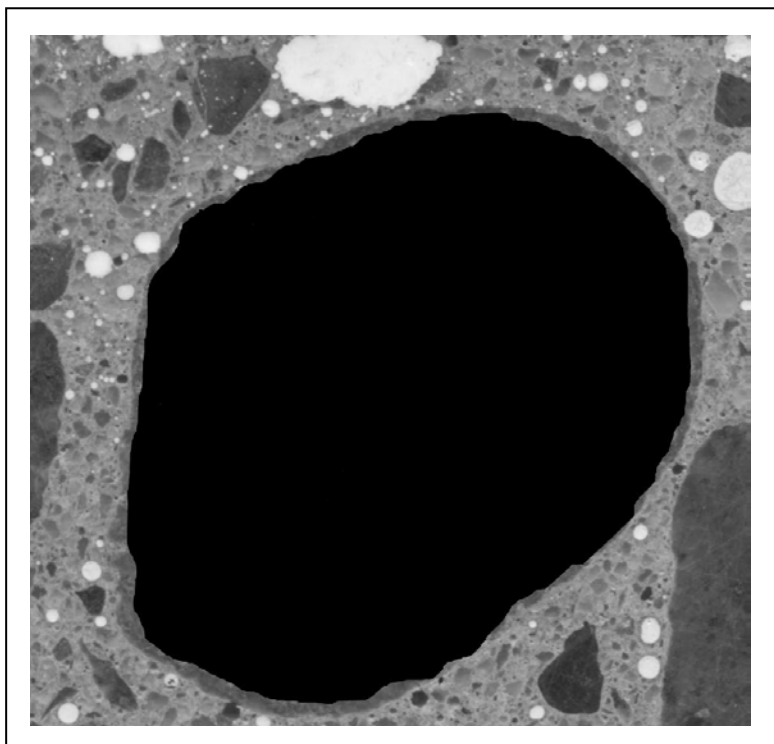


Figure 3.3.3.1.4 Fully filled porous aggregate ready for a calculation of porosity

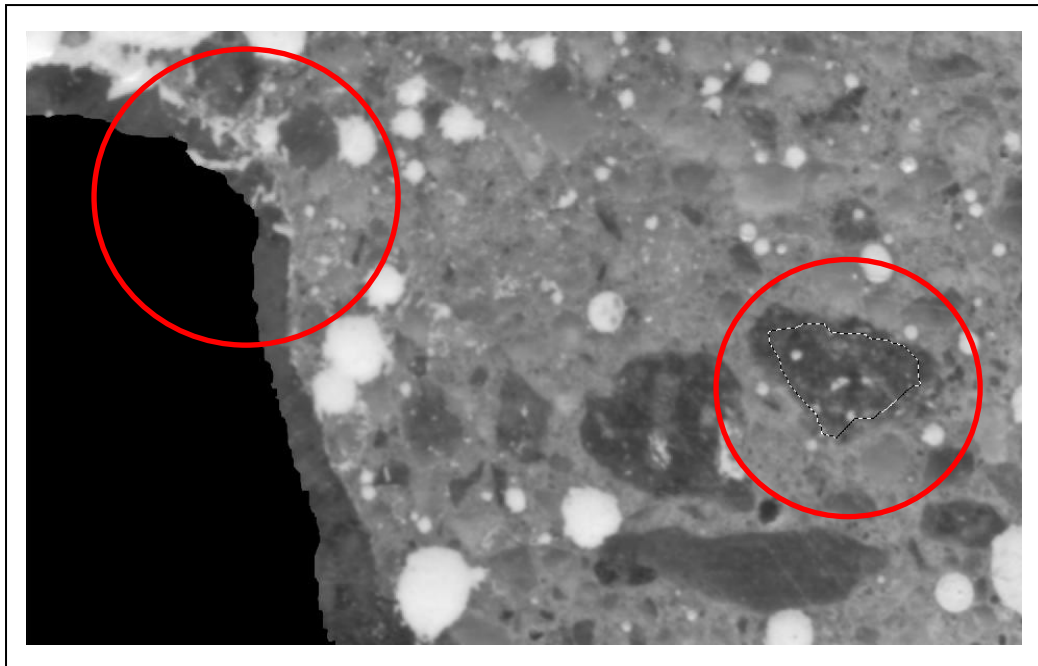


Figure 3.3.3.1.5 Careful selection, and masking inside of the circumference of a large porous aggregate (on the left), removes its porosity from digital analysis, but retains surface cracking on the outside surface of the aggregate; the lasso on a small aggregate (on the right) selects the area inside of the aggregate required to be masked in black

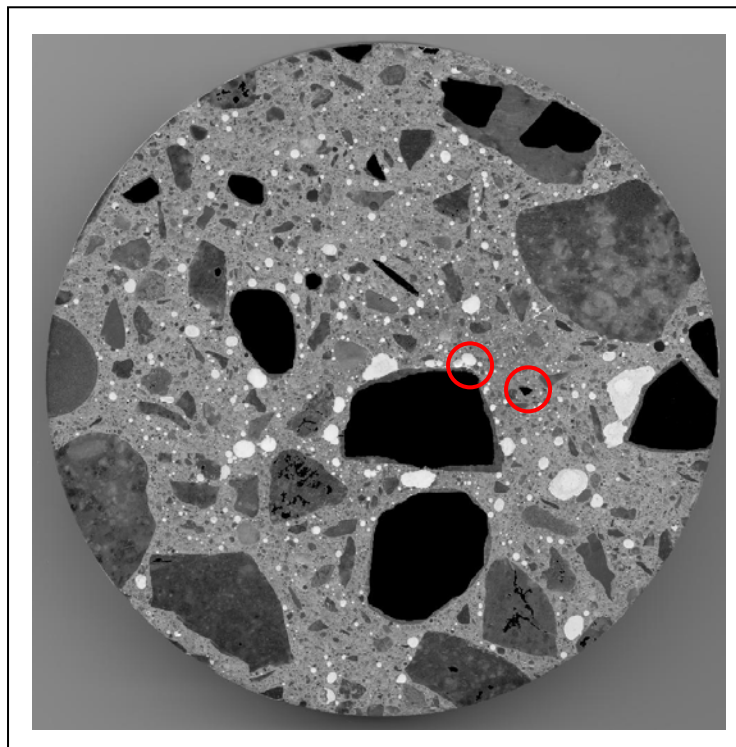


Figure 3.3.3.1.6 Fully filled Reference Sample 5b, ready for automatic digital analysis, and calculation of the percentage porosity

Detailed Procedures for Calculations of Porosity

1. Open ImageJ programme;
2. On Menu bar click File, then click Open and select the picture file of the image to open on the screen;

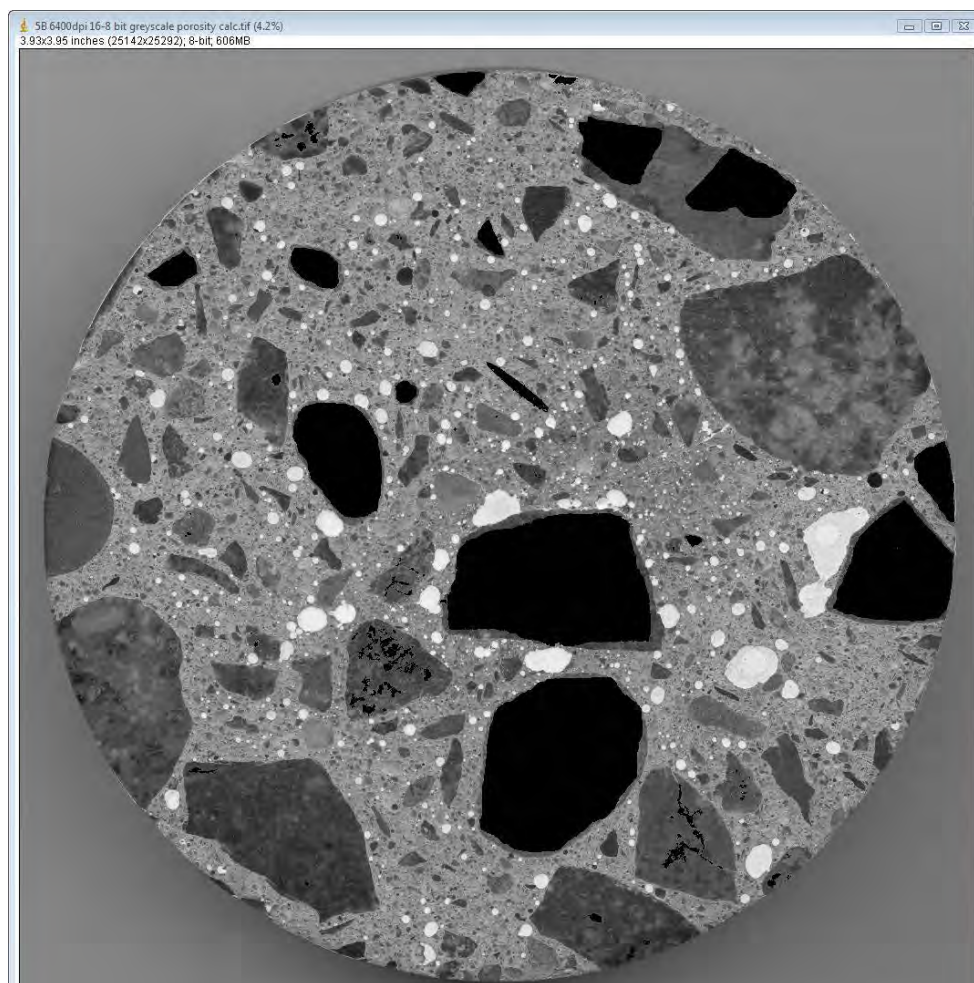
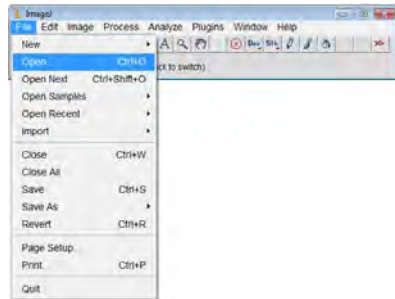



Figure 3.3.3.1.7 Open the image in ImageJ (pixels 25142 x 25292, size 606 MB, 8-bit greyscale, scanned 6400 dpi in true optical resolution)

3. Choose the Elliptical tool  on the toolbar and carefully select the circumference of the image (yellow circle in Figure 3.3.3.1.8);

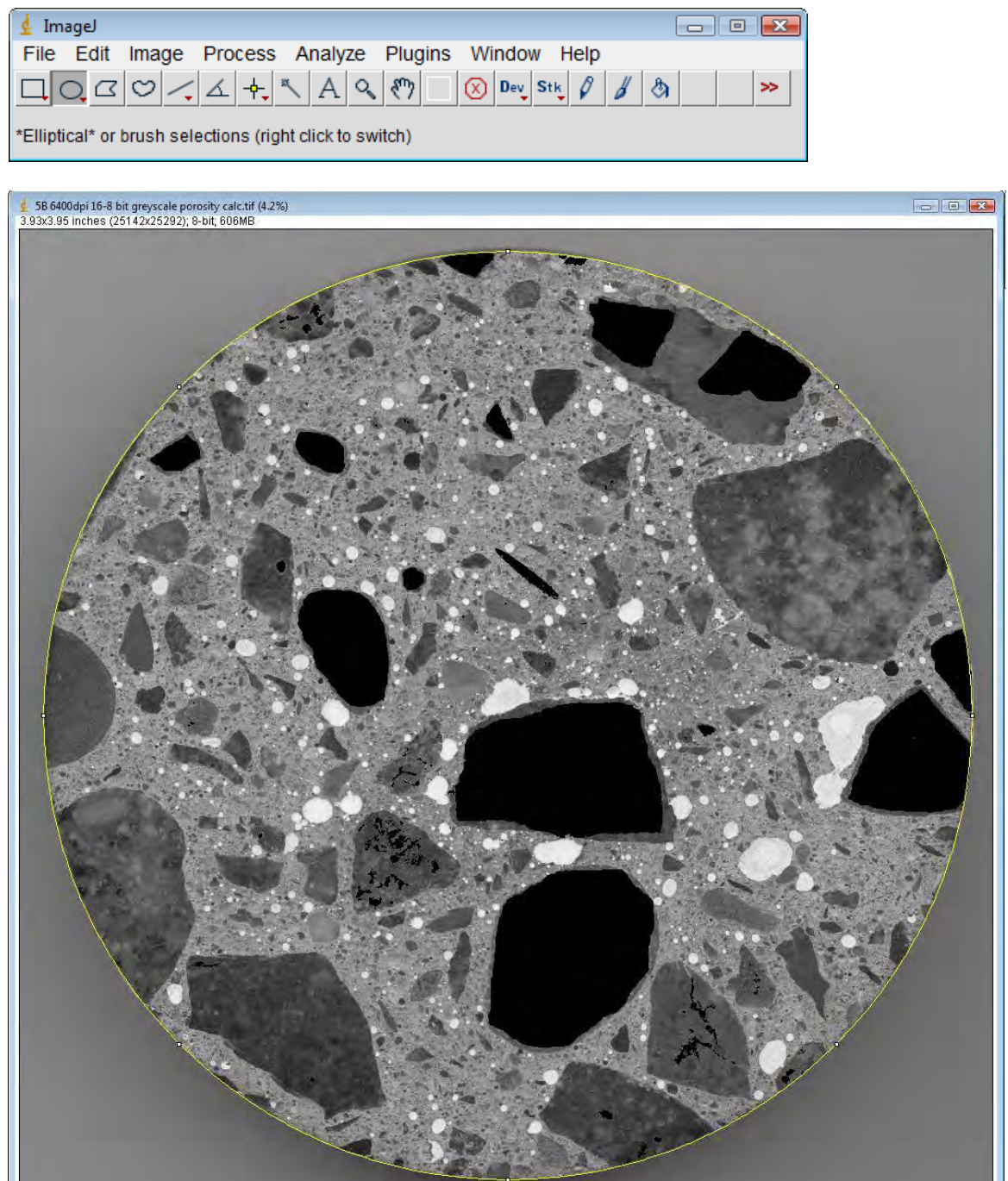


Figure 3.3.3.1.8 Select carefully the circumference of the Sample with Elliptical tool on the menu bar

4. On the Menu bar click Image, then Type, then select 8-bit to change the colour image into the greyscale image if not already in that format;

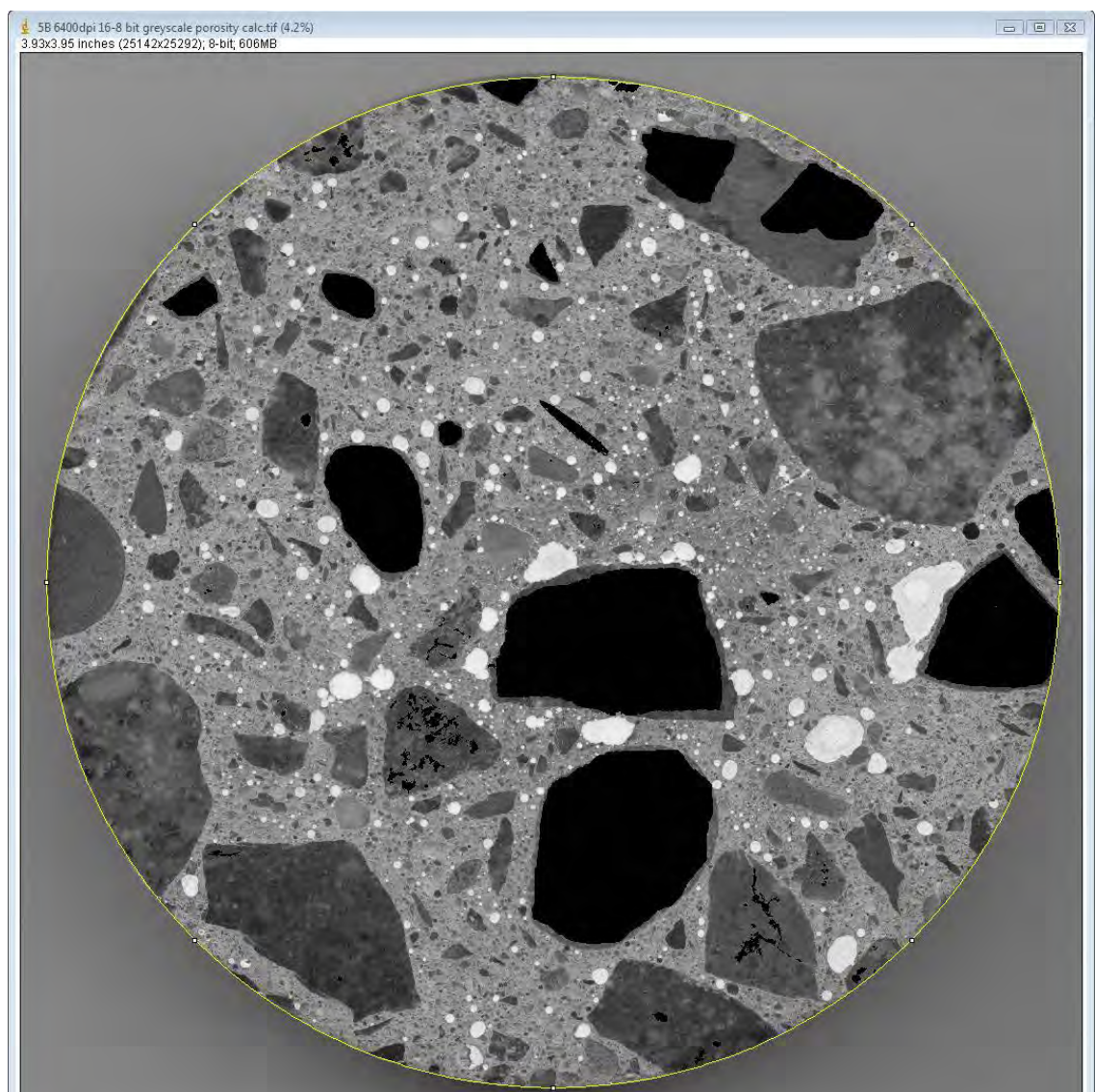
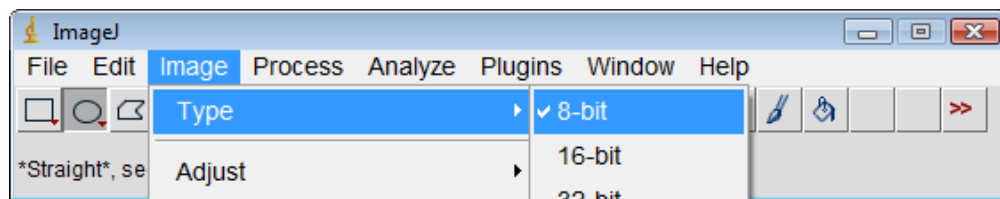


Figure 3.3.3.1.9 Type of the image is changed to 8-bit for the calculation

5. On the Menu bar click Image, then Adjust, then Threshold and keep the Default on Red colour;

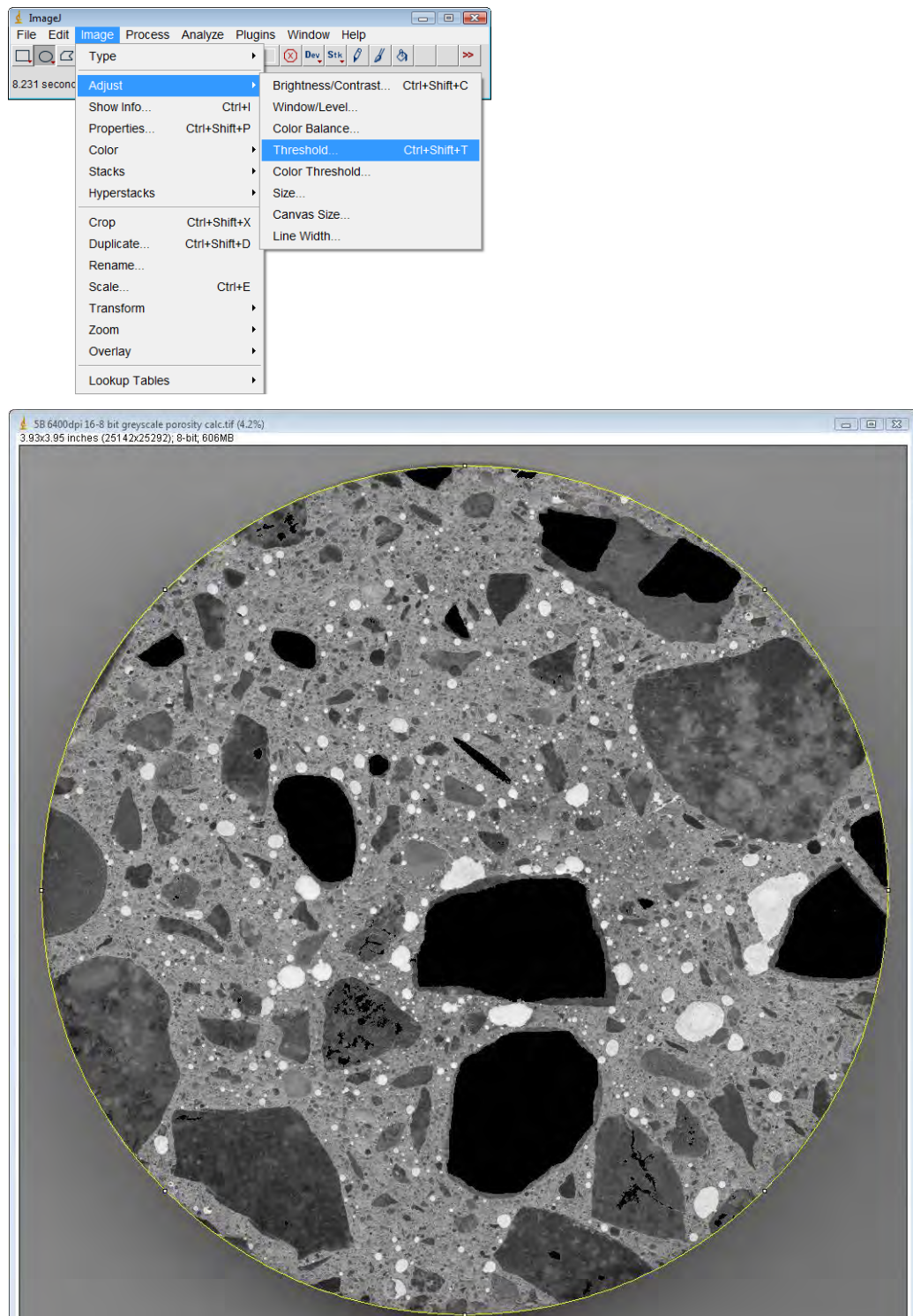


Figure 3.3.3.1.10 Select Image, Adjust and Threshold to start the calculation

The image on the screen will look similar to the Figure 3.3.3.1.11 below, with the threshold selected automatically by the software;

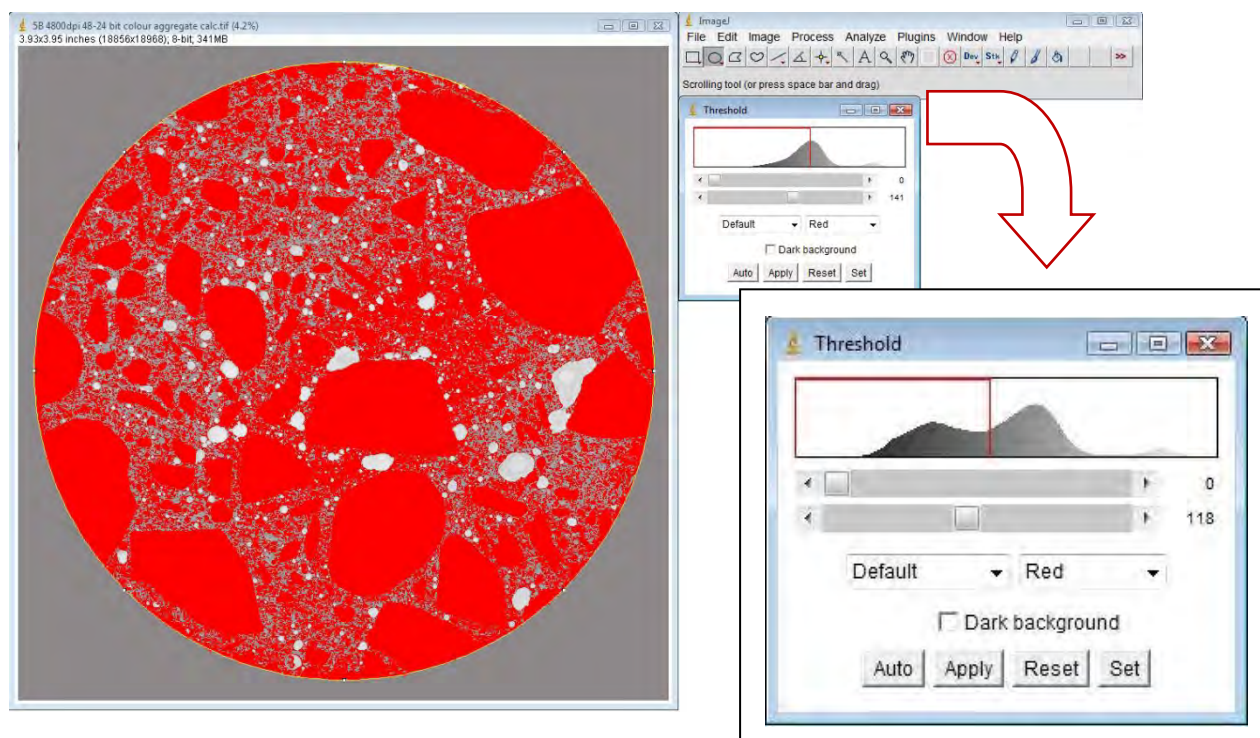


Figure 3.3.3.1.11 Automatic selection of the threshold by the software that needs to be manually adjusted in the following steps

6. Adjust the toolbars in the threshold manually - the bottom button to 255 as below:

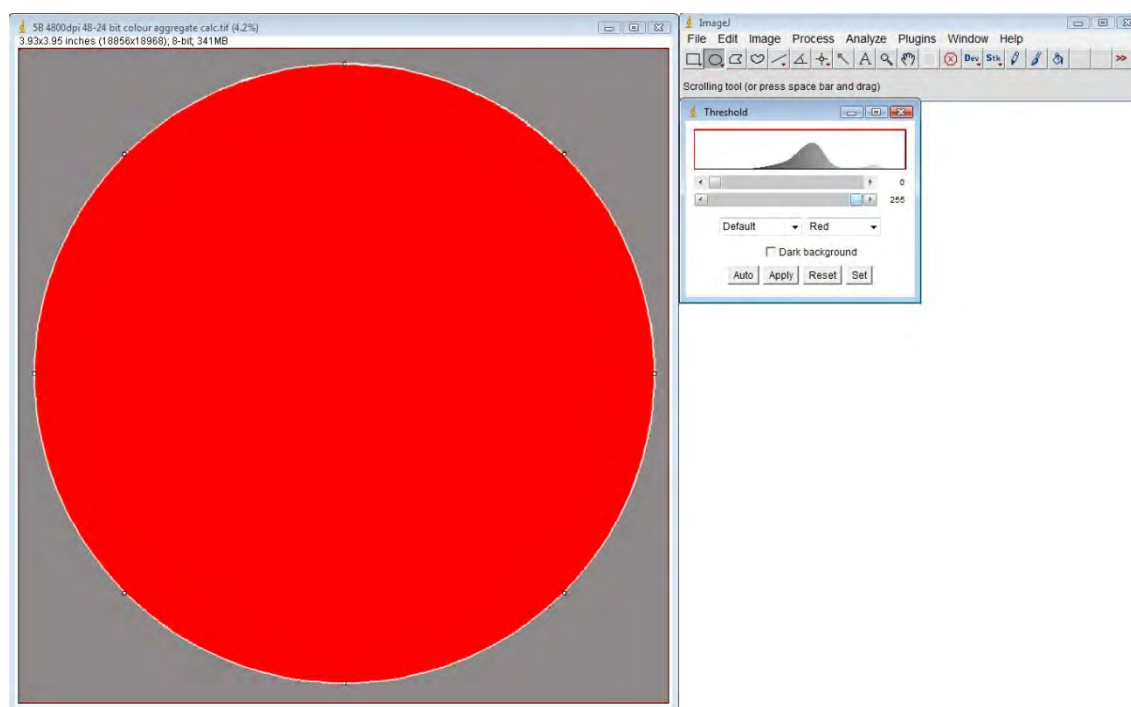


Figure 3.3.3.1.12 The bottom button in the threshold gets adjusted to 255 (full red fill)

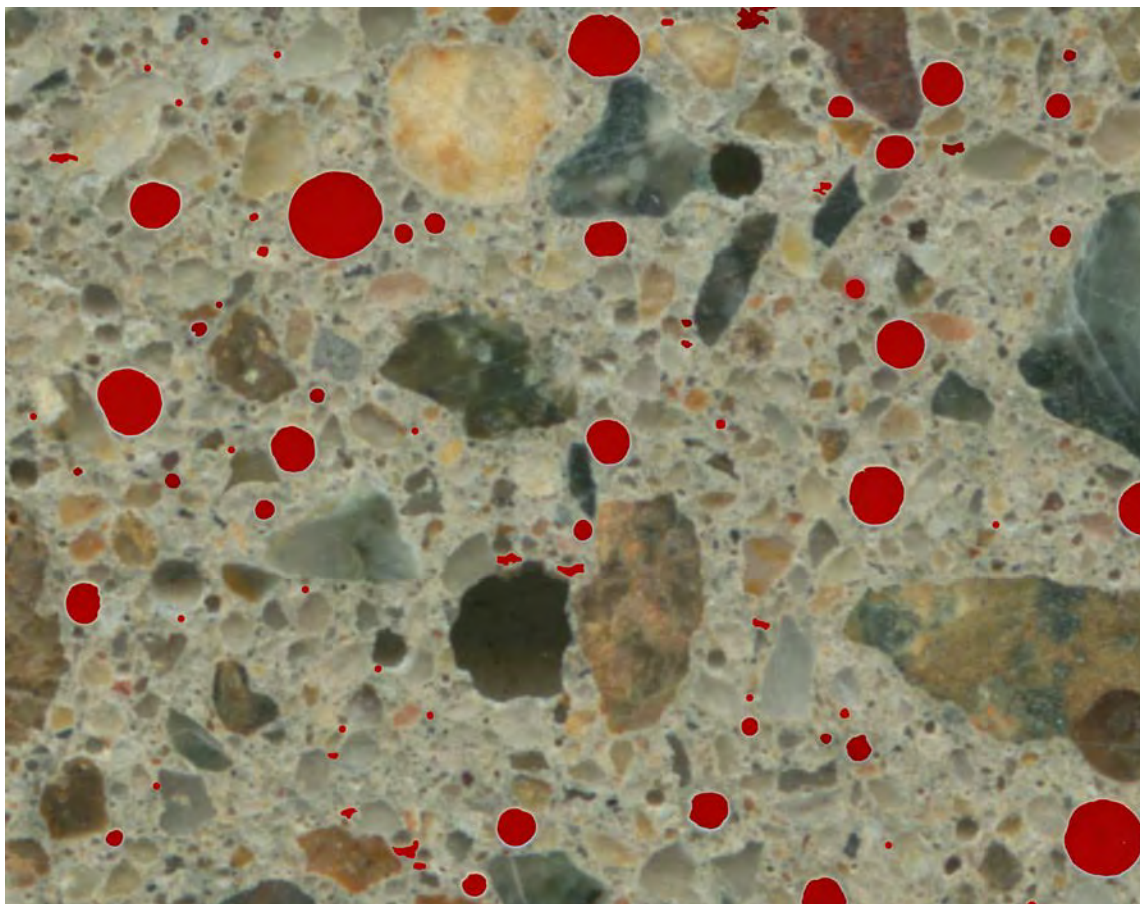


Figure 3.3.3.1.13 Red coloured entrained micro-pores on the original colour scanned image

Figure 3.3.3.1.13 displays coloured pores on the original colour picture of the image. Image size was 1.78 GB in 6400 dpi, 48-bit colour.

Some of these entrained micro-pores are very small. 64-bit ImageJ is able to very accurately detect the true circumferences, thus accurately calculating the true void area in 2D. This can be then quantitatively related to 3D volumetric percentage air voids.

64-bit ImageJ was unable to analyse 6400 dpi 48-bit colour digital image. For this reason the image was reduced to 8-bit greyscale for quantitative calculations.

7. Adjust the top button to the value (the pixels with brightness values greater than or equal to this threshold value display in red) - in this case 180 - to display the porosity in red while watching in a zoomed image the calibration of 5-10 μ micro pores on the screen to make sure that they are fully selected;

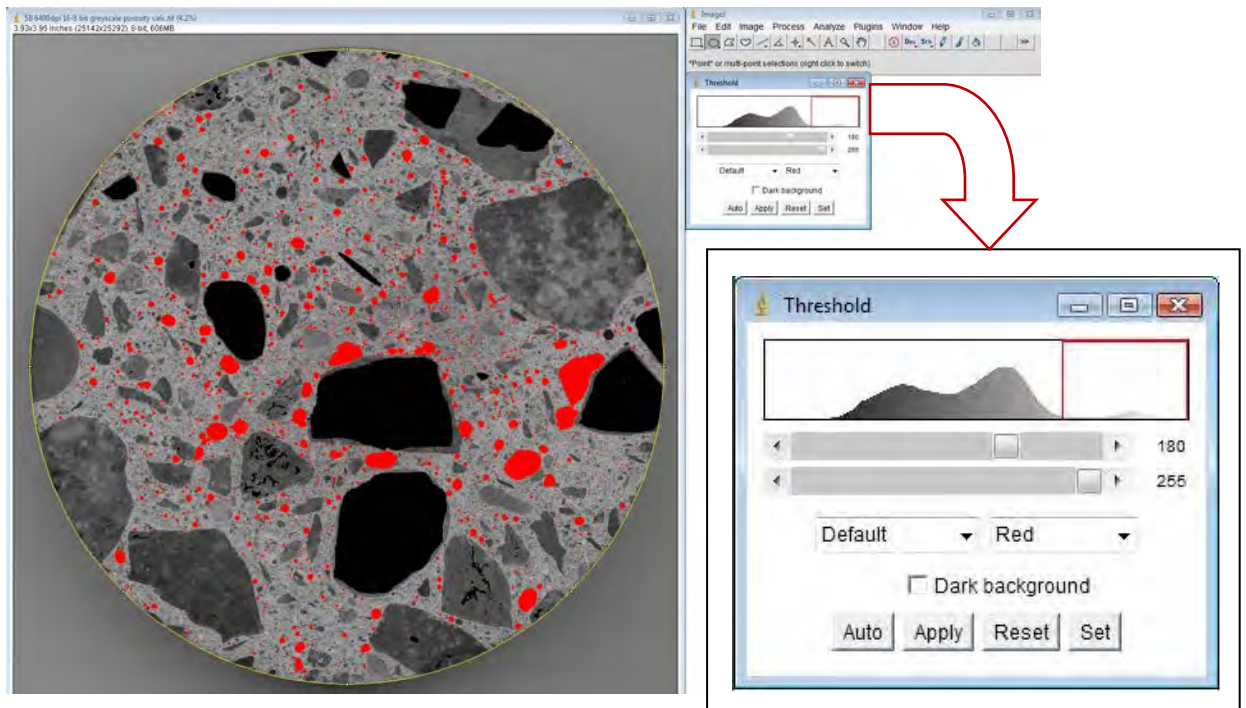
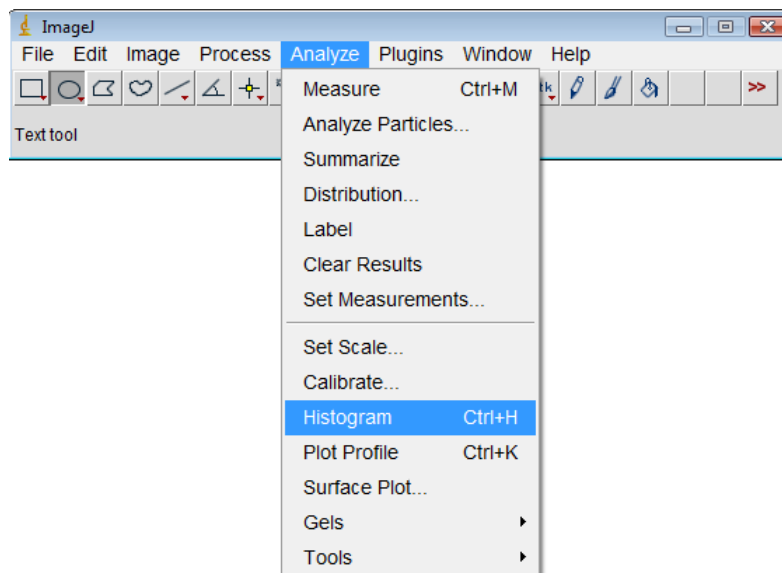


Figure 3.3.3.1.14 Porosity (originally in white) is now covered in red for the calculation

8. On the Menu bar select Analyze, then Histogram:



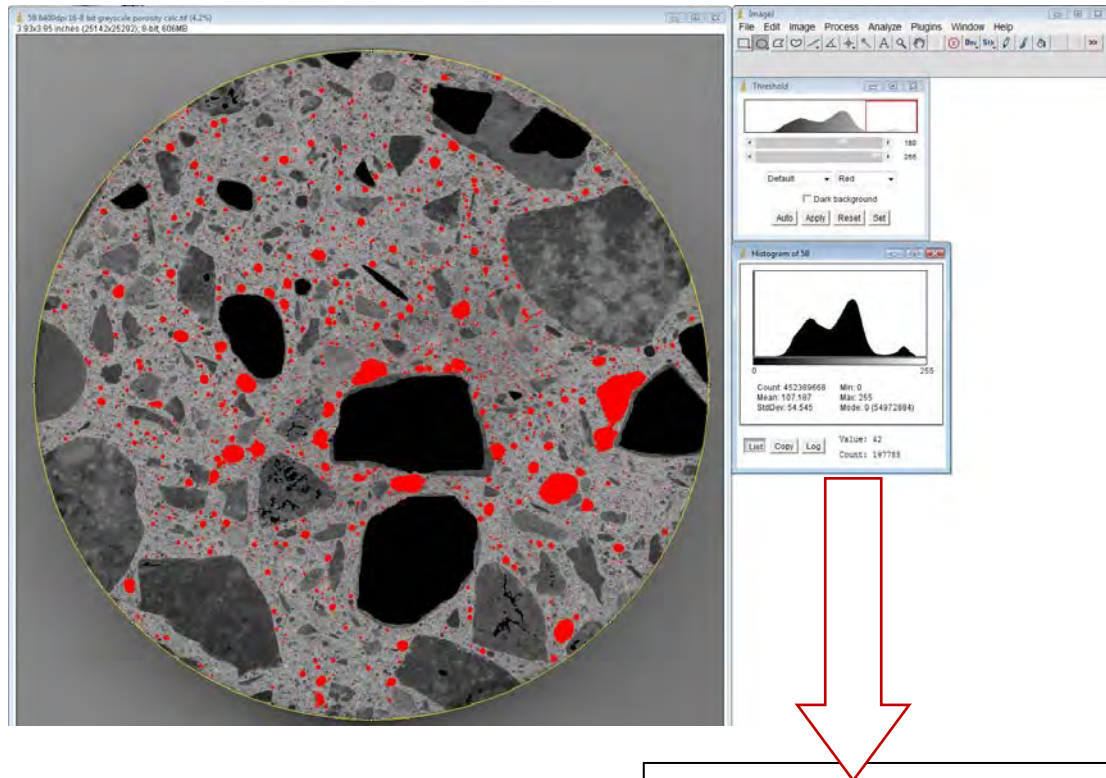
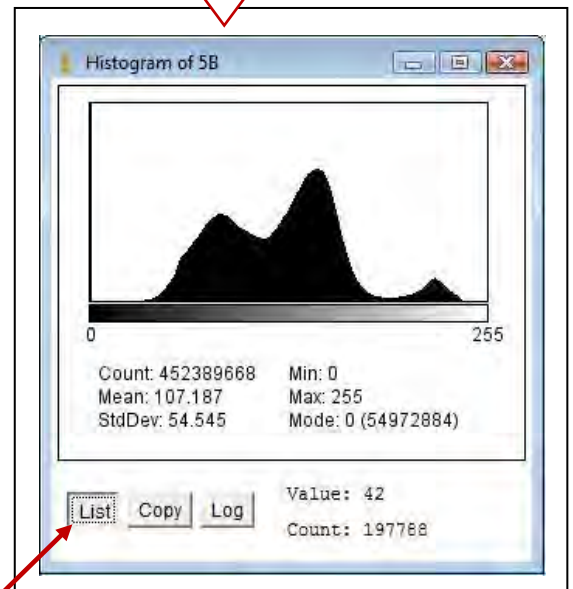


Figure 3.3.3.1.15 Select the Histogram under the Analyze on the Menu bar to calculate the values of the selected area to calculate



9. In the Histogram now select List to display values of the selected range of bits and their count;

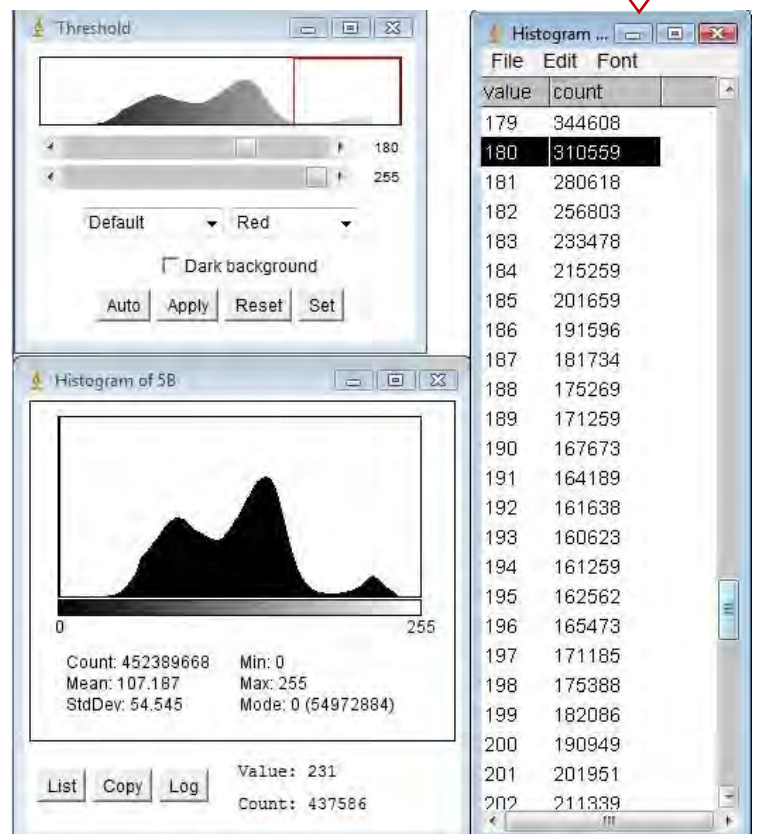
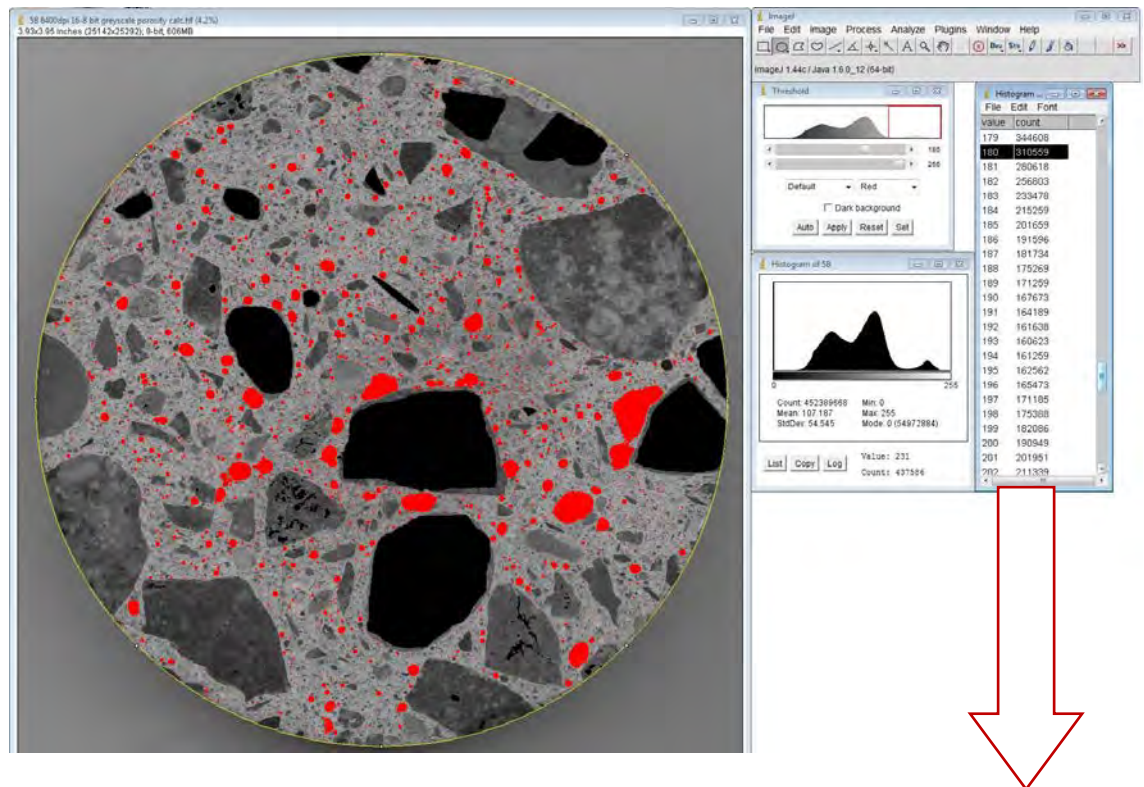


Figure 3.3.3.1.16 List of values is displayed from bits 0 to 255 where the first selection will be in this case the value at the bit 180, after that slide down to the value of 255 and copy the whole selection (between 180 to 255) into the Clipboard

10. Open Microsoft Excel and paste the selection of values into the spreadsheet;

	1B	2B	3B	4B	5B
1	179	371289	182	297188	183
2	180	367339	183	273790	186
3	181	339524	184	261305	187
4	182	328786	185	246637	188
5	183	322342	186	237747	189
6	184	315704	187	229897	190
7	185	312211	188	225991	191
8	186	309476	189	221255	192
9	187	313950	190	219714	193
10	188	310553	191	218356	194
11	189	324254	192	221327	195
12	190	328013	193	226455	196
13	191	316661	194	229778	197
14	192	346884	195	237085	198
15	193	356626	196	248625	199
16	194	346786	197	257036	200
17	195	362176	198	267153	201
18	196	398638	199	322536	202
19	197	416062	200	357769	203
20	198	453184	201	414712	204
21	199	500794	202	512662	205
22	200	483186	203	533996	206
23	201	504002	204	578428	207
24	202	529968	205	605409	208
25	203	556658	206	641186	209
26	204	583938	207	684755	210
27	205	613958	208	738729	211
28	206	643952	209	797430	212
29	207	673762	210	847291	213
30	208	701550	211	875092	214
31	209	727448	212	907239	215
32	210	752770	213	943687	216
33	211	777580	214	980547	217
34	212	796446	215	101915	218
35	213	819750	216	105882	219
36	214	839364	217	109954	220
37	215	863189	218	114054	221
38	216	883318	219	118240	222
39	217	899624	220	122541	223
40	218	954135	221	138164	224
41	219	930678	222	142727	225
42	220	941472	223	148070	226
43	221	972220	224	157978	227
44	222	907486	225	174910	228
45	223	874230	226	161223	229
46	224	84230	227	159195	230

Figure 3.3.3.1.17 Values of selected bits from the List in the Histogram are pasted into the spreadsheet

11. Underneath of the pasted values a formula for the sum of the values will be selected to provide the calculation of all pixels in the selected range (180 to 255);

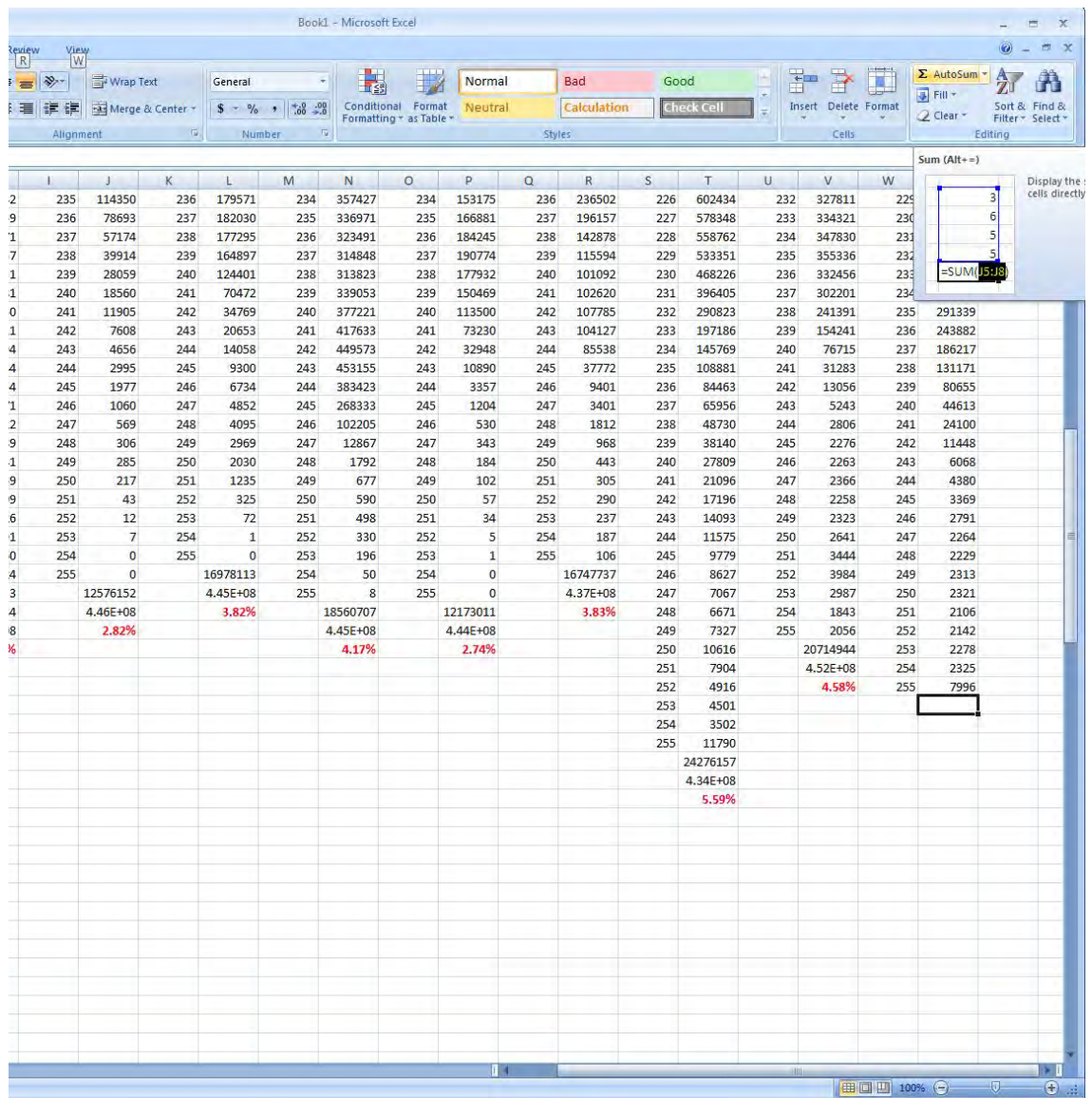


Figure 3.3.3.1.18 Formula for the sum of values is selected on the Menu bar

12. The sum that is offered by the software gets checked if correct and inserted by pressing the Enter key;

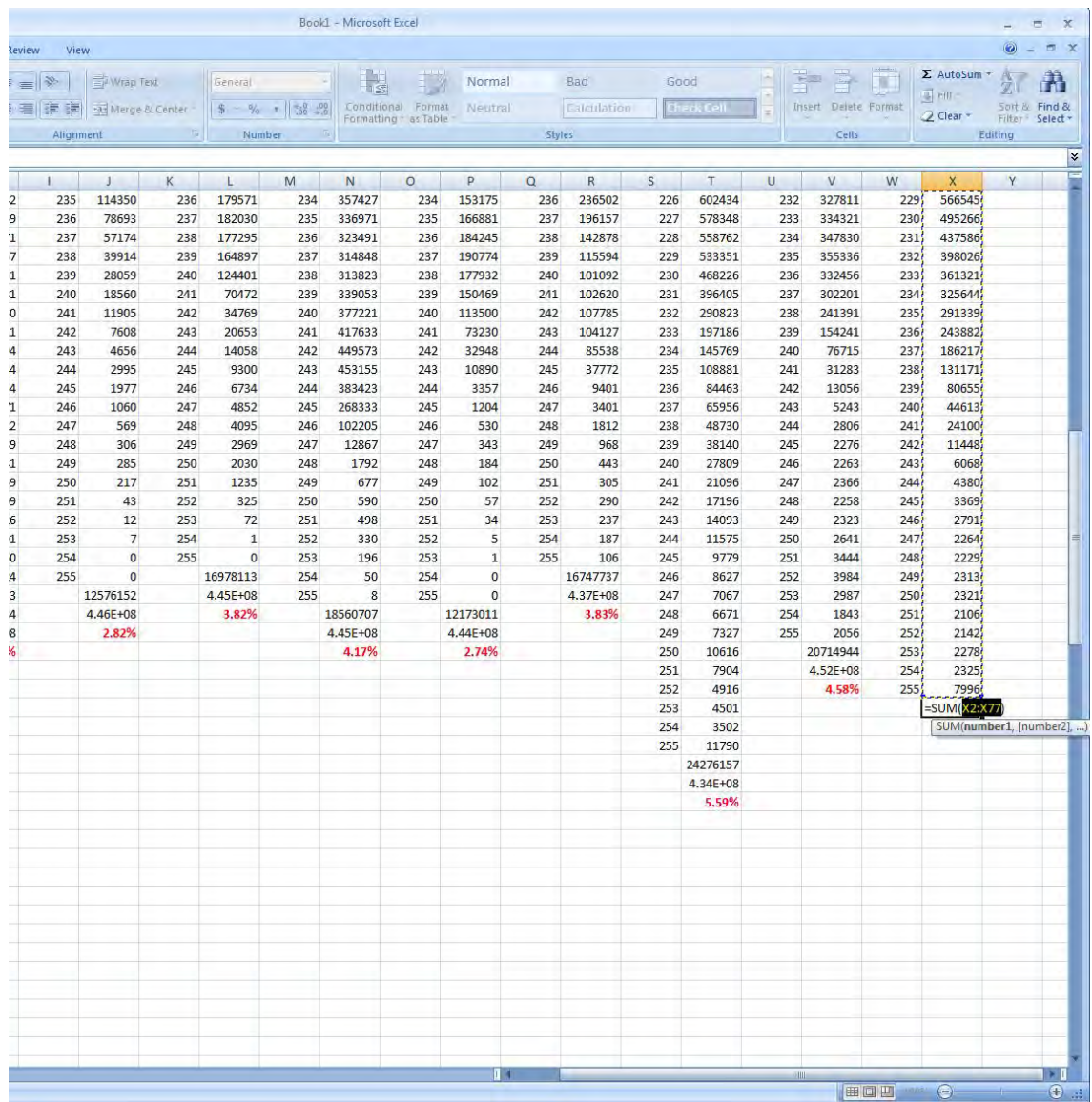


Figure 3.3.3.1.19 Sum is inserted underneath

13. The result of the sum is now underneath and the value at the Total Count of pixels in the whole object is manually copied underneath from the Histogram:

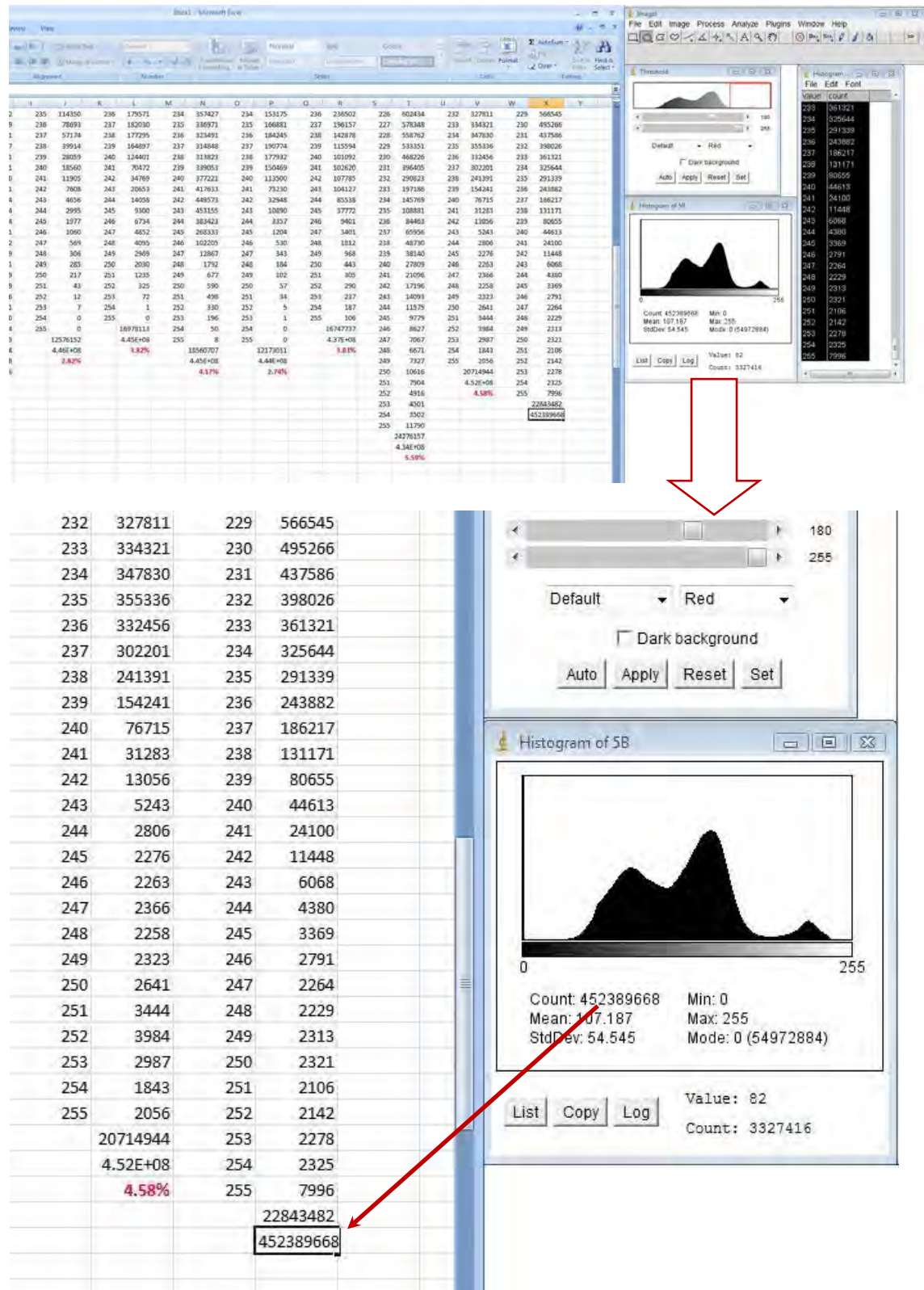


Figure 3.3.3.1.20 Copy the value for total Count underneath

14. The formula to calculate the percentage of the summed values in the range of bits between 180 to 255 against the 100% Total Count of pixels is inputted underneath (formula = the partial sum/the total sum):

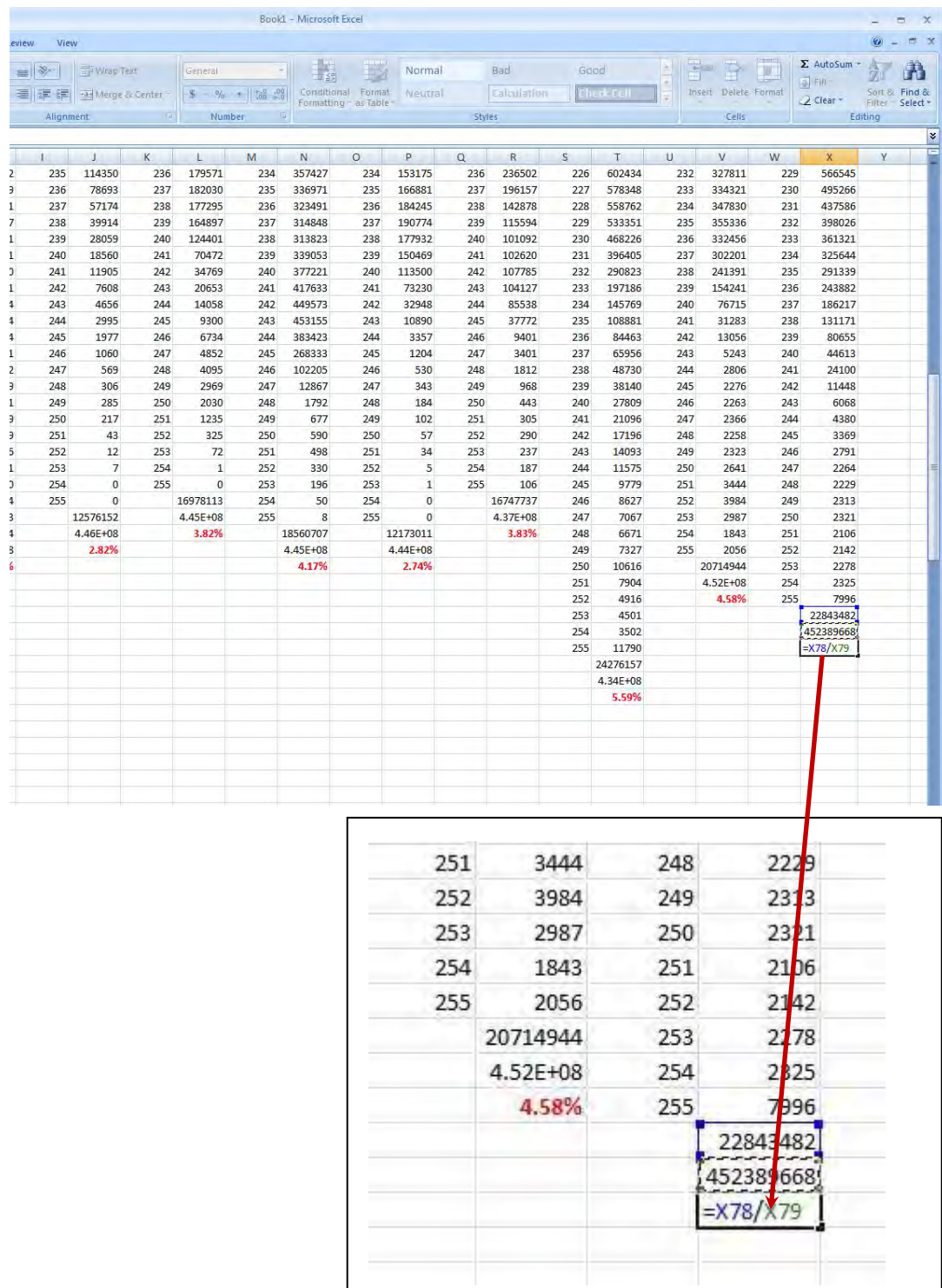
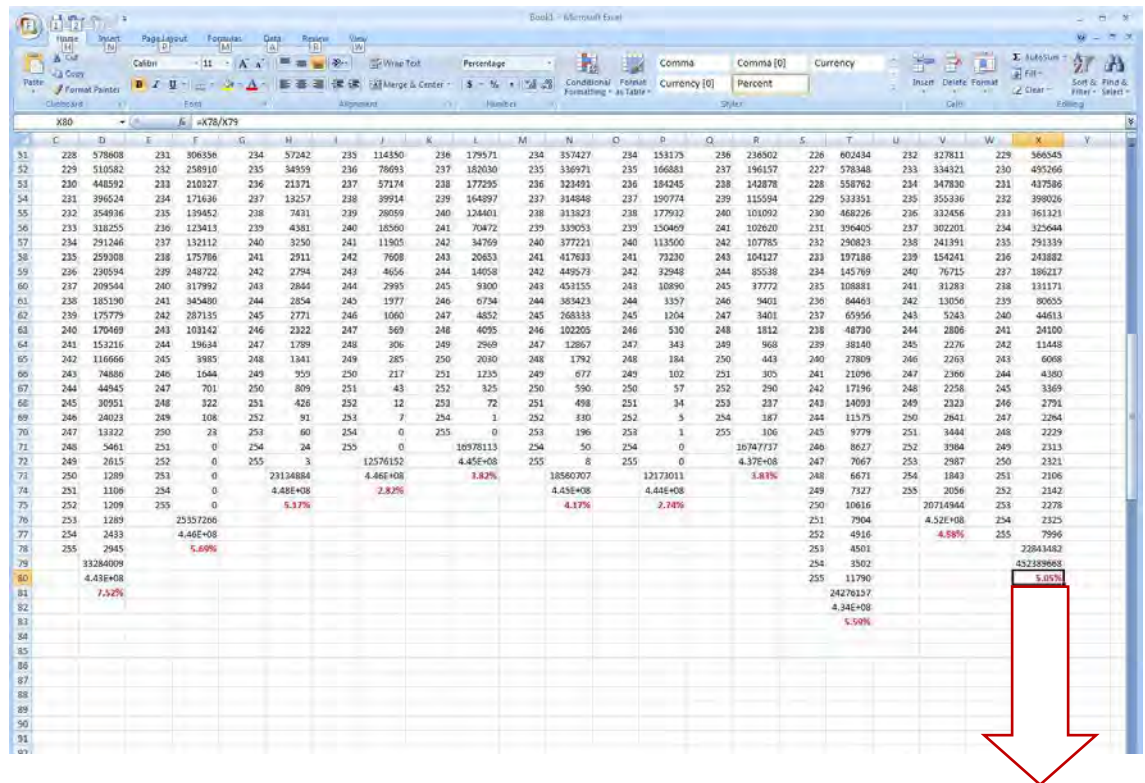


Figure 3.3.3.1.21 Formula for the calculation of the porosity is manually inputted

15. In the last step the calculation for the percentage of the porosity gets formatted:



1843	251	2106
2056	252	2142
20714944	253	2278
4.52E+08	254	2325
4.58%	255	7996
		22843482
		452389668
		5.05%

Figure 3.3.3.1.22 Formula gets formatted, the final value of **5.05%** for Reference Sample 5b

3.3.3.2 Study 3 - A Procedure for 100% Quantitative Calculations of Coarse Aggregate Using 64-bit Adobe PhotoShop Elements 7.0, SilverFast Epson SE, 64-bit ImageJ and Microsoft Excel in 64-bit Windows

Samples were scanned in 4800 ppi 48-24 bit colour for digital analysis. Each Sample was then opened in the 64-bit Adobe PhotoShop Elements 7.0 and with the help of this programme adjusted for the calculation.

All aggregate is of different colours and shapes. To concentrate onto the sizes and shapes of the coarse aggregate that needed to be calculated, the aggregate was selected with a magnetic lasso tool exactly on the circumference of the aggregate and then coloured in black. This way the aggregate then was ready for the exact quantitative calculation.

The following Figures (3.3.3.2.1 to 3.3.3.2.3) are showing in detail the process of colouring/masking the aggregate.

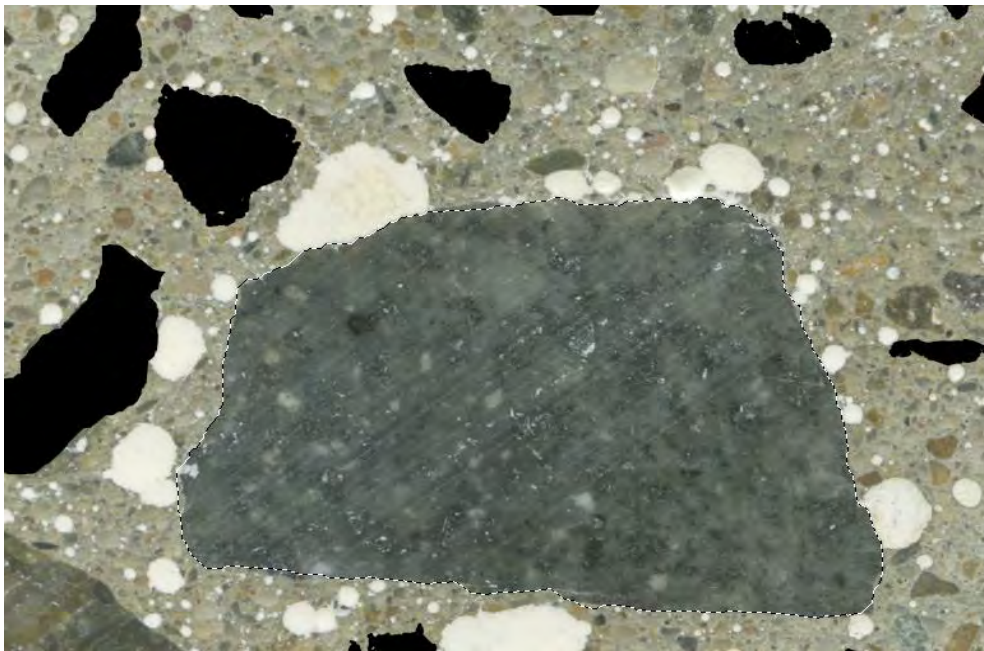


Figure 3.3.3.2.1 Magnetic lasso tool selects the circumference of the aggregate

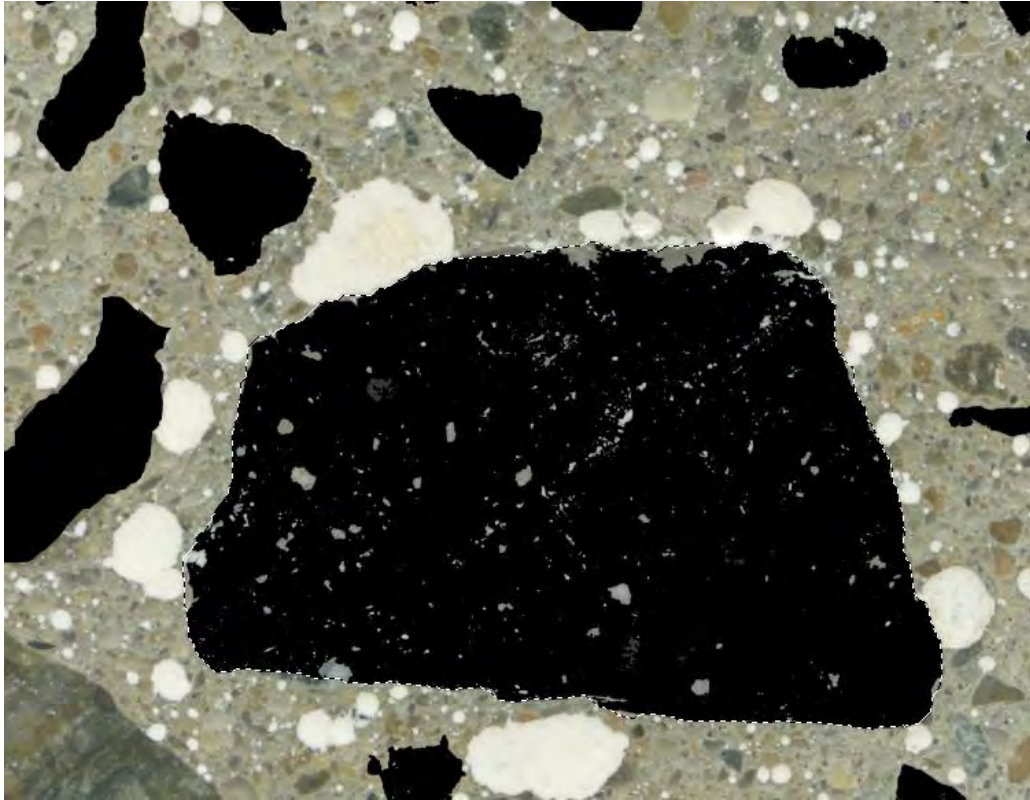


Figure 3.3.3.2.2 The bucket tool gradually fills the object with black colour

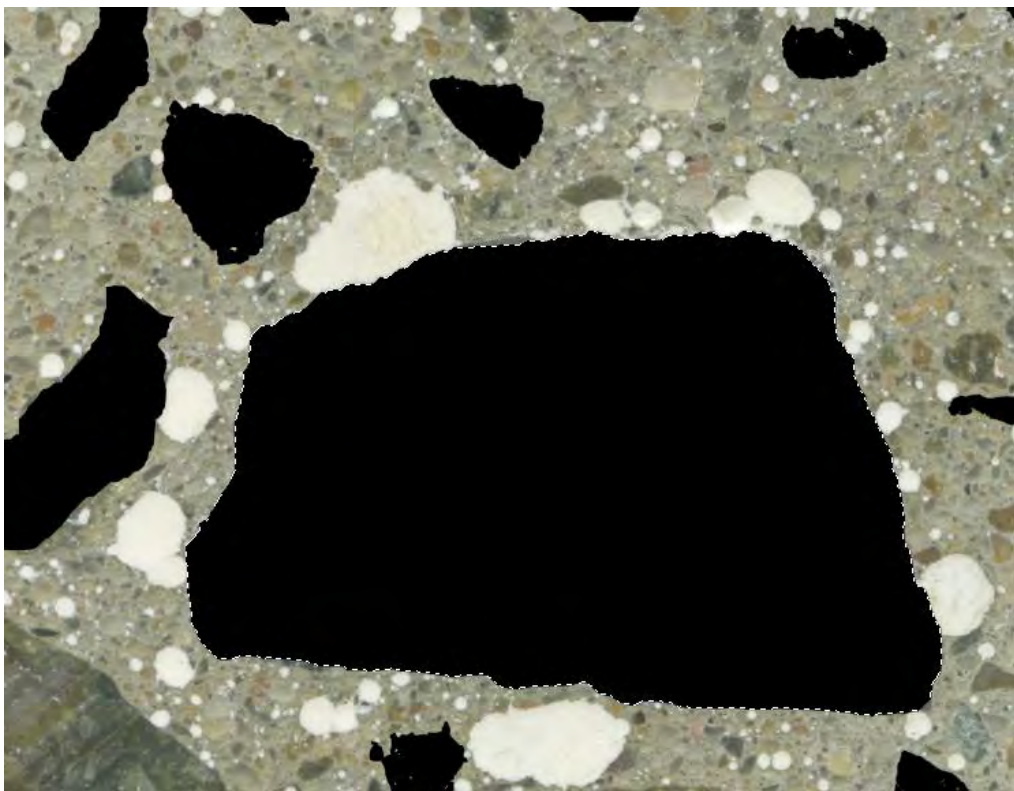


Figure 3.3.3.2.3 Fully filled aggregate

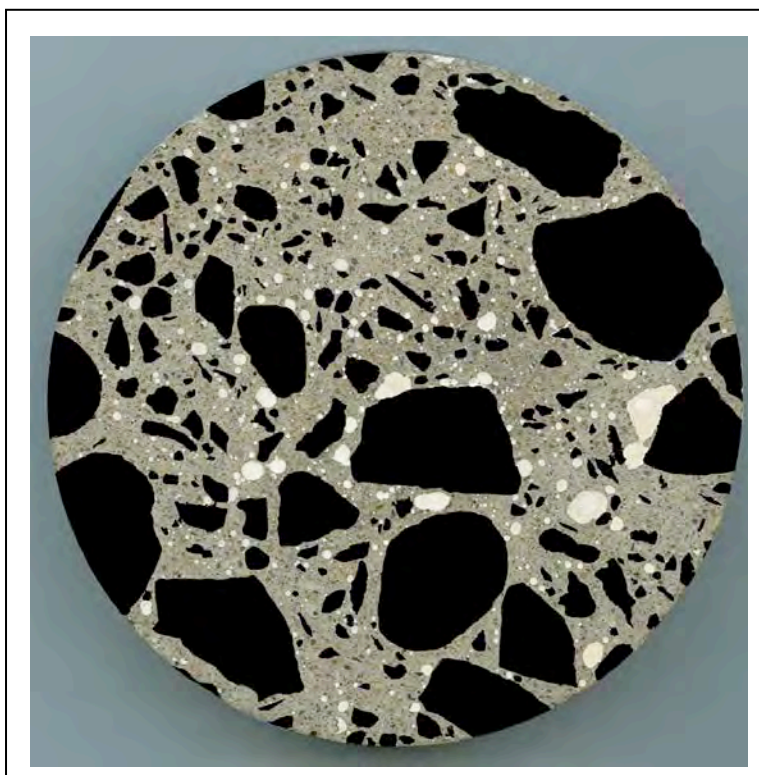


Figure 3.3.3.2.4 Fully filled Reference Sample 5b 4800 ppi, 48-24 bit colour, 1GB, 18856 x 18968 pixels (ready for a calculation in ImageJ)



Figure 3.3.3.2.5 Original Reference Sample 5b 4800 ppi, 48-24 bit colour, 1.78 GB, 25142 x 25292 pixels

Detailed Procedures for 100% Quantitative Calculations of Coarse Aggregate

1. Open ImageJ;
2. Click File, then click Open and select the picture file of the image to open on the screen;

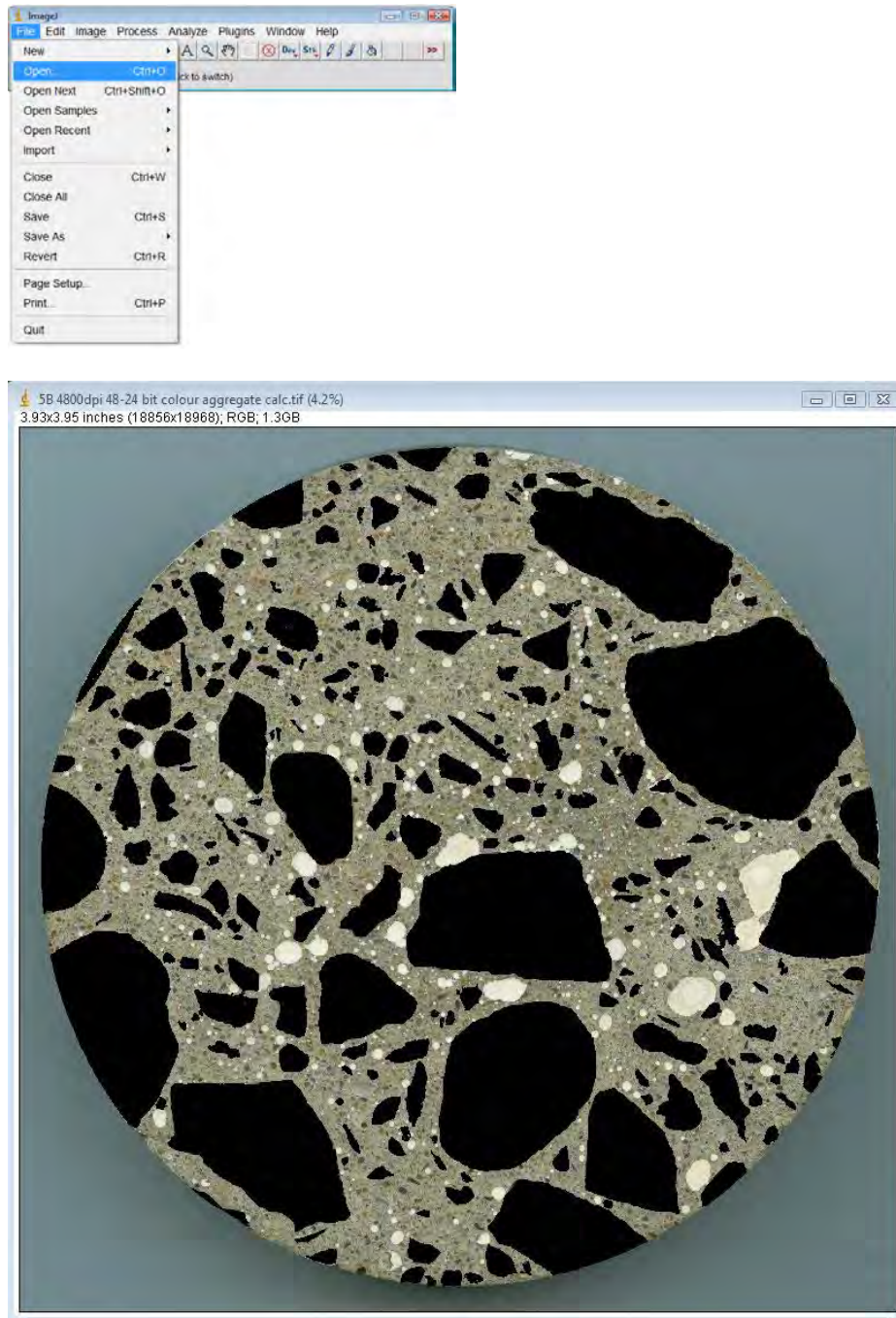



Figure 3.3.3.2.6 Open the image in ImageJ (pixels 18856 x 18968, 48 00 ppi, size 1.3 GB, 24-bit colour depth)

3. Choose the Elliptical tool  on the toolbar and carefully select the circumference of the image (yellow circle in Figure 3.3.3.2.7);

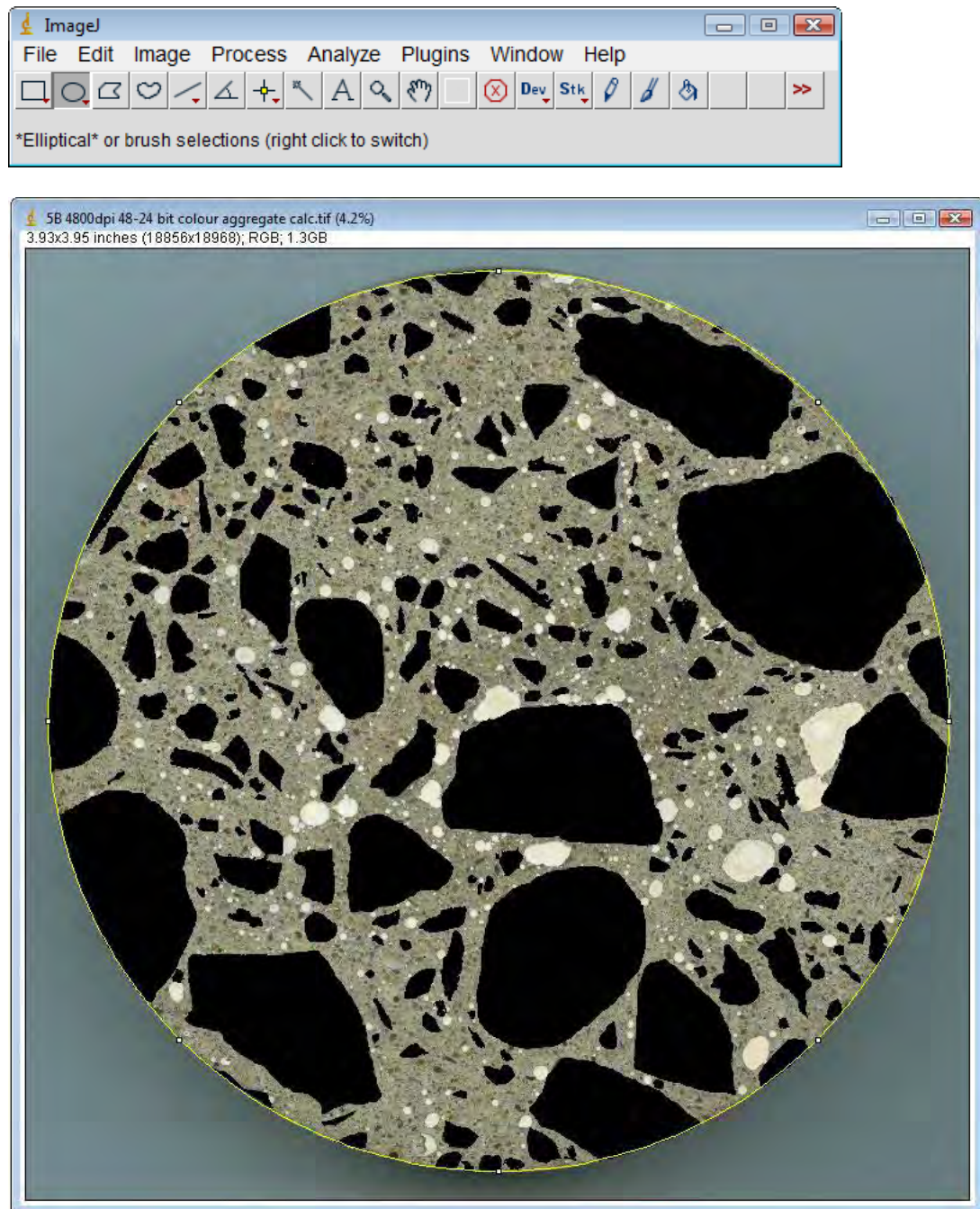


Figure 3.3.3.2.7 Select carefully the circumference of the Sample with Elliptical tool on the menu bar

4. Click Image, then Type and then 8-bit to change the colour image into the black and white image if not already in that format;

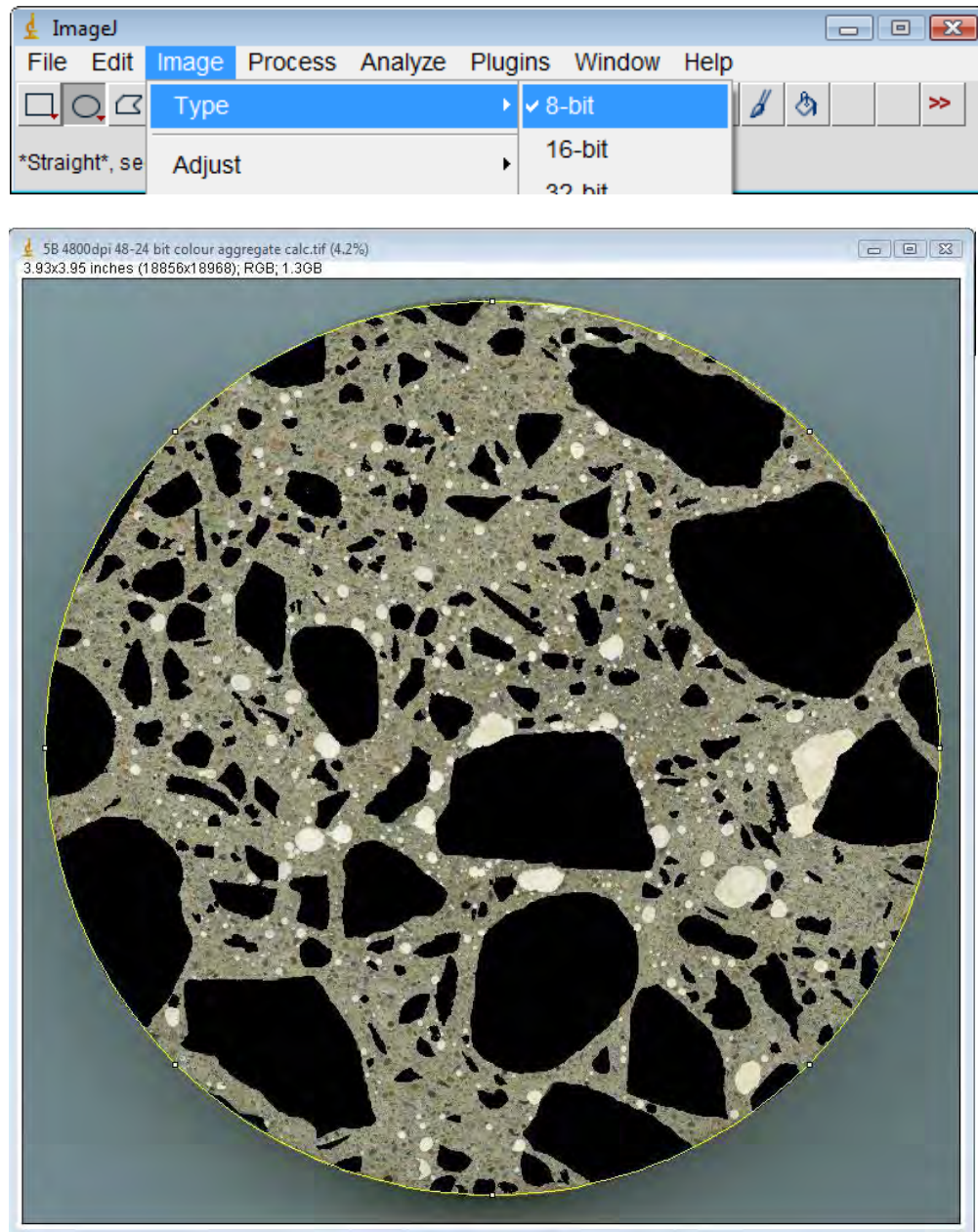


Figure 3.3.3.2.8 Type of the image is changed to 8-bit for the calculation

5. Click Image, then click Adjust, then click Threshold and keep the Default on Red colour;

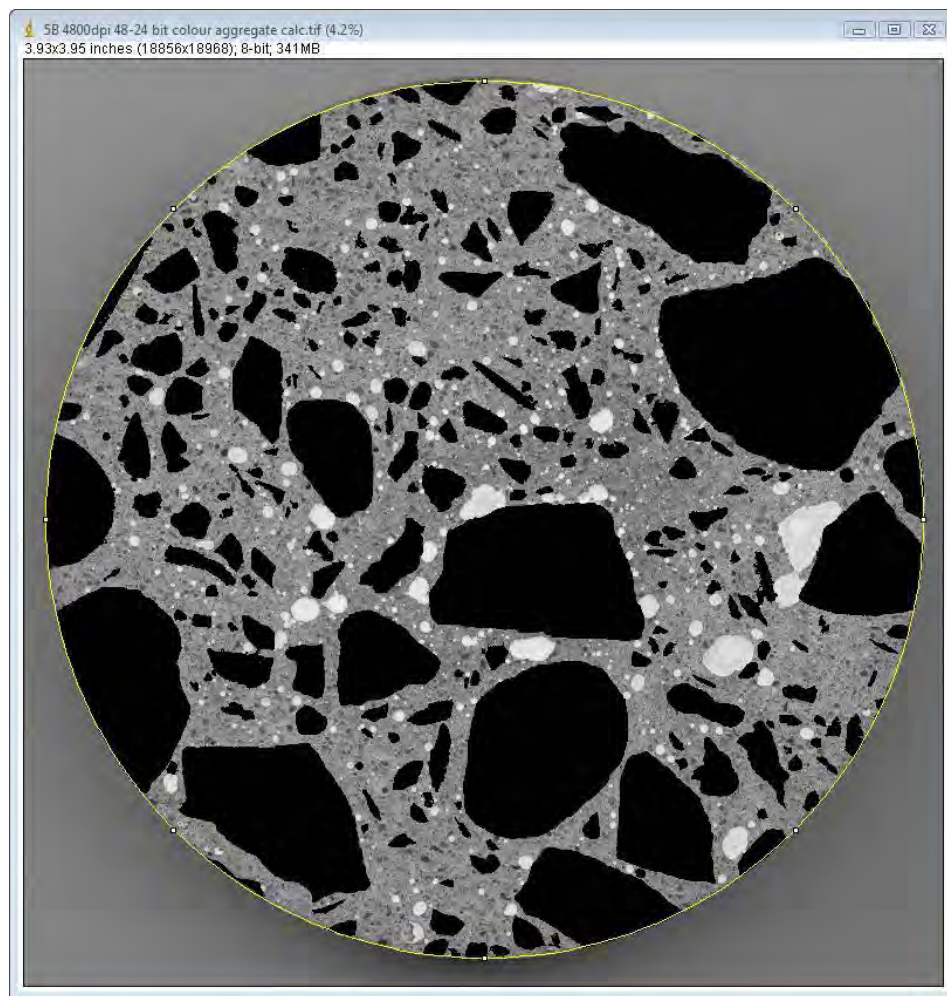
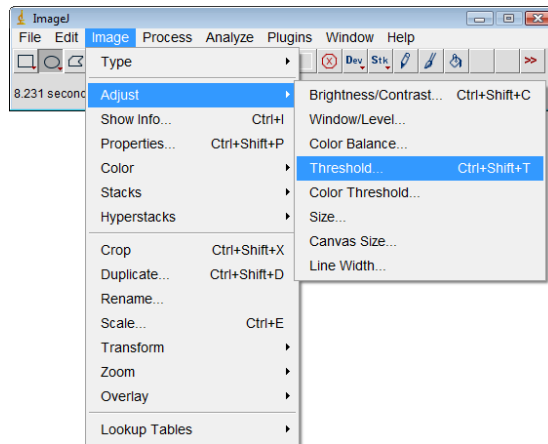


Figure 3.3.3.2.9 Select Image, Adjust and Threshold to start the calculation

The image on the screen will look similar to the Figure 3.3.3.2.10 on the next page, note
 - the threshold gets selected automatically by the software;

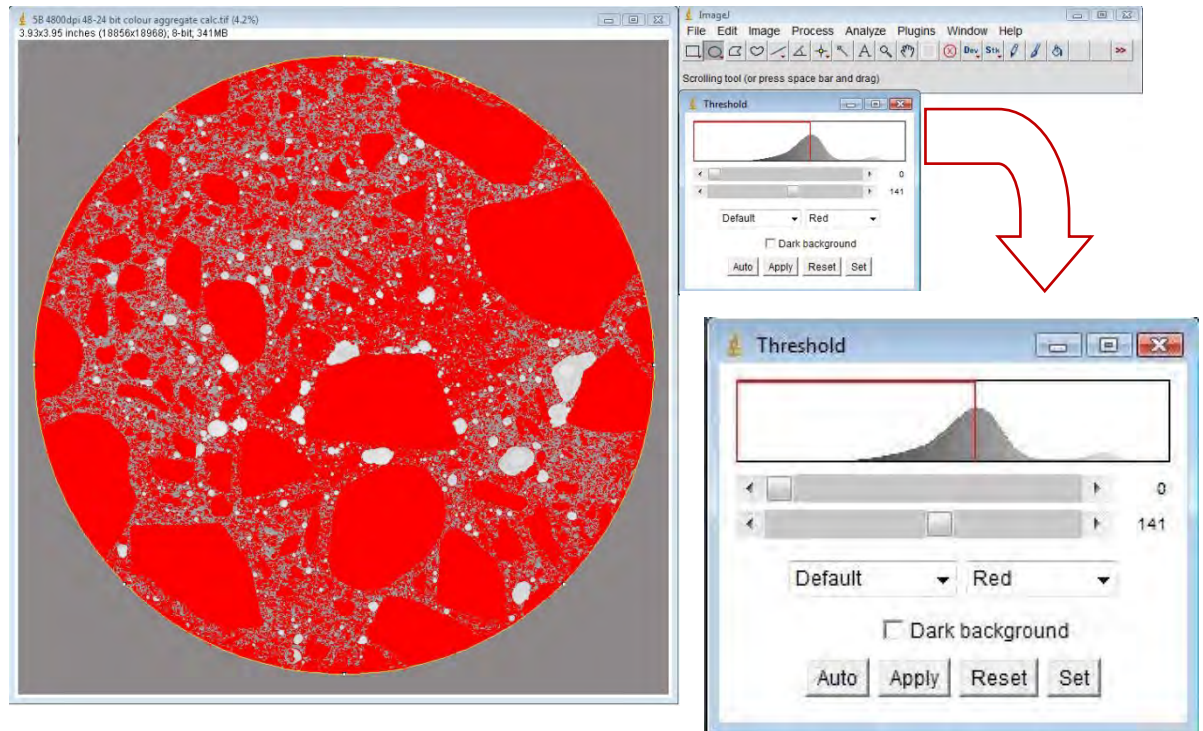


Figure 3.3.3.2.10 Automatic selection of the threshold by the software that needs to be manually adjusted in the following steps

6. Adjust the toolbars in the threshold manually - the bottom button to 255 as below:

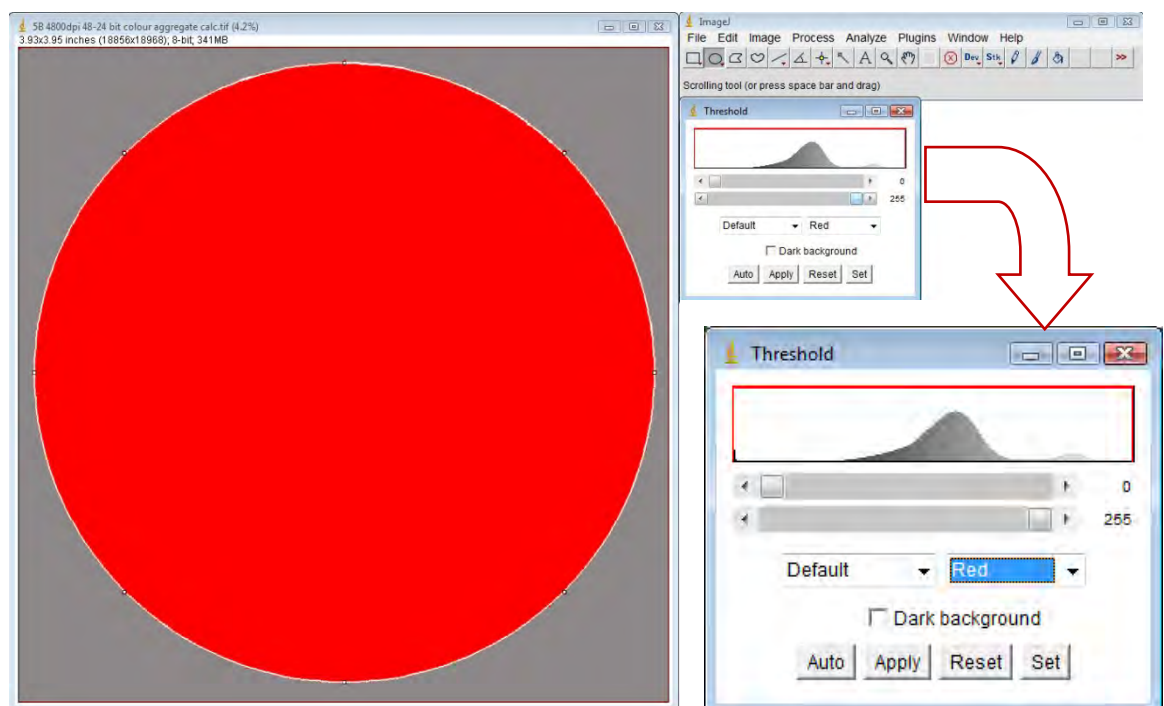


Figure 3.3.3.2.11 The bottom button in the threshold gets adjusted to 255 (full red fill)

7. Adjust the top button to the value suggested as the first solid value shown on the picture above the toolbar - in this case 72 - to display the aggregate in black while watching the colouring in the paste on the screen to make sure that the selection of aggregate is done well;

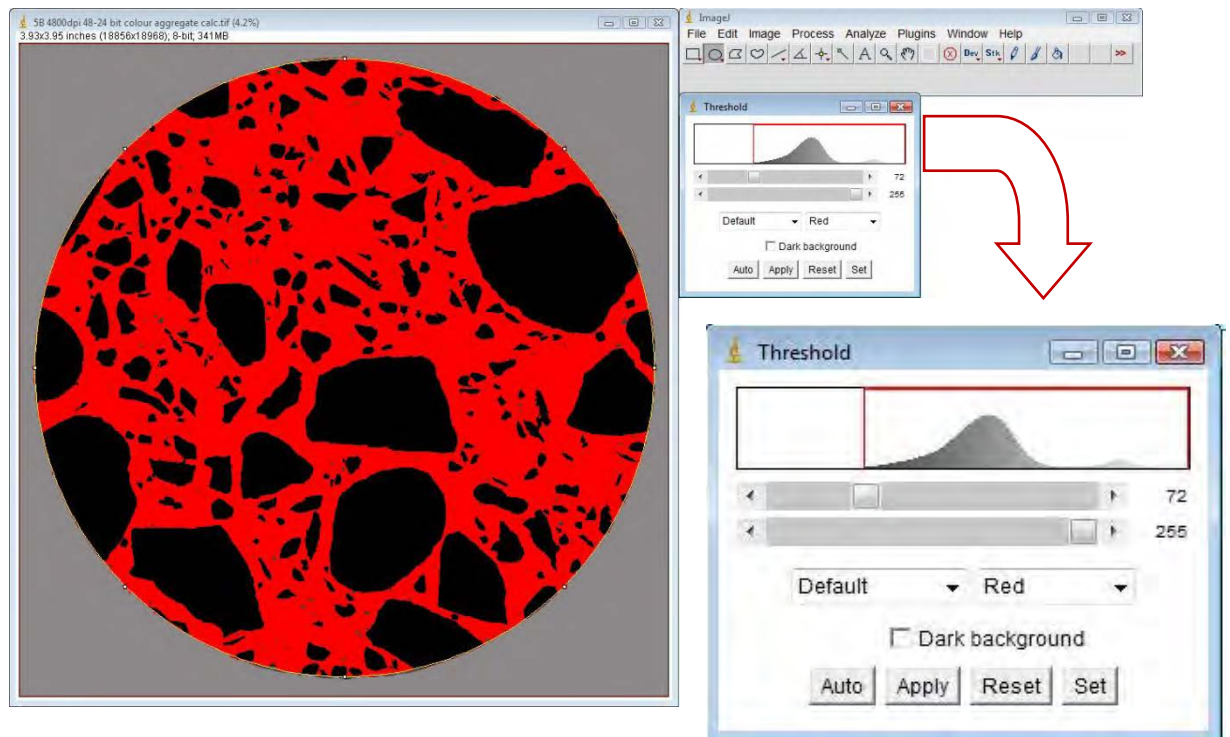


Figure 3.3.3.2.12 Aggregate in black and the rest is in red ready for the calculation

8. On the menu bar select Analyze, then Histogram:

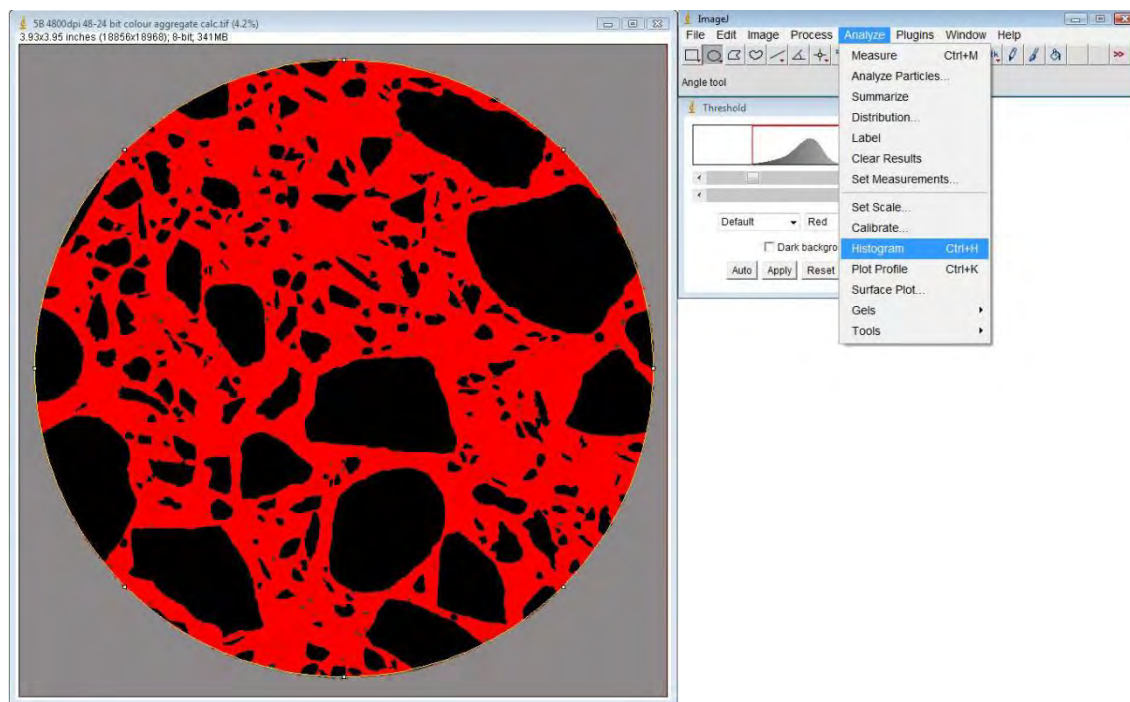
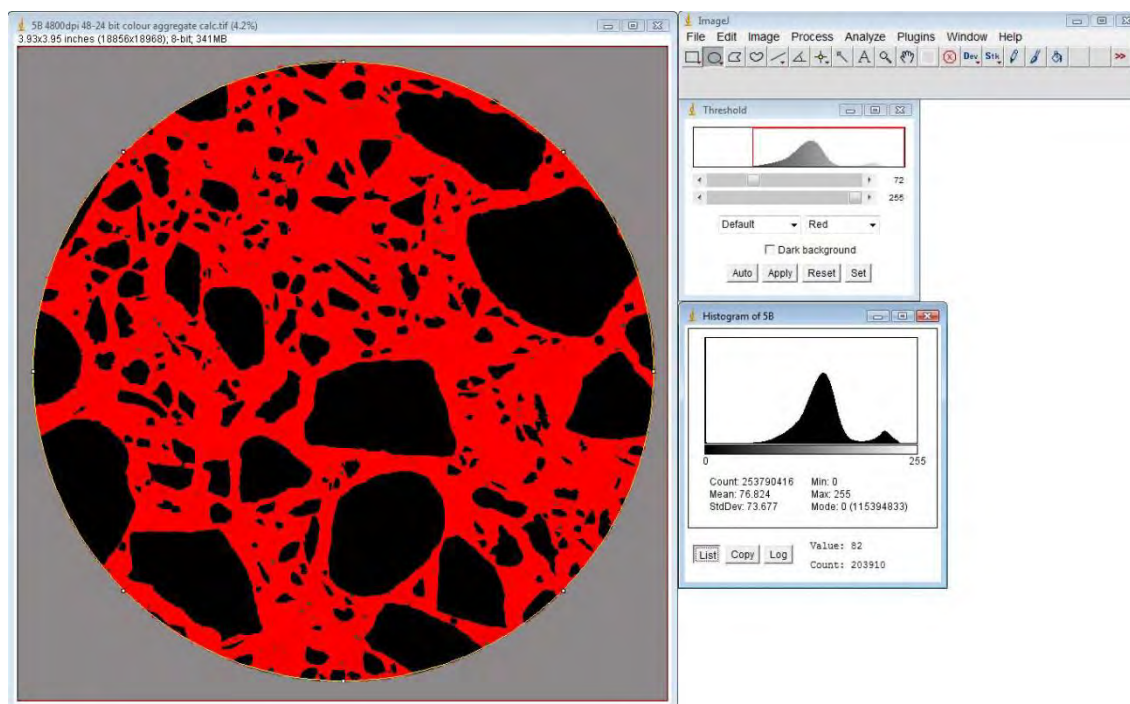


Figure 3.3.3.2.13 Select the Histogram under the Analyze on the menu bar to calculate the values of the selected area



Histogram in detail on the next page

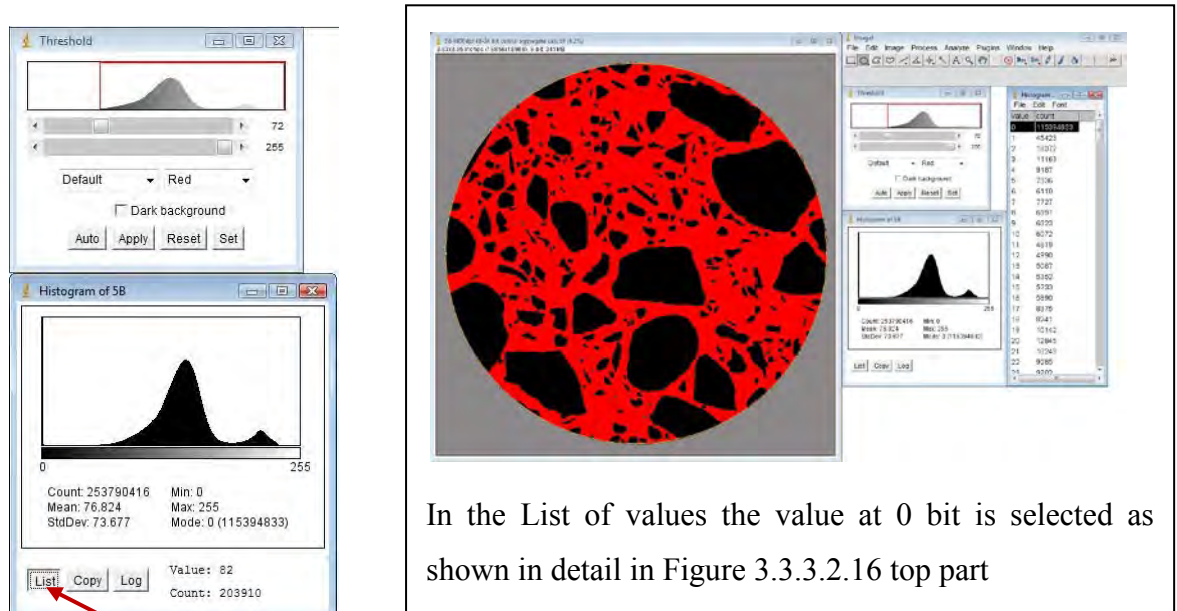


Figure 3.3.3.2.14 Histogram is displayed on the screen

9. In the Histogram now select List to display values of the selected range of bits and their count;

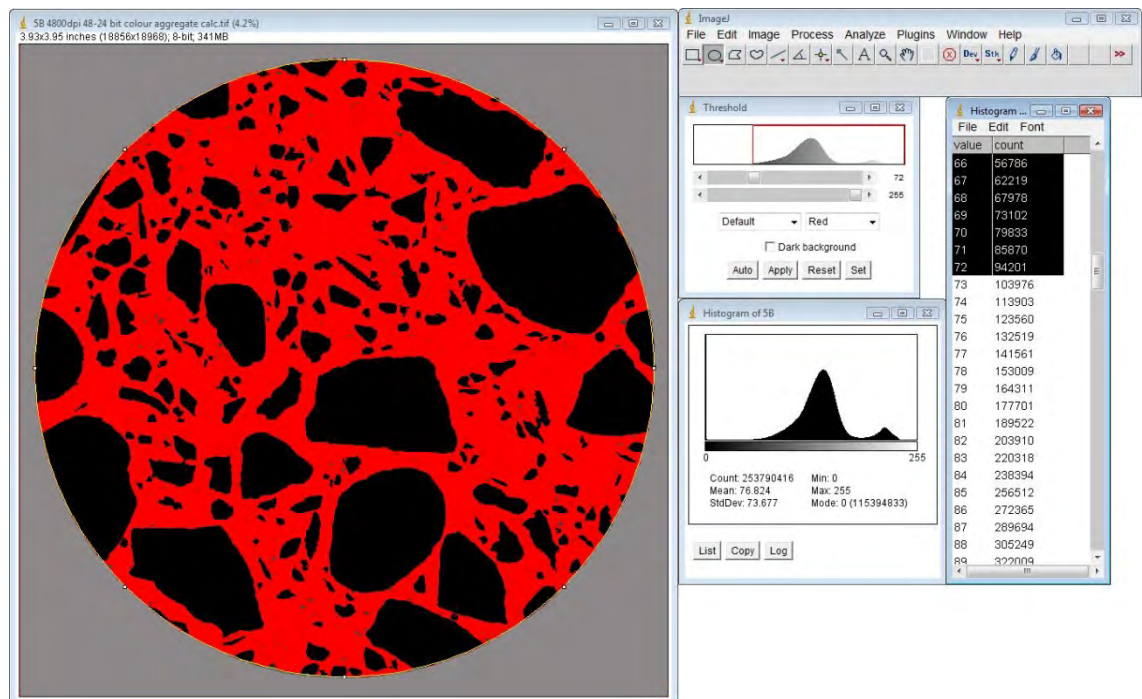


Figure 3.3.3.2.15 List of values is displayed from bits 0 to 255 where the first selection will be in this case the value at the bit 0, after that slide down to the value of 72 and copy the whole selection (between 0 to 72) into the Clipboard as shown in detail in Figure 3.3.3.2.16 bottom part

10. Values of bits 0 to 72 are copied and pasted into the spreadsheet:

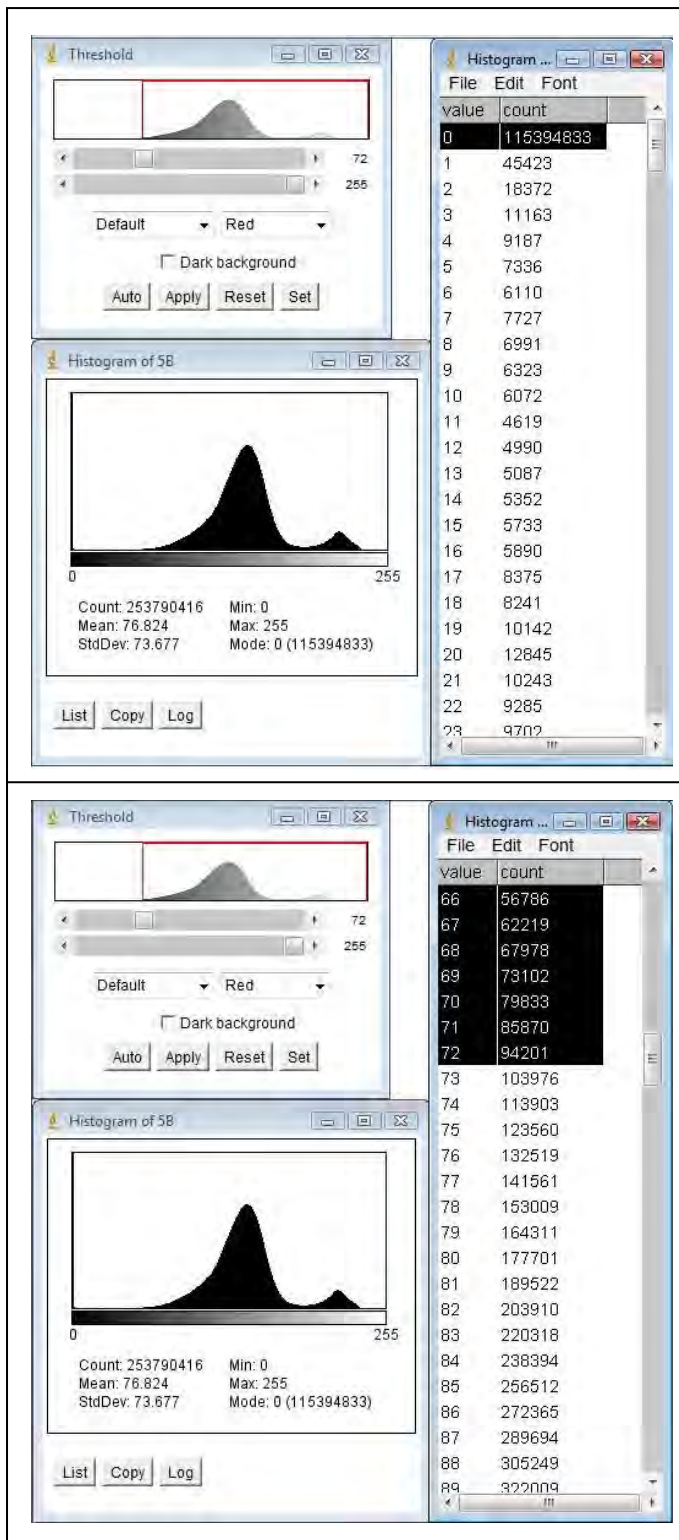


Figure 3.3.3.2.16 Selection of values in the range of 0 to 72 bits is copied and pasted into the Microsoft Excel for calculations

11. Microsoft Excel is used for the calculation:

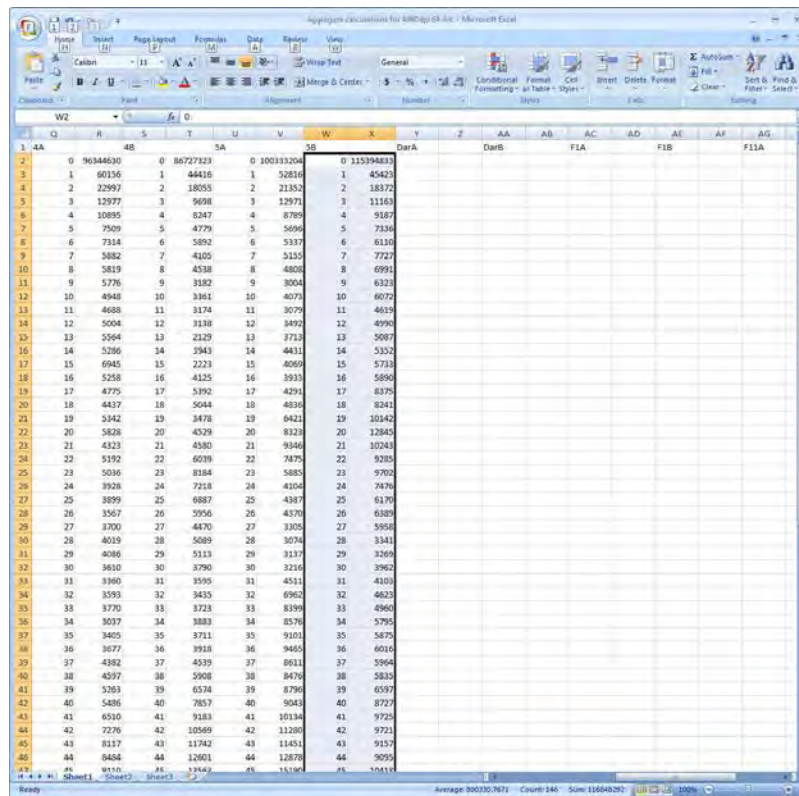


Figure 3.3.3.2.17 Values are copied onto the spreadsheet

12. A formula to sum the pixel values of the selected range is inserted with the help of the software:

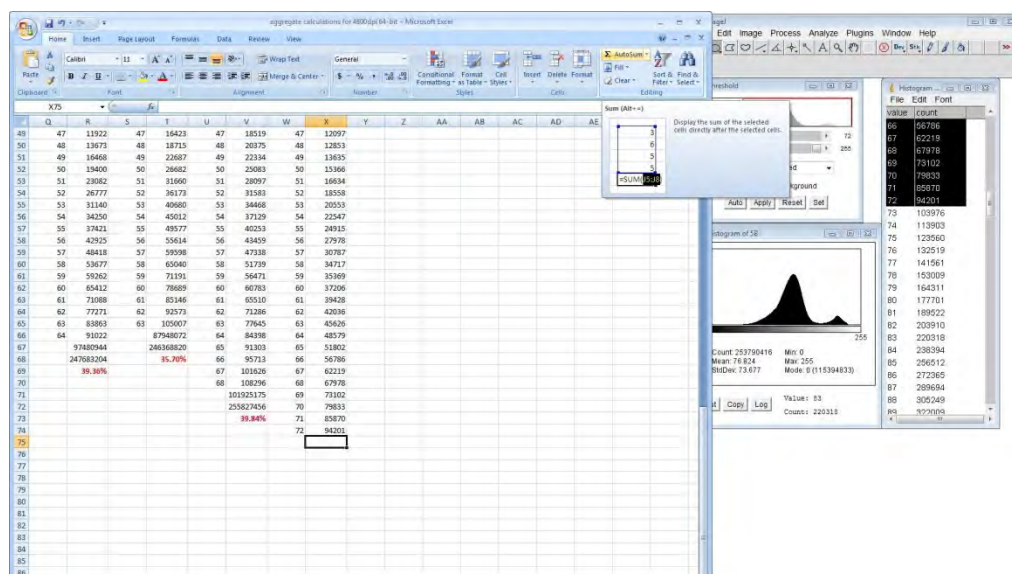


Figure 3.3.3.2.18 The Sum formula gets inserted

13. The sum is inserted and calculated

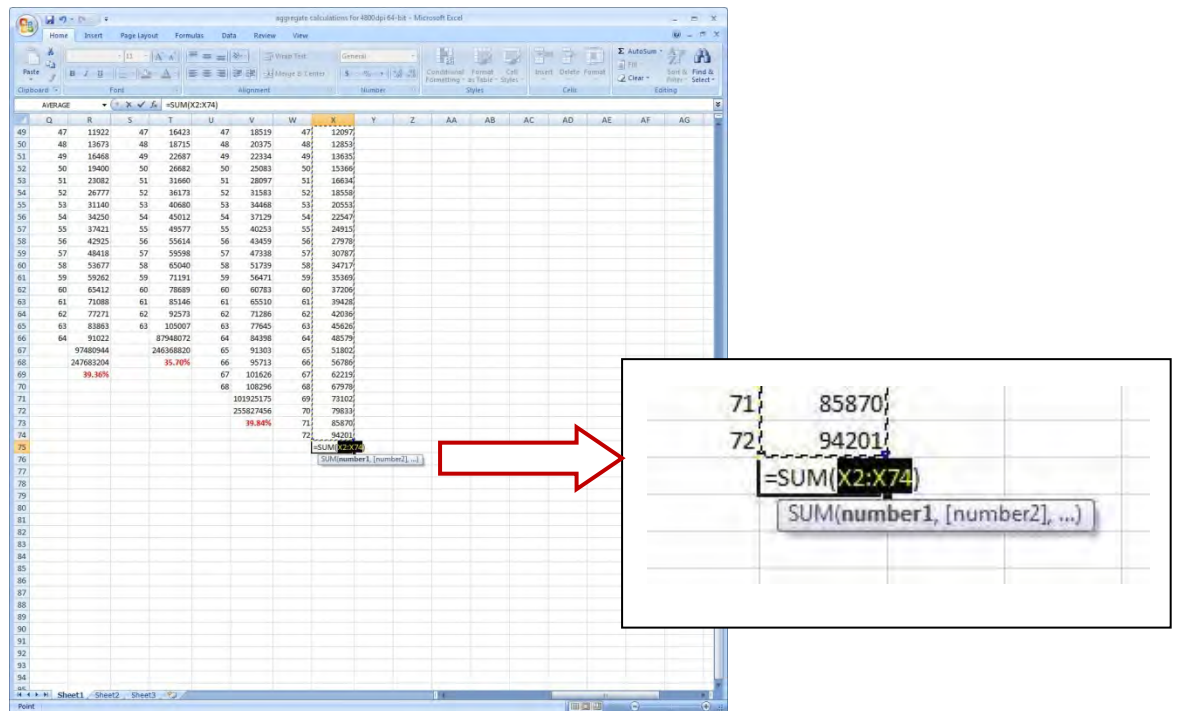


Figure 3.3.3.2.19 The Sum gets calculated

14. Value of Total sum of pixels in the selected shape are copied manually from the Histogram into the spreadsheet

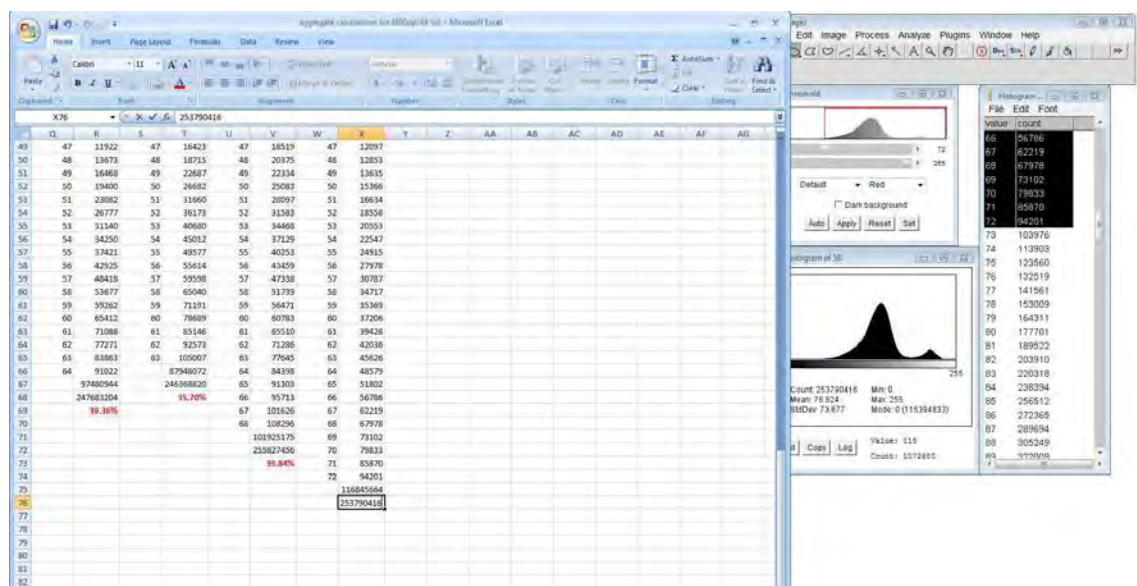


Figure 3.3.3.2.20 Total sum of pixels is copied manually into the spreadsheet as shown in detail on the following page in Figure 3.3.3.2.21

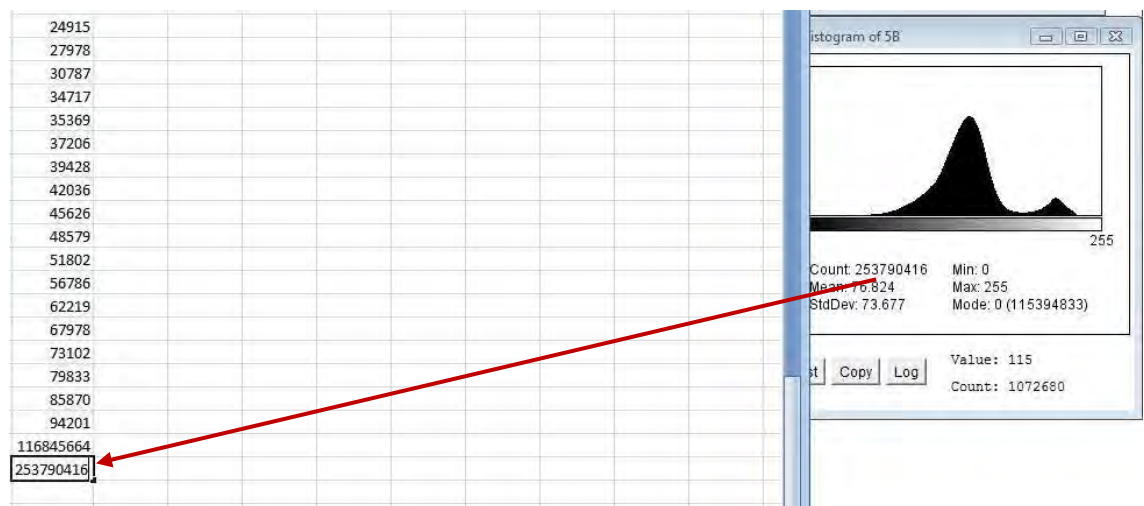


Figure 3.3.3.2.21 The value of the sum of all pixels in the selected object is copied into the spreadsheet manually

15. Formula to calculate the percentage of the aggregate is manually inserted into the spreadsheet:

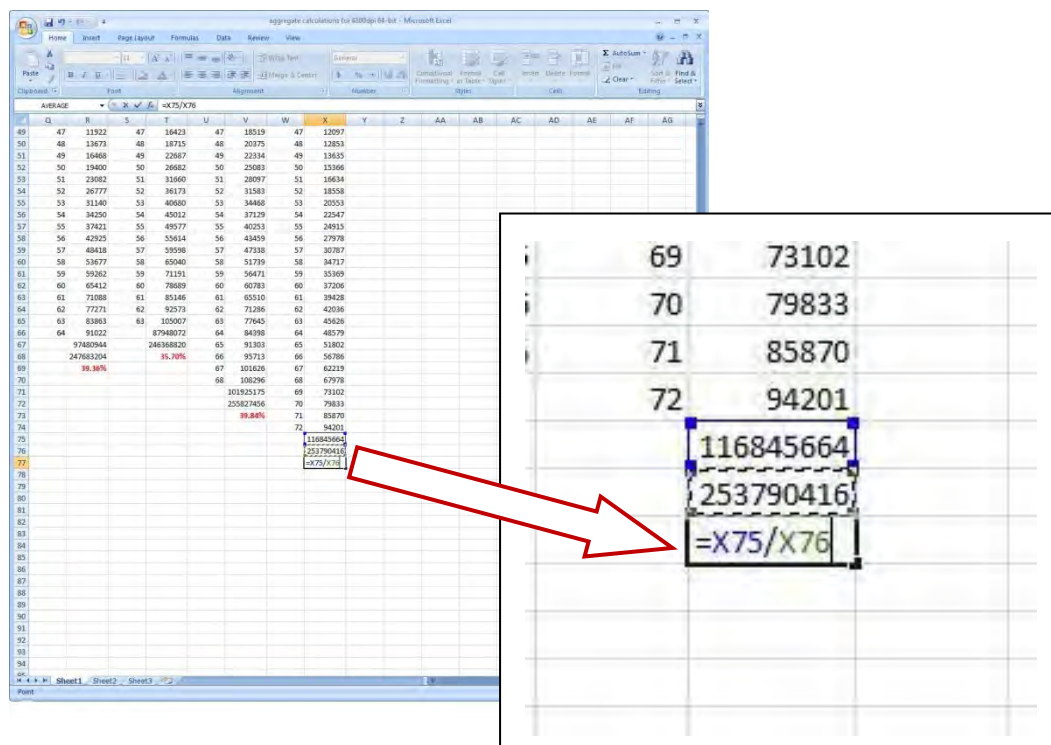


Figure 3.3.3.2.22 Formula is inserted to calculate the percentage of the aggregate

16. The last step is to format the result of the calculation:

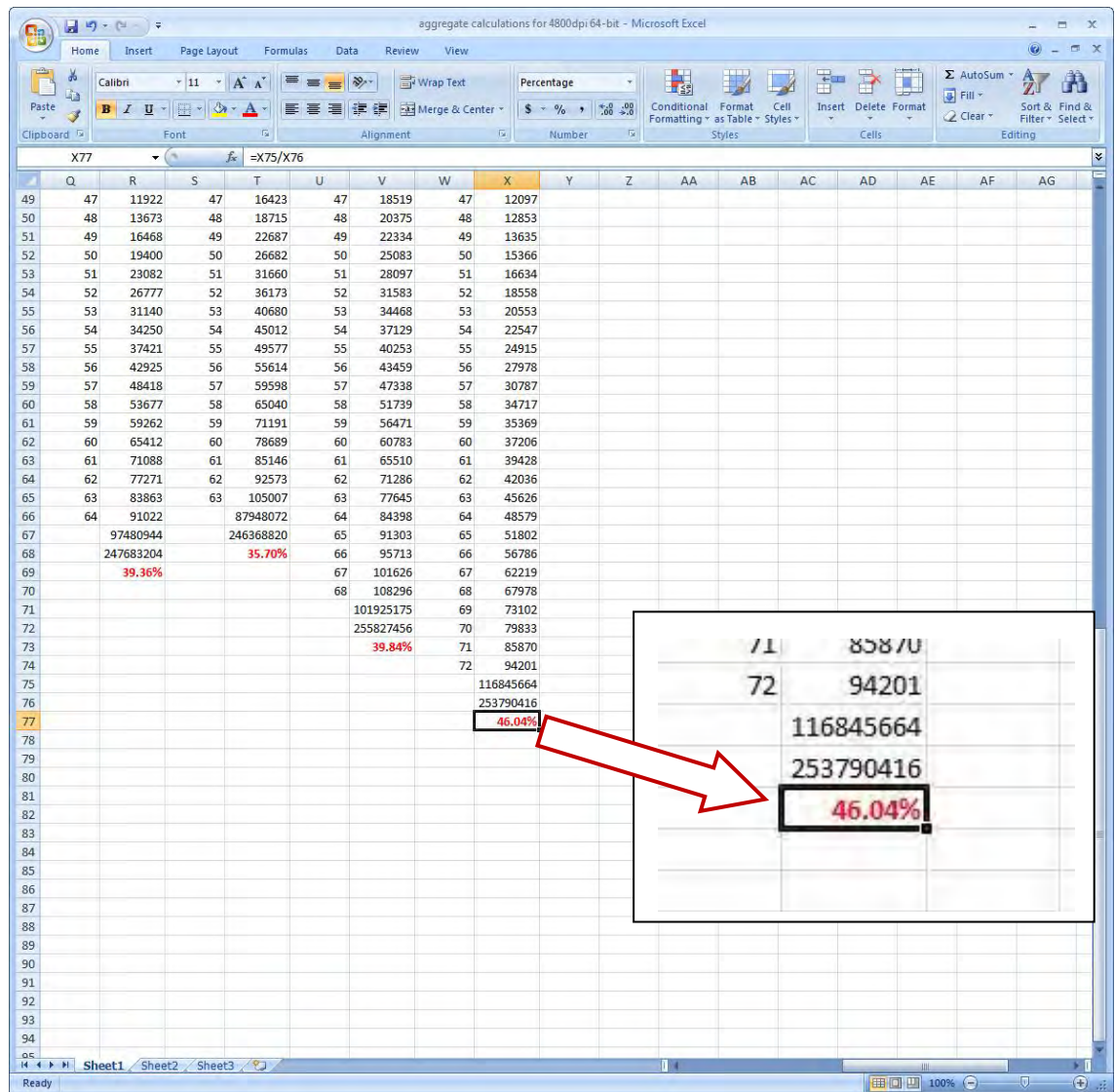


Figure 3.3.3.2.23 The resulting calculation gets formatted

3.3.3.3 Study 3 - A Procedure for Auto Calculations of Coarse Aggregate Using 64-bit Adobe PhotoShop Elements 7.0, SilverFast Epson SE, 64-bit ImageJ and Microsoft Excel in 64-bit Windows

1. Open ImageJ;
2. Click File, then click Open and select the picture file of the image to open on the screen (in this case the original scanned picture without any adjustments);

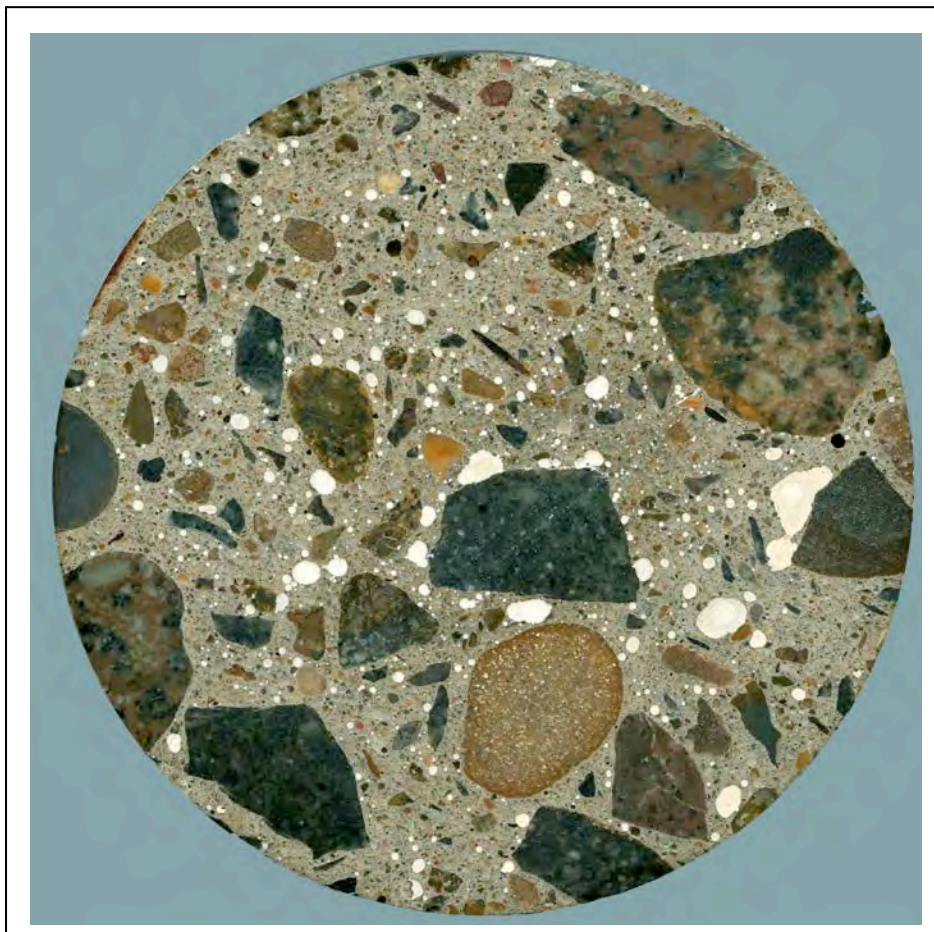


Figure 3.3.3.3.1 Open the image

3. Select the circumference of the object;

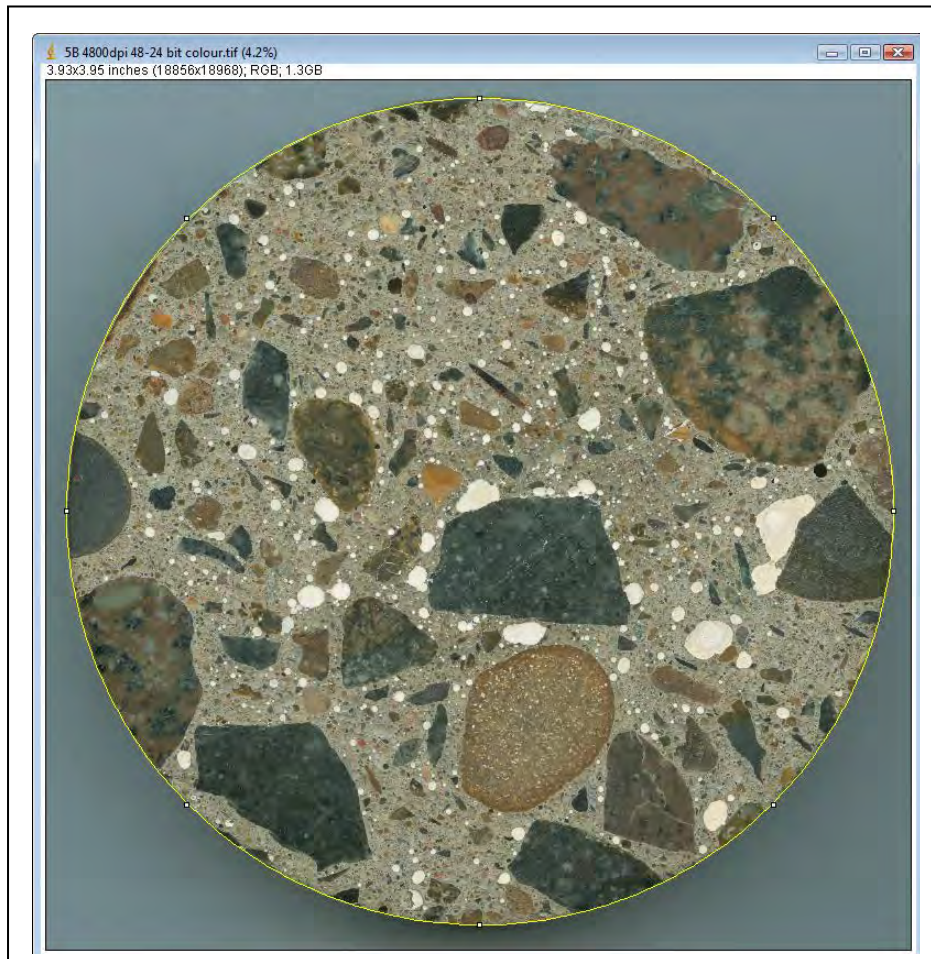


Figure 3.3.3.3.2 Select the circumference

4. Select the Image, Type, 8-bit

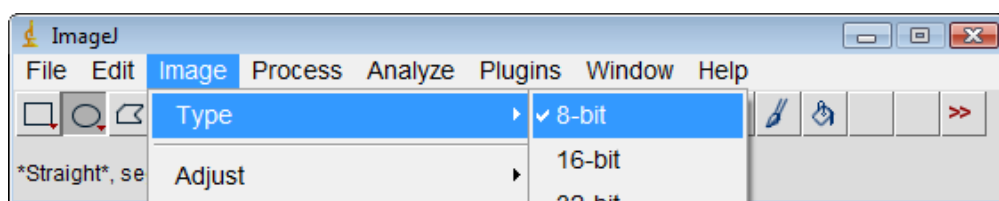


Figure 3.3.3.3.3 Select the Type

5. Select Image, Adjust, Threshold - the object will look similarly as the one in Figure 3.3.3.3.4 with the red colour preselected in the Threshold window;

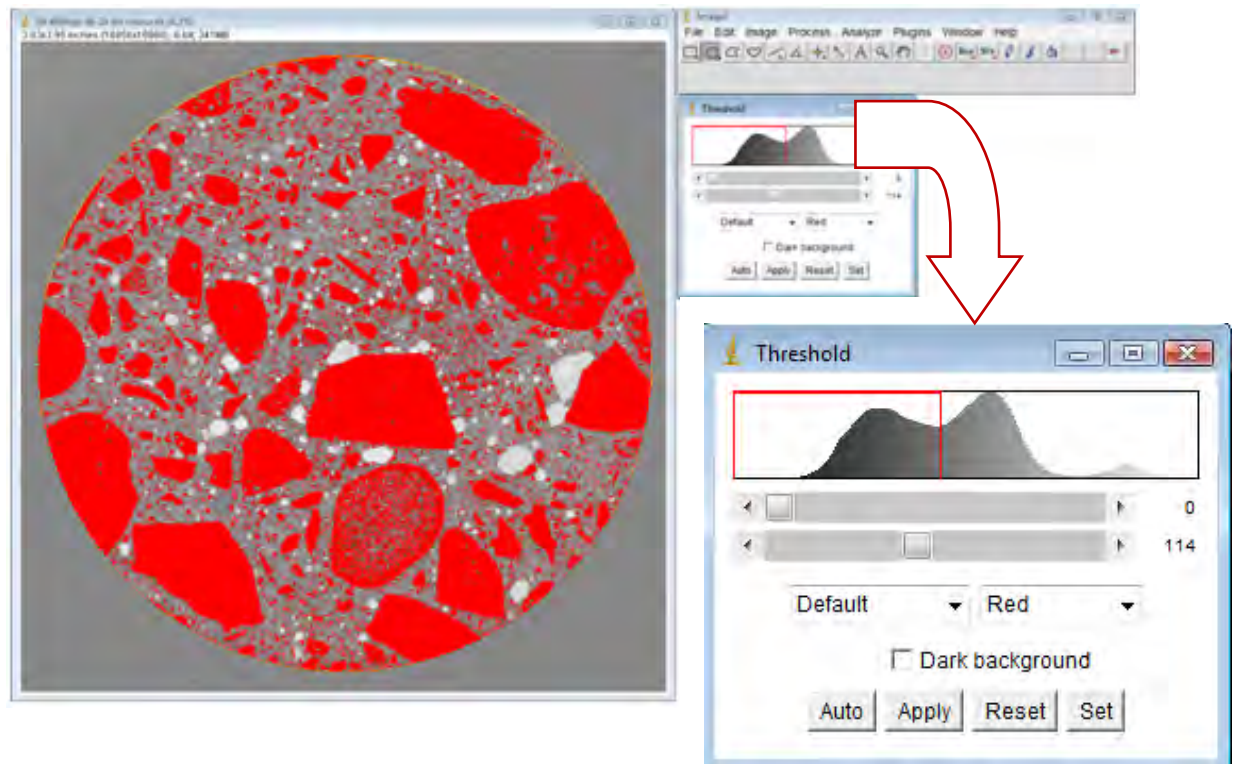


Figure 3.3.3.3.4 Select Image, Adjust, Threshold

6. Select Analyze, Histogram and List in the Histogram window and then select values from 0 to 114 in the list of values (as the previous figure showed in the Threshold after the ImageJ automatically displays the maximum value next to the bar) to copy into the Clipboard;

In case that all aggregate is not selected in ImageJ when compared to the original colour picture of the Sample, then the best solution to this is to place the original picture of the image into the PhotoShop Elements, mask the "invisible" aggregate and then place back into the ImageJ and let the ImageJ calculate the aggregate automatically. By doing this the procedure of the automatic calculation of the aggregate then falls within 1% of the 100% quantitative value. Figure 3.3.3.3.5 shows such an example.

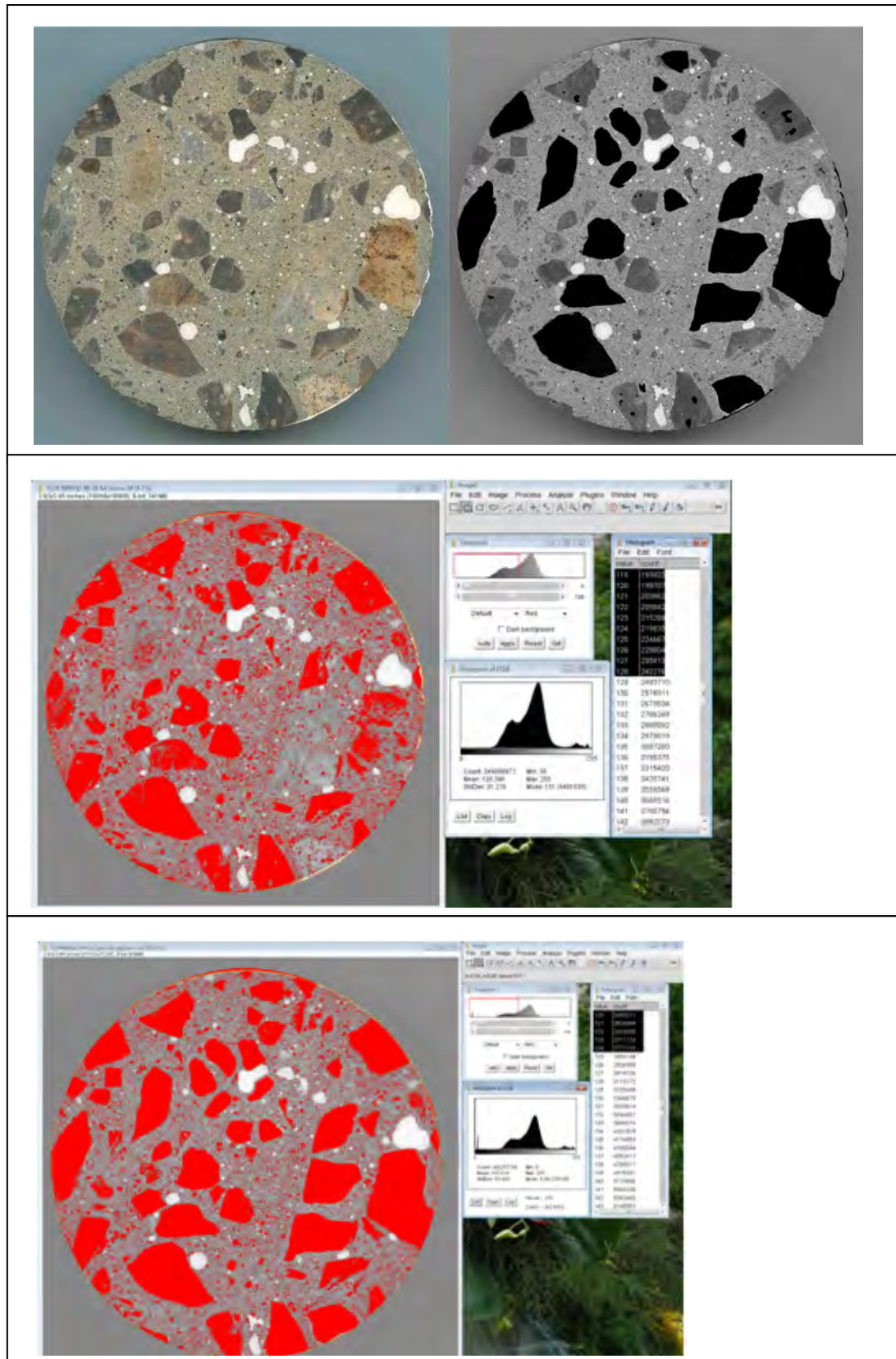


Figure 3.3.3.3.5 Calibration masking of the "invisible" aggregate for an automatic calculation is shown here on Sample FIIB

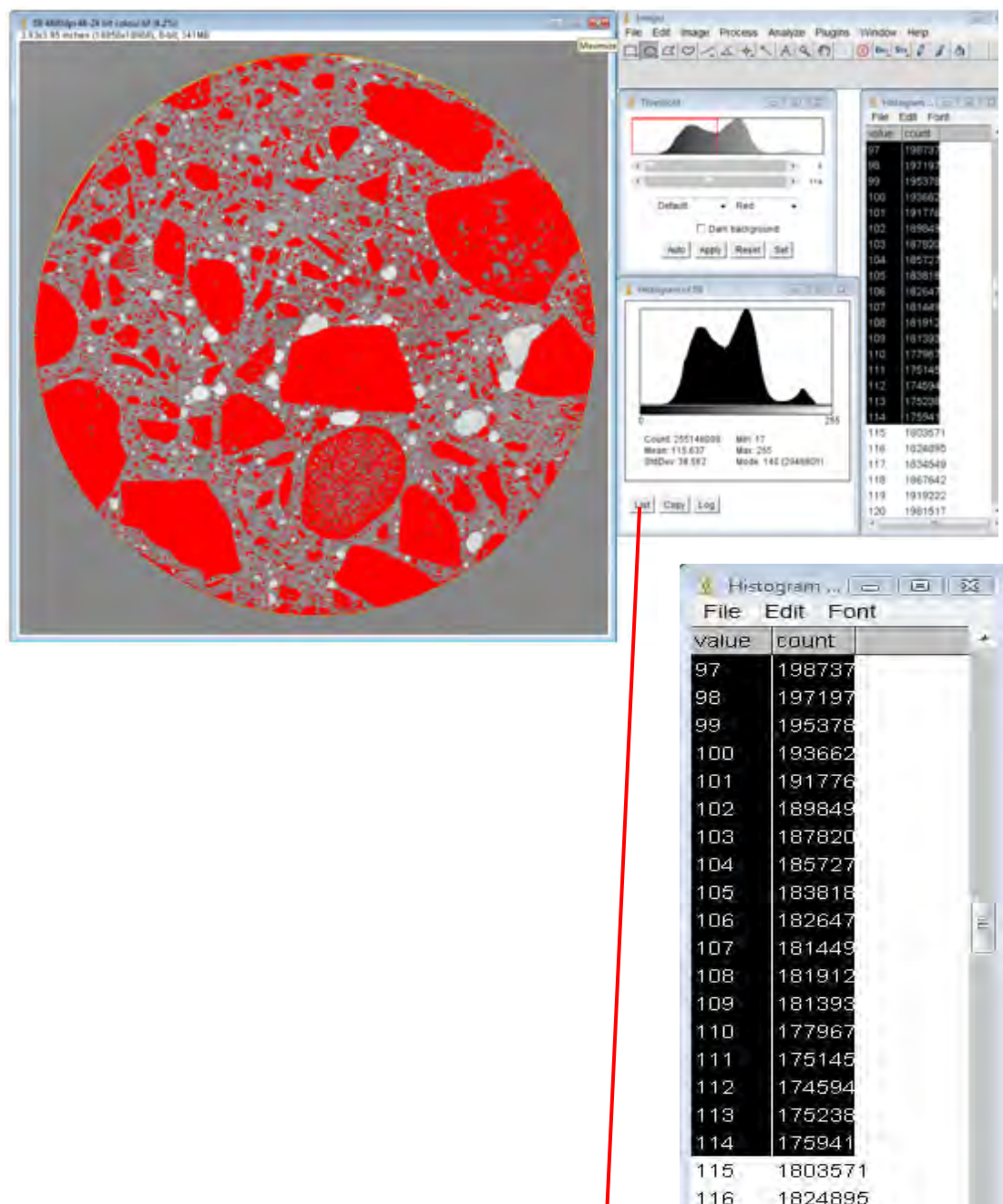


Figure 3.3.3.3.6 Select Analyze, Histogram and List in the Histogram, then select the values in the List of values to copy into the Clipboard

8. Open the Microsoft Excel and paste the list of values into the spreadsheet to calculate the result as previously done in the full 100% quantitative calculation of the Coarse Aggregate in chapter 3.3.3.2, Figures 3.3.3.2.17 to 3.3.3.2.23;

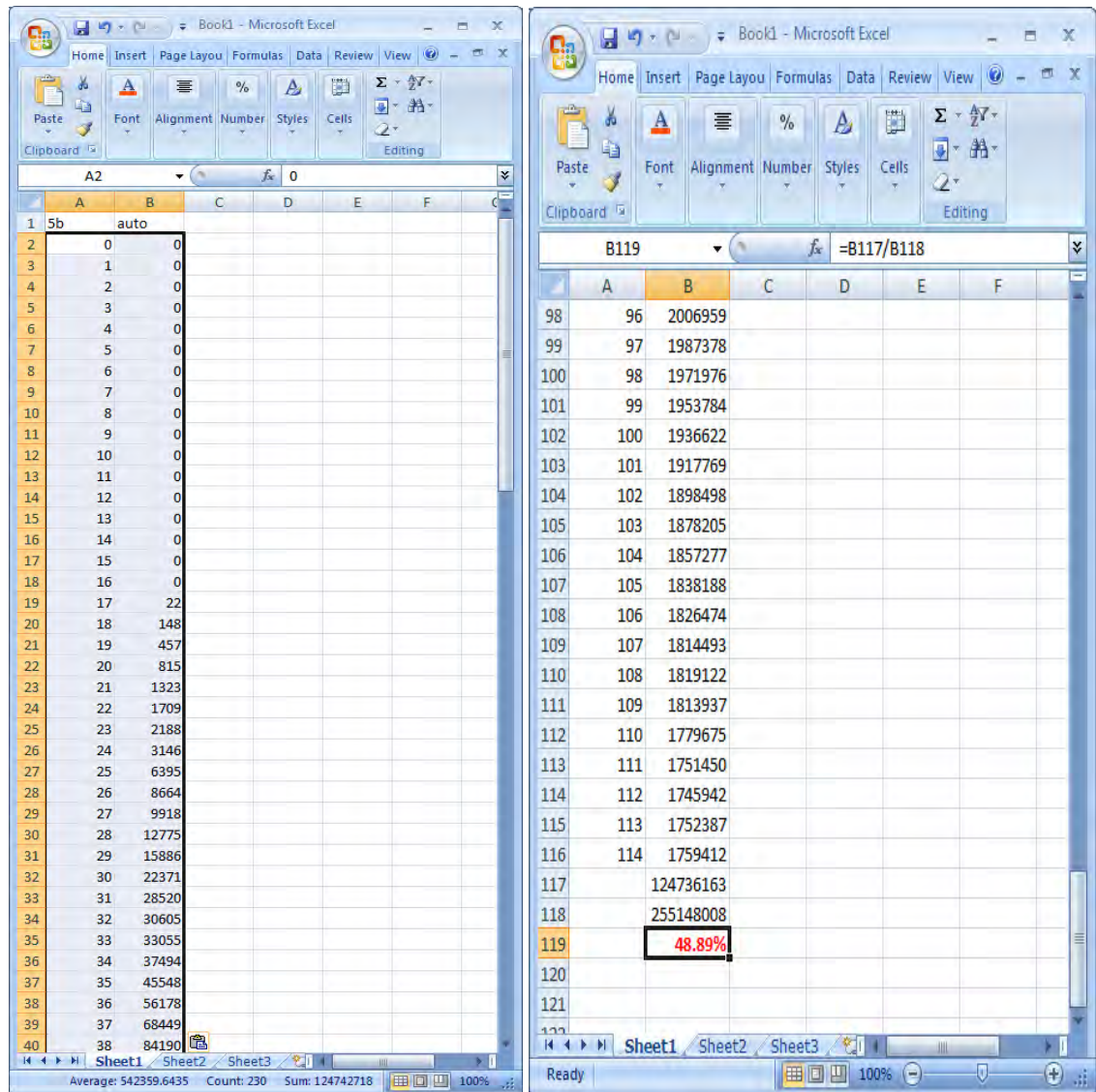


Figure 3.3.3.3.7 Calculate the automatic percentage of Coarse Aggregate

3.3.3.4 Study 3 - Calibration of Micro-Porosity in Cement Matrix

A small section 10 x 10 mm was chosen from the 100 mm diameter reference core sample 5 (5B) with very fine micro pores. The procedure was the same as in Study 3 for calculations of the percentage of porosity.

This section was scanned in true optical resolutions:

- **72 ppi** - represents the resolution of the Canon EOS 20D 8.2 Megapixel digital camera used in **Study 1**
- 200 ppi - represents the scanning resolution of documents
- 1200 ppi - represents the high detailed image for printing
- **2400 ppi** - represents the highest true optical resolution of the HP office scanner used in **Study 2**
- **4800 ppi** - represents the resolution of the Epson Perfection V700 Photo scanner used in **Study 3** for calculating percentage of aggregate
- **6400 ppi** - represents the highest true optical resolution of the Epson Perfection V700 Photo scanner used in **Study 3** for calculating percentage of porosity

Figures 3.3.3.4.1 and 3.3.3.4.2 show the detail of the small section studied on the Sample and its scanned 6400 ppi true optical resolution ($3.97\ \mu$), 48-bit HDR colour image.

Figure 3.3.3.4.1, real size of 100 x 100 mm, has an image file size 3.48 GB, dimensions 25142 x 25292 pixels, 48 bit depth. Figure 3.3.3.4.2, real size of 10 x 10 mm, has an image file size 38 MB, dimensions 2574 x 2488 pixels, 48 bit depth.

Figure 3.3.3.4.3 shows the screen dump of the calculation of porosity in ImageJ for the section scanned in 6400 ppi, where Figure 3.3.3.4.4 shows the calibration for calculation of $10\ \mu$ pores which will be zoomed in ImageJ if needed.

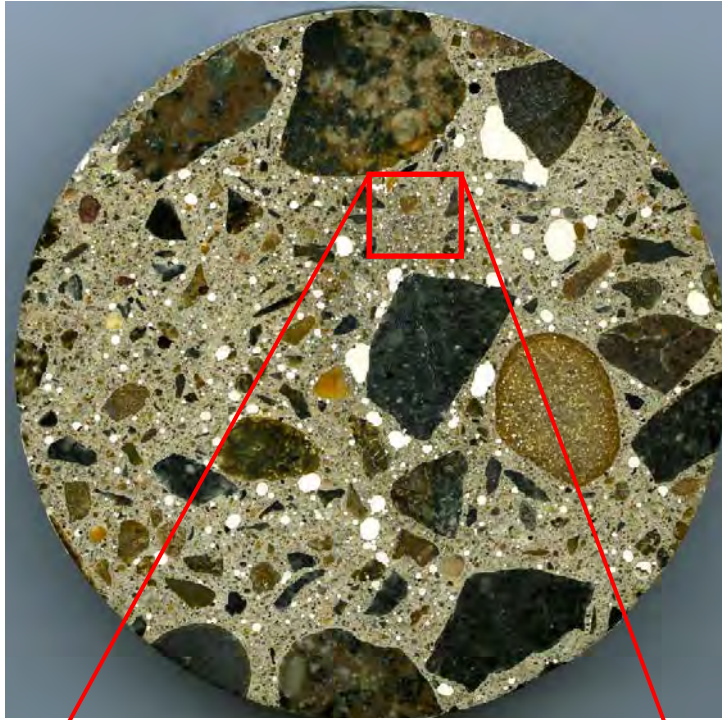


Figure 3.3.3.4.1 Small section 10x10 mm on Sample 5B

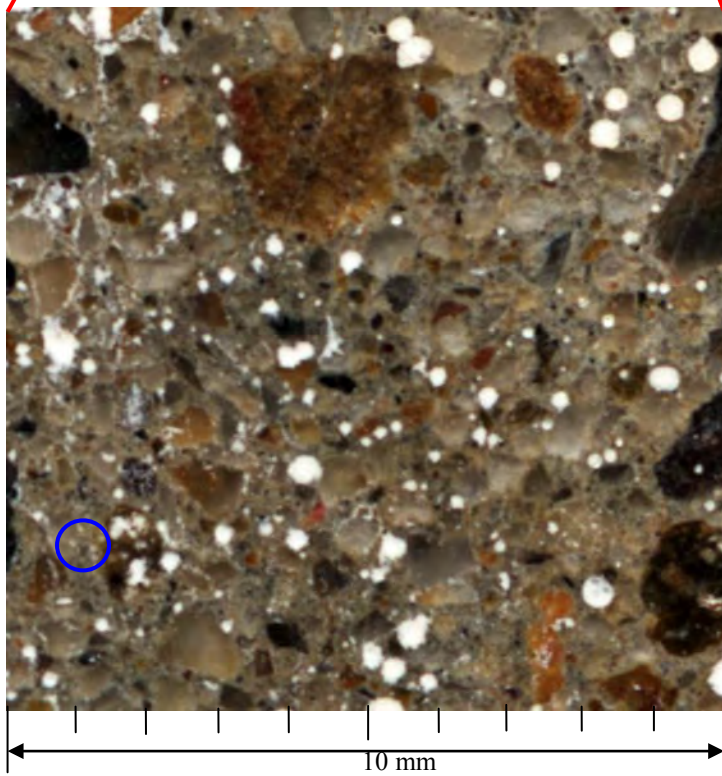


Figure 3.3.3.4.2 6400 ppi 48 bit HDR colour scanned image of the section 10 mm²

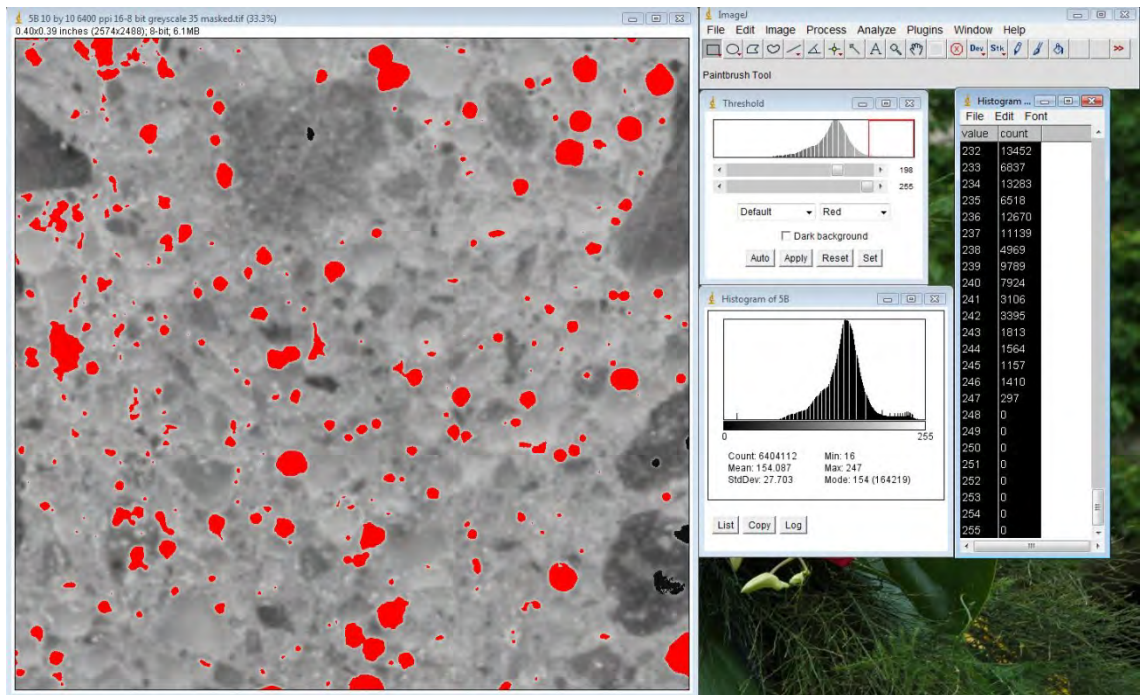


Figure 3.3.3.4.3 Screen dump of the quantitative calculation of percentage micro-porosity for sample 6400 ppi

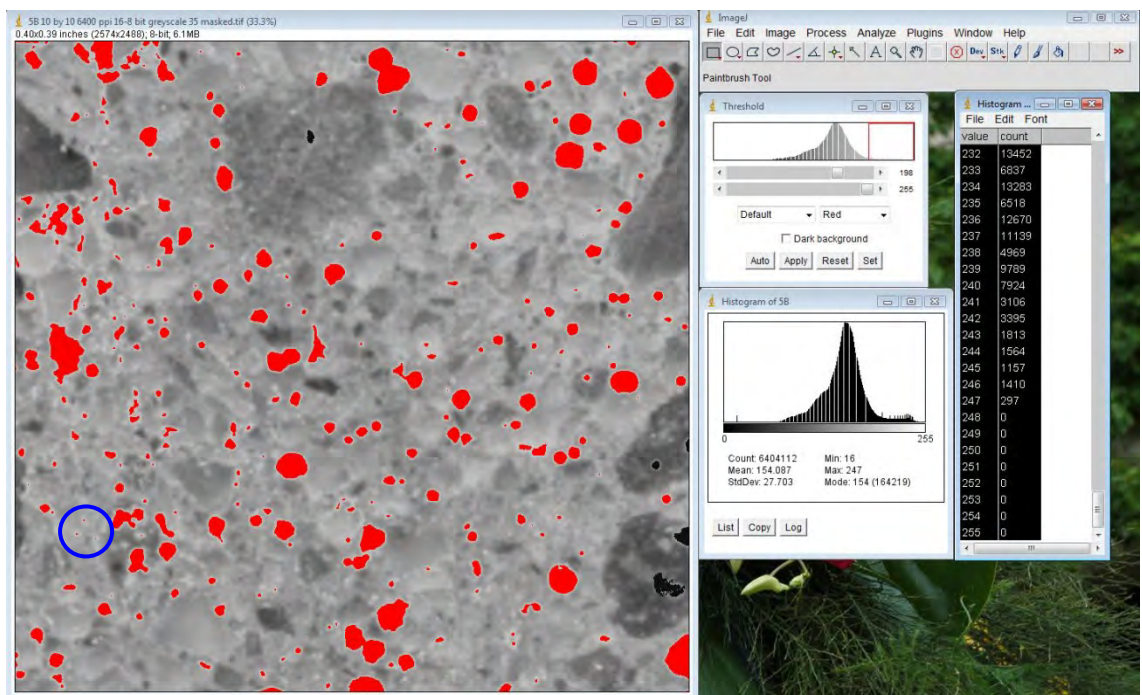


Figure 3.3.3.4.4 Blue circle highlights the 10 μ diameter pores used for quantitative calibration and calculation of percentage air void porosity

3.4 OPTICAL MICROSCOPY OF CEMENT PASTE MICROSTRUCTURE

Samples were cut into smaller sections of about $\sim 1 \text{ cm}^2$. They were then mounted in phenolic resin and polished to a mirror finish.

Multiple images of all polished Samples were taken in 300X magnification on the Nikon Epiphot 200 Microscope showing below and digital images were saved.



Figure 3.4.1 Nikon Epiphot 2000 Microscope

The microstructure observed was of the sand particles, spherical (circular in 2-D) air-voids and bonding matrix.

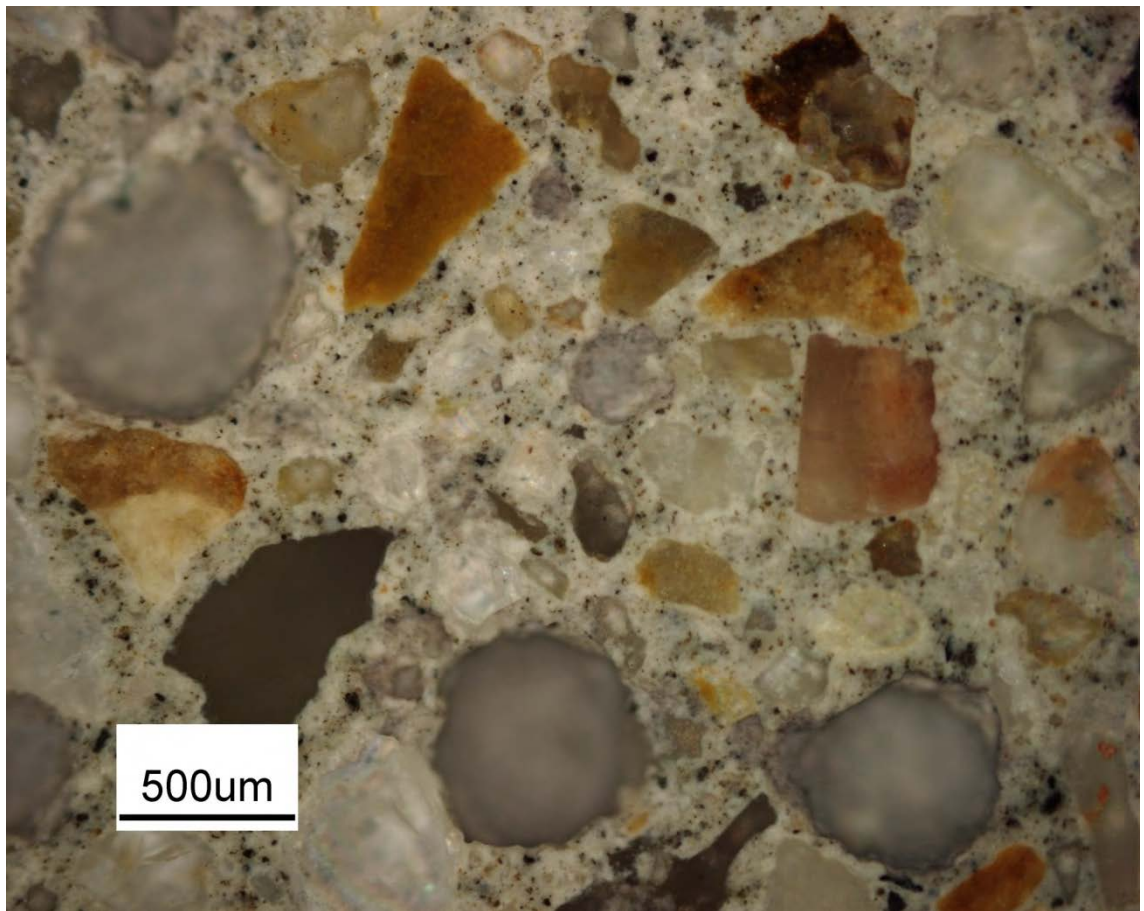


Figure 3.4.2 Detail of Sample 5B microstructure showing micro pores $\sim 500\ \mu\text{m}$ in diameter

3.5 Vickers Micro Hardness of Cement Matrix

Introduction

The cement bonding matrixes of all samples were tested for micro hardness. This value could be related to the relative compressive strength of the mixes.

The Vickers micro indenter uses a 136° pyramidal diamond indenter that forms a square indent. The indenter is pressed into the sample by an accurately controlled test force. The force is maintained for a specific dwell time, normally 10 – 15 seconds (according to ASTM E384 - micro force ranges 10g to 1 kg).

After the dwell time is complete, the indenter is removed leaving an indent in the sample that appears square shaped on the surface.

The size of the indent is determined optically by measuring the two diagonals of the square indent.

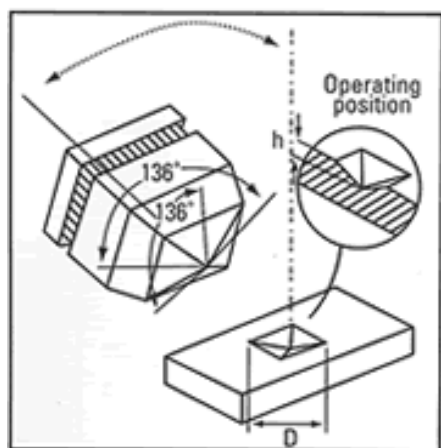


Figure 3.5.1 Diagram of the indenter

The Vickers hardness number is a function of the test force divided by the surface area of the indent. The average of the two diagonals is used in the formula to calculate the Vickers hardness. All calculations are performed by the software within the machine.

Vickers Hardness Formula (HV)

$$HV = 0.102 F/S$$

$$= 0.102 \times F \sin (\theta/2) d^2$$

$$= 0.1891/d^2$$

F: Test Force (N)

S: Superficial area of indentation (mm²)

d: Averaged diagonal length of indentation (mm)

θ: Included point angle of diamond indenter (= 136°)

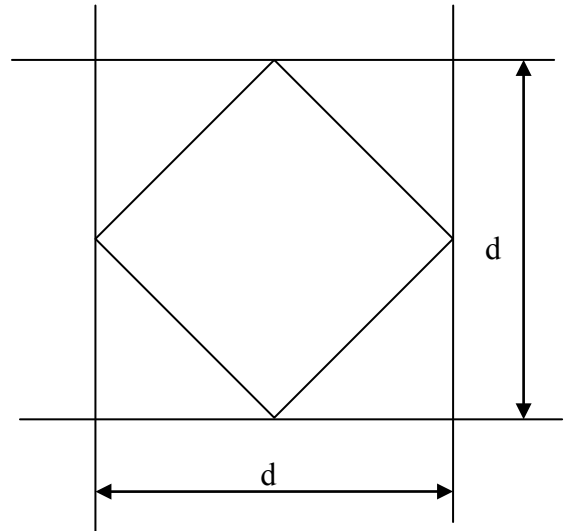


Figure 3.5.2 Indent shape

Experimental Procedure

The bonding matrix between the fine sand particles was tested for hardness.

Parameters used for measuring Vickers micro hardness indenter were:

- a weight of 300 g,
- held for 15 seconds.

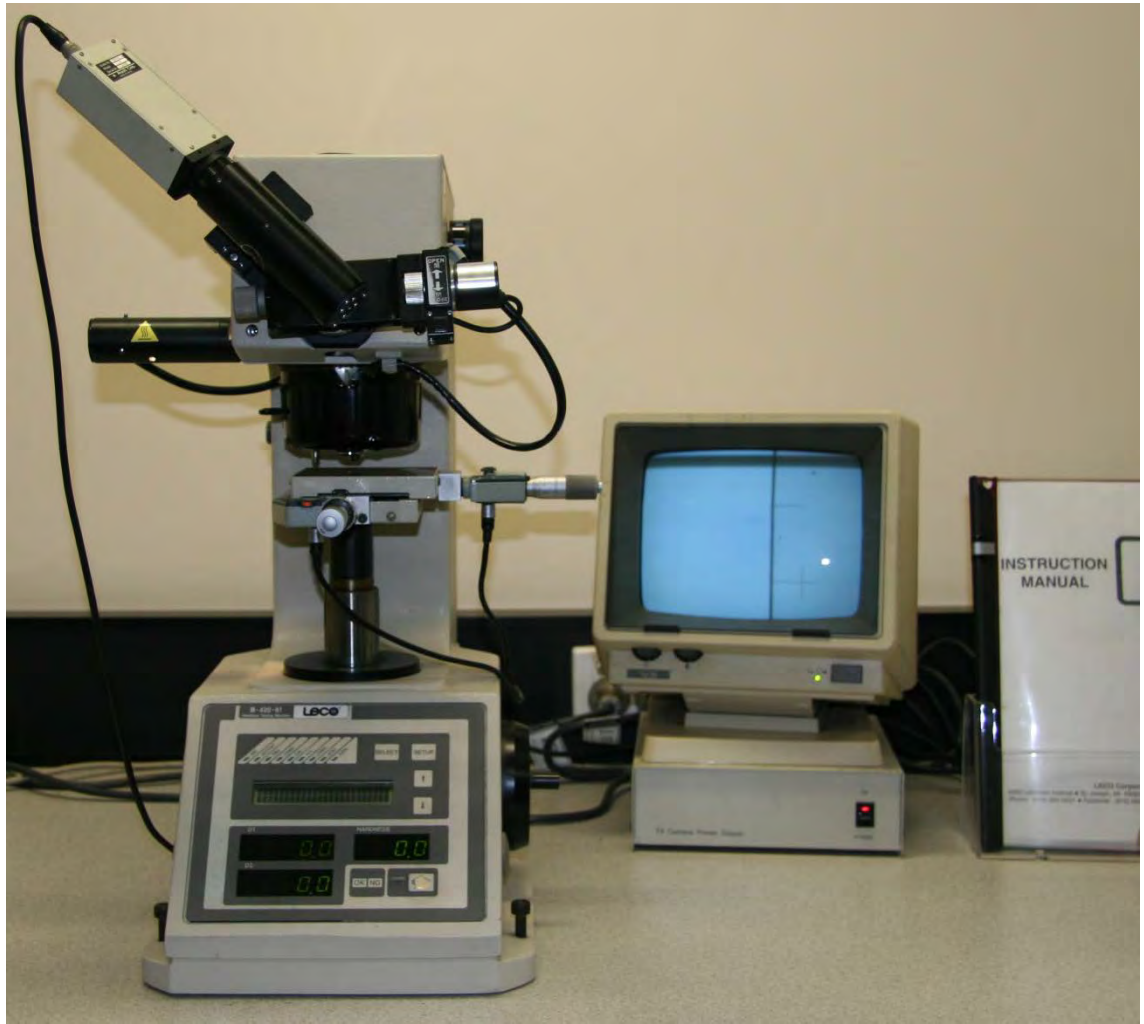


Figure 3.5.3 Vickers micro indenter used

4 EXPERIMENTAL RESULTS

Introduction

The compiled data and its interpretation are presented to answer the question from the thesis outline.

The results and data analysis below will explain the meaning of the comparative forensic data collected in research and explain why the likely cause of the damage to the concrete slab.

Results presented are as follows:

- 4.1 Bulk density and apparent porosity
- 4.2 High resolution X-Ray specific imaging for micro-cracking
- 4.3 Digital image analysis of the pores and coarse aggregate
- 4.4 Optical microscopy
- 4.5 Vickers Micro-hardness

4.1 Bulk Density and Apparent Porosity Results

Sample	Mass Dried g	Mass saturated suspended in water g	Mass saturated suspended in air g	Bulk Density kg/m ³	Apparent Porosity %	Water Absorption %
Sample 1-1	6.2528	3.7445	6.6259	2170	12.9	6.0
Sample 1-2	7.2313	4.4625	7.6396	2276	12.9	5.6
Sample 1-3	6.2416	3.8846	6.5236	2365	10.7	4.5
Sample 1-4	7.2560	4.4617	7.7263	2223	14.4	6.5
Sample 1-5	6.9267	4.2447	7.4082	2190	15.2	7.0
Sample 1-6	3.9304	2.4188	4.1269	2301	11.5	5.0
Average				2254	12.9	5.8
Sample 2-1	8.2081	5.0780	8.5941	2334	11.0	4.7
Sample 2-2	6.9471	4.2537	7.2153	2346	9.1	3.9
Sample 2-3	6.8408	4.1821	7.1401	2313	10.1	4.4
Sample 2-4	7.4057	4.5390	7.7139	2333	9.7	4.2
Sample 2-5	7.4544	4.5871	7.7495	2357	9.3	4.0
Sample 2-6	6.3445	3.8162	6.7426	2168	13.6	6.3
Average				2308	10.5	4.6
Sample 3-1	7.8580	4.8213	8.2621	2284	11.7	5.1
Sample 3-2	6.1703	3.7542	6.4483	2290	10.3	4.5
Sample 3-3	6.7256	4.1123	6.9851	2341	9.0	3.9
Sample 3-4	6.7706	4.0854	7.1905	2180	13.5	6.2
Sample 3-5	7.8720	4.7500	8.2417	2254	10.6	4.7
Sample 3-6	7.6179	4.6134	8.0006	2249	11.3	5.0
Average				2267	11.1	4.9
Sample 4-1	6.6443	4.0324	7.0538	2199	13.6	6.2
Sample 4-2	7.1099	4.3105	7.4824	2242	11.7	5.2
Sample 4-3	7.3901	4.5338	7.6890	2342	9.5	4.0
Sample 4-4	7.8743	4.7491	8.3548	2184	13.3	6.1
Sample 4-5	6.3706	3.8325	6.7898	2154	14.2	6.6
Sample 4-6	8.9986	5.4775	9.4126	2287	10.5	4.6
Average				2235	12.1	5.5
Sample 5-1	7.3044	4.5072	7.6559	2320	11.2	4.8
Sample 5-2	7.1150	4.3748	7.4511	2313	10.9	4.7
Sample 5-3	7.4028	4.5950	7.6911	2391	9.3	3.9
Sample 5-4	7.1961	4.4031	7.5108	2316	10.1	4.4
Sample 5-5	7.8603	4.7638	8.3400	2198	13.4	6.1
Sample 5-6	7.7760	4.7361	8.2606	2206	13.7	6.2
Sample 5-7	6.7304	4.1111	7.0238	2311	10.1	4.4
Sample 5-8	7.0858	4.3604	7.4038	2328	10.4	4.5
Sample 5-9	7.6278	4.7032	7.9696	2335	10.5	4.5
Sample 5-10	6.7064	4.0820	7.0977	2224	13.0	5.8
Average				2294	11.3	4.9
Sample RM1	6.7991	4.1038	7.1141	2259	10.5	4.6
Sample RM2	6.5855	3.9643	6.9245	2225	11.5	5.1
Sample RM3	6.1203	3.6350	6.4774	2153	12.6	5.8
Sample RM4	6.5319	3.9186	6.8847	2202	11.9	5.4
Sample RM5	6.6612	4.0564	7.0101	2255	11.8	5.2
Sample RM6	6.4373	3.8450	6.7848	2190	11.8	5.4
Average				2294	11.7	5.3
Sample DAR1	7.0365	4.4201	7.3490	2402	10.7	4.4
Sample DAR2	6.9573	4.3636	7.2912	2376	11.4	4.8
Sample DAR3	6.3280	3.9239	6.6570	2315	12.0	5.2
Sample DAR4	6.0080	3.7594	6.2964	2368	11.4	4.8
Sample DAR5	8.0263	5.0759	8.3441	2456	9.7	4.0
Sample DAR6	6.6900	4.1472	7.0257	2324	11.7	5.0
Average				2374	11.1	4.7

Table 4.1.1 Bulk Density and Apparent Porosity

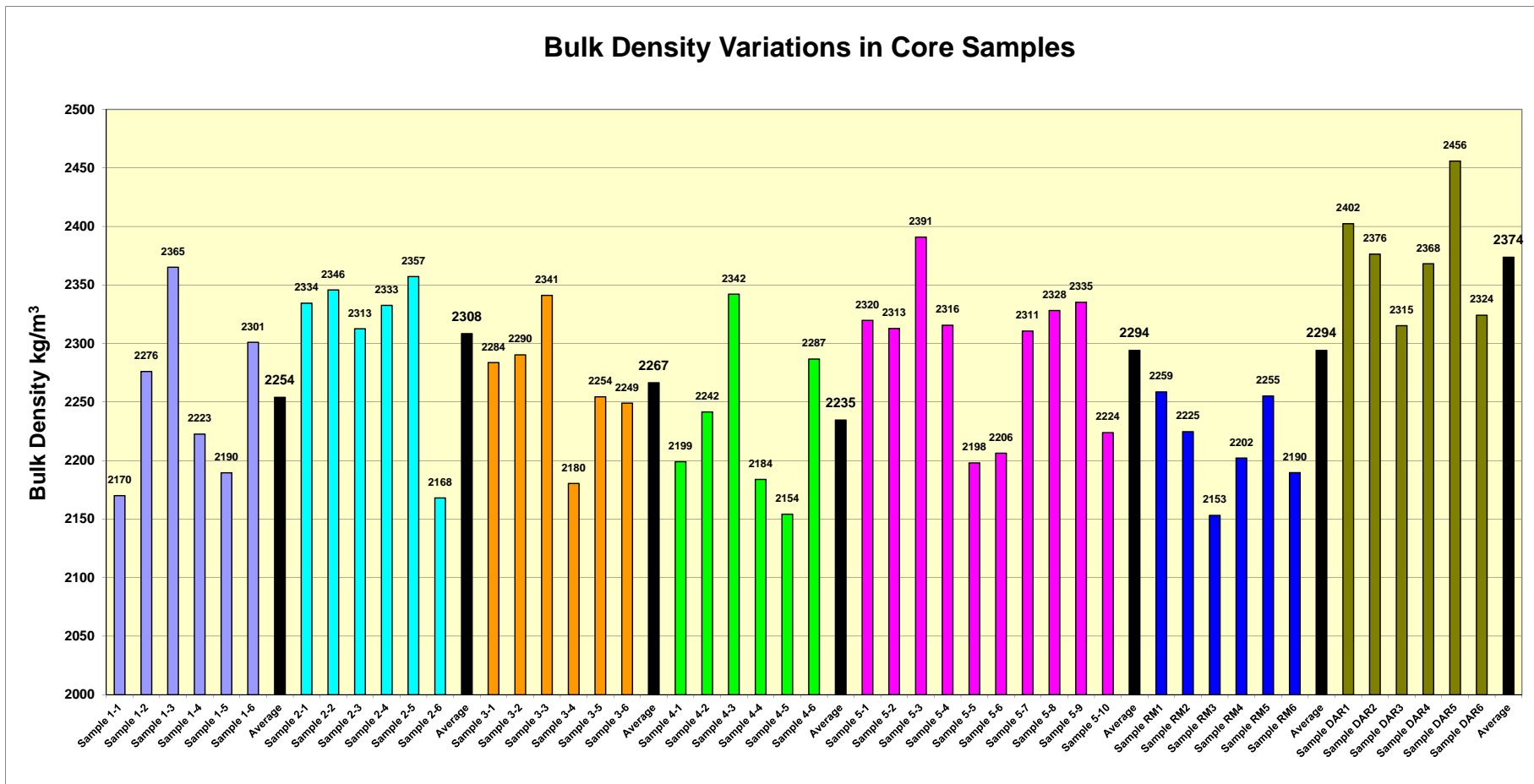


Figure 4.1.1 Bulk Density Variations in Core Samples

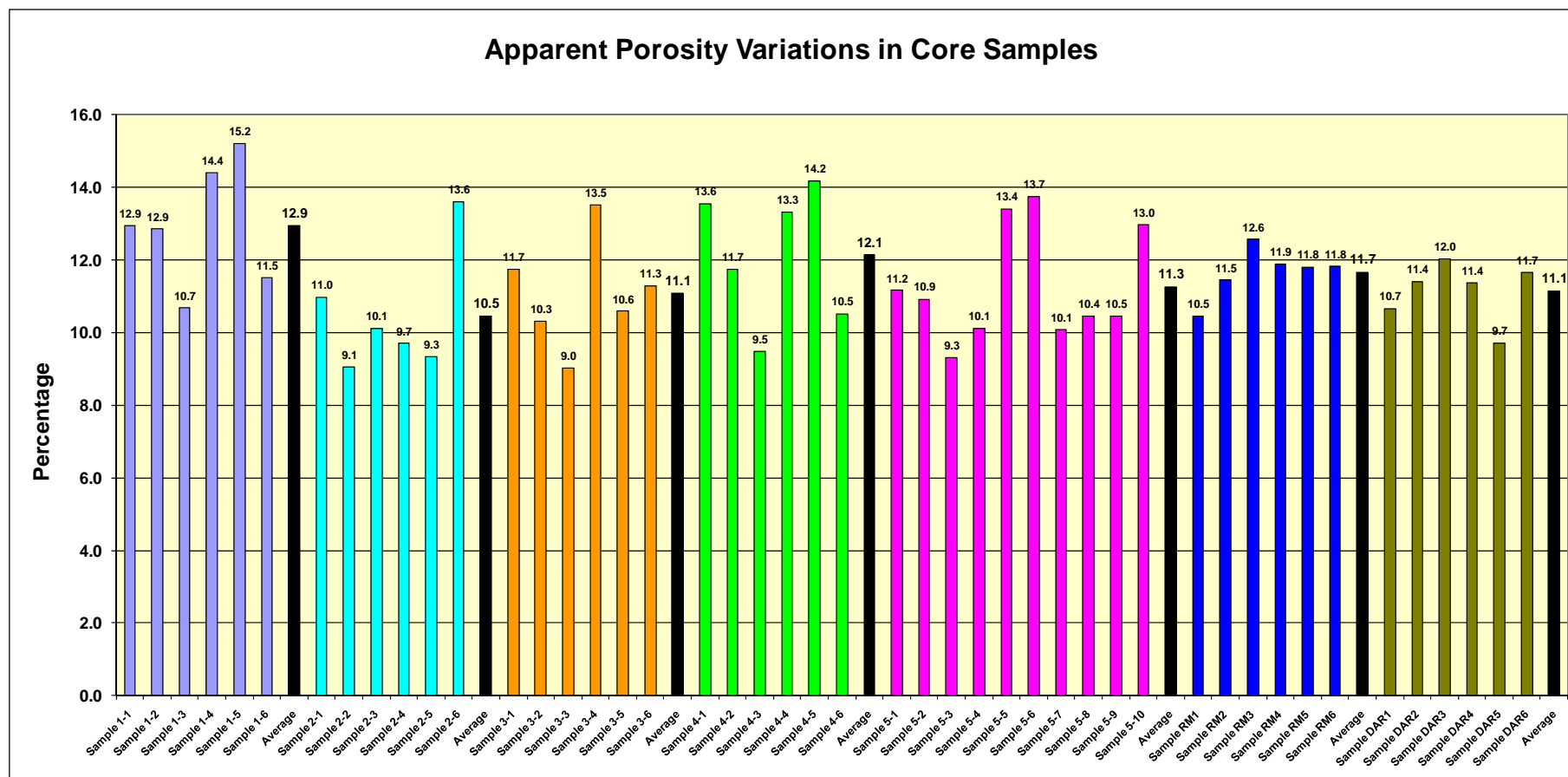


Figure 4.1.2 Apparent Porosity Variations in Core Samples

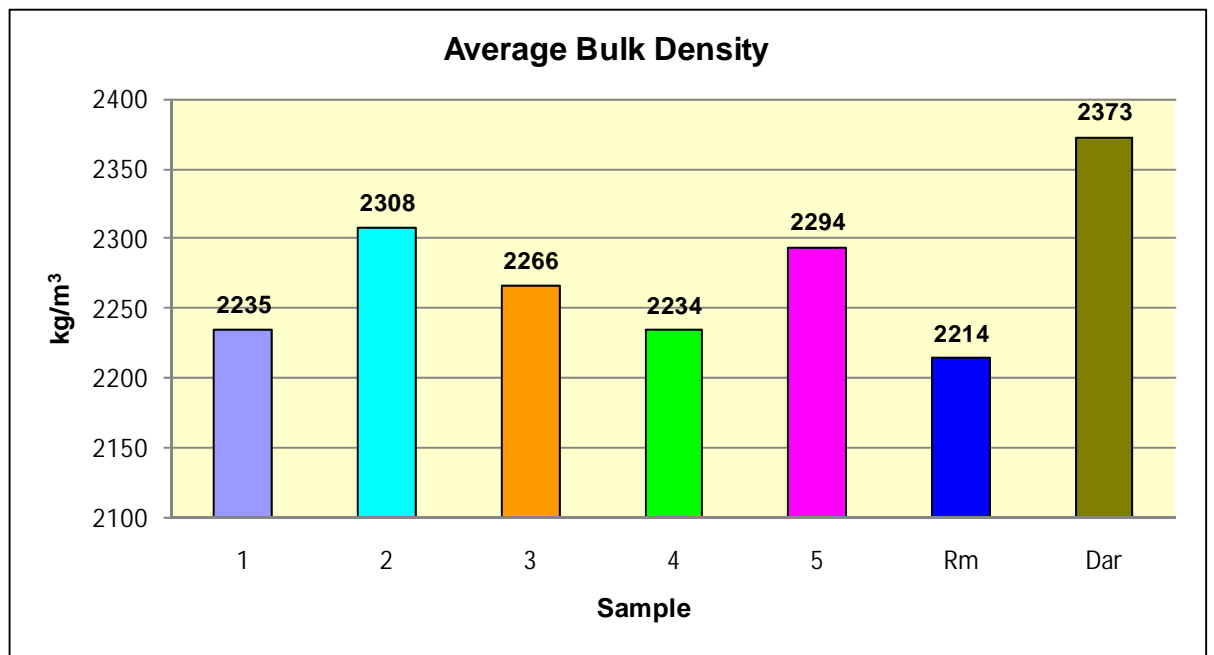


Figure 4.1.3 Average Bulk Density

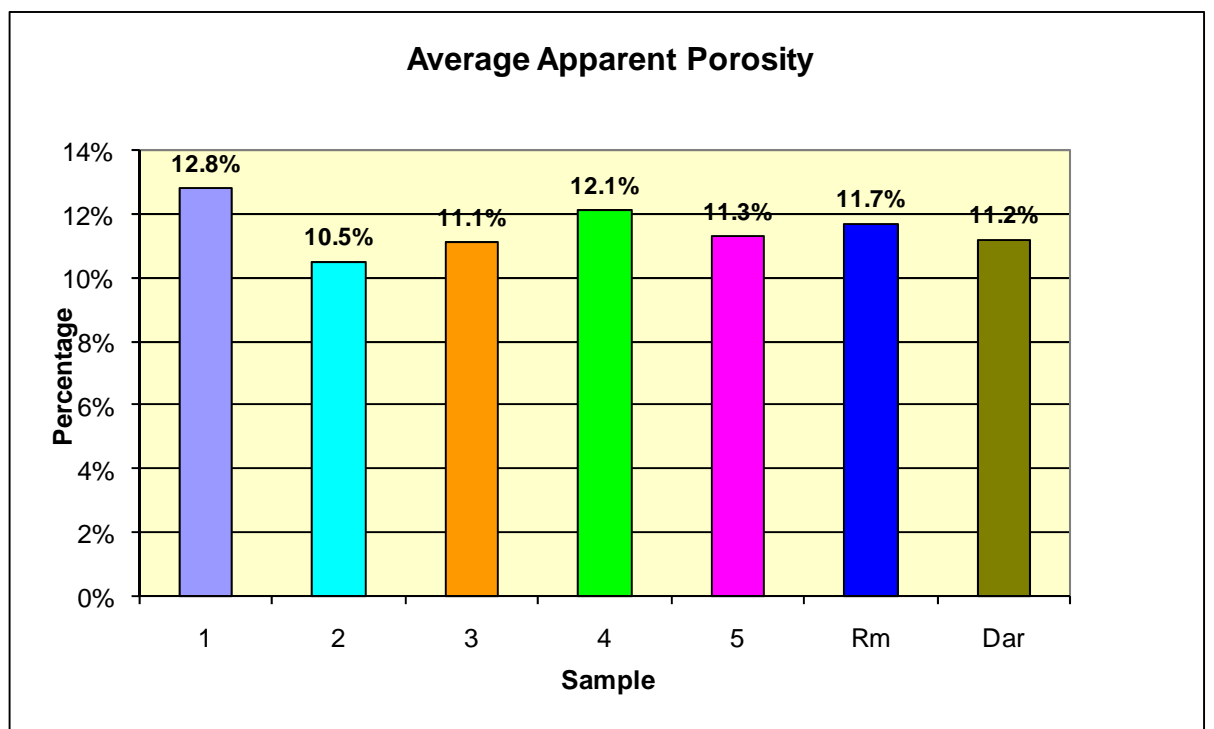


Figure 4.1.4 Average Apparent Porosity

4.1.1 Discussion of Results

Observations and Explanations

- Samples 1 (2235 kg/m^3) and 4 (2234 kg/m^3) had the lowest Bulk Density out of Samples 1 to 5 from the warehouse floor;
- Samples 1 (12.8%) and 4 (12.1%) had the highest Apparent Porosity out of Samples 1 to 5 from the warehouse floor;
- Samples Rm and Dar are used in the chart for comparison only and were not a part of the forensic study;
- Samples 1 to 5 and Rm have similar average apparent porosities;
- Sample Dar has higher bulk density than the others measured.
- The most damaged section of the concrete floor was Sample 1 followed by Sample 4 (Figure 4.1.1.1);
- Samples 1 and 4 were apparently the softest;
- Sample 1 was laminated and very crumbly due to its high porosity and low bulk density;
- Sample Dar has the higher average bulk density because of its dense blue metal coarse aggregate.
- Samples 1 to 5 and Rm contain river gravel coarse aggregate, hence lower bulk densities;
- Sample Dar contains higher bulk density blue metal coarse aggregate, hence the highest bulk density.

The question remains –

Was the specified mix substandard in the areas where the Samples 1 and 4 were cored from?

4.2 Skyscan X-Ray Microtomograph Results

4.2.1 Variable (Random) Cuts

Figure 4.2.1.1 shows the whole sample cut 1-1. The 1-1A is an X-Ray image of the bottom section of 1-1. The 1-1B is an X-Ray image of the top section of 1-1.

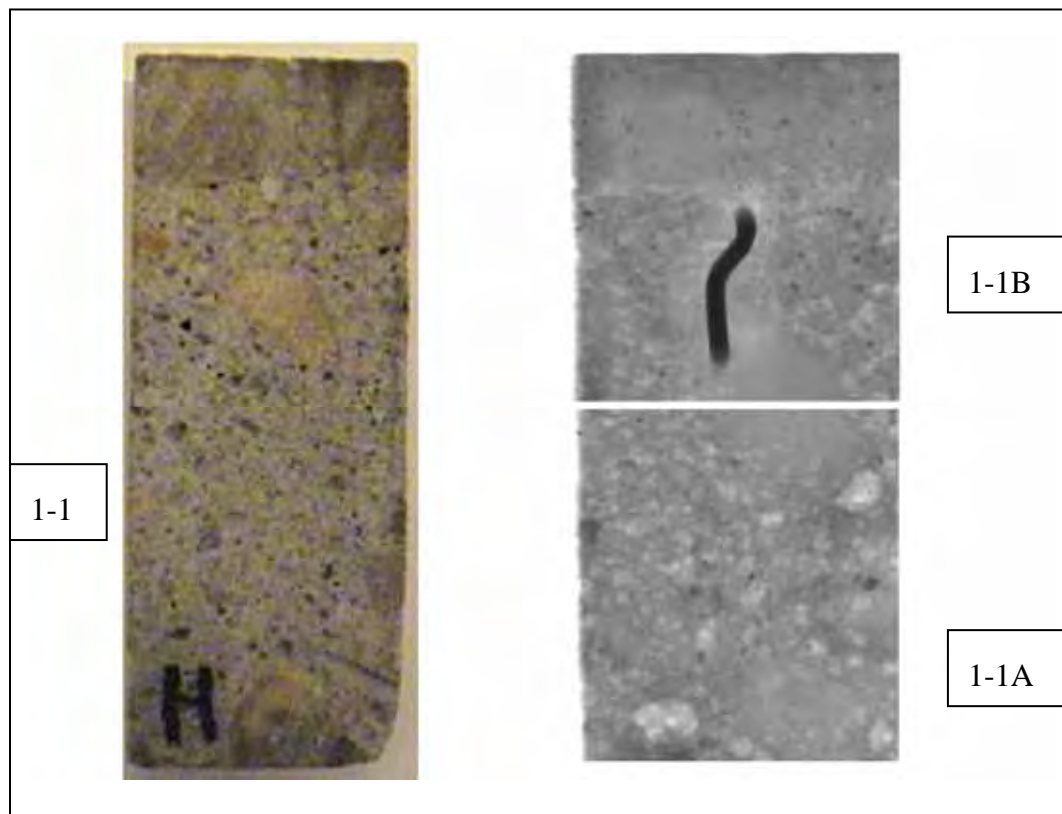


Figure 4.2.1.1 (in detail) Random cut 1-1 from Concrete Core Sample 1 with its 2 X-Ray images 1-1B and 1-1A on the right

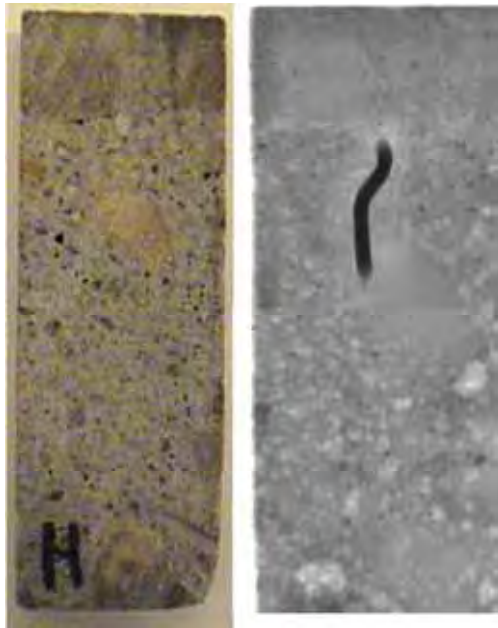


Figure 4.2.1.1 Sample 1-1

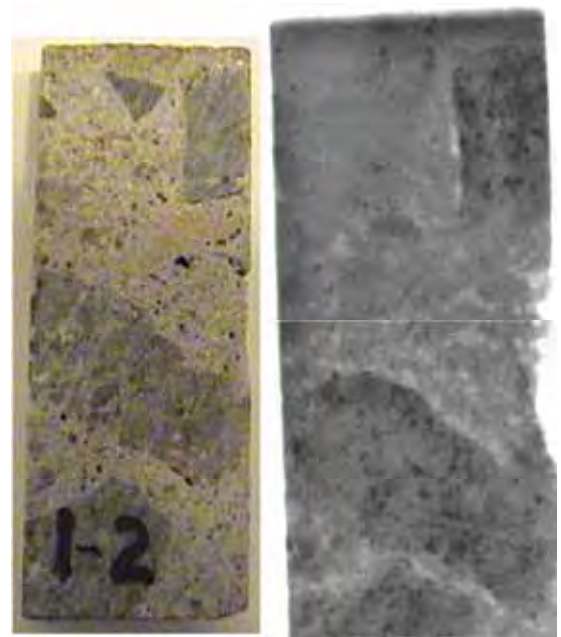


Figure 4.2.1.2 Sample 1-2

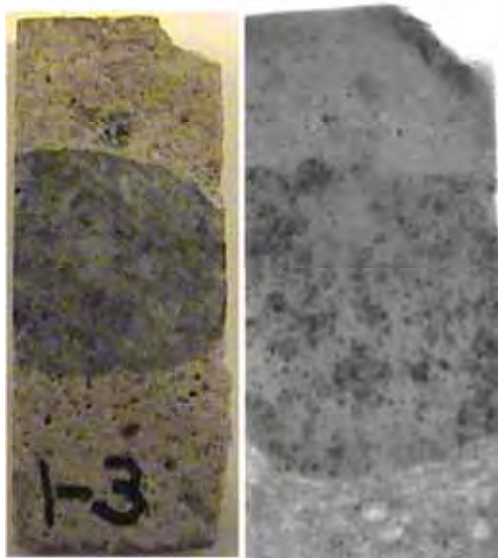


Figure 4.2.1.3 Sample 1-3

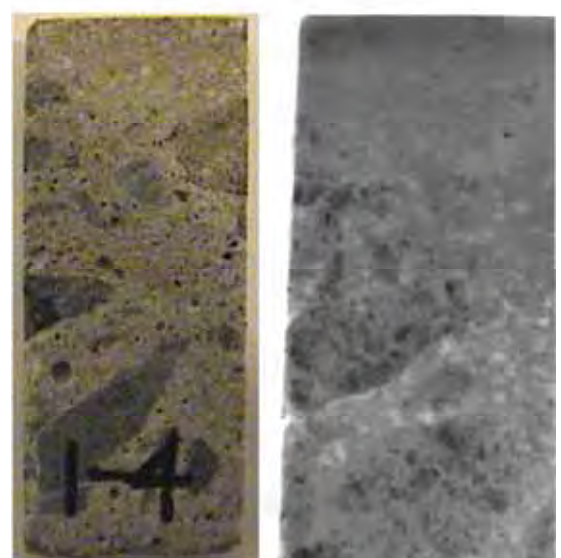


Figure 4.2.1.4 Sample 1-4

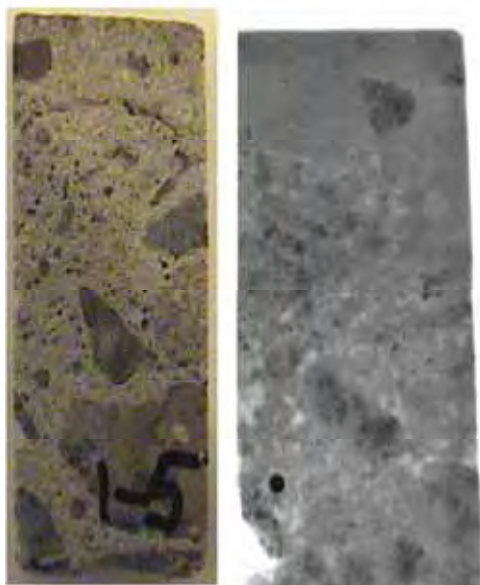


Figure 4.2.1.5 Sample 1-5

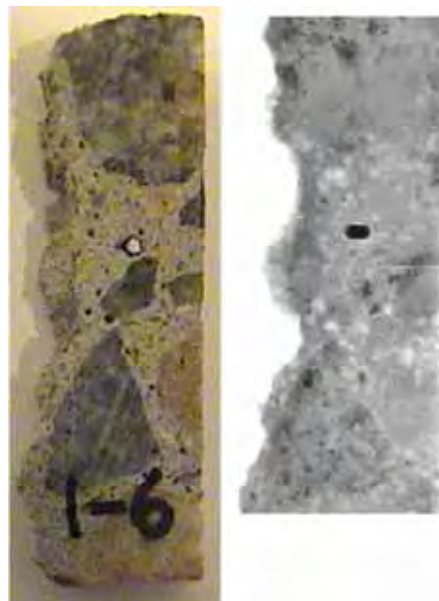


Figure 4.2.1.6 Sample 1-6

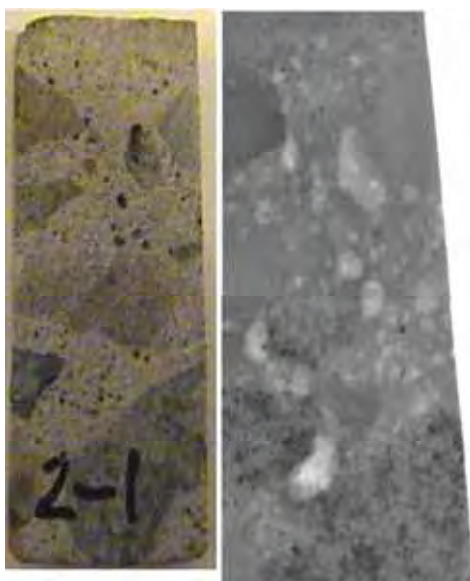


Figure 4.2.1.7 Sample 2-1

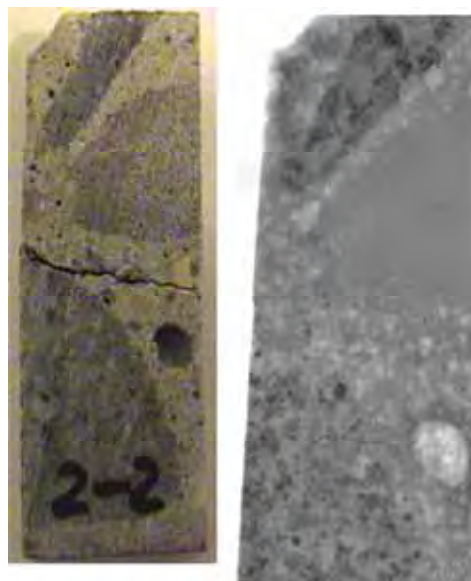


Figure 4.2.1.8 Sample 2-2

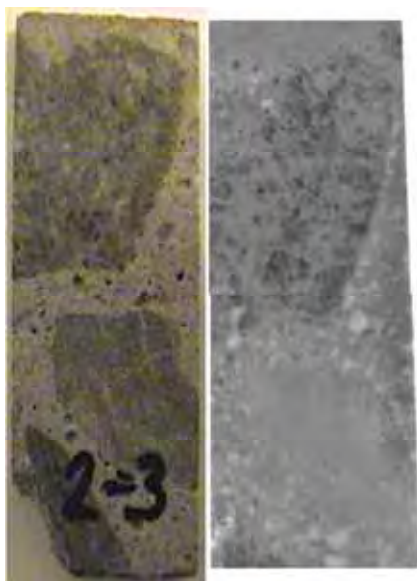


Figure 4.2.1.9 Sample 2-3

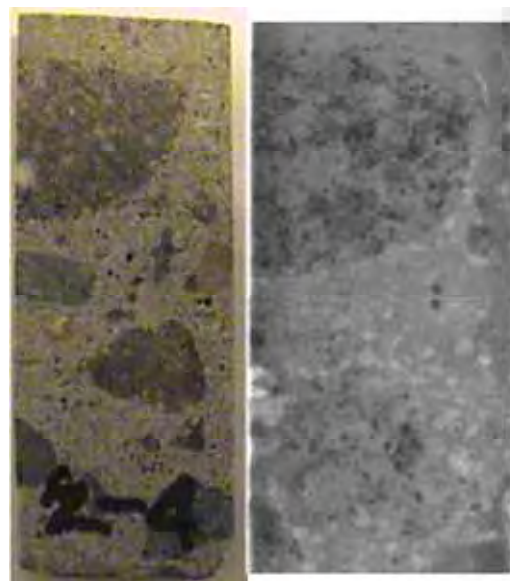


Figure 4.2.1.10 Sample 2-4

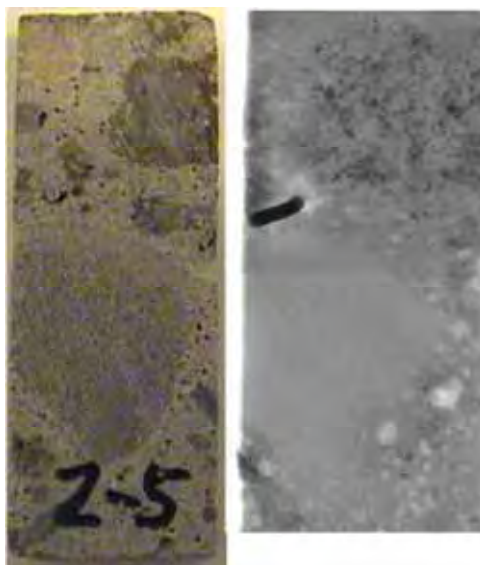


Figure 4.2.1.11 Sample 2-5

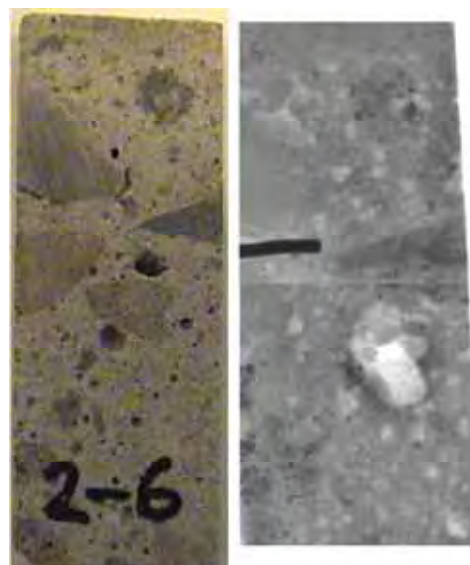


Figure 4.2.1.12 Sample 2-6

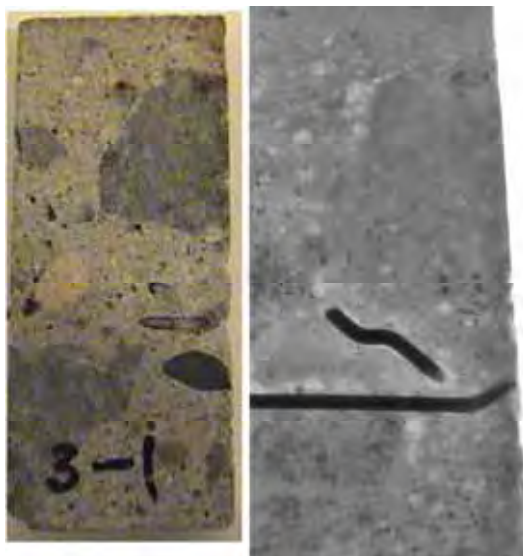


Figure 4.2.1.13 Sample 3-1

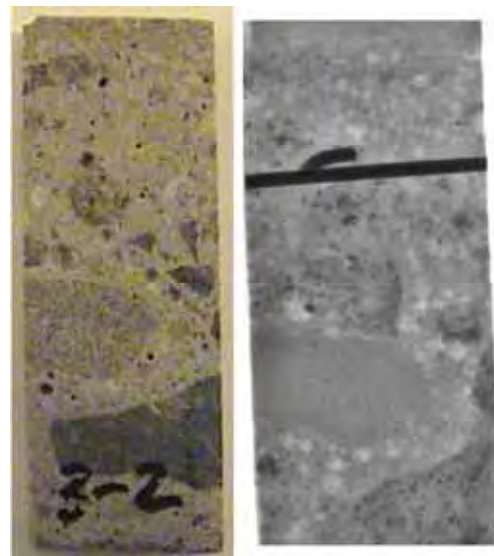


Figure 4.2.1.14 Sample 3-2

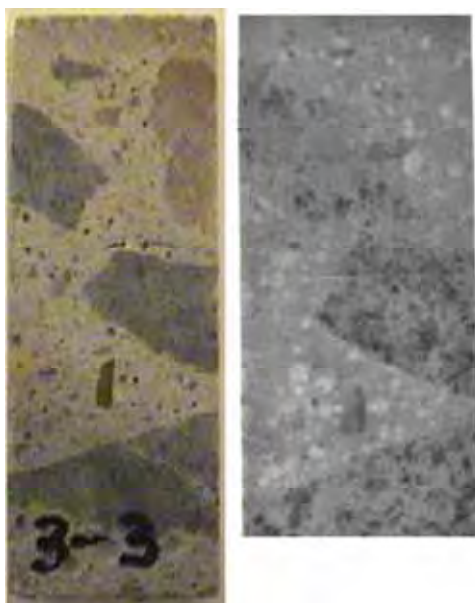


Figure 4.2.1.15 Sample 3-3

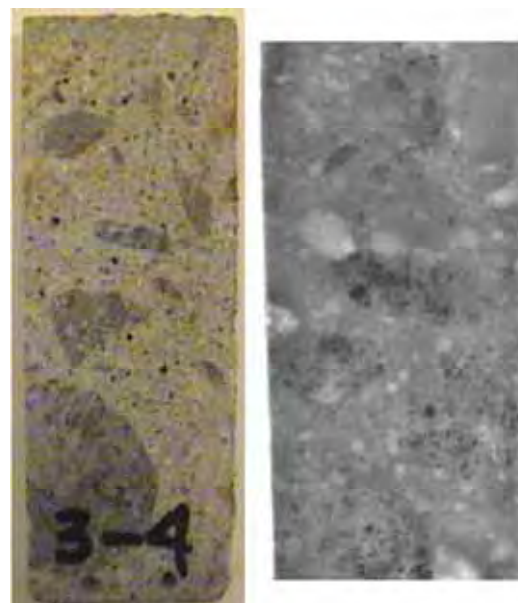


Figure 4.2.1.16 Sample 3-4



Figure 4.2.1.17 Sample 3-5



Figure 4.2.1.18 Sample 3-6



Figure 4.2.1.19 Sample 4-1



Figure 4.2.1.20 Sample 4-2

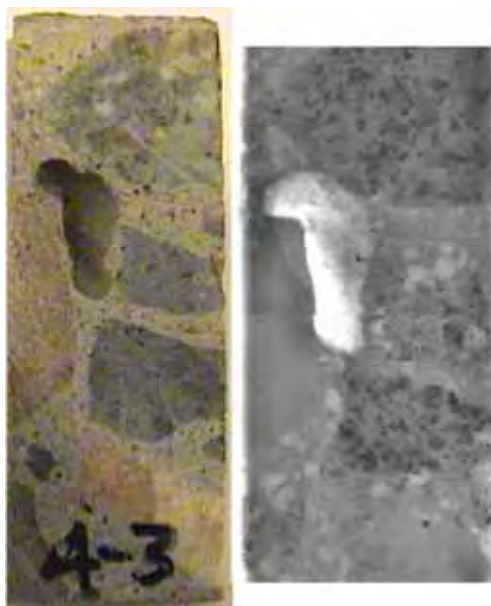


Figure 4.2.1.21 Sample 4-3

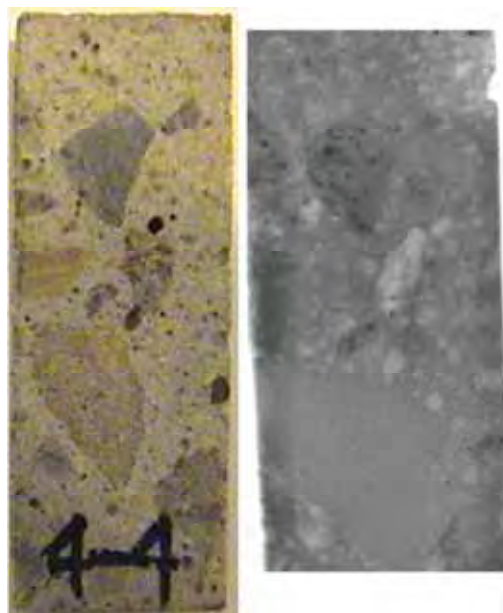


Figure 4.2.1.22 Sample 4-4

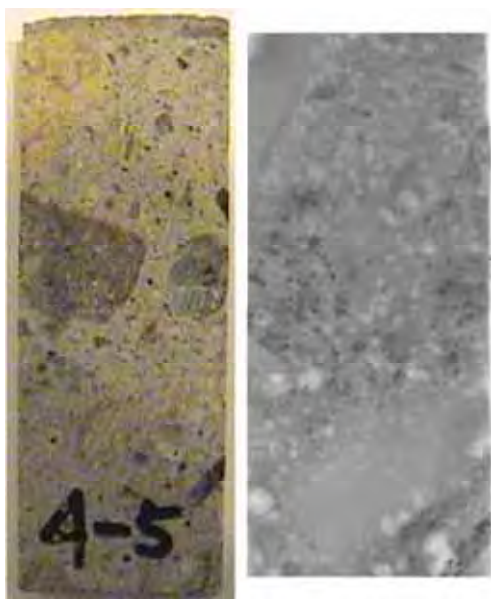


Figure 4.2.1.23 Sample 4-5

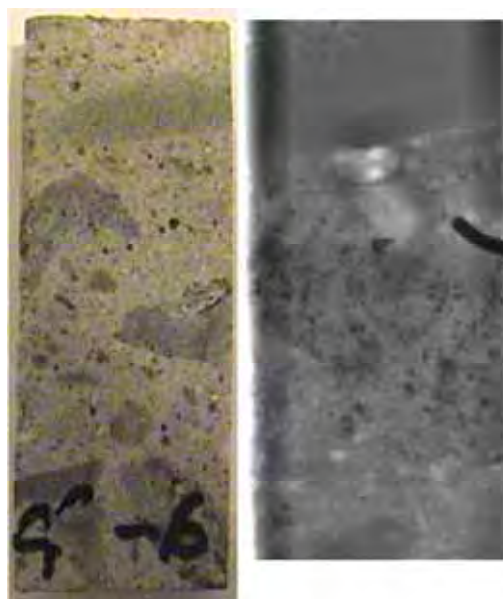


Figure 4.2.1.24 Sample 4-6

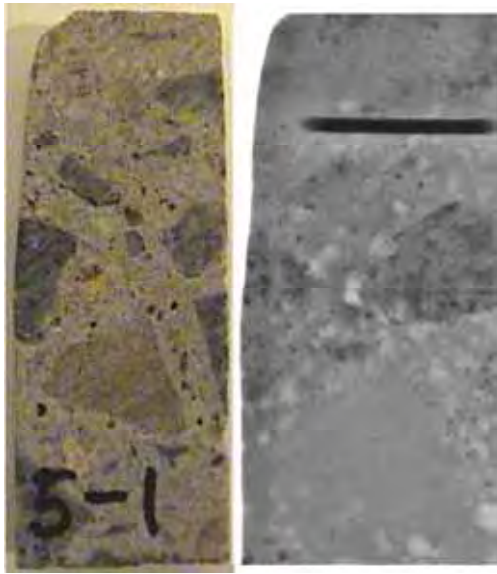


Figure 4.2.1.25 Sample 5-1

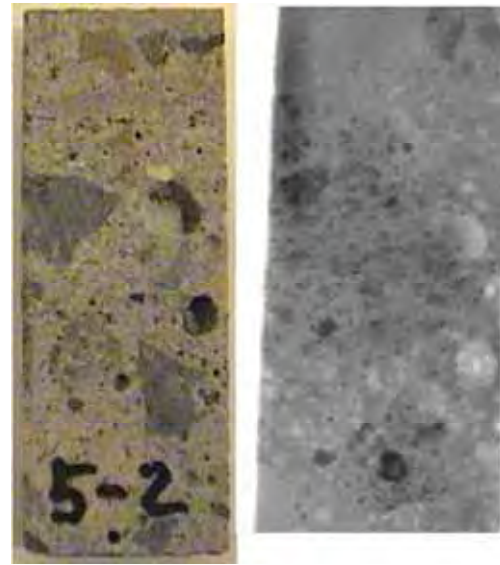


Figure 4.2.1.26 Sample 5-2

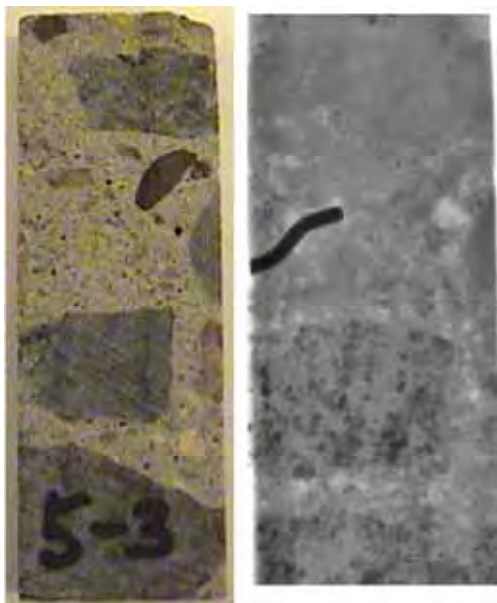


Figure 4.2.1.27 Sample 5-3

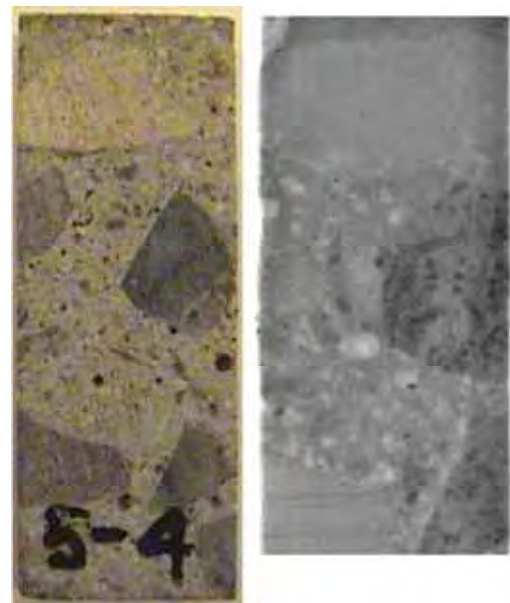


Figure 4.2.1.28 Sample 5-4



Figure 4.2.1.29 Sample 5-5



Figure 4.2.1.30 Sample 5-6



Figure 4.2.1.31 Sample 5-7

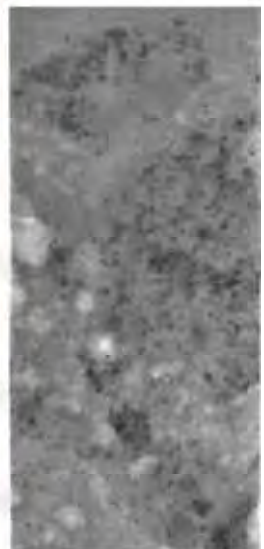


Figure 4.2.1.32 Sample 5-8

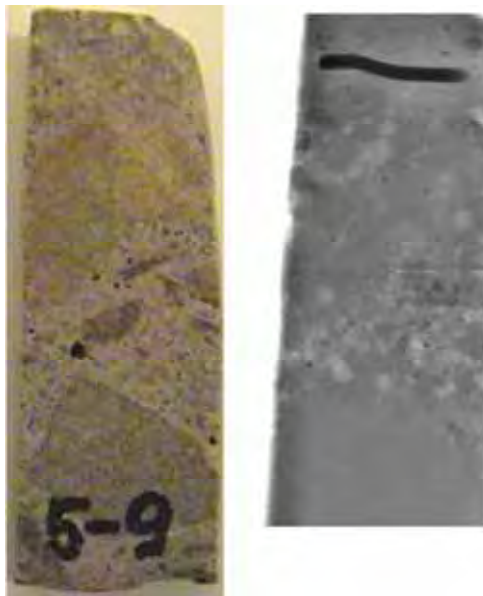


Figure 4.2.1.33 Sample 5-9

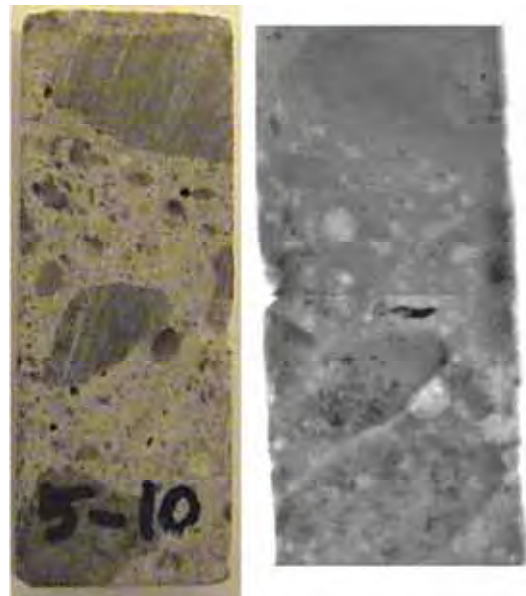


Figure 4.2.1.34 Sample 5-10

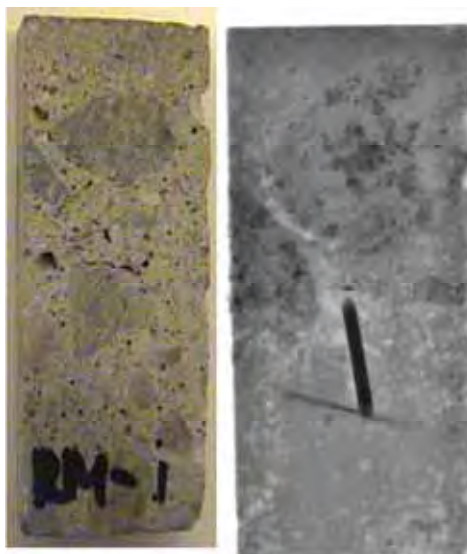


Figure 4.2.1.35 Sample Rm-1

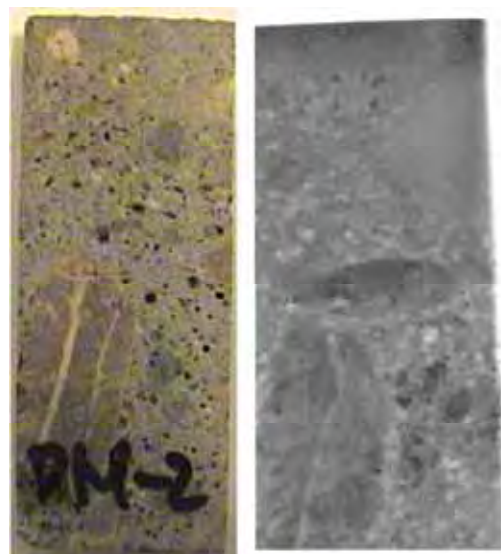


Figure 4.2.1.36 Sample Rm-2



Figure 4.2.1.37 Sample Rm-3



Figure 4.2.1.38 Sample Rm-4

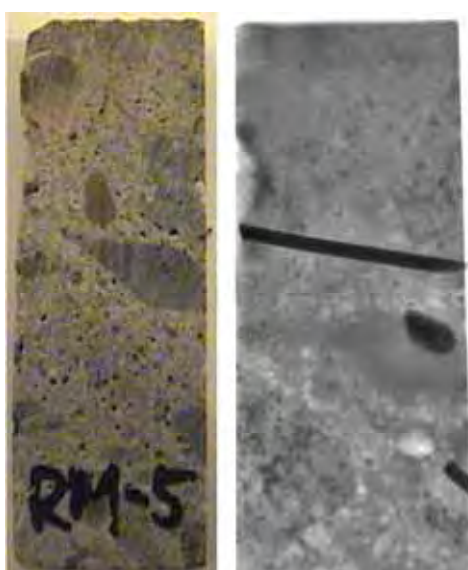


Figure 4.2.1.39 Sample Rm-5

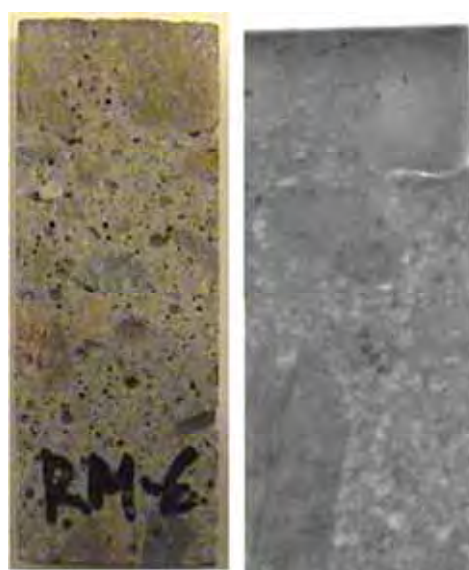


Figure 4.2.1.40 Sample Rm-6

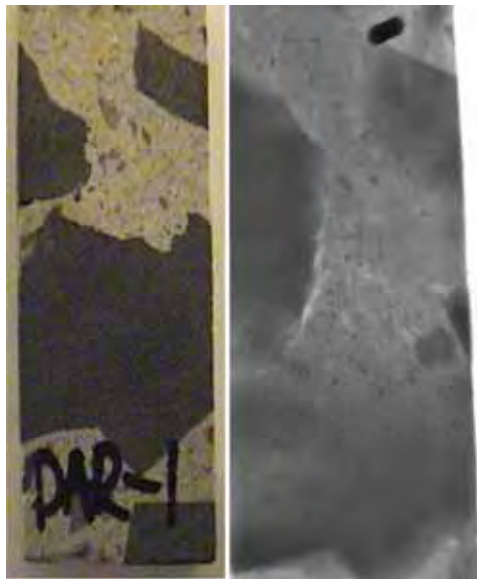


Figure 4.2.1.41 Sample Dar-1

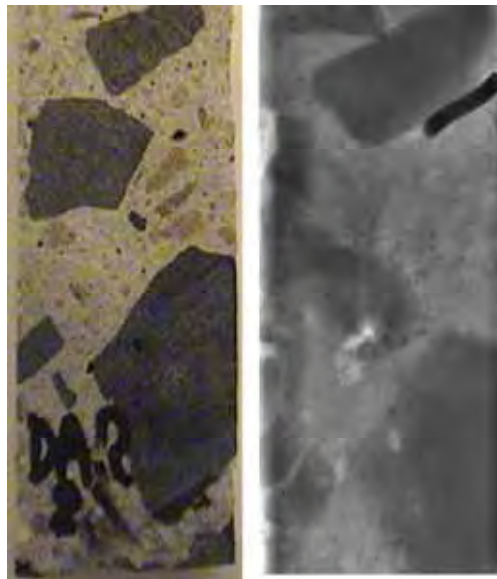


Figure 4.2.1.42 Sample Dar-2

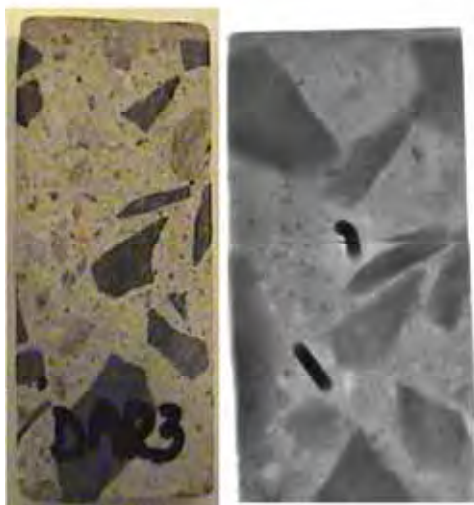


Figure 4.2.1.43 Sample Dar-3

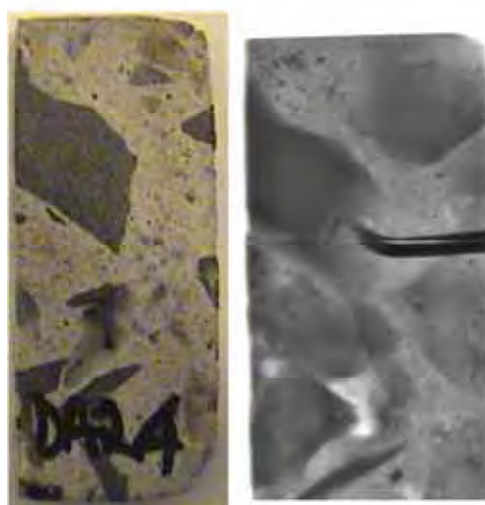


Figure 4.2.1.44 Sample Dar-4



Figure 4.2.1.45 Sample Dar-5

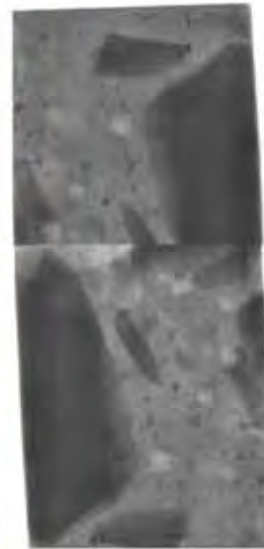


Figure 4.2.1.46 Sample Dar-6

4.2.2 Samples Cut Perpendicular to the Notch

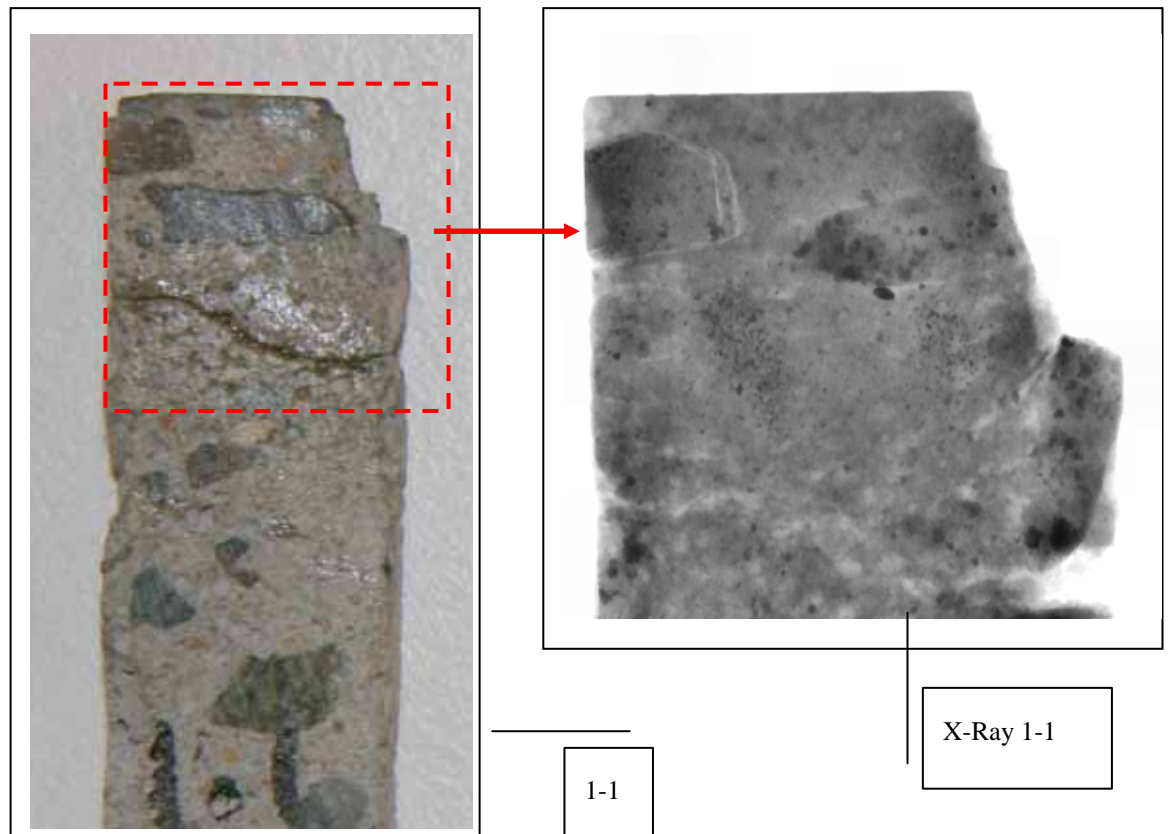


Figure 4.2.2.1 (in detail) Perpendicular cut from Concrete Core Sample 1-1 with its X-Ray image

Large X-Ray Images of all Perpendicular cut Samples 1 to 4, 5(Reference), Rm, Dar, FI, and FII, follow with initial observations for each Sample.

Detailed analysis of each X-ray image follows, to differentiate forensic samples 1 to 4, reference sample 5, and comment on two other mixes of the same compressive strength (Rm - ReadyMix and Dar - Western Suburbs), and two later samples of higher compressive strength and differing micro-structures (FI and FII).

Sample 1-1 X-Ray Perpendicular cut

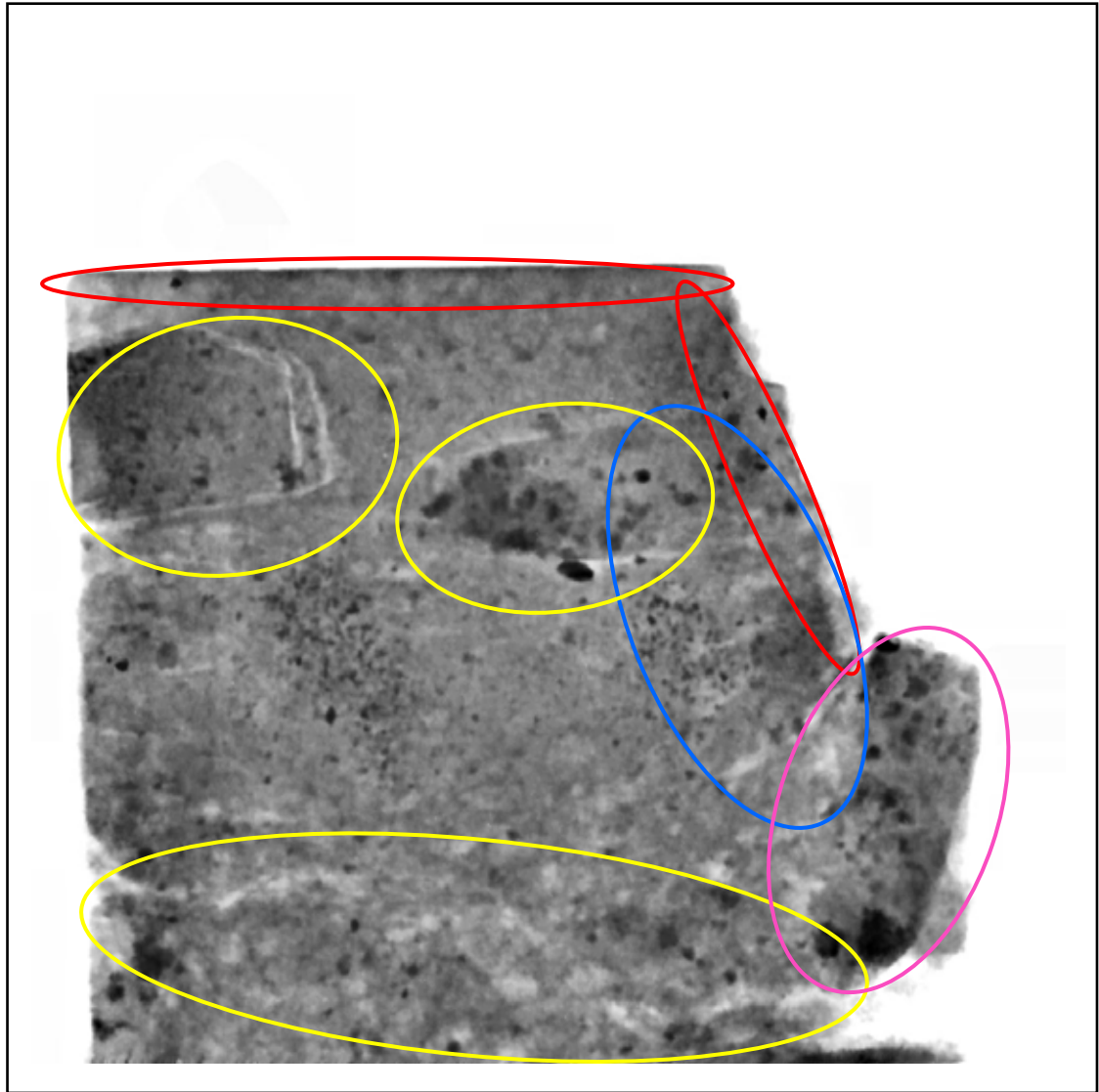


Figure 4.2.2.1 X-Ray Detail of Sample 1-1

- Darkened areas around notch, diamond cut edge, and top
 - Radial cracks from notch
 - Interfacial zone cracking around aggregates, and throughout cement matrix
 - Shadowed from aggregate, not compression
- Numerous air voids, porosity

Sample 1-2 X-Ray Perpendicular cut

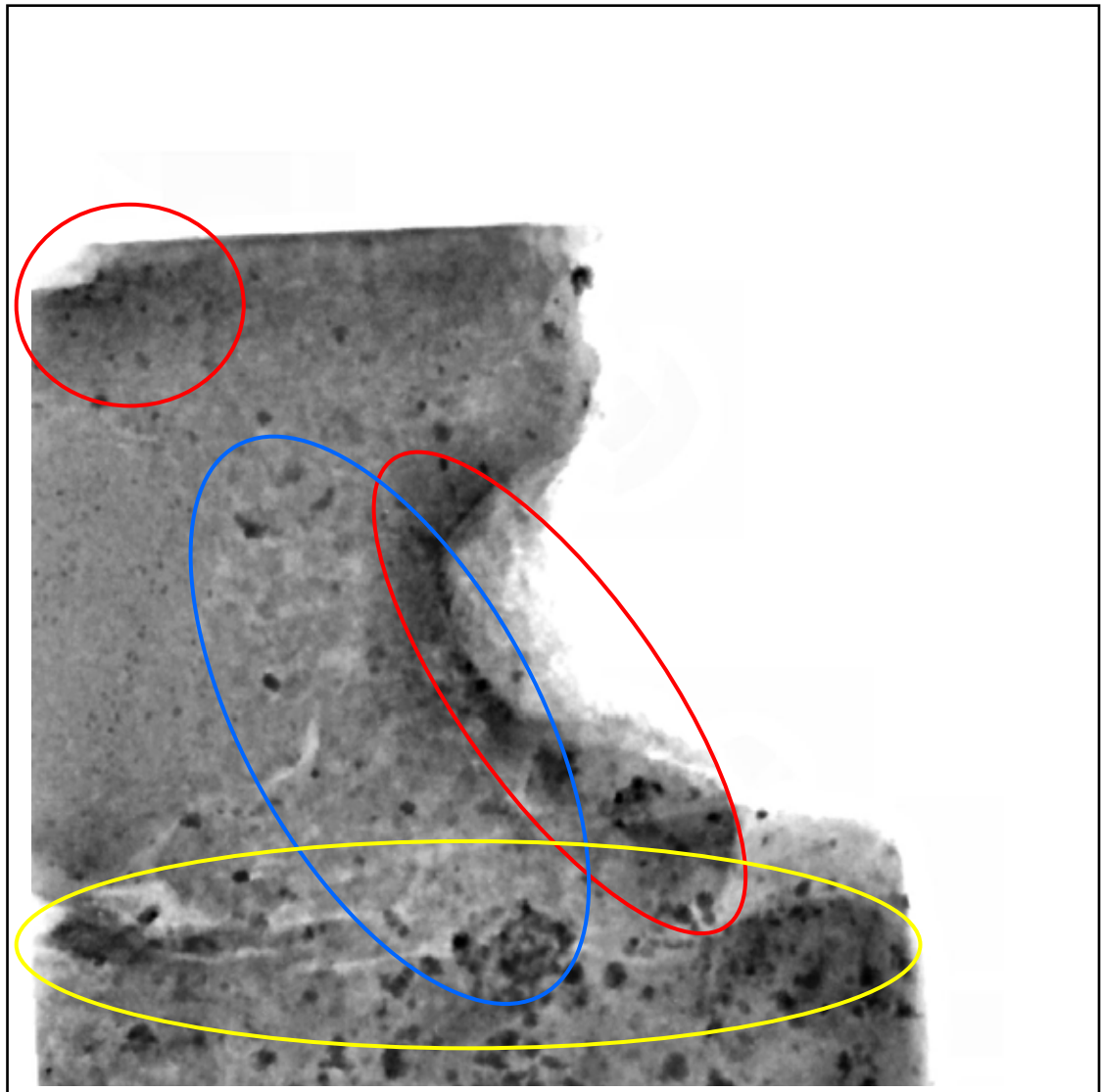


Figure 4.2.2.2 X-Ray Detail of Sample 1-2

- Obvious compression ahead of damaged notch (not from aggregate) and top corner
- Heavy radial cracking
- Interfacial zone cracking and laminations around top of aggregate

Sample 1-3 X-Ray Perpendicular cut

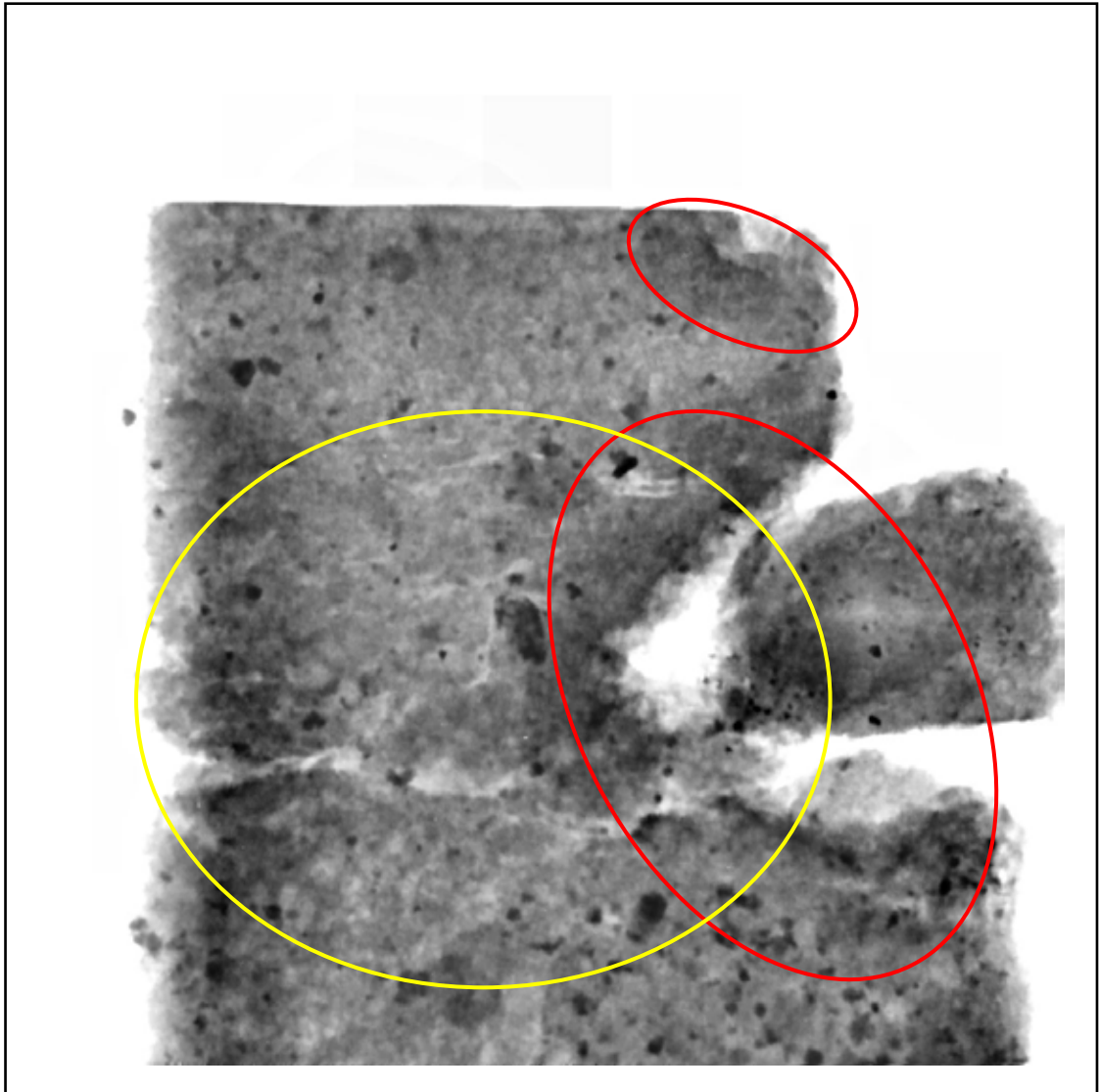




Figure 4.2.2.3 X-Ray Detail of Sample 1-3

Similar to Sample 1-2

-  Darkening areas around notch (some from aggregate) and top right corner compressed
-  Interfacial zone heavy cracking

Sample 1-4 X-Ray Perpendicular cut

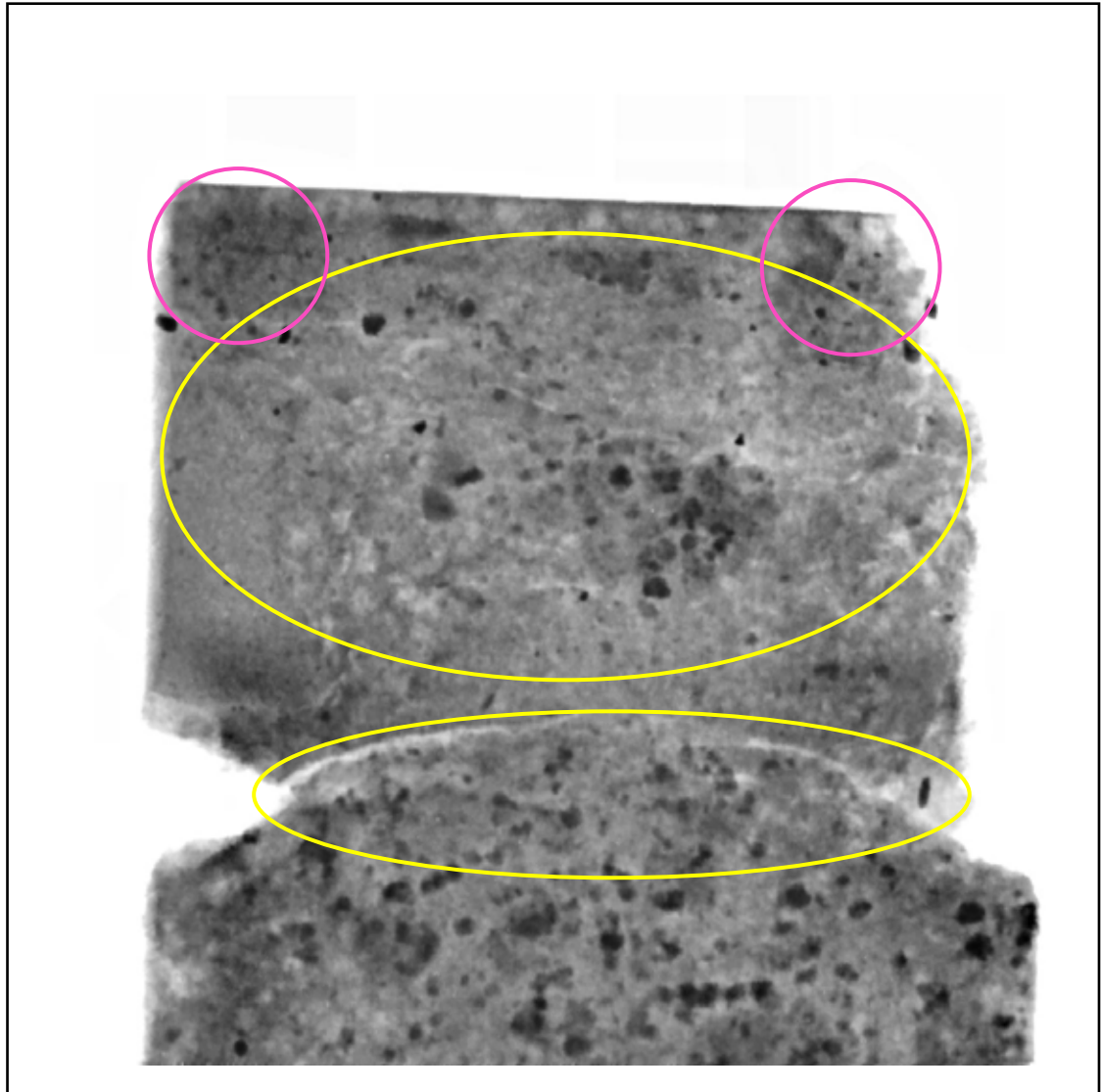


Figure 4.2.2.4 X-Ray Detail of Sample 1-4

- Heavy interfacial transition zone cracking around aggregate and cement matrix
- Both top corners shadowed

Sample 2-1 X-Ray Perpendicular cut

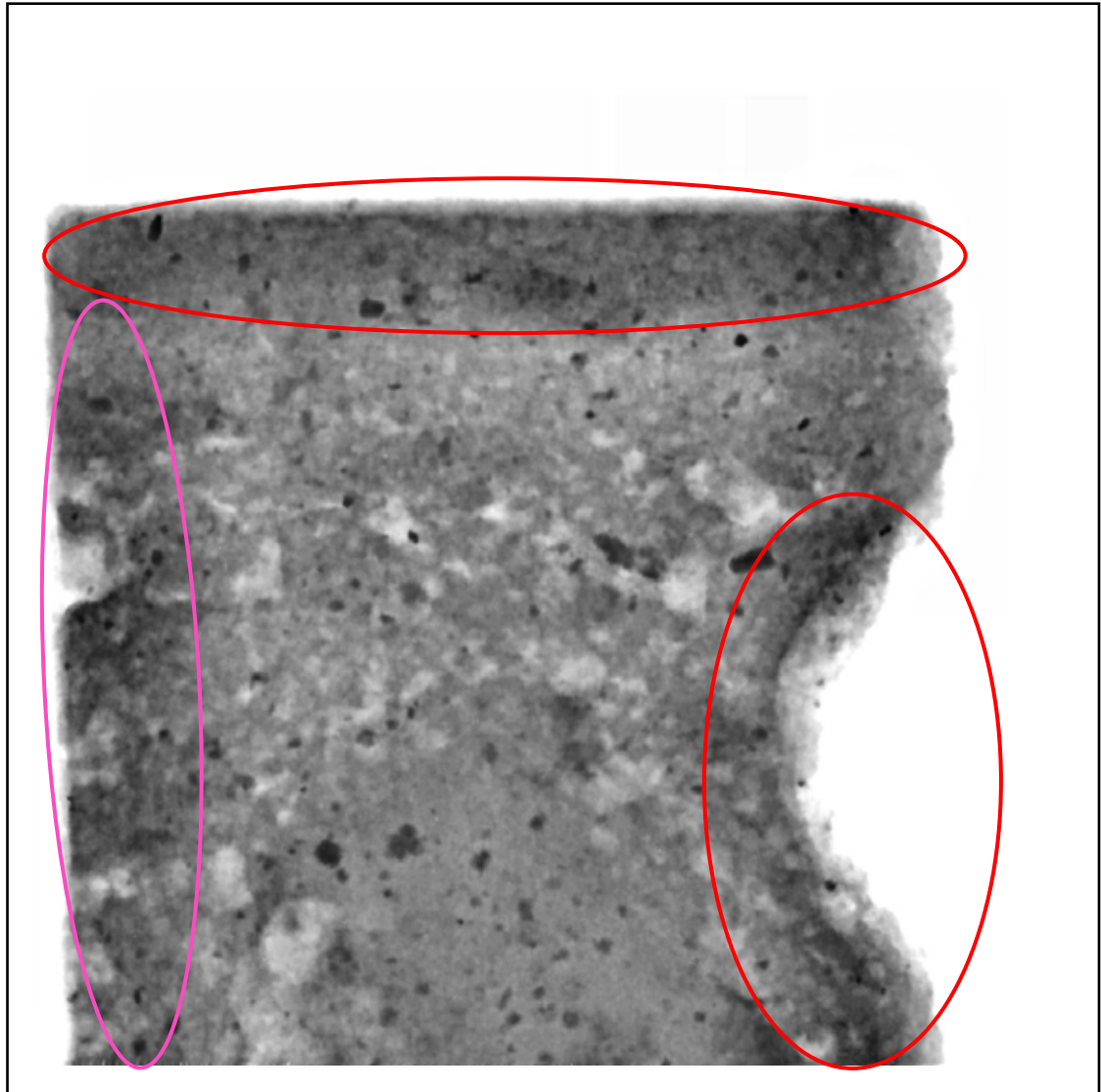




Figure 4.2.2.5 X-Ray Detail of Sample 2-1

-  Darkened areas compressed around notch, diamond cut edge, and top
 -  Cut darkening from aggregate
- Lot of porosity, large air voids

Sample 2-2 X-Ray Perpendicular cut

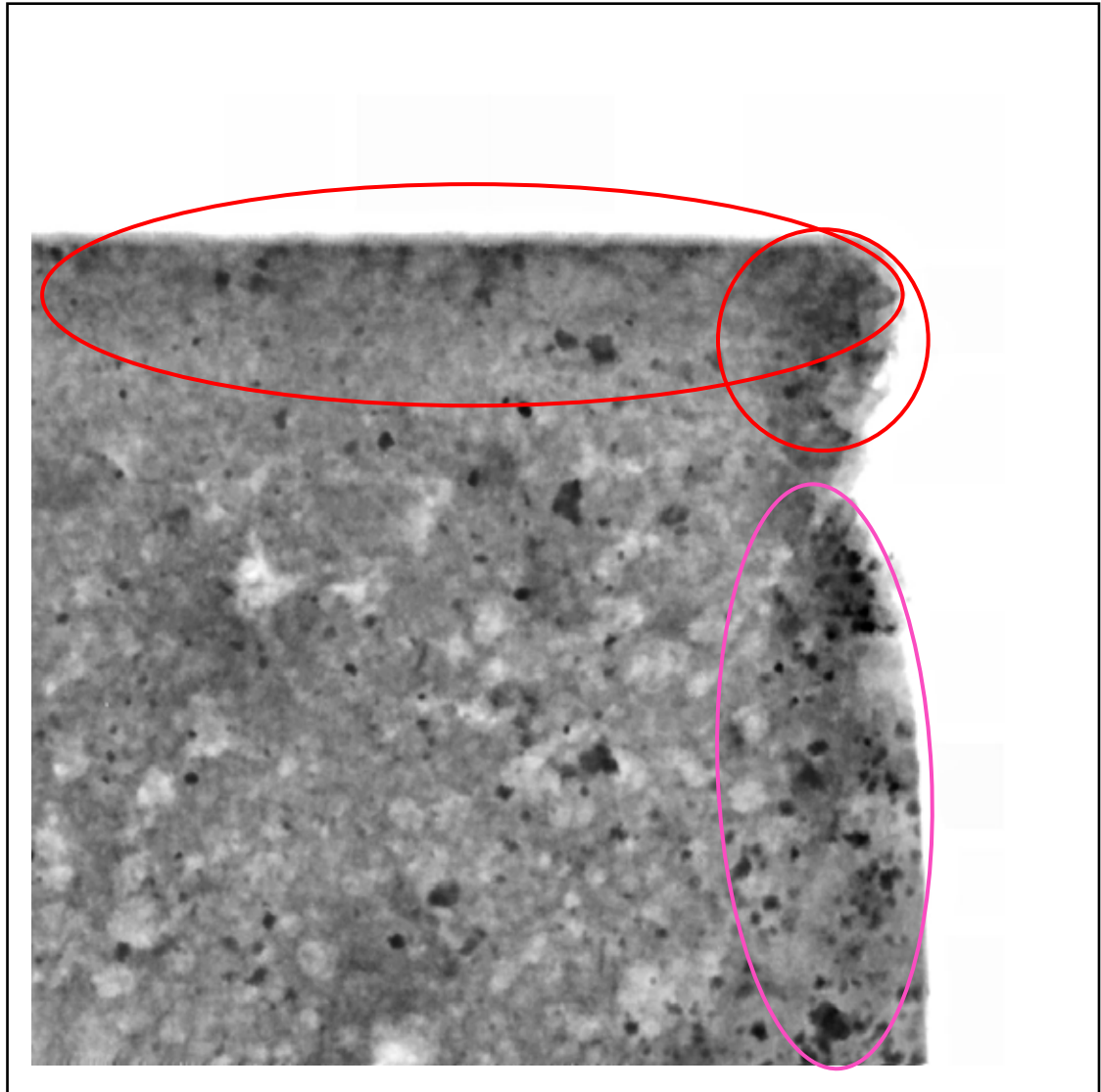




Figure 4.2.2.6 X-Ray Detail of Sample 2-2

-  Darkened compressed on top
-  Shadow in notch from aggregate
- Lot of porosity, large air voids

Sample 2-3 X-Ray Perpendicular cut

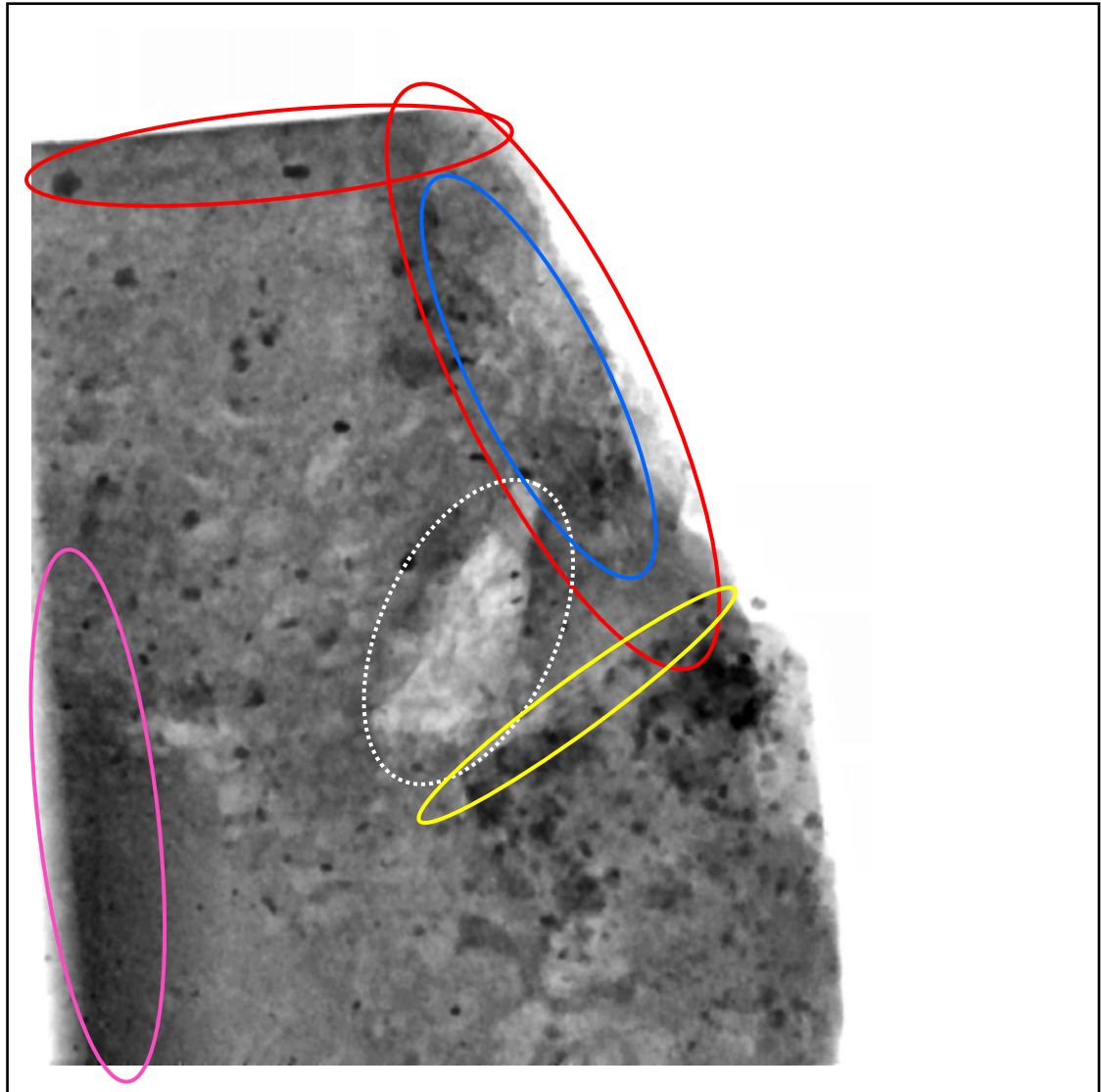






Figure 4.2.2.7 X-Ray Detail of Sample 2-3

-  Darkening in notch and on cut from aggregate
-  Radial cracks from notch
-  Darkening in aggregate – evidence of compression from cutting
-  Interfacial zone cracking and lamination around aggregates

Large void cavity (dashed white)

Downward cut causes lateral compression – notch darkening is not from cutting

Sample 2-4 X-Ray Perpendicular cut

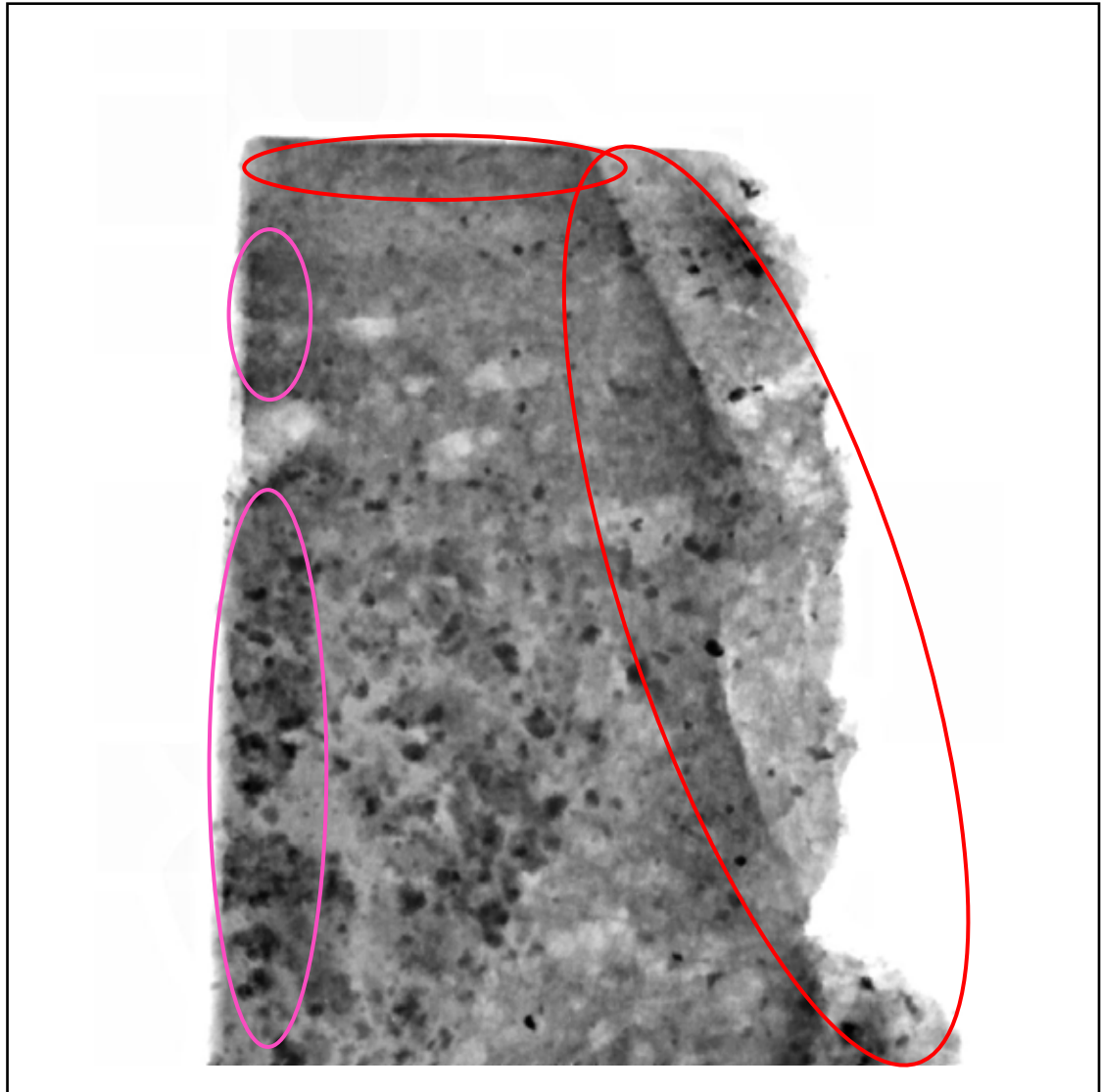




Figure 4.2.2.8 X-Ray Detail of Sample 2-4

-  Crack wake can be seen clearly on right side – light to right and shadow to left and some darkening on top
-  Cut edge, and shadow from aggregate
- Large pores (air voids)
- Good bonding of aggregate and paste

Sample 2-5 X-Ray Perpendicular cut

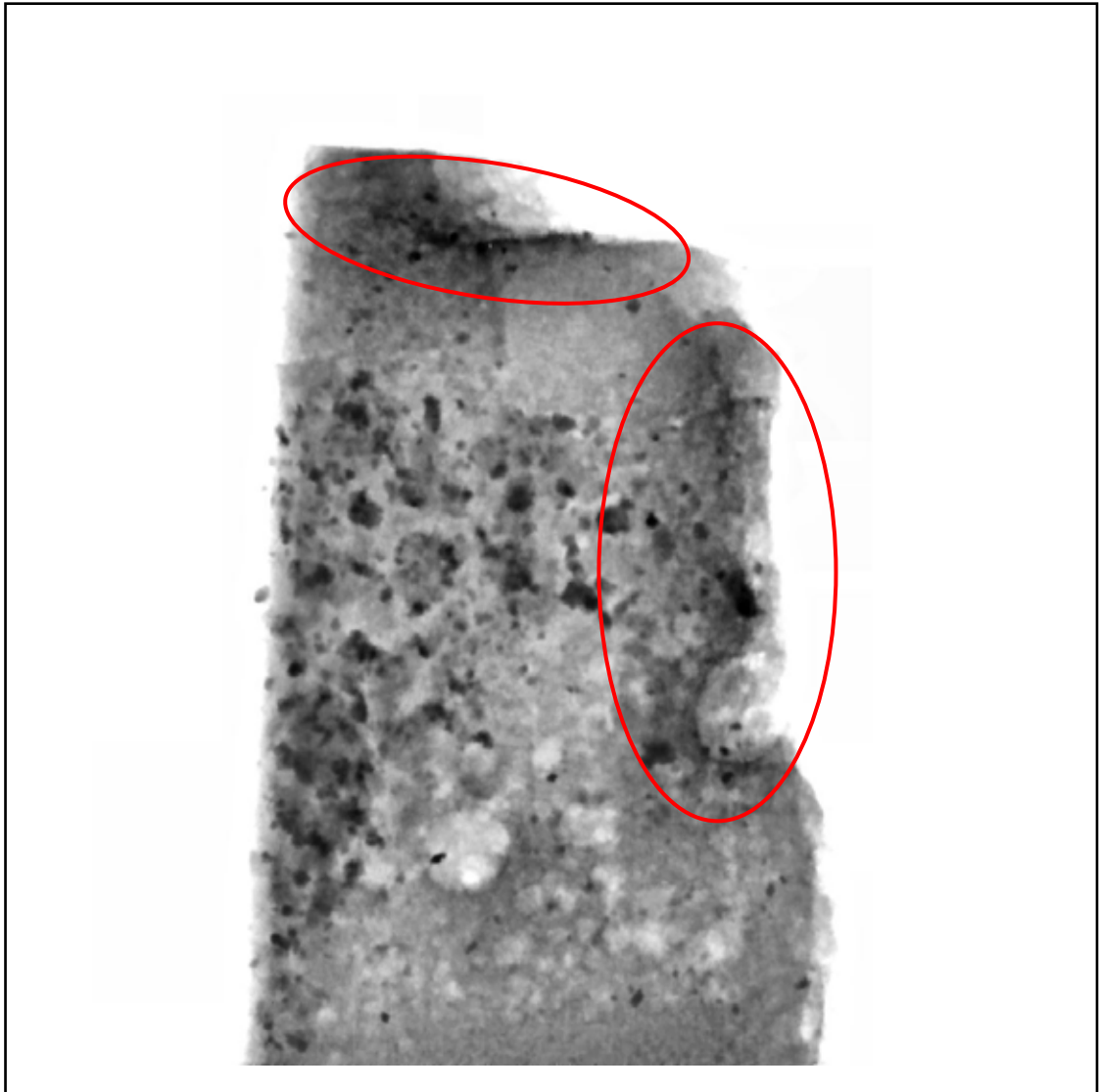



Figure 4.2.2.9 X-Ray Detail of Sample 2-5

-  Darkened areas compressed around notch, diamond cut edge, and top
- Large pores (air voids)
- Good bonding of aggregate and paste

Sample 2-6 X-Ray Perpendicular cut

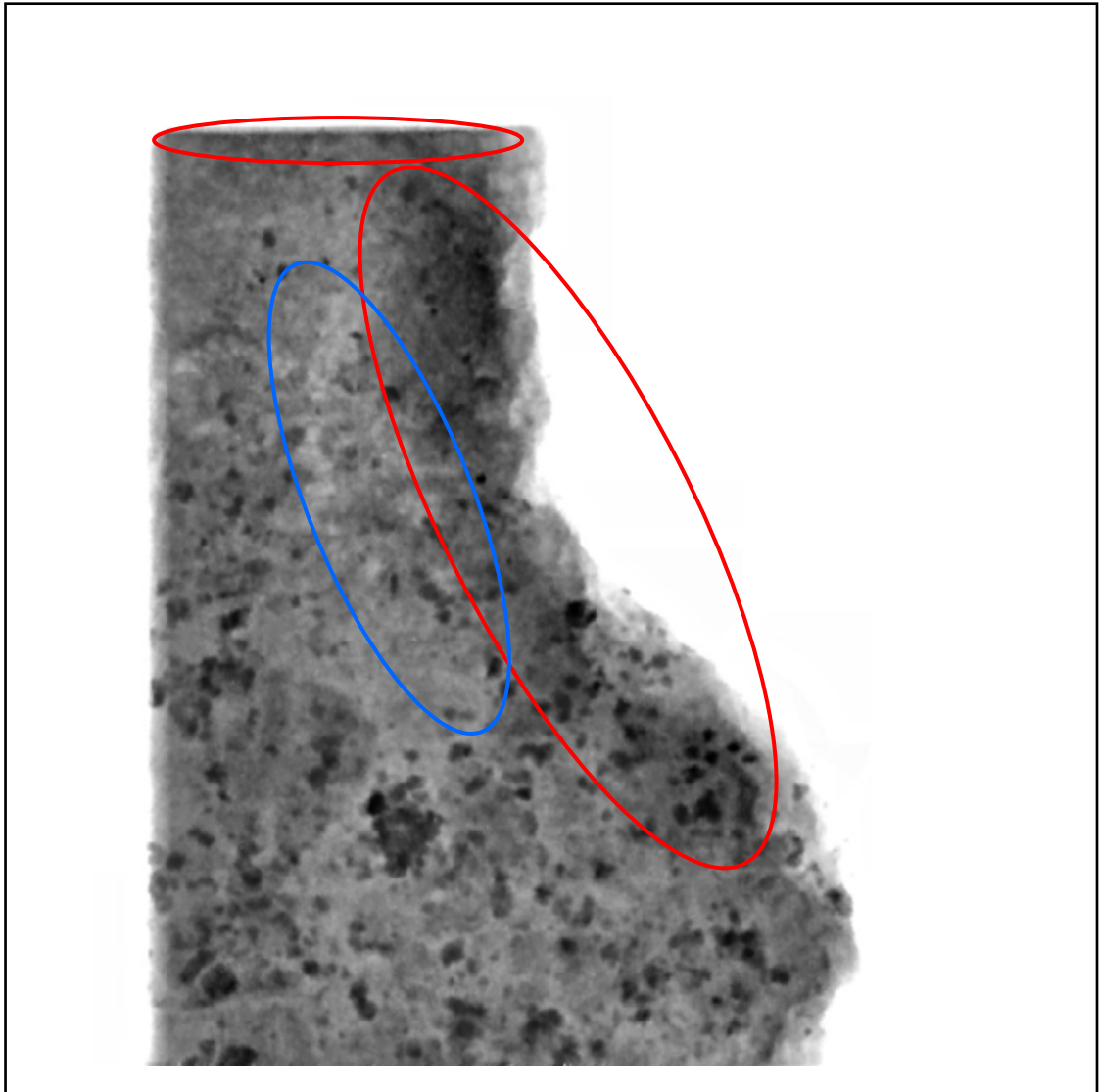


Figure 4.2.2.10 X-Ray Detail of Sample 2-6

- Darkened areas around notch, diamond cut edge, and top
- Radial cracks from notch

Note small aggregate particle in notch but no enhanced darkening

No darkening on cut (left vertical edge)

Good bonding of aggregate and paste

Sample 3-1 X-Ray Perpendicular cut

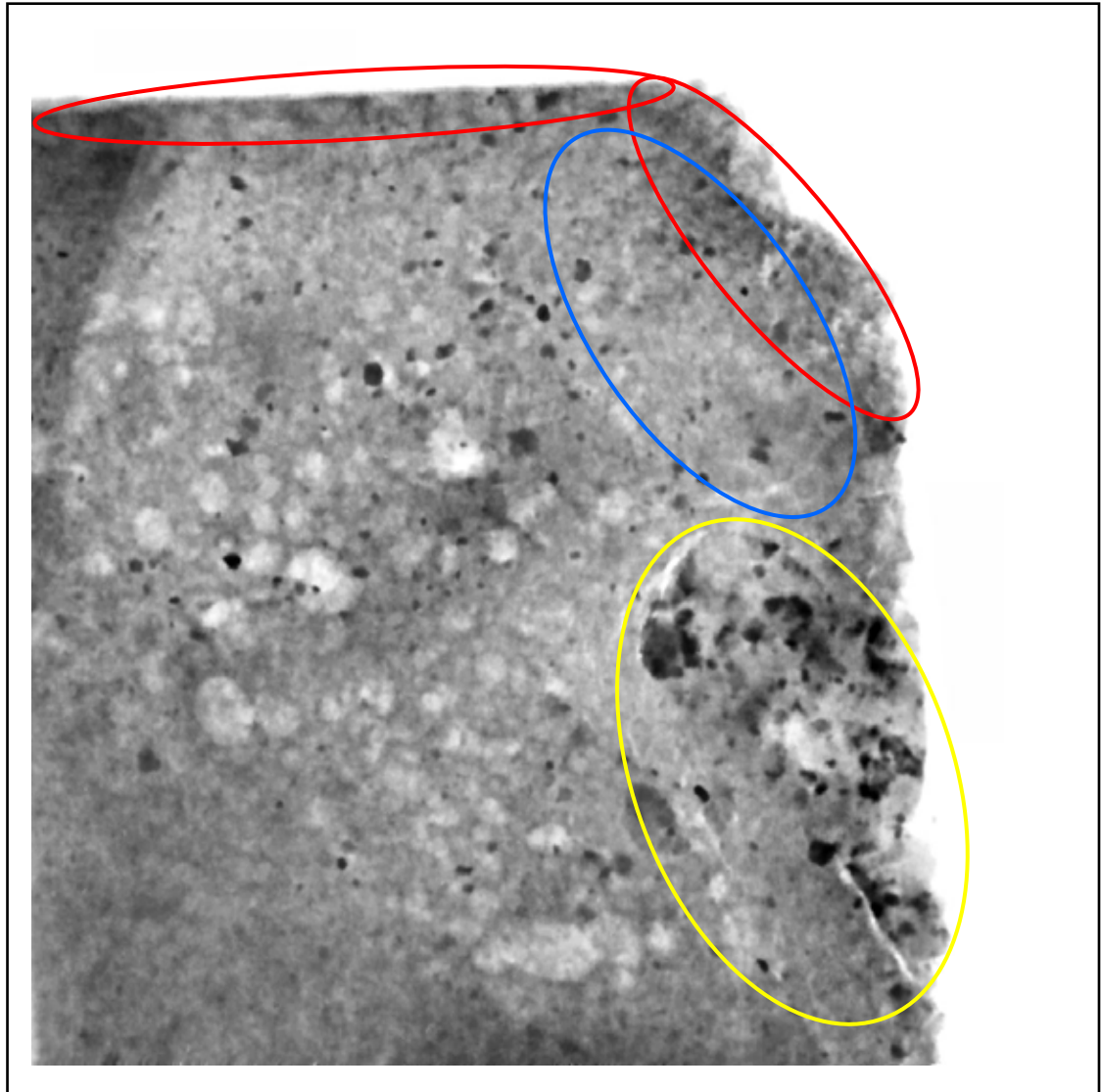


Figure 4.2.2.11 X-Ray Detail of Sample 3-1

- Darkened areas around notch, diamond cut edge, and top
 - Radial cracks from notch
 - Lamination and cracking around aggregate, and fine cracking throughout paste
- Large and numerous air voids

Sample 3-2 X-Ray Perpendicular cut

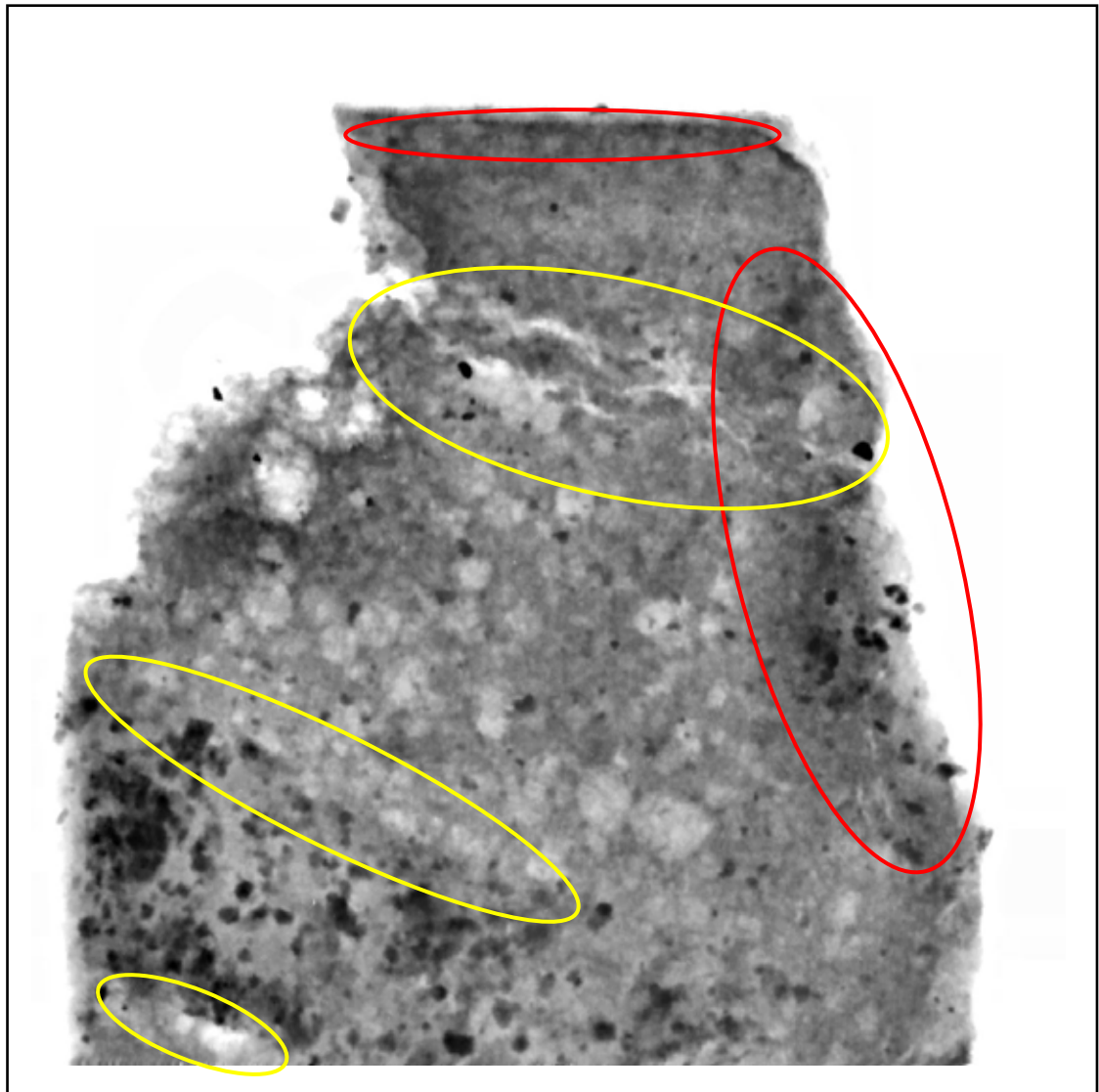


Figure 4.2.2.12 X-Ray Detail of Sample 3-2

- Darkened areas around notch, and top
- Interfacial zone cracking around aggregates, and throughout cement matrix
- Numerous large air voids
- Interfacial zone cracking around aggregates and throughout cement matrix
- Piece fell off left side during diamond cutting sample

Sample 4-1 X-Ray Perpendicular cut

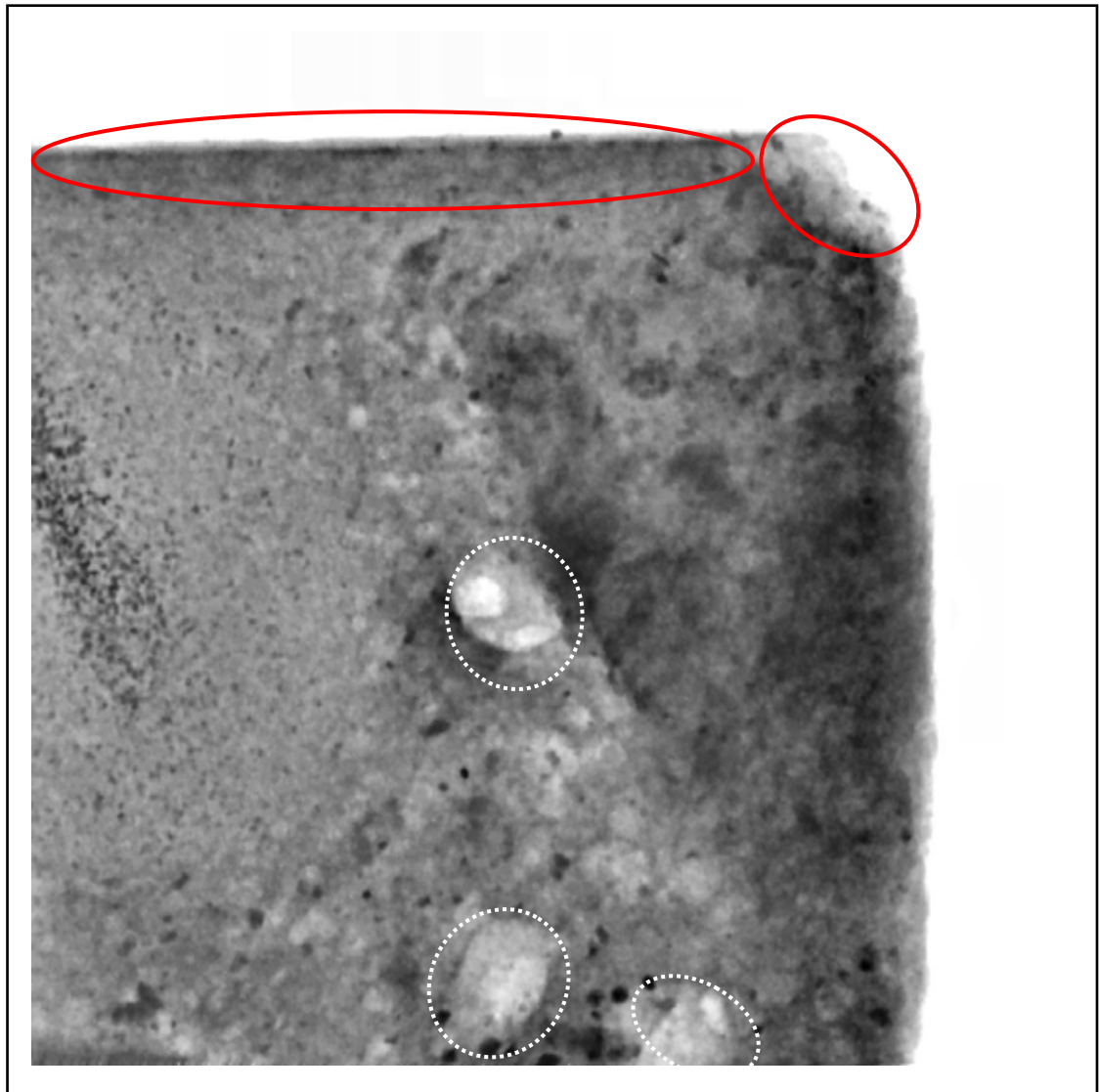


Figure 4.2.2.13 X-Ray Detail of Sample 4-1

- Notch shows little degradation (degradation stops at hard aggregate), darkening clearly along the line of notch confirms compression from cutting notch, darkening top
- Large voids (dashed white)

Sample 4-2 X-Ray Perpendicular cut

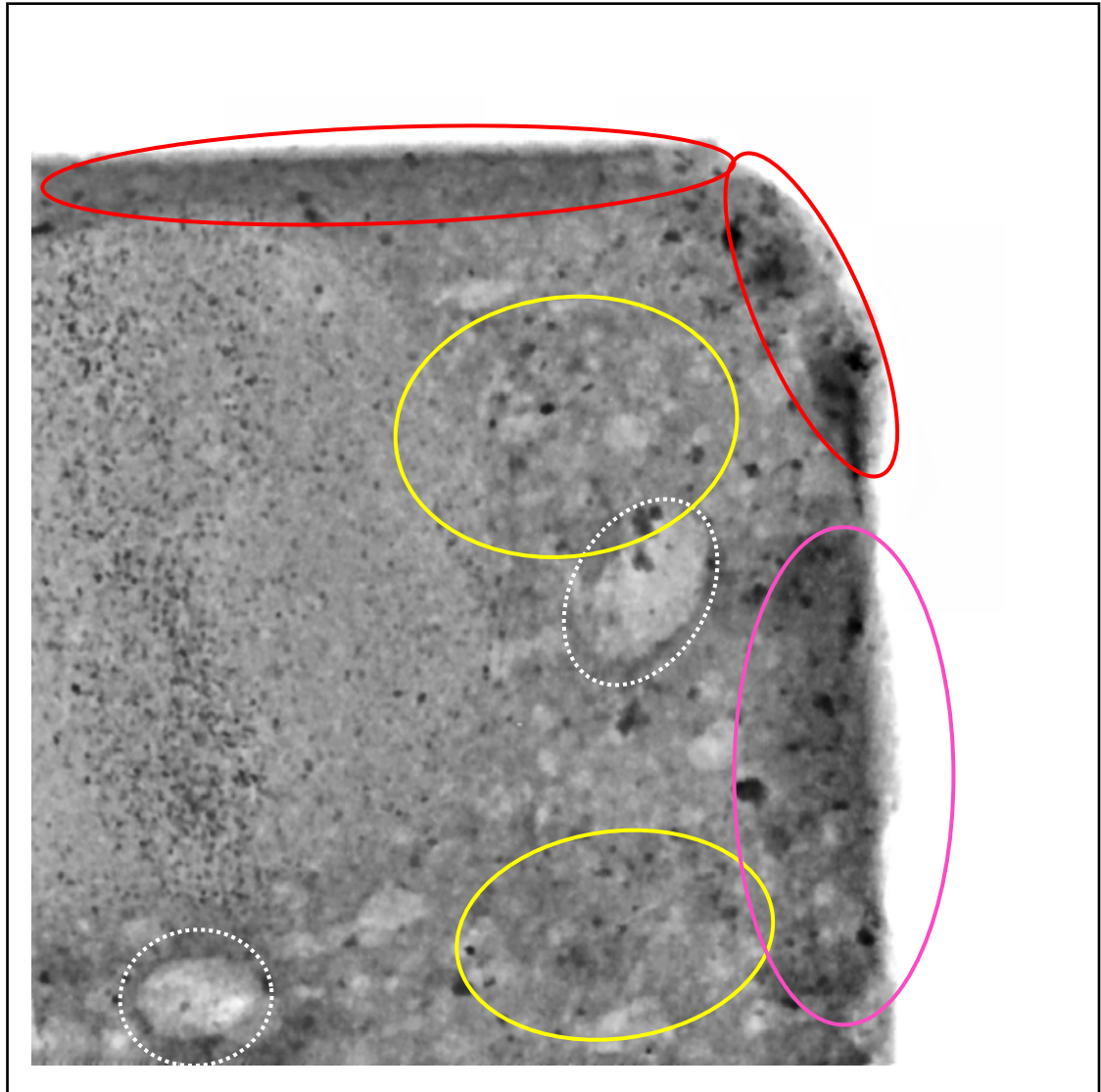





Figure 4.2.2.14 X-Ray Detail of Sample 4-2

-  Top darkening blocked by aggregate, darkened areas around notch
-  Fine cracking around aggregates, and throughout cement matrix
-  Shadowed from aggregate, not compression
- Large air voids (dashed white)

Sample 5-1 X-Ray Perpendicular cut

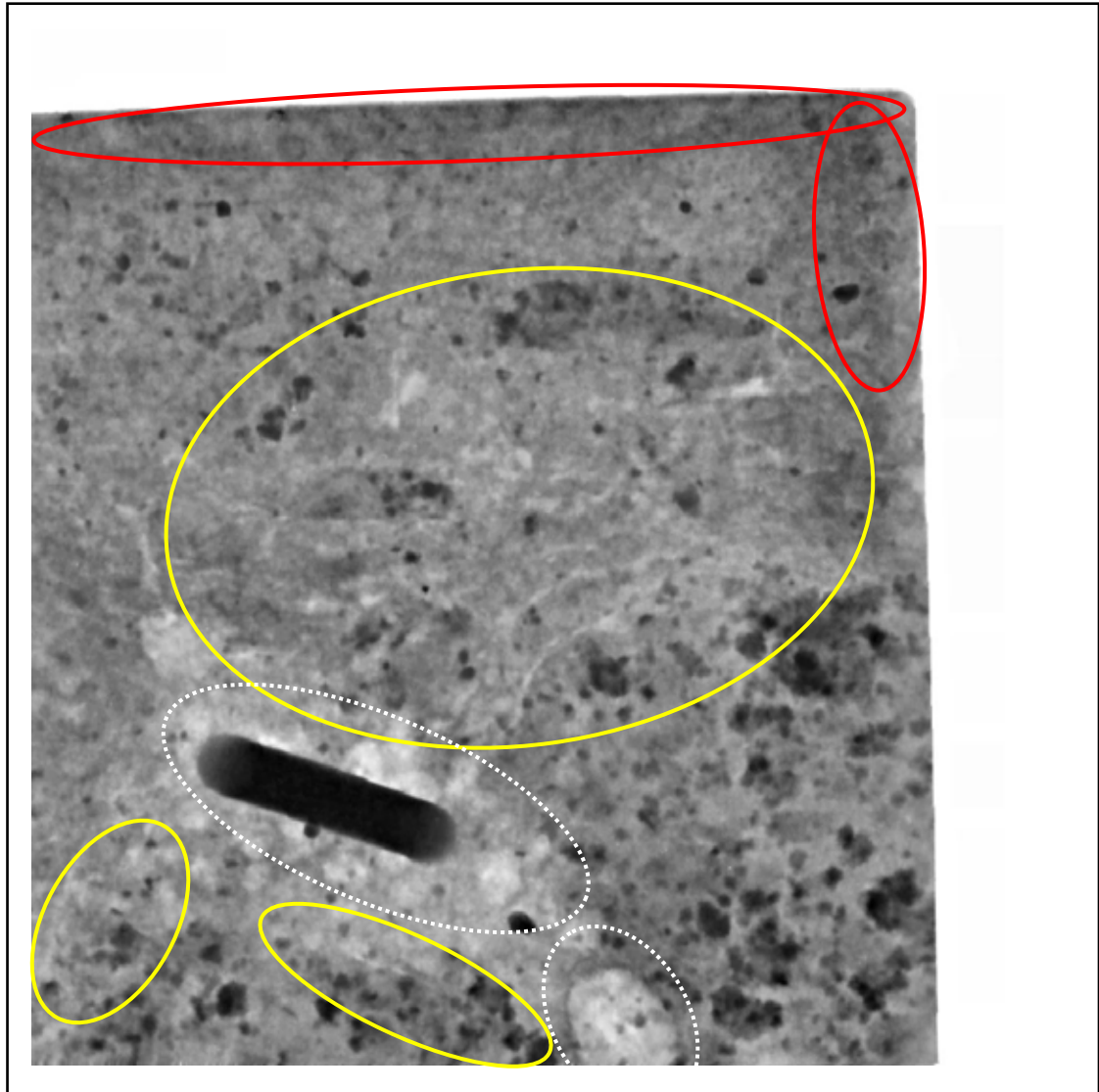


Figure 4.2.2.15 X-Ray Detail of Sample 5-1

Reference Sample, no notch, no damage

- Slight darkening on top, slight darkening on cut- right due to compression of diamond sawing Sample
- Interfacial zone cracking around aggregates, and throughout cement matrix
- Large air voids (dashed white) around metal pin re-enforcement

Sample 5-2 X-Ray Perpendicular cut

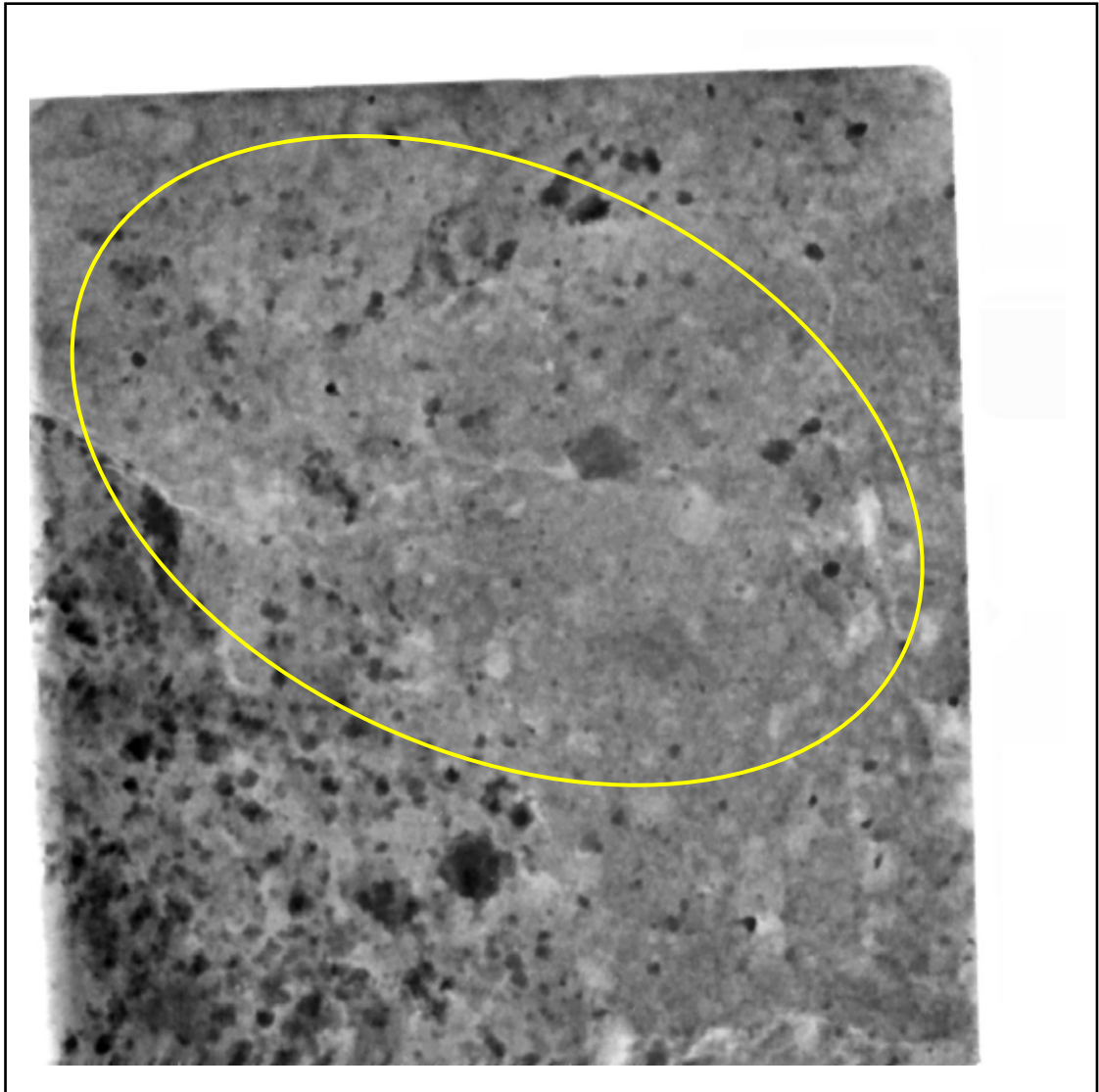


Figure 4.2.2.16 X-Ray Detail of Sample 5-2

○ Interfacial zone micro-cracking around aggregates, and throughout cement matrix

No evidence of darkening

Air voids

Sample Rm-1 X-Ray Perpendicular cut

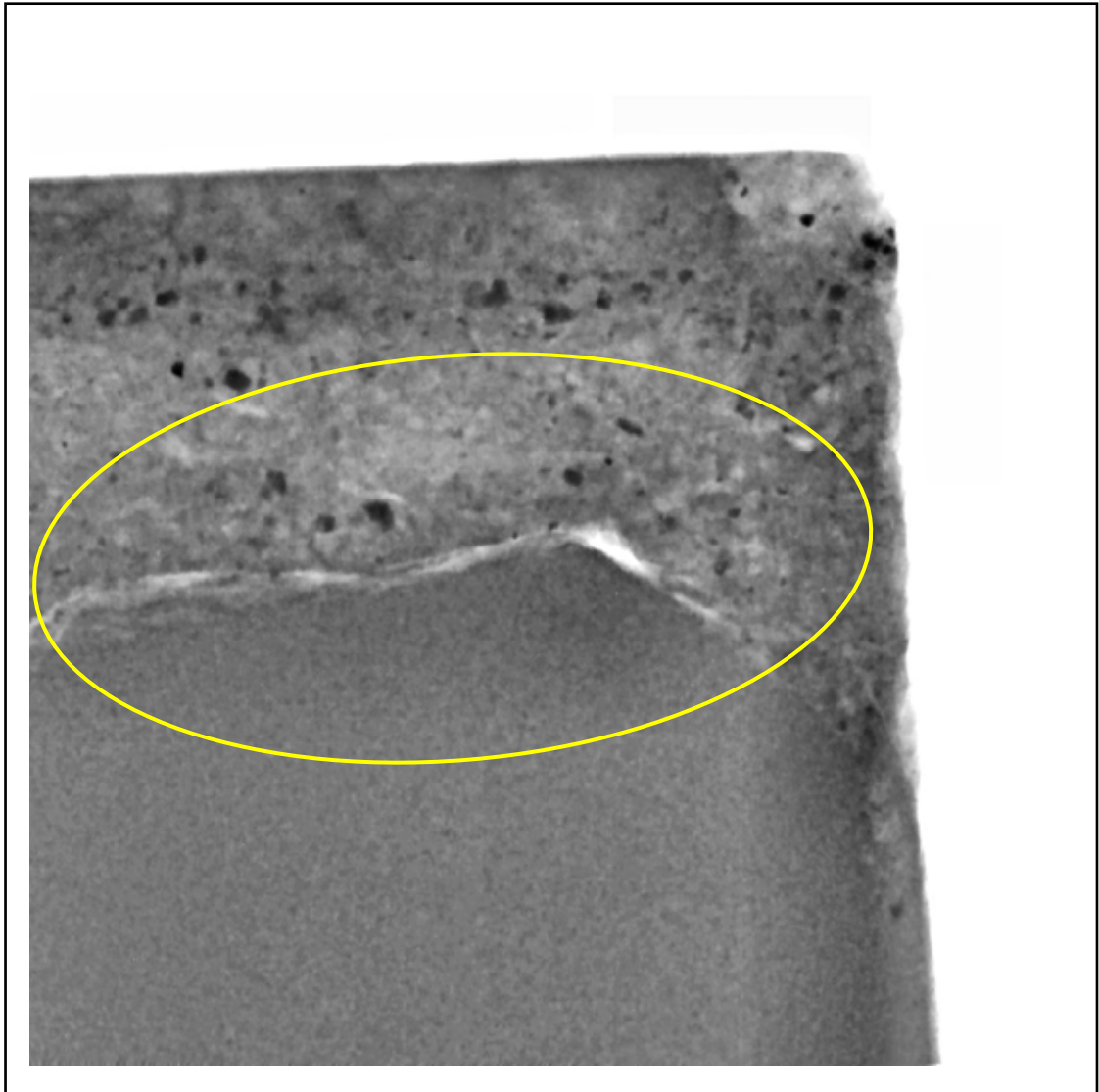



Figure 4.2.2.17 X-Ray Detail of Sample Rm-1

Reference mix assumed to be similar to Samples 1 to 5

-  Interfacial zone cracking around aggregates, and throughout cement matrix, large lamination crack around aggregate

Sample Rm-2 X-Ray Perpendicular cut

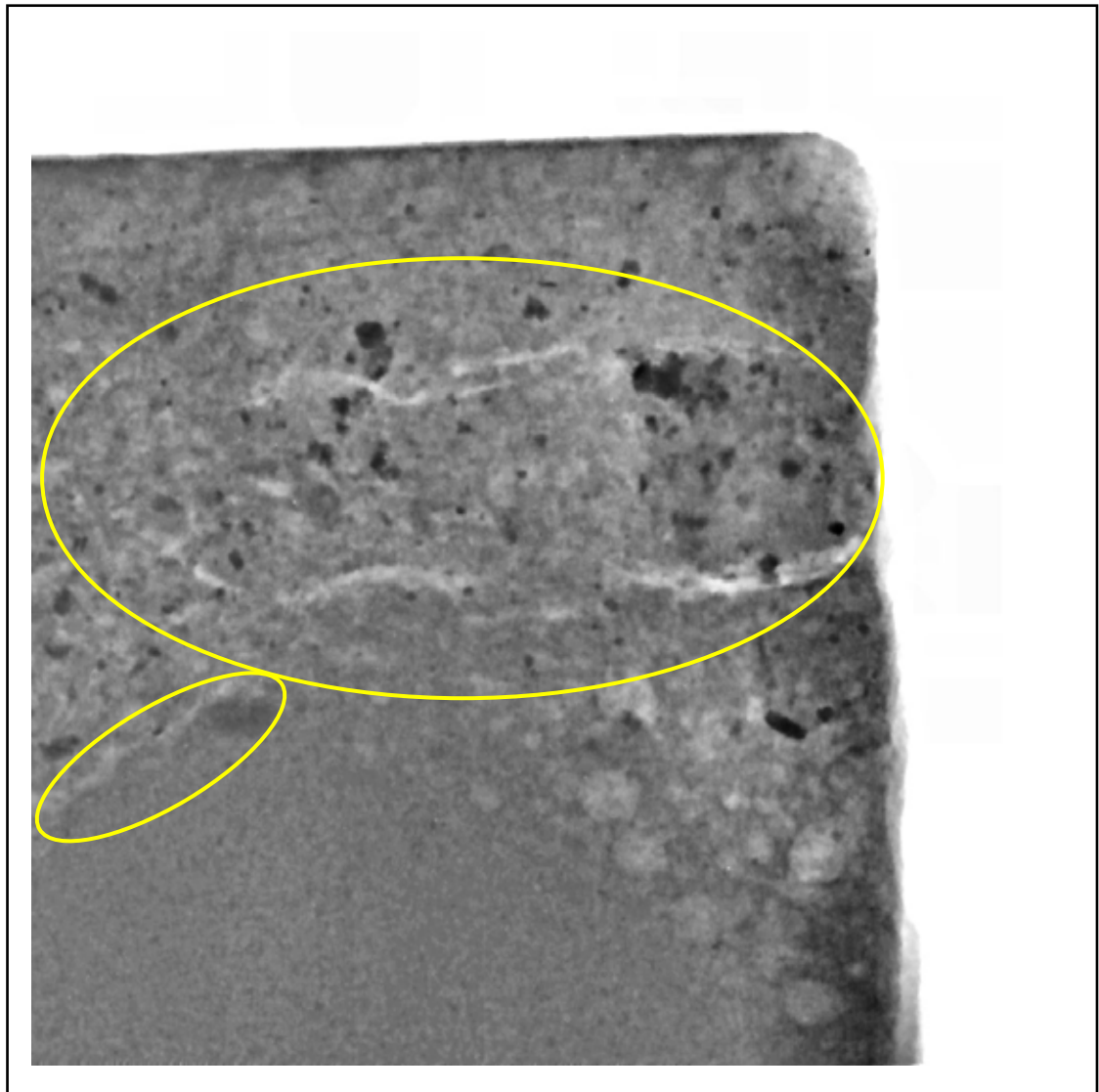



Figure 4.2.2.18 X-Ray Detail of Sample Rm-2

-  Large cracks around aggregate
- Air voids

Sample Rm-3 X-Ray Perpendicular cut

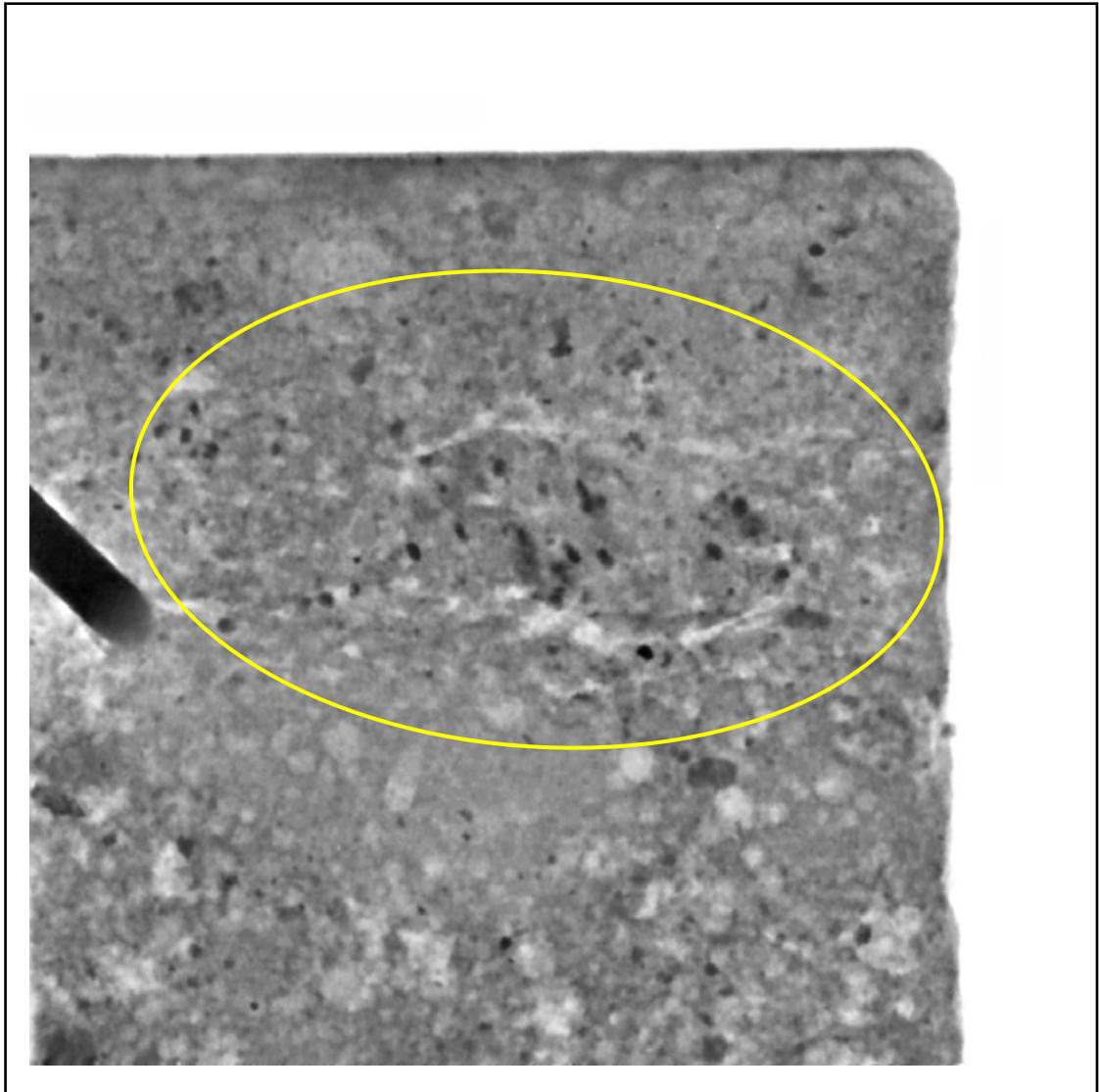


Figure 4.2.2.19 X-Ray Detail of Sample Rm-3



Cracks around aggregate

No darkening

Numerous air voids, porosity around metal pin re-enforcement

Sample Dar-1 X-Ray Perpendicular cut

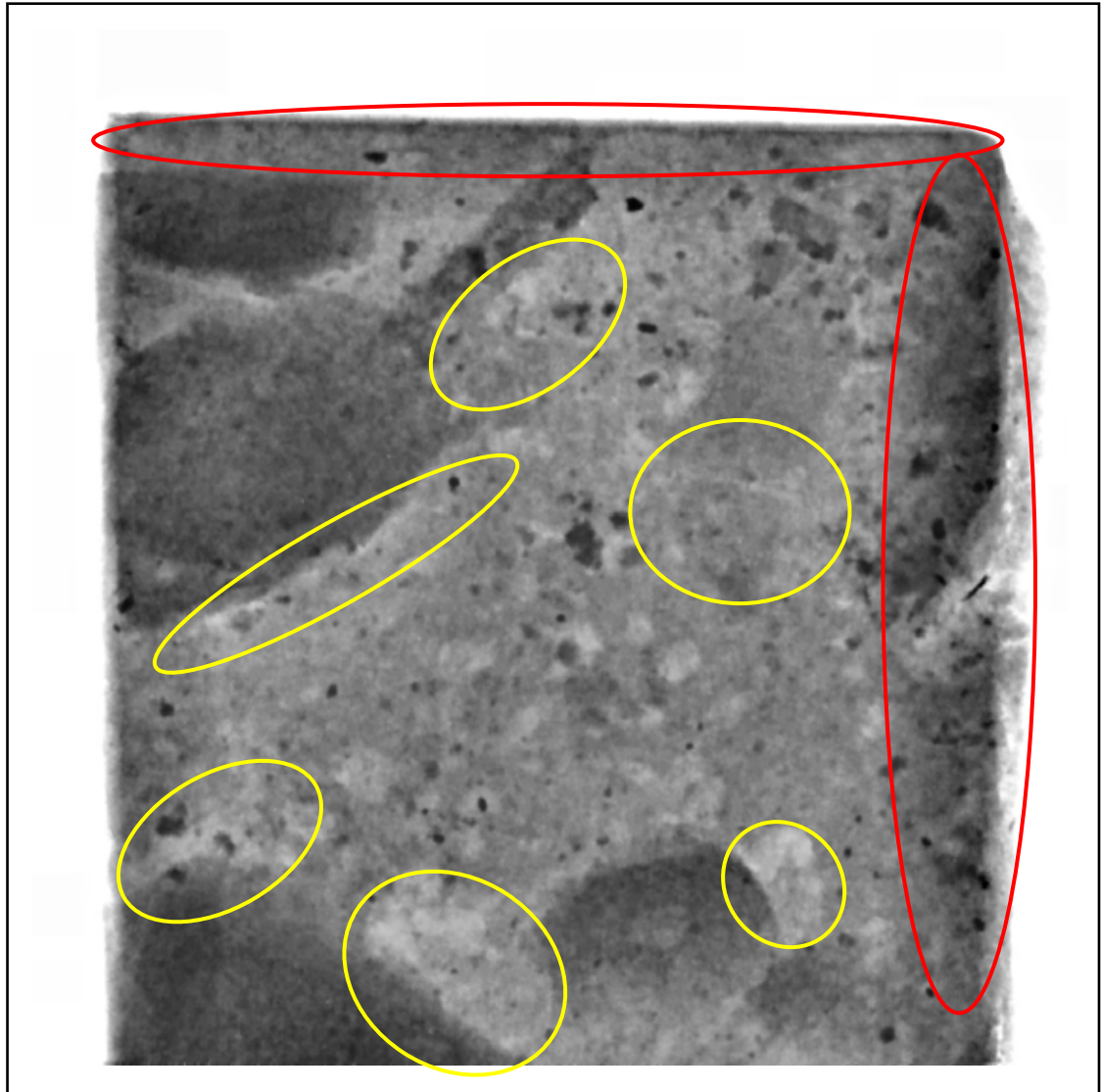




Figure 4.2.2.20 X-Ray Detail of Sample Dar-1

-  Slight darkening on top, slight darkening on cut- right due to compression of diamond sawing Sample
-  Interfacial zone cracking around aggregates, and throughout cement matrix
- Numerous air voids

Sample Dar-2 X-Ray Perpendicular cut

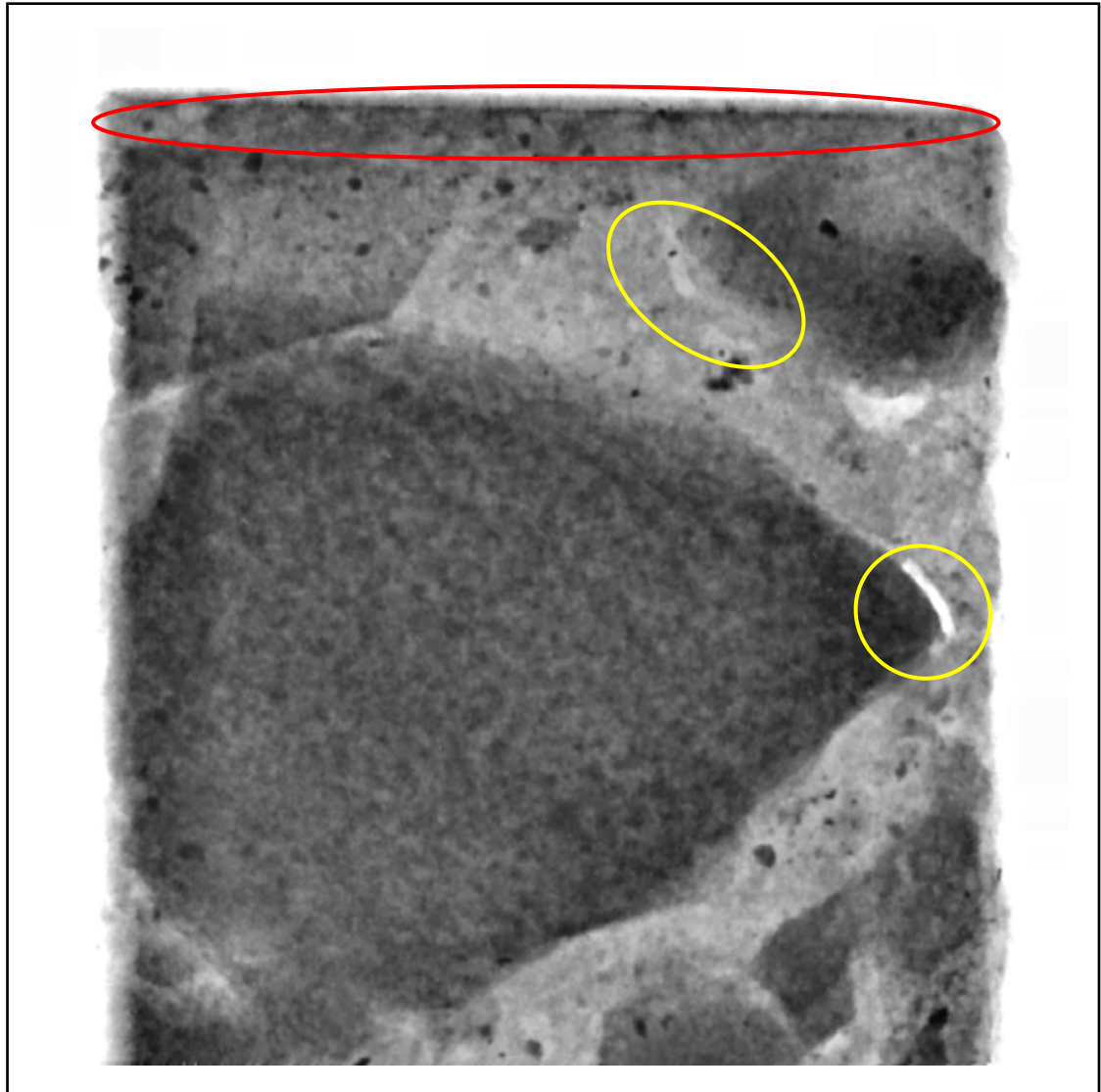


Figure 4.2.2.21 X-Ray Detail of Sample Dar-2

- Slight darkening on top
- Interfacial zone cracking around aggregates, and throughout cement matrix
- Angular blue metal aggregate, good bonding between aggregate and cement matrix
- Porosity

Sample FI-1 X-Ray Perpendicular cut

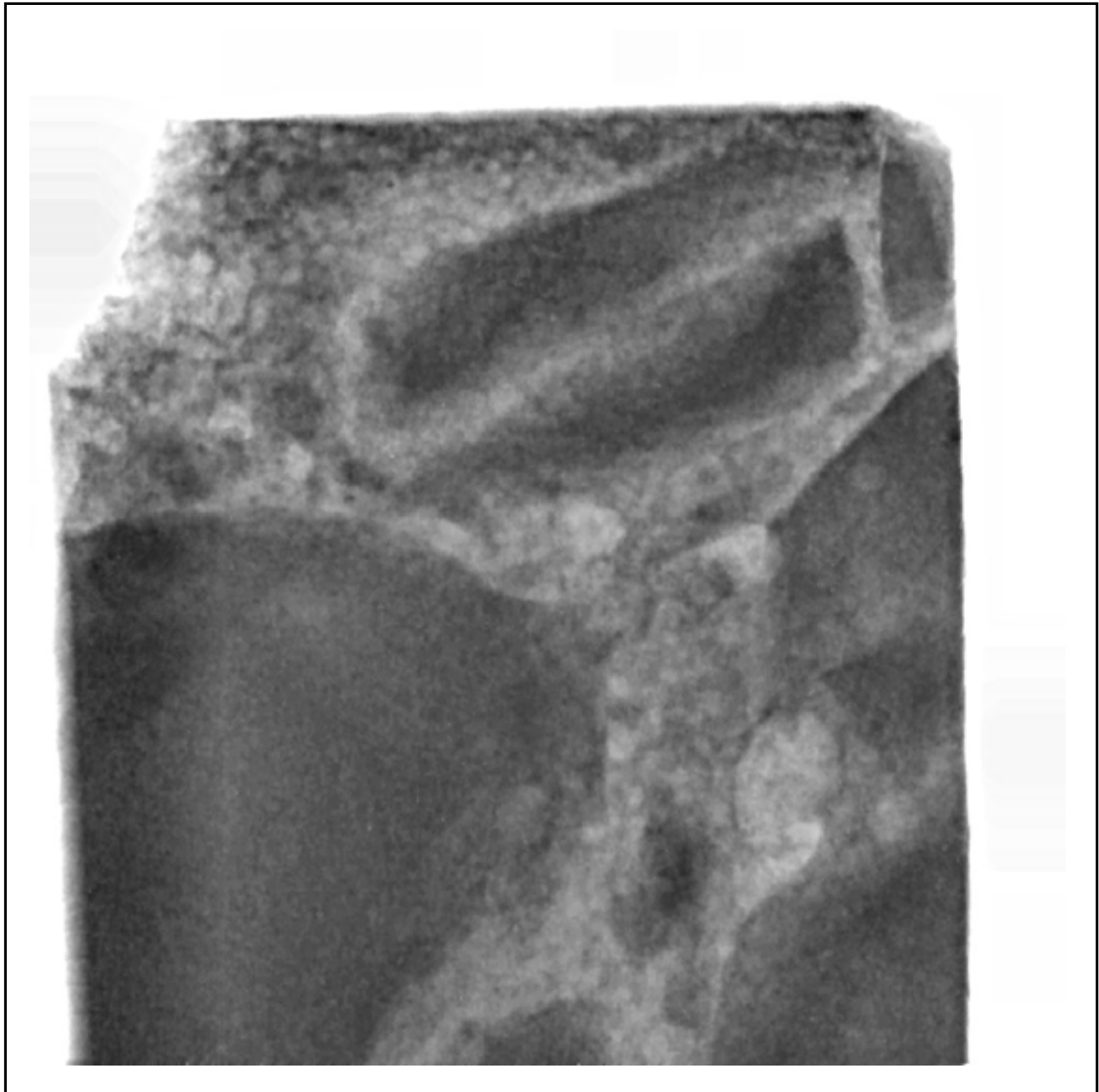


Figure 4.2.2.22 X-Ray Detail of Sample FI-1

Dense hard aggregate

Air voids

Good bond between angular aggregate and paste matrix

Sample FI-2 X-Ray Perpendicular cut

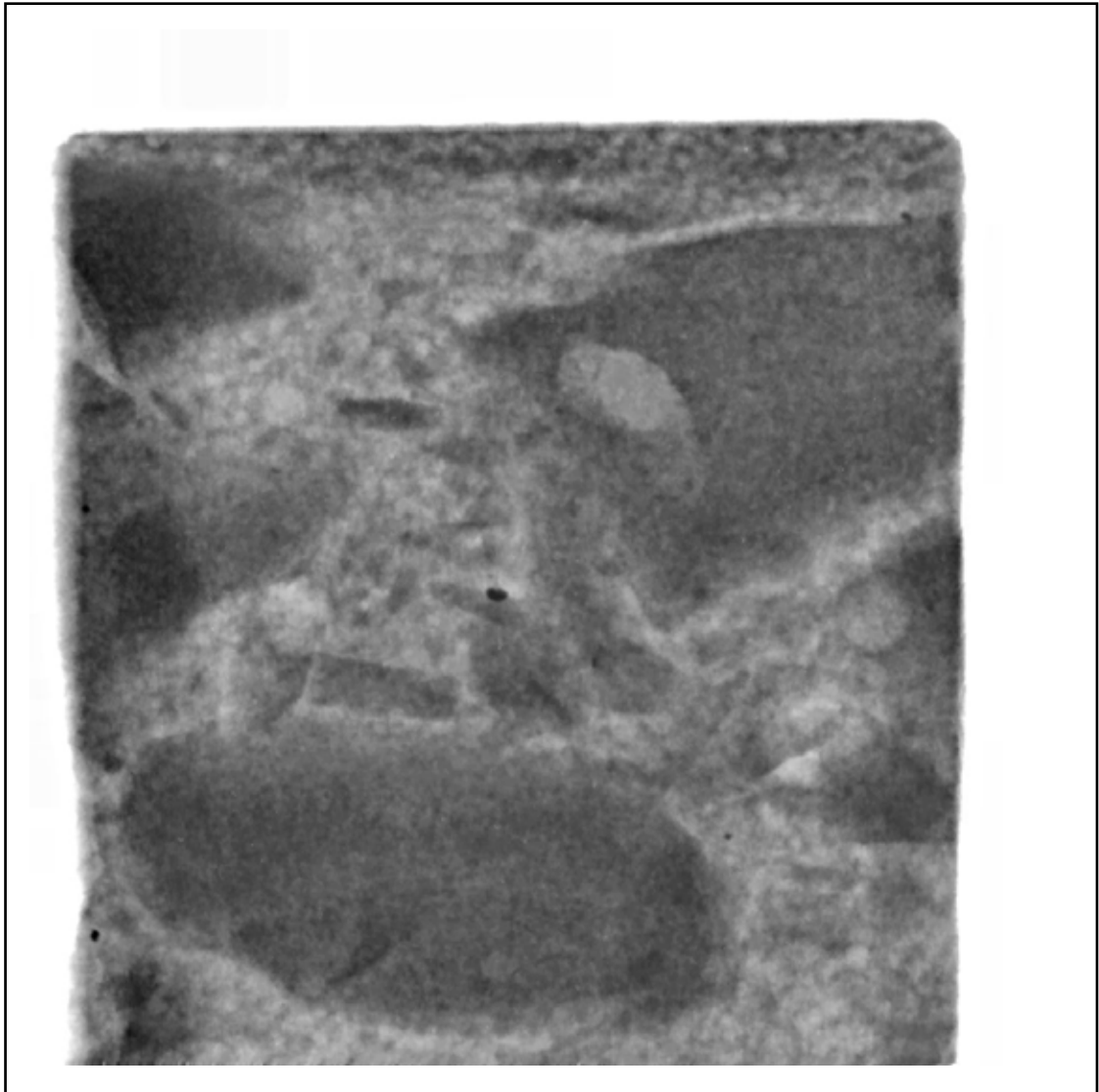


Figure 4.2.2.23 X-Ray Detail of Sample FI-2

Dense hard aggregate

Air voids

Absence of cracking

Sample FI-3 X-Ray Perpendicular cut

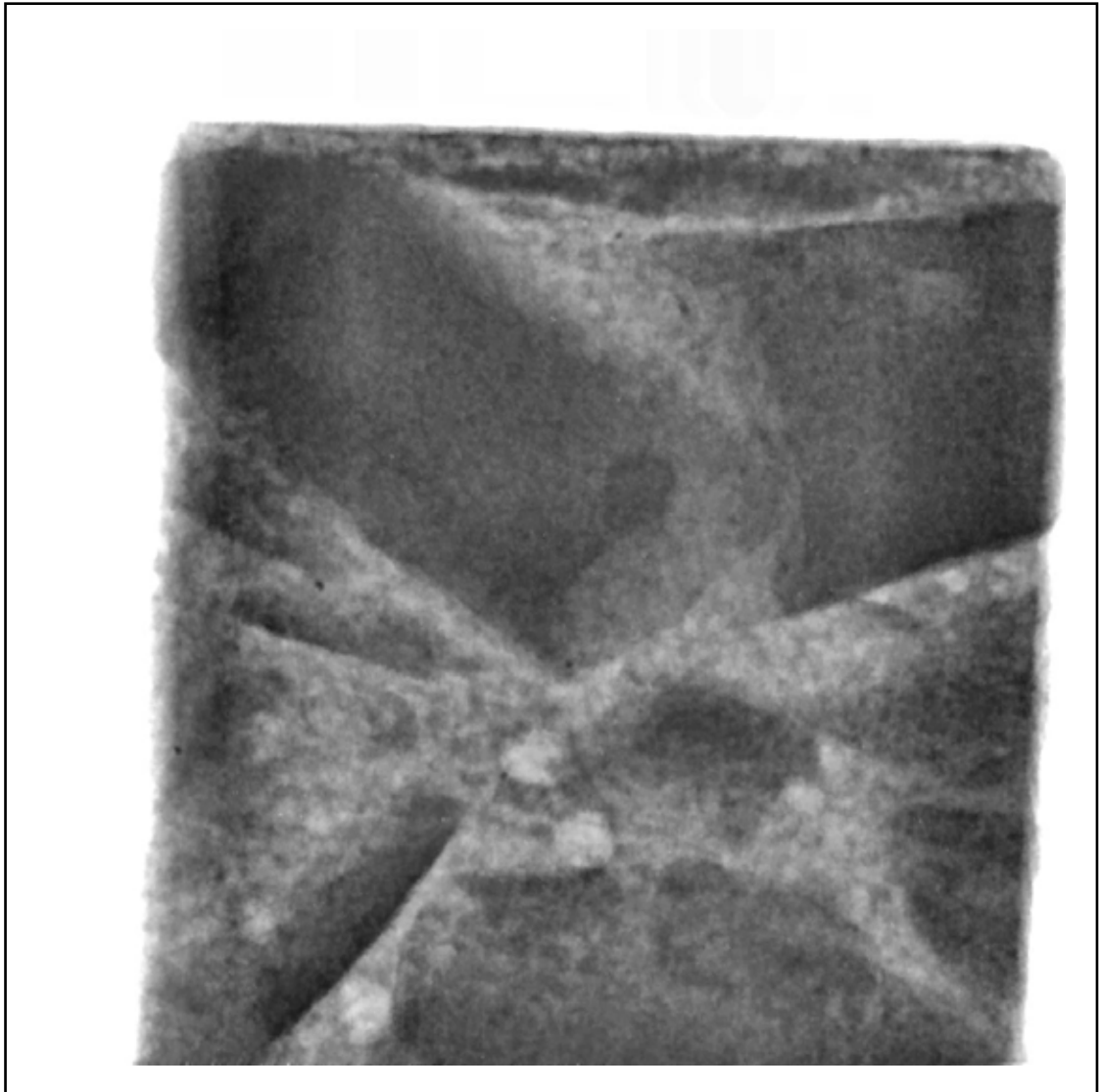


Figure 4.2.2.24 X-Ray Detail of Sample FI-3

Air voids

Absence of cracking

Good aggregate matrix bond

Dense angular aggregate

Sample FII-1 X-Ray Perpendicular cut

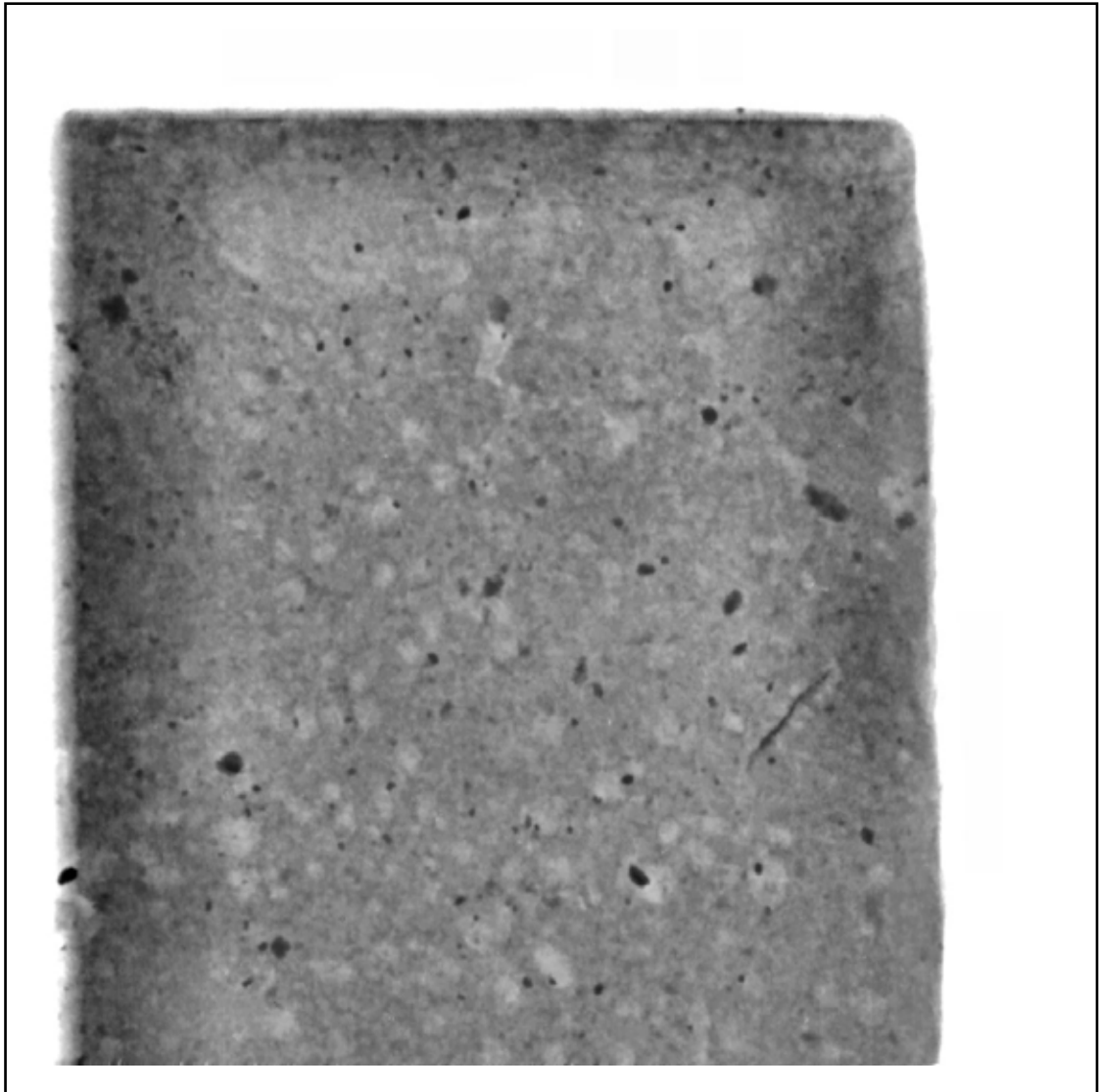


Figure 4.2.2.25 X-Ray Detail of Sample FII-1

Lot of fine capillary joined air voids

Sample FII-2 X-Ray Perpendicular cut

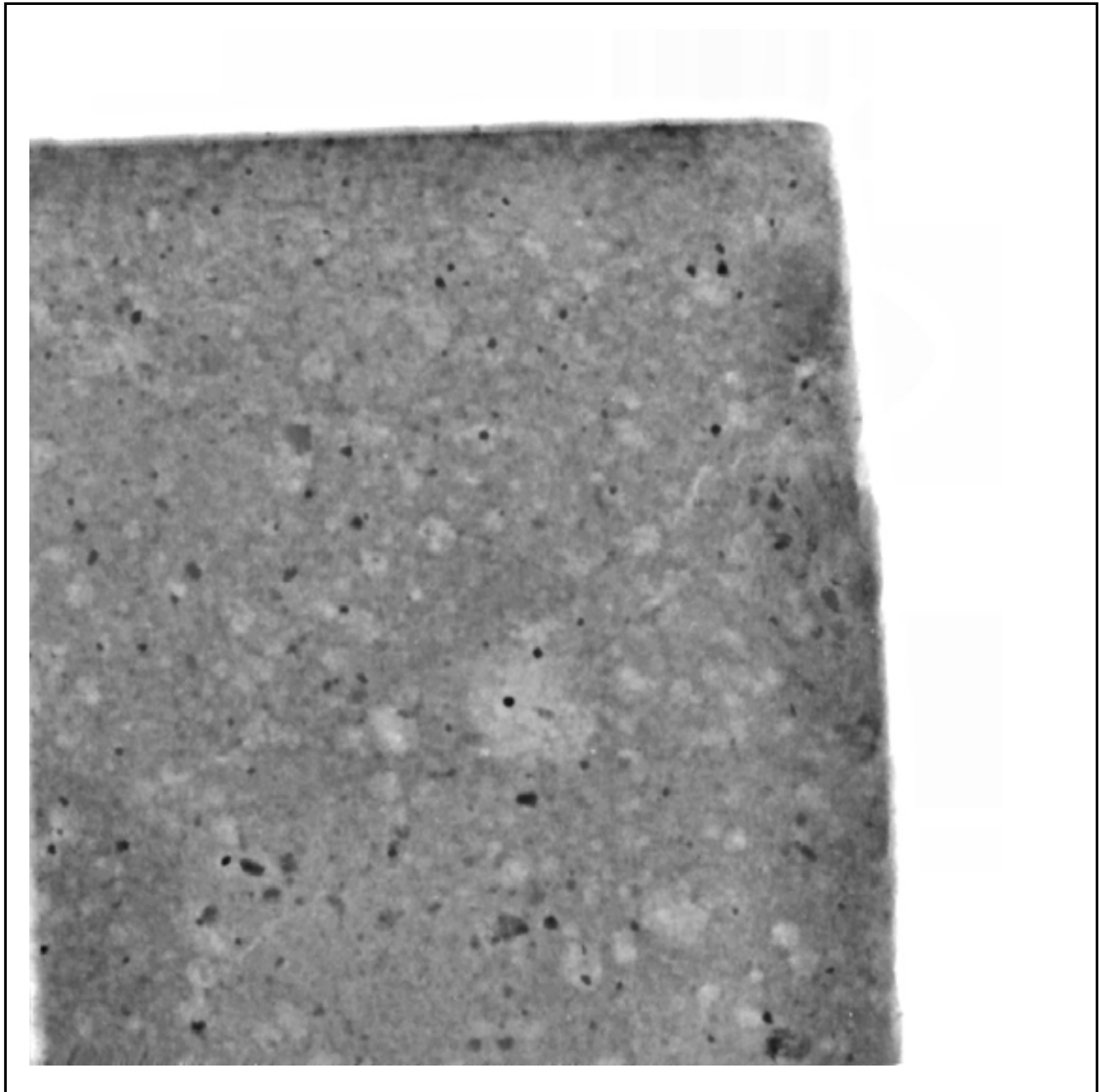


Figure 4.2.2.26 X-Ray Detail of Sample FII-2

Fine structure

A couple of fine capillary joined air voids as in FII-1

Sample FII-3 X-Ray Perpendicular cut

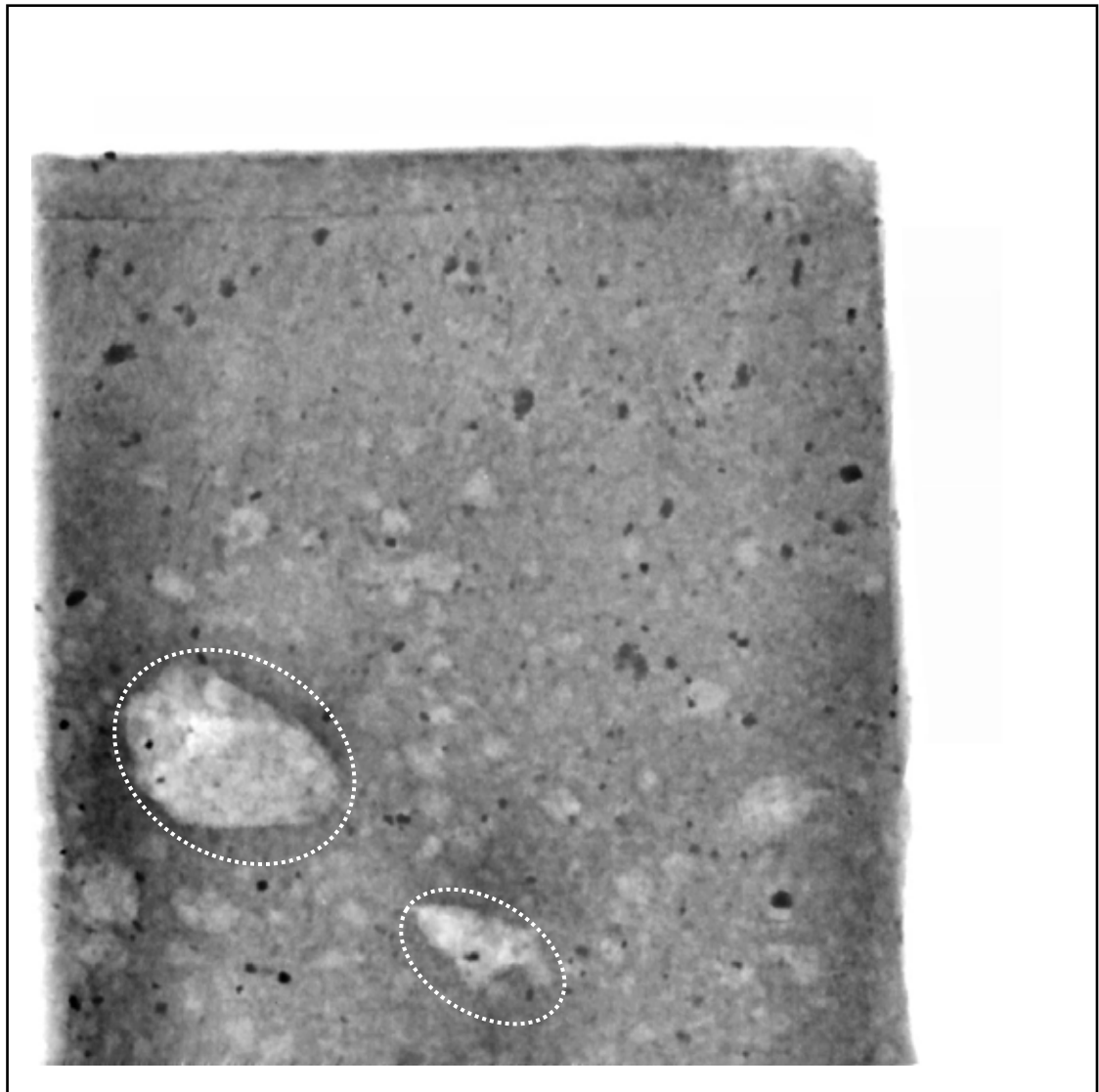


Figure 4.2.2.27 X-Ray Detail of Sample FII-3

Large air voids (dashed white)

Fine structure, absence of cracking

4.2.3 Discussion of Results

Observations of Variable Cut Samples

Sample 1

Worst sample – very crumbly

Heavy concentration of cracks through entire body, especially around the aggregates

Corner apparently compressed (darkened)

Sample 2

Fewer cracks than Sample 1

Some cracks around aggregates

One large pore

Sample 3

Very few cracks, even around aggregates

Sample 4

Very few cracks, even around aggregates, very large pore

Sample 5

Reference sample – no notch

More cracks than in Samples 2 to 4

Cracks in both body and around aggregates

Rm

Many cracks in body and around aggregates

Crack density equivalent to that of Sample 1 but not nearly as weak

Cracks in aggregate suggest shale

Dar

Very difficult to cut

Some cracks in body

Lower porosity than in Samples 1 to 5

Scarcely any cracks around the aggregates

Two large pores

Observations of Perpendicular Cut Samples

Sample 1-1

Darkened areas around notch, diamond but, and top

Radial crack from notch

Many parallel cracks

Cut edge is shadowed from aggregate

Sample 1-2

Obvious compression ahead of notch (not from aggregate)

Relatively heavy cracking

Sample 1-3

Similar to Sample 12

Darkening on cut (some from aggregate)

Top corner compressed

Heavy cracking

Sample 1-4

Heavy cracking

Both top corners shadowed

Sample 2-1

Cut darkening from aggregate

Sample 2-2

Darkening on top

Darkening in notch from aggregate

Sample 2-3

Darkening in notch and on cut from aggregate

Darkening in aggregate – evidence of compression from cutting

Downward cut causes lateral compression – notch darkening is not from cutting

Sample 2-4

Crack wake can be seen clearly – light to right and shadow to left

Some darkening on top

Sample 2-5

Darkening on top

Darkening in notch

Sample 2-6

No darkening on cut

Clear darkening in notch

Note small aggregate particle in notch but no enhanced darkening

Sample 3-1

Darkening on cut (spurs left from cutting)

Darkening on top

Darkening in notch

Sample 3-2

Piece fell off

Darkening in notch (a little)

Sample 4-1

Notch shows little degradation

Darkening clearly along the line of notch confirms compression from cutting notch

Abraded notch corner shows no compression

Sample 4-2

Top darkening blocked by aggregate

Smooth notch depth darkened

Slight darkening on abraded notch corner

Sample 5-1

Slight darkening on top

Slight darkening on cut

Sample 5-2

No evidence of darkening

Sample Rm-1

Large crack around aggregate

Darkening on top

Darkening in notch

Darkening in aggregate directly below notch

Sample Rm-2

Two large radial cracks around aggregate

Darkening in notch

Sample Rm-3

Cracks around aggregate

No darkening

Sample Dar-1

Slight darkening on top

Darkening in notch

Sample Dar-2

Slight darkening on top

Sample FI-1 to Sample FII-3

These samples were not a part of the study

Explanations

The concrete core samples were of variable quality. Core 1 was inferior to the others in that it was difficult to cut since it was crumbly. Cores 2 to 5 and Rm exhibited approximately similar characteristics during diamond cutting in that they were typical of normal concretes. Core Dar was very difficult to cut.

The X-Ray images confirmed these qualitative observations. The samples from Core 1 were heavily cracked through the entire body. The samples from Cores 2 to 5 and Rm contained fewer cracks, these being associated mainly with the aggregates. The samples from Core Dar showed lower porosity and lower crack densities. Most of the observed cracking was associated with the aggregates. It is likely that this resulted from concrete shrinkage.

The darkening of the notch corner in one sample from Core 1 (variable cut) suggested that compression (increased density and hence X-Ray shadow) from impact may have occurred. This was one of the factors that led to the preparation of samples cut perpendicular to the notch.

The perpendicular cut samples confirmed that compression occurred as a result of diamond cutting during notching and sample preparation as well as from impact and load-bearing that occurs during use. The compression is not associated with cracks since there was no correlation between crack location and darkening.

It is likely that the observed deterioration of the notch corners occurred as a result of repeated impact and resultant compression. This cyclic damage did not appear to cause rapid crack propagation (except as shown by the crack wake in Sample 2-4) but instead caused gradual weakening and abrasion.

The sky scan looked at the largest size 35 x 15 mm and 5 mm thick of samples possible that could be placed inside. The 16-bit greyscale TIFF files that were saved in a lower resolution of 15.19 μ is not an issue in this study since it is a qualitative comparative study of cracking and porosity. This resolution was able to show the relationship between the damage and an apparent durability of the concrete.

The interfacial transition zones could be clearly seen between the aggregate and the cement matrix. Also the porosity could be clearly identified.

From the X-Ray images the degree of darkness indicated the relative density of the aggregates and also the compression in the damages areas of the notch.

Note: The dense blue metal aggregate appeared black and the porous river gravel was in various shades of grey. The matrix was of light grey and the pores appeared white.

4.3 Digital Analysis Results

4.3.1.1 Study 1 - Results for Calculations of Porosity 72 ppi Digital Images

1A		1B		1C		1D		2A		2B	
190	4169	184	8253	197	5188	195	4137	196	3238	197	3766
191	4181	185	7920	198	5562	196	4120	197	3472	198	3834
192	4086	186	7804	199	5319	197	4185	198	3234	199	3646
193	4206	187	7709	200	5159	198	4070	199	3365	200	3596
194	4040	188	7418	201	5013	199	4115	200	3095	201	3513
195	3759	189	7403	202	5108	200	4000	201	3113	202	3405
196	3860	190	7045	203	5145	201	4116	202	2990	203	3516
197	3919	191	6907	204	5291	202	4186	203	3060	204	3293
198	4023	192	6646	205	5068	203	4151	204	3010	205	3345
199	3904	193	6611	206	5173	204	4202	205	2891	206	3362
200	3905	194	6459	207	5189	205	4199	206	2892	207	3341
201	3901	195	6336	208	5068	206	4102	207	2957	208	3307
202	3820	196	6276	209	5132	207	3951	208	2787	209	3254
203	4038	197	5908	210	5401	208	4147	209	2808	210	3300
204	4039	198	6103	211	5248	209	4058	210	2868	211	3260
205	4051	199	5942	212	5300	210	4163	211	2808	212	3310
206	4060	200	5917	213	5528	211	4268	212	2768	213	3321
207	3874	201	5795	214	5775	212	4196	213	2750	214	3242
208	4076	202	5691	215	5768	213	4348	214	2647	215	3176
209	4086	203	5827	216	5838	214	4419	215	2748	216	3302
210	4210	204	5630	217	5867	215	4439	216	2821	217	3368
211	4244	205	5615	218	6090	216	4479	217	2707	218	3531
212	4178	206	5507	219	6134	217	4721	218	2852	219	3501
213	4225	207	5347	220	6195	218	4796	219	2745	220	3523
214	4358	208	5293	221	6515	219	4536	220	2899	221	3552
215	4465	209	5488	222	6768	220	4794	221	2830	222	3694
216	4540	210	5377	223	6891	221	4964	222	2875	223	3741
217	4731	211	5182	224	6860	222	5077	223	2949	224	3835
218	4737	212	5281	225	6926	223	5070	224	2949	225	4217
219	4756	213	5230	226	7601	224	5183	225	3007	226	4221
220	4868	214	5319	227	7569	225	5114	226	3089	227	4260
221	4903	215	5309	228	7913	226	5149	227	3036	228	4133
222	5270	216	5228	229	8509	227	5485	228	3176	229	4330
223	5136	217	5268	230	8439	228	5529	229	3213	230	4423
224	5173	218	5447	231	8533	229	5548	230	3155	231	4600
225	5275	219	5219	232	8250	230	5590	231	3236	232	4813
226	5392	220	5633	233	8662	231	5747	232	3044	233	4579
227	5845	221	5402	234	8434	232	5722	233	3222	234	4804
228	5927	222	5366	235	9113	233	5796	234	3293	235	4772
229	6206	223	5335	236	9458	234	5937	235	3396	236	4853
230	6346	224	5528	237	9468	235	6075	236	3612	237	5197
231	6361	225	5652	238	9112	236	6198	237	3621	238	5297
232	6517	226	5693	239	8958	237	6125	238	3613	239	5175
233	6594	227	5810	240	8674	238	5960	239	3442	240	5323
234	6905	228	5840	241	8113	239	5898	240	3526	241	5313
235	6643	229	6006	242	9022	240	6228	241	3423	242	5101
236	7085	230	6161	243	9260	241	6196	242	3701	243	5107
237	6723	231	6467	244	9164	242	6185	243	3652	244	5287
238	6718	232	6438	245	8274	243	6180	244	3663	245	5123
239	6690	233	6325	246	7953	244	6134	245	3643	246	5087
240	6959	234	6216	247	7410	245	6216	246	3642	247	5431
241	6673	235	6225	248	6722	246	6157	247	3747	248	5193
242	6522	236	6679	249	6395	247	6466	248	3823	249	5144
243	6374	237	6988	250	6175	248	6582	249	4074	250	5314
244	6351	238	6906	251	7073	249	6297	250	3964	251	5927
245	6205	239	6607	252	7416	250	6106	251	4359	252	6823
246	6128	240	6409	253	9697	251	6157	252	4779	253	8742
247	6457	241	6523	254	14013	252	7064	253	6970	254	11833
248	5915	242	6619	255	14411	253	8894	254	9927	255	13638
249	5578	243	6600	pores	424310	254	12397	255	11807	pores	270894
250	5525	244	6535	255	3308622	255	12145	pores	213083	255	3498260
251	5729	245	6354	percentag	12.82%	pores	332469	255	3521446	percentag	7.74%
252	6480	246	6165			255	3488388	percentag	6.05%		
253	9185	247	6323			percentag	9.53%				
254	11231	248	5885								
255	10898	249	5965								
pores	357228	250	5662								
255	3432300	251	5912								
percentag	10.41%	252	5952								
		253	9022								
		254	13383								
		255	13257								
		pores	457553								
		255	3327654								
		percentag	13.75%								

Table 4.3.1.1.1 Percentage of Porosity Samples 1A to 2B

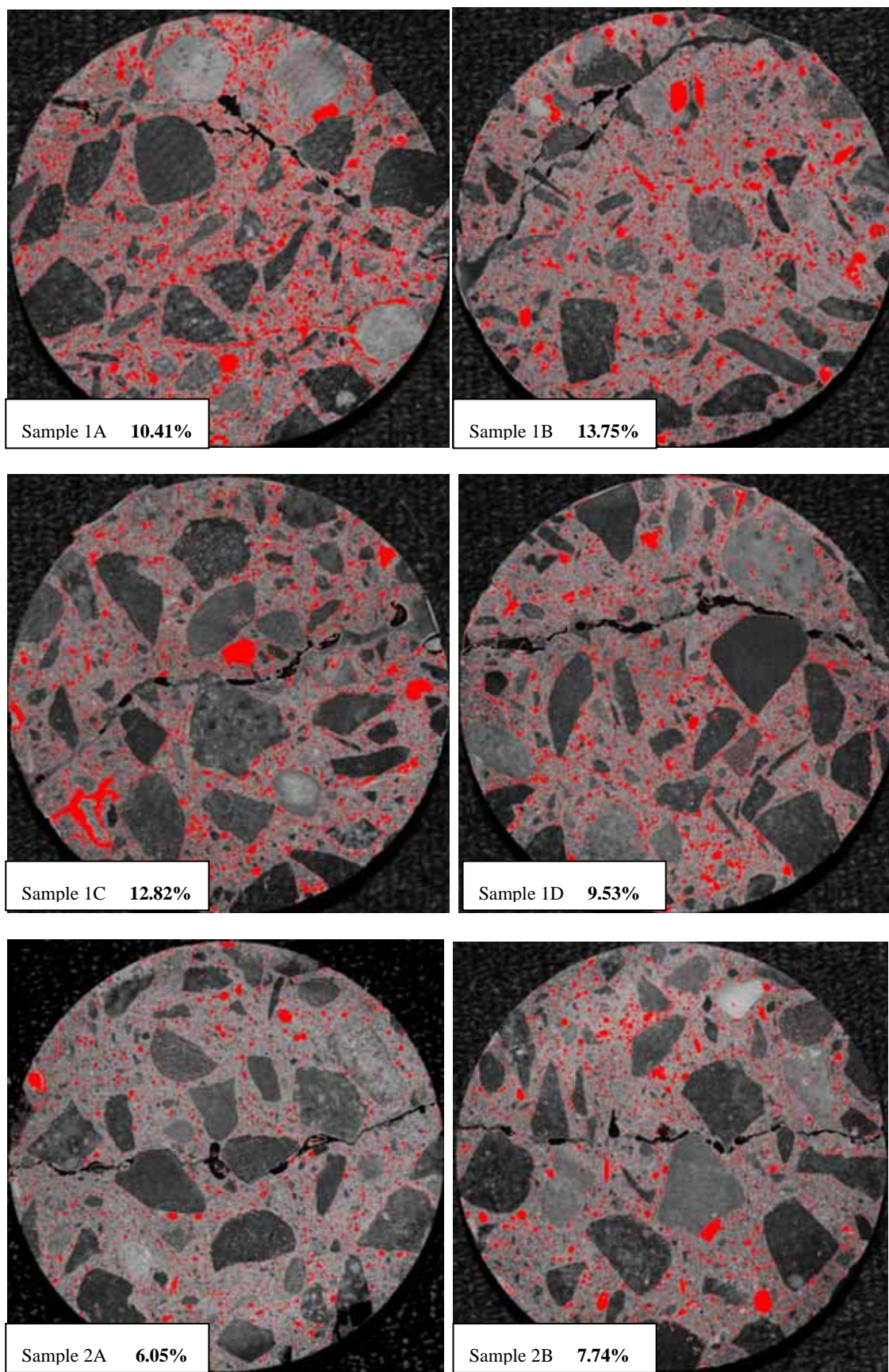


Figure 4.3.1.1.1 Porosity images 1A to 2B from ImageJ

Sample 3a		Sample 3b		Sample 4a		Sample 4b		Sample 5a		Sample 5b	
191	3664	202	3447	207	3301	196	4001	179	4182	190	4595
192	3774	203	3370	208	3304	197	3989	180	3933	191	4188
193	3541	204	3328	209	3053	198	3940	181	3764	192	4227
194	3623	205	3248	210	2902	199	3641	182	3573	193	4089
195	3469	206	3028	211	2797	200	3673	183	3624	194	3881
196	3342	207	3124	212	2781	201	3698	184	3610	195	3734
197	3106	208	2979	213	2801	202	3715	185	3418	196	3784
198	3300	209	2994	214	2838	203	3687	186	3254	197	3557
199	3042	210	3048	215	2599	204	3639	187	3047	198	3593
200	3050	211	2981	216	2575	205	3691	188	3051	199	3390
201	3169	212	2947	217	2525	206	3727	189	3195	200	3397
202	3005	213	2925	218	2608	207	3679	190	3078	201	3274
203	2935	214	2940	219	2488	208	3714	191	3059	202	3284
204	2850	215	2801	220	2517	209	3719	192	2887	203	3134
205	2833	216	2851	221	2480	210	3595	193	2687	204	3116
206	2892	217	2812	222	2487	211	3692	194	2897	205	3158
207	2848	218	2840	223	2404	212	3655	195	2793	206	2964
208	2888	219	2765	224	2337	213	3743	196	2700	207	2852
209	2769	220	2781	225	2486	214	3906	197	2608	208	2952
210	2700	221	2789	226	2567	215	3797	198	2566	209	3048
211	2776	222	2730	227	2556	216	3724	199	2492	210	2940
212	2779	223	2775	228	2566	217	3686	200	2539	211	2788
213	2700	224	2862	229	2406	218	4207	201	2576	212	2827
214	2926	225	2770	230	2437	219	4003	202	2531	213	2861
215	2825	226	2881	231	2615	220	3920	203	2504	214	2884
216	2868	227	2891	232	2555	221	3906	204	2481	215	2949
217	2766	228	2846	233	2721	222	3768	205	2405	216	2961
218	2764	229	2898	234	2655	223	3875	206	2467	217	2893
219	2891	230	3061	235	2760	224	4006	207	2545	218	3024
220	2924	231	3114	236	2828	225	4134	208	2462	219	3068
221	3012	232	3027	237	2893	226	4080	209	2425	220	2935
222	3034	233	3063	238	3036	227	4111	210	2488	221	3085
223	3131	234	3126	239	3260	228	4173	211	2440	222	2811
224	3102	235	3310	240	3544	229	4332	212	2474	223	3144
225	3302	236	3565	241	3558	230	4248	213	2542	224	2997
226	3525	237	3651	242	3725	231	4300	214	2640	225	3215
227	3608	238	3590	243	3913	232	4128	215	2606	226	3286
228	3657	239	3638	244	4084	233	4189	216	2749	227	3462
229	3674	240	3747	245	4369	234	4290	217	2651	228	3492
230	3722	241	3890	246	4621	235	4195	218	2830	229	3552
231	3931	242	4197	247	4963	236	4229	219	3040	230	3628
232	3978	243	4214	248	4933	237	4529	220	2958	231	3669
233	4266	244	4488	249	5190	238	4516	221	3078	232	3728
234	4206	245	4603	250	5293	239	4398	222	3100	233	3888
235	4316	246	4650	251	5645	240	4557	223	3204	234	3725
236	4399	247	5107	252	6345	241	4452	224	3287	235	3968
237	4440	248	4912	253	8570	242	4633	225	3383	236	4418
238	4590	249	5471	254	11826	243	4621	226	3438	237	4398
239	4732	250	5371	255	23787	244	4371	227	3485	238	4488
240	5051	251	5678	pores	193504	245	4396	228	3664	239	4247
241	4949	252	6201	percentage	3497808	246	4203	229	4012	240	4488
242	4845	253	7988		5.53%	247	4442	230	3886	241	4528
243	4690	254	11293			248	4482	231	4146	242	4742
244	4942	255	17238			249	4492	232	3922	243	4877
245	4930	pores	214844			250	4581	233	4153	244	5018
246	5024	percentage	3660789			251	4913	234	4248	245	4748
247	5188		5.87%			252	5153	235	4472	246	4637
248	4797					253	7495	236	4653	247	4896
249	4625					254	12442	237	4916	248	4747
250	4683					255	15309	238	4771	249	4852
251	4766					pores	268390	239	5090	250	4800
252	5211					percentage	3557874	240	5095	251	5330
253	7516						7.54%	241	5238	252	5169
254	10334							242	5339	253	8179
255	9974							243	5375	254	11972
pores	255169							244	5385	255	21340
percentage	3378224							245	4946	pores	275871
	7.55%							246	4884	percentage	3536592
								247	5289		7.80%
								248	4933		
								249	4738		
								250	4765		
								251	5224		
								252	4648		
								253	6983		
								254	10850		
								255	22002		
								pores	301373		
								percentage	3389840		
									8.89%		

Table 4.3.1.1.2 Percentage of Porosity Samples 3A to 5B

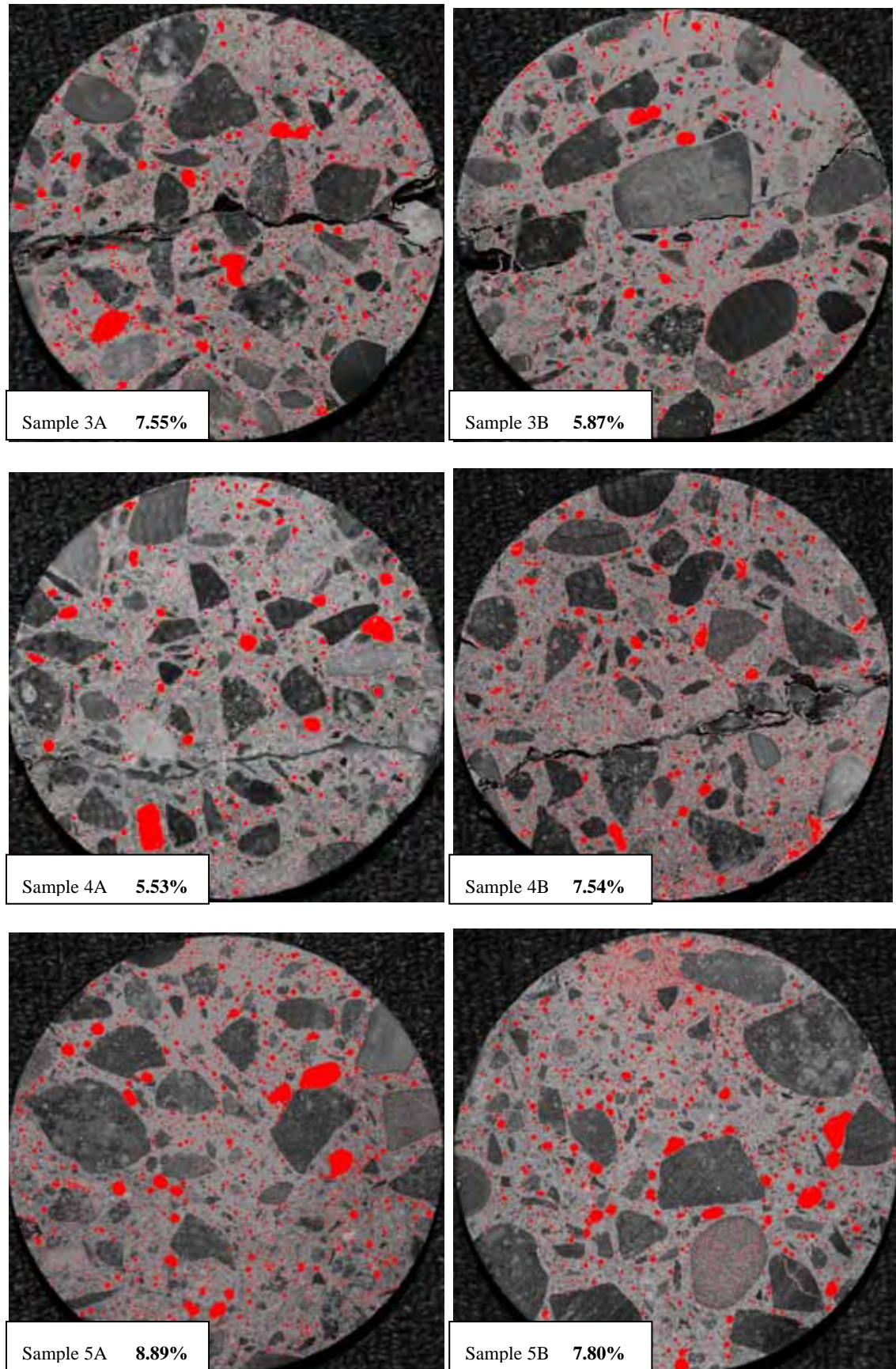


Figure 4.3.1.1.2 Porosity images 3A to 5B from ImageJ

Sample RMa		Sample RMb		Sample DARa		Sample DARb	
184	5904	187	7268	217	3246	203	3606
185	5570	188	7001	218	3301	204	3497
186	5500	189	6811	219	3166	205	3289
187	5493	190	6542	220	3196	206	3072
188	5514	191	6131	221	3030	207	3040
189	5335	192	6079	222	3119	208	3020
190	5027	193	6106	223	3121	209	2931
191	4968	194	5950	224	2962	210	3080
192	4954	195	5616	225	3179	211	2910
193	4918	196	5467	226	3128	212	2731
194	4945	197	5189	227	3133	213	2641
195	4843	198	5315	228	2973	214	2816
196	4657	199	4974	229	2996	215	2714
197	4599	200	5012	230	2920	216	2775
198	4784	201	4531	231	2997	217	2686
199	4682	202	4484	232	3033	218	2628
200	4435	203	4346	233	3035	219	2650
201	4244	204	4337	234	2965	220	2615
202	4215	205	4333	235	2949	221	2665
203	4220	206	4290	236	2838	222	2641
204	4119	207	4169	237	2937	223	2652
205	4105	208	4054	238	2893	224	2559
206	3990	209	4109	239	2984	225	2654
207	3938	210	4111	240	3095	226	2779
208	4128	211	4055	241	3003	227	2806
209	3954	212	3825	242	2869	228	2920
210	4033	213	3850	243	3016	229	3011
211	4035	214	3829	244	3012	230	3127
212	3854	215	3797	245	2985	231	3198
213	4088	216	3659	246	3015	232	3336
214	3886	217	3795	247	3503	233	3530
215	3923	218	3788	248	3184	234	3480
216	3917	219	3643	249	3294	235	3693
217	3938	220	3655	250	3340	236	3781
218	3794	221	3574	251	3742	237	3764
219	3884	222	3744	252	4600	238	4025
220	3995	223	3703	253	6913	239	4074
221	4068	224	3645	254	12761	240	4353
222	4010	225	3680	255	17304	241	4281
223	3985	226	3653	pores	149737	242	4373
224	3942	227	3626	255	3669402	243	4277
225	4079	228	3658	percentage	4.08%	244	4236
226	4234	229	3919			245	4362
227	4380	230	3831			246	4428
228	4184	231	3888			247	4531
229	4325	232	3803			248	4388
230	4382	233	4068			249	4493
231	4445	234	4024			250	4331
232	4696	235	4065			251	4241
233	4780	236	4014			252	4895
234	4678	237	4112			253	6123
235	4715	238	4010			254	9883
236	5118	239	4049			255	11671
237	4978	240	4275			pores	198262
238	5045	241	4038			255	3585088
239	4739	242	4116			percentage	5.53%
240	4963	243	4021				
241	5213	244	4061				
242	5117	245	4207				
243	5145	246	4142				
244	5315	247	4313				
245	5027	248	4331				
246	5210	249	4342				
247	5299	250	4461				
248	5235	251	4620				
249	5557	252	5560				
250	5516	253	6707				
251	6038	254	9632				
252	5782	255	12825				
253	8675	pores	322838				
254	11015	255	3376758				
255	11743	percentage	9.56%				
pores	352021						
255	3463471						
percentage	10.16%						

Table 4.3.1.1.3 Percentage of Porosity Samples RmA to DarB

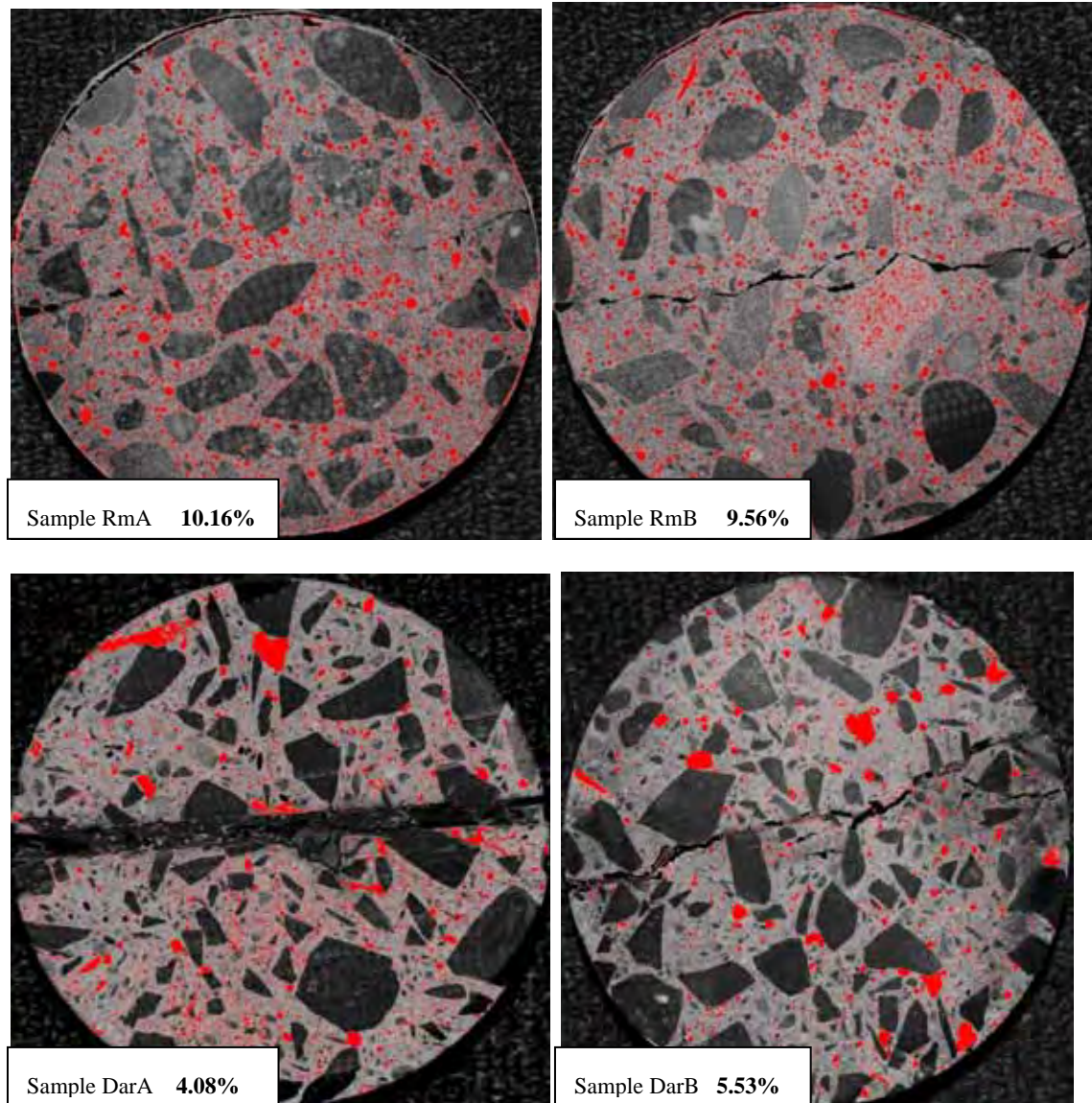


Figure 4.3.1.1.3 Porosity images RmA to DarB from ImageJ

Sample F1a		Sample F1b		Sample F11a		Sample F11b	
214	1906	194	2097	208	3537	210	3723
215	1912	195	2088	209	3511	211	3531
216	1799	196	1937	210	3539	212	3472
217	1763	197	1978	211	3483	213	3482
218	1639	198	1810	212	3456	214	3310
219	1603	199	1739	213	3279	215	3316
220	1613	200	1696	214	3415	216	3095
221	1609	201	1718	215	3414	217	3180
222	1546	202	1624	216	3182	218	3009
223	1505	203	1578	217	3203	219	2895
224	1510	204	1518	218	3005	220	2916
225	1555	205	1457	219	2999	221	2811
226	1513	206	1486	220	2925	222	2933
227	1391	207	1396	221	3140	223	2865
228	1400	208	1336	222	3027	224	2853
229	1525	209	1352	223	2862	225	2820
230	1412	210	1258	224	2929	226	2908
231	1364	211	1229	225	2783	227	2970
232	1371	212	1196	226	2925	228	2929
233	1304	213	1129	227	2946	229	2876
234	1392	214	1120	228	3017	230	3031
235	1361	215	1078	229	2928	231	3107
236	1403	216	1069	230	3115	232	3087
237	1387	217	1086	231	3209	233	3254
238	1406	218	1028	232	3079	234	3278
239	1358	219	991	233	3360	235	3423
240	1299	220	909	234	3263	236	3588
241	1451	221	936	235	3371	237	3805
242	1421	222	933	236	3436	238	3797
243	1473	223	850	237	3463	239	3789
244	1485	224	912	238	3583	240	4102
245	1585	225	877	239	3749	241	4245
246	1673	226	867	240	3943	242	4526
247	1958	227	779	241	3994	243	4652
248	1918	228	797	242	4097	244	4874
249	2628	229	773	243	4012	245	5015
250	2473	230	786	244	4435	246	4931
251	2559	231	816	245	4478	247	5313
252	3064	232	738	246	4733	248	5149
253	4668	233	744	247	5046	249	6087
254	8426	234	777	248	5074	250	5787
255	9118	235	699	249	5323	251	6770
pores	86746	236	728	250	5694	252	6898
255	3434000	237	697	251	6240	253	8816
percentage	2.53%	238	741	252	6357	254	11561
		239	698	253	8682	255	20847
		240	663	254	11170	pores	205626
		241	704	255	15050	255	3568314
		242	711	pores	201461	percentage	5.76%
		243	704	255	3453797		
		244	808	percentage	5.83%		
		245	810				
		246	871				
		247	986				
		248	1019				
		249	961				
		250	1066				
		251	1156				
		252	1486				
		253	2860				
		254	6954				
		255	10339				
		pores	86149				
		255	3498344				
		percentage	2.46%				

Table 4.3.1.1.4 Percentage of Porosity Samples FIA to FIIB

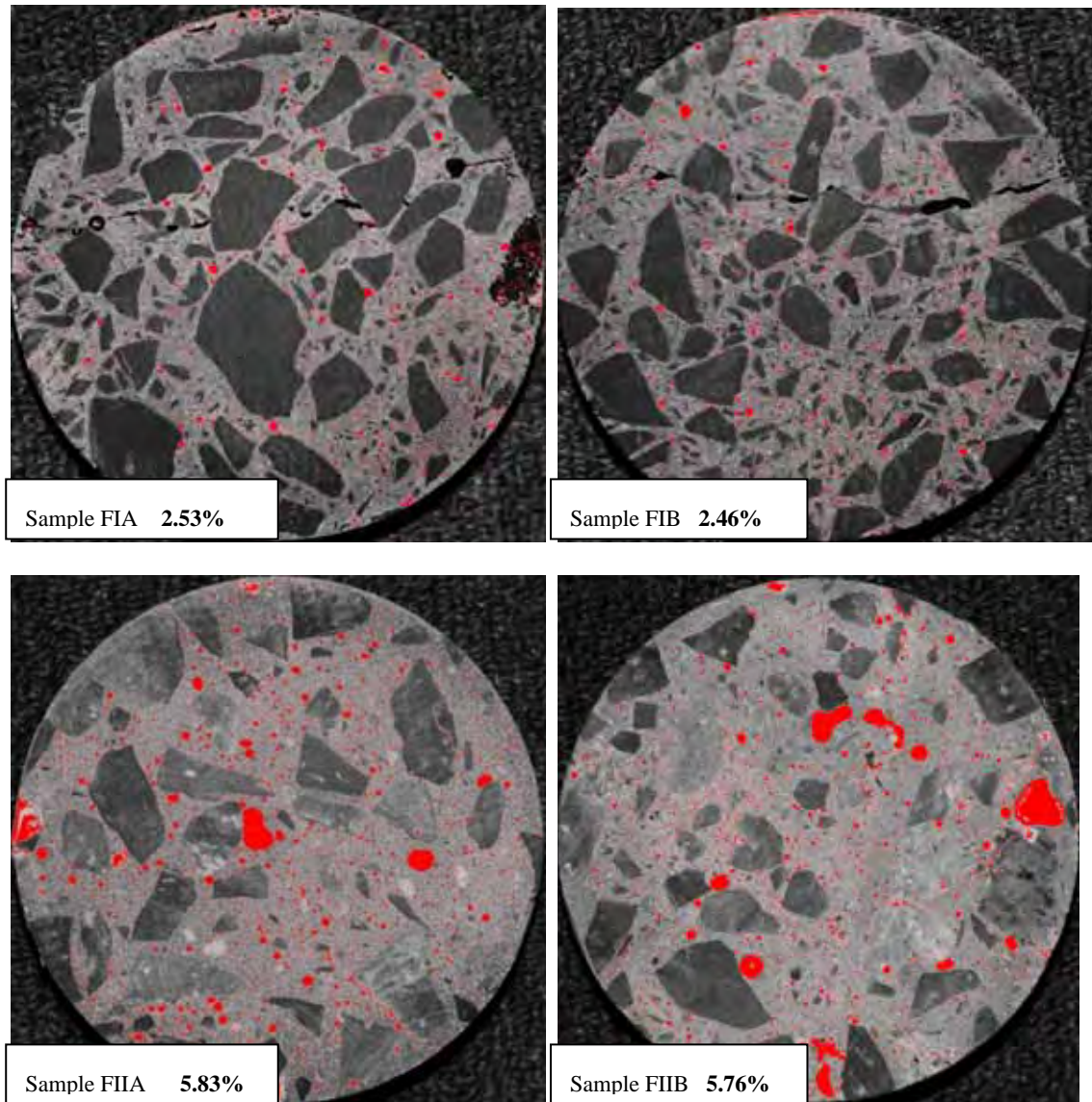


Figure 4.3.1.1.4 Porosity images FIA to FIIB from ImageJ

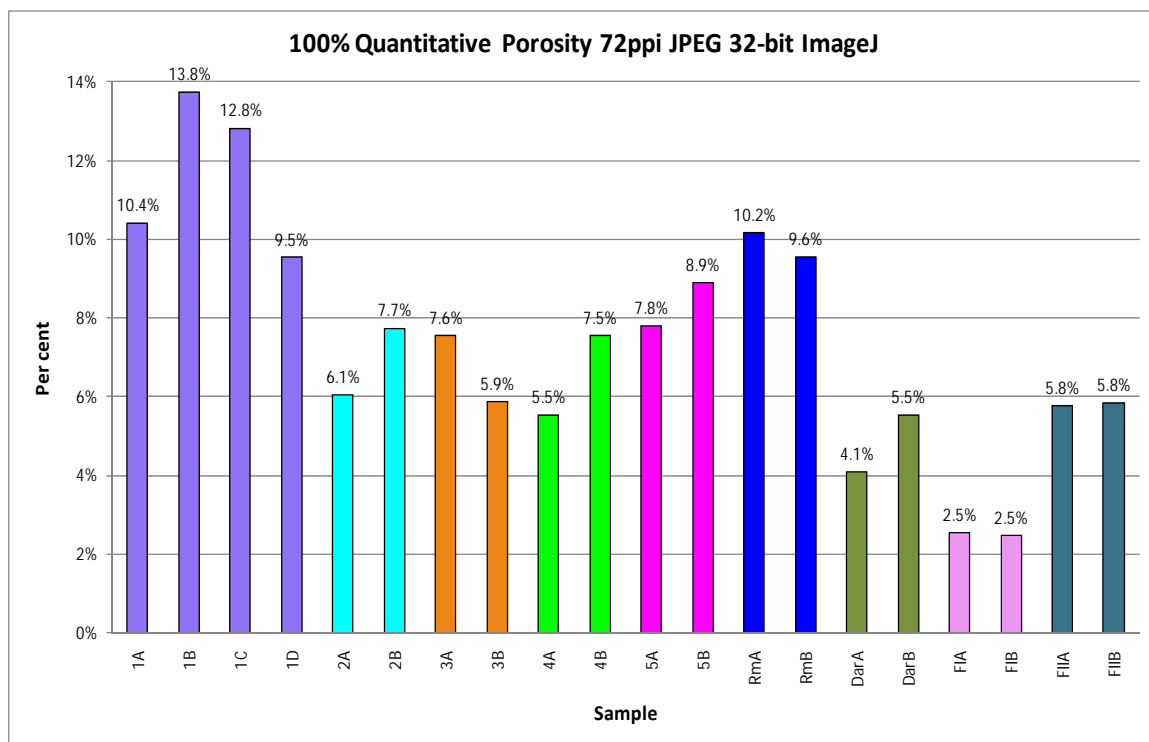


Figure 4.3.1.1.5 Percentage of Porosity in all samples

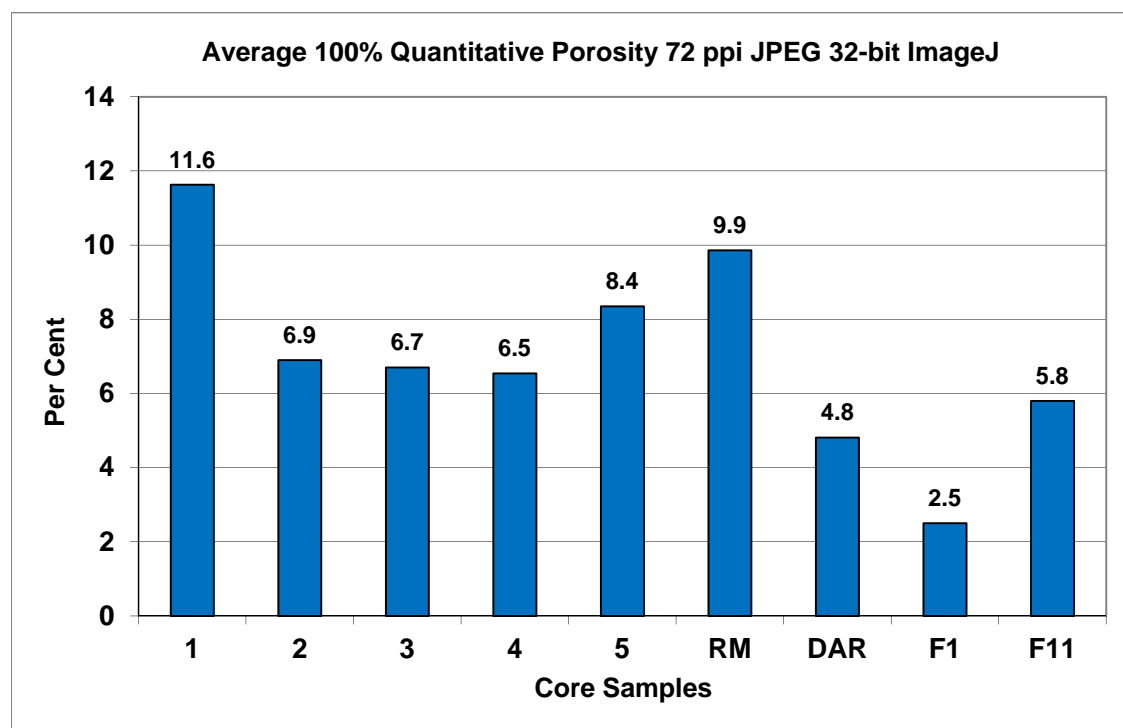


Figure 4.3.1.1.6 Average Percentage of Porosity in each core sample

Observations and Explanations

These first observations confirm Sample 1 as the most porous. The fine porosity was over-calculated by up to 50% due to the low resolution digital camera images, image files saved by the camera in JPEG, rough surface preparation and a 32-bit image analysis software used.

A part from all this, the initial comparisons between core samples were revealed.

4.3.1.2 Study 1 - Results for 100% Quantitative Calculations of Coarse Aggregate Percentage 72 ppi in 32-bit ImageJ

Sample 1a		Sample 1b		Sample 1c		Sample 1d		Sample 2a		Sample 2b	
86	6469	99	14214	92	15567	80	9046	100	9736	77	7392
87	6755	100	15045	93	16436	81	8837	101	10400	78	7606
88	6844	101	15590	94	16849	82	9338	102	11017	79	8073
89	6991	102	16189	95	17424	83	9553	103	11653	80	8122
90	7179	103	16438	96	17551	84	10084	104	12430	81	8513
91	7390	104	17267	97	18197	85	10563	105	12925	82	8675
92	7659	105	17692	98	18912	86	10560	106	13283	83	8976
93	7964	106	18407	99	19652	87	10636	107	14139	84	9121
94	8139	107	18608	100	20598	88	10934	108	14485	85	9605
95	8344	108	18757	101	21316	89	11164	109	15142	86	9802
96	8682	109	19557	102	22060	90	11447	110	15565	87	10414
97	8817	110	20027	103	23248	91	11662	111	16410	88	10388
98	9064	111	21320	104	23558	92	12344	112	17146	89	10983
99	9499	112	22642	105	24094	93	12517	113	18273	90	11344
100	9849	113	23554	106	23942	94	12992	114	18959	91	11995
101	10391	114	23834	107	24758	95	13250	115	19650	92	12607
102	10973	115	23684	108	25193	96	13555	116	19882	93	12768
103	11328	116	24143	109	24543	97	13766	117	20165	94	13233
104	12017	117	24664	110	25167	98	14058	118	20765	95	13790
105	12530	118	24850	111	25590	99	14402	119	21213	96	14467
106	13049	119	25306	112	25804	100	15067	120	21795	97	14857
107	13057	120	26288	113	27182	101	15930	121	21718	98	15300
108	13437	121	26625	114	26884	102	16284	122	22690	99	15422
109	13706	122	26124	115	26869	103	17286	123	23535	100	16382
110	14314	123	26859	116	26699	104	17813	124	23984	101	17244
111	14568	124	27354	117	26943	105	18282	125	23722	102	17802
112	15203	125	27175	118	26939	106	18428	126	25531	103	18437
113	15504	126	27988	119	26899	107	19069	127	27013	104	18751
114	16086	127	28257	120	26865	108	19541	128	27296	105	19536
115	16431	128	28105	121	26494	109	19365	129	27595	106	19907
116	16281	129	27955	122	25686	110	19377	130	28737	107	20195
117	16351	130	28762	123	25885	111	19944	131	28353	108	20712
118	16660	131	29072	124	25240	112	20528	132	28218	109	21060
119	17369	132	28021	125	23842	113	21473	133	28098	110	21212
120	17661	133	28424	126	23502	114	21935	134	28769	111	22472
121	17946	134	28108	127	22994	115	22256	135	28275	112	23131
122	17950	135	27328	128	22022	116	22240	136	28692	113	23951
123	18550	136	27066	129	21998	117	23046	137	28184	114	24199
240	7290	253	10335	246	6942	234	7537	254	12422	231	4605
241	7310	254	14785	247	7339	235	7574	255	15482	232	4669
242	7509	255	15137	248	6701	236	7863		1756796	233	4622
243	7314		2066672	249	6443	237	7628	255	3526572	234	4730
244	7424	255	3324830	250	6345	238	7343		49.82%	235	4687
245	7227		62.16%	251	6560	239	7428		50.18%	236	4865
246	7292		37.84%	252	7378	240	7656			237	5010
247	7024			253	10674	241	7654			238	5212
248	6956			254	14416	242	7476			239	5143
249	6849			255	15865	243	7373			240	5182
250	6732				1810772	244	7346			241	5192
251	6945			255	3437312	245	7332			242	5167
252	7003				52.68%	246	7210			243	5081
253	9910				47.32%	247	7613			244	5405
254	24009					248	7469			245	5245
255	8041					249	7104			246	5164
	1858353					250	6861			247	5597
255	3311898					251	6926			248	5406
	56.11%					252	7841			249	5254
	43.89%					253	10042			250	5568
						254	13669			251	6324
						255	13166			252	7156
							1933361			253	9374
						255	3508182			254	12649
							55.11%			255	15013
							44.89%				1912651
										255	3513281
											54.44%
											45.56%

Table 4.3.1.2.1 Percentage of Coarse Aggregate Samples 1A to 2B

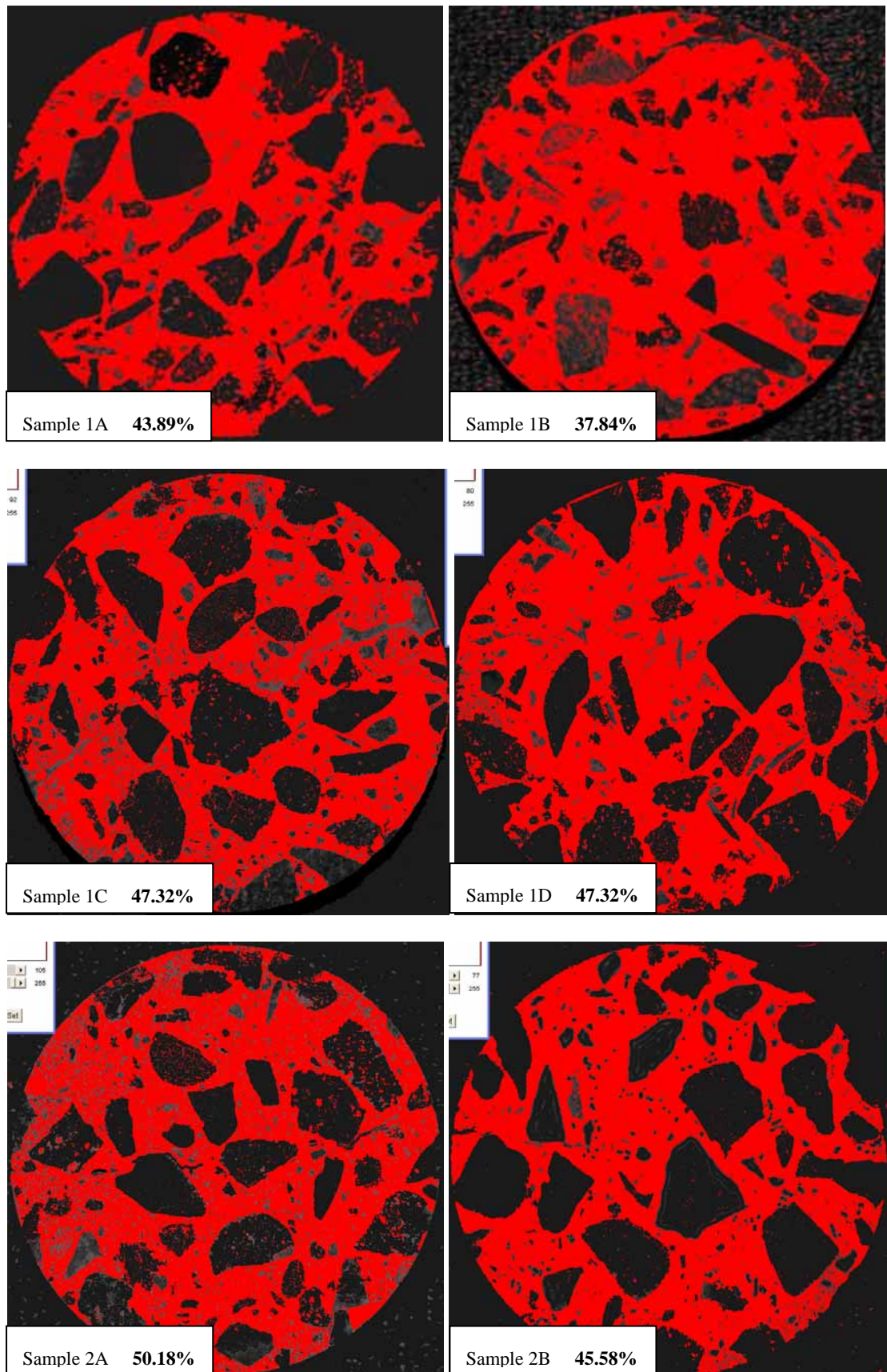


Figure 4.3.1.2.1 Coarse Aggregate Images 1A to 2B from ImageJ

Sample 3a		Sample 3b		Sample 4a		Sample 4b		Sample 5a		Sample 5b	
101	8721	86	4148	87	4583	68	5106	77	4828	86	3545
102	8823	87	4321	88	4731	69	5248	78	5087	87	3627
103	9328	88	4617	89	4795	70	5377	79	5346	88	3778
104	9676	89	4919	90	5146	71	5445	80	5493	89	3813
105	10031	90	5223	91	5240	72	5411	81	5777	90	3885
106	10341	91	5522	92	5440	73	5508	82	5916	91	4136
107	10899	92	5647	93	5639	74	5752	83	6191	92	4036
108	11257	93	6067	94	5675	75	5691	84	6529	93	4287
109	11363	94	6189	95	6143	76	6015	85	6875	94	4360
110	11834	95	6552	96	6373	77	6042	86	7025	95	4533
111	12481	96	6506	97	6391	78	6258	87	7385	96	4559
112	13103	97	6981	98	6908	79	6285	88	7680	97	4694
113	13755	98	7227	99	7229	80	6381	89	8060	98	5057
114	14612	99	7493	100	7553	81	6913	90	8230	99	5267
115	14779	100	7945	101	7984	82	6887	91	8798	100	5490
116	15653	101	8707	102	8397	83	7088	92	9125	101	5823
117	16317	102	9171	103	8878	84	7353	93	9668	102	6164
118	16851	103	9877	104	9421	85	7666	94	10025	103	6420
119	17481	104	10084	105	9754	86	7793	95	10331	104	6745
120	18464	105	10852	106	10355	87	7917	96	11014	105	6927
121	18288	106	11479	107	10518	88	8205	97	11555	106	7164
122	19688	107	12059	108	10855	89	8219	98	11807	107	7465
123	20284	108	12349	109	11565	90	8600	99	12526	108	7970
124	20684	109	13023	110	12088	91	9004	100	13348	109	8022
125	20987	110	13879	111	12653	92	9288	101	14007	110	8532
126	22299	111	14414	112	13312	93	9768	102	14809	111	9136
127	23094	112	15536	113	14002	94	9982	103	15448	112	9627
128	24000	113	16065	114	14708	95	10371	104	16399	113	9912
129	24642	114	16837	115	15367	96	10648	105	17189	114	10559
130	25449	115	17765	116	16309	97	11046	106	17442	115	11023
131	25656	116	18490	117	16913	98	11703	107	18475	116	11364
132	26054	117	18867	118	17458	99	12216	108	19203	117	12019
133	26801	118	19647	119	17923	100	12908	109	19554	118	12318
134	27893	119	20305	120	19372	101	13864	110	20350	119	12799
135	28426	120	21164	121	19789	102	14427	111	21384	120	13971
136	28510	121	22276	122	20362	103	15275	112	21693	121	14584
137	28642	122	23223	123	21135	104	15852	113	22149	122	15711
138	28633	123	23880	124	21363	105	16425	114	22934	123	16347
251	5380	236	3933	237	2866	219	4206	228	3451	237	4093
252	5889	237	4034	238	2965	220	4100	229	3736	238	4157
253	8763	238	4050	239	3253	221	4066	230	3651	239	4075
254	13070	239	4004	240	3481	222	3971	231	3756	240	4239
255	13606	240	4161	241	3514	223	4077	232	3704	241	4283
	1750183	241	4283	242	3690	224	4129	233	3881	242	4592
255	3399580	242	4631	243	3831	225	4315	234	4010	243	4612
	51.48%	243	4596	244	4069	226	4225	235	4152	244	4781
	48.52%	244	4875	245	4364	227	4253	236	4319	245	4513
		245	5018	246	4559	228	4374	237	4606	246	4518
		246	5029	247	4892	229	4446	238	4475	247	4730
		247	5440	248	4850	230	4370	239	4822	248	4588
		248	5258	249	5149	231	4383	240	4776	249	4773
		249	5722	250	5204	232	4279	241	4896	250	4828
		250	5667	251	5622	233	4248	242	4963	251	5269
		251	5905	252	6333	234	4309	243	5113	252	5489
		252	6531	253	8534	235	4368	244	4940	253	8742
		253	8326	254	11726	236	4350	245	4564	254	11888
		254	11666	255	23585	237	4553	246	4612	255	17666
		255	17366		2001818	238	4544	247	4862		1747016
			1803968	255	3478252	239	4445	248	4633	255	3548288
		255	3638972		57.55%	240	4564	249	4343		49.24%
			50.43%		42.45%	241	4464	250	4696		50.76%
						242	4606	251	4763		
						243	4595	252	4628		
						244	4407	253	6949		
						245	4391	254	9319		
						246	4303	255	11798		
						247	4433		1738069		
						248	4518	255	3428952		
						249	4626		50.69%		
						250	4598		49.31%		
						251	4809				
						252	5082				
						253	7495				
						254	12278				
						255	14561				
							2035637				
						255	3583160				
							56.81%				
							43.19%				

Table 4.3.1.2.2 Percentage of Coarse Aggregate Samples 3A to 5B

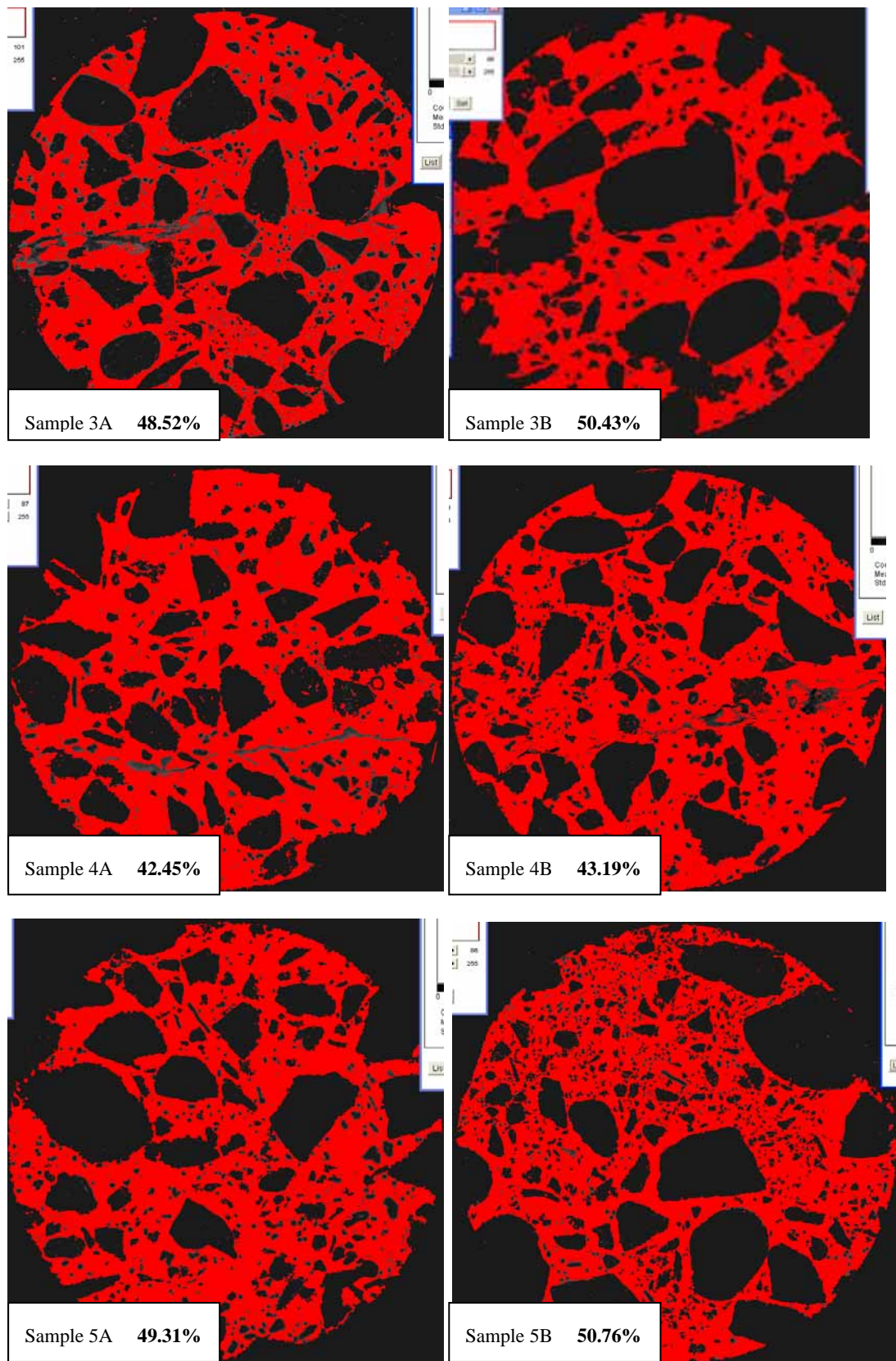


Figure 4.3.1.2.2 Coarse Aggregate Images 3A to 5B from ImageJ

Sample RMa		Sample RMb		Sample DARa		Sample DARb	
81	11412	80	8601	85	2338	84	4556
82	11351	81	8920	86	2362	85	4554
83	11529	82	9108	87	2453	86	4752
84	11603	83	9344	88	2408	87	4948
85	11824	84	9546	89	2515	88	4952
86	11941	85	9759	90	2602	89	5188
87	12230	86	10001	91	2635	90	5425
88	12467	87	10204	92	2774	91	5575
89	12869	88	10388	93	2798	92	5661
90	12949	89	10427	94	2873	93	5958
91	13297	90	10849	95	2948	94	6245
92	13711	91	11201	96	3094	95	6366
93	13682	92	11463	97	3081	96	6502
94	13858	93	11707	98	3144	97	6779
95	14257	94	12186	99	3258	98	6887
96	14299	95	12352	100	3414	99	7295
97	15141	96	12769	101	3527	100	7527
98	15258	97	13224	102	3638	101	7954
99	15446	98	13324	103	3864	102	8078
100	15878	99	13702	104	3754	103	8654
101	16770	100	14314	105	4083	104	9097
102	16950	101	14602	106	4261	105	9094
103	17753	102	15009	107	4361	106	9490
104	17849	103	15609	108	4494	107	9744
105	18011	104	15764	109	4537	108	10101
106	18622	105	16255	110	4771	109	10331
107	18884	106	16567	111	4990	110	10606
108	19171	107	16781	112	5396	111	11048
109	19816	108	17265	113	5499	112	11408
110	19794	109	17771	114	5870	113	11890
111	20155	110	17824	115	6105	114	12718
112	20761	111	18260	116	6412	115	13049
113	21011	112	18809	117	6751	116	13537
114	21905	113	19185	118	6950	117	13773
115	21761	114	19349	119	7308	118	14713
116	21928	115	19723	120	7503	119	14856
117	22574	116	20492	121	7811	120	15422
				122	8139	121	15949
240	4169	239	3878	244	3759	244	5142
241	4259	240	3885	245	3759	244	5142
242	4365	241	3824	246	3723	245	5395
243	4265	242	3752	247	4074	246	5346
244	4273	243	3752	248	3778	247	5575
245	4217	244	3833	249	3818	248	5471
246	4272	245	3798	250	3752	249	5660
247	4177	246	3797	251	4146	250	5443
248	4293	247	3862	252	4879	251	5505
249	4512	248	3823	253	6780	252	6326
250	4494	249	3984	254	11559	253	7918
251	4707	250	4023	255	14313	254	12629
252	4655	251	4210		1870780	255	14703
253	6446	252	4668	255	3679574		1894500
254	7765	253	5537		50.84%	255	3590104
255	8812	254	7443		49.16%		52.77%
	1897326	255	9954				47.23%
255	3513297		1833990				
	54.00%	255	3429010				
	46.00%		53.48%				
			46.52%				

Table 4.3.1.2.3 Percentage of Coarse Aggregate Samples RmA to DarB

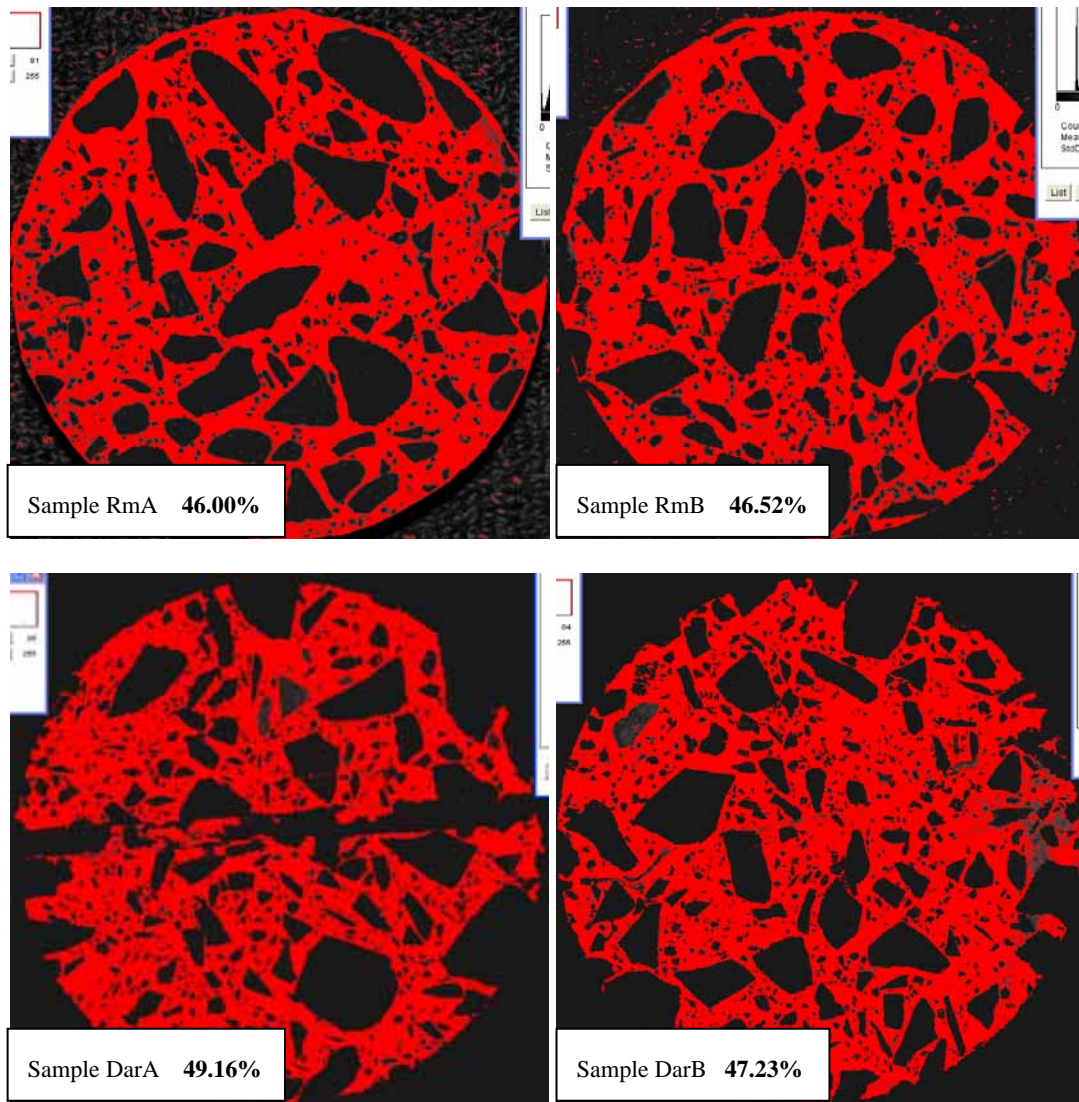


Figure 4.3.1.2.3 Coarse Aggregate Images RmA to DarB from ImageJ

Sample F1a		Sample F1b		Sample F11a		Sample F11b	
94	18000	94	25694	86	7705	90	6389
95	18401	95	25706	87	7972	91	6287
96	18108	96	25151	88	8202	92	6596
97	17703	97	25305	89	8478	93	6714
98	17548	98	25386	90	9065	94	6768
99	17267	99	26408	91	9269	95	7001
100	17714	100	27480	92	9852	96	6986
101	17881	101	28512	93	10165	97	7265
102	18474	102	29038	94	10464	98	7132
103	18790	103	29540	95	11004	99	7461
104	19140	104	30900	96	11403	100	7821
105	19084	105	31191	97	11883	101	8064
106	18854	106	31498	98	12366	102	8290
107	19841	107	32597	99	12885	103	8489
108	19924	108	32842	100	13448	104	8820
109	20226	109	32459	101	13896	105	9002
110	20065	110	32722	102	14410	106	9461
111	20571	111	32921	103	15157	107	9927
112	21258	112	33678	104	15723	108	10186
113	21758	113	34289	105	16170	109	10469
114	22496	114	33635	106	16441	110	10893
115	22897	115	33751	107	17171	111	11348
116	22988	116	32843	108	17338	112	11966
117	22555	117	32630	109	17920	113	12396
118	22741	118	32073	110	18092	114	13048
119	23208	119	33043	111	18959	115	13437
120	23915	120	33890	112	19261	116	14054
121	24287	121	33438	113	20270	117	14755
122	24531	122	33097	114	20821	118	15067
123	24358	123	33276	115	21502	119	15665
124	24007	124	32363	116	22159	120	16338
125	23968	125	32140	117	21987	121	16882
126	24272	126	31407	118	22277	122	17610
127	25371	127	32991	119	22992	123	18695
128	25508	128	31958	120	23468	124	19354
129	25164	129	32173	121	23969	125	19612
130	25096	130	32218	122	24368	126	20810
131	25159	131	31698	123	25138	127	21408
239	1904	239		232	2731	236	3096
240	1859	240	759	233	2847	237	3232
241	1963	241	788	234	2868	238	3289
242	1990	242	827	235	2912	239	3321
243	1977	243	817	236	3057	240	3467
244	2042	244	896	237	3152	241	3759
245	2179	245	943	238	3096	242	3862
246	2259	246	1011	239	3307	243	4010
247	2609	247	1107	240	3519	244	4100
248	2585	248	1165	241	3516	245	4110
249	3644	249	1183	242	3607	246	4228
250	3414	250	1213	243	3640	247	4400
251	3846	251	1472	244	3997	248	4358
252	4363	252	1619	245	4049	249	4937
253	5798	253	2529	246	4224	250	5050
254	11377	254	8291	247	4651	251	5433
255	17278	255	26397	248	4453	252	5622
	1880285		2067241	249	4865	253	7424
255	3453672	255	3534950	250	5350	254	9346
	54.44%		58.48%	251	5435	255	14201
	45.56%		41.52%	252	5859		1899347
				253	7829	255	3598538
				254	9406		52.78%
				255	9641		47.22%
					1855894		
				255	3478484		
					53.35%		
					46.65%		

Table 4.3.1.2.4 Percentage of Coarse Aggregate Samples FIA to FIIB

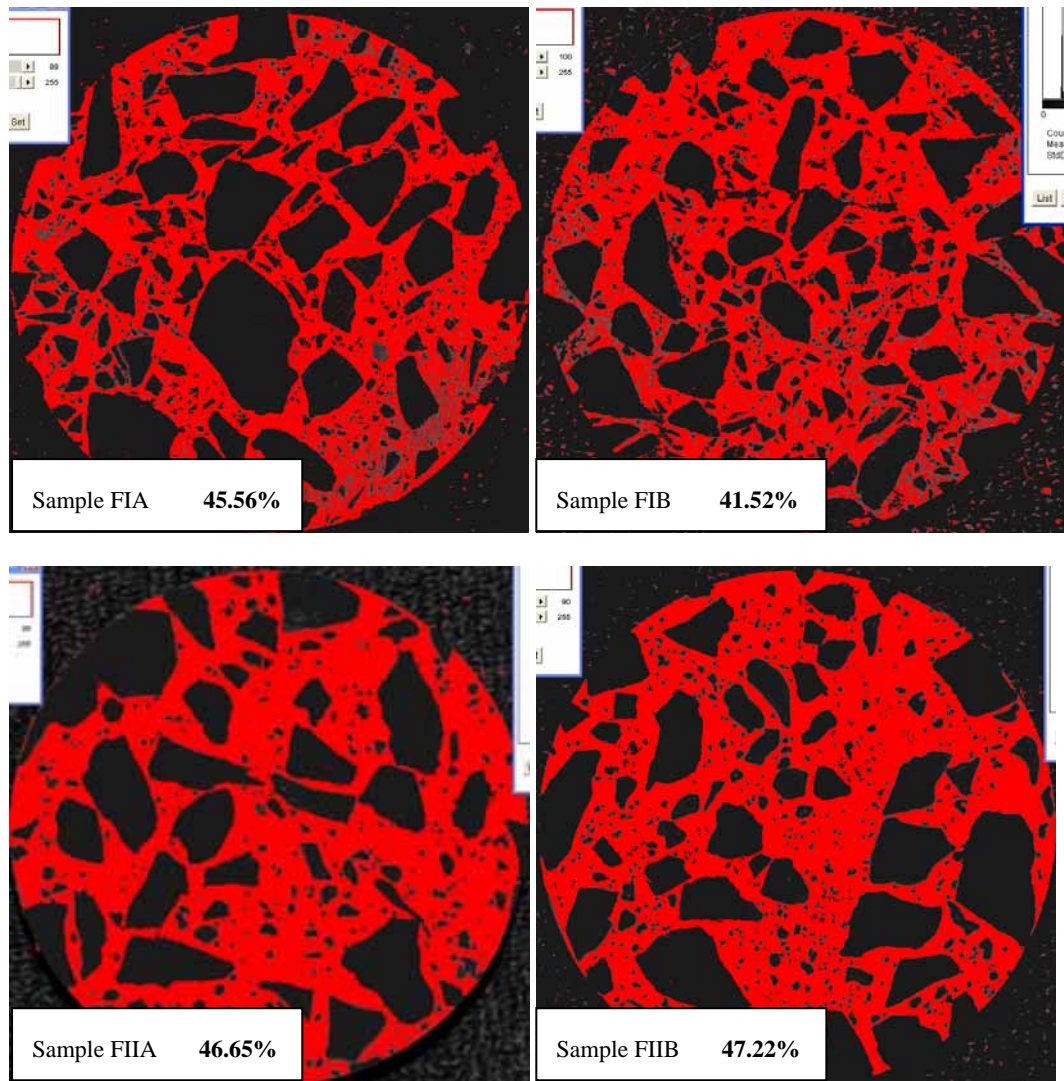


Figure 4.3.1.2.4 Coarse Aggregate Images FIA to FIIB from ImageJ

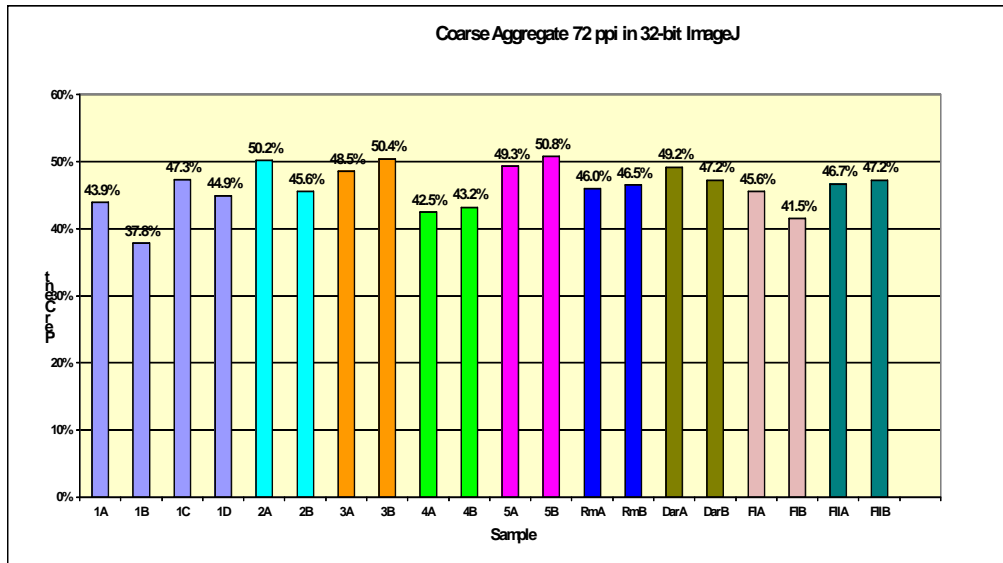


Figure 4.3.1.2.5 Percentage of Coarse Aggregate of all samples

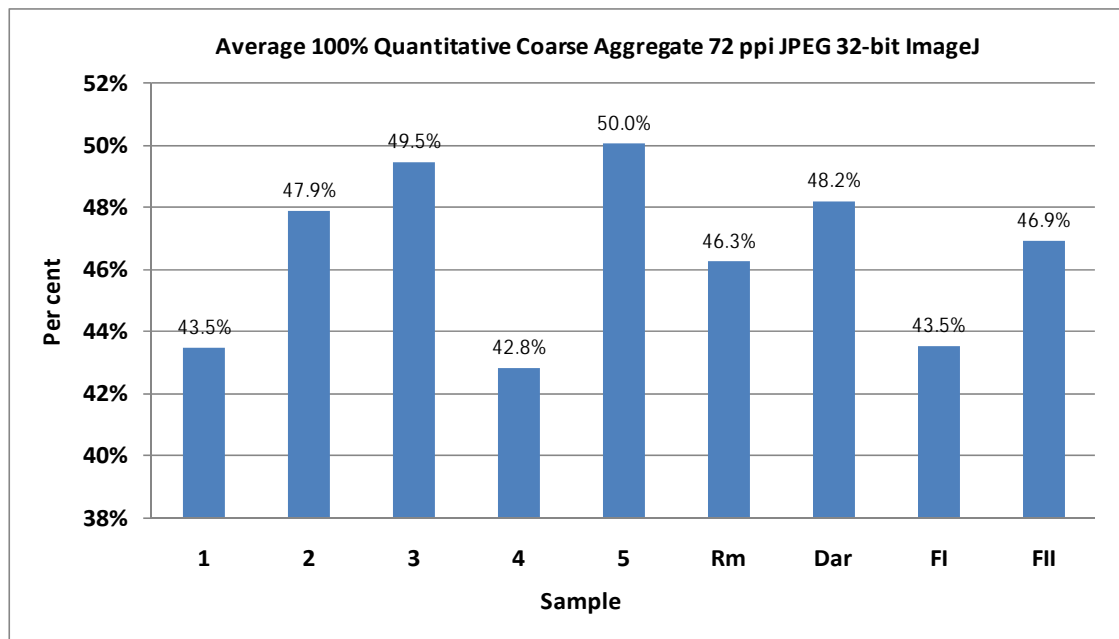


Figure 4.3.1.2.6 Average Percentage of Coarse Aggregate of each core sample

Observations and Explanations

Core samples 1 and 4 had the lowest percentage coarse aggregate, on average 3 to 5% below the others in the study (core samples 1 to 5).

This correlated with the highest damage.

4.3.2.1 Study 2 - Results for Calculations of Porosity 2400 ppi Digital Images

1A		1B		1C		1D		2A		2B	
204	53797	206	48133	200	51168	210	49389	204	56989	209	53663
205	50453	207	45742	201	46952	211	45483	205	49696	210	48683
206	48174	208	44172	202	44424	212	42791	206	44093	211	44169
207	45886	209	43435	203	42481	213	40786	207	38983	212	39805
208	45106	210	43641	204	40761	214	38953	208	35446	213	36172
209	44308	211	43504	205	39837	215	37984	209	32065	214	32979
210	43720	212	44258	206	39198	216	37222	210	29618	215	30046
211	43949	213	44890	207	38349	217	37160	211	28143	216	28025
212	44355	214	46220	208	38305	218	36955	212	26411	217	26937
213	45087	215	47841	209	38681	219	37066	213	24842	218	25534
214	45840	216	49196	210	39596	220	37556	214	23953	219	24984
215	46894	217	51613	211	40222	221	38251	215	23151	220	25074
216	48092	218	53192	212	40818	222	38672	216	22473	221	25037
217	49547	219	56077	213	42046	223	40039	217	22032	222	25661
218	50926	220	58684	214	43838	224	41798	218	21961	223	26112
219	52422	221	61782	215	45809	225	42765	219	21783	224	27409
220	54526	222	65029	216	47963	226	44616	220	21339	225	27936
221	55787	223	68467	217	50093	227	45909	221	21401	226	29173
222	58050	224	72097	218	52826	228	48107	222	21429	227	30461
223	60158	225	76434	219	55514	229	50615	223	21779	228	32415
224	62223	226	80317	220	59285	230	53488	224	22054	229	33919
225	64533	227	84774	221	62983	231	56052	225	22749	230	36535
226	67169	228	90320	222	67568	232	58890	226	23773	231	38364
227	69481	229	95177	223	72133	233	62827	227	24957	232	40893
228	72078	230	100942	224	76692	234	66532	228	25978	233	43688
229	74789	231	105055	225	82476	235	71143	229	27460	234	46994
230	76952	232	111161	226	88022	236	76285	230	29550	235	50327
231	80168	233	116049	227	94009	237	82100	231	31475	236	53711
232	83134	234	121099	228	99610	238	89045	232	33554	237	57594
233	86409	235	126603	229	106205	239	96033	233	35935	238	61985
234	88992	236	131403	230	111805	240	103756	234	38511	239	66220
235	92652	237	134464	231	118516	241	112324	235	41255	240	71599
236	95096	238	138040	232	124374	242	120110	236	44427	241	77557
237	97954	239	141029	233	130546	243	127841	237	47398	242	82735
238	100044	240	143330	234	135311	244	134627	238	51376	243	88316
239	101806	241	146202	235	139396	245	141368	239	54906	244	93541
240	101739	242	146733	236	143436	246	144423	240	59550	245	98216
241	101416	243	147568	237	144807	247	145519	241	62920	246	101933
242	99967	244	147619	238	144756	248	143452	242	67221	247	105879
243	97657	245	146872	239	142238	249	137605	243	71539	248	107009
244	93942	246	144592	240	136579	250	126021	244	74621	249	108113
245	89688	247	142502	241	130085	251	110318	245	77762	250	104907
246	84172	248	138228	242	119593	252	89102	246	80461	251	95970
247	78415	249	133258	243	108421	253	63988	247	81434	252	79424
248	71971	250	126755	244	95800	254	42597	248	81997	253	63480
249	65748	251	117486	245	82121	255	36946	249	80089	254	57272
250	58901	252	104594	246	68269	pores	3324509	250	77734	255	117157
251	52798	253	91262	247	55588	total	62181952	251	72262	pores	2623613
252	47660	254	85846	248	44669	percentage	5.35%	252	61493	total	62182648
253	47740	255	216459	249	37844			253	47681	percentage	4.22%
254	58052	pores	4820146	250	37163			254	33231		
255	136861	total	61512000	251	41911			255	40090		
pores	3587284	percentage	7.84%	252	49917			pores	2213030		
total	61594996			253	55971			total	62099516		
percentage	5.82%			254	45409			percentage	3.56%		
				255	36746						
				pores	4169135						
				total	62098544						
				percentage	6.71%						

Table 4.3.2.1.1 Percentage of Porosity Samples 1A to 2B

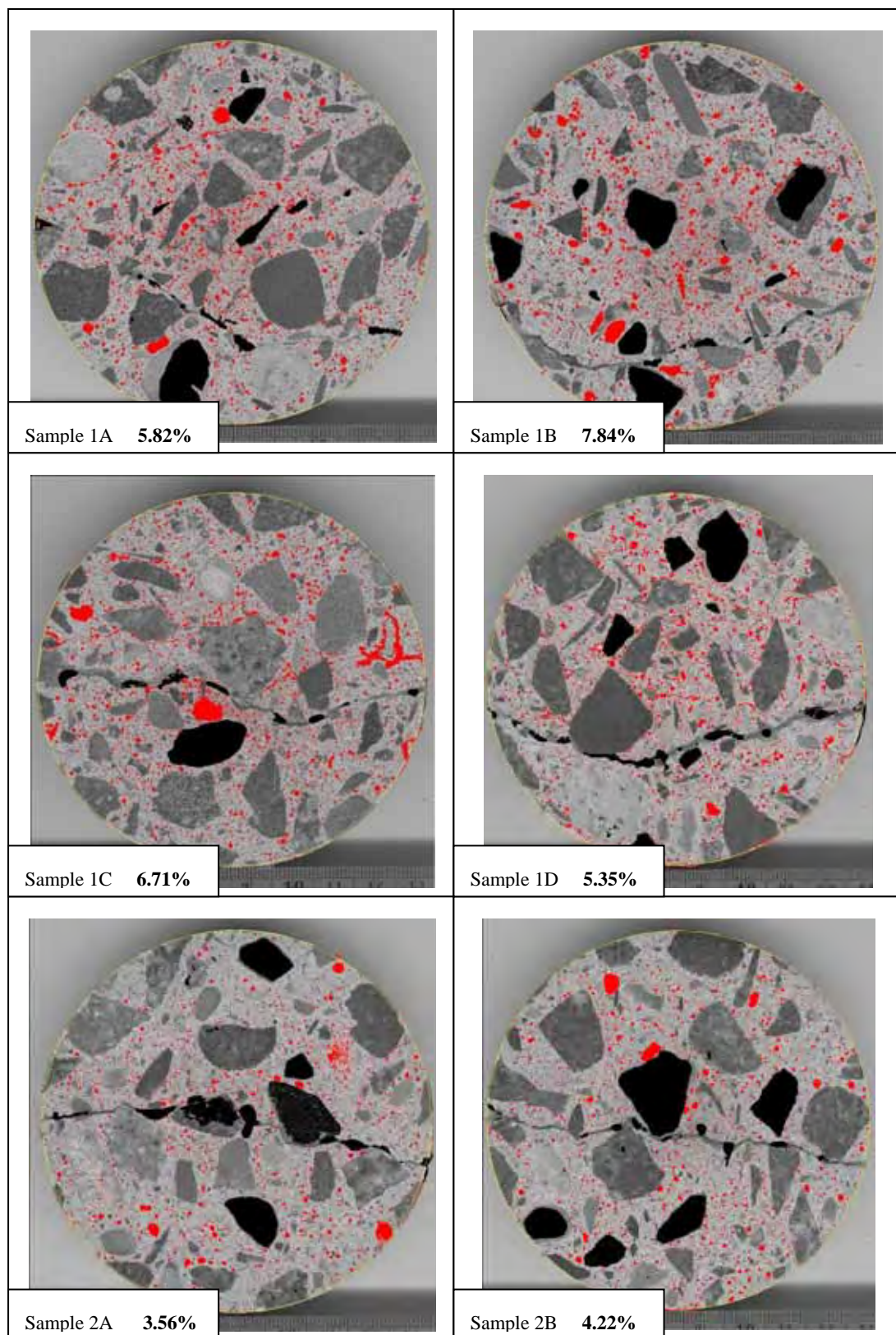


Figure 4.3.2.1.1 Porosity images 1A to 2B from ImageJ

3A		3B		4A		4B		5A		5B	
197	33513	211	56827	205	49791	197	52329	201	51445	204	51603
198	29410	212	47825	206	41952	198	49393	202	43231	205	44673
199	26389	213	40802	207	36320	199	46681	203	36495	206	39229
200	23752	214	34886	208	31446	200	44690	204	31583	207	35007
201	21916	215	30562	209	28610	201	43526	205	27625	208	31337
202	20366	216	26763	210	25387	202	42350	206	24982	209	28446
203	20040	217	24260	211	24037	203	42486	207	22938	210	26537
204	18931	218	22076	212	22516	204	41704	208	21004	211	24384
205	18356	219	20608	213	21800	205	41194	209	20267	212	23522
206	18306	220	19554	214	21434	206	41662	210	19492	213	22442
207	18415	221	18775	215	21363	207	41963	211	19351	214	22260
208	18690	222	18315	216	21668	208	42659	212	19520	215	22094
209	18727	223	17987	217	22145	209	43318	213	19739	216	22300
210	19394	224	18042	218	22375	210	43867	214	20430	217	23029
211	20055	225	18243	219	22862	211	45074	215	21152	218	22982
212	20740	226	18670	220	24098	212	46418	216	22298	219	23594
213	21683	227	19297	221	25082	213	47634	217	23896	220	24626
214	22661	228	19786	222	26037	214	49048	218	25041	221	25523
215	23864	229	20614	223	27670	215	50482	219	27250	222	26995
216	25282	230	21290	224	29041	216	52186	220	29329	223	28460
217	27146	231	22294	225	30357	217	54241	221	31951	224	30437
218	29025	232	23024	226	32704	218	56961	222	35231	225	31815
219	30599	233	24383	227	34689	219	59592	223	38708	226	34203
220	33484	234	25887	228	37413	220	62931	224	42748	227	37113
221	35606	235	27146	229	40193	221	65650	225	47479	228	39369
222	38302	236	29108	230	43510	222	69656	226	52750	229	42700
223	41319	237	30775	231	47143	223	73132	227	58464	230	46104
224	44712	238	33248	232	51531	224	77503	228	64896	231	50414
225	47865	239	35233	233	56171	225	81015	229	72847	232	54955
226	51665	240	37482	234	61716	226	84550	230	79614	233	59473
227	55677	241	40199	235	66012	227	88598	231	86544	234	64963
228	60260	242	43129	236	72536	228	91394	232	93179	235	70379
229	64598	243	46737	237	78042	229	94062	233	98226	236	77232
230	69033	244	50111	238	83723	230	96466	234	102812	237	83528
231	74208	245	54355	239	89942	231	97878	235	106216	238	91244
232	79769	246	58764	240	95432	232	99305	236	108306	239	99476
233	83733	247	63979	241	100735	233	100027	237	108155	240	106736
234	86552	248	69987	242	104837	234	99663	238	106810	241	114502
235	89689	249	75933	243	107833	235	99758	239	104724	242	121624
236	90622	250	80667	244	109041	236	98912	240	101718	243	127983
237	88733	251	81895	245	109524	237	97473	241	98534	244	133209
238	85893	252	77531	246	107850	238	96646	242	96201	245	134903
239	82109	253	67614	247	103897	239	95575	243	93846	246	135191
240	77133	254	62307	248	98455	240	93769	244	92344	247	132146
241	72520	255	257592	249	91088	241	92840	245	90873	248	126026
242	66851	pores	1934562	250	80337	242	91071	246	90561	249	118585
243	62112	total	62098544	251	71018	243	90486	247	89502	250	109203
244	56914	percentage	3.12%	252	64332	244	88390	248	88459	251	100453
245	52892			253	65731	245	87328	249	86345	252	92761
246	50545			254	80671	246	86290	250	81955	253	83169
247	49748			255	146544	247	84710	251	75230	254	69482
248	50964		pores	2908641	248	81254	252	60741	255	74793	
249	54186		total	60920600	249	76224	253	39433	pores	3263214	
250	58312		percentage	4.77%	250	66760	254	22069	total	62856180	
251	61862				251	55184	255	13377	percentage	5.19%	
252	63668				252	41305	pores	3187916			
253	60606				253	27473	total	62940440			
254	49843				254	18876	percentage	5.06%			
255	28758				255	41161					
pores	2748003				pores	3972773					
total	61597892				total	60514060					
percentage	4.46%				percentage	6.57%					

Table 4.3.2.1.2 Percentage of Porosity Samples 3A to 5B

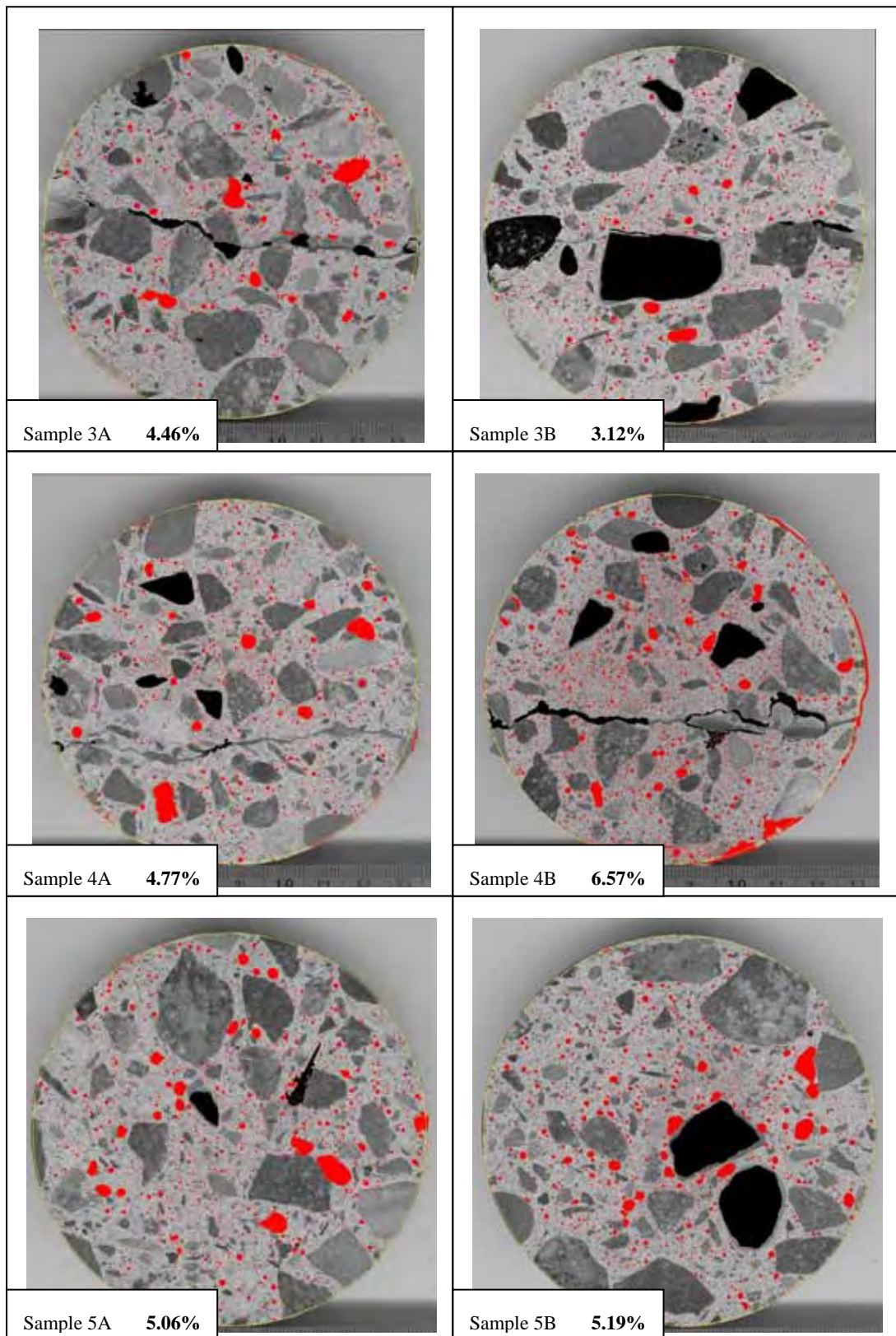


Figure 4.3.2.1.2 Porosity images 3A to 5B from ImageJ

RmA		RmB		DarA		DarB	
204	41252	204	40270	213	47293	206	35501
205	36967	205	37005	214	39163	207	29192
206	34137	206	34162	215	32722	208	24347
207	31750	207	31961	216	28173	209	21389
208	30301	208	30260	217	24091	210	19087
209	28711	209	28895	218	21236	211	17450
210	28146	210	27646	219	19014	212	15909
211	27096	211	26981	220	17345	213	15383
212	27028	212	26533	221	16233	214	14877
213	27169	213	26139	222	15304	215	15008
214	26897	214	26241	223	14640	216	15307
215	27323	215	26132	224	14595	217	15729
216	27901	216	26337	225	14662	218	16172
217	28431	217	26743	226	14584	219	17157
218	29085	218	27131	227	14576	220	17874
219	29847	219	27556	228	14886	221	19318
220	30713	220	27860	229	15450	222	20609
221	31966	221	28712	230	15592	223	22347
222	32638	222	29504	231	16120	224	24239
223	33930	223	30609	232	16591	225	27039
224	35250	224	32205	233	17501	226	29663
225	37021	225	33314	234	18165	227	32777
226	38557	226	34723	235	18983	228	36432
227	40104	227	36738	236	20144	229	40407
228	41761	228	38671	237	20923	230	44886
229	43546	229	40754	238	22017	231	49409
230	45175	230	43316	239	23348	232	54329
231	47239	231	46187	240	24281	233	58409
232	49305	232	49410	241	25565	234	63417
233	52229	233	52359	242	27118	235	67404
234	54474	234	55865	243	28401	236	71611
235	57131	235	59900	244	30269	237	74751
236	59509	236	63806	245	31609	238	76619
237	62590	237	68966	246	33728	239	77596
238	65971	238	72676	247	36558	240	76887
239	69506	239	77985	248	40616	241	75114
240	72520	240	82844	249	45686	242	71757
241	77563	241	88200	250	51369	243	67631
242	81684	242	93466	251	59437	244	62746
243	86264	243	99063	252	66211	245	56730
244	92177	244	103953	253	71999	246	50198
245	98038	245	110000	254	76106	247	44352
246	105558	246	114476	255	128699	248	40857
247	114775	247	118201	pores	1331003	249	38908
248	126403	248	120795	total	61931684	250	40339
249	138398	249	121062	percentage	2.15%	251	44489
250	152430	250	118236			252	49490
251	161090	251	111805			253	52087
252	161071	252	100843			254	45679
253	149010	253	85040			255	39491
254	129214	254	69913			pores	2038399
255	193169	255	123882			total	62433768
	3350020	pores	3055331			percentage	3.26%
	63871724	total	63109312				
	5.24%	percentage	4.84%				

Table 4.3.2.1.3 Percentage of Porosity Samples RmA to DarB

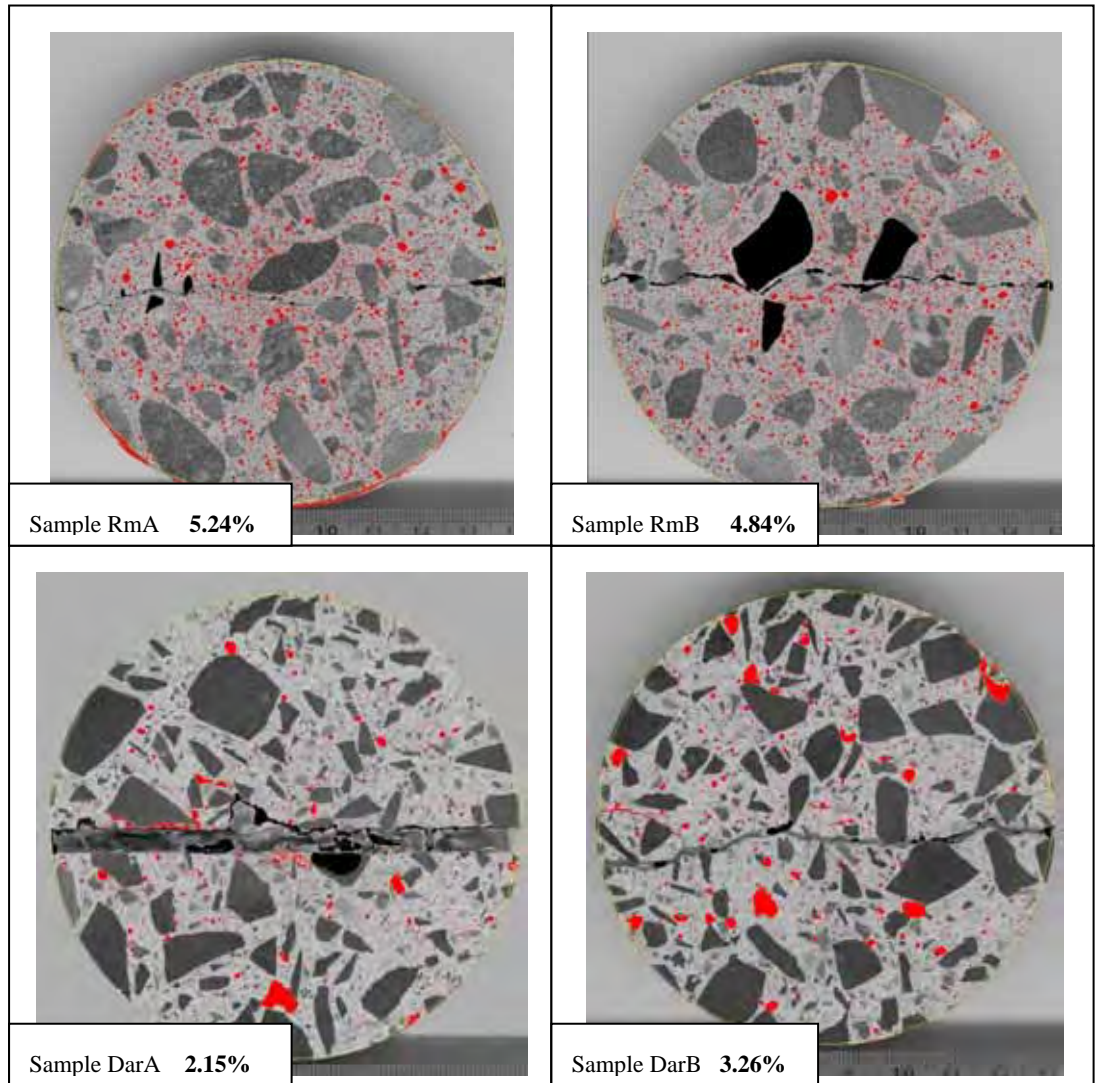


Figure 4.3.2.1.3 Porosity images DarA to DarB from ImageJ

F1A		F1B		F11A		F11B	
193	29853	193	30167	198	33355	200	69627
194	26291	194	26381	199	29013	201	61572
195	23306	195	22842	200	26180	202	54637
196	19990	196	19898	201	23152	203	49025
197	17584	197	17588	202	21037	204	43862
198	15851	198	15368	203	19500	205	39925
199	13976	199	13590	204	17964	206	36099
200	12424	200	12062	205	16935	207	33077
201	11080	201	10806	206	16263	208	30216
202	10104	202	9561	207	15930	209	27858
203	9317	203	8947	208	15221	210	25760
204	8672	204	8270	209	15171	211	24302
205	7994	205	7496	210	15013	212	22326
206	7764	206	7020	211	15172	213	21475
207	7481	207	6658	212	15598	214	20410
208	6978	208	6280	213	15785	215	19441
209	6599	209	6171	214	16116	216	19356
210	6400	210	5924	215	16554	217	18719
211	6203	211	5824	216	16757	218	18911
212	6021	212	5604	217	17756	219	19016
213	5953	213	5555	218	18537	220	19393
214	5818	214	5459	219	19427	221	19822
215	5730	215	5398	220	20166	222	20620
216	5713	216	5424	221	21599	223	21608
217	5583	217	5393	222	22983	224	22922
218	5563	218	5360	223	24367	225	25005
219	5708	219	5552	224	25961	226	27179
220	5703	220	5595	225	27973	227	29809
221	5672	221	5405	226	29933	228	33397
222	5725	222	5641	227	32332	229	37761
223	5922	223	5652	228	34682	230	42093
224	5918	224	5718	229	37399	231	48010
225	6128	225	5844	230	40268	232	54007
226	6488	226	5913	231	43452	233	59910
227	6567	227	5918	232	46217	234	66160
228	6920	228	6294	233	49834	235	71358
229	7213	229	6476	234	52867	236	75396
230	7558	230	6654	235	56264	237	77373
231	7553	231	6878	236	58743	238	77729
232	8482	232	7145	237	61057	239	76696
233	8577	233	7485	238	62921	240	74569
234	9109	234	7786	239	63563	241	70973
235	9348	235	8027	240	63176	242	66441
236	10077	236	8272	241	60646	243	62223
237	10576	237	8491	242	57977	244	57752
238	10999	238	8737	243	54407	245	53179
239	11707	239	9141	244	50980	246	48301
240	12284	240	9306	245	48589	247	44280
241	12797	241	9693	246	46813	248	40768
242	13394	242	9903	247	47030	249	39242
243	14085	243	10170	248	47589	250	41783
244	14390	244	10714	249	47877	251	49091
245	15259	245	10985	250	45837	252	59716
246	16136	246	11522	251	40656	253	73522
247	16862	247	12193	252	31194	254	87162
248	17628	248	13001	253	20687	255	94820
249	18332	249	13879	254	10961		2525684
250	18948	250	15365	255	5208		62015936
251	19567	251	16254		1908644		4.07%
252	20134	252	16824		61764772		
253	21249	253	15638		3.09%		
254	22139	254	12970				
255	71789	255	18922				
	775191		629009				
	62686312		62183120				
	1.24%		1.01%				

Table 4.3.2.1.4 Percentage of Porosity Samples FIA to FIIB

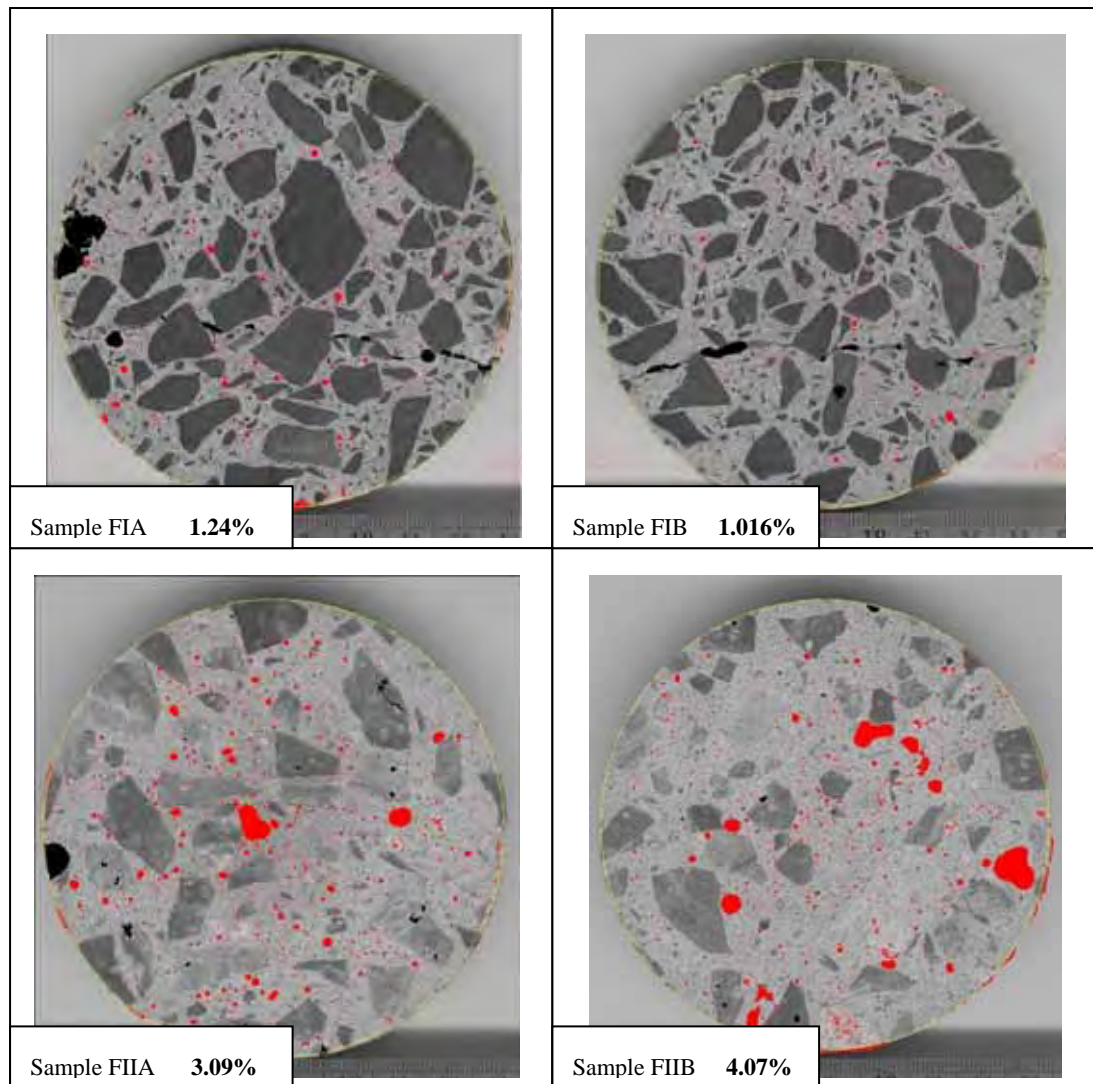


Figure 4.3.2.1.4 Porosity images FIA to FIIB from ImageJ

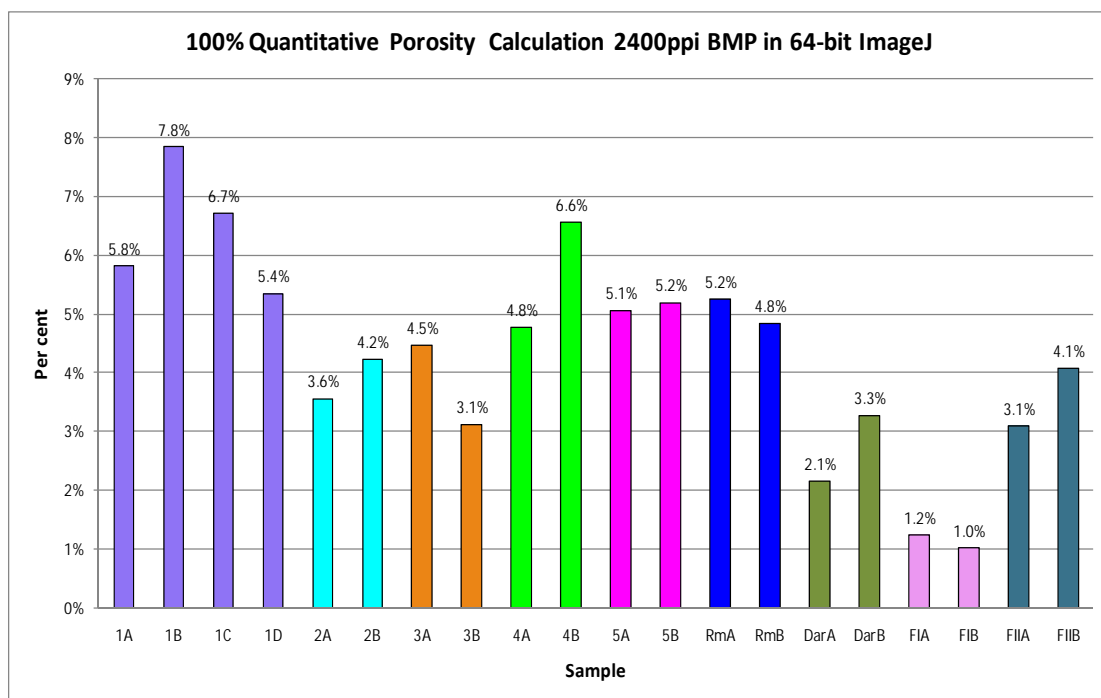


Figure 4.3.2.1.5 Percentage of Porosity of all samples

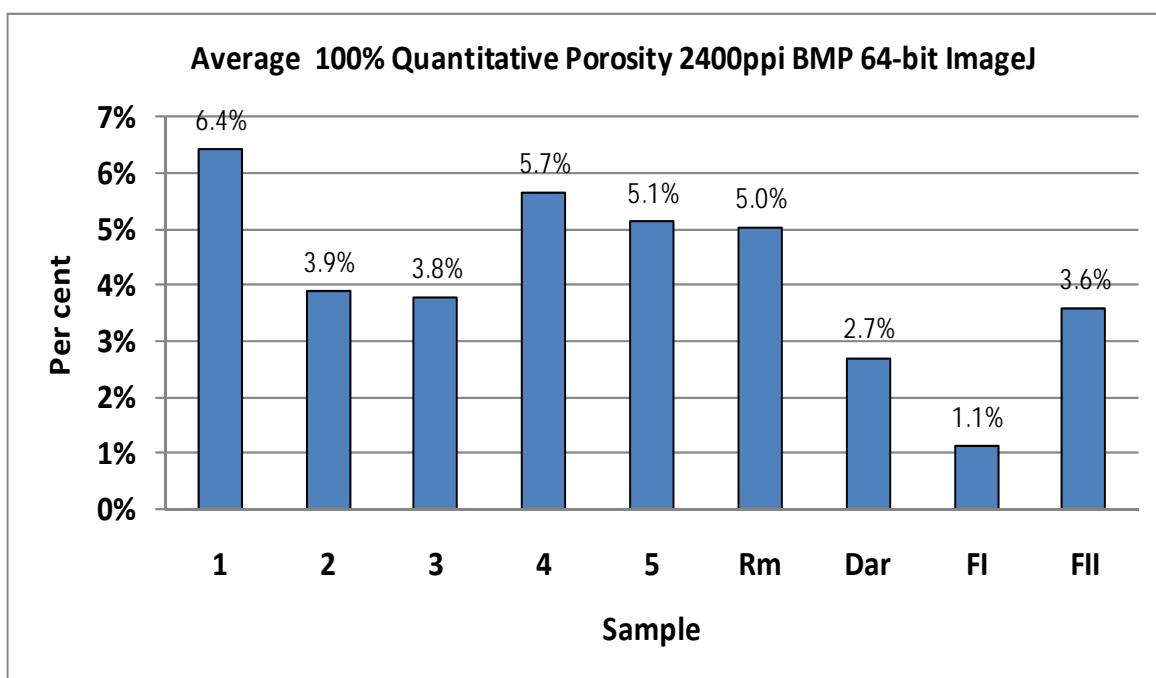


Figure 4.3.2.1.6 Average Percentage of Porosity of each core sample

Observations and Explanations

The scanned images in resolution 2400 ppi were calculated in 64-bit ImageJ image analysis software hence the results were much more accurate. Lower percentage porosity was achieved in all samples under this study.

It is very interesting that the consistency must have been very good because in comparing two Studies at this stage now (72 ppi and 2400 ppi) in Figure 4.3.2.1.7 the chart follows a similar profile. (Figure 4.3.2.1.8 shows the resulting comparison of all three Studies.)

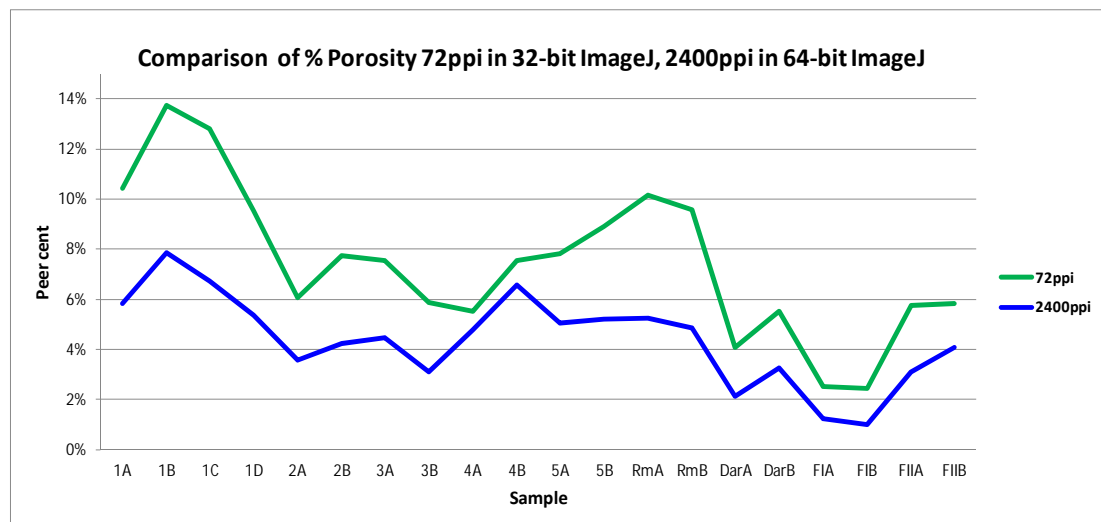


Figure 4.3.2.1.7 Comparison % Porosity for 72 ppi and 2400 ppi

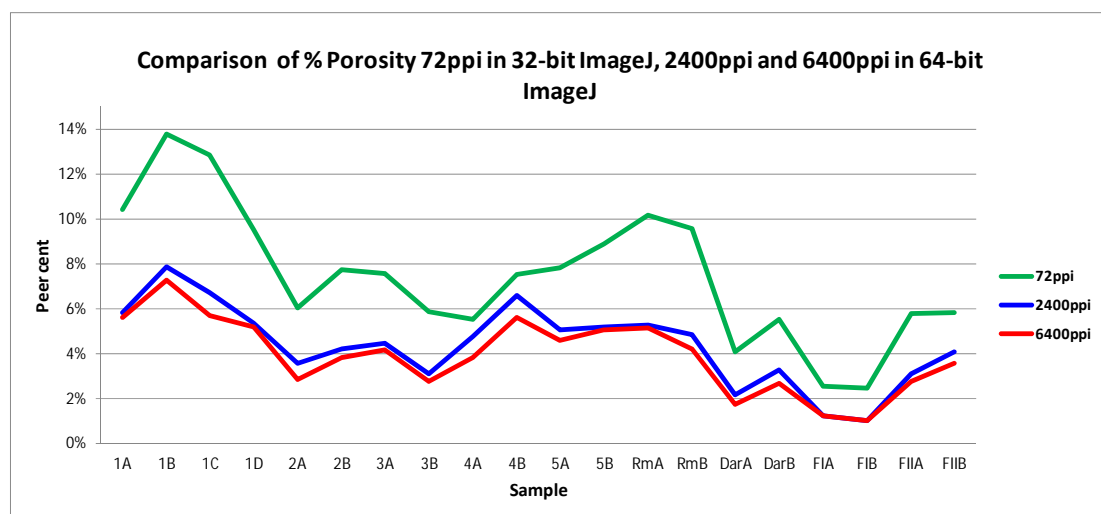


Figure 4.3.2.1.8 Comparison % Porosity for 72 ppi, 2400 ppi and 6400 ppi

4.3.2.2 Study 2 - Results for Auto Calculations of Coarse Aggregate Percentage 2400 ppi in 64-bit ImageJ

1A	1B	1C	1D	2A	2B	
						6024
						2606
82	396292	82	269932	82	274680	300186
83	417784	83	286788	83	293187	316814
84	436814	84	302193	84	310339	334594
85	454566	85	318683	85	327940	349431
86	468663	86	332675	86	345370	364580
87	479519	87	346992	87	361142	379495
88	488959	88	361141	88	378921	392253
89	493370	89	373647	89	395847	402062
90	495904	90	385057	90	410718	411761
91	496299	91	395594	91	426180	422011
92	492152	92	403604	92	438455	428633
93	488479	93	410912	93	453299	433654
94	481875	94	419141	94	467419	438604
95	473344	95	423377	95	479852	440998
96	466117	96	427807	96	491680	442512
97	459179	97	432017	97	503339	442297
98	449853	98	433494	98	515021	443671
99	442167	99	437099	99	526092	442004
100	435429	100	438272	100	537582	441594
101	428876	101	437693	101	550609	439150
102	423053	102	437780	102	559092	436433
103	418303	103	438545	103	569388	435354
104	411832	104	434483	104	574928	432879
105	408315	105	431956	105	580430	428987
106	404565	106	427755	106	579308	427336
107	399999	107	422976	107	577223	423961
108	396154	108	418409	108	573619	421281
109	391733	109	414045	109	565258	418011
						4640
						6800
130	328982	130	313113	130	393358	378309
131	329932	131	314248	131	391065	379806
132	332746	132	320058	132	388284	379129
133	335806	133	323169	133	386441	381036
134	338244	134	327357	134	385722	379203
135	343051	135	331076	135	387354	381181
136	345271	136	338691	136	387290	384064
137	351370	137	344678	137	389519	384823
138	356751	138	351001	138	393574	387252
	25844334	139	358098	139	397599	391309
	62265588	140	365786	140	403275	395539
	41.51%	141	374236	141	409165	26519432
			25109667		29854180	62603100
			62682848		62517884	42.36%
			40.06%		47.75%	
					39.95%	
						43.86%

Table 4.3.2.2.1 Percentage of Coarse Aggregate Samples 1A to 2B

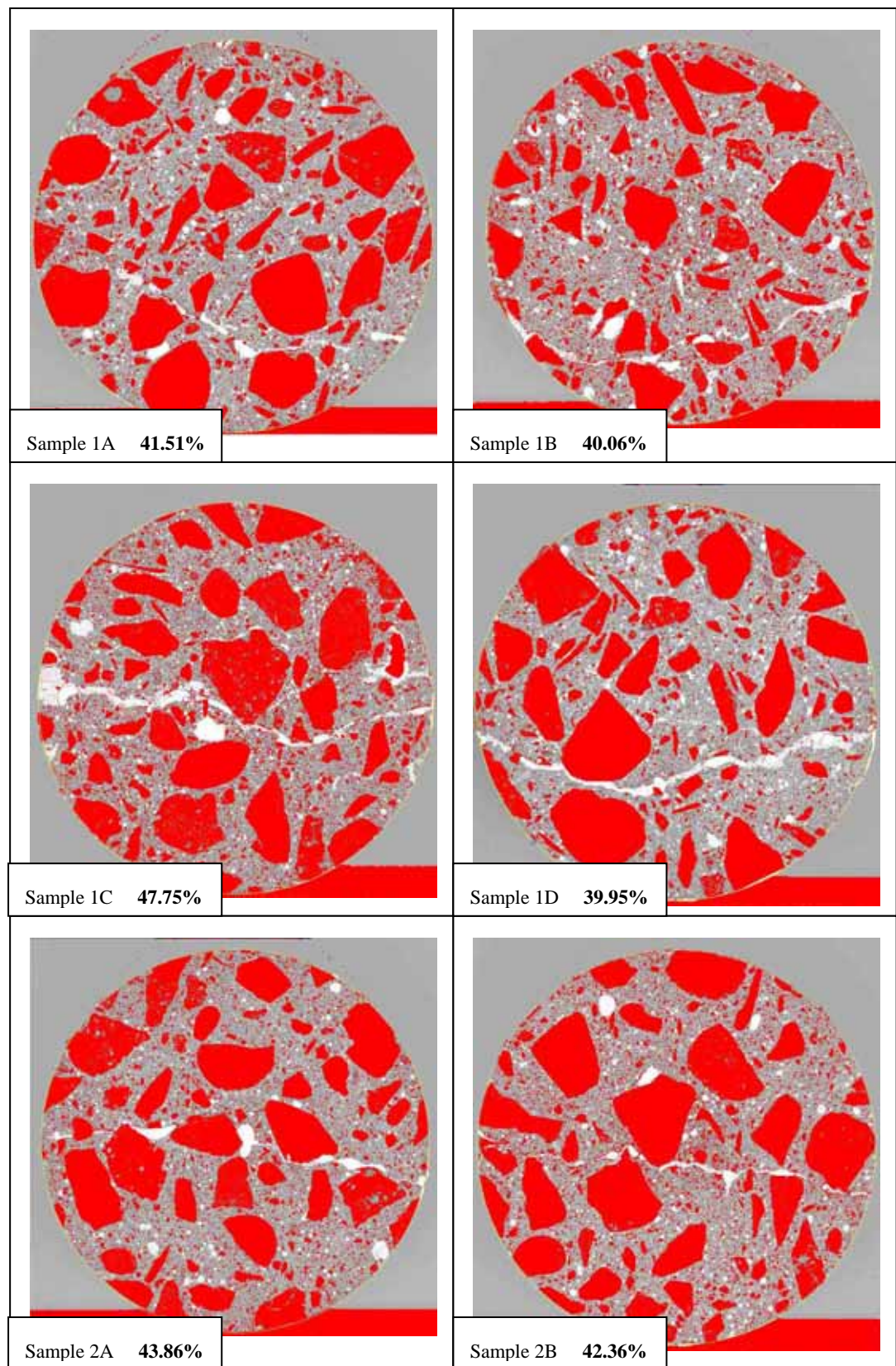


Figure 4.3.2.2.1 Coarse Aggregate Images 1A to 2B from ImageJ

3A		3B		4A		4B		5A		5B	
82	277010	82	203544	82	168463	82	312419	82	298021	82	271632
83	297927	83	212566	83	181933	83	322370	83	309338	83	291091
84	320327	84	222493	84	195344	84	330073	84	317416	84	309632
85	341214	85	231306	85	210224	85	338594	85	326315	85	330152
86	363483	86	241942	86	225399	86	347266	86	334714	86	348504
87	381987	87	250644	87	240695	87	355481	87	341313	87	367020
88	400983	88	261550	88	255516	88	361866	88	348340	88	384558
89	418007	89	271430	89	271651	89	370089	89	353395	89	402072
90	436089	90	281048	90	284731	90	377113	90	358846	90	419120
91	450095	91	290348	91	299008	91	384290	91	363238	91	434330
92	463617	92	301538	92	312395	92	390234	92	367712	92	447685
93	473638	93	312158	93	325869	93	399068	93	371708	93	463139
94	482680	94	320800	94	338713	94	404819	94	376971	94	475242
95	489481	95	331923	95	350824	95	411351	95	380634	95	486591
96	492928	96	340685	96	362629	96	416667	96	384751	96	498328
97	496989	97	349661	97	372961	97	421008	97	389339	97	507825
98	495544	98	358304	98	382360	98	426800	98	394352	98	515708
99	491633	99	367617	99	392025	99	429482	99	399563	99	523227
100	486829	100	376096	100	401511	100	431414	100	404037	100	529148
101	480184	101	384925	101	408342	101	432913	101	408621	101	533294
102	472234	102	393011	102	414540	102	431314	102	412816	102	537847
103	464692	103	402234	103	419909	103	428094	103	417153	103	540733
104	456549	104	409625	104	422522	104	425093	104	422958	104	541724
105	453657	105	416728	105	425761	105	421160	105	426667	105	544075
106	448823	106	423279	106	425992	106	415703	106	429552	106	542402
107	448087	107	428798	107	425599	107	411366	107	431713	107	539726
108	446182	108	434550	108	424240	108	408054	108	432312	108	534443
109	446709	109	437731	109	421960	109	403015	109	432700	109	528370
110	447908	110	438996	110	420489	110	397427	110	429768	110	522515
111	451209	111	439354	111	417754	111	393356	111	429253	111	516188
112	452920	112	437937	112	416663	112	387748	112	428398	112	508162
113	456216	113	437395	113	414977	113	382514	113	428654	113	500349
114	458460	114	435574	114	413532	114	378128	114	429340	114	491625
115	461327	115	433329	115	409419	115	372306	115	431219	115	482086
116	462240	116	432046	116	422418	116	367497	116	432046	116	472240
135	430241	135	405205	135	370866	135	418914	135	402490	135	399910
136	431287	136	405538	136	369521		25390189	136	399177	136	399933
137	434210	137	406383	137	371926		62260224	137	397403	137	399904
138	438110	138	409076	138	373295		40.78%	138	396846	138	400435
	27816786	139	408538	139	376477			139	395805	139	401475
	62855452	140	410476	140	379581			140	394710	140	402219
	44.26%	141	413575	141	382806			141	396109	141	406359
		142	416126	142	387815				27665559		29297103
		143	417308	143	391694				63787232		63447864
		144	419755	144	397798				43.37%		46.18%
		145	422977		24578484						
			26850195		61092476						
			62686312		40.23%						
			42.83%								

Table 4.3.2.2.2 Percentage of Coarse Aggregate Samples 3A to 5B

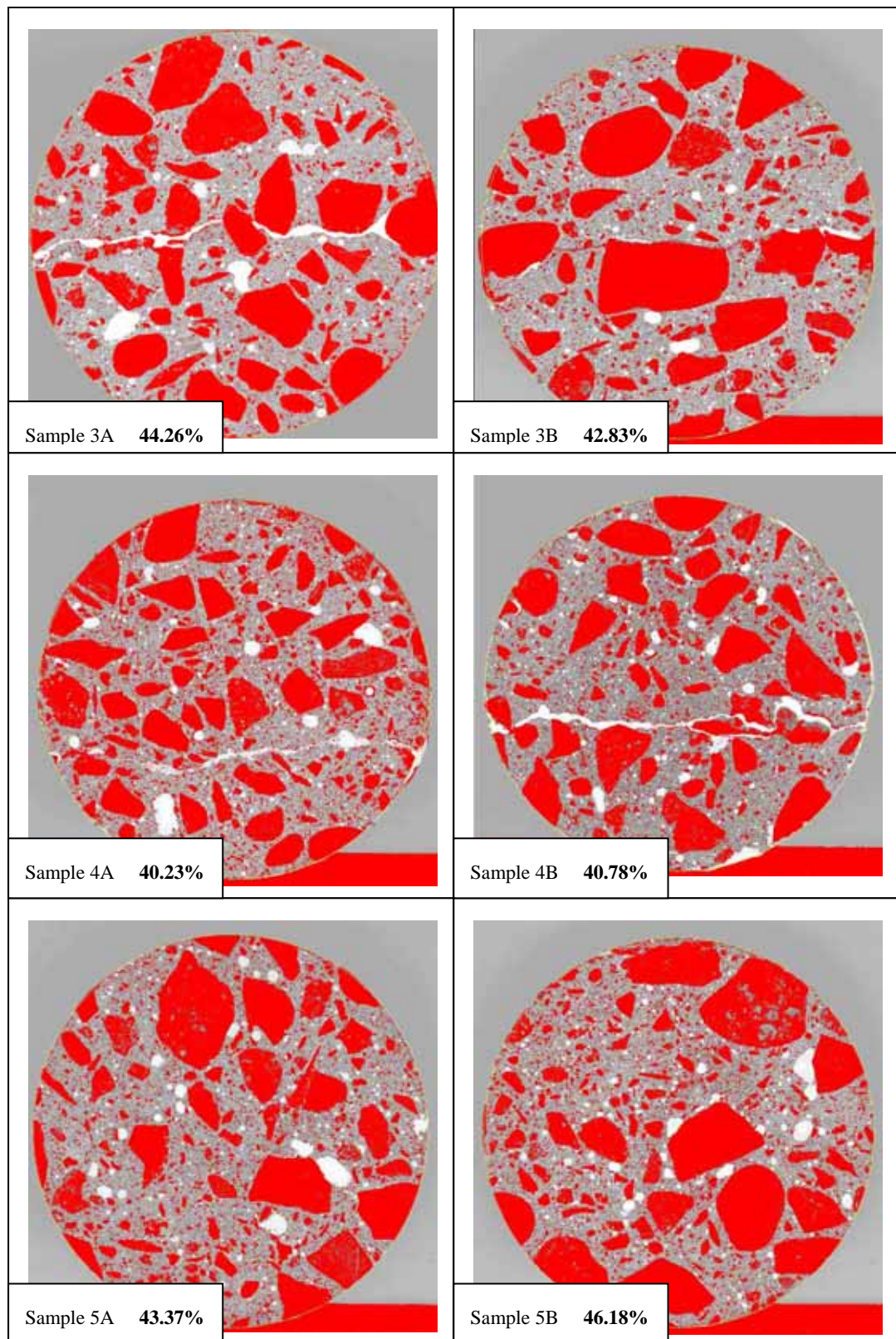


Figure 4.3.2.2.2 Percentage of Coarse Aggregate Samples 3A to 5B

RmA		RmB		DarA		DarB	
79	246291	79	169008	79	601004	79	602594
80	265033	80	185466	80	609179	80	561299
81	283290	81	201149	81	612732	81	517038
82	300272	82	218059	82	612622	82	474665
83	317261	83	234853	83	607579	83	432106
84	332452	84	251026	84	598950	84	393316
85	347567	85	267177	85	584968	85	356500
86	362270	86	284044	86	567964	86	324061
87	373922	87	299110	87	548780	87	293970
88	386677	88	312659	88	524833	88	267878
89	396758	89	325838	89	499958	89	245139
90	405389	90	338322	90	472979	90	225683
91	414685	91	352252	91	444983	91	210485
92	421516	92	363704	92	417714	92	195474
93	429735	93	374587	93	393424	93	184289
94	436005	94	384890	94	366696	94	174748
95	442103	95	394611	95	343929	95	167382
96	448654	96	403354	96	320756	96	160465
97	453512	97	411244	97	301023	97	156250
98	458391	98	419194	98	282761	98	152284
99	464078	99	426477	99	266546	99	149688
100	468850	100	432189	100	253074	100	147550
101	472907	101	437016	101	240734	101	145135
127	455580	127	387877	127	155368		25973940
128	449727	128	387316	128	155774		63278236
129	445670	129	384880	129	157692		41.05%
130	442155	130	384143	130	158713		
131	438934	131	383788	131	160206		
132	437000	132	385129	132	162489		
133	435992	133	388461	133	164624		
134	433379	134	390777		26280238		
135	433126	135	394010		63447428		
136	431136	136	396070		41.42%		
137	430643	137	401243				
138	431216	138	405475				
139	430864	139	410840				
140	432596	140	417385				
	29908298		28753926				
	64126784		64042192				
	46.64%		44.90%				

Table 4.3.2.2.3 Percentage of Coarse Aggregate Samples RmA to DarB

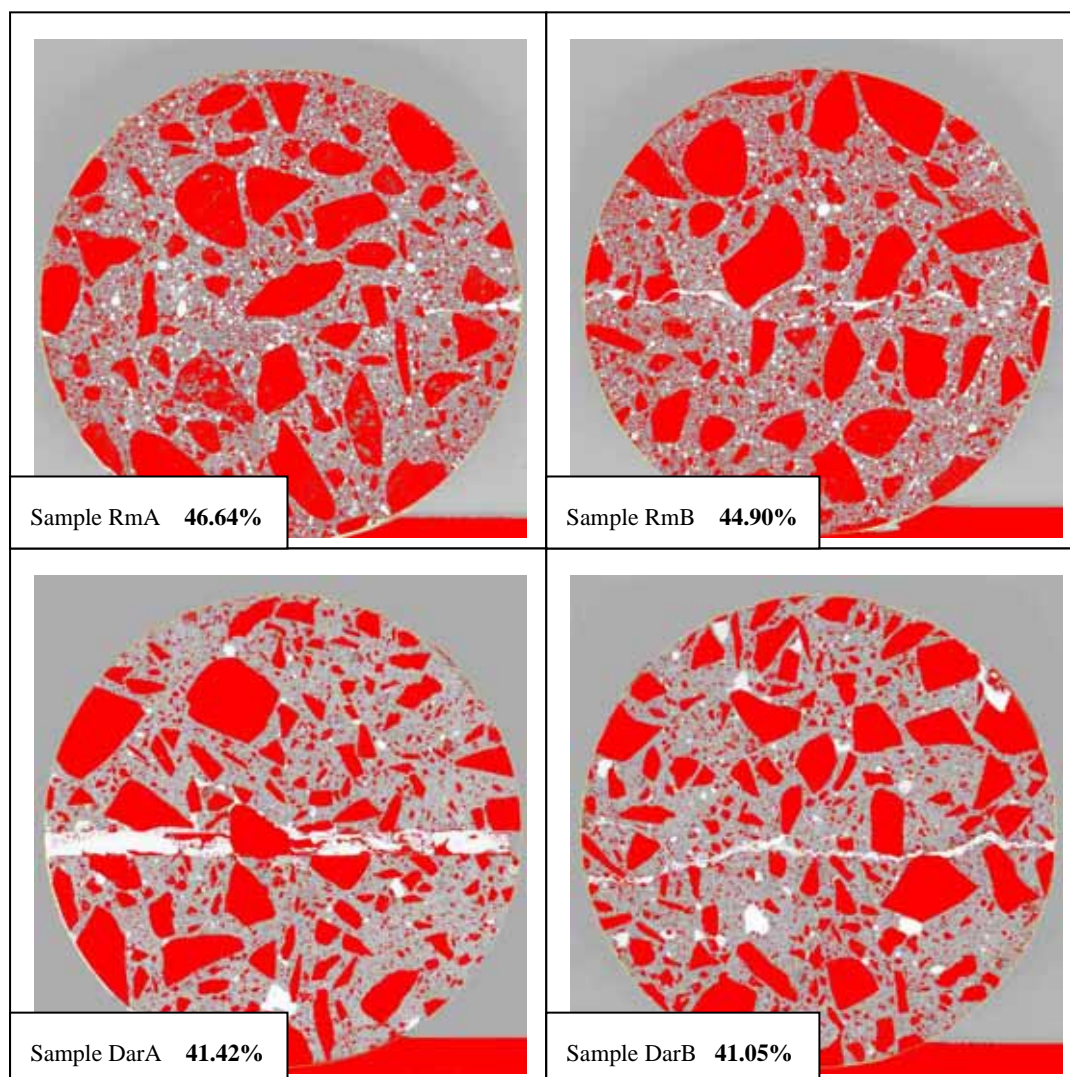


Figure 4.3.2.2.3 Coarse Aggregate Images RmA to DarB from ImageJ

FIA		FIB		FIIA		FIIB	
79	988306	79	990136	79	46624	79	188431
80	967928	80	991517	80	51391	80	200737
81	936121	81	982726	81	57207	81	212811
82	894665	82	957332	82	63420	82	223861
83	848527	83	924082	83	70007	83	234975
84	796602	84	881436	84	78579	84	246353
85	741158	85	831511	85	86778	85	255762
86	684388	86	774006	86	97237	86	265568
87	629419	87	715680	87	108307	87	273645
88	575679	88	657127	88	121663	88	280934
89	522727	89	599198	89	135799	89	286575
90	474078	90	543613	90	151773	90	292446
91	429301	91	490660	91	170533	91	296281
92	389168	92	441584	92	187819	92	299126
	31035819	117	163671	117	401880	117	324981
	62183120		27465526	118	409274	118	334035
	49.91%		62266948	119	416485	119	347055
			44.11%	120	423226	120	360366
				121	431931	121	375299
				122	439736	122	395122
				123	446938	123	412843
				124	456800	124	435074
				125	463668	125	460777
				126	473563		28386165
				127	482798		61764772
				128	492637		45.96%
				129	501808		
				130	511951		
				131	524028		
				132	532223		
				133	542377		
				134	552160		
				135	562124		
				136	572947		
				137	584673		
				138	594583		
				139	607631		
				140	619371		
				141	633559		
				142	648636		
					23446335		
					61681340		
					38.01%		

Table 4.3.2.2.4 Percentage of Coarse Aggregate Samples FIA to FIIB

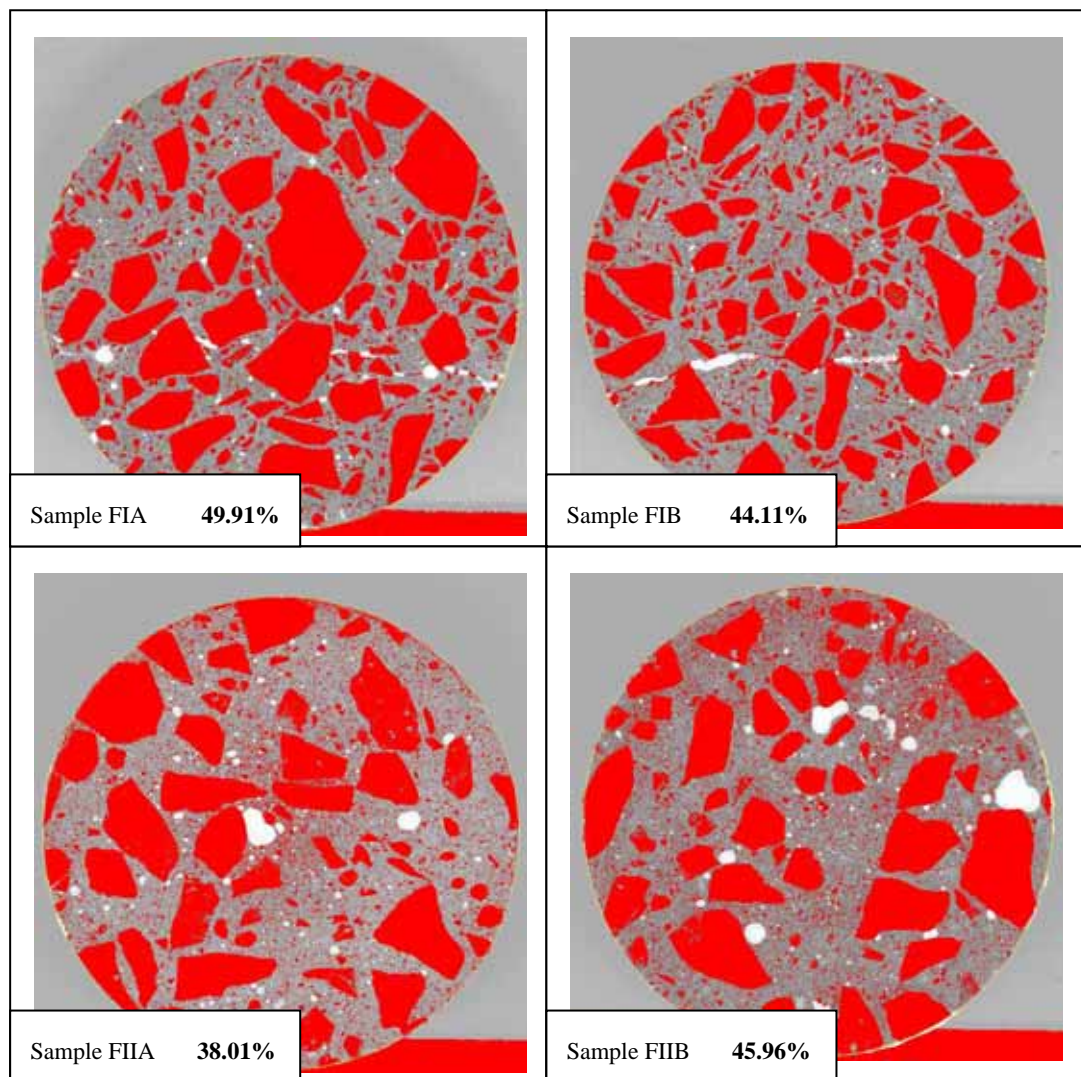


Figure 4.3.2.2.4 Coarse Aggregate Images FIA to FIIB from ImageJ

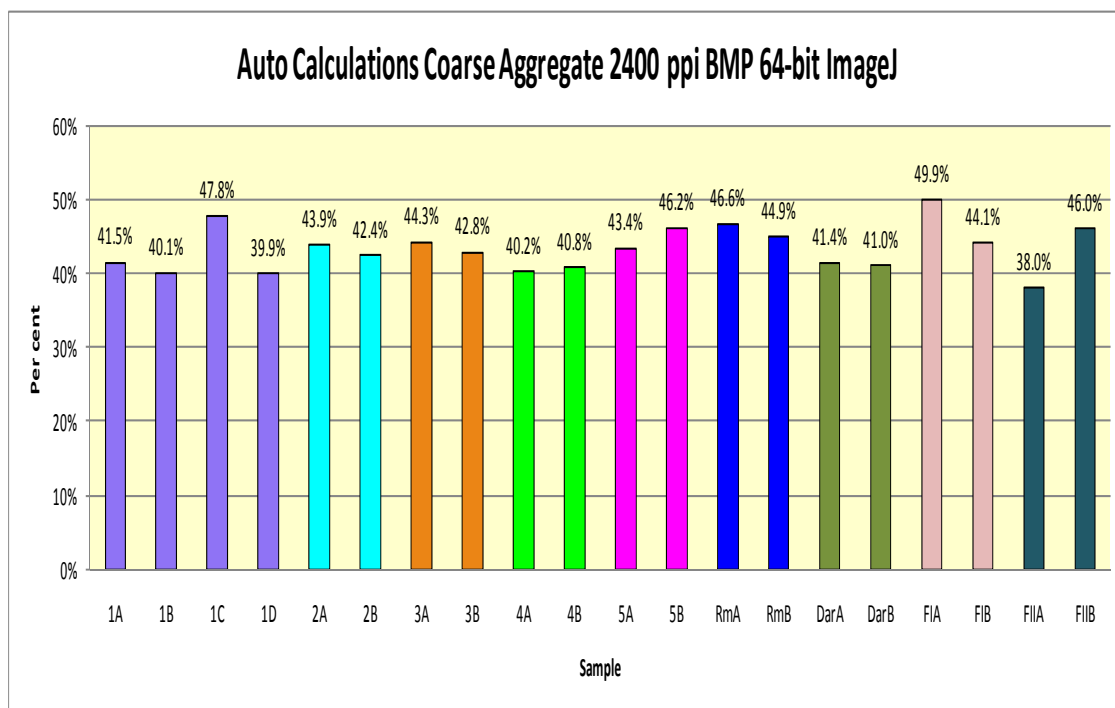


Figure 4.3.2.2.5 Percentage of auto calculations Coarse Aggregate of all samples

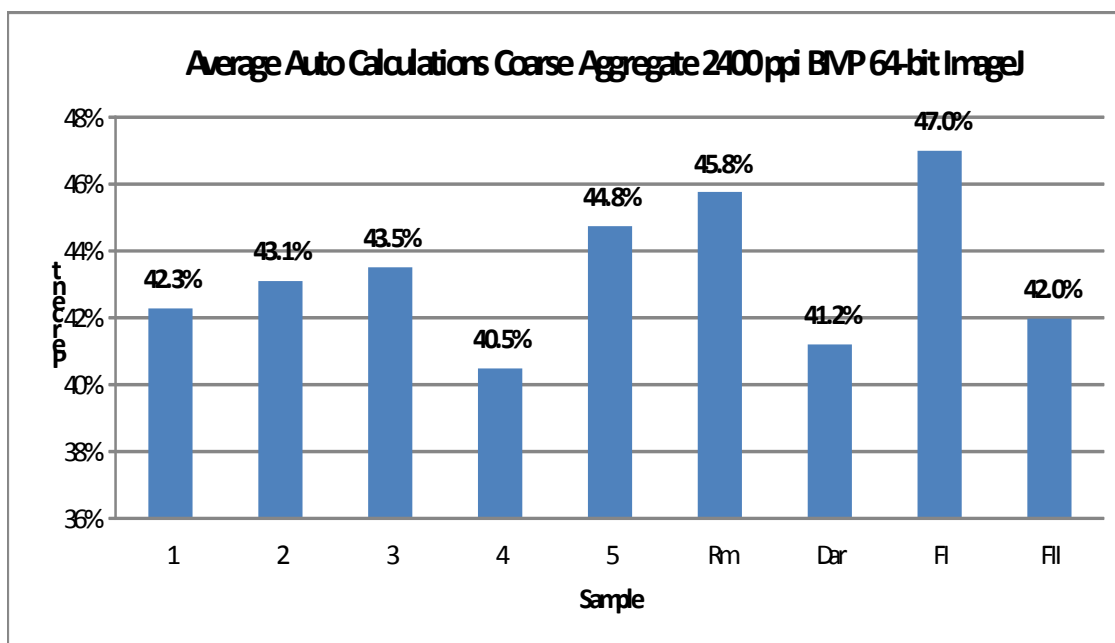


Figure 4.3.2.2.6 Average percentage of auto calculations Coarse Aggregate of each core sample

Observations and Explanations

Figure 4.3.2.2.7 shows the first comparison the differences between the different resolutions of the images studied and also the difference of the accuracy of the image analysis software in 32-bit and 654-bit versions.

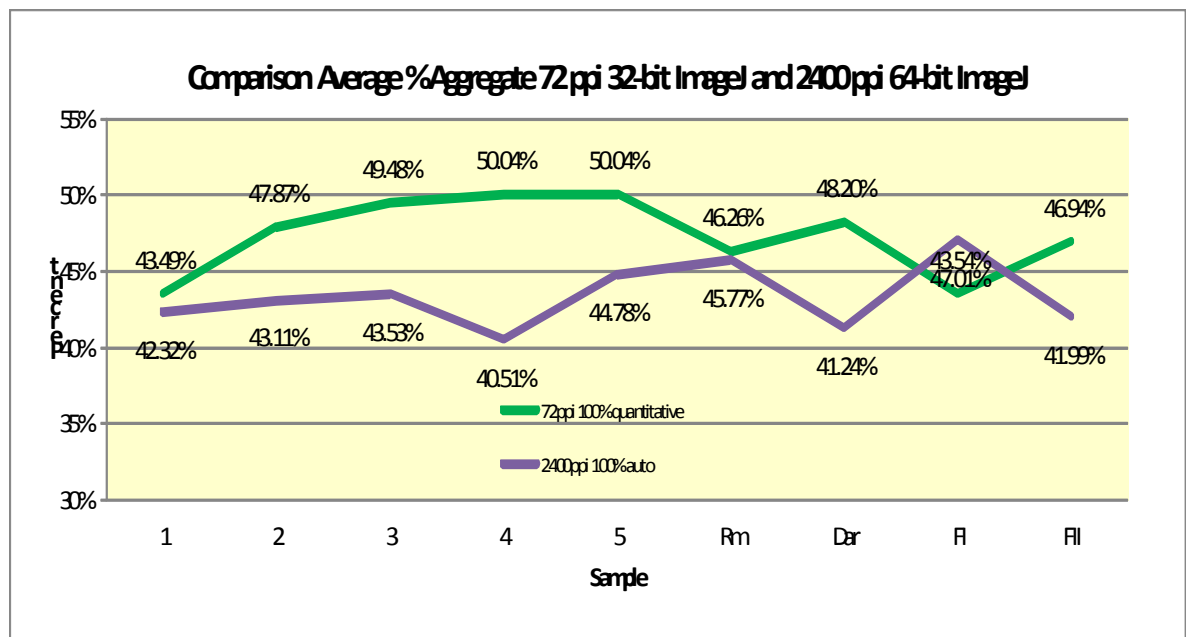


Figure 4.3.2.2.7 Comparison % Coarse Aggregate 72 ppi and 2400 ppi

4.3.3.1 Study 3 - Results for Calculations of Porosity 6400 ppi Digital Images

1A		1B		1C		1D		2A		2B	
180	385274	182	324489	182	297168	185	304049	186	159053	187	171573
181	336817	183	317814	183	275390	186	290978	187	146794	188	165328
182	324220	184	311261	184	261305	187	280301	188	136476	189	160331
183	315062	185	307707	185	246637	188	271576	189	128432	190	155580
184	307262	186	304963	186	237747	189	265395	190	120595	191	153999
185	300720	187	309653	187	229897	190	261841	191	116294	192	152393
186	298631	188	312616	188	225091	191	259292	192	111667	193	152450
187	297788	189	320682	189	223155	192	258413	193	109145	194	154470
188	298956	190	324797	190	219714	193	260307	194	107328	195	156929
189	302325	191	333814	191	218556	194	262119	195	107687	196	161067
190	304907	192	344119	192	221327	195	265939	196	108070	197	167340
191	309865	193	353780	193	224945	196	270132	197	110006	198	174205
192	314642	194	365906	194	229778	197	276289	198	113010	199	199512
193	319695	195	379162	195	237085	198	283219	199	128966	200	189000
194	327581	196	395351	196	246625	199	312070	200	123066	201	197256
195	336667	197	412923	197	257036	200	300286	201	127905	202	205789
196	346588	198	432029	198	267153	201	310657	202	134508	203	215565
197	359428	199	497605	199	322536	202	321488	203	141852	204	226043
198	370945	200	480371	200	297769	203	337849	204	148995	205	237896
199	416461	201	501105	201	314732	204	351535	205	159659	206	250760
200	395354	202	526913	202	332662	205	372446	206	168811	207	264898
201	407265	203	553969	203	353996	206	394062	207	178340	208	280688
202	420728	204	581222	204	378428	207	420242	208	188764	209	296220
203	431076	205	611140	205	405459	208	446557	209	199699	210	314542
204	447196	206	640515	206	431186	209	476843	210	210819	211	333897
205	464595	207	669225	207	458475	210	507546	211	227247	212	354682
206	478456	208	698990	208	488729	211	535831	212	240842	213	378742
207	492326	209	725181	209	519072	212	574100	213	256340	214	402014
208	506405	210	750705	210	547291	213	617847	214	273444	215	428983
209	521364	211	771825	211	578092	214	665279	215	290227	216	455153
210	534654	212	794823	212	607239	215	717166	216	311454	217	486934
211	545887	213	818307	213	634667	216	773788	217	330795	218	542915
212	559155	214	838077	214	660547	217	831887	218	367056	219	564499
213	571884	215	861780	215	681935	218	905590	219	379298	220	589141
214	585730	216	881840	216	710382	219	938351	220	404408	221	598366
215	598439	217	898298	217	739514	220	972279	221	433458	222	601921
216	609244	218	953078	218	801054	221	976504	222	459071	223	586644
217	619173	219	925223	219	795470	222	953409	223	483554	224	563021
218	653110	220	933458	220	817541	223	887709	224	501369	225	535105
219	629032	221	926584	221	833614	224	808136	225	499697	226	499856
220	620735	222	906921	222	827827	225	727814	226	493635	227	465616
221	607152	223	873565	223	800930	226	644049	227	480859	228	432540
222	582031	224	835550	224	767978	227	566233	228	453608	229	404563
223	551827	225	785333	225	714910	228	467563	229	419973	230	388249
224	512645	226	724252	226	661223	229	359195	230	385967	231	383682
225	471591	227	651284	227	590303	230	263675	231	336373	232	382349
226	433239	228	577847	228	515293	231	192526	232	290181	233	343921
227	397354	229	510312	229	437532	232	137726	233	234686	234	255584
228	357354	230	448574	230	365391	233	92907	234	168279	235	196143
229	317784	231	396523	231	306356	234	57242	235	114350	236	179571
230	289720	232	354937	232	258910	235	34959	236	78693	237	182030
231	262050	233	318262	233	210327	236	21371	237	57174	238	177295
232	233760	234	291250	234	171636	237	13257	238	39914	239	164897
233	208612	235	259308	235	139452	238	7431	239	28059	240	124401
234	187483	236	230594	236	123413	239	4381	240	18560	241	70472
235	172158	237	209544	237	132112	240	3250	241	11905	242	34769
236	167486	238	185190	238	175786	241	2911	242	7608	243	20653
237	177045	239	175779	239	248722	242	2794	243	4656	244	14058
238	179119	240	170469	240	317992	243	2844	244	2995	245	9300
239	180423	241	153216	241	345480	244	2854	245	1977	246	6734
240	164551	242	116666	242	287135	245	2771	246	1060	247	4852
241	140349	243	74886	243	103142	246	2322	247	569	248	4095
242	122570	244	44945	244	19634	247	1789	248	306	249	2969
243	118108	245	30951	245	3985	248	1341	249	285	250	2030
244	92698	246	24023	246	1644	249	959	250	217	251	1235
245	56733	247	13322	247	701	250	809	251	43	252	325
246	32579	248	5461	248	322	251	426	252	12	253	72
247	17642	249	2615	249	108	252	91	253	7	254	1
248	10727	250	1289	250	23	253	60	254	0	255	0
249	8214	251	1106	251	0	254	24	255	0		16978113
250	7203	252	1209	252	0	255	3		12576152		444728720
251	6048	253	1289	253	0		23134884		445619884		3.82%
252	4772	254	2433	254	0		447872632		2.82%		
253	3627	255	2945	255	0		5.17%				
254	2318		32073150		25357266						
255	1322		441166730		445626308						
	24743936		7.27%		5.69%						
	440658572										
	5.62%										

Table 4.3.3.1.1 Percentage of Porosity Samples 1A to 2B

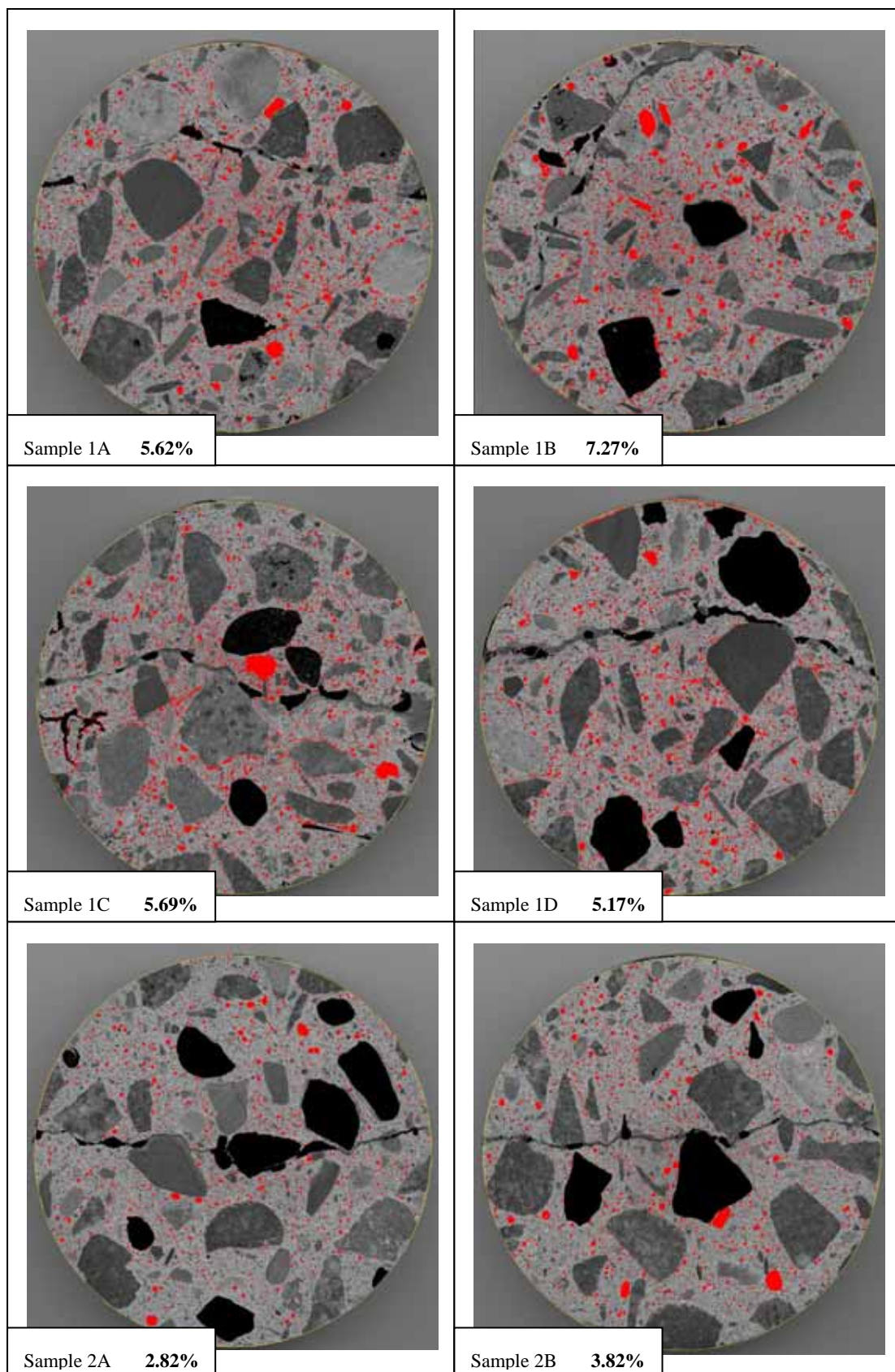


Figure 4.3.3.1.1 Porosity images 1A to 2B from ImageJ

3A		3B		4A		4B		5A		5B	
185	167664	185	189989	187	198217	177	352300	183	174281	180	312000
186	154845	186	173894	188	180871	178	335446	184	163923	181	282041
187	145029	187	162442	189	169614	179	320724	185	156522	182	258172
188	135412	188	153045	190	157704	180	306478	186	151756	183	234805
189	130305	189	147043	191	150689	181	296755	187	148032	184	216427
190	124025	190	142039	192	143759	182	288462	188	144084	185	202886
191	120779	191	138167	193	140436	183	281473	189	141844	186	192755
192	119437	192	136538	194	138759	184	275273	190	141293	187	182856
193	117505	193	135266	195	139306	185	271840	191	141018	188	176327
194	117492	194	134497	196	141131	186	269771	192	143851	189	172262
195	118784	195	136635	197	142887	187	267156	193	147059	190	168673
196	120514	196	138814	198	147883	188	264586	194	150873	191	165217
197	123593	197	143215	199	167258	189	263066	195	156251	192	162571
198	127863	198	147370	200	156395	190	263657	196	162461	193	161554
199	147407	199	163261	201	162355	191	264426	197	169358	194	162146
200	139300	200	158700	202	168813	192	264184	198	172460	195	163462
201	146866	201	165057	203	177019	193	268073	199	179359	196	166464
202	154131	202	172949	204	184074	194	272284	200	192110	197	172081
203	162693	203	181410	205	194135	195	276508	201	206122	198	176307
204	171881	204	191607	206	203130	196	283004	202	223686	199	182828
205	183725	205	202792	207	215279	197	290386	203	243577	200	191640
206	195845	206	214514	208	228043	198	300844	204	267698	201	202593
207	208701	207	228218	209	241948	199	311667	205	293493	202	211946
208	222718	208	243263	210	255245	200	326324	206	323606	203	224860
209	237366	209	255370	211	269383	201	342706	207	352448	204	239481
210	254151	210	271219	212	286568	202	358092	208	384056	205	256111
211	270869	211	286477	213	304669	203	376034	209	421500	206	275255
212	288099	212	301615	214	323247	204	394639	210	462278	207	296794
213	309336	213	314267	215	345676	205	415047	211	507640	208	319526
214	332749	214	329341	216	370907	206	434699	212	553234	209	341717
215	354410	215	347348	217	402239	207	455209	213	604058	210	368341
216	378161	216	357691	218	444219	208	473011	214	654291	211	399935
217	404669	217	362424	219	459731	209	485063	215	698740	212	433823
218	445093	218	367655	220	497381	210	493840	216	722718	213	472359
219	460856	219	355435	221	528704	211	497806	217	722503	214	517952
220	487708	220	351126	222	557033	212	500570	218	731132	215	565802
221	514686	221	342496	223	584648	213	509875	219	726464	216	617797
222	539714	222	330802	224	605517	214	522187	220	708630	217	672596
223	555289	223	322571	225	616649	215	540787	221	691705	218	739648
224	553223	224	304944	226	607811	216	555899	222	648889	219	804155
225	544078	225	274726	227	606032	217	575509	223	611330	220	859040
226	525407	226	245513	228	594303	218	598642	224	584351	221	889701
227	498659	227	223760	229	566055	219	622469	225	547117	222	895885
228	471676	228	199063	230	518979	220	640019	226	503968	223	868153
229	460450	229	176527	231	462829	221	650039	227	452637	224	826270
230	448898	230	160718	232	398585	222	667491	228	410286	225	780031
231	431966	231	145977	233	348877	223	674193	229	378982	226	735612
232	405077	232	140333	234	318139	224	657596	230	353376	227	687022
233	377439	233	145027	235	277391	225	628105	231	334763	228	632232
234	357427	234	153175	236	236502	226	602434	232	327811	229	566624
235	336971	235	166881	237	196157	227	578348	233	334321	230	495349
236	323491	236	184245	238	142878	228	558762	234	347830	231	437627
237	314848	237	190774	239	115594	229	533351	235	355336	232	398047
238	313823	238	177932	240	101092	230	468226	236	332456	233	361342
239	339053	239	150469	241	102620	231	396405	237	302201	234	325657
240	377221	240	113500	242	107785	232	290823	238	241391	235	291350
241	417633	241	73230	243	104127	233	197186	239	154241	236	243893
242	449573	242	32948	244	85538	234	145769	240	76715	237	186223
243	453155	243	10890	245	37772	235	108881	241	31283	238	131180
244	383423	244	3357	246	9401	236	84463	242	13056	239	80662
245	268333	245	1204	247	3401	237	65956	243	5243	240	44617
246	102205	246	530	248	1812	238	48730	244	2806	241	24100
247	12867	247	343	249	968	239	38140	245	2276	242	11448
248	1792	248	184	250	443	240	27809	246	2263	243	6068
249	677	249	102	251	305	241	21096	247	2366	244	4380
250	590	250	57	252	290	242	17196	248	2258	245	3369
251	498	251	34	253	237	243	14093	249	2323	246	2791
252	330	252	5	254	187	244	11575	250	2641	247	2264
253	196	253	1	255	106	245	9779	251	3444	248	2229
254	50	254	0		16747737	246	8627	252	3984	249	2313
255	8	255	0		437062508	247	7067	253	2987	250	2321
	18560707		12173011		3.83%	248	6671	254	1843	251	2106
	444728720		444266820			249	7327	255	2056	252	2142
	4.17%		2.74%			250	10616		20714944	253	2278
						251	7904		452389056	254	2325
						252	4916		4.58%	255	7996
						253	4501				22878812
						254	3502				453294176
						255	11790				5.05%
							24276157				
							433998884				
							5.59%				

Table 4.3.3.1.2 Percentage of Porosity Samples 3A to 5B

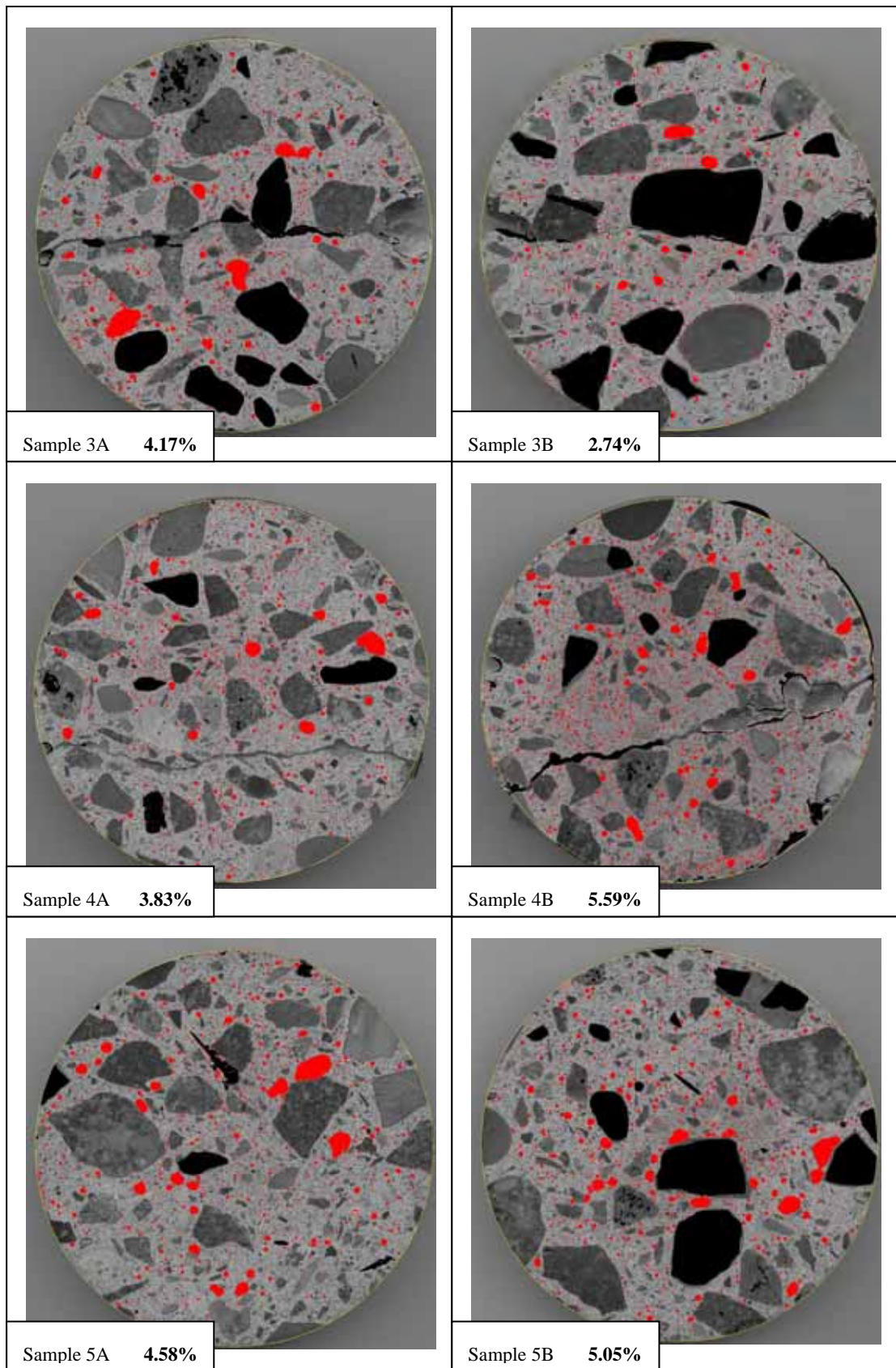


Figure 4.3.3.1.2 Porosity images 3A to 5B from ImageJ

RmA		RmB		DarA		DarB	
171	313630	181	186367	186	214319	188	152080
172	285680	182	183356	187	183048	189	136732
173	262261	183	181149	188	156911	190	125665
174	243577	184	180234	189	136508	191	118170
175	227131	185	180097	190	119368	192	111252
176	215622	186	181266	191	106928	193	107465
177	207197	187	182079	192	96994	194	104264
178	200549	188	185444	193	87551	195	103088
179	195886	189	187618	194	80923	196	103579
180	192391	190	191221	195	74812	197	104041
181	190577	191	195222	196	70434	198	105409
182	191298	192	200267	197	66617	199	107065
183	191659	193	206269	198	64792	200	111288
184	190965	194	214822	199	63511	201	115990
185	193743	195	223032	200	62368	202	121341
186	196892	196	233892	201	62212	203	128495
187	201304	197	244623	202	63305	204	140081
188	204411	198	260936	203	64845	205	152212
189	209266	199	274863	204	67051	206	166153
190	213923	200	292802	205	70460	207	181513
191	220767	201	312459	206	73502	208	198237
192	227416	202	332271	207	77577	209	216644
193	235171	203	357429	208	82602	210	242125
194	243744	204	384401	209	87471	211	270289
195	251584	205	416541	210	92374	212	294277
196	259653	206	446718	211	98753	213	318116
197	270035	207	478128	212	106397	214	340480
198	281751	208	508073	213	115405	215	362745
199	293541	209	537776	214	123997	216	369758
200	305086	210	572616	215	133425	217	370923
201	317715	211	602678	216	143274	218	364354
202	330284	212	631790	217	152552	219	358100
203	344698	213	661096	218	161888	220	355792
204	359214	214	684879	219	170213	221	361953
205	375155	215	703142	220	179278	222	369999
206	393843	216	720247	221	186202	223	374344
207	410771	217	724529	222	190760	224	364380
208	431935	218	710173	223	194489	225	366651
209	452879	219	680834	224	197393	226	361028
210	473726	220	649941	225	206448	227	335995
211	495657	221	603978	226	211539	228	282302
212	519697	222	543848	227	211615	229	236458
213	548193	223	475038	228	212948	230	213466
214	570791	224	404957	229	215825	231	188478
215	591477	225	346156	230	210637	232	153950
216	616282	226	284470	231	202956	233	129292
217	635628	227	228996	232	182184	234	113200
218	660821	228	181916	233	172701	235	103481
219	682707	229	147937	234	171255	236	101264
220	691233	230	120394	235	177205	237	108709
221	684200	231	96718	236	196983	238	118366
222	668680	232	78952	237	218587	239	128807
223	650731	233	57939	238	215816	240	145968
224	615467	234	37721	239	190360	241	174374
225	571325	235	22296	240	148828	242	225429
226	526271	236	11442	241	76982	243	283373
227	475241	237	4861	242	37011	244	170792
228	418825	238	2335	243	20313	245	35857
229	363225	239	1373	244	10083	246	7143
230	308417	240	662	245	4861	247	3438
231	257162	241	422	246	3402	248	2352
232	204620	242	352	247	2429	249	1914
233	163269	243	293	248	1707	250	1878
234	130142	244	286	249	1736	251	1590
235	107377	245	273	250	2165	252	1124
236	86883	246	255	251	2361	253	445
237	68006	247	208	252	2441	254	96
238	54633	248	193	253	2468	255	7
239	45608	249	136	254	3287		12025626
240	34674	250	72	255	7418		450127480
241	24352	251	65		7805060		2.67%
242	17577	252	132		447872632		
243	12004	253	199		1.74%		
244	7780	254	177				
245	5155	255	71				
246	2928		18956403				
247	1661		451936108				
248	1309		4.19%				
249	784						
250	360						
251	199						
252	103						
253	88						
254	65						
255	0						
	23328537						
	454651360						
	5.13%						

Table 4.3.3.1.3 Percentage of Porosity Samples RmA to DarB

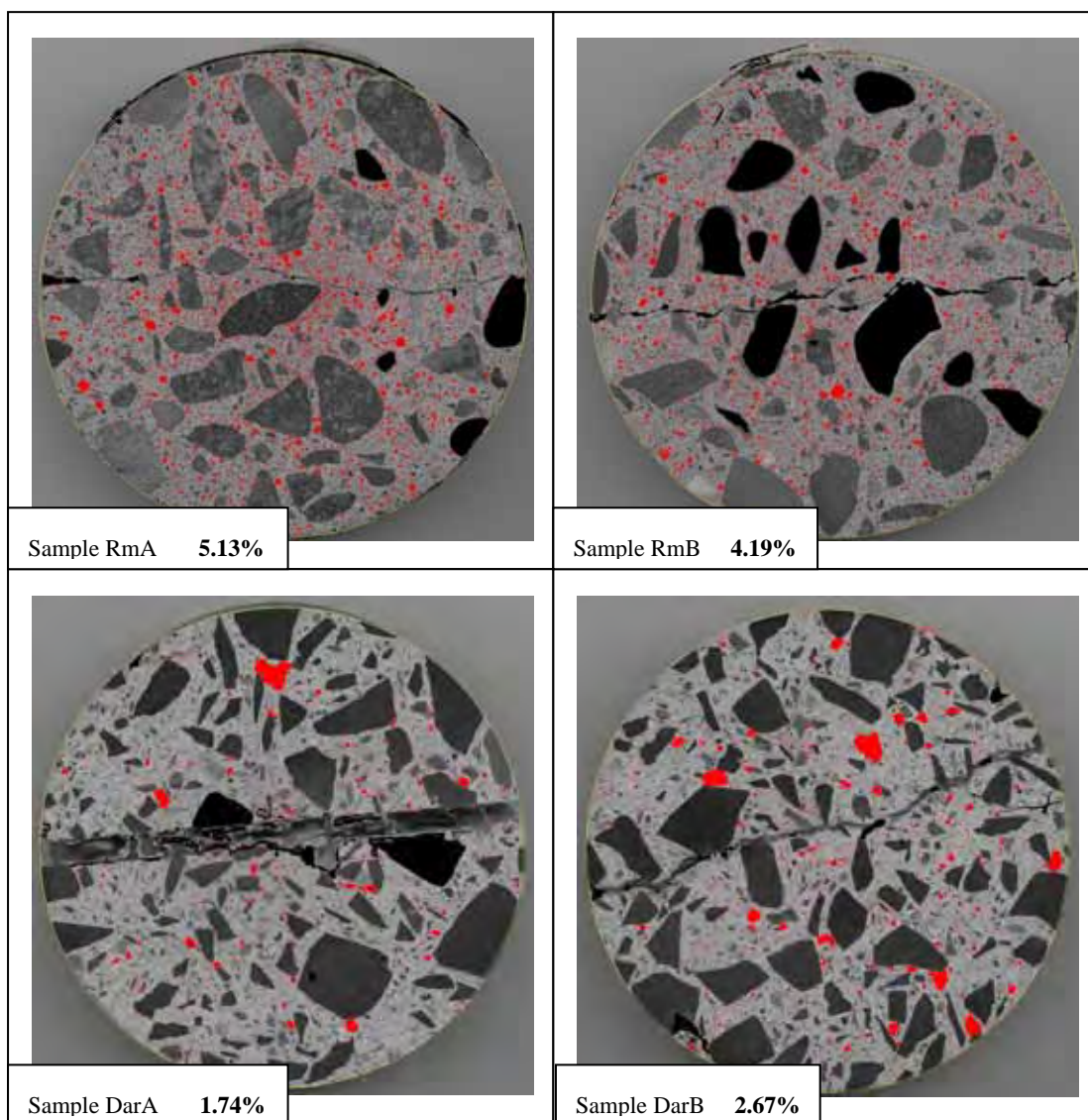


Figure 4.3.3.1.3 Porosity images RmA to DarB from ImageJ

F1A		F1B		F11A		F11B	
160	159098	160	167615	190	118485	184	203743
161	151073	161	155517	191	111869	185	184190
162	125143	162	133051	192	104924	186	167012
163	111231	163	118376	193	100621	187	153977
164	101107	164	106357	194	96401	188	143828
165	93808	165	96773	195	94637	189	134706
166	87293	166	87733	196	93959	190	128101
167	80523	167	79643	197	92839	191	123835
168	75366	168	74042	198	91817	192	121169
169	71145	169	68879	199	90408	193	120020
170	66406	170	65226	200	90007	194	116215
171	62197	171	61302	201	89782	195	109924
172	59087	172	58511	202	90111	196	103486
173	55731	173	56268	203	91905	197	99255
174	52621	174	53967	204	94625	198	96213
175	49694	175	51997	205	96856	199	94171
176	47782	176	50732	206	98954	200	92423
177	46600	177	49521	207	101274	201	91712
178	45641	178	48450	208	104322	202	91459
179	44409	179	47323	209	108957	203	92284
180	46060	180	48260	210	114619	204	93670
181	41180	181	45436	211	120344	205	95259
182	40882	182	44702	212	126079	206	97417
183	39719	183	44036	213	133465	207	99797
184	38552	184	43399	214	142809	208	103403
185	37997	185	43293	215	153703	209	107684
186	38029	186	43098	216	165625	210	114312
187	38662	187	43191	217	180150	211	120919
188	38757	188	43045	218	193309	212	129980
189	39240	189	43485	219	211121	213	141647
190	39913	190	43661	220	229844	214	154603
191	40984	191	45078	221	249906	215	168964
192	41735	192	45716	222	269283	216	189019
193	43741	193	46176	223	293602	217	213431
194	45874	194	44468	224	316684	218	244011
195	46217	195	44362	225	336268	219	279081
196	48147	196	44575	226	350957	220	313576
197	51826	197	46735	227	366956	221	348972
198	54065	198	48283	228	377229	222	396498
199	58822	199	52602	229	385807	223	451618
200	57908	200	51817	230	386307	224	512501
201	61975	201	53413	231	375053	225	566386
202	65385	202	54653	232	358194	226	597072
203	68295	203	55340	233	340874	227	589520
204	72355	204	57102	234	321706	228	550068
205	76706	205	58718	235	296209	229	500105
206	79661	206	59126	236	274840	230	437054
207	84924	207	60849	237	253780	231	369971
208	89182	208	62305	238	241055	232	315735
209	94620	209	63828	239	234736	233	282359
210	100597	210	66835	240	228104	234	258656
211	103095	211	69404	241	237616	235	245677
212	104126	212	71061	242	293857	236	247003
213	105176	213	72722	243	432846	237	261222
214	105456	214	73647	244	419479	238	265390
215	104866	215	74065	245	264255	239	245144
216	104447	216	73656	246	188934	240	181102
217	103000	217	73629	247	131995	241	146347
218	102517	218	74326	248	84298	242	144824
219	96114	219	71096	249	39971	243	173141
220	95551	220	68435	250	7818	244	227168
221	95052	221	64104	251	405	245	300755
222	91320	222	59640	252	158	246	386972
223	82520	223	54609	253	45	247	476179
224	76350	224	51901	254	0	248	491939
225	70943	225	49705	255	0	249	354182
226	67434	226	46334		12093048	250	179831
227	60172	227	45402		437583712	251	58156
228	48085	228	42728		2.76%	252	21109
229	32685	229	38741			253	5704
230	21165	230	32209			254	1971
231	15131	231	22710			255	1889
232	14285	232	17696				15726716
233	14698	233	13258				440699568
234	15671	234	10609				3.57%
235	17269	235	7629				
236	18669	236	5245				
237	20525	237	4470				
238	22710	238	3058				
239	29157	239	2484				
240	40187	240	1970				
241	52814	241	1355				
242	48483	242	848				
243	21189	243	560				
244	3558	244	362				
245	1493	245	118				
246	1358	246	31				
247	1508	247	28				
248	1589	248	22				
249	1658	249	8				
250	1873	250	3				
251	2289	251	1203				
252	3280	252	0				
253	3352	253	0				
254	2332	254	0				
255	114560	255	0				
	5447677		4479951				
	441147584		444282868				
	1.23%		1.01%				

Table 4.3.3.1.4 Percentage of Porosity Samples FIA to FIIB

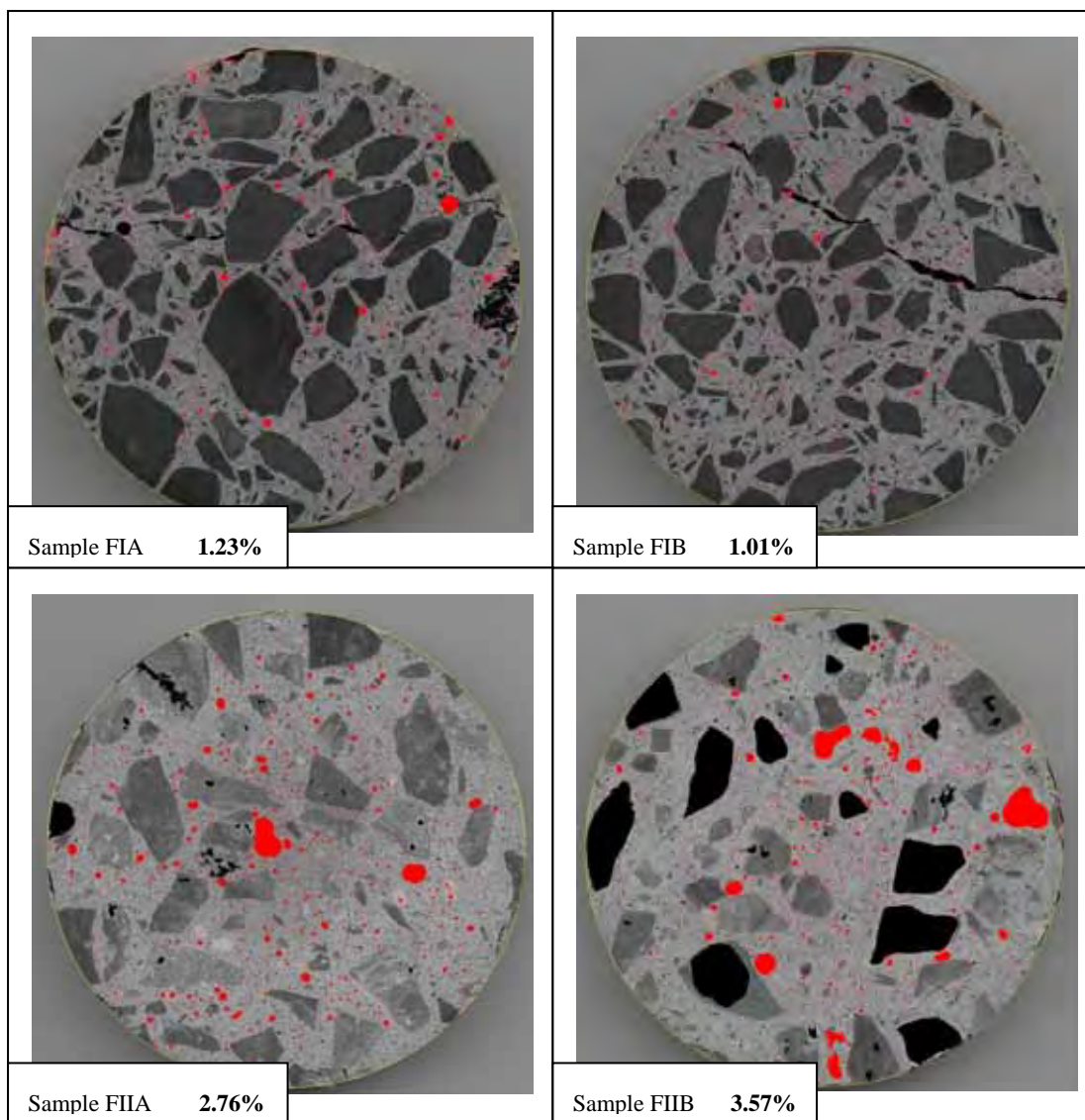


Figure 4.3.3.1.4 Porosity images FIA to FIIB from ImageJ

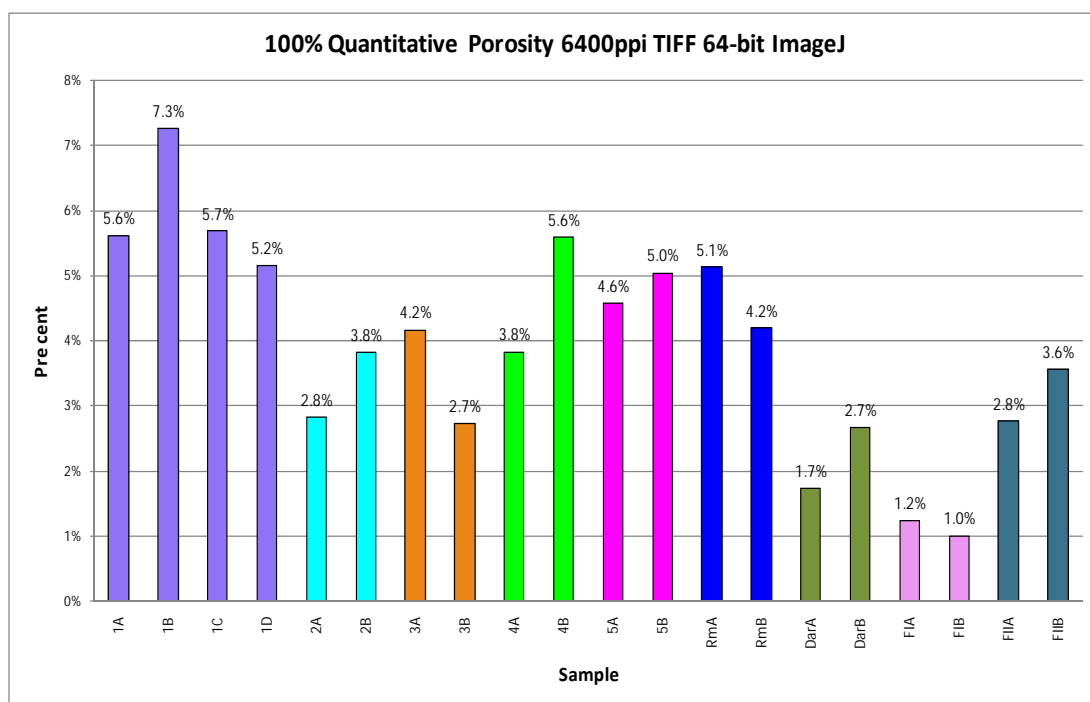


Figure 4.3.3.1.5 Percentage of Porosity of all samples

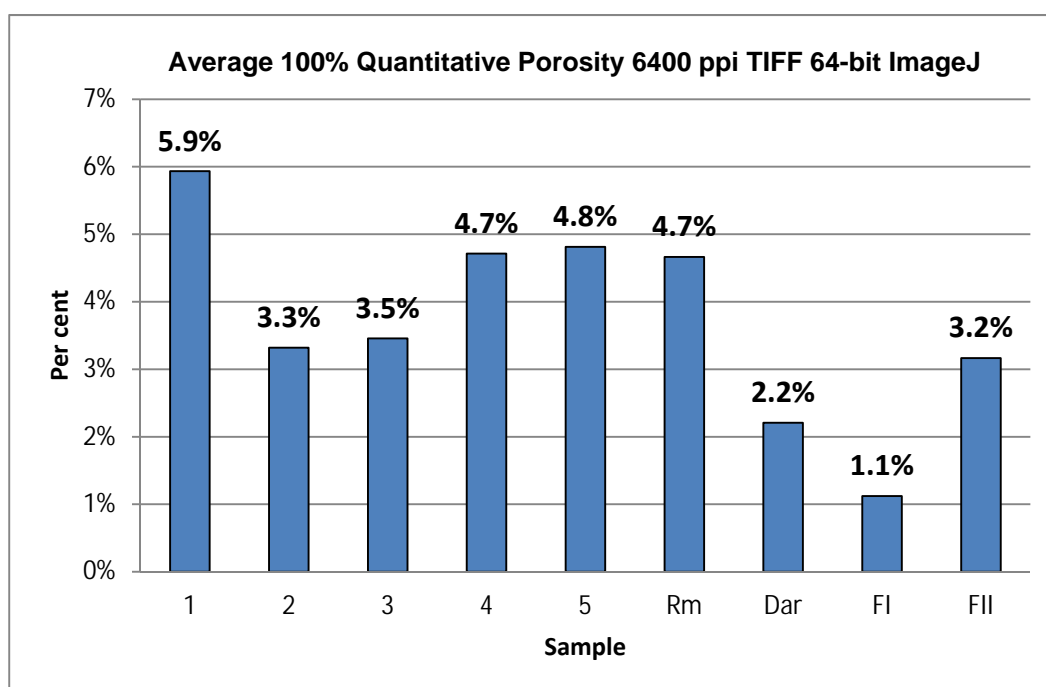


Figure 4.3.3.1.6 Average Percentage of Porosity of each core sample

Observations and Explanations

Figures 4.3.3.1.5 and 4.3.3.1.6 are 100% quantitative results. The 6400 ppi was the most accurate analysis in the thesis. The profiles of both calculations are very close.

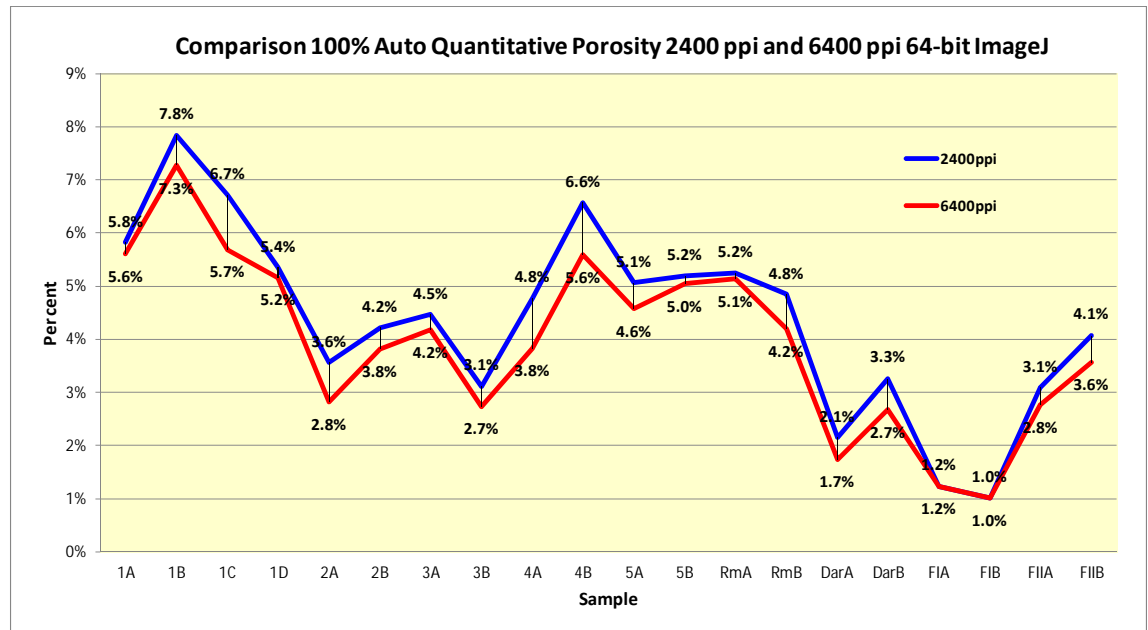


Figure 4.3.3.1.7 Comparison % Porosity 2400 ppi and 6400 ppi 64-bit ImageJ

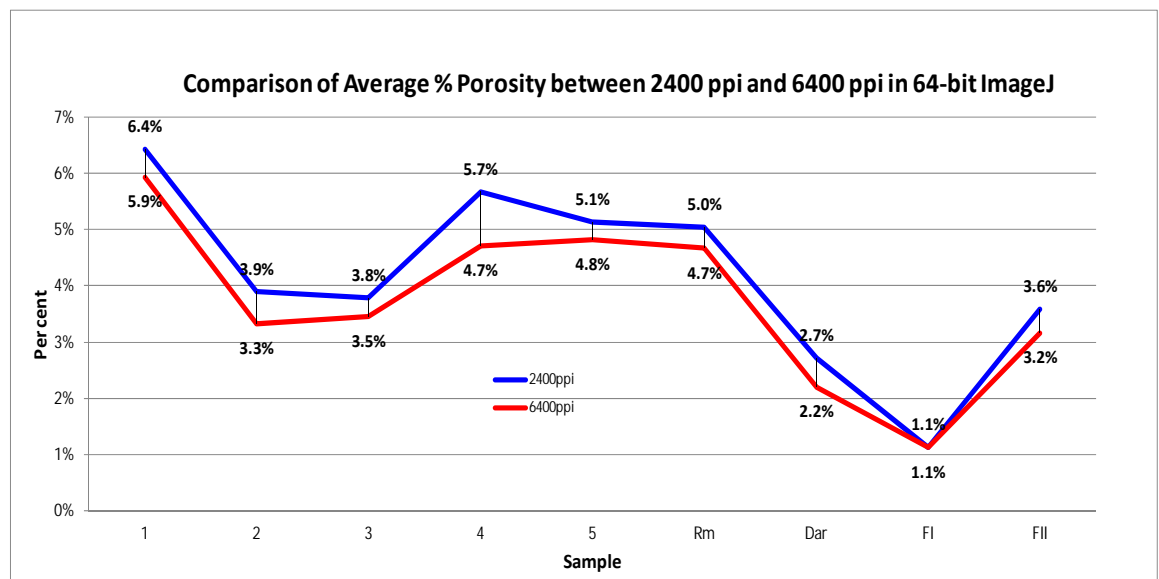


Figure 4.3.3.1.8 Comparison Average % Porosity 2400 ppi and 6400 ppi

4.3.3.2 Study 3 - Results for 100% Quantitative Calculations of Coarse Aggregate Percentage 4800 ppi in 64-bit ImageJ

1A		1B		1C		1D		2A		2B	
14	7159	14	18895	14	18688	14	7702	14	3302	14	5090
15	8421	15	13111	15	23272	15	15154	15	4662	15	5115
16	8360	16	17960	16	19804	16	15707	16	4040	16	4119
17	9543	17	21780	17	15589	17	13663	17	2640	17	4471
18	11773	18	24000	18	21918	18	13634	18	3559	18	5020
19	12691	19	30144	19	17988	19	15170	19	3174	19	7705
20	11281	20	24607	20	22953	20	14683	20	3960	20	6260
21	9437	21	20716	21	27857	21	15893	21	4785	21	4535
22	7410	22	14020	22	31874	22	9838	22	6161	22	2713
23	8585	23	12783	23	22199	23	13149	23	6268	23	2996
24	9472	24	11452	24	20346	24	15351	24	3810	24	3058
25	7639	25	12405	25	15696	25	13930	25	2865	25	3616
26	6892	26	11204	26	13272	26	9761	26	3290	26	3540
27	4728	27	9619	27	11812	27	11311	27	2603	27	2831
28	4278	28	10398	28	10171	28	10072	28	2335	28	3145
29	3876	29	13658	29	8941	29	8469	29	1907	29	3542
30	4749	30	11728	30	11324	30	8391	30	2145	30	3648
31	4583	31	7909	31	12797	31	10903	31	2532	31	3188
32	4081	32	9511	32	13090	32	10287	32	2853	32	3141
51	25828	51	42497	51	43482	51	35070	51	41536	51	49764
52	28966	52	45818	52	46712	52	38775	52	46527	52	54935
53	31964	53	50601	53	50622	53	44401	53	52248	53	60721
54	34440	54	56415	54	52987	54	48796	54	56723	54	65544
55	37903	55	64950	55	57150	55	52251	55	60360	55	68955
56	41286	56	74596	56	65440	56	58241	56	62255	56	73352
57	44179	57	80861	57	70412	57	63809	57	62754	57	75197
58	48241	58	87607	58	75984	58	67718	58	65261	58	78327
59	51570	59	93831		103843791	59	72456	59	66898	59	81899
60	55695	60	102914		251083472	60	80033	60	68399		108612901
61	60490		83019546		41.36%	61	85863	61	70671		250406648
62	65121		247726696				108686951	62	74019		43.37%
63	71463		33.51%				251757980	63	79559		
64	79221						43.17%	64	86007		
65	87291								110048409		
	113858409								250409736		
	248044340								43.95%		
	45.90%										

Table 4.3.3.2.1 Percentage of Coarse Aggregate Samples 1A to 2B

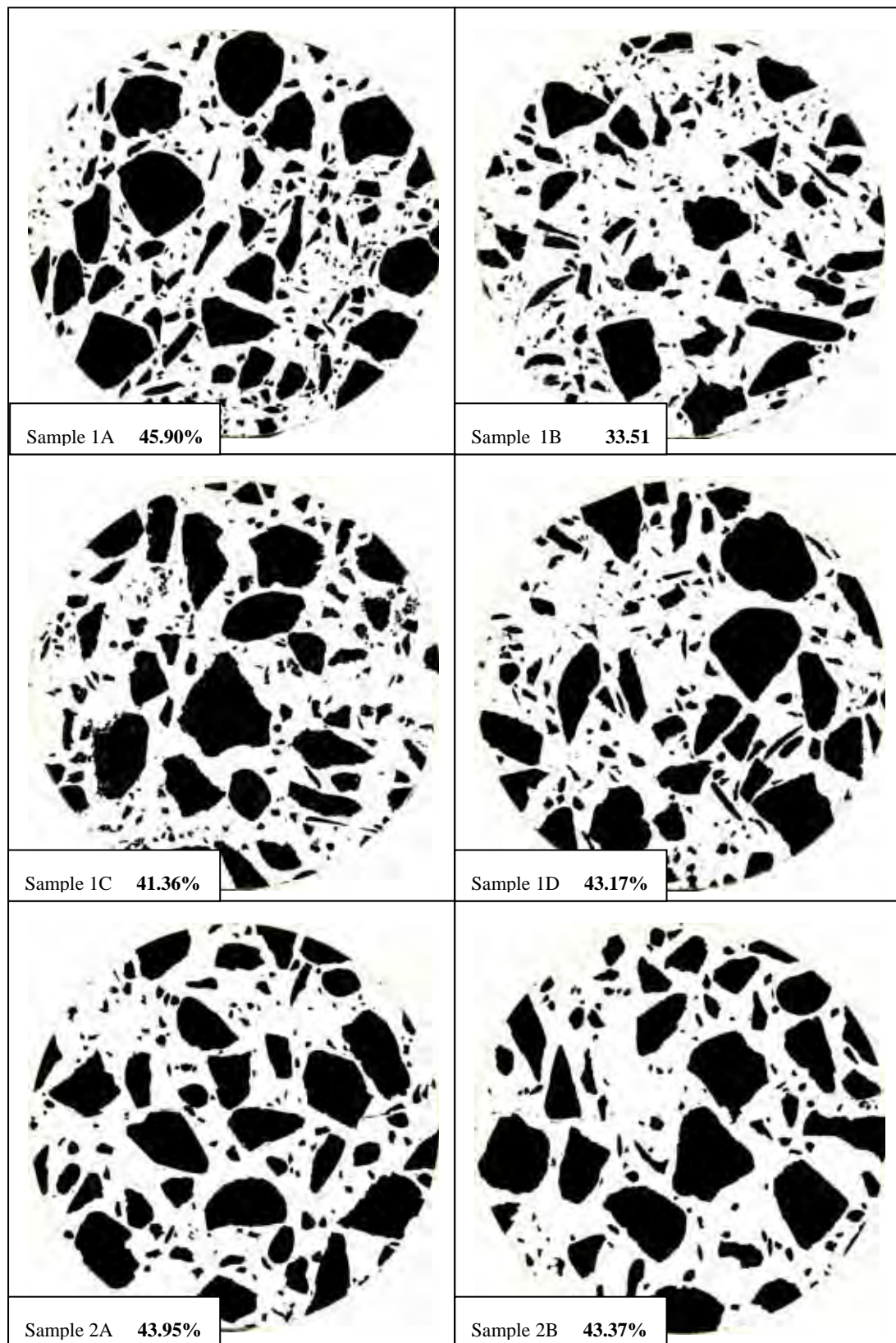


Figure 4.3.3.2.1 Coarse Aggregate Images 1A to 2B from ImageJ

3A		3B		4A		4B		5A		5B	
								3361	10	4073	10
12	6858	12	4519	12	5004	12					4930
13	5407	13	4510	13	5564	13	2129	13	3713	13	5087
14	4917	14	5437	14	5286	14	3943	14	4431	14	5352
15	4339	15	5069	15	6945	15	2223	15	4069	15	5733
16	5387	16	3874	16	5258	16	4125	16	3933	16	5890
17	7020	17	3434	17	4775	17	5392	17	4291	17	8375
18	10213	18	3305	18	4437	18	5044	18	4836	18	8241
19	8119	19	3288	19	5342	19	3478	19	6421	19	10142
20	6443	20	3581	20	5828	20	4529	20	8323	20	12845
21	5740	21	3414	21	4323	21	4580	21	9346	21	10243
22	4245	22	3472	22	5192	22	6039	22	7475	22	9285
23	4422	23	2750	23	5036	23	8184	23	5885	23	9702
24	4839	24	3083	24	3928	24	7218	24	4104	24	7476
25	4969	25	3571	25	3899	25	6887	25	4387	25	6170
26	5592	26	3394	26	3567	26	5956	26	4370	26	6389
27	4177	27	4007	27	3700	27	4470	27	3305	27	5958
28	4221	28	3841	28	4019	28	5089	28	3074	28	3341
29	4254	29	3817	29	4086	29	5113	29	3137	29	3269
30	5127	30	4906	30	3610	30	3790	30	3216	30	3962
31	5562	31	4704	31	3360	31	3595	31	4511	31	4103
32	6040	32	5765	32	3593	32	3435	32	6962	32	4623
33	7271	33	6786	33	3770	33	3723	33	8399	33	4960
						34	3883	34	8576	34	5785
55	44947	55	69728	55	37421	55					21913
56	47607	56	71765	56	42925	56	55614	56	43459	56	27978
57	49775	57	73003	57	48418	57	59598	57	47338	57	30787
58	52265	58	75079	58	53677	58	65040	58	51739	58	34717
59	53769	59	75957	59	59262	59	71191	59	56471	59	35369
60	57299	60	76220	60	65412	60	78689	60	60783	60	37206
61	60384	61	75852	61	71088	61	85146	61	65510	61	39428
62	63571	62	77935	62	77271	62	92573	62	71286	62	42036
63	67903	63	81701	63	83863	63	105007	63	77645	63	45626
64	73174	64	85654	64	91022		87948072	64	84398	64	48579
65	81009	65	90871		97480944		246368820	65	91303	65	51802
66	85875	66	94429		247683204		35.70%	66	95713	66	56786
67	89857		111366586		39.36%			67	101626	67	62219
68	96448		250745036					68	108296	68	67978
69	104490		44.41%						101925175	69	73102
	107312582								255827456	70	79833
	250745036								39.84%	71	85870
	42.80%									72	94201
											116845664
											253790416
											46.04%

Table 4.3.3.2.2 Percentage of Coarse Aggregate Samples 3A to 5B

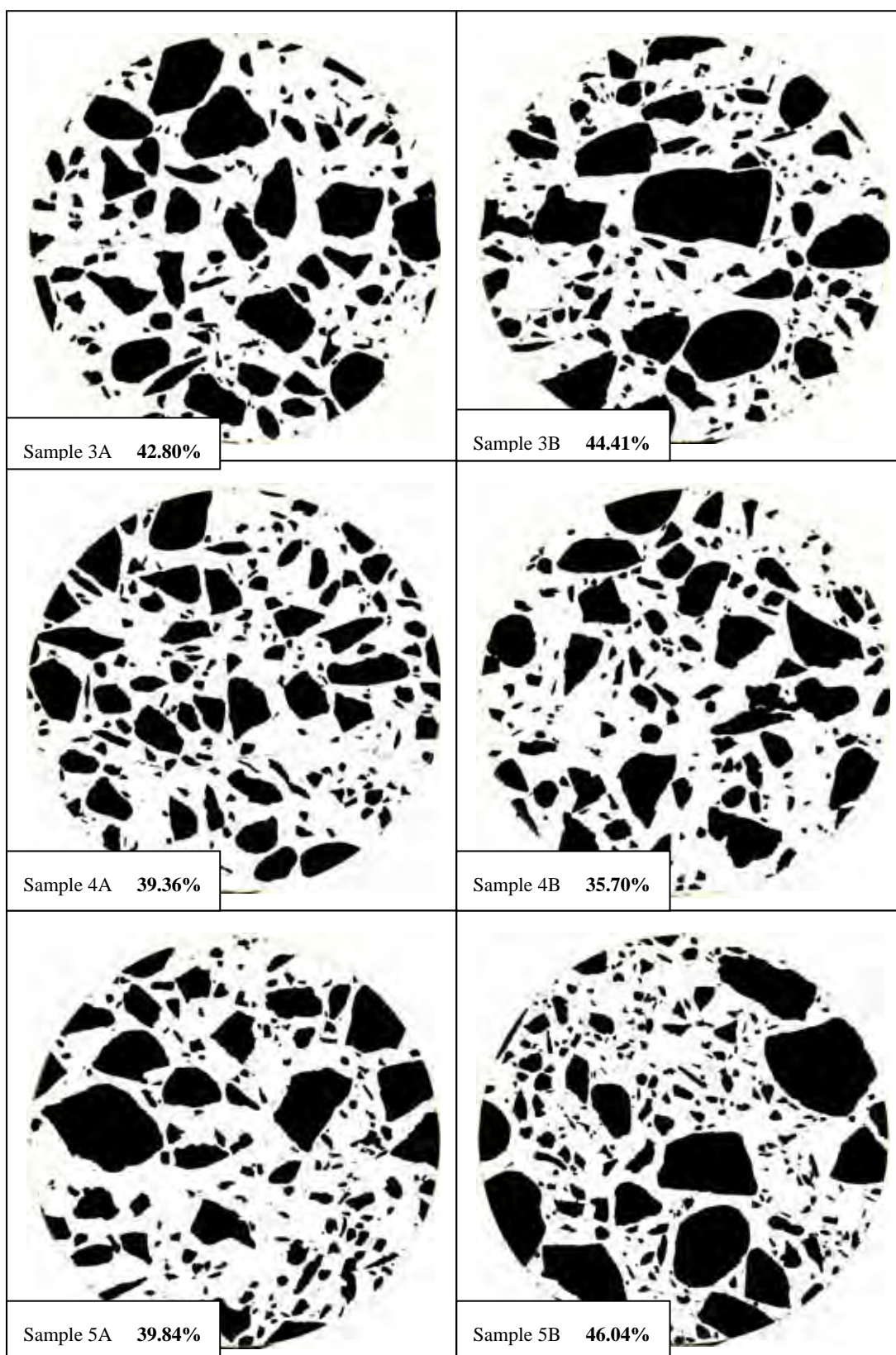


Figure 4.3.3.2.2 Coarse Aggregate Images 3A to 5B from ImageJ

RmA		RmB		DarA		DarB	
12		12	2597	12	8712	12	6447
14	2459	14	751				
15	3331	15	5718	15	12945	15	7407
16	4257	16	6017	16	18881	16	7031
17	4865	17	5034	17	22085	17	7604
18	4301	18	6860	18	21811	18	7195
19	4108	19	8943	19	25355	19	7982
20	6771	20	7806	20	25650	20	8589
21	5879	21	6698	21	24592	21	7708
22	4153	22	7123	22	27218	22	7033
23	3829	23	3322	23	26866	23	7885
24	3896	24	3070	24	26450	24	7959
40	27113	40	17758		249740780	40	19452
41	36673	41	20191		42.05%	41	23525
42	45678	42	23015			42	27326
43	53609	43	27089			43	31098
44	59284	44	31592			44	35367
45	62193	45	36071			45	39459
46	65205	46	40195			46	43264
47	69404	47	44151			47	47548
48	74647	48	50660			48	51412
49	81136	49	57344			49	55846
50	87244	50	63717			50	60528
51	94314	51	70999			51	63282
	107095441	52	77941			52	66527
	255147576	53	84119			53	69945
	41.97%	54	86969			54	71976
		55	88999			55	73569
		56	91884			56	75906
		57	95148			57	80914
		58	99027			58	85847
			104039107			59	89672
			255147576			60	94072
			40.78%			61	98368
						62	102843
						63	107010
						64	112168
						65	118167
						66	121194
							100076202
							253109720
							39.54%

Table 4.3.3.2.3 Percentage of Coarse Aggregate Samples RmA to DarB

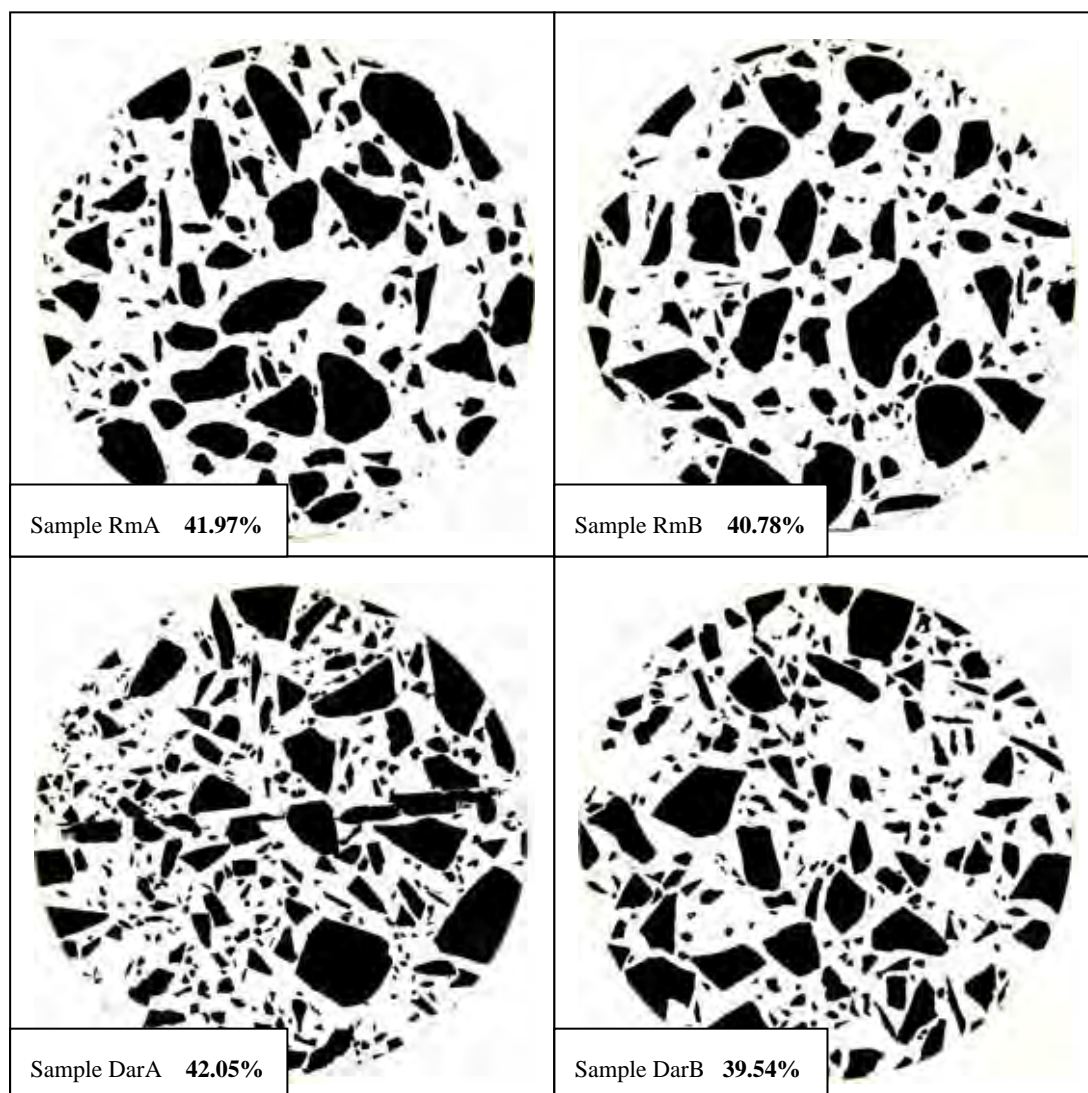


Figure 4.3.3.2.3 Coarse Aggregate Images RmA to DarB from ImageJ

F1A		F1B		F11A		F11B	
				3	9071	3	9444
5	5420	5					
6	6992	6	7083	6	3071	6	3404
7	6797	7	7557	7	2429	7	3202
8	7610	8	6376	8	2314	8	4011
9	5930	9	8007	9	1422	9	2091
10	6630	10	7854	10	1708	10	2243
11	8560	11	9141	11	1235	11	2133
12	7076	12	7930	12	1192	12	1655
			7480	13	1155	13	1533
	119272240		102582193	49	5420	49	7979
	247392864		248733604	50	5970	50	8123
	48.21%		41.24%	51	6738	51	8714
				52	8029	52	9093
				53	9258	53	10152
				54	10170	54	10665
				55	11106	55	11120
				56	12303	56	11982
				57	13389	57	13018
				58	14769	58	14764
				59	15709	59	16167
				60	16859	60	17410
				61	17832	61	19158
				62	18503	62	20880
				63	20270	63	22751
				64	21442	64	24700
				65	22767	65	27284
				66	23420	66	29051
				67	25101	67	30658
				68	26642	68	31589
				69	28632	69	32408
				70	30416	70	33428
				71	32481	71	34653
				72	35413	72	36877
				73	39417	73	38759
				74	42348	74	40030
				75	46685	75	42226
				76	50581	76	43861
				77	54417	77	46094
				78	59200	78	49055
				79	64839	79	51575
				80	70713	80	54078
				81	77321	81	58188
				82	83089	82	63100
				83	89778	83	68572
				84	96164	84	73645
				85	102717	85	79341
					104372744	86	85002
					247058888	87	92229
					42.25%	88	101831
						89	110686
							109135304
							248398092
							43.94%

Table 4.3.3.2.4 Percentage of Coarse Aggregate Samples F1A to FIIB

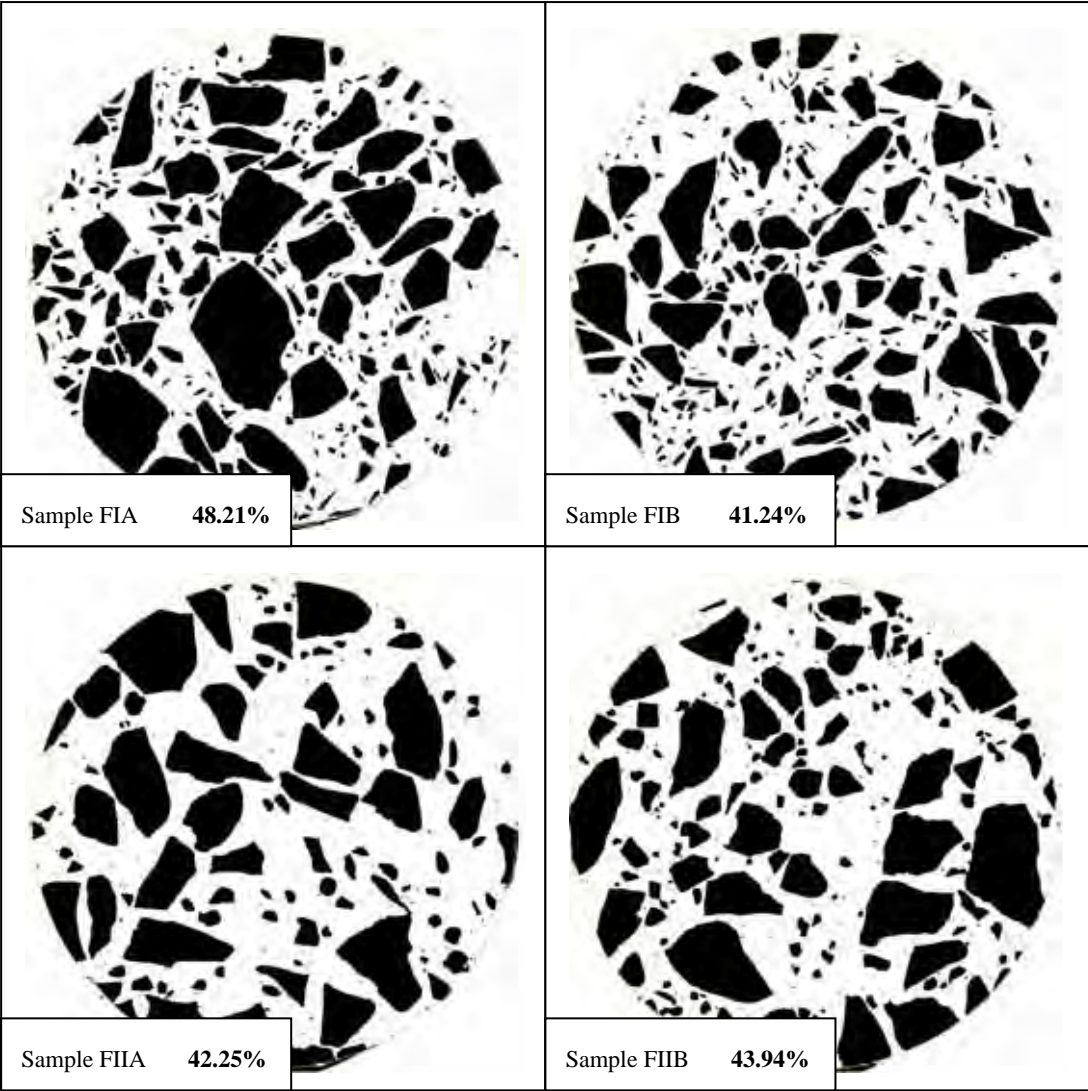


Figure 4.3.3.2.4 Coarse Aggregate Images FIA to FIIB from ImageJ

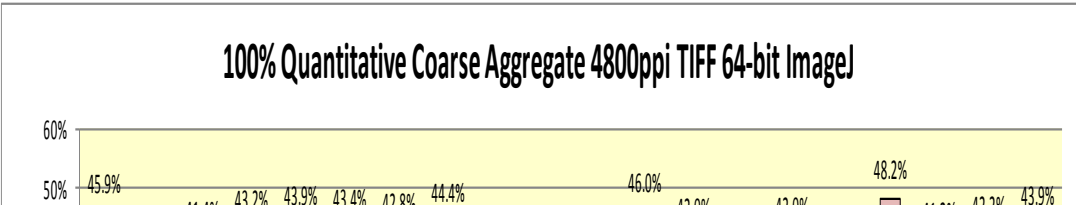


Figure 4.3.3.2.5 Percentage of Coarse Aggregate of all samples

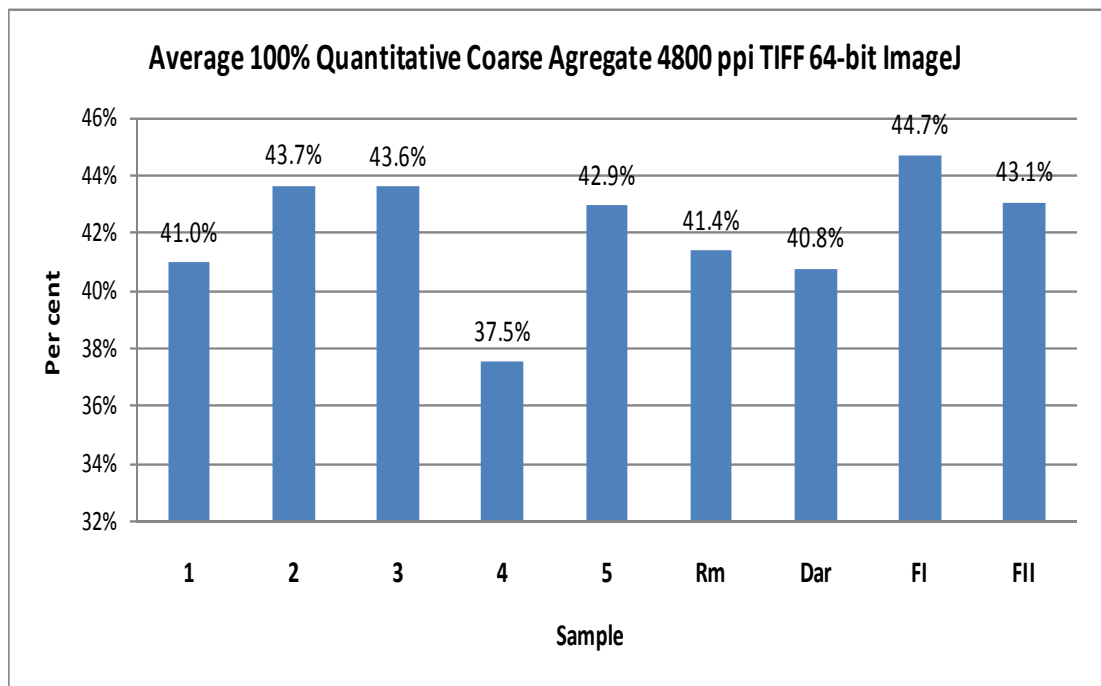


Figure 4.3.3.2.6 Average Percentage of Coarse Aggregate of each core sample

Observations and Explanations

All results in this study are 100% quantitative and 100% calculated.

In the following Study 4.3.3.3 automatic calculations will be compared and calibrated against the reference values from this study.

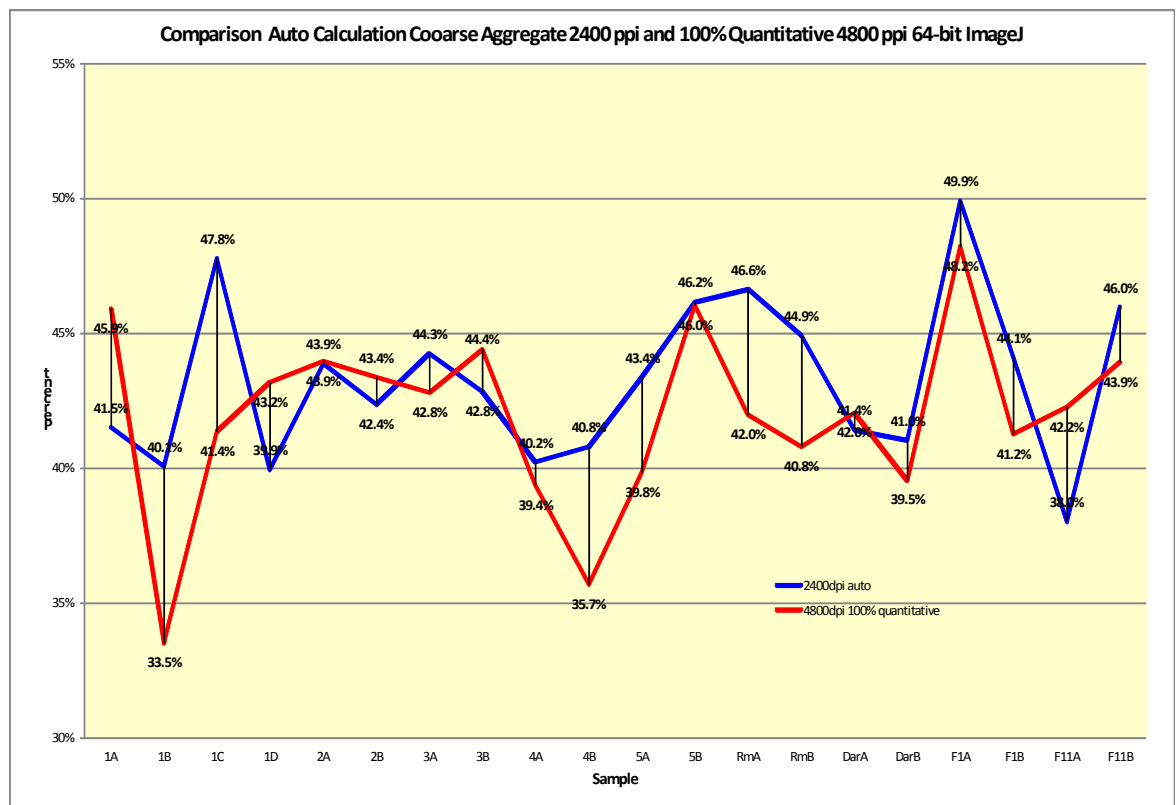


Figure 4.3.3.2.7 Comparison Auto 2400 ppi and 100% Quantitative 4800 ppi

As the 4800 ppi was done 100% Quantitative method and 2400 ppi automatic calculation method, only some samples correlate in Figure 4.3.3.2.7.

4.3.3.3 Study 3 - Results for Automatic Calculations of Coarse Aggregate Percentage 4800 ppi in 64-bit ImageJ

1A	1B	1C	1D	2A	2B
60	1026418	60	1366509	60	823230
61	3370365	61	1433850	61	900165
62	2349242	62	1512735	62	2054628
63	2459546	63	1601634	63	2133623
64	1420245	64	1693150	64	2219118
65	3190325	65	1791449	65	2277722
66	2572394	66	1828572	66	2324530
67	2217029	67	1880066	67	2282204
68	1615691	68	1932537	68	2261049
69	2654654	69	1982582	69	2225024
70	2292725	70	2035288	70	2177629
71	1960303	71	2066025	71	2116475
72	1623872	72	2093220	72	2044083
73	2255960	73	2116020	73	1986418
74	2057200	74	2142697	74	1928708
75	1799655	75	2159402	75	1876453
76	1595881	76	2160818	76	1810863
77	1989987	77	2160127	77	1743235
78	1969069	78	2157222	78	1687428
79	1715205	79	2138672	79	1846369
80	1609529	80	2114389	80	1781951
81	1486181	81	2071646	81	1731607
82	1359838	82	2071646	82	1731607
83	122454568	83	2071646	83	1731607
84	249725076	84	2071646	84	1731607
85	49.04%	85	2071646	85	1731607
86		86	2071646	86	1731607
87		87	2071646	87	1731607
88		88	2071646	88	1731607
89		89	2071646	89	1731607
90		90	2071646	90	1731607
91		91	2071646	91	1731607
92		92	2071646	92	1731607
93		93	2071646	93	1731607
94		94	2071646	94	1731607
95		95	2071646	95	1731607
96		96	2071646	96	1731607
97		97	2071646	97	1731607
98		98	2071646	98	1731607
99		99	2071646	99	1731607
100		100	2071646	100	1731607
101	1209163	101	1530379	101	1339148
102	1138509	102	1514685	102	1335693
103	1164872	103	1530313	103	1335693
104	1350147		91894478	104	1368074
105	1159888		248733604	105	1343557
106	1121260		36.94%	106	1346480
107	1194225			107	1361567
108	122454568			108	1376310
109	249725076			109	1396015
110	49.04%			110	1418443
111				111	1466988
112				112	1489086
113				113	1544836
114				114	1569407
115				115	1615028
116				116	1661214
117				117	1710464
118				118	1778967
119				119	1828052
120				120	1870167
121				121	1914932
122				122	1974124
123				123	2033391
124				124	2092771
125				125	2152247
126				126	2211824
127				127	2271502
128				128	2331281
129				129	2391161
130				130	2451142
131				131	2511224
132				132	2571407
133				133	2631691
134				134	2692076
135				135	2752562
136				136	2813149
137				137	2873837
138				138	2934626
139				139	2995516
140				140	3056507
141				141	3117600
142				142	3178794
143				143	3239990
144				144	3301187
145				145	3362386
146				146	3423586
147				147	3484787
148				148	3545989
149				149	3607192
150				150	3668396
151				151	3729601
152				152	3790807
153				153	3852014
154				154	3913222
155				155	3974431
156				156	4035641
157				157	4096852
158				158	4158063
159				159	4219275
160				160	4280487
161				161	4341699
162				162	4402912
163				163	4464125
164				164	4525338
165				165	4586551
166				166	4647764
167				167	4708977
168				168	4770190
169				169	4831403
170				170	4892616
171				171	4953829
172				172	5015042
173				173	5076255
174				174	5137468
175				175	5198681
176				176	5259894
177				177	5321107
178				178	5382320
179				179	5443533
180				180	5504746
181				181	5565959
182				182	5627172
183				183	5688385
184				184	5749598
185				185	5810811
186				186	5872024
187				187	5933237
188				188	5994450
189				189	6055663
190				190	6116876
191				191	6178089
192				192	6239302
193				193	6300515
194				194	6361728
195				195	6422941
196				196	6484154
197				197	6545367
198				198	6606580
199				199	6667793
200				200	6729006
201				201	6790219
202				202	6851432
203				203	6912645
204				204	6973858
205				205	7035071
206				206	7096284
207				207	7157497
208				208	7218710
209				209	7279923
210				210	7341136
211				211	7402349
212				212	7463562
213				213	7524775
214				214	7585988
215				215	7647201
216				216	7708414
217				217	7769627
218				218	7830840
219				219	7892053
220				220	7953266
221				221	8014479
222				222	8075692
223				223	8136905
224				224	8198118
225				225	8259331
226				226	8320544
227				227	8381757
228				228	8442970
229				229	8504183
230				230	8565396
231				231	8626609
232				232	8687822
233				233	8749035
234				234	8810248
235				235	8871461
236				236	8932674
237				237	8993887
238				238	9055100
239				239	9116313
240				240	9177526
241				241	9238739
242				242	9299952
243				243	9361165
244				244	9422378
245				245	9483591
246				246	9544804
247				247	9606017
248				248	9667230
249				249	9728443
250				250	9789656
251				251	9850869
252				252	9912082
253				253	9973295
254				254	10034508
255				255	10095721
256				256	10156934
257				257	10218147
258				258	10279360
259				259	10340573
260				260	10401786
261				261	10462999
262				262	10524212
263				263	10585425
264				264	10646638
265				265	10707851
266				266	10769064
267				267	10830277
268				268	10891490
269				269	10952703
270				270	11013916
271				271	11075129
272				272	11136342
273				273	11197555
274				274	11258768
275				275	11319981
276				276	11381194
277				277	11442407
278				278	11503620
279				279	11564833
280				280	11626046
281				281	11687259
282				282	11748472
283				283	11809685
284				284	11870898
285				285	11932111
286				286	11993324
287				287	12054537
288				288	12115750
289				289	12176963
290				290	12238176
291				291	12299389
292				292	12360602
293				293	12421815
294				294	12483028
295				295	12544241
296				296	12605454
297				297	12666667
298				298	12727880
299				299	12789093
300				300	12850306

Table 4.3.3.3.1 Percentage of Coarse Aggregate Samples 1A to 2B

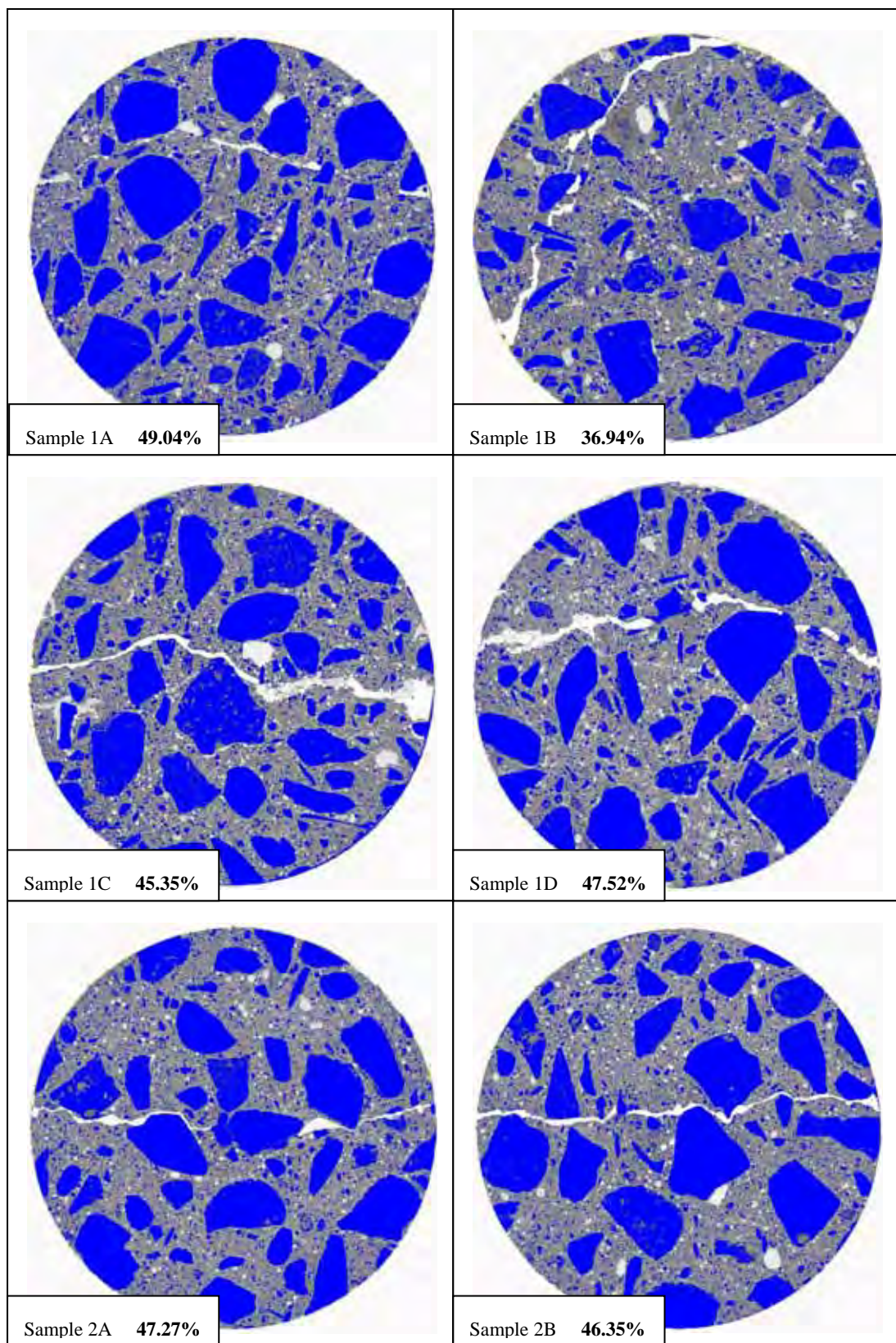


Figure 4.3.3.3.1 Coarse Aggregate Images 1A to 2B from ImageJ

3A		3B		4A		4B		5A		5B	
66	1092213	66	1303435	66	1030388	67	1528919	67	1527594	67	1940842
67	1205103	67	1357517	67	1119924	68	1563814	68	1562312	68	1992441
68	1324906	68	1406810	68	1188167	69	1611207	69	1609545	69	2042629
69	1448631	69	1456514	69	1256534	70	1663678	70	1661563	70	2105285
70	1579806	70	1514910	70	1329792	71	1704792	71	1702018	71	2161531
71	1682253	71	1548699	71	1381234	72	1746247	72	1743217	72	2212702
72	1788004	72	1596702	72	1430205	73	1790195	73	1787068	73	2270477
73	1893410	73	1646397	73	1478344	74	1826727	74	1823382	74	2319156
74	1990194	74	1705685	74	1518923	75	1855373	75	1851965	75	2354256
75	2077659	75	1756414	75	1558714	76	1871303	76	1867807	76	2371800
76	2135290	76	1804478	76	1590946	77	1897235	77	1893650	77	2375737
77	2193418	77	1860855	77	1627966	78	1925065	78	1921472	78	2371848
78	2235315	78	1920027	78	1666183	79	1932561	79	1929077	79	2372892
79	2245047	79	1961453	79	1689767	80	1943933	80	1940579	80	2377201
80	2249728	80	2017689	80	1724488	81	1970874	81	1967428	81	2378317
81	2253085	81	2088843	81	1765554	82	1987438	82	1987438	82	2378317
96	2108251	96	2067936	96	1901286	97	1702362	97	1695624	97	1972650
97	2145191	97	2064144	97	1895531	98	1693299	98	1686638	98	1955739
98	2166635	98	2039798	98	1877855	99	1672202	99	1665663	99	1935086
99	2162397	99	2006929	99	1839685	100	1657789	100	1651650	100	1916775
100	2154459	100	1975709	100	1802818	101	1648309	101	1642528	101	1897890
101	2141937	101	1939594	101	1776227	102	1630205	102	1624606	102	1877936
102	2097872	102	1902784	102	1732599	103	1621822	103	1615919	103	1855198
103	2075156	103	1898384	103	1712398	104	1643633	104	1637068	104	1834980
104	2097198	104	1930622	104	1720114	105	1621403	105	1610327	105	1816030
105	2019775	105	1889732	105	1668562	106	1630687	106	1608653	106	1803430
106	1976978	106	1875133	106	1660055	107	1618750	107	1601720	107	1788473
107	1937530	107	1874104	107	1647386	108	1610328	108	1602721	108	1776761
108	1891082	108	1864049	108	1633874	109	1615849	109	1610661	109	1760359
109	1828133	109	1850975	109	1618578	110	1623861	110	1646926	110	1742677
110	1787558	110	1856547	110	1623861	111	1643687	111	1708189	111	1727055
111	1770444	111	1881946	111	1643687	112	1625673	112	1732381	112	1722484
112	1718360	112	1845287	112	1625673	113	1650873	113	1800617	113	1725654
113	1718326	113	1865226	113	1650873	114	1653881	114	1872519	114	1734302
114	1713569	114	1870340	114	1653881	115	1673364	115	1976394	115	1762212
115	1726923	115	1883461	115	1673364	116	1684891	116	109925373	116	125482994
116	1763355	116	1891890	116	1684891	117	1690403	117	252774544	117	253452112
117	1775326	117	1872794	117	1690403	118	1715918	118	43.49%	118	49.51%
118	1783394	118	1872206	118	1715918	119	1729007	119		119	
119	1797384	119	118934858	119	1729007	120	1730022	120		120	
120	1789480	120	248060464	120	1730022	121	1734601	121		121	
	116360998		47.95%	121	1734601	122	1754331	122		122	
	248396728			122	1754331	123	1782236	123		123	
	46.84%			123	1782236	124	108457848	124		124	
				124	108457848	125	245695012	125		125	
				125	245695012	126	44.14%	126		126	

Table 4.3.3.3.2 Percentage of Coarse Aggregate Samples 3A to 5B

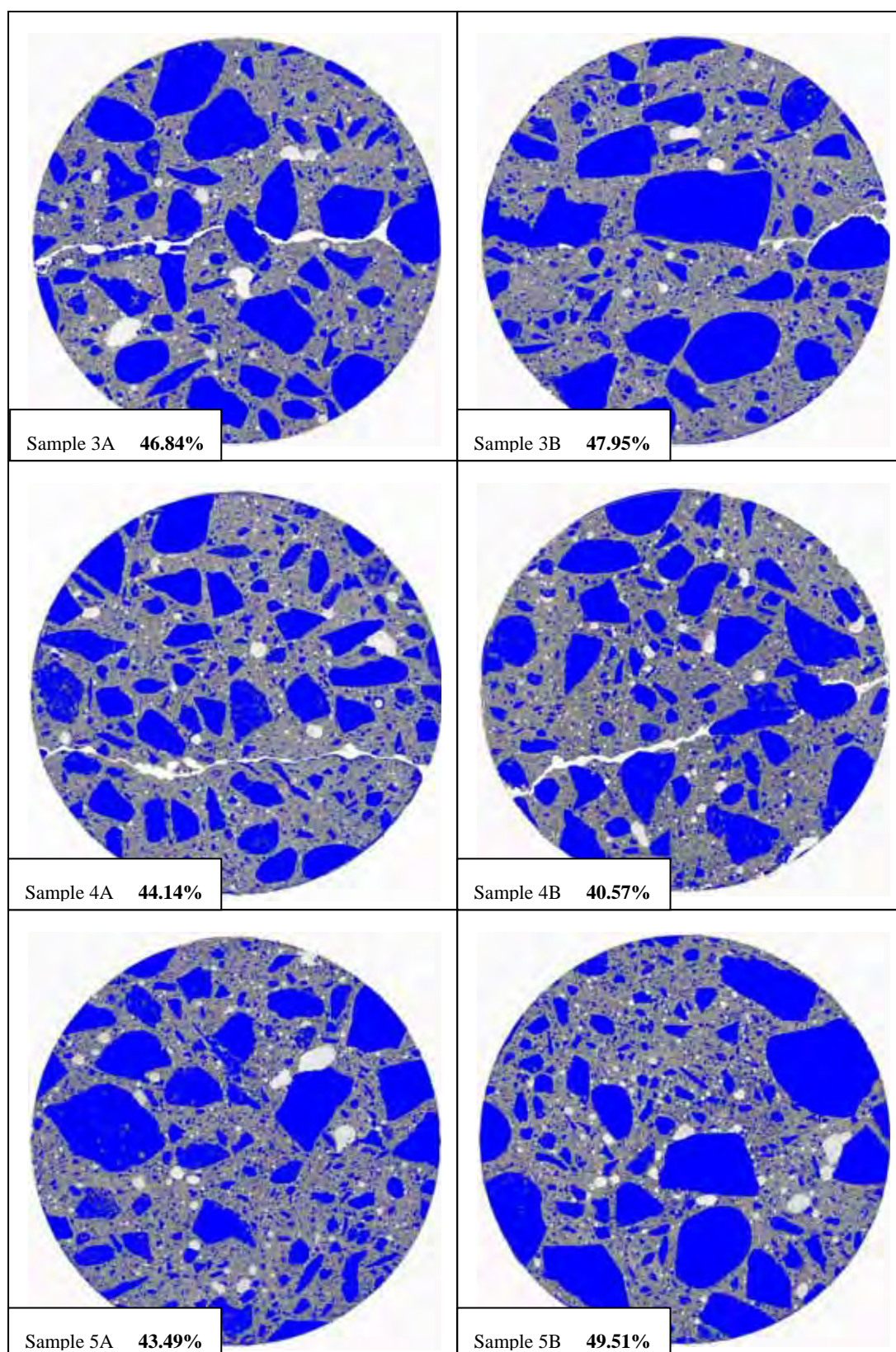


Figure 4.3.3.3.2 Coarse Aggregate Images 3A to 5B from ImageJ

RmA		RmB		DarA		DarB	
58	1377400	58	920220				
59	1462804	59	991414	59	2442209	59	2032791
60	1544261	60	1063307	60	2237741	60	1747115
61	1634889	61	1136809	61	2063534	61	1521912
62	1728239	62	1213503	62	1923930	62	1351196
63	1810205	63	1298602	63	1794472	63	1217663
64	1869170	64	1390901	64	1683678	64	1113601
65	1910178	65	1472360	65	1581731	65	1025749
66	1943033	66	1549467	66	1476593	66	951917
67	1969783	67	1616578	67	1376861	67	884165
68	2001379	68	1673850	68	1286420	68	828219
69	2028484	69	1731101	69	1209654	69	781539
70	2054896	70	1784134	70	1144611	70	741994
71	2086197	71	1840096	71	1092413	71	709084
72	2119560	72	1886561	72	1049810	72	681547
101	2040430	101	1928175	102	755118	102	641270
102	2016933	102	1928175	102	755118	102	641270
103	1991846	103	1915560	103	771938	103	647748
104	1970977	104	1905702	104	793541	104	655307
105	1954264	105	1907162	105	803759	105	662127
106	1947123	106	1912429	106	792279	106	671234
107	1931883	107	1923962		106526018		106208245
108	1922788	108	1935242		250409736		252093980
	118660760	109	1945275		42.54%		42.13%
	254468508	110	1954950				
	46.63%	111	1971546				
		112	2005165				
		113	2044707				
		114	2100717				
			114960390				
			254129800				
			45.24%				

Table 4.3.3.3.3 Percentage of Coarse Aggregate Samples RmA to DarB

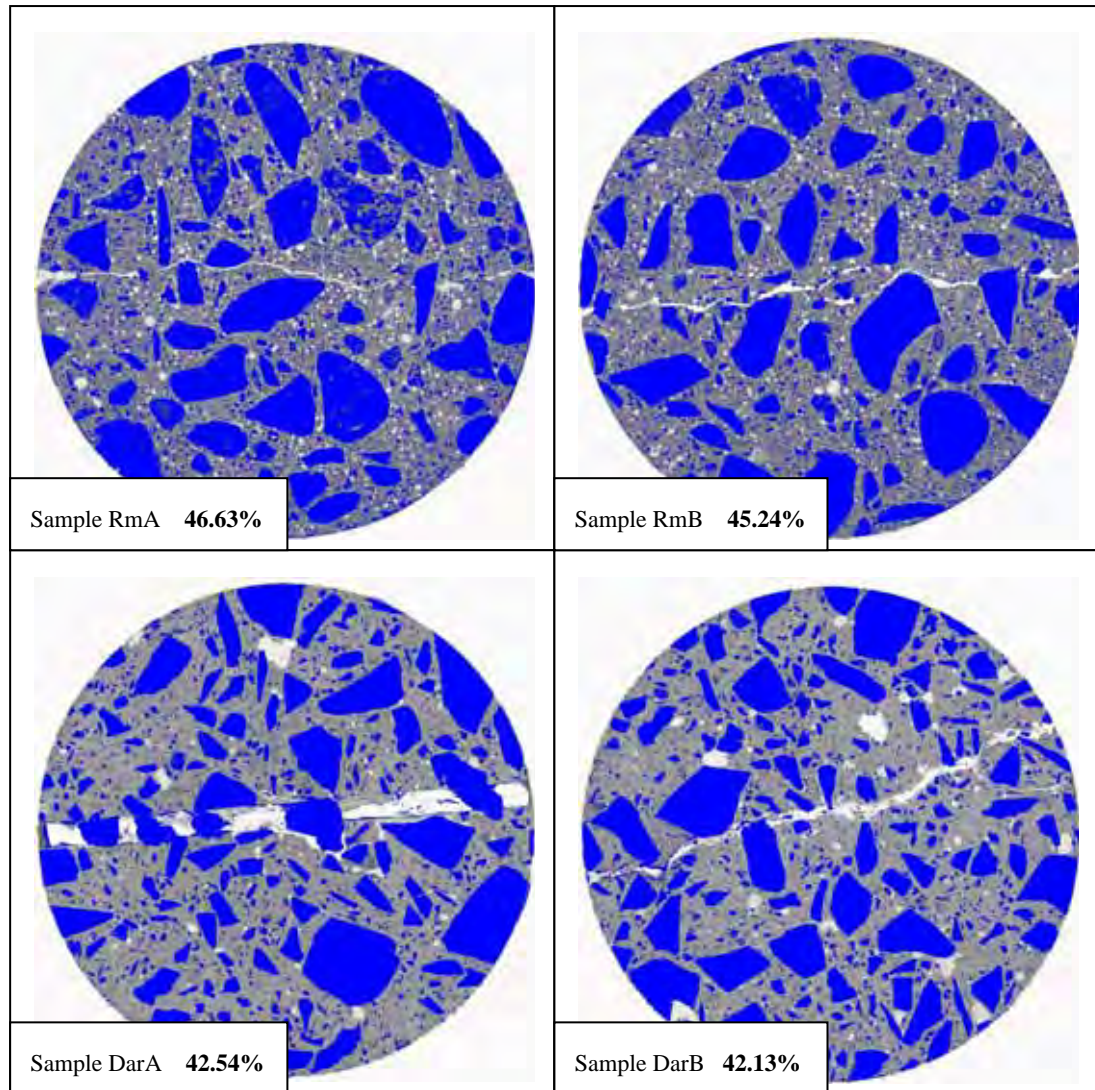


Figure 4.3.3.3.3 Coarse Aggregate Images RmA to DarB from ImageJ

FIA		FIB		FIIA		FIIB	
				100	2050125	100	2054768
63	1411488	63	1516875	101	2074552	101	2064819
64	1285848	64	1385673	102	2087197	102	2047433
65	1178260	65	1264447	103	2092260	103	2023328
66	1083126	66	1152706	104	2096143	104	1997470
67	999867	67	1048276	105	2110848	105	1982572
68	927367	68	953337	106	2133538	106	1979863
69	867259	69	874834	107	2165508	107	1982193
70	815211	70	806969	108	2189883	108	1993079
71	773330	71	748558	109	2210373	109	1993658
72	736216	72	698711	110	2232237	110	1997199
73	705940	73	657359	111	2248534	111	1986500
74	677054	74	619827	112	2266580	112	1990753
75	649885	75	591904	113	2294261	113	2013887
76	625528	76	566197	114	2329593	114	2055500
77	605665	77	549629	115	2365324	115	2108836
78	592066	78	540335	116	2413457	116	2154152
79	581632	79	533417	117	2465629	117	2225156
80	570918	80	531632	118	2528371	118	2303718
81	564848	81	532689	119	2590193	119	2377247
82	561098	82	537689	120	2659537	120	2455211
83	563798	83	545410	121	2715631	121	2526549
84	568726	84	558672	122	2768895	122	2618095
85	581210	85	576756	123	2828299	123	2711113
86	602884	86	602881	124	2888012	124	2777118
	122912936		108625414		106650200		198841245
	247728048		248733604		245720012		440257248
	49.62%		43.67%		43.40%		45.16%

Table 4.3.3.3.4 Percentage of Coarse Aggregate Samples FIA to FIIB

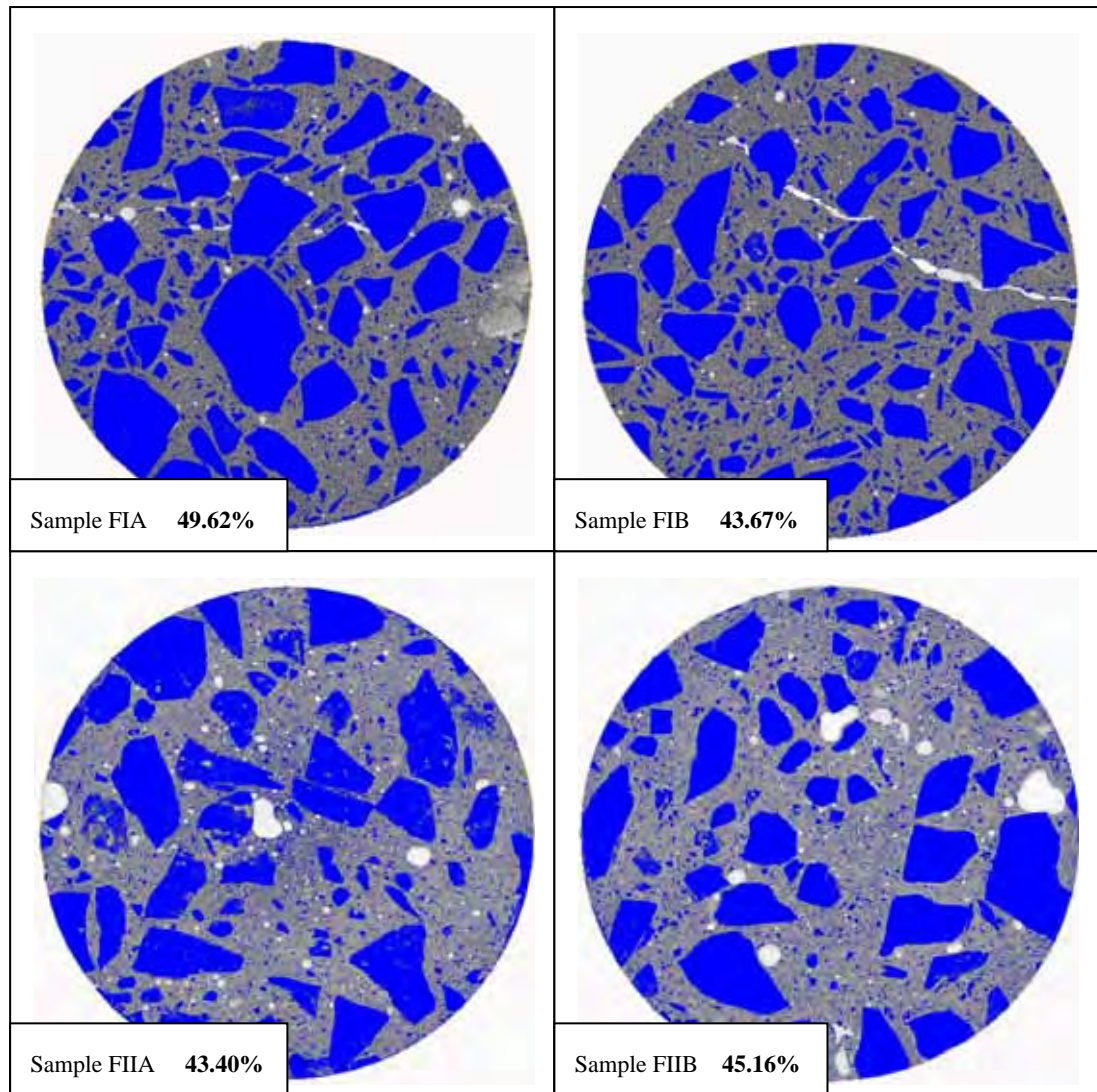


Figure 4.3.3.3.4 Coarse Aggregate Images FIA to FIIB from ImageJ

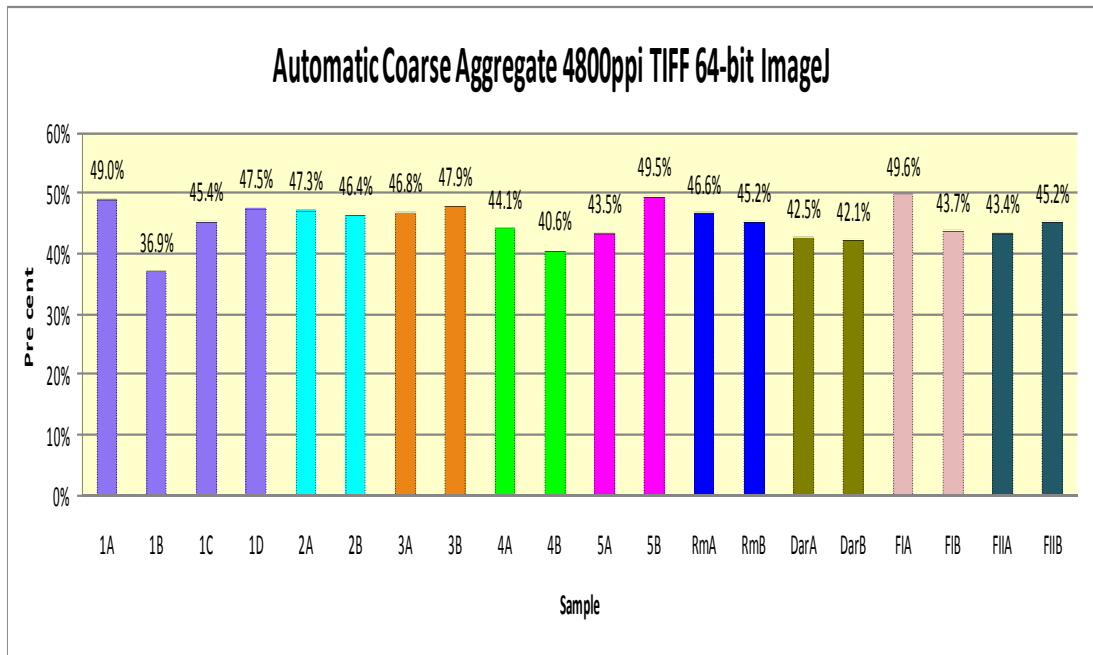


Figure 4.3.3.3.5 Percentage of Coarse Aggregate of all samples

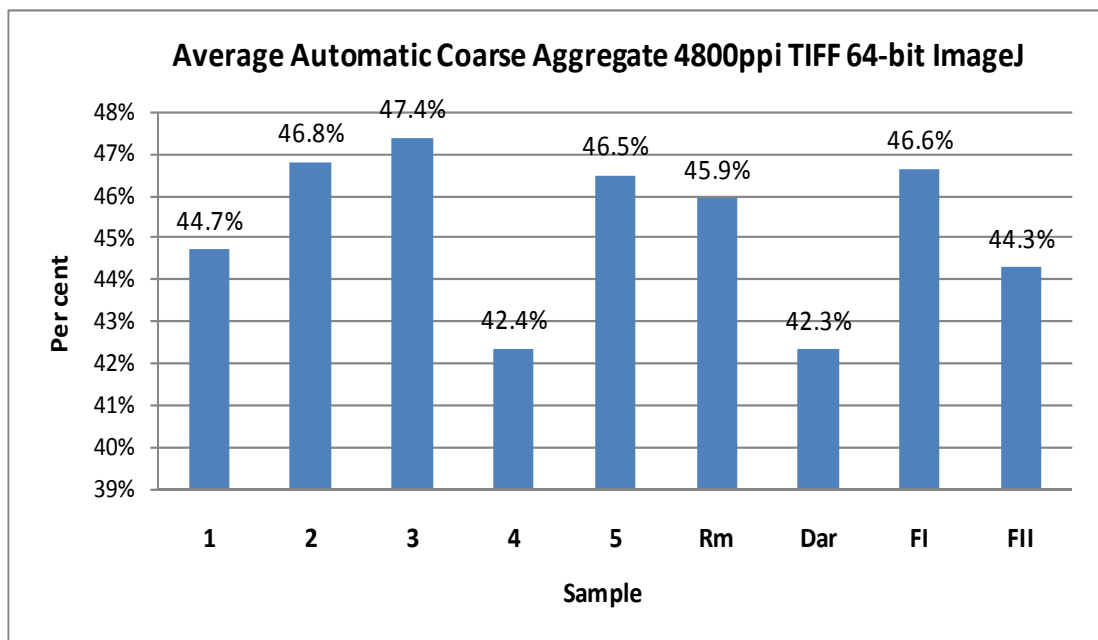


Figure 4.3.3.3.6 Average Percentage of Coarse Aggregate of each core sample

Observations and Explanations

This is the first comparison that can be made between 100% automatic method results and 100% quantitative method results. The auto results are only about 1.2% to 4.8% different to quantitative, averaging 3.14% for all samples and 3.94% for the studied samples 1-5 and Rm as Table 4.3.3.3.5 and Figure 4.3.3.3.7 show.

	4800ppi 100% Auto	Quantitative	Difference
1	44.71%	40.99%	3.73%
2	46.81%	43.66%	3.15%
3	47.40%	43.61%	3.79%
4	42.36%	37.53%	4.83%
5	46.50%	42.94%	3.56%
Rm	45.93%	41.37%	4.56%
Dar	42.34%	40.79%	1.54%
FI	46.64%	44.73%	1.92%
FII	44.28%	43.09%	1.19%
Average 1-Rm			3.94%
Average all			3.14%

Table 4.3.3.3.5 Difference between 100% Auto and 100% Quantitative calculations

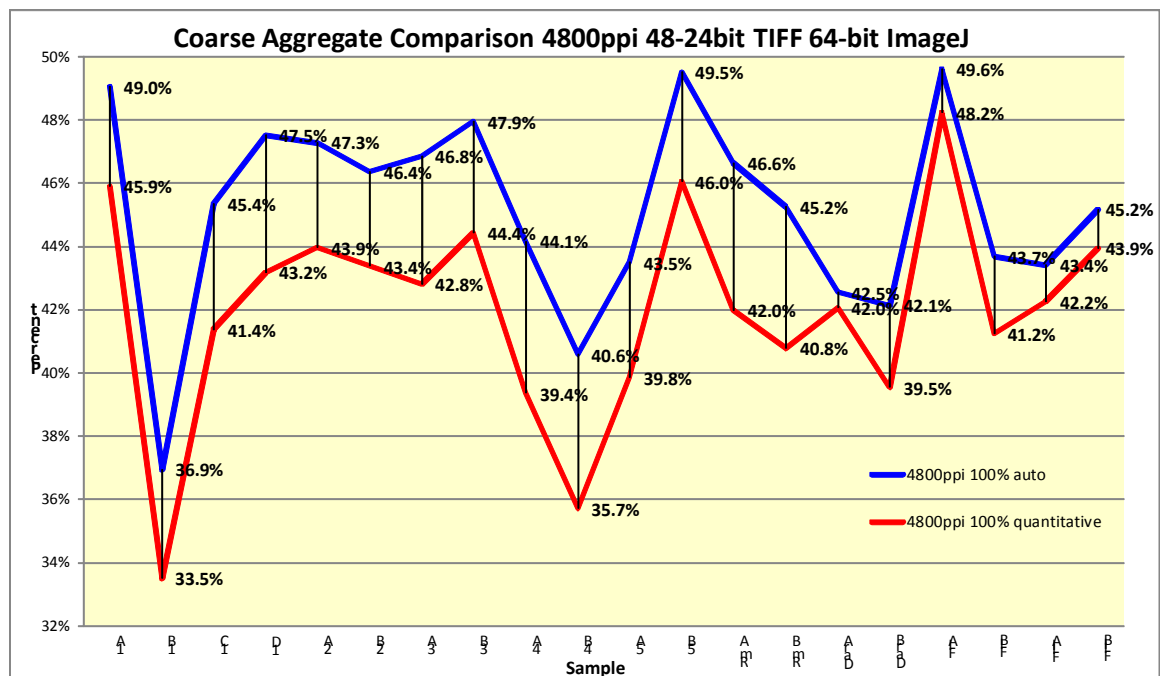


Figure 4.3.3.3.7 Comparison coarse aggregate 100% auto and 100% quantitative methods

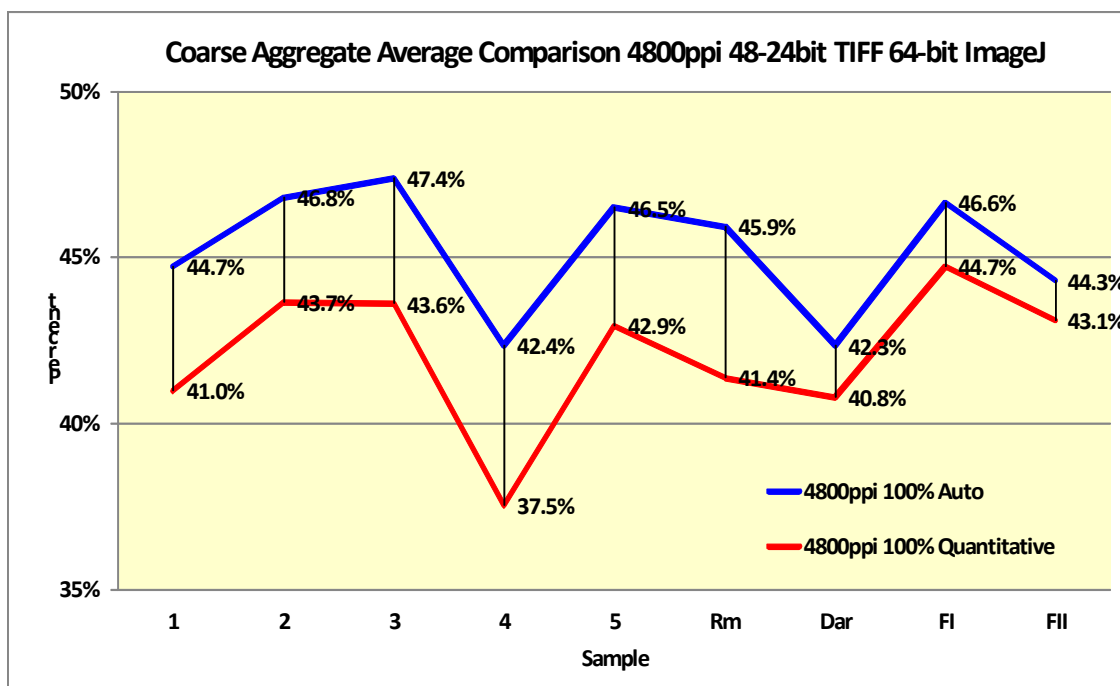


Figure 4.3.3.3.8 Comparison Average coarse aggregate Auto and 100% Quantitative

In Figure 4.3.3.3.8 the blue metal aggregate samples Dar and FI calculated by auto method were only 2% different from a quantitative method. The multi coloured river aggregates in other samples were 3.15% to 4.56% different from the quantitative method. The accuracy of calculations from correctly calibrated 64-bit ImageJ is totally amazing.

Spce	4800ppi Auto	4800ppi Quantitative	Difference	4800ppi Auto	Percentage Difference
1	44.7%	41.0%	3.7%	48%	-0.2%
2	46.8%	43.7%	3.1%	49%	-0.8%
3	47.4%	43.6%	3.8%	45%	-0.2%
4	42.4%	37.5%	4.9%	34%	0.9%
5	46.5%	42.9%	3.6%	46%	-0.4%
Rm	45.9%	41.4%	4.5%	40%	0.6%
Average Rm			3.94%		-0.2%

Table 4.3.3.3.6 Auto calibrated average values in Samples 1 to 5 and Rm

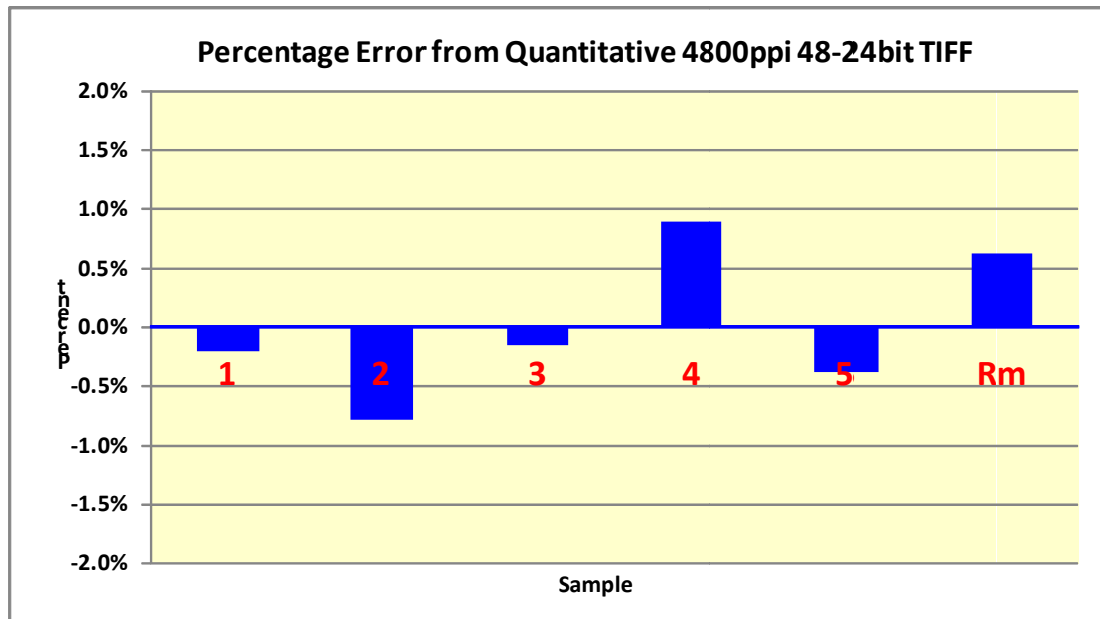


Figure 4.3.3.3.9 Percentage error auto calibrated from 100% quantitative method

Figure 4.3.3.3.10 Coarse aggregate average comparison between quantitative method and auto calibrated values in Samples 1 to 5 and Rm

Table 4.3.3.3.6 demonstrates how the calibration was done. The difference between the auto method and quantitative method was averaged then subtracted from the auto values which simply created the calibrated auto values for samples 1 to 5 and Rm.

As the Table 4.3.3.3.6 shows in the last column the median percentage error for the auto calibrated in comparison to quantitative values is only -0.2%. The true range of error is well documented in Figure 4.3.3.3.9 and Figure 4.3.3.3.10 which show accuracy within 1% of the quantitative accurate values.

Sample	Auto	Quantitative	Difference	Auto Calibrated	Percentage error from Quantitative
1A	40%	49%	31%	45%	-0%
1B	39%	35%	34%	32%	-0%
1C	44%	44%	40%	46%	02%
1D	45%	42%	43%	47%	06%
2A	43%	49%	33%	45%	-04%
2B	44%	44%	30%	46%	-08%
3A	48%	42%	40%	41%	03%
3B	47%	44%	32%	49%	-05%
4A	41%	34%	48%	44%	10%
4B	46%	37%	49%	38%	11%
5A	45%	38%	36%	37%	-01%
5B	45%	40%	35%	47%	-03%
Avg Difference 1A-5B			38%	Median	-02%

Table 4.3.3.3.7 Samples 1A to 5B auto calibrated

Samples 1A to 5B were auto calibrated the same way as the averages in Table 4.3.3.3.6.

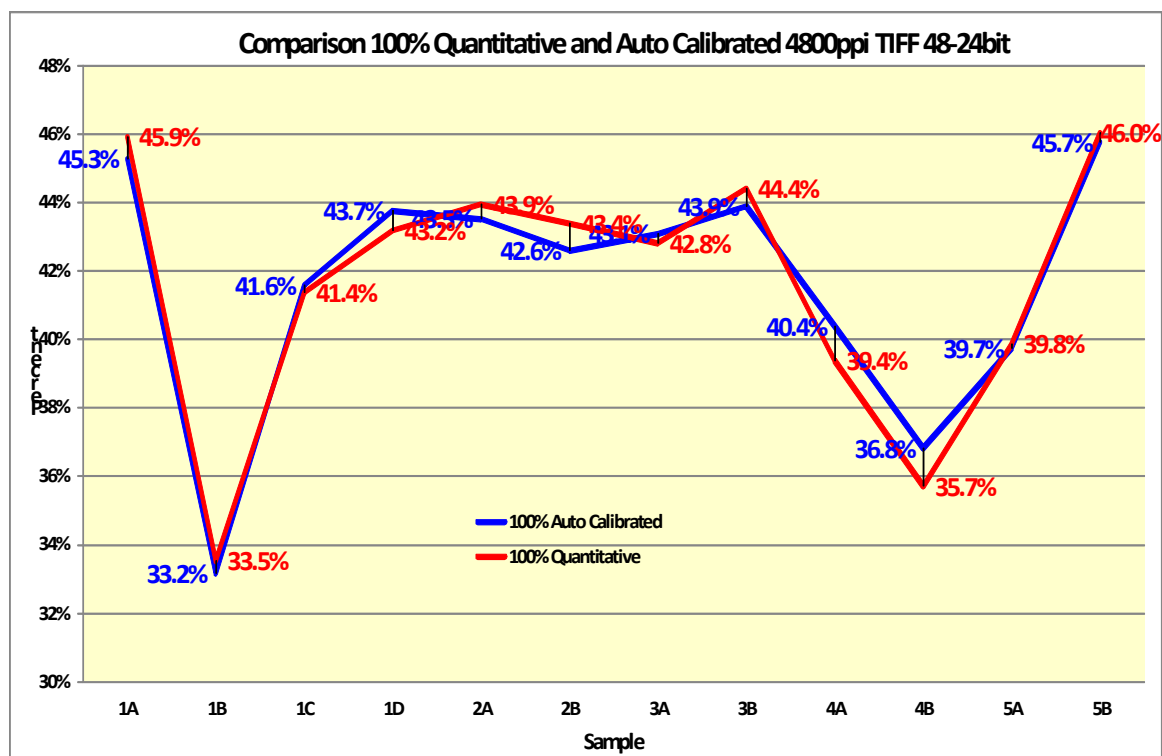


Figure 4.3.3.3.11 Comparison of Samples from the damaged Warehouse floor

Figure 4.3.3.3.11 shows a comparison between the auto calibrated values of percentage of coarse aggregate and 100% quantitative values.

An automatic analysis technique/method for calculating a percentage of coarse aggregate was successfully developed. The automatic method can accurately differentiate varying microstructures within the large concrete core samples.

Figures 4.3.3.3.12 and 4.3.3.3.13 show that the auto calibrated method developed in this study is within 1% of accurate quantitative percentage coarse aggregate.

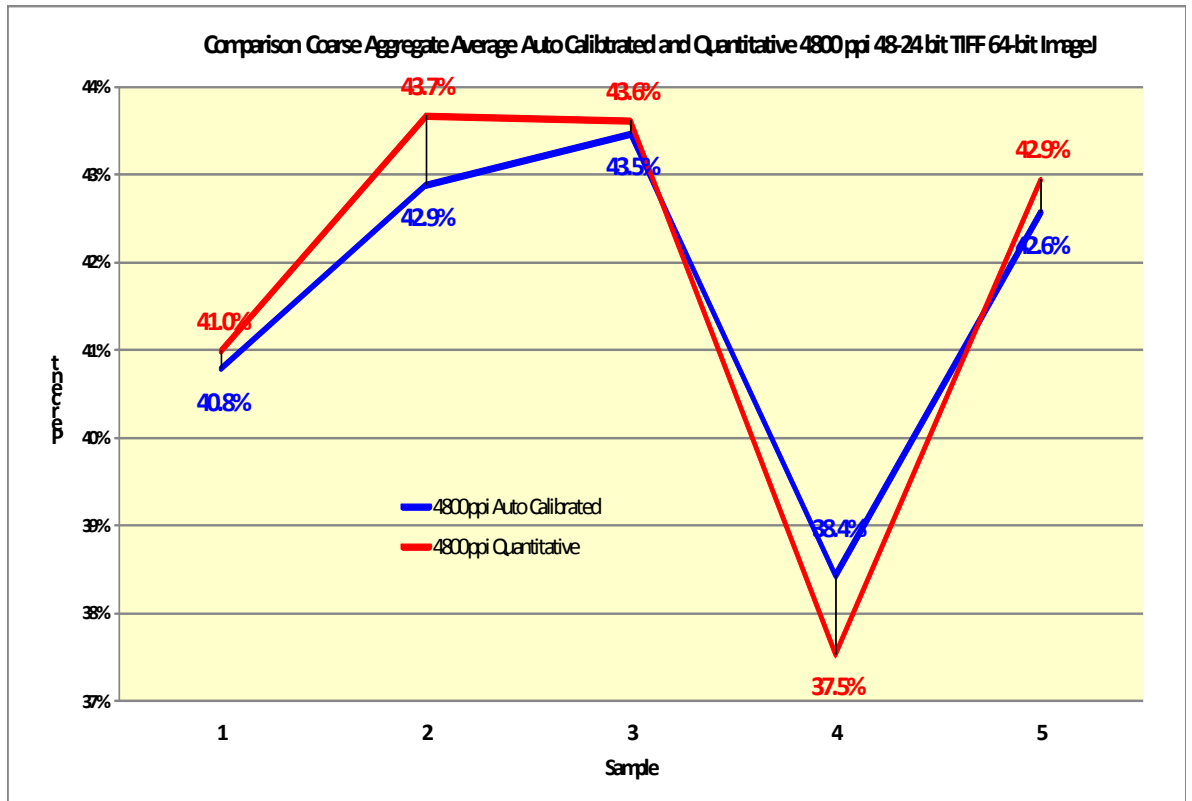


Figure 4.3.3.12 Comparison coarse aggregate between auto calibrated and quantitative

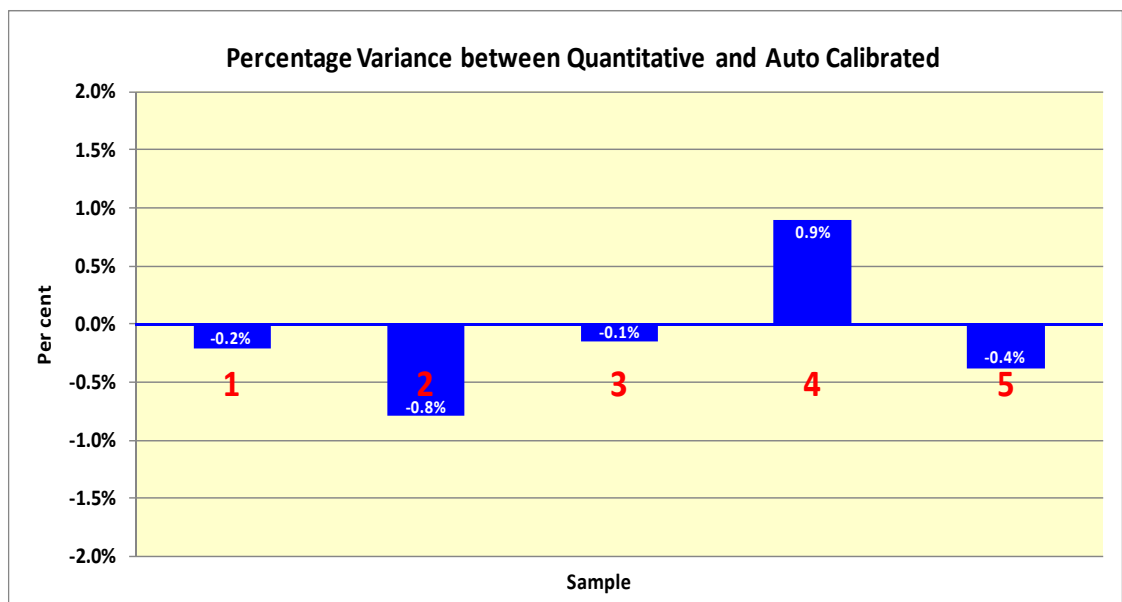


Figure 4.3.3.13 Variance between auto calibrated and quantitative values

4.3.3.4 Study 3 - Results For Calibration of Micro-Porosity in Cement Matrix Calculated in 64-bit ImageJ

72 ppi		200 ppi		1200 ppi		2400 ppi		4800 ppi		6400 ppi	
178	6	188	27	194	441	195	1675	197	5790	198	9574
179	5	189	10	195	386	196	1504	198	5440	199	9305
180	0	190	5	196	367	197	1399	199	5181	200	8675
181	3	191	13	197	359	198	1390	200	4969	201	16507
182	7	192	12	198	343	199	1343	201	9280	202	7752
183	6	193	10	199	338	200	1168	202	4259	203	7117
184	1	194	14	200	334	201	2348	203	4029	204	7000
185	3	195	14	201	586	202	1066	204	3877	205	6625
186	5	196	8	202	265	203	1008	205	3811	206	6524
187	2	197	7	203	258	204	969	206	3761	207	6397
188	3	198	11	204	235	205	937	207	3532	208	6232
189	2	199	4	205	238	206	889	208	3429	209	5960
190	2	200	7	206	212	207	946	209	3459	210	5848
191	0	201	23	207	213	208	854	210	3301	211	11530
192	0	202	4	208	220	209	849	211	6547	212	5730
193	1	203	5	209	222	210	840	212	3139	213	5717
194	2	204	11	210	216	211	1597	213	3221	214	5643
195	0	205	7	211	392	212	794	214	3097	215	5640
196	0	206	7	212	227	213	810	215	3199	216	5609
197	1	207	7	213	170	214	778	216	3093	217	11030
198	1	208	9	214	214	215	802	217	6284	218	5442
199	2	209	5	215	217	216	750	218	3083	219	5427
200	2	210	6	216	187	217	1572	219	2998	220	5462
201	0	211	18	217	382	218	770	220	3018	221	11058
202	1	212	9	218	194	219	778	221	6179	222	5523
203	0	213	7	219	184	220	737	222	3153	223	5768
204	0	214	11	220	174	221	1517	223	3147	224	11352
205	0	215	5	221	390	222	810	224	6480	225	5691
206	0	216	4	222	189	223	801	225	3211	226	5672
207	0	217	10	223	206	224	1582	226	3160	227	11262
208	0	218	4	224	399	225	821	227	6346	228	5767
209	0	219	8	225	216	226	743	228	3213	229	5782
210	1	220	7	226	201	227	1582	229	3233	230	12068
211	0	221	7	227	403	228	780	230	6715	231	6320
212	0	222	8	228	187	229	807	231	3588	232	13452
213	1	223	3	229	211	230	1651	232	7455	233	6837
214	1	224	6	230	428	231	885	233	3884	234	13283
215	0	225	2	231	211	232	1832	234	7520	235	6518
216	1	226	4	232	494	233	982	235	3643	236	12670
217	2	227	4	233	259	234	1833	236	7105	237	11139
218	1	228	6	234	492	235	882	237	6321	238	4969
219	0	229	10	235	217	236	1739	238	2750	239	9789
220	1	230	8	236	428	237	1575	239	5458	240	7924
221	0	231	1	237	429	238	680	240	4482	241	3106
222	0	232	5	238	184	239	1375	241	1747	242	3395
223	0	233	6	239	340	240	1102	242	1964	243	1813
224	0	234	8	240	282	241	411	243	1075	244	1564
225	0	235	8	241	132	242	481	244	860	245	1157
226	0	236	6	242	143	243	257	245	677	246	1410
227	1	237	5	243	78	244	227	246	834	247	297
228	0	238	3	244	63	245	174	247	208	248	0
229	0	239	4	245	42	246	206	248	3	249	0
230	0	240	1	246	61	247	51	249	0	250	0
231	0	241	1	247	20	248	0	250	0	251	0
232	0	242	0	248	1	249	0	251	0	252	0
233	0	243	1	249	0	250	0	252	0	253	0
234	0	244	2	250	0	251	0	253	0	254	0
235	0	245	1	251	0	252	0	254	0	255	0
236	0	246	0	252	0	253	0	255	0		356332
237	0	247	0	253	0	254	0		206208		6404112
238	0	248	0	254	0	255	0		3601380		5.56%
239	0	249	0	255	0		54359		5.73%		
240	0	250	0		14280		901310				
241	0	251	0		225078		6.03%				
242	0	252	0		6.34%						
243	0	253	0								
244	0	254	0								
245	0	255	0								
246	0		419								
247	0		6240								
248	0		6.71%								
249	0										
250	0										
251	0										
252	0										
253	0										
254	0										
255	0										
	64										
	812										
	7.88%										

Table 4.3.3.4.1 Percentage of micro porosity from Sample 5B in various resolutions

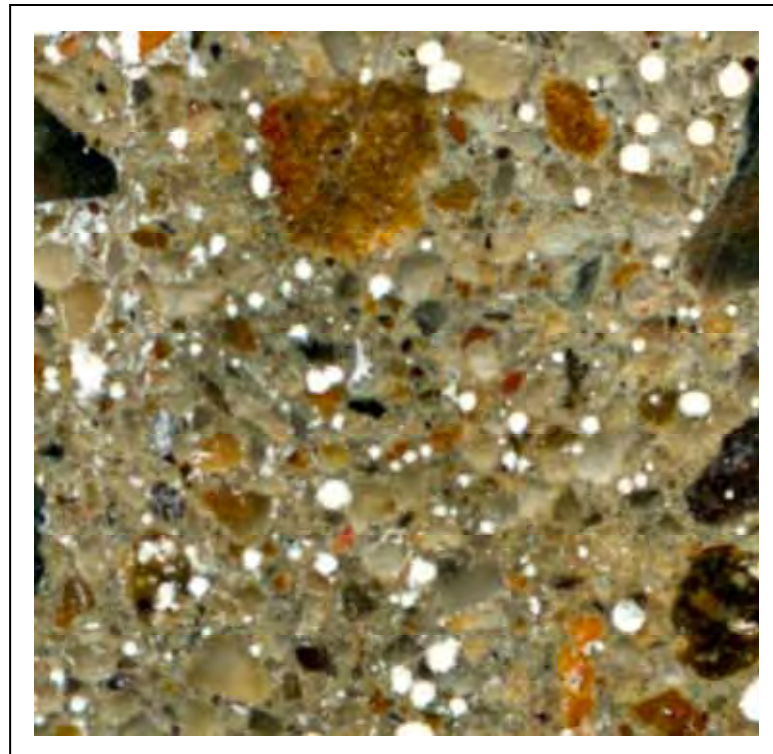


Figure 4.3.3.4.1 Original image in 6400 ppi of the selected section

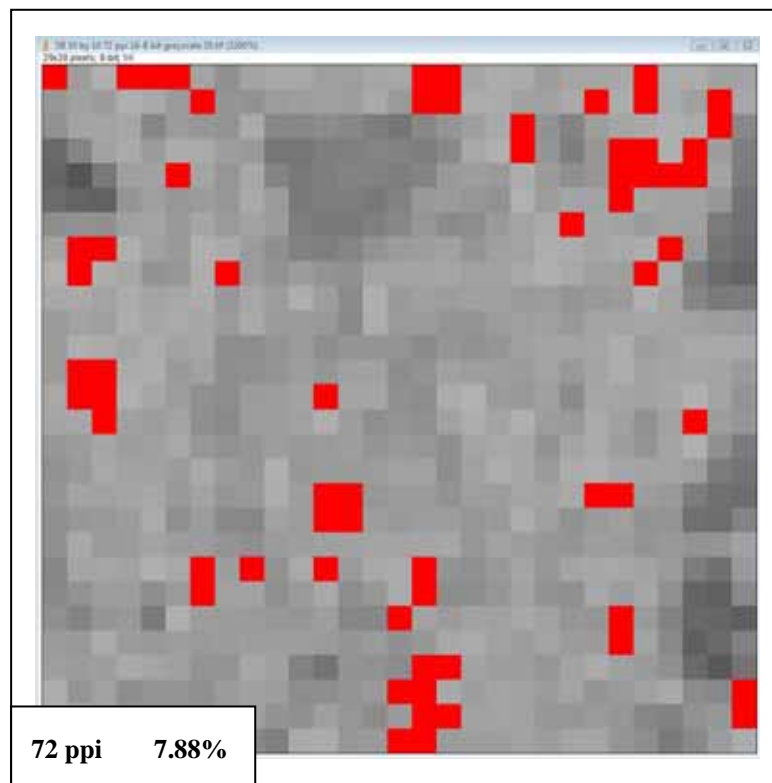


Figure 4.3.3.4.2 72 ppi resolution micro porosity calculated

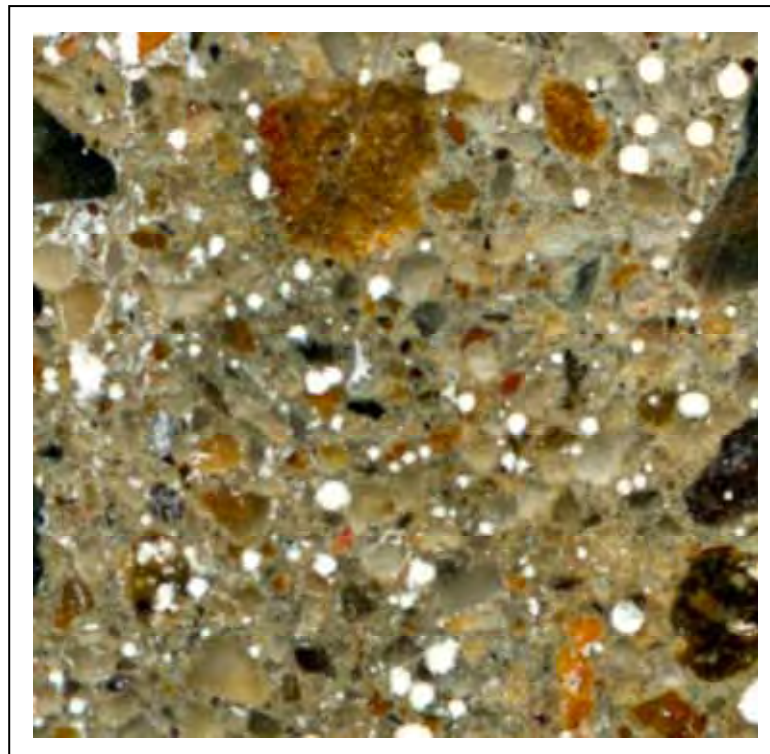


Figure 4.3.3.4.3 Original image in 6400 ppi of the selected section

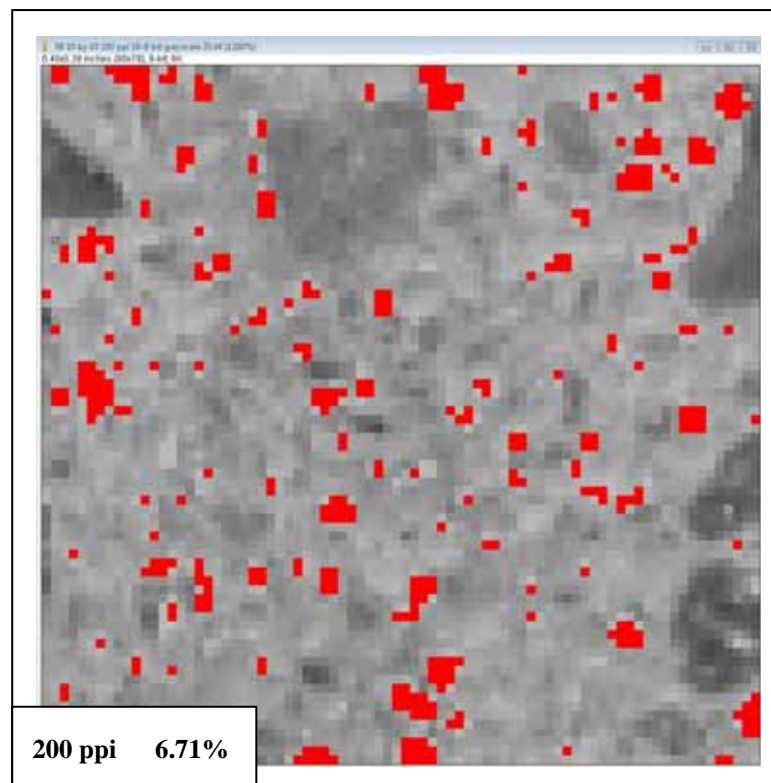


Figure 4.3.3.4.4 200 ppi resolution micro porosity calculated

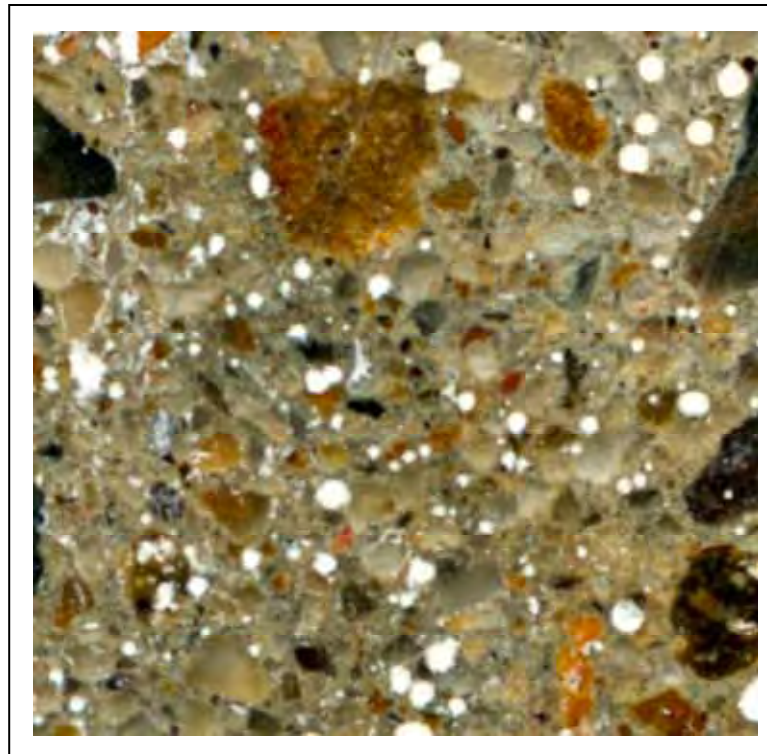


Figure 4.3.3.4.5 Original image in 6400 ppi of the selected section

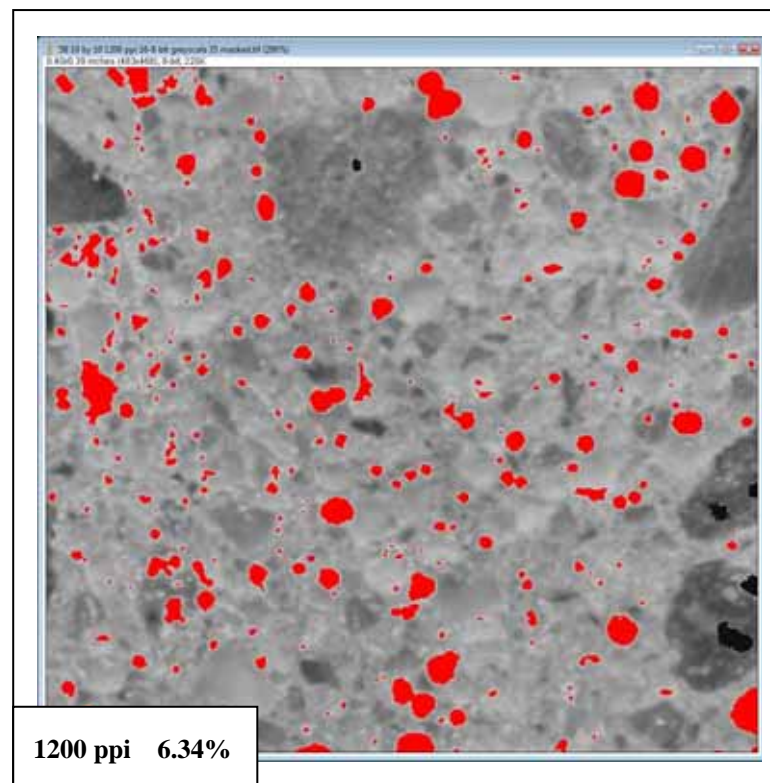


Figure 4.3.3.4.6 1200 ppi resolution micro porosity calculated

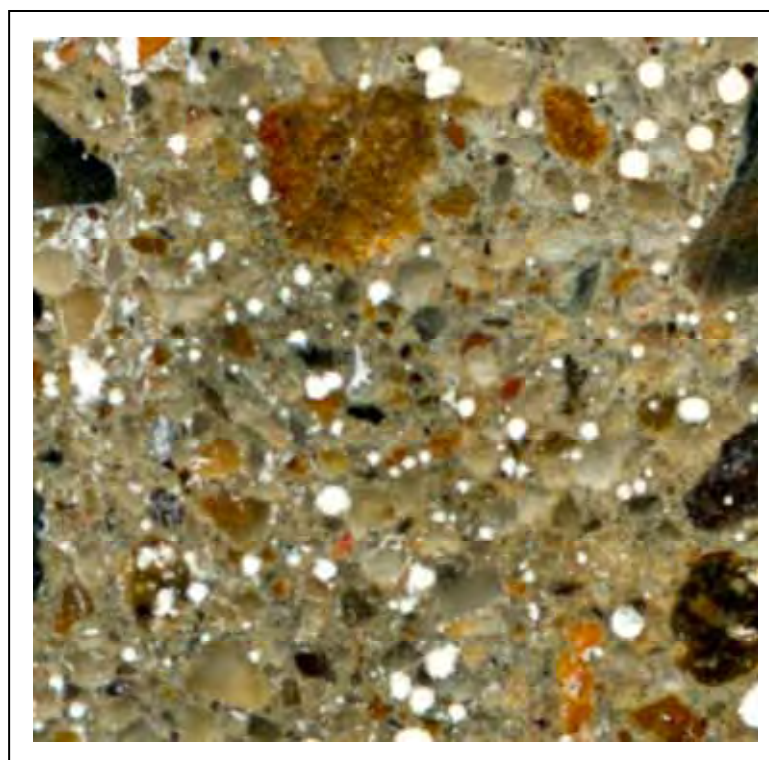


Figure 4.3.3.4.7 Original image in 6400 ppi of the selected section

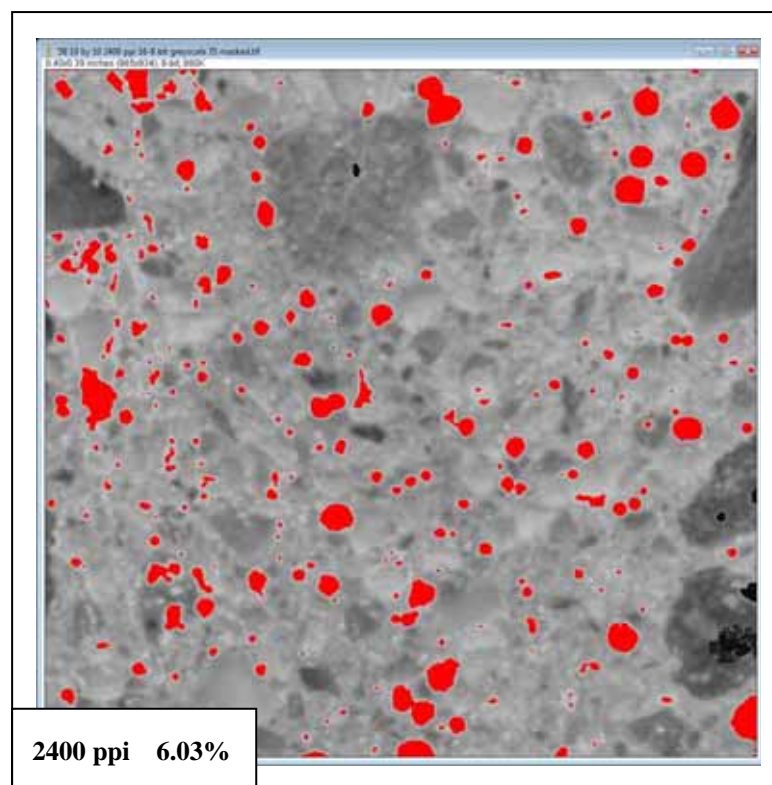


Figure 4.3.3.4.8 2400 ppi resolution micro porosity calculated

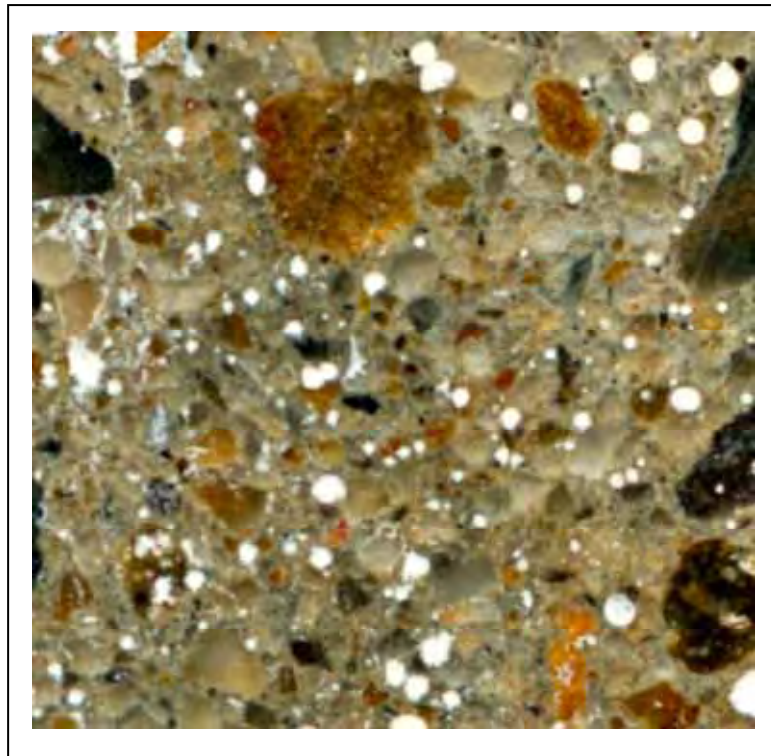


Figure 4.3.3.4.9 Original image in 6400 ppi of the selected section

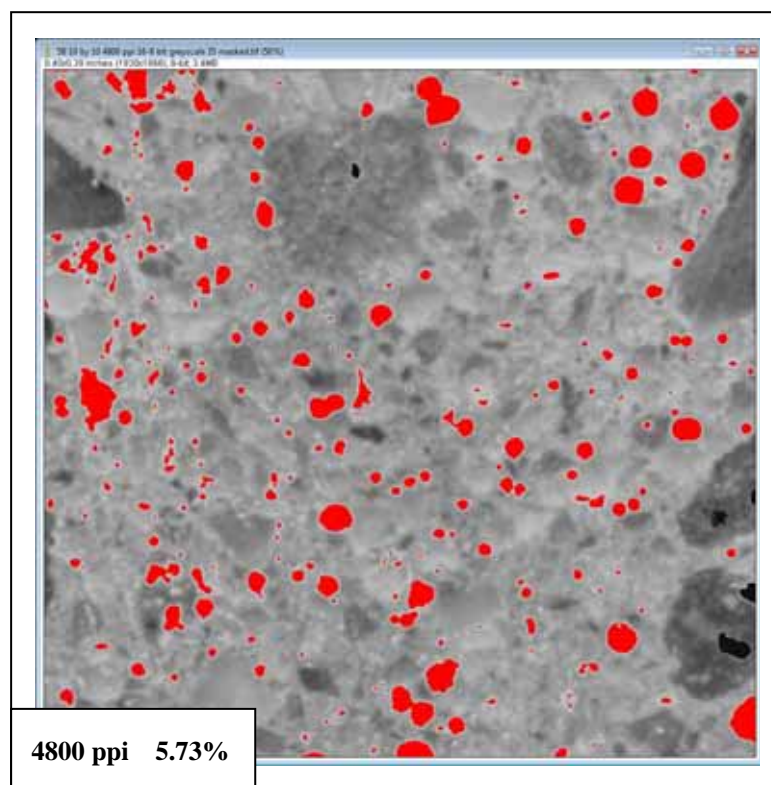


Figure 4.3.3.4.10 4800 ppi resolution micro porosity calculated

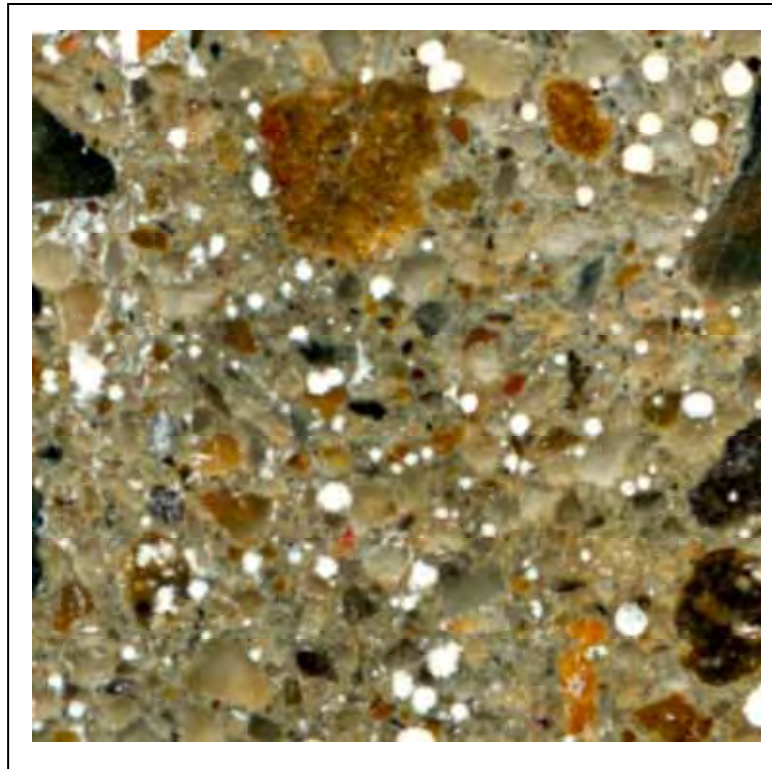


Figure 4.3.3.4.11 Original image in 6400 ppi of the selected section

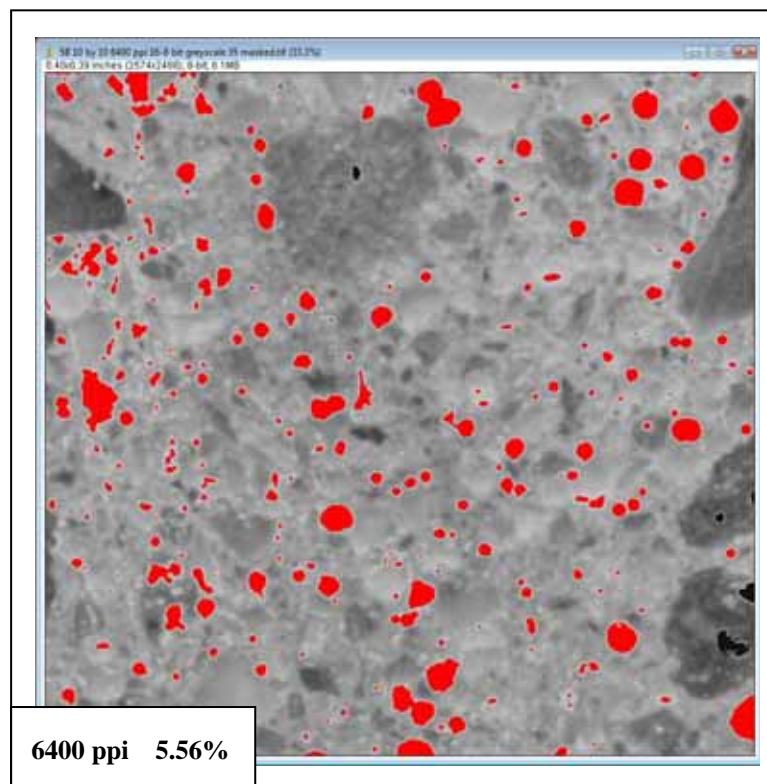


Figure 4.3.3.4.12 6400 ppi resolution micro porosity calculated

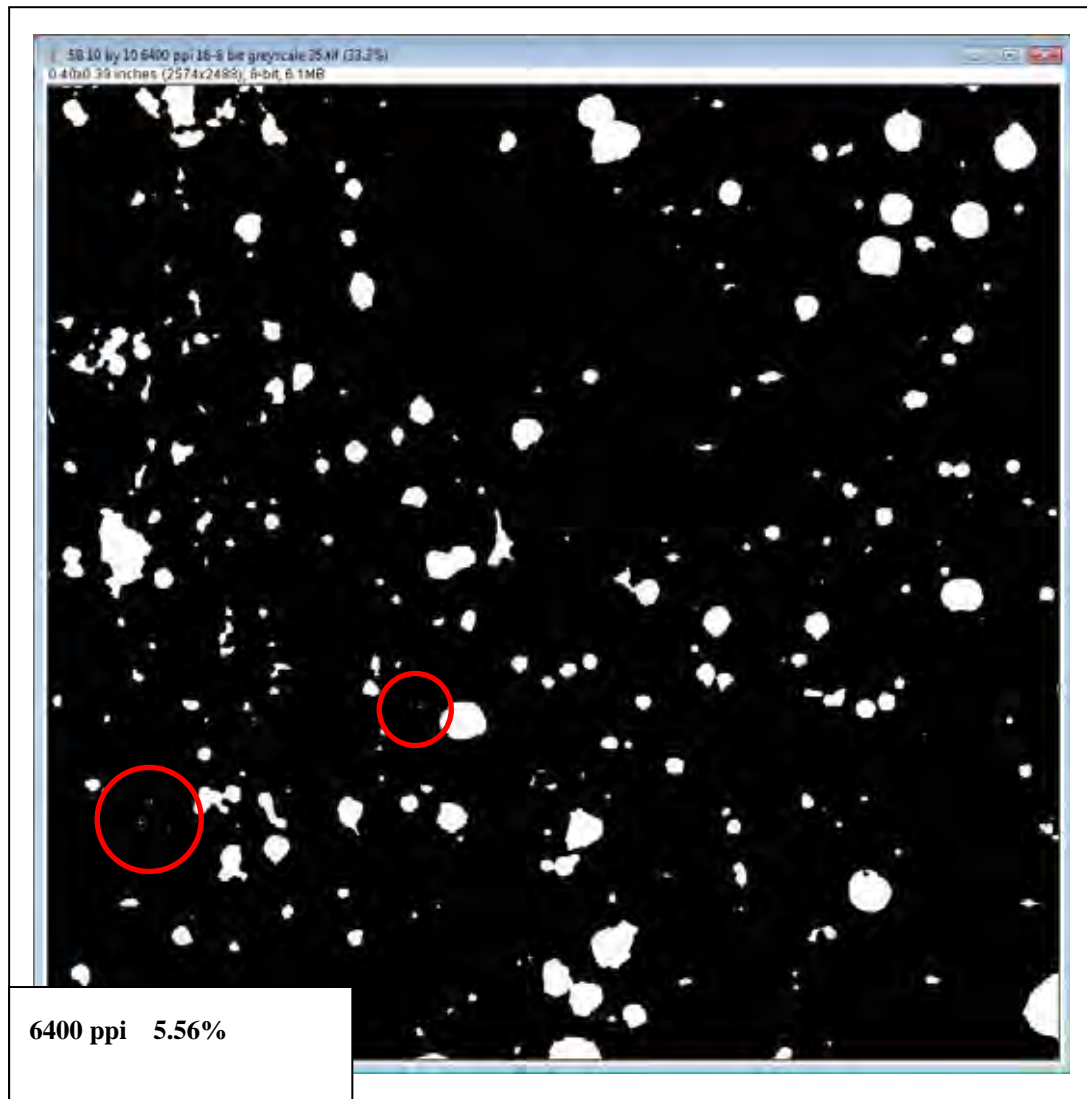


Figure 4.3.3.4.13 6400 ppi resolution micro porosity in B&W

Figure 4.3.3.4.13 shows the exact size of the pores in white colour. The fine 10 μ diameter pores within the red circles are the quantitative calibration constants of all porosity measurements in the full core samples (image size 3.48 GB).

Scanned resolution (ppi)	Image file size 48 bit colour (kB)	Image file size 8 bit greyscale (kB)	Image size in pixel dimensions	Pixel size (μ)
72	448	2.2	29 x 29	352.7
200	481	26.0	80 x 78	127.0
1200	1720	245.0	483 x 466	21.2
2400	5590	905.0	965 x 934	10.6
4800	21000	3450.0	1930 x 1866	5.3
6400	38000	4130.0	2574 x 2488	4.0

Table 4.3.3.4.2 Data for the small section image 10 x 10 mm

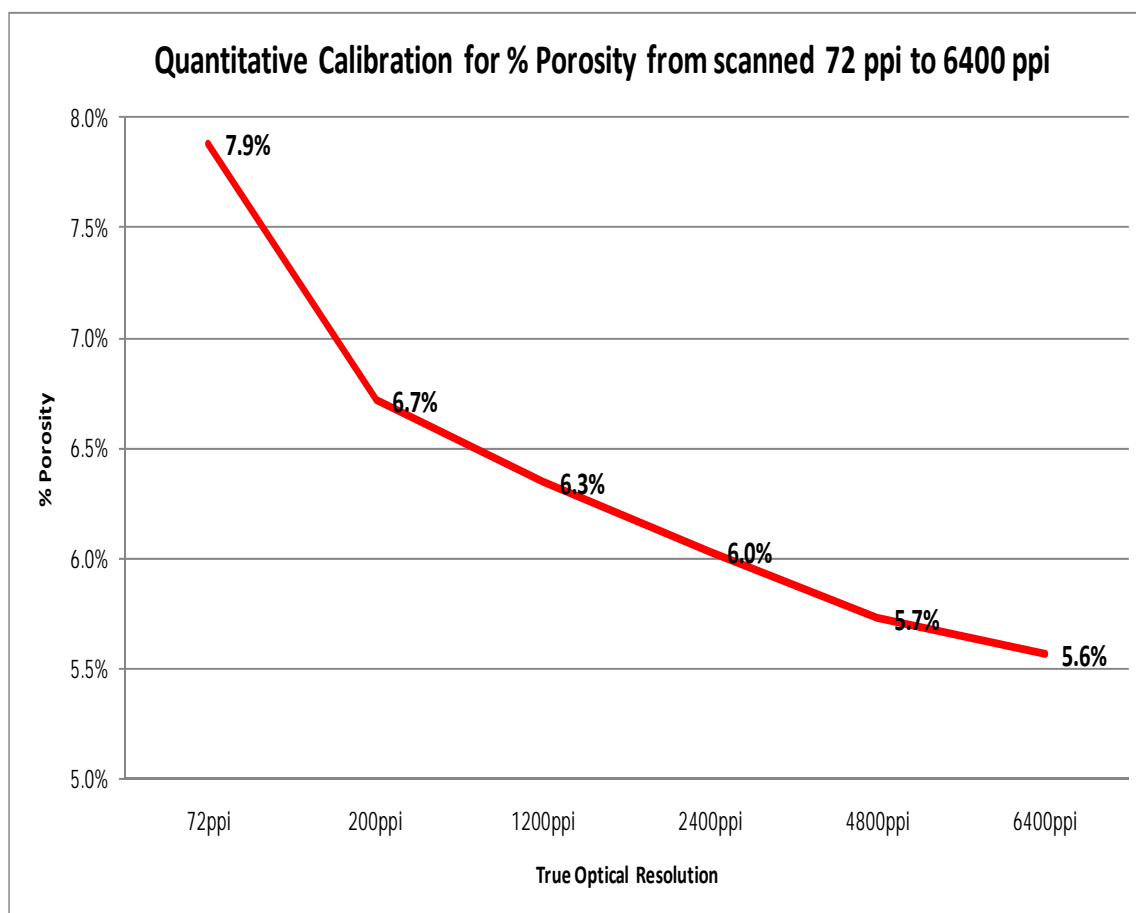


Figure 4.3.3.4.14 Quantitative calibration for % porosity from 72 ppi to 6400 ppi

Observations and Explanations

Table 4.3.3.4.2 shows that when the high depth 48-bit colour image file is reduced to 8-bit greyscale in 64-bit ImageJ analysis the true optical pixel resolution remains the same for calculations.

Figure 4.3.3.4.14 shows and proves the higher the scanned resolution the more accurate is the calculated value of micro porosity.

The calibration of 6400 ppi scanned image resolution of the micro porosity in this small section (37 MB TIFF) guarantees that the 3.48 GB TIFF image file of the 100 mm diameter core section is also fully calibrated and quantitative.

As the true optical pixel resolution of the scanned image becomes smaller and smaller the 64-bit ImageJ software can more and more accurately pick the true perimeter of the micro pores.

The smallest pores accurately calculated in this study were approximately 10 μ in diameter as quantitatively calibrated in Figure 4.3.3.4.13.

4.3.3.5 Summary of Digital Analysis Studies

Most of the samples under study were composed of complex multi coloured and transparent river gravel aggregates.

The accurate results in digital analysis are obtainable, if the three simple procedures are followed -

1. Fine diamond lapping sample preparation;
2. 64-bit image analysis software of uncompressed, untouched TIFF image;
3. High resolution scanning combined with 64-bit image capture software.

At 6400 ppi true optical resolution the percentage porosity in all samples was within 1% of quantitative value calculated in 64-bit ImageJ.

At 4800 ppi true optical resolution the percentage of coarse aggregate in all samples was within 1% of quantitative value calculated in 64-bit ImageJ.

4.4 Optical Microscopy of Cement Paste Microstructure Results

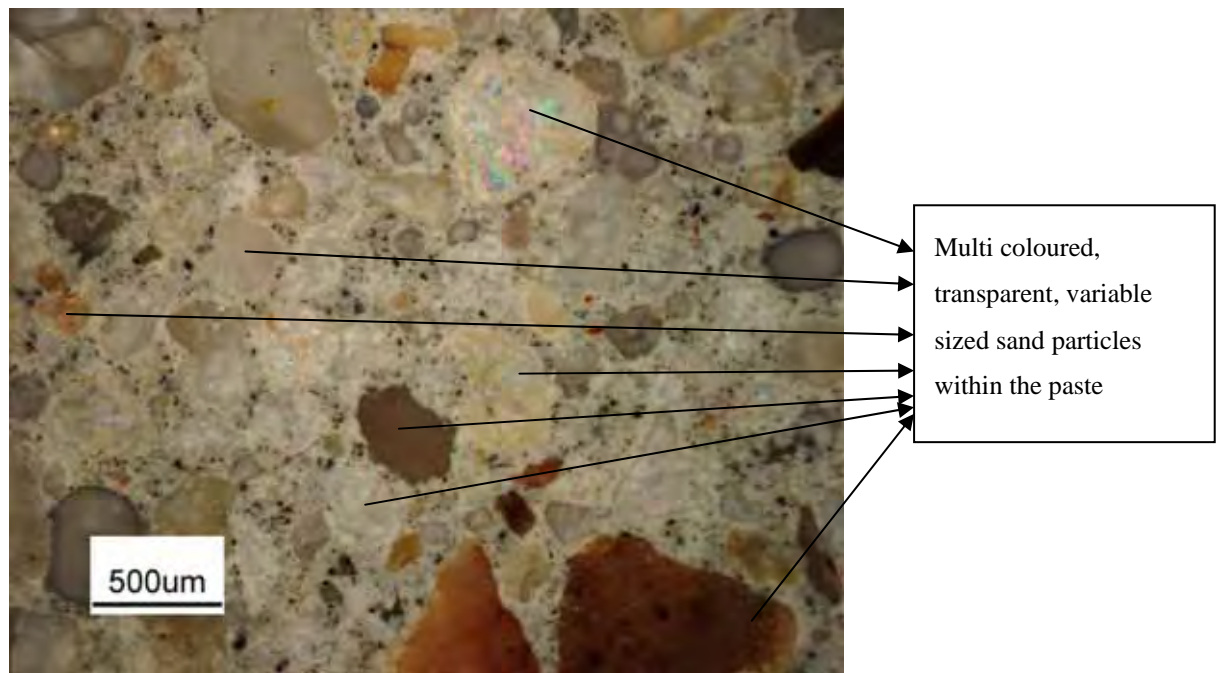


Figure 4.4.1 Core Sample 1 section 1

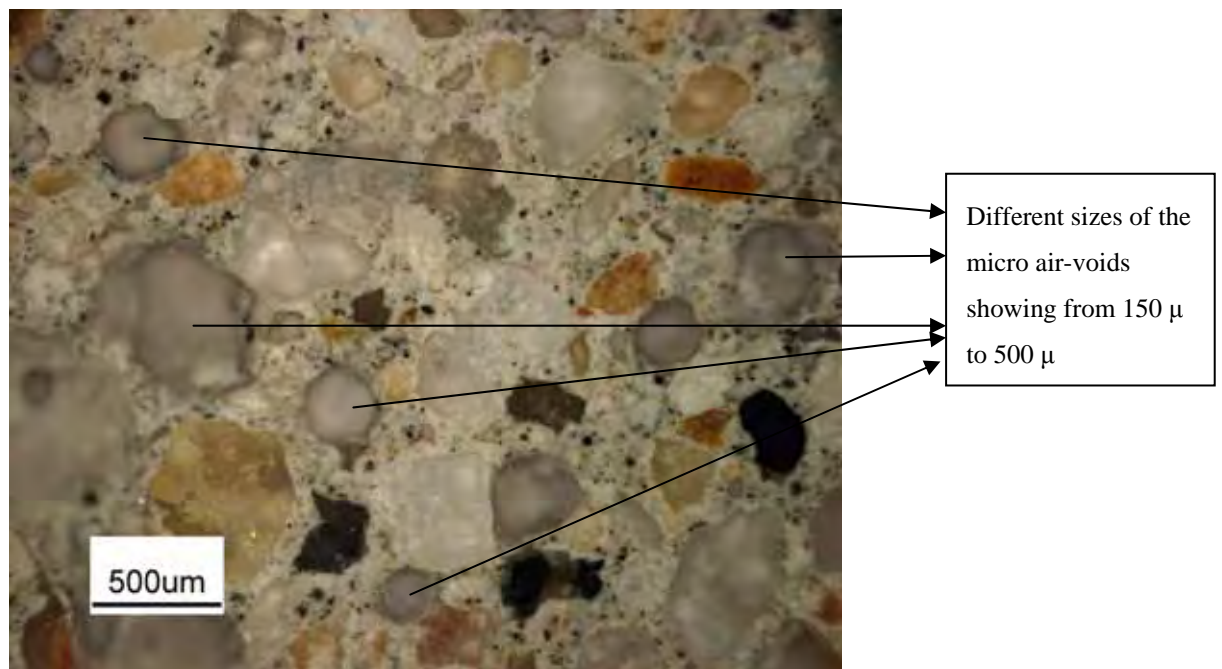


Figure 4.4.2 Core Sample 1 section 2



Figure 4.4.3 Core Sample 2 section 1

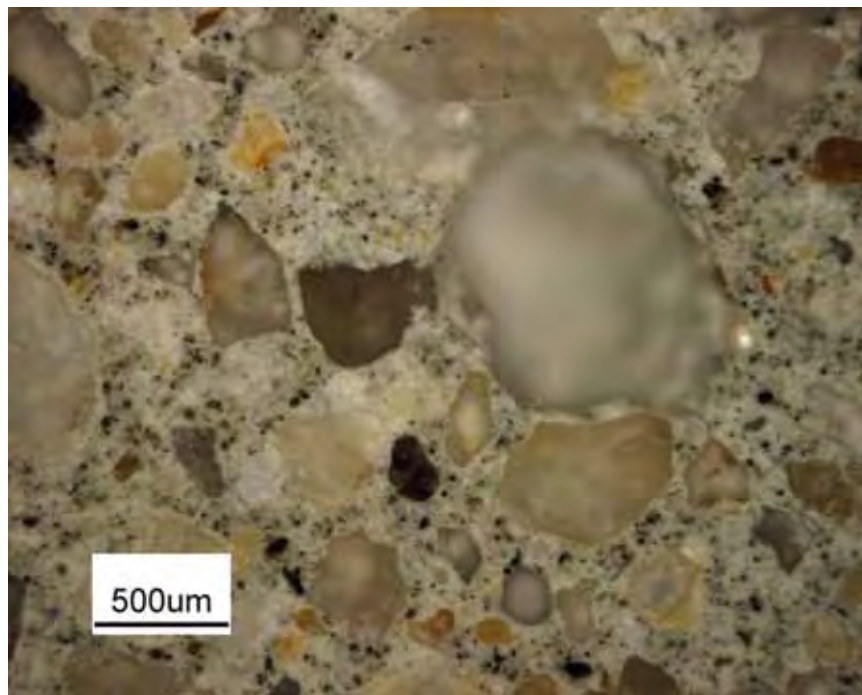


Figure 4.4.4 Core Sample 2 section 2



Figure 4.4.5 Core Sample 3 section 1

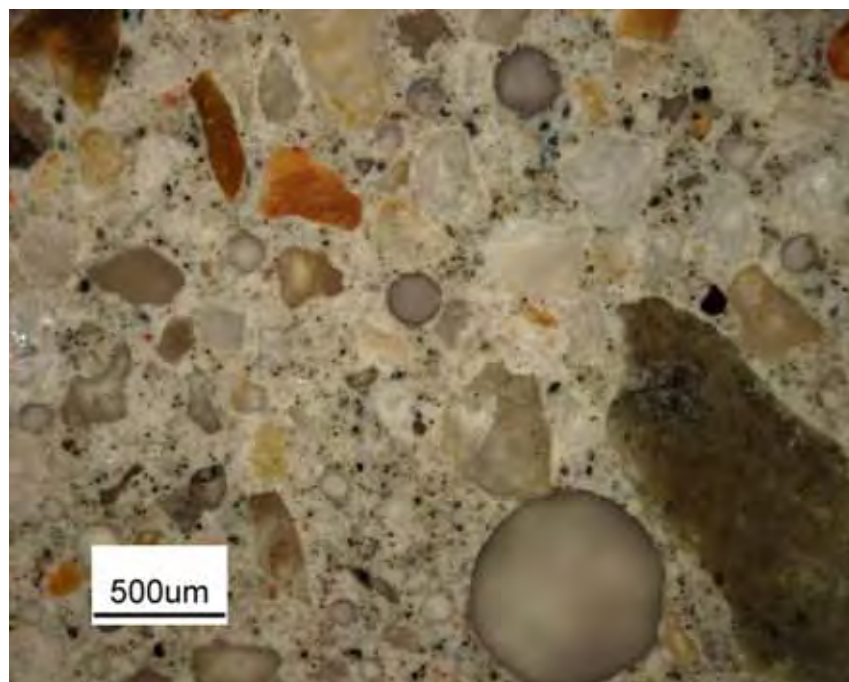


Figure 4.4.6 Core Sample 3 section 2

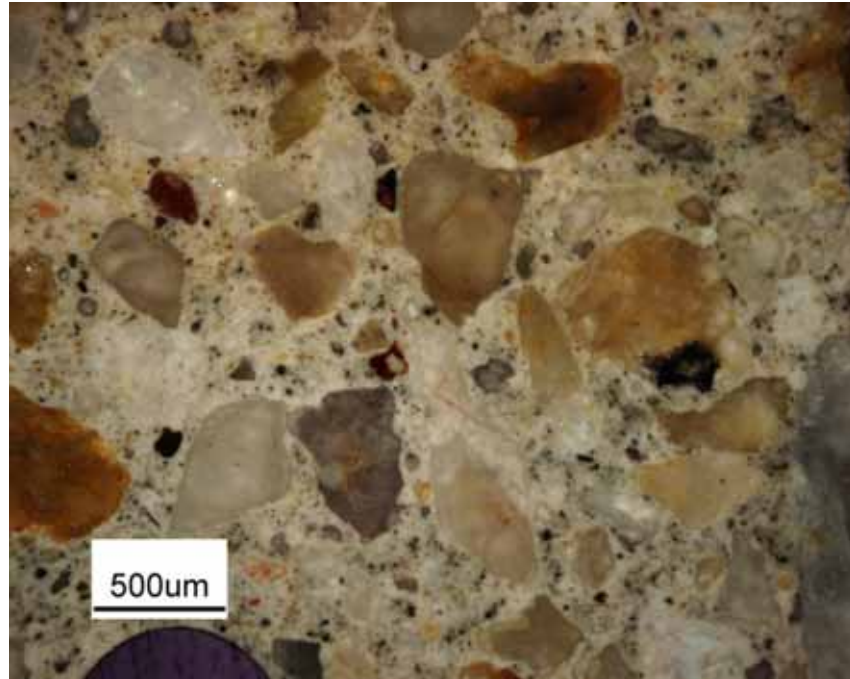


Figure 4.4.7 Core Sample 4 section 1

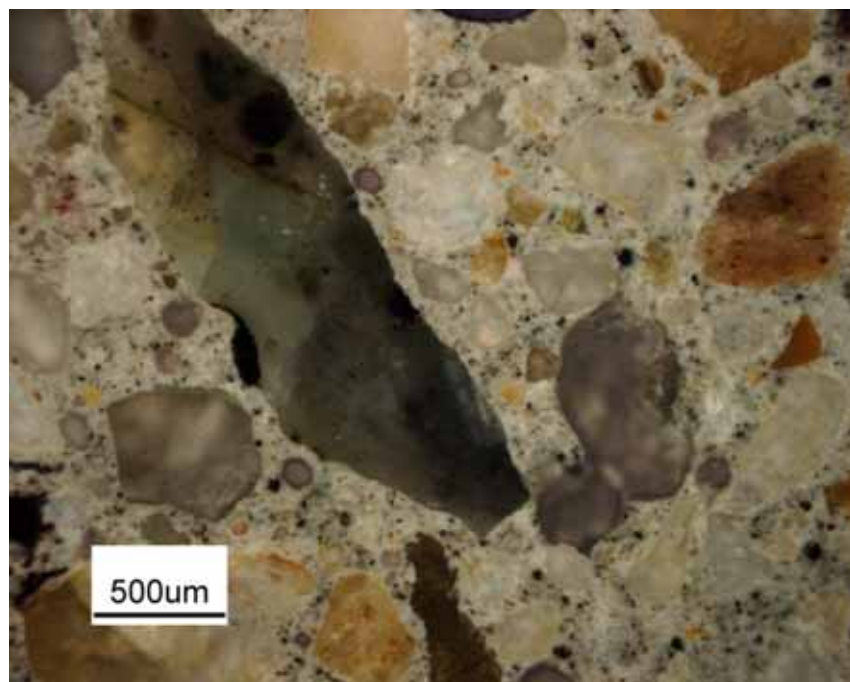


Figure 4.4.8 Core Sample 4 section 2

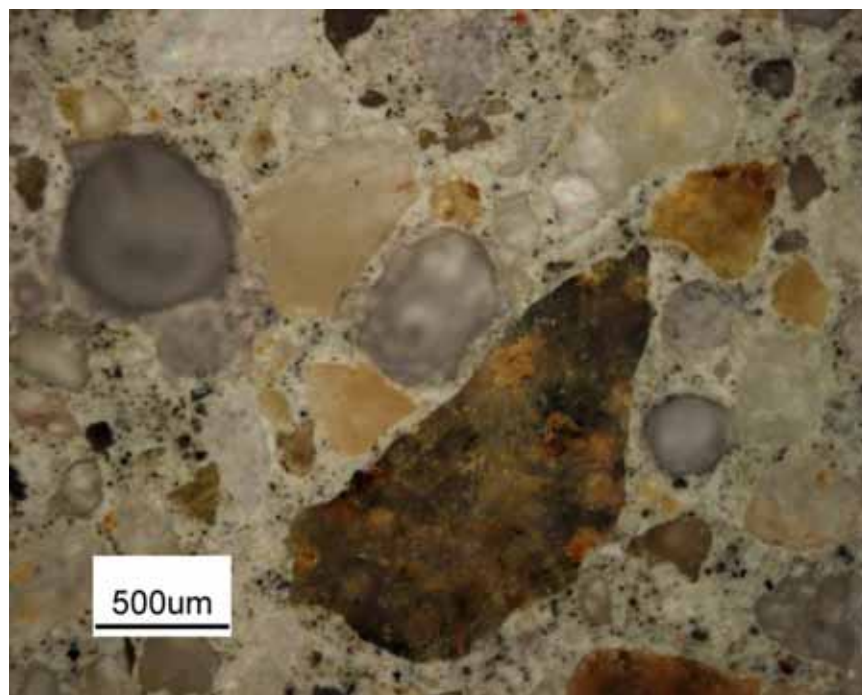


Figure 4.4.9 Core Sample 5 section 1

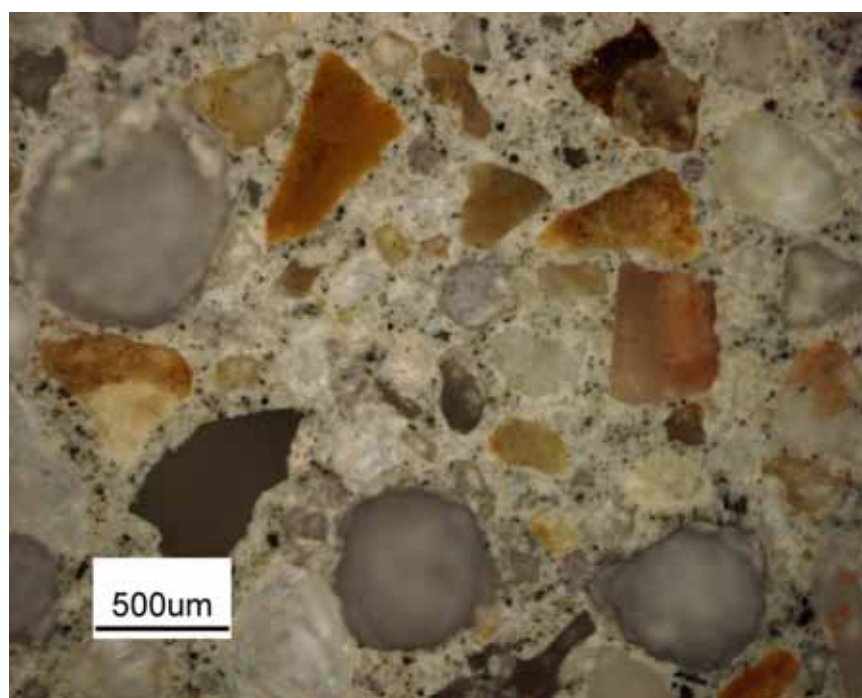


Figure 4.4.10 Core Sample 5 section 2

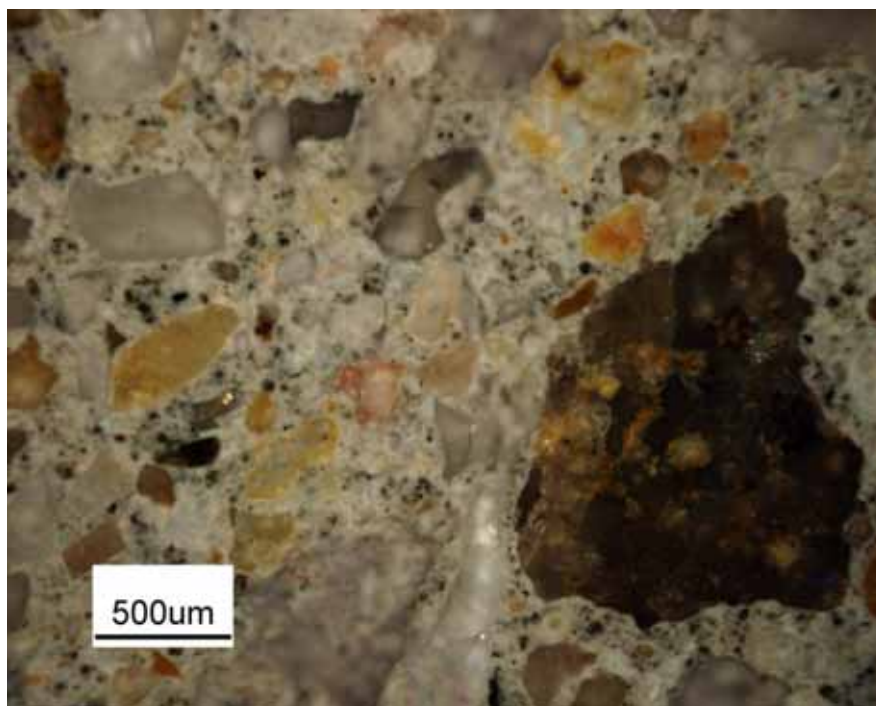


Figure 4.4.11 Core Sample Rm section 1

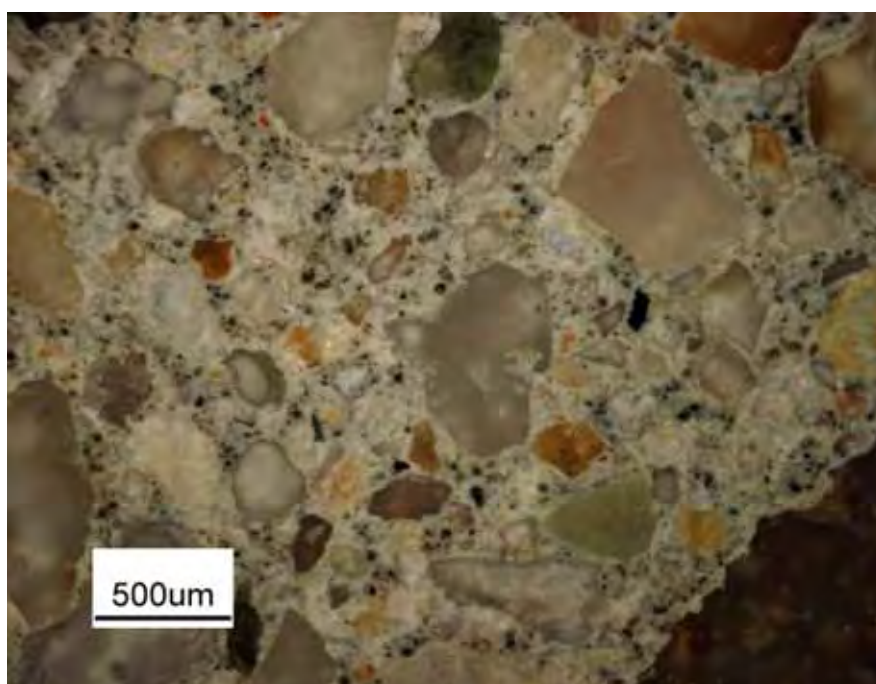


Figure 4.4.12 Core Sample Rm section 2

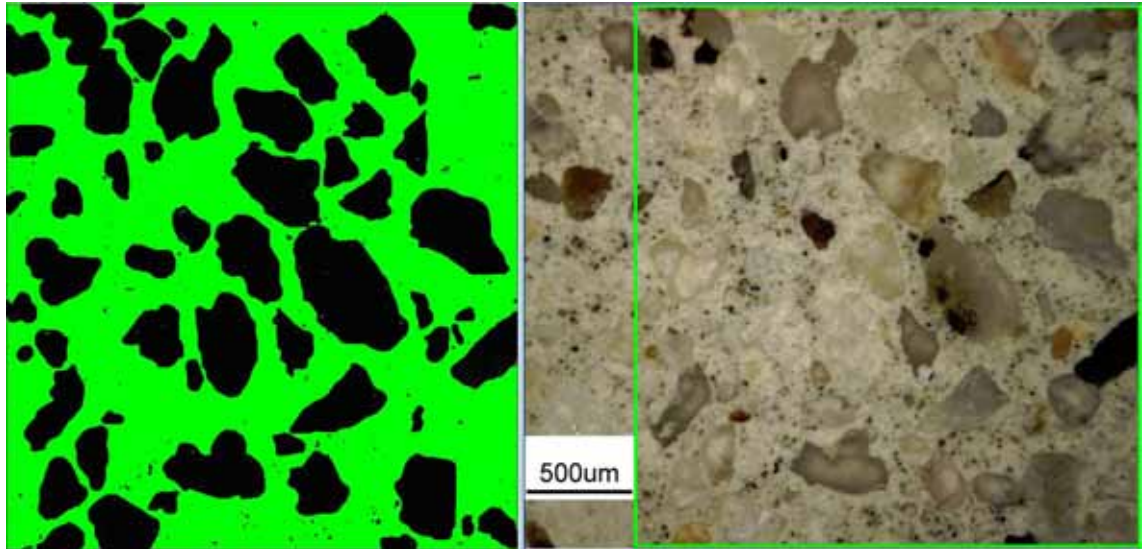


Figure 4.4.13 Core Sample Dar section 1, latest research of quantitative percentages of components in cement paste (Appendix A)

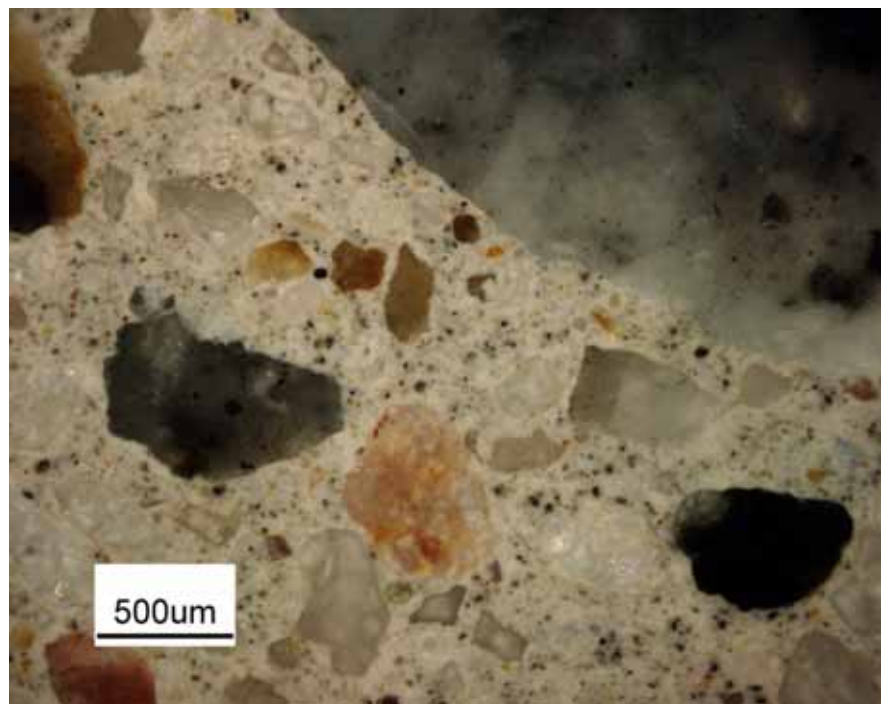


Figure 4.4.14 Core Section Dar section 2

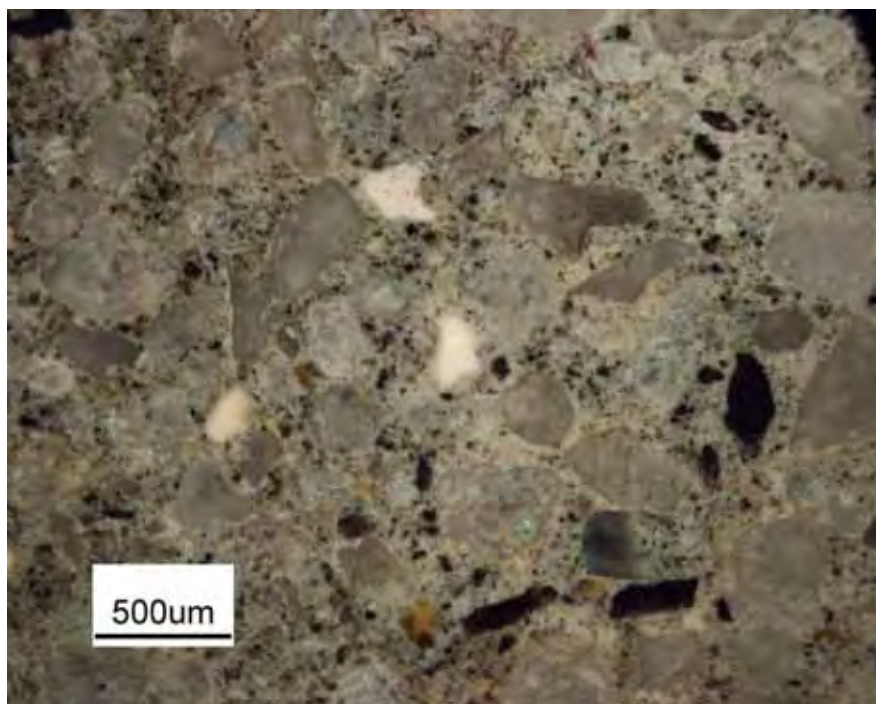


Figure 4.4.15 Core Sample FI section 1

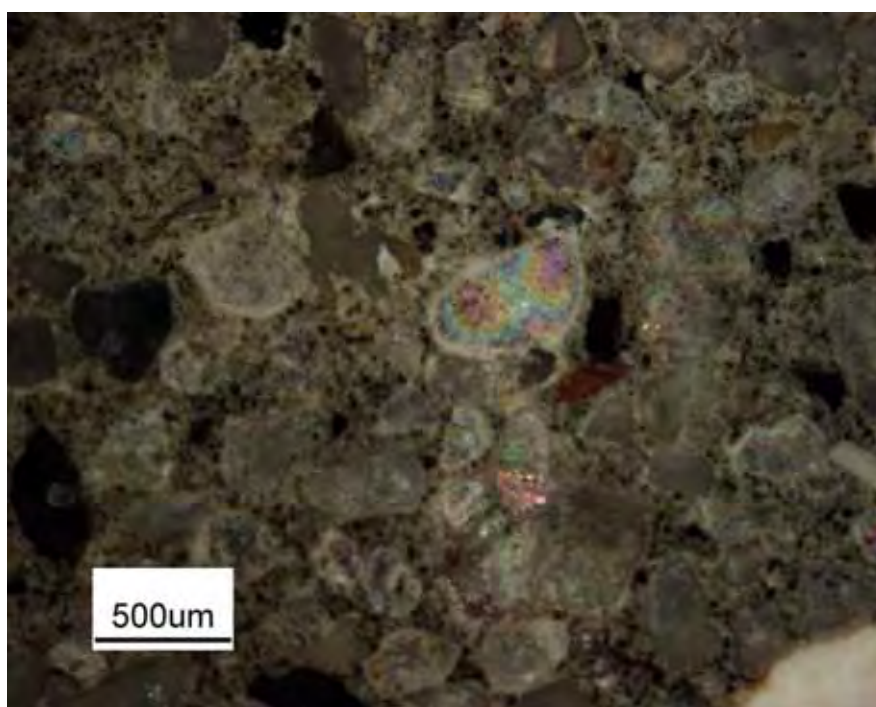


Figure 4.4.16 Core Sample FI section 2

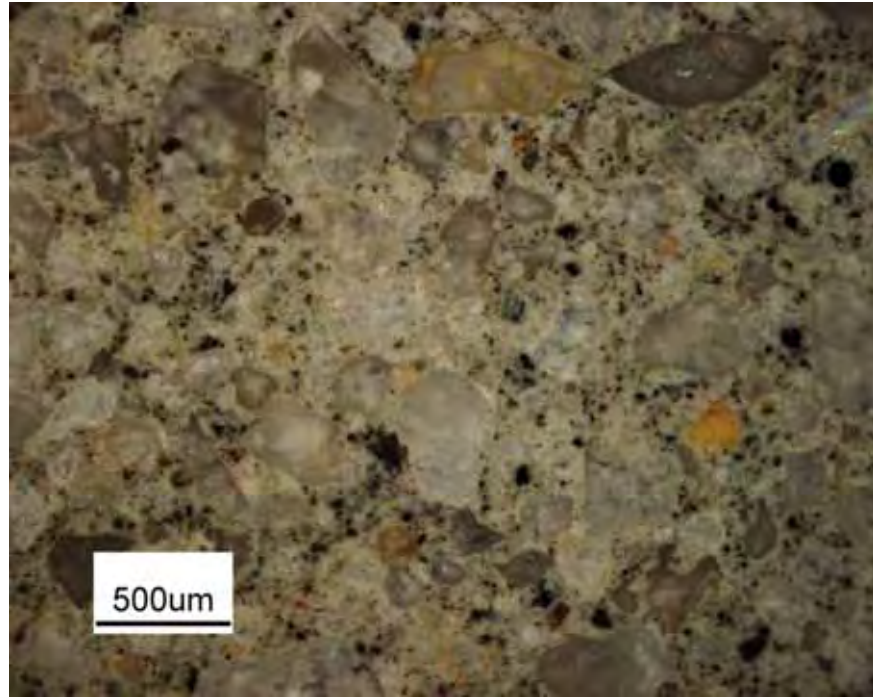


Figure 4.4.17 Core Sample FII section 1

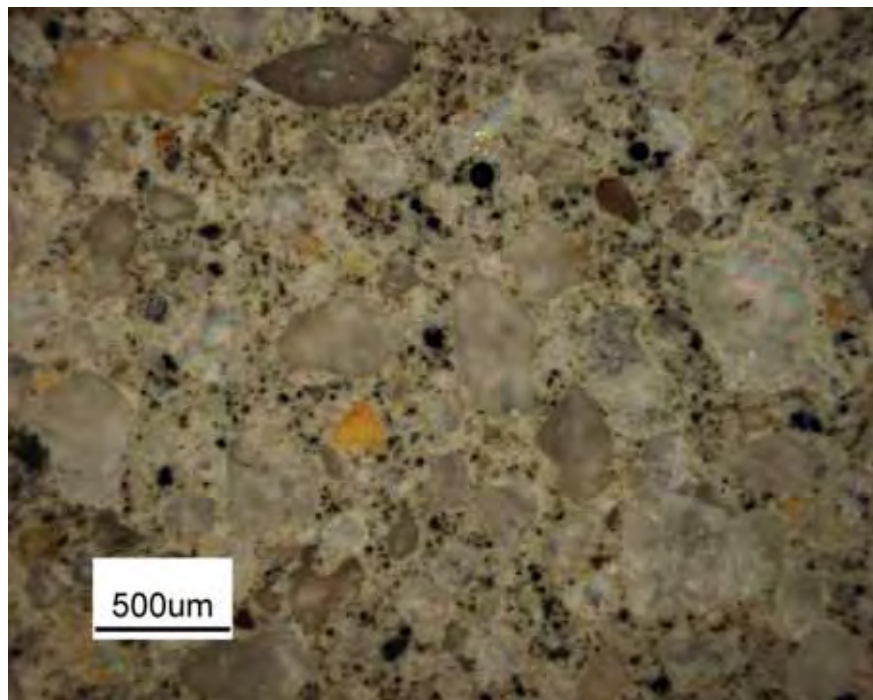


Figure 4.4.18 Core Sample FII section 2

4.4.1 Discussion of Results

Observations and Explanations

Samples were examined on the Nikon Epiphot 200 Microscope. The diagnosis of the microstructure was used for a selection of solid paste matrix areas for testing the Vickers micro hardness on each one of them.

Microscope digital images of the Samples were taken and kept in a folder on a PC in a format shown above in Figures 4.4.1 to 4.4.18.

Digital analysis of the matrix microstructure was not part of this thesis; hence it was not carried out on these digital images.

These digital images were of the size 3840 x 3072 pixels (11.8 megapixels). They were saved in 24-bit colour with an optical resolution of 1.2 μ pixel size.

With traditional paste staining techniques and the accurate filling of micro pores and cracks with fluorescent white epoxy, 64-bit image analysis will be very accurate in analysing quantitative values for percentage paste, percentage fine sand/fine aggregate, percentage micro pores, down to 400 nano metres. For digital analysis below 400 nano metres would require imaging by SEM to find cracks and pores in the 1- 2- nano metre range. This would complete the study from macro to nano structural analysis. The 64-bit image analysis software is far more accurate than the currently used 32-bit version.

My latest research carried out is documented in **Appendix A**.

4.5 Vickers Micro Hardness of Cement Matrix Results

Micro Vickers Hardness of Cement Matrix and Aggregate (300g load)														
Sample	Test 1	Test 2	Test 3	Test 4	Test 5	Test 6	Test 7	Test 8	Test 9	Test 10	Test 11	Test 12	Average	Avg Aggregate
1	43.2	35.6	29.5	23.4	26.3	36	34.5	29.2	26.9	34.9	22.8	36.7	31.6	
2	30.6	50.8	32.2	34.2	24.1	30	39.2	38.1	26.2	30.2	29.4	47.3	34.4	
3	37.4	43	30.7	29.4	33.4	31	25.3	30.9	37.5	29.9	40.3	40	34.1	
4	32.5	41.3	43.2	37.8	47.8	38.8	34.8	42.3	39.4	30.8	28.9	32.5	37.5	54.8
5	28.3	38.4	40.2	24.1	30	33.9	25.8	36.7	35.8	27.6	24.9	41.1	32.2	
Rm	36.1	20.3	18.9	43.2	40.3	29.1	41.2	30.2	39.8	20.9	34.2	27.4	31.8	
Dar	36.4	30.8	41.6	40.4	43.4								38.5	
FI	57.9	77.9	68.7	62	79.7	59.7	73.4	74.5	67.1	75.3	69.9	64.5	69.2	225
FII	55.2	49.8	79	58.6	51.9								58.9	

Table 4.5.1 Vickers Micro Hardness table

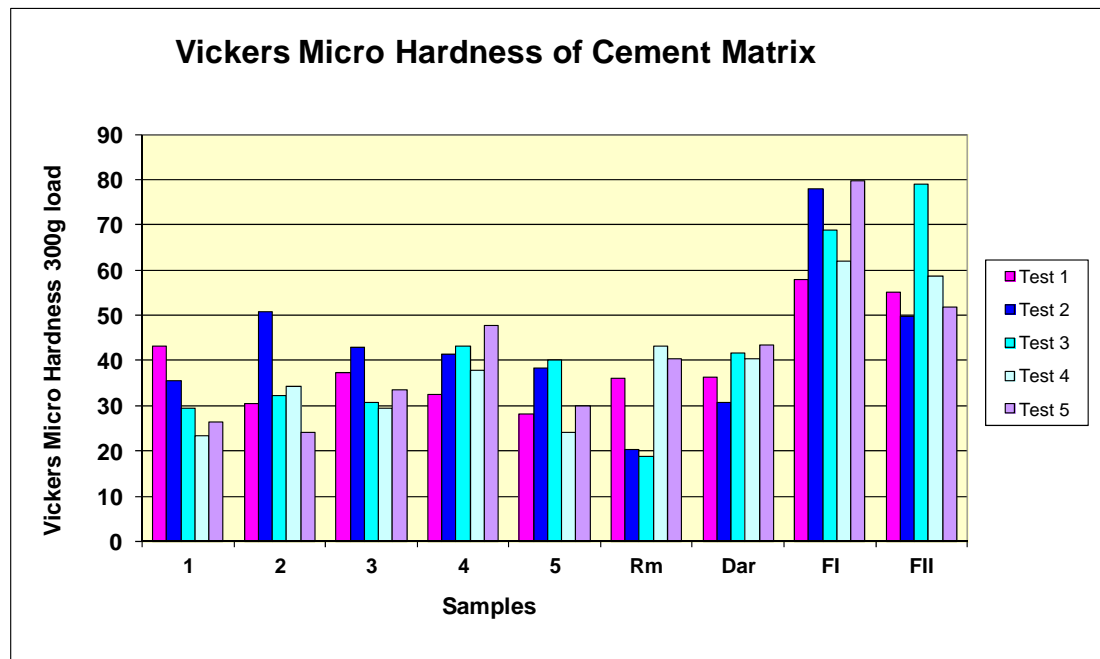


Figure 4.5.1 Vickers Micro Hardness Comparison of all Samples

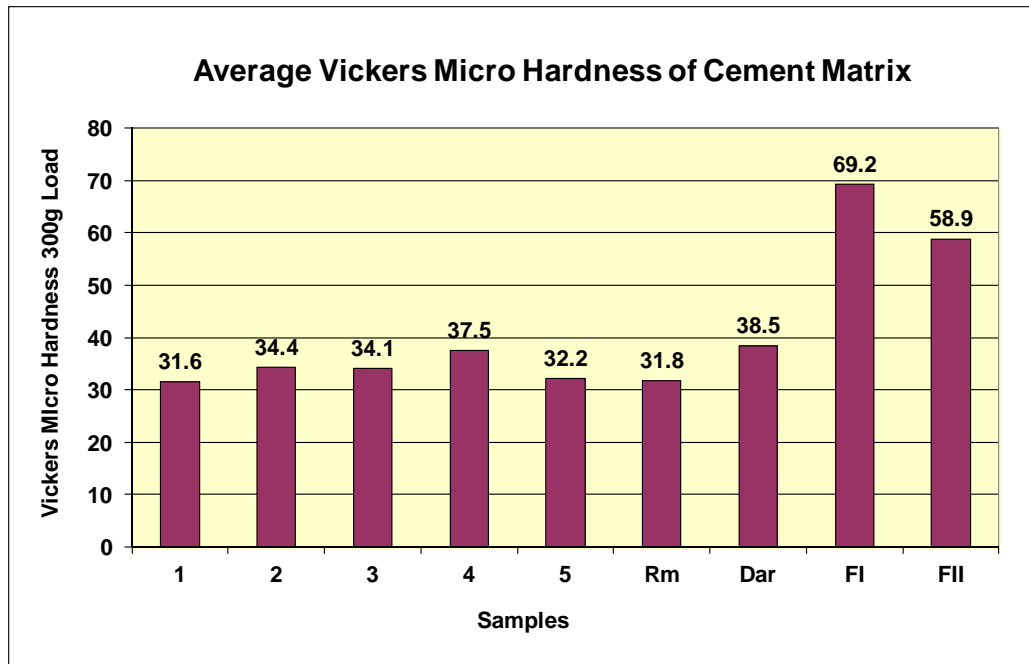


Figure 4.5.2 Average Vickers Micro Hardness of all samples

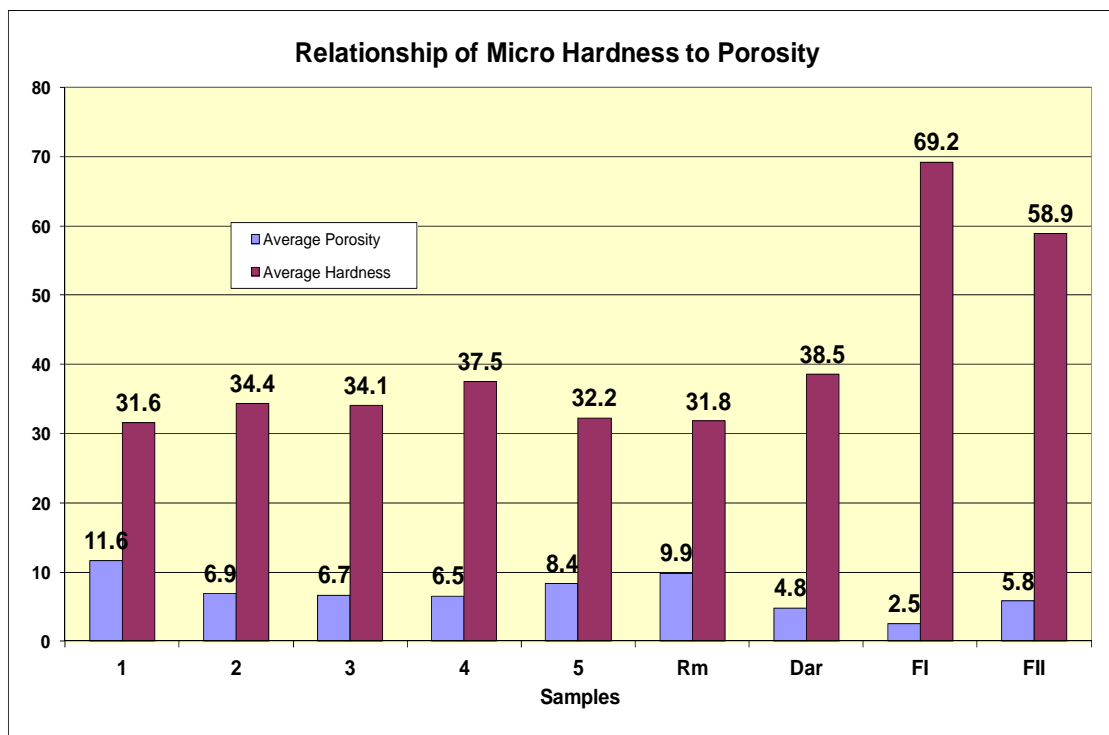


Figure 4.5.3 Relationship of Vickers Micro Hardness to Apparent Porosity

4.5.1 Discussion of Results

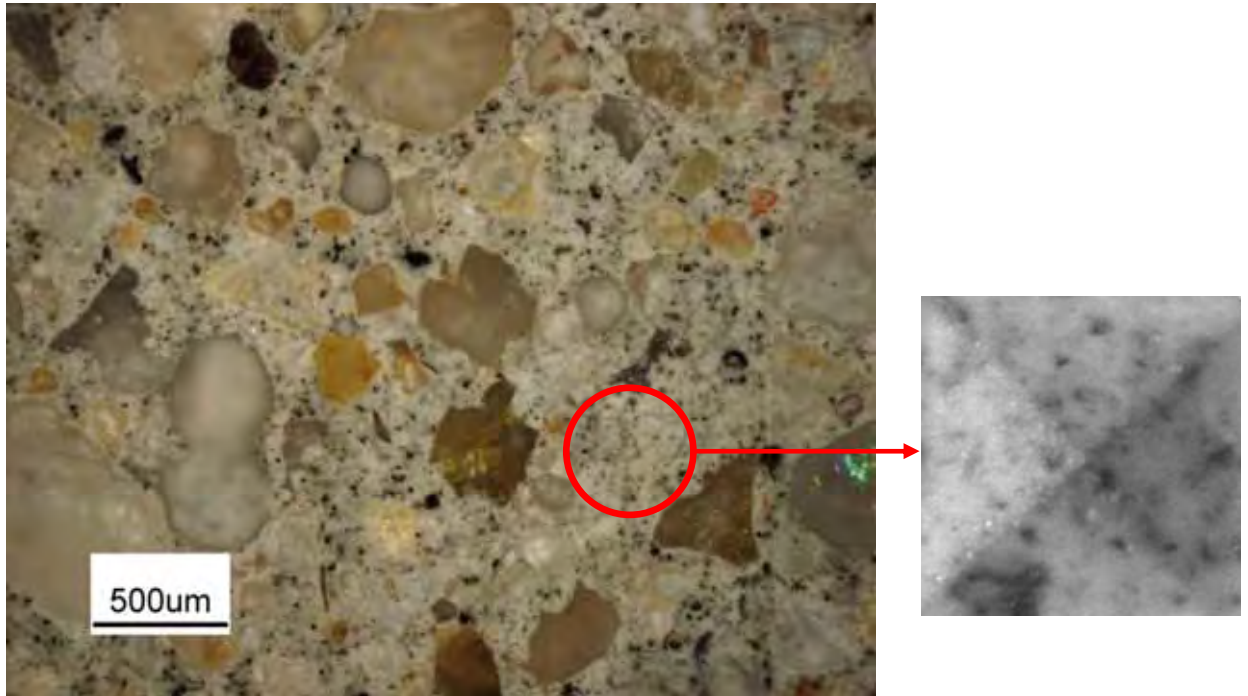


Figure 4.5.1.1 Example of an area in the matrix and Vickers micro hardness indent

Observations and Explanations

To further understand the difference in durability in the samples the hardness of the river gravel aggregate in Sample 4 and blue metal aggregate in Sample FI were tested.

The damaged floor samples 1A to 4B – the average aggregate hardness was only 1.5x the hardness of the bonding matrix. Therefore the aggregate was only marginally stronger than the cement matrix but it was adequate for this grade of concrete.

In samples FI and FII – the blue metal aggregate hardness was on average 4x the hardness of the much stronger bonding matrix. These mixes had a much stronger compressive strength and were higher cement content mixes.

5 CONCLUSION

Four core samples drilled through expansion joints from a damaged structural concrete floor slab were quantitatively examined and compared.

Some traditional testing was employed but mostly newer micro CT X-Ray scanning technology, and digital image analyses were used. Three detailed studies of varying high resolution digital analyses of the micro-structures provided the necessary mega files to quantitatively compare tests and analysis results required for forensic comparison.

Core sample 1 was the most porous, yet had similar cement/sand paste micro-hardness (similar compressive strength) to core samples 2 to 4 drilled from the same floor slab.

The core samples 1 to 4 varied, but were within (what the consultant, Mr Jim Griffiths, considered) normal specification parameters. The porosity, coarse aggregate, micro-cracking, etc. compared favourably with reference core sample 5 and the core sample Readymix (Rm).

It was finally concluded after thorough analyses that the damage to areas of the slab, particularly apparent from core samples 1 and 4, was due to specific point impact damage and not to an incorrect durability concrete specification, or batching error.

Questions arose as to the suspected variability in pumping, laying, vibrating, and float finishing procedures followed throughout construction.

It was revealed after the test analyses were completed that very heavily stacked steel wheeled trolleys had crossed over the notched areas during the installation of steel pallet racking during the warehouse fit-out, damaging many areas. The damage

occurred because these point loads exceeded the impact compressive strength of the mix, even though it was correctly purpose specified for its durability.

The result of the court action or party that ultimately settled was never revealed, but restoration work to the new warehouse slab floor amounted to several hundred thousands of dollars.

This is the first time, as far as I can establish, that at Materials Science and Engineering at UNSW fine diamond surface lapped full cross sections of concrete cores have been digitally scanned in 6400 ppi x 6400 ppi (4 micron) true optical resolution. Very large data image files (between 700 MB to 3.48 GB) were saved for analysis in 48-bit HDR colour.

Up until recently this detailed research analysis was only possible within private concrete consultant laboratories utilising proprietary high resolution scanners and 64-bit image analysis software.

This study has well and truly confirmed that by using 64-bit Windows 7 (or Vista Ultimate) operating systems, 64-bit Office 2010, 64-bit ImageJ and image data files of ~ 3 GB, that had been optically scanned to at least 4800 ppi but preferably 6400 ppi (true optical resolution of 4 micron), the automated quantitative digital analysis is almost 100% accurate for basalt aggregate. The analysis is about 99% accurate for quantitatively calibrated multi-coloured river gravels. In all samples tested, the quantitative total air void porosity resolved to 4 microns true optical resolution which was 99% accurate to ASTM C 457 and EN 480-11 standards.

Multi-coloured and transparent aggregates, fine silt and sand grains are yet to be accurately quantified in a fully automated 64-bit image analysis mode and may need 128-bit image analysis software that will run in Windows 8 (the anticipated 128-bit operating system due for release in 2013).

There is an urgent need for Materials Science and Engineering at UNSW to develop optical laser scanners to <0.25 microns ($>100,000$ ppi) to compete and excel against the current quantitative research data from proprietary laboratories and overseas research centres, that are currently able to resolve larger samples of cement micro-structures to 0.5 micron (50800 ppi).

The future for automated quantitative analyses of complex micro-structures within ever larger sized ceramic samples is exciting indeed.

REFERENCES

1. Ammouche, A., Riss, J., Breysse, D., Marchand, J., *Cement and Concrete Composites*, Special Issue: Image Analysis, 2001
2. ASTM Committee C-9, *Significance of Tests and Properties of Concrete and Concrete-Making Materials*, ASTM, Philadelphia, USA, 1978
3. ASTM C 457: *Standard Test Method for Microscopical Determination of Parameters of the Air-Void System in Hardened Concrete*
4. Benz, D.P., Halleck, P.M., Grader, A.S., and Robert, J.W., *Four Dimensional X-Ray Micro-tomography Study of Water Movement during Internal Curing*, Proceedings of the International RILEM Conference - Volume Changes of Hardening Concrete: Testing and Mitigation, Eds. O.M. Jensen, P. Lura, and K. Kovler, RILEM Publications S.A.R.L., 2006
5. Bentz, D.P., Stutzman, Paul, E., *Curing, Hydration, and Microstructure of Cement Paste*, ACI Materials Journal, Sep/Oct 2006
6. Chini, A., Villevicencio, E., Rinker, M., *Detection of Microcracks in Concrete Cured at Elevated Temperature*, Florida Department of Transport Contract No BD 545-50 Final Report Submitted to School of Building Construction, University of Florida July, 2006
7. *Concrete Design Handbook in Accordance with AS3600*, a joint publication of Cement and Concrete Association of Australia and Standards Australia, 1994

8. Dhir, R., *Controlling Concrete Degradation*, Thomas Telford Publications, London, UK, 1999
9. Dhir, R., *Creating with Concrete*, University of Dundee, Scotland, 1999
10. Dhir, R., *Extended Performance of Concrete Structures*, Thomas Telford Publications, London, UK, 1999
11. Dhir, R., *Radical Design and Concrete Practices*, Thomas Telford Publications, London, UK, 1999
12. Dolar, L., *Handbook of Concrete Aggregates - A Petrographic and Technological Evaluation*, Noyes Publications, Park Ridge, New Jersey, USA, 1983
13. EN 480-11, *Admixtures for concrete, mortar and grout – test methods – Part 11: Determination of air void characteristics in hardened concrete*
14. Erlin/Stark editors, *Petrography Applied to Concrete and Concrete Aggregates*, ASTM, Philadelphia, USA, 1990
15. Garboczi, E.J., Bentz, D.P., *Digital Simulation of the Aggregate-Cement Paste Interfacial Zone in Concrete*, Maryland, USA, 1990
16. Glinicki, M, A., Litorowicz, A., *Crack System Evaluation in Concrete Elements at Mesoscale*, Bulletin of the Polish Academy of Sciences Technical Services
17. Glinicki, Michal A., Litorowitz, Agnieszka, *Diagnostyka Rys w Kompozytach O matrycy cementowej metoda Komputerowej analizy obrazu*, Drogi i Mosty Publication, Warszawa, Poland, 2007 - from a personal contact with Dr. Glinicki in Polish language

18. Glinicki, M., Litorowicz, A., *Digital Analysis of Microscopic Images for Crack System Evaluation in Concrete Elements*, Institute of Fundamental Technological Research, Polish Academy of Sciences, Świątokrzyska 21, 00-049 Warszawa, Poland, 2006

19. Glinicki, M., Zielinski, M., *Depth-sensing indentation method for evaluation of secondary cementitious materials*, Cement and Concrete Research Volume 34, Issue 4, April 2004, Pages 721-724.

20. Green, H., *Impact strength of concrete*, Proc. Inst. C.E., 28, pp. 383 - 96, Building Research Establishment, Crown copyright, London, 1964

21. *Handbook of Reinforced Concrete Design in Accordance with AS3600*, 2001/2002

22. Hooton, R. D., Bickley, J., Hover, K. C., *Preparation of a Performance-based Specification for Cast-in-Place Concrete*, RMC Research Foundation, 2006

23. Jana, D.A., *Round Robin Test on Measurements of Air-Void Parameters in Hardened Concrete by Various Automated Image Analysis and Astm C457 Methods*, 29th ICMA proceedings. Quebec, Canada, May 20-24; 2007

24. Jakobsen, U., Pade, C., Thaulow, N., Brown, D., Sahu, S., Magnusson, O., De Buck, S., De Schutter, G., *Automated Air Void Analysis of Hardened Concrete-A Round Robin Study*, Cement and Concrete Research Volume 36, Issue 8, August 2006, pages 1444-1452 10th EUROSEMINAR on microscopy applied to building materials, University of Paisley, June 21-25, 2005

25. Kim, K., Milstein, F., *Relation Between Hardness and Compressive Strength of Polymer Concrete*, Construction and Building Materials Volume 1, Issue 4, December 1987, Pages 209-214

26. Kosmatka, S.H., Kerkhoff, B., Panarese, W.C., *Design and Control of Concrete Mixtures*, Fourteenth Edition, Portland Cement Association, USA, 2002
27. Litorowicz, A., *Identification and Quantification of Cracks in Concrete by Optical Fluorescent Microscopy*, Cement and Concrete Research, Warszawa, Poland, 2006
28. *Modelling of cement based materials properties and performance through a multi scale approach*, Concrete Materials 351-371, Nova Science Publishers, Inc., Hauppauge. NY, USA, 2009
29. Meyers, Chawla, *Mechanical Behaviour of Materials*, Pages 162-168, 1999
30. Mindess, S., Young, J.F., *Concrete*, Prentice Hall, New Jersey, USA, 1981
31. Metropolitan Water Sewerage and Drainage Board Sydney, *Concrete Manual*, Sydney Water Board Production, 1983
32. Neville, A. M., *Properties of Concrete*, Longman Scientific & Technical, Longman Group UK Limited, 1989
33. Neville, A.M., Brooks, J.J., *Concrete Technology*, Pearson Prentice Hall, UK, 2008
34. Pade, C., Jakobsen, U.H., Elsen, J., *A New Automatic Analysis System for Analyzing the Air Void System in Hardened Concrete*, Proceedings of the International Cement Microscopy Association, ed. Jany, L, and Nisperos, A., San Diego, 2002
35. Patty, T., *PowerPoint Presentation of Concrete Petrography*, Austin Petrographic Laboratory, WJE Austin, 2008

36. Peterson, K. W., Swartz, R. A., Sutter, L., Van Dam, T. J., *Hardened Concrete Air Void Analysis with a Flatbed Scanner*, Annual Meeting

37. Peterson, K., *Automated Air-Void System Characterization of Hardened Concrete: Helping Computers to Count Air-Voids Like People Count Air-Voids – Methods for Flat Bed Scanner Calibration*, PhD. Dissertation, Michigan Technological University, Houghton, MI, USA, 2008

38. Peterson, K., Carlson, J., Sutter, L., Van Dam, T., *Methods for Threshold Optimization From Images Collected From Contrast Enhanced Concrete Surfaces For Air-Void System Characterization*, Materials Characterization Vol 60 issue 7 Pages 710-715 Journal 2009

39. Promentilla, M.A.B., Sugiyama, T., Hitomi, T. And Takeda, N., *Characterizing the 3d Pore Structure of Hardened Cement Paste With Synchrotron Microtomography*, Journal of Advanced Concrete Technology. Japan Concrete Institute. Vol. 6(2), pp. 703-713, 2008

40. Promentilla, M., Sugiyama, T., Hitomi, T., Takeda, N., *Quantification of Tortuosity in Hardened Cement Pastes Using Synchrotron-Based X-Ray Computed Microtomography*, Cement and Concrete Research Volume 39. Issue 6, June 2009

41. Portland Cement Association, *Design and Control of Concrete Mixtures*, Illinois, USA, 1968

42. Ranachowski, Glinicki, *Application of acoustic emission method for concrete component identification during micro hardness testing*, Cement Wapno Beton [1425-8129], Vol. 15, Iss. 4, pg 202, Poland, 2010

43. Rasband, W.S., *ImageJ*, U. S. National Institutes of Health, Bethesda, Maryland, USA, <http://rsb.info.nih.gov/ij/>, 1997-2009

44. Rasband, W., *ImageJ Image Processing and Analysis in Java*, National Health Institute, 2007
45. Ramezaniapour, A.M., Hooton, R.D., *Evaluation of Two Automated Methods for Air-Void Analysis of Hardened Concrete*, Journal of ASTM International Volume 7, Issue 2, February 2010
46. Ryan, W.G., Samarin, A., *Australian Concrete Technology*, Longman Cheshire, Australia 1992
47. Ramachandran, V.S., Beaudoin, J.J., *Handbook of Techniques in Concrete Science and Technology*, Stnadard Publishers Distributors, Delhi, India, 2006
48. Sahu, S., Badger, S., Thaulow, N., and Lee, R. J., *Determination of Water-Cement Ratio of Hardened Concrete by Scanning Electron Microscopy*, Cement and Concrete Composites Volume 26, Issue 8, Pages 987-992, November 2004
49. StJohn, D., *Concrete Petrography - A Handbook of Investigative Techniques*, Arnold Hodder Deadlone Group, London, 1998
50. Sutter, L. Research Brief, No. 0092-03-16, September 2007
51. The Specifier's Guide to Durable Concrete Item Code: EB221, 2005
52. Transportation Research Board No 80, Washington DC, Etats-Unis, No 1775, pp 36-43, 2001
53. Warner, R., Foster, S., Kilpatrick, A., *Reinforced Concrete Basics, Analysis and Design of Reinforced Concrete Structures*, Pearson, Australia, 2007

APPENDIX A

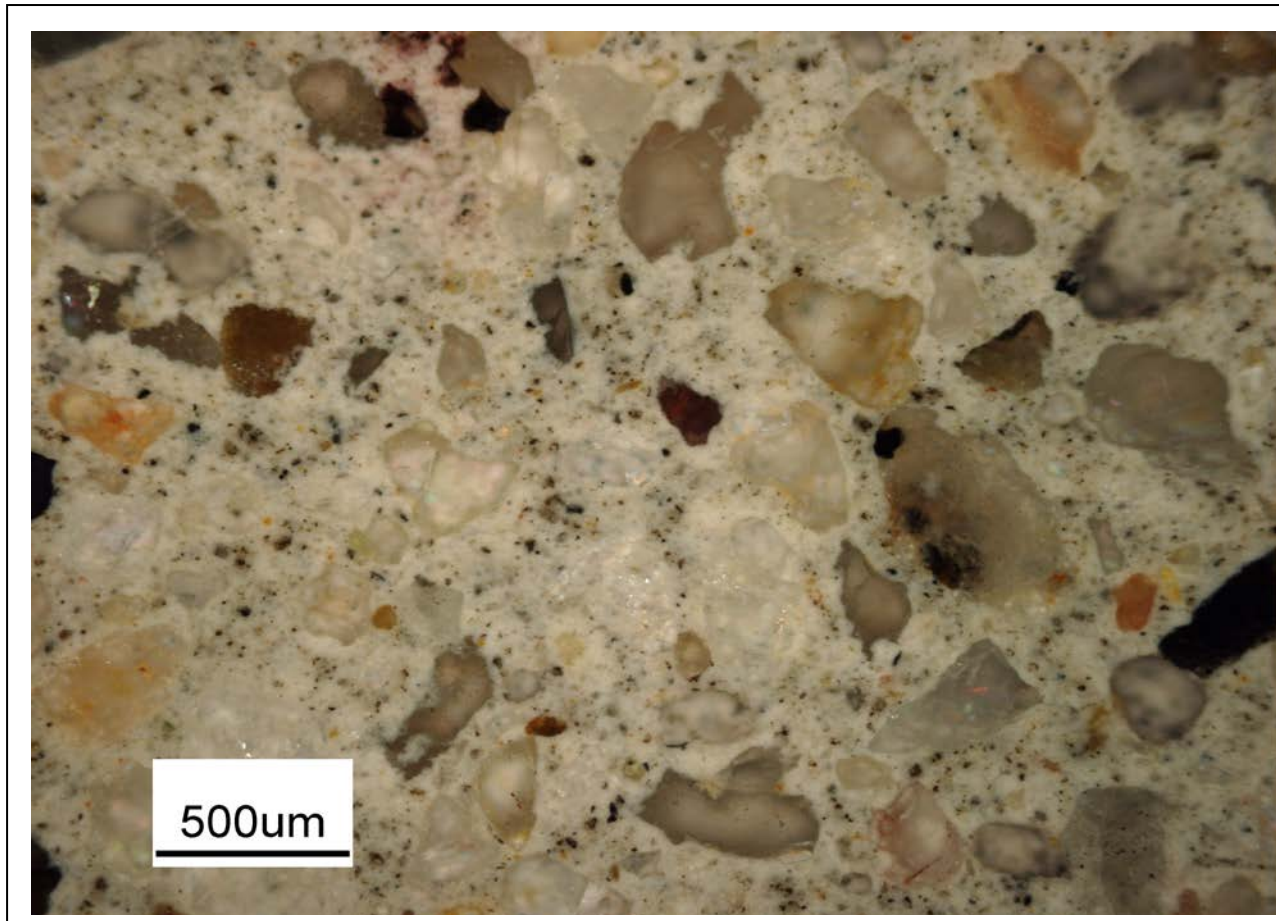
On the following pages is the beginning of a break through method of a quantitative study of the nanostructures within the cement matrix from digital images acquired from the Optical Microscope.

A small region of paste containing fine sand particles, all less than 500 μ , varying in sizes between 200 to 500 μ , small pores of air are visible throughout the structure as well.

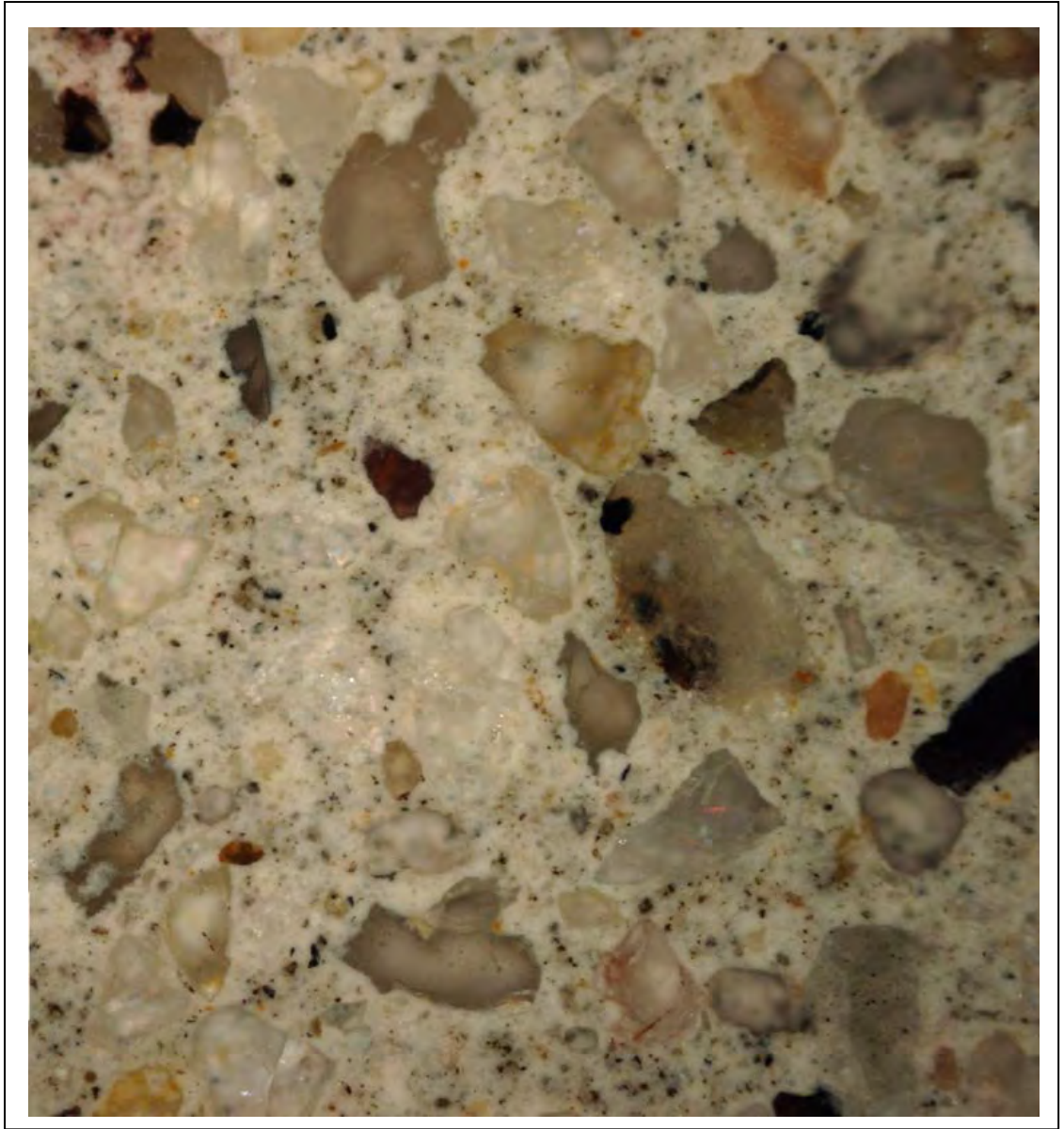
A digital analysis of this image in 64-bit ImageJ gave these results:

1. Percentage sand particles - 40.4%, therefore by difference the cement paste is 59.6%; (pages 354, 357 and 360)
2. Fine porosity was calculated to be 3.9% in this region, the analysis of a full 100 mm diameter core calculated on average 2.2%; calculating only a small section in this case $\sim 4.7 \text{ mm}^2$, the percentage porosity was about 80% higher than the quantitative on the full sample in Study 3 (pages 355, 359 and 360)
3. Dark particles within the cement paste quantitatively calculated between 0.8% to 2.2% (page 358).

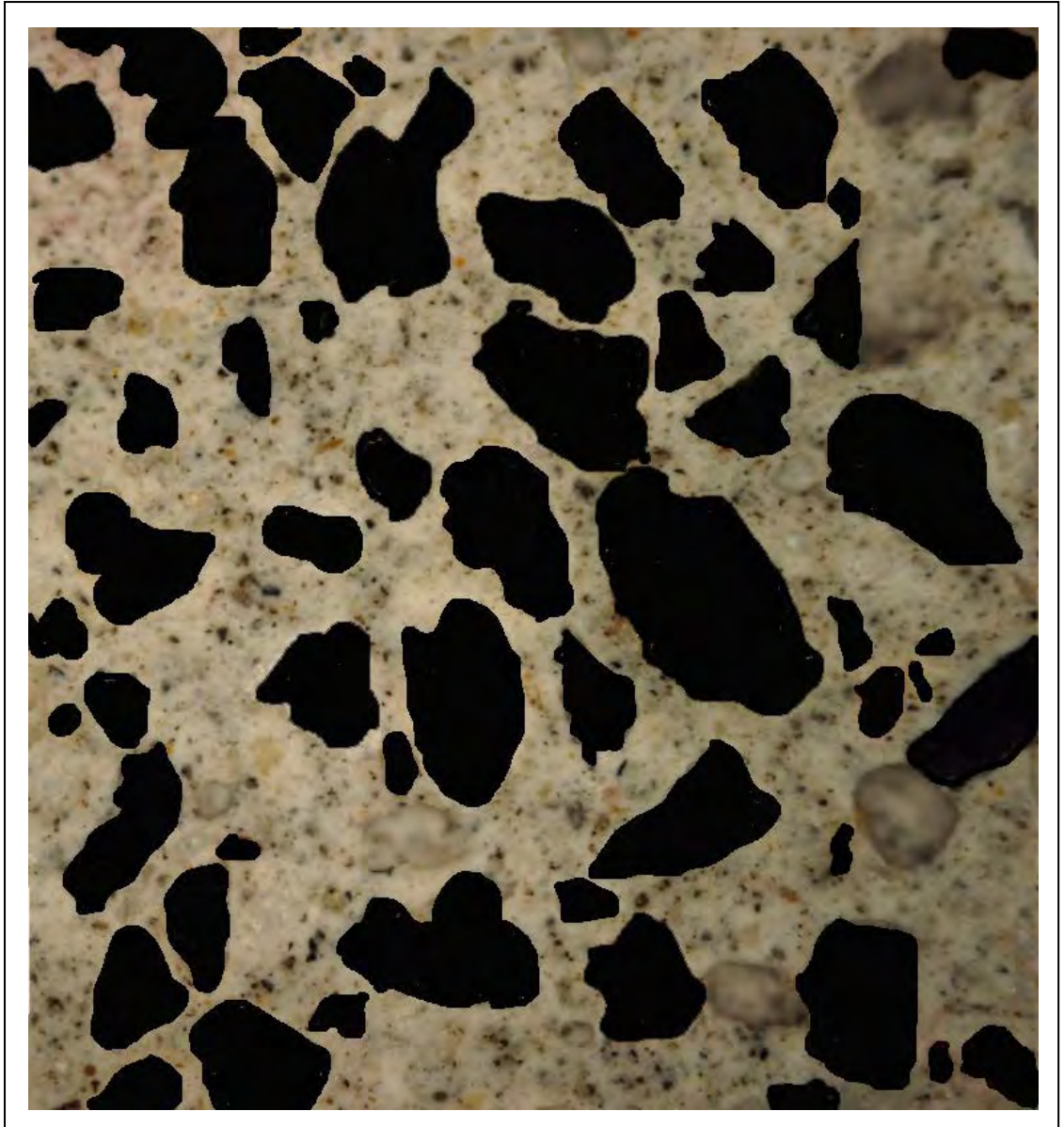
When analysing a digital image that has a resolution less than 0.3 μ , the 64-bit ImageJ easily locates perimeters of particles and can calculate to an extreme accuracy. These images could not be analysed in 32-bit ImageJ.



Original microscope digital image of Dar1



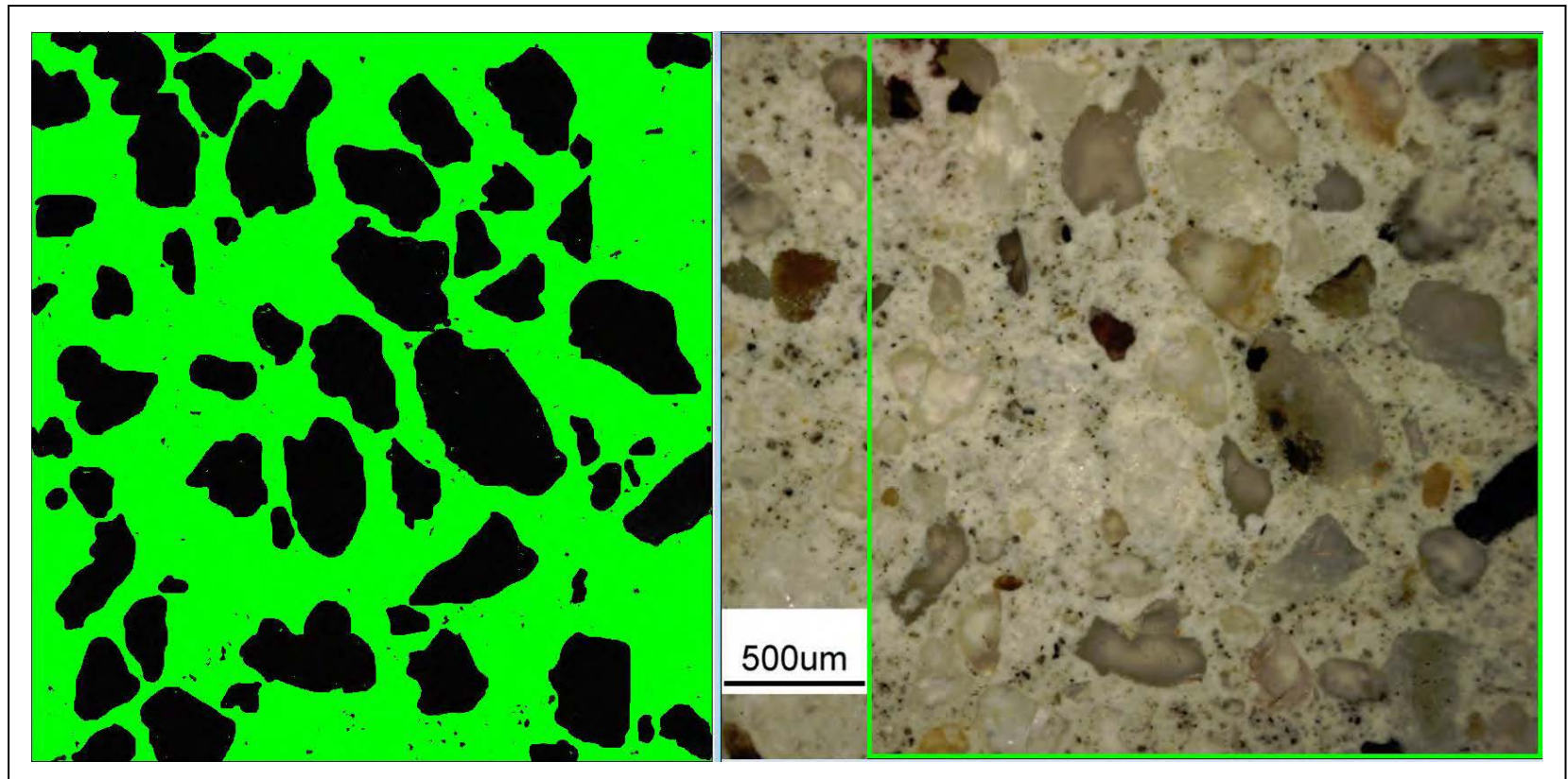
2 - Selected area for analysis from 1 - Original Dar1



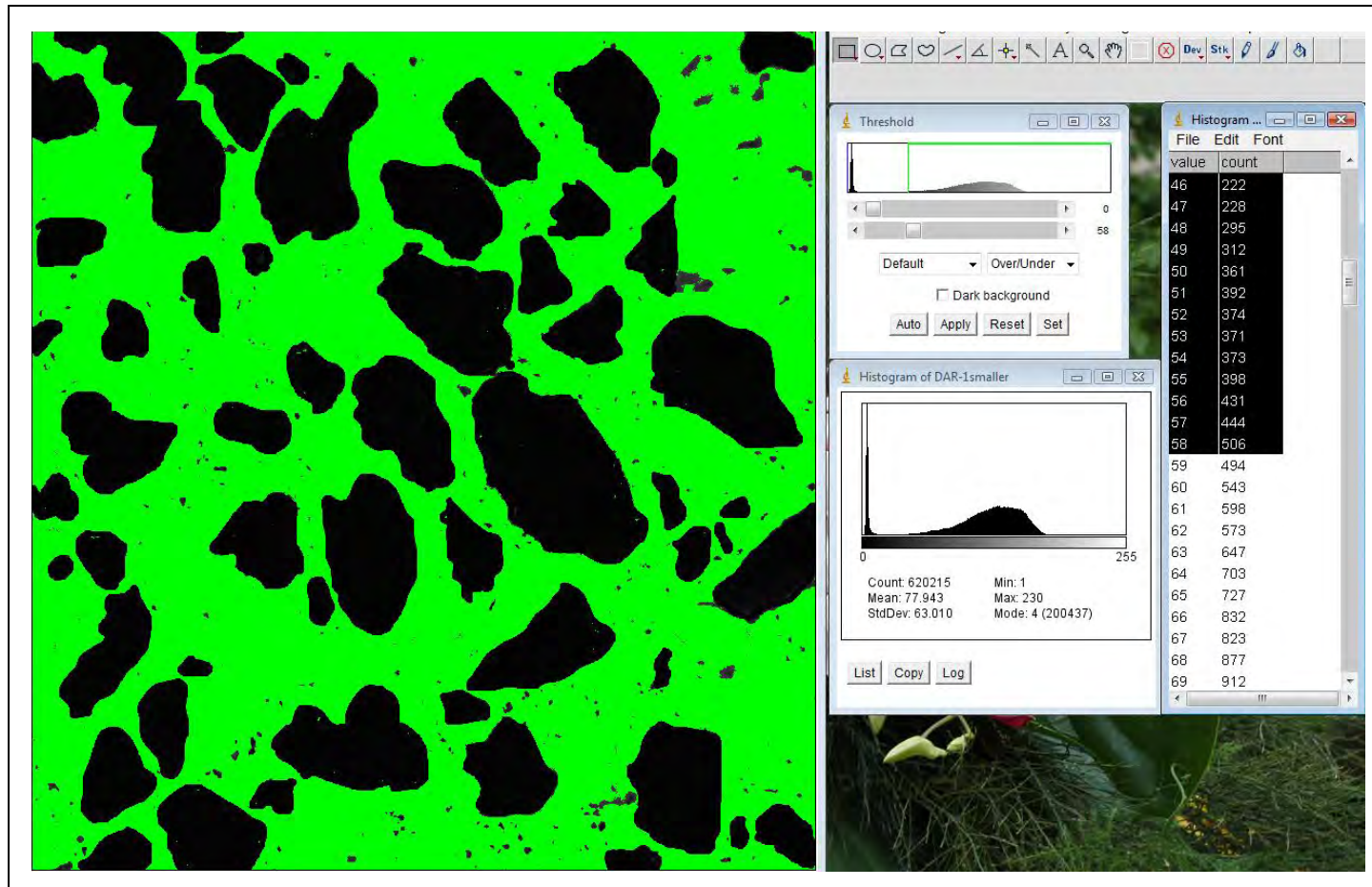
3 - Masked sand particles Dar1



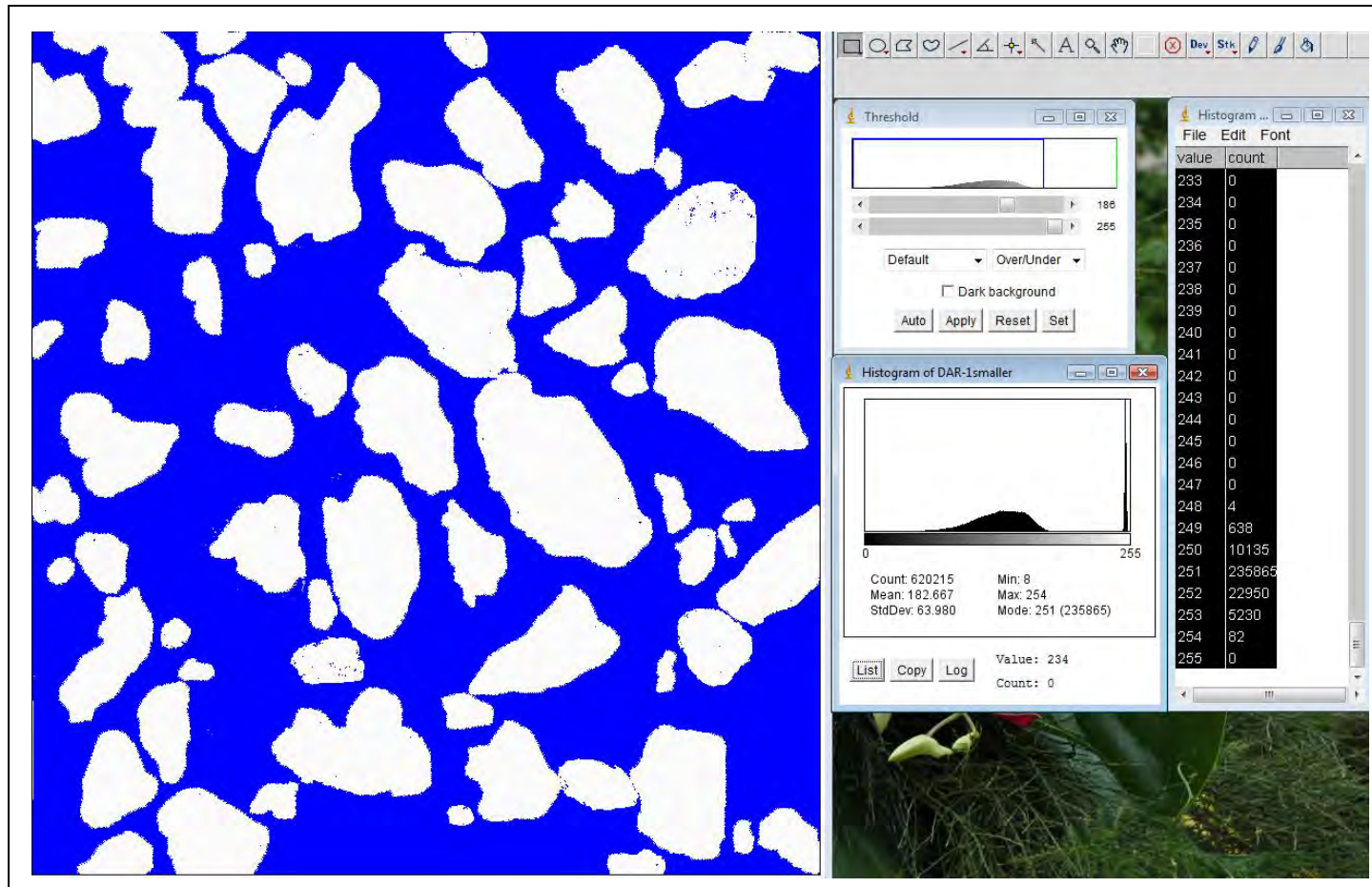
4 - Masked sand particles and porosity in white - Dar1



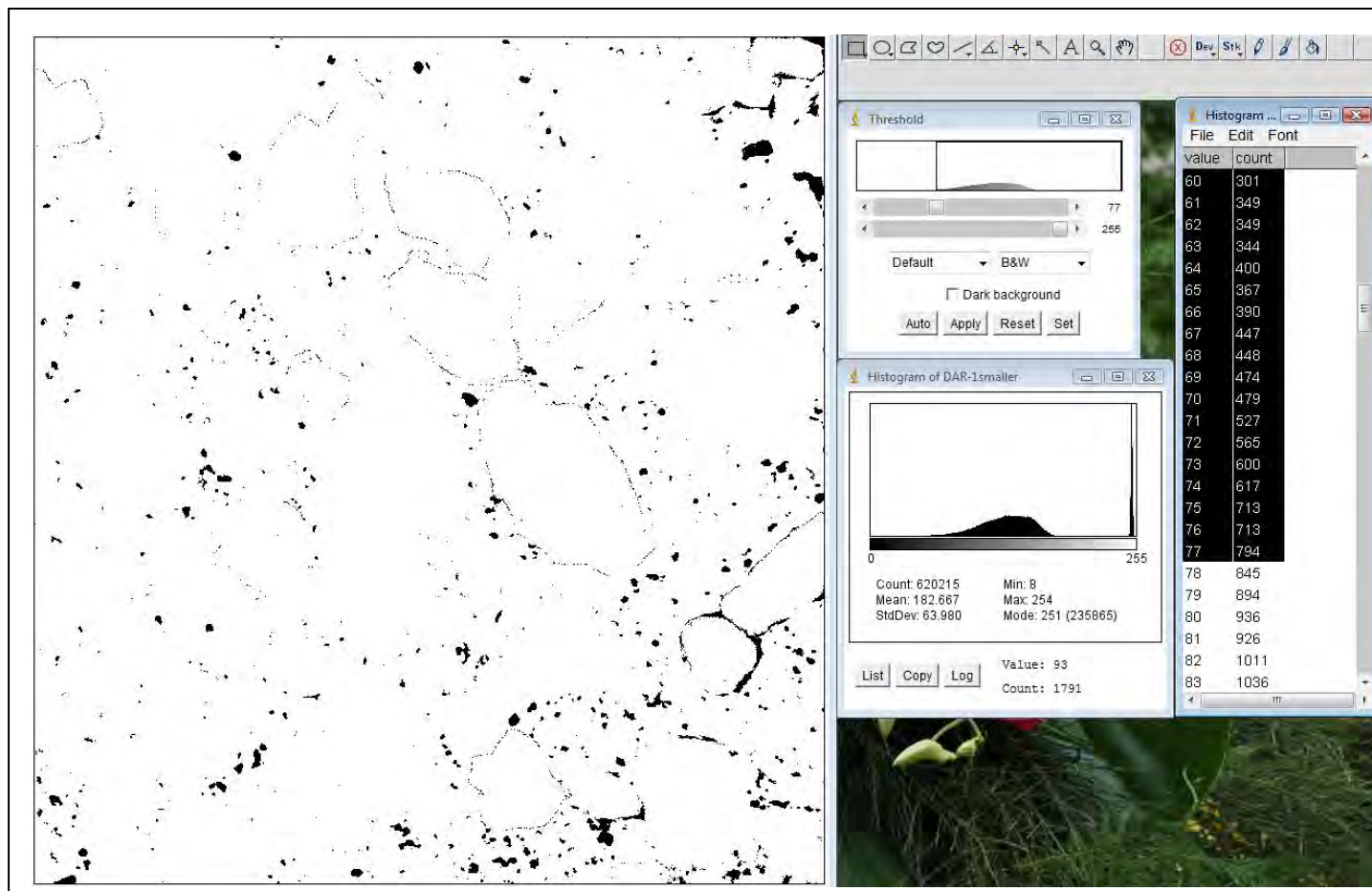
5 - Original microscope digital image and its calculation on masked sand particles in 64-bit ImageJ in green



6 - Calculation in 64-bit ImageJ of sand particles - Dar1



8 - Calculation in 64-bit ImageJ of sand particles and paste - Dar1



8 - Calculation in 64-bit ImageJ of particles in paste - Darl

Dar1	sand		sand +pores		black specks	
0	0		186	22	0	0
1	25		187	11	1	0
2	1878		188	8	2	0
3	15474		189	5	3	0
4	200437		190	4	4	0
5	17068		191	3	5	0
6	3259		192	1	6	0
7	1229		193	5	7	0
8	855		194	1	8	2
9	589		195	0	9	2
10	412		196	1	10	1
11	333		197	2	11	3
12	292		198	0	12	6
13	212		199	0	13	6
14	173		200	1	14	10
15	161		201	0	15	7
16	107		202	1	16	7
17	116		203	0	17	7
18	96		204	0	18	9
19	91		205	0	19	20
20	94		206	0	20	24
21	82		207	1	21	22
22	82		208	0	22	28
23	90		209	2	23	31
24	82		210	2	24	37
25	88		211	0	25	34
26	95		212	3	26	33
27	102		213	1	27	40
28	97		214	1	28	55
29	107		215	0	29	52
30	105		216	2	30	48
31	119		217	5	31	61
32	117		218	3	32	68
33	101		219	6	33	64
34	118		220	11	34	58
35	132		221	16	35	81
36	136		222	9	36	93
37	142		223	4	37	79
38	140		224	7	38	75
39	150		225	4	39	100
40	158		226	2	40	89
41	171		227	4	41	113
42	165		228	6	42	111
43	185		229	2	43	115
44	167		230	1	44	108
45	227		231	0	45	146
46	222		232	0	46	138
47	228		233	0	47	143
48	295		234	0	48	172
49	312		235	0	49	165
50	361		236	0	50	211
51	392		237	0	51	220
52	374		238	0	52	222
53	371		239	0	53	206
54	373		240	0	54	232
55	398		241	0	55	209
56	431		242	0	56	240
57	444		243	0	57	260
58	506		244	0	58	281
	250766		245	0	59	280
	620215		246	0	60	301
	40.4%		247	0	61	349
			248	4	62	349
			249	638	63	344
			250	10135	64	400
			251	235865	65	367
			252	22950	66	390
			253	5230	67	447
			254	82	68	448
			255	0	69	474
				275061	70	479
				620215	71	527
				44.3%	72	565
					73	600
					74	617
					75	713
					76	713
					77	794
						13701
						620215
						2.2%

9 - Calculations of sand particles, sand and pores, and black particles in paste - Dar1

APPENDIX B

The following Petrographic Data is included to assist the reader understand the correlation between traditional Analysis, and the full core sectioned Automatic Quantitative Digital Analysis of Hardened Concrete Micro-Structures analysed in my thesis.

Petrographic Methods of Examining Hardened Concrete:

A Petrographic Manual

Publication No. FHWA-HRT-04-150
July 2006



FOREWORD

Petrographic Methods of Examining Hardened Concrete: A Petrographic Manual was originally published in 1992 by the Virginia Transportation Research Council (VTRC) as Report VTRC-92-R14. Authored by Hollis N. Walker, it was the culmination of a quarter century of work by her in concrete petrography at the VTRC.

This edition, revised by D. Stephen Lane, senior research scientist at the VTRC, builds on the original work. It has been revised and updated to reflect recent advances in techniques and work in concrete petrography. Major additions to the manual include a new chapter (chapter 14, written by Paul E. Stutzman, physical scientist, National Institute of Standards and Technology) on the use of the scanning electron microscope to examine concrete and concrete making materials, and additional information on the identification and classification of rocks and minerals in aggregates (appendix D). Chapter 10, Alkali-Aggregate Reactions, was re-organised to outline the process one would follow to investigate a case of concrete deterioration and illustrate the features that provide evidence of alkali-silica or alkali-carbonate reactions. It is hoped that the manual will be of great use both to those entering the field of concrete petrography and to the experienced petrographer.

The following Petrographic Data is included to assist the reader understand the correlation between traditional Analysis, and the full core sectioned Automatic Quantitative Digital Analysis of Hardened Concrete Micro-Structures analyzed in my thesis

Petrographic Methods of Examining Hardened Concrete: A Petrographic Manual

**Publication No. FHWA-HRT-04-150
July 2006**

[View PDF Version](#)  (25.82 MB)



FOREWORD

Petrographic Methods of Examining Hardened Concrete: A Petrographic Manual was originally published in 1992 by the Virginia Transportation Research Council (VTRC) as Report VTRC-92-R14. Authored by Hollis N. Walker, it was the culmination of a quarter century of work by her in concrete petrography at the VTRC.

This edition, revised by D. Stephen Lane, senior research scientist at the VTRC, builds on the original work. It has been revised and updated to reflect recent advances in techniques and work in concrete petrography. Major additions to the manual include a new chapter (chapter 14, written by Paul E. Stutzman, physical scientist, National Institute of Standards and Technology) on the use of the scanning electron microscope to examine concrete and concretemaking materials, and additional information on the identification and classification of rocks and minerals in aggregates (appendix D). Chapter 10, Alkali-Aggregate Reactions, was reorganized to outline the process one would follow to investigate a case of concrete deterioration and illustrate the features that provide evidence of alkali-silica or alkali-carbonate reactions. It is hoped that the manual will be of great use both to those entering the field of concrete petrography and to the experienced petrographer.

This edition is an example of the continuing cooperation in infrastructure research and development between State and Federal agencies.

The following quotation from K. Mather (1966), serves as a mission statement for concrete petrographers:

The best petrographic examination is the one that finds the right questions and answers them with maximum economy in minimum time, with a demonstration clear to all concerned that the right questions were answered with all necessary and no superfluous detail. In practice, the approach to the ideal varies depending on the problem, the skill with which the questions are asked, and the skill of the petrographer. One measure of the petrographer's skill is knowing when to stop, either because the problem is adequately solved, or, in some cases, because it has been shown to be insoluble under the circumstances.

Katherine Mather served as chair of the American Society for Testing and Materials Subcommittee on Petrography of Concrete and Aggregates for many years. She was an expert in the practice and use of petrography, contributed to many publications, and participated actively in cement and concrete research carried on by the U.S. Army Corps of Engineers, Vicksburg, Mississippi

CHAPTER 4. CRACKS

4.1 OVERVIEW

Cracks in HCC may have several causes (see ACI 201.1R and ACI 224.1R): plastic shrinkage, settlement, drying shrinkage, thermal stresses, chemical reactions, weathering (freezing and thawing, wetting and drying, heating and cooling), corrosion of reinforcement, poor construction practices (e.g., retempering), construction overloads, errors in design and detailing, and externally applied loads. For our purposes, nine types of cracks are discussed:

1. Microcracks.
2. Crazing.
3. Scaling.
4. Cracks caused by insufficient air-void content.
5. Cracks caused by delamination at the reinforcement.
6. Cracks caused by a chemical reaction.
7. Cracks caused by drying shrinkage.
8. Cracks caused by thermal volume change.
9. Cracks caused by plastic shrinkage.

4.2 TYPES OF CRACKS

4.2.1 Microcracks

The term *microcracks* includes all very fine cracks, in any direction, at the surface or within the mass of the concrete that are not easily visible with the unaided eye, but may be seen with a

magnifying glass or microscope. Microcracks are often extremely difficult to observe on the textured surface of a placement. Chapter 8 provides instructions on the observation and recording of microcracks.

4.2.2 Crazeing

Crazeing is a fine, very shallow pattern of cracking that occurs in the exposed surface of a concrete placement. Usually it cannot be seen while the observer is in motion in a vehicle. It occurs when the thin surface layer shrinks significantly relative to the interior mass of the concrete and may result from excessive paste or water content in the surface layer or rapid drying. Crazeing usually has a very fine pattern, with the individual uncracked central portions usually no more than 50 mm across. The depth of craze cracking should be recorded. Paste-rich surface layers can also impede the rise of bleed water, trapping it just beneath the surface. If the surface layer flakes off, usually to a depth of about 3 mm, it may be called *paper scaling*. The underside of any loose flakes of concrete should be examined for clean sand grains and calcium hydroxide that would indicate trapping of bleed water and the casts of ice crystals that would indicate freezing before hardening.

4.2.3 Scaling

Scaling is a local flaking or peeling of the mortar at the surface and can be classified as light (without exposure of coarse aggregate), medium (5 to 10 mm deep), severe (11 to 20 mm deep), or very severe (> 20 mm deep) (ACI 201.1R). Scaling is usually attributable to a weak surface layer exposed to the physical effects of freezing and thawing cycles or deicing chemicals.

4.2.4 Cracks Caused by Cycles of Freezing and Thawing While Concrete Is Critically Saturated

Concrete that lacks either sufficient strength (maturity) or an adequate air-void system will develop laminar cracking if critically saturated and exposed to freezing and thawing cycles (see figures 26 and 80). The deterioration will usually proceed from the exterior inward as progressive scaling.

4.2.5 Cracks Caused by Reinforcement Corrosion

Corrosion and the resulting expansion of the reinforcement will cause lateral cracking in the plane in which the reinforcement is situated. Normally, the high pH of concrete protects the reinforcing steel from oxidation. The passivating effect of concrete on steel can be negated by the intrusion of chloride ions or by carbonation of the paste surrounding the reinforcement. The concrete between the reinforcement and the outer surface of the element thus serves as a barrier to the ingress of chloride ions or carbon dioxide. Construction plans should specify the concrete cover thickness, usually around 50 to 68 mm. Cracks extending from the exposed surfaces toward the level of the reinforcement may significantly decrease the effectiveness of the cover concrete as a barrier, especially if the cracking is over an extensive area. The concrete is considered to have only the depth of protection that exists from the bottom of the cracks to the reinforcement (see figures 27 and 28).

4.2.6 Cracks Caused by a Chemical Reaction

Chemical reactions may take place between concrete constituents (the aggregates and the paste) and ionic species in solution within the concrete mass. Cracking resulting from AAR is discussed in chapter 10.

4.2.7 Cracks Caused by Drying Shrinkage

The term *drying shrinkage* is commonly used in connection with shrinkage cracking that occurs after the HCC has attained final set and a particular degree of bonding has developed between the aggregate and the paste. After the concrete has reached final set, the paste behaves as a brittle material.

Most HCC shows evidence of drying shrinkage. Cracking can be minimized by good workmanship, proper proportioning of the mixture, and sufficient jointing performed soon after hardening. In jointed concrete, uncontrolled cracks may form if the joints were not formed early enough, are not working properly, or the shrinkage in the hardened state is excessive. In continuously reinforced HCC, very narrow, fairly regularly spaced transverse cracks are expected to form. The cracks allow for the changes in volume of the concrete with drying and varying temperatures.

4.2.8 Cracks Caused by Thermal Volume Change

Thermal effects on concrete volume can cause cracking with a disposition similar to that caused by drying shrinkage and, in fact, thermal and drying effects will often occur in concert. The coefficient of thermal expansion (CTE) of concrete is a proportional function of the CTE of its constituent materials. Since common aggregate materials differ considerably in their CTE, they consequently exert considerable influence on the concrete CTE (Scanlon and McDonald, 1994; Lane, 1994).

Thermal cracking is a predominant concern in mass concrete placements if the heat of hydration is not controlled and large temperature differences are allowed to develop between the inner core and cooling outer skin of the placement. In thin members, such as pavements and bridge decks, thermal cracking is most likely to present problems when the concrete undergoes large temperature swings during the first several days after placement. Such effects are most pronounced in heavily reinforced structures such as continuously reinforced concrete pavement and decks; however, they can present serious problems for plain jointed pavements if midslab cracks result. HIPERPAV software, published by FHWA, provides a means to predict potential thermal cracking problems for pavements (FHWA, 2003).

4.2.9 Cracks Caused by Plastic Shrinkage

Plastic shrinkage is a form of drying shrinkage that occurs while the HCC is unhardened and malleable, and the bond between the components of the material is very weak. Plastic shrinkage cracking is caused by excessive evaporation of the water at the concrete surface because of improper curing procedures for a concrete under the climatic conditions existing at the time of

placement (see appendix B and Lerch, 1957; Price, 1982; and Scott, Lane, and Weyers, 1997). Plastic shrinkage occurs in the first few hours after placement before final set (when the rate of evaporation exceeds the rate of bleeding). At this stage, the HCC has some properties of a solid, but no appreciable bond exists between the aggregate particles and the cement paste. This sort of cracking is also called *early cracking or morning cracking*, the latter because it is often the concrete that was placed in the morning and then exposed to afternoon drying conditions that exhibits this type of cracking (see figures 33 through 40).

Plastic shrinkage cracking often occurs in high-quality HCCs when curing is not promptly or adequately applied and appropriate measures to avoid excessive evaporation have not been taken. The intrinsic quality of the concrete is not necessarily adversely affected by plastic cracking. Provided the concrete was adequately moisture cured, the defect is more cosmetic in nature, except in situations where the concrete is intended to provide protection for the reinforcement.

A form of early cracking where the cracks are located directly over the steel can occur when the depth of cover over the reinforcement is shallow (Price, 1982; Dakhil, et al., 1975). This cracking is directly related to shrinkage and settlement of the concrete over the steel as the bleed water leaves the concrete and the volume of the paste is diminished. It may be accompanied by segregation of the coarse aggregate from the paste. As with HCCs with a lower w/cm, this condition is exacerbated by drying atmospheric conditions. Evidence of this type of fault can be seen on interior surfaces of specimens of these HCCs. This type of cracking is commonly called *settlement or subsidence cracking* (ACI 224R).

Occasionally, there may be severe bleed channels in HCC that might be confused with plastic shrinkage cracking. However, upon close inspection, such bleed channels show clear evidence of being a waterway, whereas plastic shrinkage cracks show clear evidence of having been pulled open by the shrinkage of the concrete. Bleed channels are trains of water voids caused by the upward movement of mixing water as the fine solids settle. Such trains of voids may occur in HCCs with a high w/cm. Some forms of plastic shrinkage cracking may have zones of such void trains. In HCCs with a low w/cm, incomplete consolidation may cause fold lines and collections of voids. Cracks occurring in HCCs can usually be distinguished by the nature of the associated voids and the appearance of the fracture surfaces (showing signs of either brittle or plastic deformation) (see section 4.3).

The following may occur in unusual and extreme cases of rapid evaporation, causing drying of the HCC before hardening:

- Surface carbonation and associated shrinkage may take place when the relative humidity at the surface falls much below the saturated state.
- As surface paste loses its moisture by evaporation, unhydrated cement may be concentrated in a weak, thin, surface zone.

These are features of extreme drying and are not usually present in HCCs affected by plastic shrinkage cracking. The absence of these features in HCC exhibiting plastic cracking does not

indicate that it was not subjected to deleterious drying conditions during or shortly after placement.

4.3 DISTINGUISHING BETWEEN PLASTIC SHRINKAGE CRACKING AND DRYING SHRINKAGE CRACKING

4.3.1 Overview

For transportation departments and other purchasers of concrete placed by a contractor (or other agency), it is frequently important to distinguish between early plastic shrinkage cracking and the brittle cracking that may occur because of structural stress or later drying shrinkage. The contractor is obligated to prevent the dehydration (and consequent cracking) of the fresh concrete that can occur when wind, low humidity, or both promote rapid drying. HCC with a low w/cm (0.40 or less) and latex-modified concretes are more apt to suffer this sort of failure than are concretes with a high w/cm ratio. When it can be shown that the cracking is caused by a failure of the contractor to refrain from placing concrete during unfavorable weather conditions, employ sufficient methods to prevent drying, or both, the contractor may be obligated to provide a new surface or accept a lower payment.

The usual rule of thumb in the literature is: If the cracks go through the aggregate particles and cause them to break, the cracking should not be considered plastic cracking. Many observers call any crack that goes around the aggregate particles a plastic/early shrinkage crack. This can be in error. There may be other reasons for the crack to go around the aggregate particles.

Some aggregates are more fragile than others and some may crack during final placing and finishing. It is possible to judge a crack to be a later crack on the criterion of broken aggregate when, in reality, the aggregate particle just happened to have a zone of weakness in the crack plane and the crack was an early crack. The specimen examined (a cross section of a crack) is a very small portion of a crack. The interior of the crack surface is a very small, nonrepresentative portion of the crack.

Cracks that preferentially go around aggregate particles indicate that the bond between the aggregate and paste was a weak point at the time the cracking occurred. The bond may be weak because of any of the following:

- Immature concrete.
- Excess water or air voids at the aggregate surface.
- Coating on the aggregate surface.
- Ca(OH)_2 at the paste-aggregate interface that dissolved because of percolating waters or solutions, thus weakening the bond late in the life of the concrete.

Thus, it is necessary that the criteria for deciding that a specific crack is a plastic shrinkage crack be more than the fact that the crack skirts the aggregate particles.

4.3.2 Analogy With Clay Materials

The difference between drying shrinkage cracking and plastic shrinkage cracking can be explained further by use of an analogy using clay materials.

Hard brittle materials (drying shrinkage cracking): Consider a broken ceramic object (pottery) or rock. If all the pieces can be found and fitted back together, the material will solidly fill the same space as did the original object. Any internal voids will almost invariably be recognizable by either their shape or the nature of the interior surface (different from a fracture surface). If all the chips are available, the expression of the crack on the surface of a hard brittle material will be a thin sharp line.

If the material is sandy clay that was fired in a kiln ("fired" is analogous to the hardening of concrete), all the cracked surfaces will fit back together if all the fragments are preserved and there are no air pockets present. If the bond and the tensile strength of the ceramic are as strong as the tensile strength of the sand, then the crack will fracture the sand and the crack surfaces will neatly and completely fit back together. If the sand has much greater tensile strength than the fired ceramic, any cracks occurring in the material are likely to detour around the sand grains.

This logic may be directly extrapolated to cracks in hardened HCCs, hardened latex-modified HCC, and many other highway materials. In the case of these materials, the general type of void and the nature and luster of the interior of the voids should be carefully studied so that they can be recognized in the path of any crack under study.

It may be that a macrocrack occurring on the riding surface of HCC that was originally a thin sharp line was worn wider by the abrasive action of traffic. The course of the crack below the surface expression should be examined. Care must be taken to extrapolate the evidence in light of all relevant facts, including the age of the placement, the amount of traffic, the pertinent weather conditions, and the strength and general condition of the concrete placement.

Malleable materials (plastic shrinkage cracking): Now, consider a crack caused by the pulling apart of a piece of modeling clay or other such material. Because of the plastic nature of the material, there may be small "bridges" of the material spanning the crack, there will be deformation of the sides of the crack, and the two sides of the crack will not be able to be fitted back together without reshaping of the crack walls. A crack of this nature starts at the exposed surface. In the case of unhardened **HCC**, this is the driest portion. Here, the crack is the widest because the surface is the origin and tension is greatest as there is no adhesion above to resist the pulling apart. The edges of the crack are often rounded back. If the material is ceramic clay and the material was baked in a kiln in the cracked condition, it would be obvious in the finished piece that the two interior surfaces of the crack would not fit back together. If the material is malleable sandy clay, then the crack will go around the sand and the crack surfaces will show that deformation occurred while the material was plastic.

This is entirely analogous to the situation in plastic shrinkage cracking in **HCC**. The crack occurs while the material is plastic and is then "baked" (the shape is preserved) by the continuing hydration of the cement and the complete hardening of the **HCC**.

4.3.3 Procedures

Distinguishing between drying shrinkage cracking and plastic shrinkage cracking is a five-step procedure, as shown in table 12.

Table 12. Procedure for distinguishing between plastic and drying shrinkage cracking.

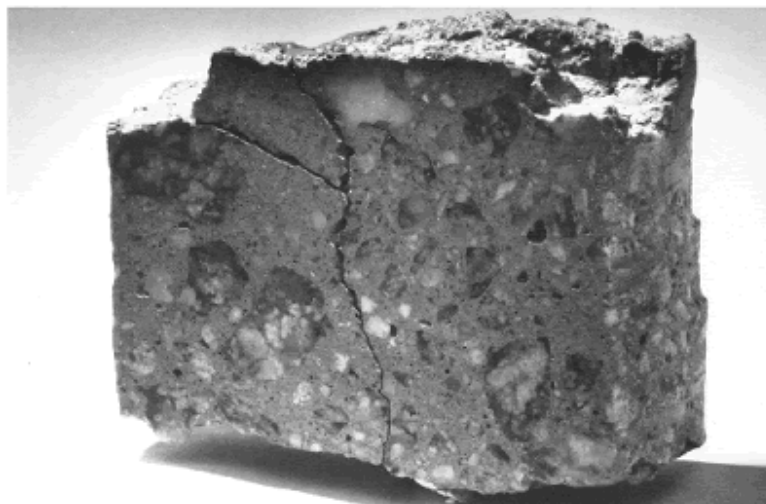
1. Study the intersection of the sidewalls of the specimen with the wearing surface.
2. Study the wearing surface of the specimen.
3. Study the expression of the crack on all cut, cored, and lapped surfaces, and focus down into the crack.
4. Examine the interior surface of the crack.
5. If necessary, study the types of voids present in other areas of the HCC and compare their surface with the various types of surfaces within the crack.

1. Study the intersection of the sidewalls of the specimen with the wearing surface:

Plastic shrinkage cracking may occur before or just after the surface is screeded and the wearing surface texture is created. In these cases, it may happen that one or more of the specimens submitted may show that mortar was worked into the top of the crack. Sometimes portions of the plug of mortar will have fallen out or been chipped off the specimen during coring and handling. It is clear that the plug is a definite indication of early plastic shrinkage cracking (see figure 33).

If the cracking occurred just before texturing, the creation of the wearing surface would naturally work mortar into the crack (see figure 34). If cracking occurred after texturing and was observed by the workers, a deliberate effort may have been made to correct the flaw.

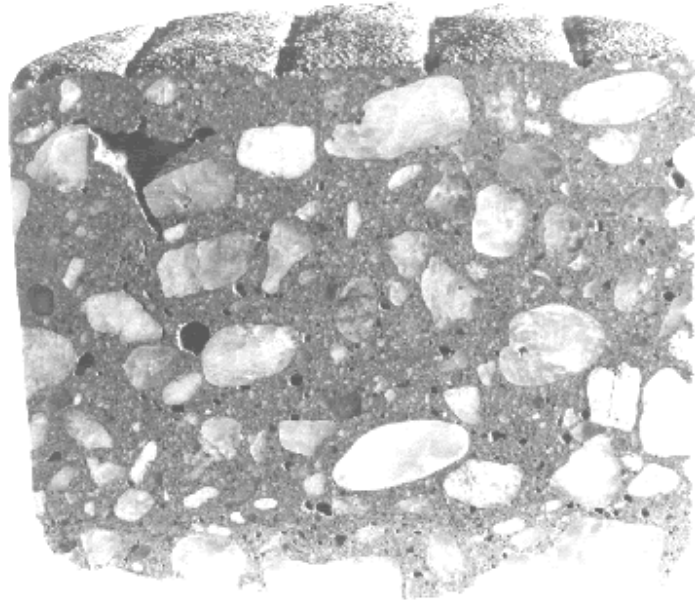
Figure 33. Plastic shrinkage cracking was covered up by mortar filling over it on top of a 100-mm core.



Mortar was worked into the top of this set of cracks before the concrete hardened. Later, the concrete cracked in the same area. Because of the lack of interlock, the new crack

follows the mortar boundaries. At the right side of the picture is a depression in the surface where a mortar plug was lost before the photograph was taken. (This specimen had to be glued together to enable the photograph to be made.)

Figure 34. Plastic shrinkage cracking occurred before a surface texture was formed.



The defect became hidden by the finishing procedures that pushed unhardened mortar over the crack.

2. **Study the wearing surface of the specimen:** With the microscope, look for features that will define the crack. Check for any features that will indicate the nature of the cracks. If photographs can be obtained of the wearing surface just after cracking but before the surface is worn by any traffic, small bridges of material may be seen stretching across the crack, which will indicate plastic shrinkage cracking (see figures 35 and 36).
3. **Study the expression of the crack on all cut, cored, and lapped surfaces, and focus down into the crack:** If you see any little bridges of paste that tie the two sides together or if any uncracked aggregate particle bridges the crack, the crack plane existing all around the particle, and the aggregate firmly attached to the hardened paste on either side, you can conclude that the crack was caused by plastic shrinkage (see figures 37 through 39). Bridges of paste or aggregate are not found in all plastic shrinkage cracks. The defining feature is the fact that the sides of the cracks have been distorted by the tensile forces because of shrinkage that occurred while the HCC was still malleable.

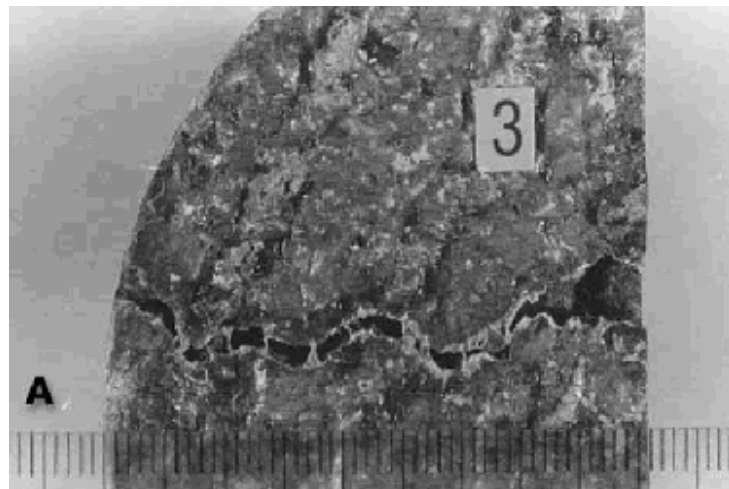
The greater the difference between the width of the crack at or near (beneath any mortar plug) the wearing surface and the width of the crack at its deep end, and the more quickly it tapers to nearly nothing, the greater the likelihood of the crack having been caused by plastic shrinkage. The V-shape of the crack is part of the distortion of the edges of the crack caused by the tensile forces. Commonly, the crack is a plastic shrinkage crack near

the surface; however, with depth, the crack is straighter and the zone of weakness has been extended after the final set by other forms of drying shrinkage or by structural stress, sometimes completely through the slab.

The path of a plastic shrinkage crack on any vertical concrete surface is usually quite tortuous because it is deflected by each piece of aggregate. Typically, the crack is wider at the top than at the bottom; however, even at the bottom, it is not the sort of crack found in a brittle ceramic (see figure 40).

Do not be confused or alarmed by the presence of abundant road dirt or mud created by the drilling of the cores. This mud may appear layered and flaky, but the structures will be fragile.

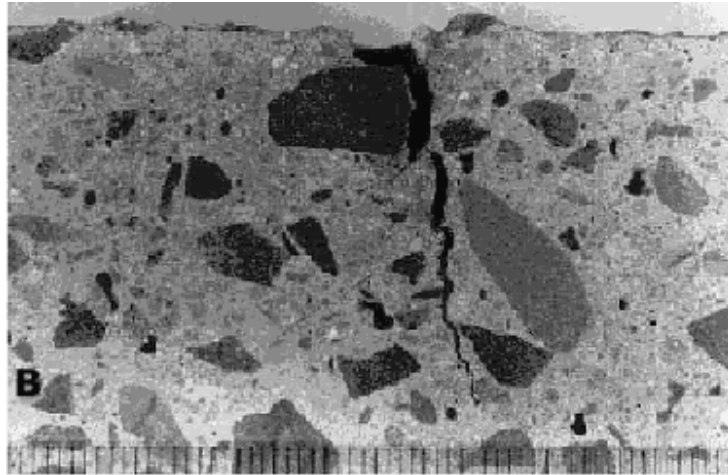
Figure 35. Plastic shrinkage cracking occurred in a latex-modified concrete overlay (top view of core (small threads of latex span the crack)).



Rules are graduated in millimeters.

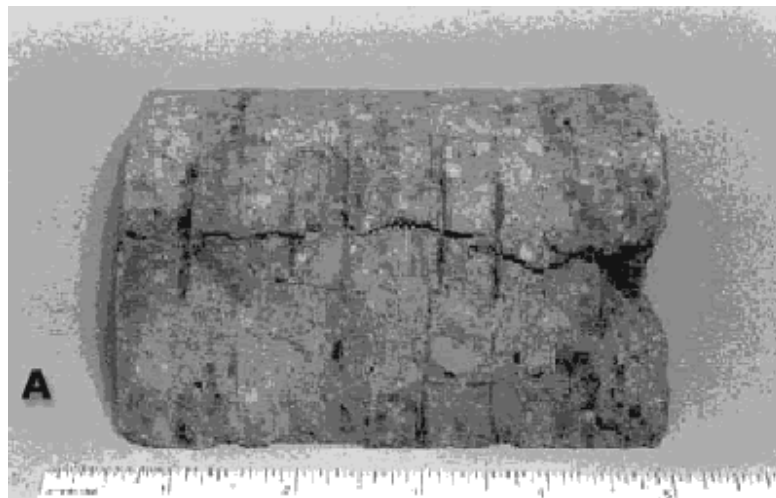
The crack shows the distortion that accompanies tension cracking in an unhardened medium. This specimen was collected before traffic destroyed these delicate structures.

Figure 36. Plastic shrinkage cracking: Small bridges of latex paste connect sides of crack.



Rules are graduated in millimeters.

Figure 37. Small bridge of paste across a crack caused by shrinkage that took place while the ordinary portland cement concrete was not hardened (100-mm core, road surface at right).



Rules are graduated in inches.

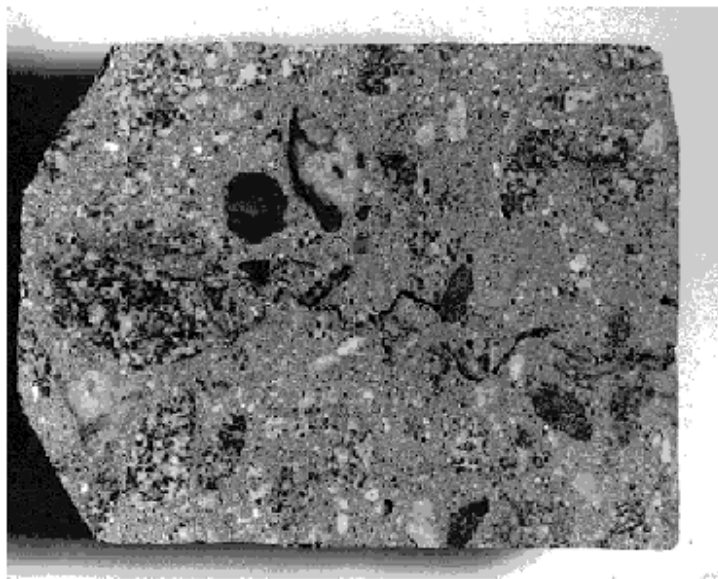
These little bridges may occasionally be found on broken, sawed, cored, or lapped surfaces.

Figure 38. Bridge of paste across plastic shrinkage crack: Closeup of bridge.



Rules are graduated in inches.

Figure 39. Tortuous path of a plastic shrinkage crack in a concrete that has not completely separated.



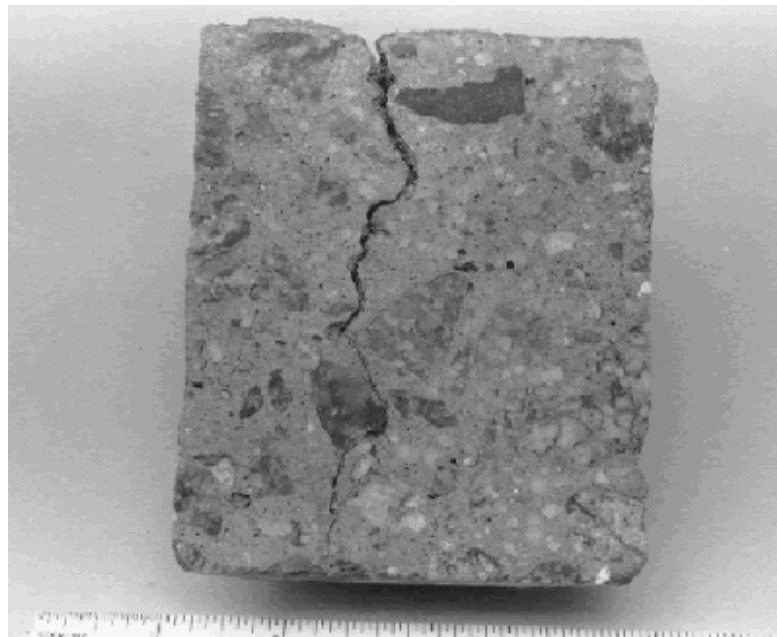
It is easy to envision how little bridges of concrete form when a crack system of this nature is stretched further. Narrow microcracks are emphasized with ink. The specimen is approximately 100 mm top to bottom.

4. **Examine the interior surface of the crack:** Delay any destructive procedures until the total surface has been studied and any air-void determinations have been made. Then, break the HCC with a hammer blow in an area away from the crack and examine the surface produced. In the most common case of a crack produced in an area not including a plastic shrinkage crack, the interior surface will be made up of a multitude of tiny angular planes with the exception of the interior of the air voids. There may be an

occasional rounded surface of an aggregate particle or of the cast of an aggregate particle; however, the major portion of the surface will be a collection of planes.

Break the HCC on the crack and examine the interior surface. Usually the interior surface of a crack produced by plastic shrinkage is made up of very tiny globules of cement paste. The surface of the paste inside the crack does not look like a cracked surface. Rather, the paste appears, as one might imagine it would, as if, when the sides of the crack were no longer in contact, minute stringers of paste had momentarily bridged the crack and then, as the tensile strength of the stringers was exceeded, the stringers coalesced into tiny globules. Each globule appears as if a paste stringer shrunk in on itself. If it is water-worn sand, none of the sand grains will be broken and they will present a naturally rounded surface. A few fragments of the coarse aggregate may be broken, as will occur in all concrete construction. If the aggregate is shaley or naturally fragile and contains a plane of weakness approximately parallel with the plane of the plastic shrinkage crack, the crack may preferentially traverse this aggregate.

Figure 40. Plastic shrinkage crack on a lapped surface (wearing surface is at the top of the photograph).



5. **If necessary, study the types of voids present in other areas of the HCC and compare their surface with the various types of surfaces within the crack.**

CHAPTER 6. VOIDS

6.1 OVERVIEW

In hardened HCC, a void is an empty space (other than a crack) in the cement paste that contains nothing but air. The type, size, shape, arrangement, and abundance of the voids are factors controlling many important properties (e.g., compressive strength, resistance to destruction by cycles of freezing and thawing, and resistance to chemical attack on the reinforcing steel and the cement paste). The percentage of air-void volume is generally specified by the design of the mixture. A large number of very small (most are not visible without magnification) air voids are desirable so that the average distance between any point in the paste and a void (spacing factor) is very short and, thus, the paste is protected from freezing and thawing. However, because voids weaken the HCC, spacing factors much less than the maximum ensuring protection from freezing and thawing are counterproductive and should be avoided.

The total air-void content (of voids larger than capillary size) of an unhardened concrete mixture is routinely determined in accordance with ASTM C 231 (pressure method) or ASTM C 173 (volumetric method). The unit weight of fresh concrete (ASTM C 138) may also be used to determine the percentage of air in the mixture. These methods do not ascertain the type of voids present; they merely measure the total void content. These measurements are important. As Bartel (1978) stated:

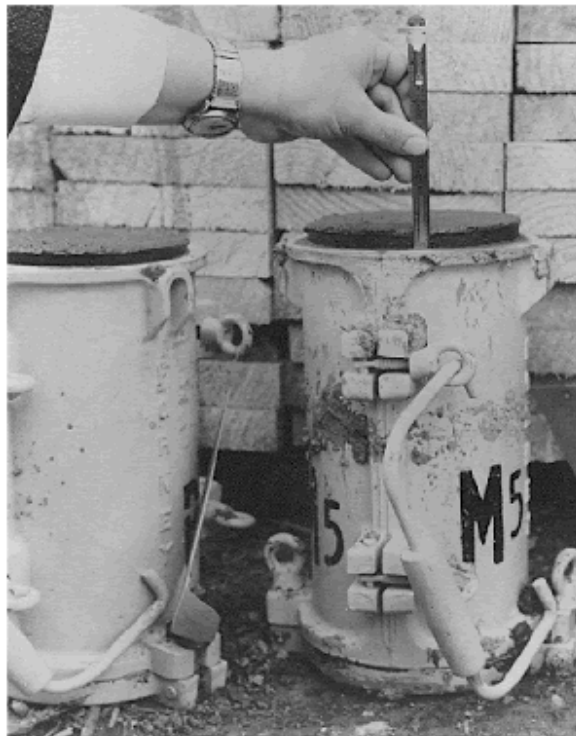
Tests for air content and unit weight of fresh concrete, carefully made in accordance with the appropriate ASTM test method, will yield an accurate measurement of the amount of air, weight, and volume of concrete being produced. Tests for air content, coupled with intelligently selected specification limits, can ensure the beneficial effects of entrained air in hardened concrete (p. 130).

Specially formed specimens of hardened HCC mixtures may be tested for resistance to the destructive forces of freezing and thawing in accordance with ASTM C 666 (resistance to rapid freezing and thawing). An HCC that is resistant generally indicates that an adequate air-void system is present and the aggregates are sound or that the HCC has not become critically saturated.

It has been variously claimed that the total air-void content increases or decreases as the concrete hardens. It appears that what really happens is that the determination of the total air-void content with field equipment made on the fresh concrete does not agree with the total air-void content determined by microscopical analysis of the hardened concrete. Except in the case of hydrogen gas being evolved by the corrosion of aluminum fragments (Newlon and Ozol, 1969) (see figure 52), no evidence has been offered showing volumetric changes in field placements or test cylinders to corroborate an increase or decrease in total air-void content.

Careful investigation by a combination of controlled sampling and testing with petrographic analyses has shown that air-void content does not change upon hardening. Rather, it may change because of outside influences (e.g., excessive vibration, the further addition of water and retempering, or pumping operations with long vertical drops). The void content in the hardened

Figure 52. Concrete that increased in volume because of corrosion of aluminum fragments.



After it was cast in the cylinder mold, the concrete increased in volume as hydrogen gas evolved from the chemical reaction of aluminum (from an aluminum delivery pipe) with the alkaline fluids of the fresh cement paste.

state will usually agree within 1 percent of the void content determined in the fresh, unhardened state. When they do not closely agree, either one of the measurements is in error or the two specimens tested do not represent the same concrete subjected to the same influences (see appendix C and Ozyildirim, 1991).

An air-void content in excess of the amount required for protection against the destructive forces of alternate freezing and thawing that occur in saturated concrete adds no benefit to concrete expected to bear loads and resist abrasion. (For a discussion of the high-air cellular concretes, see Legatski, 1994.) An excessive air-void content will lower the compressive strength of the concrete by about 5 percent for each excess percentage of voids. Because of this dual-edged nature of air entrainment, maintaining control of the air content is one of the most important facets in concrete production. It requires knowledge of the various materials and potential interactions, batching and mixing equipment and operations, and careful testing. Whiting and Nagi (1998) provide excellent information on this critical function.

6.2 TYPES OF VOIDS

The overall void content in HCC is composed of four general types of voids (as listed in table 15).

Table 15. Types of voids.

1. **Capillary voids:** Capillary voids are irregularly shaped and are very small (less than 5 μm on the lapped surface of the slice examined). They represent space originally filled by mixing water, remain after the hydration of the cement gels, and are an integral part of the paste. Although they contain air at the time of examination, they are not considered part of the air-void system.
2. **Entrained air voids:** Entrained air voids are defined by VTRC as spherical voids larger than the capillaries, but less than 1 mm on the lapped surface of the slice examined. They are formed by the folding action of the concrete mixer, and their shape, size, and abundance are influenced by the addition of surface-active, air-entraining admixtures to the mixture.
3. **Entrapped air voids:** Entrapped air voids are voids that are larger than the entrained voids, but have internal surfaces that indicate that they were formed by air bubbles or pockets. They may be spherical or irregularly shaped.
4. **Water voids:** Water voids are irregularly shaped voids whose shape, location, or internal surface indicates that they were formed by water. Usually, they are larger than entrained air voids.

6.2.1 Capillary Voids

The smallest optically visible voids in HCC are the various sizes of capillaries. A few of the larger capillary voids can be seen at the higher magnifications used to determine the parameters of the void system; however, they are generally not that large. Hearn, Hooton, and Mills (1994) provide an excellent discussion of the capillary void system in HCC. Capillary voids are spaces formed by the shape of the hydrated cement gel structures and spaces left between the gel structures as water is used in the self-desiccation of the hydration process. They were occupied by water or gas when the concrete was fresh and are larger and more abundant in concretes with a high w/cm. The extent (volume and continuity) of the capillary system is thus controlled by the w/cm and the degree of maturity of the concrete. The evenness of the distribution of the pores and capillaries is controlled by the distribution of the water. As the concrete hydrates, the water in the pores is used in the hydration of the cement. As the concrete matures, much of the capillary space becomes filled with the products of hydration and the products of any reactions occurring between the chemicals of the paste and the aggregate. Some of the finer capillaries are spaces created by differential crystal growth.

The capillaries are detected only when specialized methods are used. In laboratories thus equipped, the various types of electron microscopes can be used to view the capillary void system. In the VTRC laboratory, the abundance and location of the capillary voids are detected by use of the P/EF microscope in the study of fluorescent thin sections of the specimen concrete (see chapter 13). At the NIST laboratory, the SEM is used (see chapter 14). Rarely, capillary

voids can be noted during the determination of the parameters of the void system. In that event, capillary voids are considered to be paste.

6.2.2 Entrained Air Voids

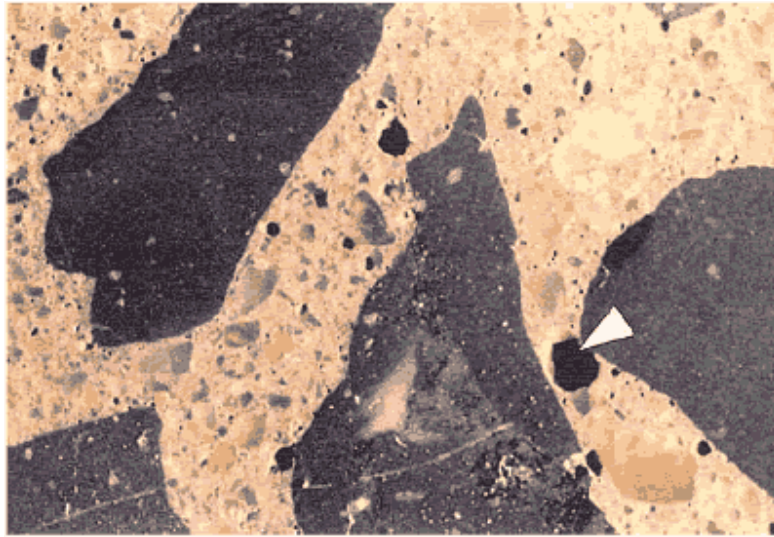
Entrained voids are small spherical voids enfolded by the mixer. Surface-active, air-entraining admixtures are added to the mixture to stabilize a specified percentage of these voids and thus protect the hardened HCC against the destructive forces of freezing and thawing. Thus, the entrained air void is a desirable void. Entrained air voids are generally considered to be larger than the capillaries (at least 5 μm in diameter), but smaller than the entrapped voids (Verbeck, 1966, 1978; Hearn, et al., 1994). Entrained air voids have so much surface tension relative to their volume that they are little affected by the shape of nearby particles. Distortion occurs in these small voids only when external forces distort the concrete after the beginning of hardening.

The presence of the proper quantity of well-distributed entrained air voids can prevent deterioration of the concrete by relieving the pressures that can develop during the freezing and thawing process (Helms, 1978; Hover, 1994; Newlon, 1978; Newlon and Mitchell, 1994; Pigeon and Pleau, 1995). Entrained air also facilitates the placement of the concrete because the entrained air voids increase the fluidity of the paste.

Very irregularly shaped small voids (maximum dimension of less than 1 mm) cannot be properly called entrained voids because they lack the characteristic shape showing that they were formed by the surface tension of the air-entraining admixture. It is not known if such voids function to protect the concrete against the deterioration caused by freezing and thawing. Small, irregular voids (particularly if not at an aggregate boundary or a wearing surface) may be evidence of retempering (see appendix C).

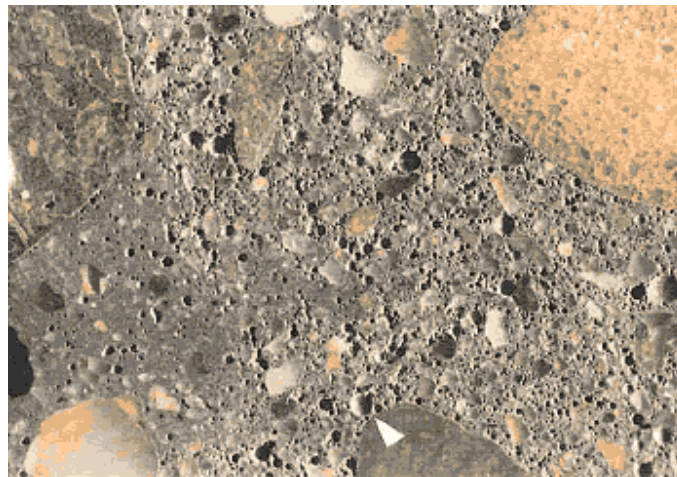
Figures 53 and 54 show concretes with different percentages of air voids.

Figure 53. Surface of finely lapped slice of concrete containing 5.6 percent total air voids.



The void content of this concrete is in the middle of the specification range. The large void marked with an arrow is about 2 mm across (larger than an entrained air void). Notice the very fine voids throughout the paste.

Figure 54. Surface of finely lapped slice of concrete containing 17 percent total air voids.



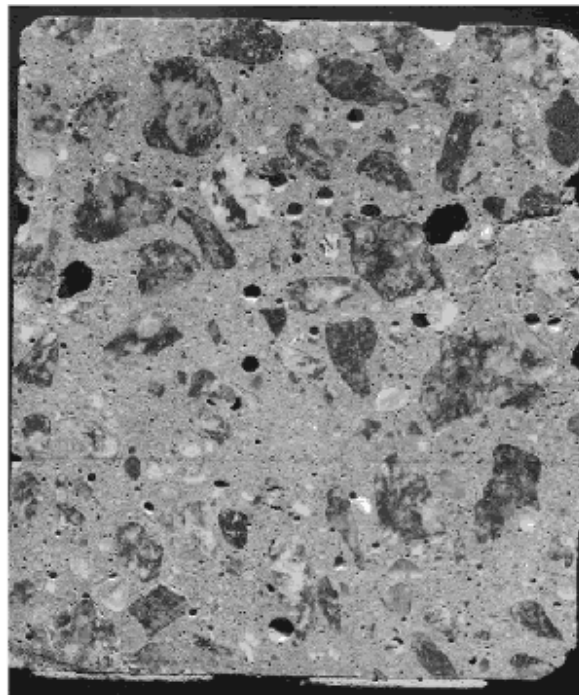
The void content of this concrete is way above the upper limit of the specification range. The void indicated by the arrow is about 1 mm across. The area of darker paste (lower left) has a lower void content. If an HCC contains more than one kind of paste, this generally indicates that the mixture had begun to hydrate before additional water was added (see section 8.4 and appendix C).

6.2.3 Entrapped Voids and Water Voids

All voids, regardless of shape, that have a maximum dimension (on the surface examined) of more than 1 mm are defined by VTRC as entrapped voids (large spherical) or water voids (large irregular). If voids occur flattened out at the boundary between the aggregate (usually coarse aggregate) and the paste, they are a class of entrapped voids called *boundary voids*.

Voids larger than entrained voids have no appreciable beneficial effect and weaken the HCC. Such voids are controlled by the efficiency of whatever system of consolidation is in use and the workability of the concrete at the time of consolidation. Particular voids may be caused by too much water in the HCC, a strong affinity of a particular aggregate lithology for water, improper consolidation, and occasionally by the dissolving away of Ca(OH)_2 . Water- or air-filled pockets not removed by consolidation will leave irregularly shaped voids (see figure 55). Water voids are irregularly shaped voids created in the HCC by bleed water prevented from rising to the surface by an aggregate particle or the hardening of the paste. Water voids contained water when the HCC was fresh and unhardened; however, in the hardened state, these voids are filled with air and thus might be more properly termed *water-formed air voids*.

Figure 55. Concrete core with about 4 percent large, irregularly shaped voids.



In this instance, the concrete, which had not yet been consolidated, became hard and unworkable while repairs were being made on the paving equipment. The specimen is 100 mm across.

6.3 QUANTITATIVE DETERMINATION OF AIR-VOID PARAMETERS

6.3.1 Overview

In hardened concrete, the air-void system may be characterized by one of two methods described in ASTM C 457—the *linear traverse method* or the *modified point-count method*. The parameters calculated include:

- **Air-void content (symbolized in ASTM C 457 by A):** It is a percentage by volume. A particular spacing of air voids is required to protect the concrete from the expansion of water during freezing. Empirical relationships were established between the void spacing and the total air content so that air content is used as the concrete design and control parameter. However, since the development of these relationships, a variety of new air-entraining admixture formulations are being used that produce void systems with characteristics significantly different from those upon which the relationships were established. Consequently, extremely low spacing factors may occur with air contents at the upper end of the specified range. Excess air-void content or very low spacing factors (i.e., < 0.10 mm) will cause the concrete to have less than the intended compressive strength.
- **Void frequency (symbolized in ASTM C 457 by n):** It is the number of voids per unit length of traverse. The void frequency is required in the calculation of the average chord in the modified point-count method.
- **Average chord length (symbolized in ASTM C 457 by l):** It is the length of the sum of the chords of the air voids divided by the number of voids encountered in the traverse.
- **Specific surface (symbolized in ASTM C 457 by α):** It is the surface area of the average void divided by the volume of the average void. It is calculated from the average chord. The unit involved can be expressed as squared units divided by cubed units or as units to the -1 power. The higher values (higher void surface area per void internal volume) indicate smaller voids. Small voids (with a shorter average chord) are desirable because they disperse throughout the concrete with small unprotected volumes of paste in between. If the same air-void content were present in larger voids, the unprotected volumes of paste would be much larger.
- **Spacing factor (ASTM C 457):** It is calculated from the specific surface, the percentage of air voids, and the percentage of paste (see section 7.1) that must be protected. It is expressed as a decimal value of the measurement unit. The spacing factor is a theoretical measure of the average distance water or expansive force must travel in HCC before it contacts an air void (i.e., half the average distance between air voids).

The air-void analyzer (AVA) is an apparatus that determines the characteristics of the air-void system from a sample of fresh concrete. Developed in Europe, the device measures the rate of air loss from a sample of mortar mixed with a viscous liquid and then uses Stoke's law to determine the size of the bubbles rising through a water column. The device reports the air content by volume of concrete contained in the entrained air voids, the specific surface of the entrained air-void system, and a value for the spacing factor. The AVA is a focus technology of the American Association of State Highway and Transportation Officials (AASHTO) Technology Implementation Group.

6.3.2 Methods and Equipment

6.3.2.1 Overview

New methods and equipment are continually being devised to monitor and determine the air-void parameters of hardened concrete. It is part of the job of the petrographer to assess the value of new methods and equipment and to decide which method is of value in which situation and, therefore, which equipment is worthy of a place in the budget of the organization. If the results of an air-void determination are to be presented in court and the testimony of opposing expert witnesses will be heard, any deviation from the principles of ASTM C 457 that has not been agreed upon by the litigants may invalidate the results of the analysis. Within an organization, particular deviations from the strict interpretation of ASTM C 457 may be acceptable if justified by their experience.

According to ASTM C 457, air-void system analyses can be efficiently performed with several methods and kinds of equipment. Suitable equipment for the determination of air-void parameters in hardened concrete includes, but is not necessarily limited to: (1) linear traverse, (2) modified point-count, and (3) image analysis equipment. Typically, the types of equipment to be used permit or facilitate the movement of the specimen of HCC on the stage of a microscope so that data may be collected over the specified area and from the specified length of traverse. Generally, the data collected are:

1. **Total length of the traverse over which the determination is made:** In the modified point-count method, the total number of points examined and the distance the equipment moves between the points are required for the calculations.
2. **Portion of the traverse that is across air voids:** In the linear traverse method, this portion is the sum of the chord lengths across air voids; in the modified point-count method, this portion is the number of points that occur in air voids multiplied by the distance the equipment moves between points.
3. **Number of voids occurring in the traverse examined:** The accuracy of the determination of the specific surface and spacing factor is completely dependent on the accuracy of the count of the number of voids on the line traversed. In the linear traverse method, the number of voids in the traverse is the number of chords collected; in the modified point-count method, it is the number of voids counted along the traverse line.

The procedures detailed in ASTM C 457 are those to be used with nonelectronic types of equipment (see ASTM C 457, figures 2 and 6). When equipment is used that includes automatic devices for moving the specimen, electric or electronic counters or totalizers and calculators, or measuring devices, the equipment must allow adherence to the principles of ASTM C 457 and permit or perform the calculation of the same parameters of the air-void system from the same data. The exact procedures followed for the operation of the equipment must be those described and specified by the fabricator of the equipment.

It is not known which type of equipment produces the most accurate results or how accurate the results need to be. Modified point-count equipment is favored by those who need speed. If the air-void parameters of spacing factor and specific surface are not required, a simple point count can be performed. Those who want a record of the chord-length distribution for research

purposes favor linear traverse equipment, whereas those who want speed and the ability to collect a lot of data and manipulate them on a computer in many different ways favor image analysis equipment. Image analysis equipment can strain the equipment budget, but requires less operator time since a human does not actually perform the examination. Research laboratories will usually require either point-count or image analysis equipment for speed in making routine determinations, and linear traverse equipment for its ability to determine chord-length distribution on a surface unaltered by the fillers and dyes required by image analysis.

NOTE: The air-paste ratio method of calculation detailed in ASTM C 457 is to be used ONLY: (1) when proportions of the ingredients in the mixture are known with some certainty; (2) when it can be assumed that no change in mixture proportions has occurred (e.g., retempering has not occurred (i.e., the amount of paste can be closely calculated)); AND (3) when, because of the lack of exposure of a generalized specimen of the HCC or because of the extremely large size of the aggregate, it is impossible to obtain a specimen of the HCC for microscopical analysis with an aggregate distribution that is representative of the placement. The air-paste ratio calculations use the aggregate-paste ratio of the mixture design to transform mathematically the air-paste ratio and other air-void properties determined microscopically to an estimated percentage of air voids, specific surface, and spacing factor for the concrete. In these situations, it is convenient to select a specimen of HCC that is low in aggregate so that the microscopist will not have to spend excess time moving over aggregate.

6.3.2.2 Linear Traverse

Using the linear traverse equipment (see figure 56), the operator tabulates the chord lengths across all phases of interest and records them for later analysis (Walker, 1988). This sort of data permits the straightforward calculation of the void parameters by the summing of the lengths of the chords and the counting of each occurrence of a phase. Because the calculations are extremely sensitive to errors made in the determination of the number of voids traversed, the method of deciding whether a void is or is not touched or transected by the line of traverse must be consistently applied throughout the analysis. If the individual lengths of the chords of the air voids are recorded and particular shape assumptions are made, a graphical representation of the chord lengths will indicate the size distribution of the air voids. The collection of the air-void data requires one pass of the microscope along the traverse line. The data necessary for calculation of the paste content may be collected at the same time or a separate determination can be made for the paste content. This procedure is further discussed in section 7.1.2. With some types of linear traverse equipment, all the air-void parameters are automatically calculated; with others, the calculations must be performed on a calculator or computer.

6.3.2.3 Point Count

With the point-count equipment, the operator records the type of substance (air void, paste, or aggregate) appearing at the index point of the reticle at a large number of points as provided by the click stop locations on the HCC specimen as the stage and specimen are moved under the microscope. The points may be randomly distributed or regularly distributed on a randomly placed grid or on a traverse line. Data concerning the relative amounts of all the phases and the voids encountered can be collected from one pass along the traverse line. If difficulty in

distinguishing the exact paste-aggregate boundary is encountered, the operator may consider a separate pass over a lightly etched surface to collect these data (see section 7.1.2). The air-void parameters may be calculated by the analysis equipment or separately calculated using a calculator or computer.

Figure 56. Partially automated linear traverse equipment for determining air-void parameters.

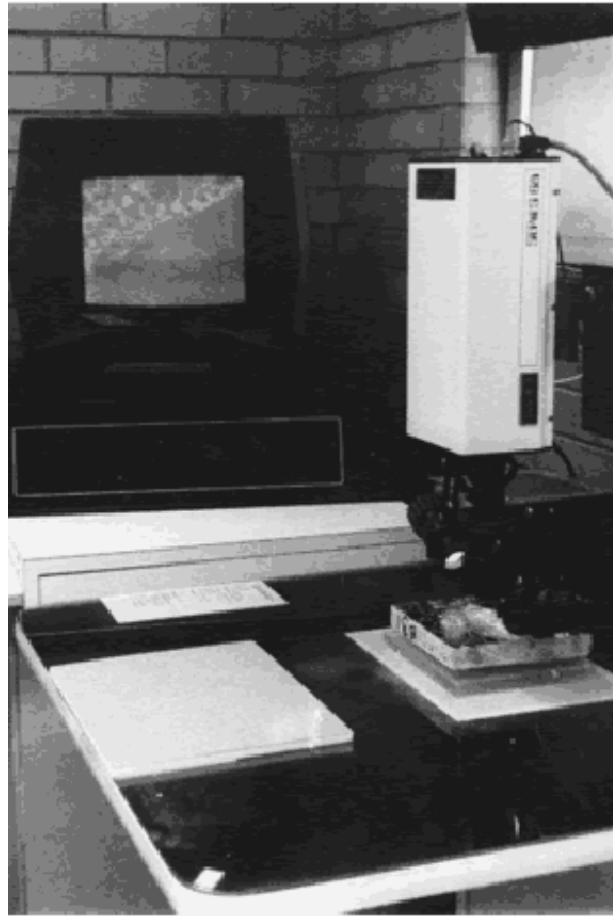


Either linear traverse or point-count software can be used to control the motion of the stage and to collect data.

6.3.2.4 Image Analysis

Image analysis systems incorporating a variety of equipment have been used to examine HCC. The typical setup uses a video camera with a magnifying lens (see figure 57) or a standard stereomicroscope with a video camera (see figure 56). Peterson, Swartz, Sutter, and Van Dam (2001) describe the use of a flatbed scanner for imaging. The collected images are then analyzed by computer software to calculate the air-void parameters. To enable the image analysis software to recognize air voids as distinct from other features requires that the specimen be specially prepared so that each of the three major phases of interest (voids, paste, and aggregate) is a distinct tone (e.g., white, black, and medium gray). A typical surface preparation is to ink the surface black, fill the voids with a white powder (e.g., kaolin) and remove the excess from the surface, and finally ink out any filled voids that the system should not classify as air voids (i.e., voids in aggregate particles). Peterson, et al. (2001) used a three-step procedure by collecting

Figure 57. Image analysis equipment.



Photograph by R.H. Howe, courtesy of PennDOT

The instrument is shown in the process of analyzing the air-void system of a slice of concrete. The screen in the background shows the progress of the analysis.

images of : (1) the untreated surface, (2) the surface treated with phenolphthalein (to differentially stain the paste), and (3) the inked and filled surface. The specimen preparation methods for image analysis can be exacting and can make the surface used useless for ordinary stereomicroscopic examination (as described in chapter 8). If it is desirable to perform normal examinations, these should be performed before the special surface treatments or, alternately, on an opposing lapped surface. Missouri DOT is currently managing a pooled-fund study to develop image analysis software with processing and pattern recognition capabilities to determine the airvoid parameters from an ordinary lapped surface (Missouri DOT, 2000).

Automatic systems that require filling the voids (thus hiding their interior surface) cannot make particular distinctions by a human operator possible. The human operator can often mentally reconstruct what the surface examined would have been if this or that flaw had not occurred. The human operator can judge whether an observed void is an air void, a fly-ash cenosphere, or the

hole left where a small round grain of sand has fallen out. These distinctions are generally possible by the study of the reaction products and the luster of the interior of the void.

6.3.2.5 Other Considerations

At VTRC, it has long been recognized that the accuracy of a linear traverse determination of the air-void parameters is as dependent or more dependent on the number of voids encountered and measured along the traverse as it is on the length of the traverse. Once 1000 voids have been measured and counted, the results from the data obtained subsequently change very little. Snyder, Hover, and Natesaiyer (1991) conducted an analytical investigation of the effect of the number of voids and the length of the traverse on the minimum expected error that can be encountered in a linear traverse determination of the void parameters in hardened HCC. Their work supports the belief that little additional accuracy is achieved if the determination includes more than 1000 voids and that almost no additional accuracy is achieved with more than 2000 voids.

When the air-void parameters are determined for intradepartmental purposes, the traverse length can be limited to that needed to count the 1000 or more voids. In such cases, the traverse length needed should be estimated and the specimen set up so that the traverse length is evenly distributed over the available surface. Under circumstances when ASTM C 457 requires 2540 mm of traverse, it is estimated that only 1270 to 1778 mm are required for the collection of data from 1000 voids in ordinary within-specification concrete. Should a legal controversy arise concerning the subject concrete, any traverse length deficiency can be made up by collecting additional data from traverse lines (also evenly distributed over the surface). If the traverse direction and starting point are randomly chosen, in both cases, the randomness of the data collection will be maintained. It is our view that spreading the data collection area over as large a surface area as possible so that any irregularities of void distribution (any clumping or areas devoid of voids) become part of the data recorded and examined is more important than the length of the traverse line.

The corollary is that if the number of voids is very small because of low air content or large voids, the length of traverse recommended in ASTM C 457 is probably not sufficient to obtain accurate air-void parameter data (Snyder, et al., 1991). Under such circumstances and with borderline compliance with specifications, it may be wise to use an additional length of traverse to ensure accuracy. In most cases, the small specific surface and large spacing factors caused by the lack of sufficient small voids will decisively indicate the inadequacy of the void system to provide freezing-thawing durability.

The method of deciding whether a void is or is not touched or transected by the line of traverse must be a simple rule that is firmly adhered to throughout any particular analysis. Pleau, et al. (1990), using the point-count method, recommended: "A simple way to guarantee a random choice is to systematically choose the constituent located in a given quadrant (of the field viewed), say the upper-left corner of the crosshairs" (p. 5). A similar method can be devised for whatever type reference point, reticle, and counting method are in use. Other researchers (e.g., Mather, 1989) have suggested that points in dispute be collected in a separate register and later distributed to the totals of the constituents in the same proportion as are the data concerning which there is no dispute.

6.3.3 Preparation of Specimens

The importance of the proper preparation of the surface of the slice of concrete cannot be overemphasized (see figures 42 through 44). In most laboratories, skilled, highly trained technicians prepare specimens. A poorly prepared specimen can cause a determination of the percentage of air present in a specimen to deviate from the true value by as much as 2 percentage points (20 percent to 50 percent of the true value). A rough surface makes it impossible to detect small voids. This will have the effect of lowering the detected percentage of air, decidedly lowering the specific surface, and thus raising the spacing factor. Quantitative determination on a surface that is undercut and wherein the edges of the voids have been chipped or worn away can provide data that indicate the presence of more air than really exists.

Chapter 5 has several suggestions for the treatment of weak or immature concrete before lapping. Pleau, et al. (1990) suggests soaking the slices (slabs) in water for a few days to promote further curing and cement hydration and thus produce a strengthened paste for lapping. This is a satisfactory procedure for recently cast concretes when the intent of the examination is merely to determine the parameters of the air-void system and its effectiveness may be improved by saturating the soaking water with lime, since soaking in plain water may leach lime and thus weaken the paste. Concretes that contain pozzolans or slag will benefit from gentle moist-heat curing (i.e., at 38°C). However, if the investigation requires a detailed examination of the paste microstructure, the potential altering effects of plain or lime-saturated water must be considered. More important, these and other effects (e.g., dissolving reaction products or liquefying expansive alkali-silica gels) must be considered before using this method in the examination of mature concretes for condition assessment or fault diagnosis.

Each method of producing a finely lapped specimen surface for microscopical study will probably produce different effects on different types of concrete (different w/cm, different kinds of aggregates, different degrees of maturity and deterioration).

In particular concretes in which the shape of the air voids has become distorted (see appendix C), all manner of overlaps and crushing of voids may occur. The operator should be alert and ready to record the data for each void in a logical and consistent manner.

6.3.4 Technician Considerations

The linear traverse and the modified point-count methods are tedious and hard on the eyes. A single determination of the air-void parameters of a concrete by means of the linear traverse method can take up to 7 h, depending on the size and quantity of the voids. A technician cannot spend more than 4 h per day doing this sort of work on a day-to-day basis. Everyone who has tried has found that the ability of their eyes to focus has deteriorated on the following day. The training and keeping of good microscopical technicians can be a major undertaking, requiring tact, skill, understanding, and a flexible schedule of rest periods.

Image analysis systems do not require that the operator be with the equipment after the initial adjustment :thus , eye fatigue and the need to train technicians to perform microscopical analyses

are eliminated. The following points are important considerations in the hiring and training of technicians for the microscopical analysis of air-void systems:

- **Try to avoid using operators for linear traverse and point-count determinations of air-void parameters who do not have good binocular vision.**
- **Keep available standard specimens of concrete with a range of different types of air-void systems:** Air-void contents of 2 percent to 14 percent are recommended. These should be specimens that have been analyzed by a number of different operators. The results previously obtained should be kept in a secure place by the supervisor. Each new operator who is trained for this work should be tested on the standard specimens, and training should continue until the results obtained by the new operator are comparable to the range of results recorded in the past.
- **Make sure that each operator knows how to adjust the positioning of the specimen so that it is flat and so that the specimen can move under the microscope and remain in the same focal plane:** Although this procedure can be tedious, it is not nearly the nuisance that continual focusing of the microscope during the traverse will prove to be if it is neglected.
- **Make sure that each operator knows how to adjust the ocular spacing for his or her interpupillary distance; the height of the chair; and any other items available for greatest visual acuity, comfort, and convenience:** The operator must understand that these adjustments are emphasized because proper adjustment adds to the accuracy of the determination. An operator suffering from a headache or backache is not as able to produce good data as a comfortable, healthy operator.
- **Make sure that the operators understand the need for good focus and how to achieve good focus on the reticle for their main eye and simultaneous good focus on the specimen for both eyes:** Each person has one eye that looks straight ahead (the main eye). The other eye observes things at an angle. Whenever an optical technique requires a reticle in one eyepiece of a binocular system, the reticle should be placed in the lens system used by the main eye.
- **If more than one person uses the microscope, make it a routine practice for each operator when beginning work to check the focus of the reticle and the focus of the surface being examined:** Emphasize that the surface should be in focus throughout an entire traverse across the specimen. If focus is lost, errors will be great and the ability to judge the type and origin of a flaw in the finish of the surface being examined will be seriously diminished.
- **Observe the actions of the operators and determine if they are following instructions:** From time to time, have the work of the operators checked by having another operator repeat the measurement of a specimen, have the operator repeat a specimen done some months ago, or have the operator repeat one or more of the standard training specimens.
- **Teach operators that great care must be taken to include in the count every void crossed by the traverse:** The air-void count should be performed slowly and accurately. Very small voids and voids that are just barely touched by the traverse line must be counted. When the linear traverse procedure is used, it may be necessary to slow the motion along the traverse almost to a stop (if not completely) to register very small voids in the count. If it is realized that a void with an essentially zero chord length (because the

traverse line is tangent to the void or because the void is very tiny) has not been counted, it is possible with some equipment to bring the motion along the traverse to a halt (so that zero chord length is recorded) and to momentarily press the button that registers the presence of the appropriate void type. The location of a void along the traverse line is not a matter of concern, and the operator can record it anywhere. In the modified point-count method, no automatic motion is usually used while air voids existing along the traverse line are counted; therefore, this error will not be made in the same way.

6.4 CLASSIFICATION OF VOIDS

6.4.1 Overview

The determination of the abundance of the various types of voids is very useful in concrete research. It can make data available that can change various practices in the mixing and placing of HCC. As an example, it was once thought that the speed of the screed pulling the vibrators through freshly placed concrete did not affect the degree of consolidation. This did not seem logical to some. The Ballenger Construction Company of North Carolina set up a series of test sections of pavement in which the speed of the screed was carefully controlled. A detailed petrographic laboratory analysis of the abundance of the various sizes of voids in the air-void system of 24 cores that had been removed from these test sections showed that there is a good inverse relationship between the speed of the screed and the degree of consolidation (Walker, 1972). As a result, the maximum speed of the screed is now limited in many specifications.

The quantitative determination of the abundance of various types of voids can be an important part of the petrographic analysis of a specimen. In the VTRC petrographic laboratory, air voids are classified as entrained or entrapped during routine point-count analyses (see table 15). With equipment designed for this purpose, this determination may be performed concurrently with the determination of the other parameters of the air-void system.

In a finely lapped slab or thin section, the size and shape of the voids can be used as indicators of the void origin and type. The luster and texture of the interior of the voids may sometimes be used in the recognition of voids caused by accumulation of water and passageways for water. The properties on which distinctions may be made between the various types of voids are arbitrary and may vary from one laboratory to the next. Because these distinctions are made on the appearance of a void on the surface of a slice (where the third dimension of the void cannot be seen), many large voids will be classified as entrained voids when they are really entrapped voids. As indicated in figures 58 and 59, a small section through a large void can be indistinguishable in two dimensions from a large section through a small void. A cross section that is larger than the defined maximum for entrained voids must be a section of an entrapped air void or a water-formed void. A significant number of large cross sections indicate a great number of large voids.

Figure 58. Illustration of various sizes of sections that may be expressed on a randomly placed plane.

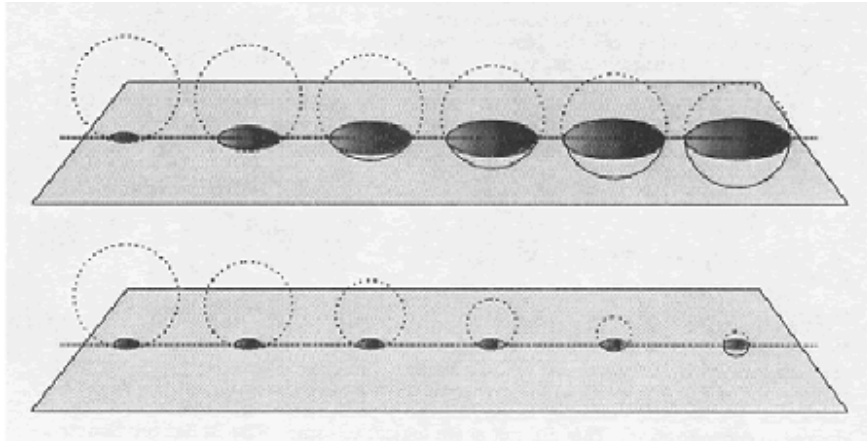
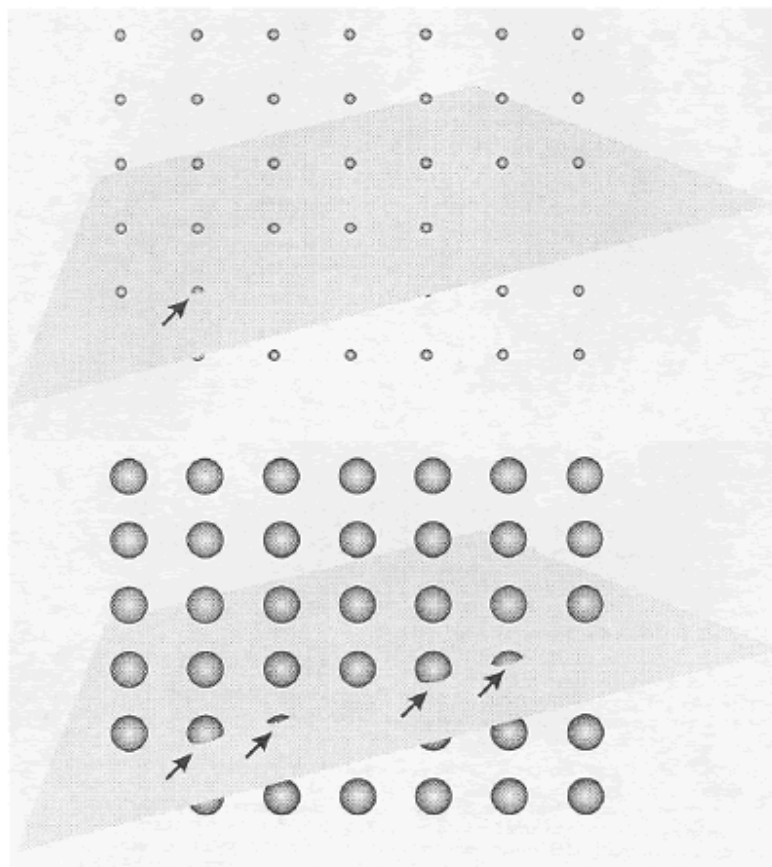


Figure 59. Two equally spaced arrays of voids.



Each array of voids is crossed by a randomly oriented plane. There is the same number of voids in a unit area in each array. Note that the plane touches more voids (see arrows) when the voids are large than when the voids are small.

6.4.2 Distinguishing Entrapped Air Voids From Water Voids

The petrographer can often distinguish between entrapped voids caused by water pockets and entrapped voids caused by air pockets. The estimate will necessitate careful observation and some extrapolation. In general, the interior surface of an air void will appear smoother, sometimes even shiny. A water void will usually have a dull interior that appears to have had small particles and precipitates deposited onto it. In the case of water-formed voids, the shapes of the bounding aggregate particles are often visible in the interior of the void. Water voids may have an interior showing water movement patterns, may be interconnected bleed-water voids, or may show by the nature of the internal deposits and asperities and by their position that they are water pockets trapped by aggregate particles.

6.4.3 Distinguishing Entrained Voids From Entrapped Voids

The determination of the size breakpoint between entrained and entrapped voids varies from laboratory to laboratory and must be interpreted in light of the method of measurement. For example, if the voids whose maximum chord on the surface examined is less than 1 mm are defined as entrained voids, then some voids whose true diameter is larger but not observable because the diameter is not in the plane of observation will be classified as entrained voids. The petrographer should maintain a clear idea of the meaning of the methods of determination in the size sorting of the voids.

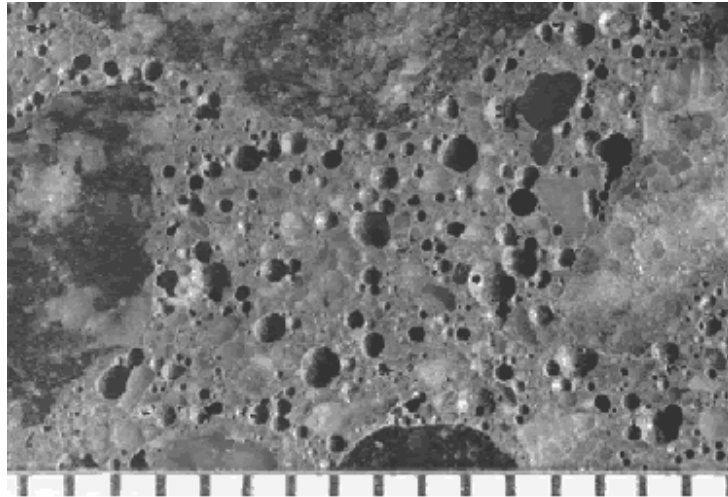
A random line of traverse through HCC has a greater chance of traversing a large void than a small one. The probability ratio is the ratio of their volumes (see figure 60). The calculations detailed in ASTM C 457 use the sums of the chord lengths and the count of the voids regardless of the desirability or relative amounts of the various sizes. If the large voids are not counted and measured as part of the overall determination of the void system (suggested by Sommer, 1979), the control against large voids provided by the determination of the specific surface and spacing factor will have been blocked and the apparent precision of the method spuriously improved (Walker, 1980).

Unless the method and the criteria used to obtain data concerning void size are rooted in statistics, the data are only rules of thumb and valid only when compared with data obtained by the same methods. Calculations can be made on the distribution of the void sizes from chord data if particular assumptions are made concerning shape, heterogeneity, and isometric distribution of air voids.

At VTRC, the diameter of the section of the void as seen on the finely lapped surface examined must be equal to or less than 1 mm for the void to be considered an entrained void. In other laboratories, the length of the chord on the traverse line across the void is the parameter measured. The latter method makes it possible to set up an automatic electronic classification and counting system for entrained versus entrapped voids. In some European laboratories, the chord must be 0.3 mm or less for the void to be considered an entrained void (Wilk, et al., 1974). A void viewed in a lapped surface may be transected by the surface either above or below its true diameter, and there is no known way to measure an actual internal diameter. Efforts have been made to peer into a void to try to get an estimate of the true diameter; however, these efforts may

serve only to confuse the issue. In many laboratories, decisions on individual void size are made on the lapped surface as viewed. A large void, more than 1 mm diameter, may be so oriented that the surface examined truncates only a small portion of the void (the extreme top or bottom) when considered from the finely lapped surface. Thus, there will always exist a larger proportion of large voids than can be recognized on the surface examined (see figure 58).

Figure 60. Void system produced by early types of high-range water reducers.



Scale is in millimeters.

Such large voids do not add to the resistance of the concrete to cycles of freezing and thawing, but do lower the compressive strength.

6.4.4 Procedures

The procedures given here are for the linear traverse method when the chord lengths are collected by an operator depressing an electronic recording device (Walker, 1988). The point-count method does not survey every void on the traverse during the percentage portion of the examination and, therefore, does not allow a classification of every void. Image analysis procedures are not discussed in detail.

This procedure is a three-step process:

1. **Examine each void when the void& leading edge comes to the index point (usually the center of the crosshairs) and determine which type of void is present:** With the wide-angle lenses and a magnification of 100X or less, voids of less than 1 mm in diameter will be completely visible in the field of view. Most voids can be classified at a glance as either entrained, entrapped, or water-formed. When borderline cases occur, use a finely marked metric ruler on the slice, in the field of the microscope, to determine void size (at low magnification, an eyepiece micrometer may be used).

2. **Record the presence of the void and the length of the chord across it in the usual manner for a linear traverse determination (by pushing down a button and holding it down until the trailing edge of the void is at the index point):** If three buttons are available for the three types of voids, each with its own tabulating device that separately measures, totals, and counts the voids, depress the appropriate button for the type of void determined in step 1. If the chord lengths are recorded by using only one button and are individually printed on paper and the void encountered is not an entrained void, stop the motion of the traverse stage and mark the paper tape at the chord measurement with a symbol to indicate the classification of the void measured. Continue with the analysis. Repeat from step 1 for each void.
3. **When the analysis has been completed, add the lengths of the chords for each type of void (if not added by the linear traverse device employed) and report the percentage by volume and the count (individual voids per specified inches of traverse) of each in the total concrete.**

6.5 MEANING OF AIR-VOID PARAMETERS

The major parameters of the air-void system are interdependent. Most concrete specifiers require only that the air-void content be within particular limits. Recently, the trend toward end-result or performance-related specifications has introduced the requirement that the spacing factor be below a particular limit or the specific surface be above a particular limit (Holley, et al., 1999; Kaderbek, Tracy, and Krauss, 2002; Schell and Konecny, 2003). Although one-sided limits on the spacing factor or specific surface do not preclude air-void contents that are too high, compressive strength requirements serve as a limit on excessive air.

Although the parameters described in ASTM C 457 remain those commonly used to describe and evaluate air-void systems, there have been attempts to develop a more meaningful descriptor. Philleo (1983) began the process using void-size distribution to determine the volume of the paste within a particular distance (0.20 mm) of an air void and thus unprotected from cycles of freezing and thawing. Furthermore, the distance at which only about 10 percent of the paste remained unprotected was coined the *Philleo factor*. Similar concepts are discussed by Attiogbe (1993); Pleau and Pigeon, 1996; Pleau, et al., 1996; and Snyder, 1997. Snyder, et al. (2001) provides a detailed examination of the practical and theoretical basis for the measurement of airvoid systems.

The following are some of the issues the air-void parameters will determine:

- **Resistance to deterioration caused by cycles of freezing and thawing:** The spacing factor is generally considered to be the most relevant measure of freezing-thawing durability provided that the concrete has adequate maturity. Adequate maturity is generally considered to have been achieved when a compressive strength of 26 to 28 megapascals (MPa) has been reached. The most often quoted maximum spacing factor value for ensuring frost resistance is 0.20 mm, with occasional references to higher values (Pigeon and Pleau, 1995). The Canadian Standards Association (CSA) has adopted a maximum average spacing factor of 0.23 mm with no single test exceeding 0.26 mm for frost resistance (Holley, et al., 1999; Schell and Konecny, 2003). Pigeon and

Pleau (1995) point out that there is no clear benefit to spacing factors much below the maximum recommended values and, in fact, that excessively low values adversely affect concrete compressive strength. Specific surface values in excess of 25 mm⁻¹ (mm²/mm³) will generally provide satisfactory spacing factors.

- **Use of specific admixtures:** The petrographer is often asked whether a particular admixture or an excess amount of a particular admixture has been used in a specific concrete. Extraordinarily low spacing factors accompanied by a high specific surface can indicate either excessive air-entraining admixture or (if the total air content is within specifications) the use of a highly specialized admixture. In the past, most air-entraining admixtures were formulations of neutralized vinsol resins. More recently, a wider variety of compounds, including vinsol resins, tall oils, and synthetic detergents are being used. Some of these newer materials produce more stable void systems with significantly smaller bubbles. For a complete discussion of the various air-entraining admixtures being used and the production of air-entrained concrete, see Whiting and Nagi (1998).

During the first trials of some of the high-range water reducers, the paste was exceedingly compact; however, many of the voids were large. This created a specific texture, as illustrated in figure 60. The high-range water reducers used in present-day mixtures do not create such a high content of large voids; however, some concrete with this texture is still in service and requests to examine these concretes still come in.

- **Flaws:** An unusually large number of voids that appear to have held water when the concrete was fresh indicate flaws in either proportioning or workmanship. An abundance of entrapped voids indicates either poor consolidation or early loss of slump.
- **Placement issues:** The data concerning the distribution of the types of voids as detailed in section 6.4 can be used to discover particular placement conditions, such as the efficiency of the consolidation and the reasons for various nonstandard conditions (such as low compressive strength or high permeability). Sometimes, when hand-held vibrators are used, there is excess entrapped air because of the persistent but erroneous belief that the specified amount of vibration will cause a loss of a portion of the required entrained air. Adequately consolidating the concrete to remove entrapped air voids will not adversely affect the ability of the entrained air-void system to provide resistance to cycles of freezing and thawing (Simon, Jenkins, and Hover, 1992).

Visually apparent "vibrator trails" have been reported from some paving operations, with longitudinal cracks developing in the trail. The distinctive "trails" result from segregation of the concrete as mortar moves into the vibrator's zones of influence. Comparison of airvoid characteristics suggested that the vibrator trails had higher spacing factors than the areas of the slab less affected by vibration (Gress, 1997).

Although the quantity of large voids and specific surface are generally not addressed in current specifications, it is important to consider these parameters and to be able to explain their meaning. In general, it is much easier to talk about a significant quantity of large voids than to explain the mathematical derivation of the specific surface. A percentage of large voids exceeding 1.5 percent is considered to be high. More than 2 percent is considered to be

excessive, and explanations for the prevalence of the large voids are sought. Does the concrete appear to have been retempered? Improperly mixed or consolidated? What is the reason?

CHAPTER 7. QUANTITATIVE ANALYSES OF PASTE, AGGREGATE, AND OTHER COMPONENTS

7.1 PASTE

7.1.1 Overview

It is necessary to calculate, estimate, or determine microscopically the volume of air-free paste in an HCC specimen in order to calculate the specific surface and the spacing factor by means of the equations in ASTM C 457 (see chapter 6).

7.1.2 Procedures

7.1.2.1 Calculation From Mixture Design

When the design of the mixture is known and it is fairly certain that all additions of water or other changes in the mixture have been properly documented, the percentage of paste can be calculated from the mixture design by adding the volumes of water and cementitious materials and expressing the volume as a percentage of the total volume of HCC produced by the mixture (ACI 211.1, ACI 211.2, ACI 211.3).

7.1.2.2 Estimation

Slight variations in paste content used in the calculations of air-void parameters do not cause much change in the values obtained. Therefore, for ordinary intradepartmental work, for preliminary work, and whenever accuracy of the spacing factor and specific surface is not required, the paste content is estimated. The normal range of paste content is 23 to 32 percent; 27 percent has often been used as a good estimate of paste content in normal concrete (ACI 211.1, ACI 211.3, ACI 221R). The petrographer should use his or her judgment to adjust this figure based on the appearance of the specimen (see figures 61 and 62). If the quantity of the paste appears to be far from normal (see figures 63 and 64), a microscopical determination of the percentage of the paste should be made to permit an accurate determination of the air-void parameters. If an estimate is to be used, the calculations may proceed and the data and method recorded in the notes for the report.

7.1.2.3 Microscopical Determination

The amount of air-free paste present is most easily determined by making a microscopical determination (linear traverse or point-count method) of the amount of aggregate present. The aggregate occurrence (the sum of the aggregate chords or the sum of the points falling in the aggregate) is calculated by dividing by the total (total traverse length or total number of points) to determine the percentage of the aggregate. Most laboratories using point-count equipment perform paste content determinations concurrently with air content determinations;

therefore, separate paste determinations are most often needed when linear traverse analyses are performed. The paste percentage is determined by subtracting the aggregate and the air percentages from 100 percent.

Figure 61. Finely lapped slices of concrete with normal paste content : Rounded to subangular quartz gravel coarse aggregate and fine sand aggregate.

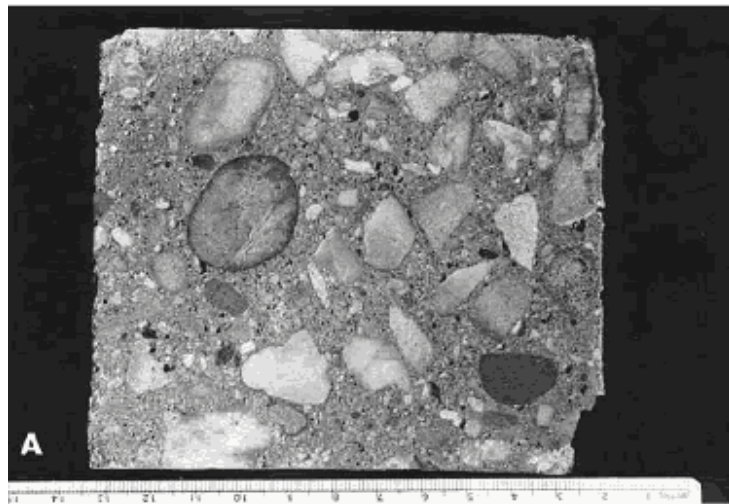


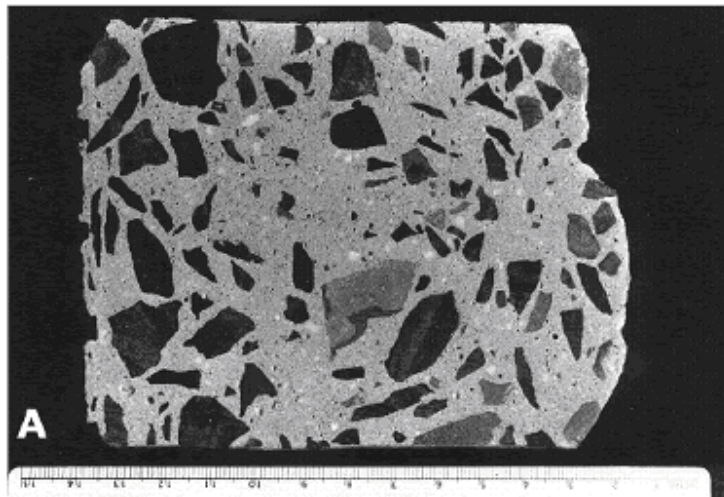
Figure 62. Finely lapped slices of concrete with normal paste content: Angular crushed granite coarse aggregate and fine sand aggregate.



To obtain the same accuracy in a microscopical determination of the aggregate as that of the air voids, at least 1000 occurrences (fragments) of the aggregate must be counted (point count) or measured (linear traverse). To determine the percentage of a substance of which there are only 200 occurrences in the traverse of the surface on which the percentage of air was determined, five such slices would have to be prepared and examined. Examining such a large number of surfaces is often economically impossible, and unless the air-void determination included these

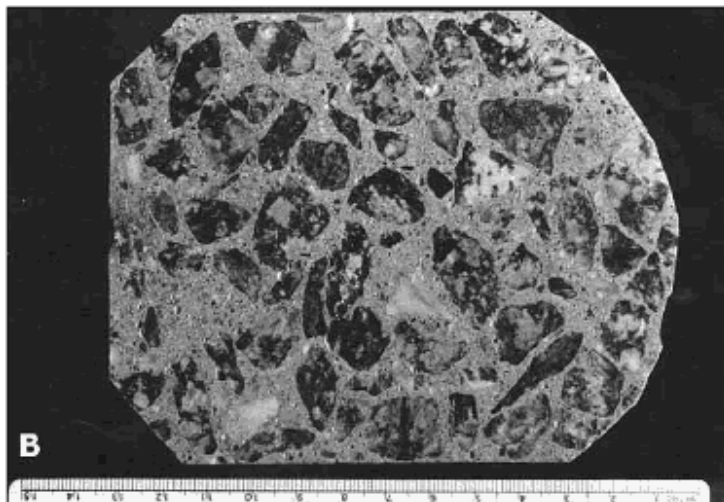
surfaces, the air content determined may not be relevant to the paste content. When there are fewer than 1000 aggregate particles along a microscopical traverse, the percentage of paste or aggregate determined should be considered an estimate.

Figure 63. Finely lapped slices of concrete with abnormal paste content: High paste content.



The coarse and medium-sized aggregate is a fine-grained metamorphosed shale, and the fine aggregate is a quartzose sand.

Figure 64. Finely lapped slices of concrete with abnormal paste content: Low paste content.



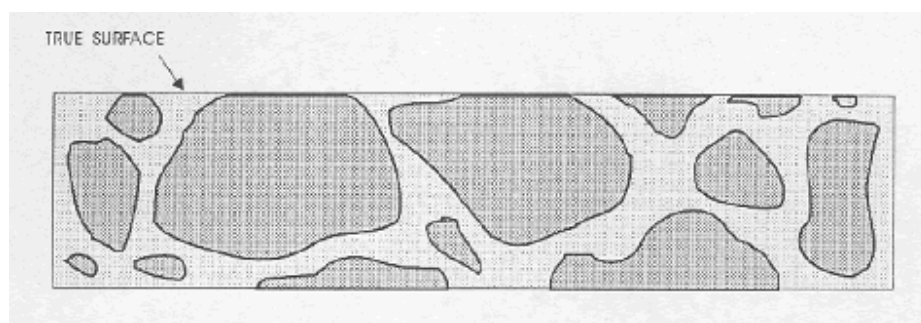
The coarse aggregate is a granitic gneiss, and the fine aggregate is a river sand.

Paste can usually be distinguished from aggregate on the basis of color, luster, internal structure, and the sort of surface produced by the lapping procedures. However, occasionally, aggregate

particles so closely resemble the paste in color, luster, and finely lapped texture that it is possible to miss small corners of coarse aggregates and fragments of sand and be quite uncertain about the exact location of the boundary between these phases. Strangely enough, carbonate aggregate is usually distinguishable by color, luster, translucence, and crystal structure. It is usually the light brown to creamy gray quartz pebbles and sands that are the most difficult to distinguish from paste.

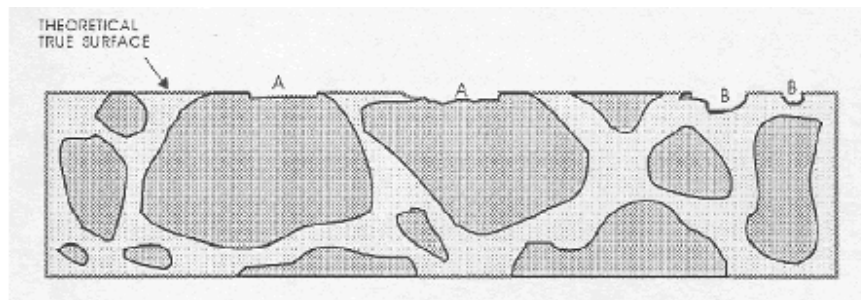
When aggregate particles are lapped in a slice of concrete, they are ground off to the level of the paste and a fine matte surface is produced on the aggregate surface remaining in the slice of concrete (see figures 65 and 66). This matte surface will be a little different for each aggregate

Figure 65. Lapped surface.



The darker line at the top surface represents the lapped, matte aggregate surface.

Figure 66. Flaws in lapped surface.



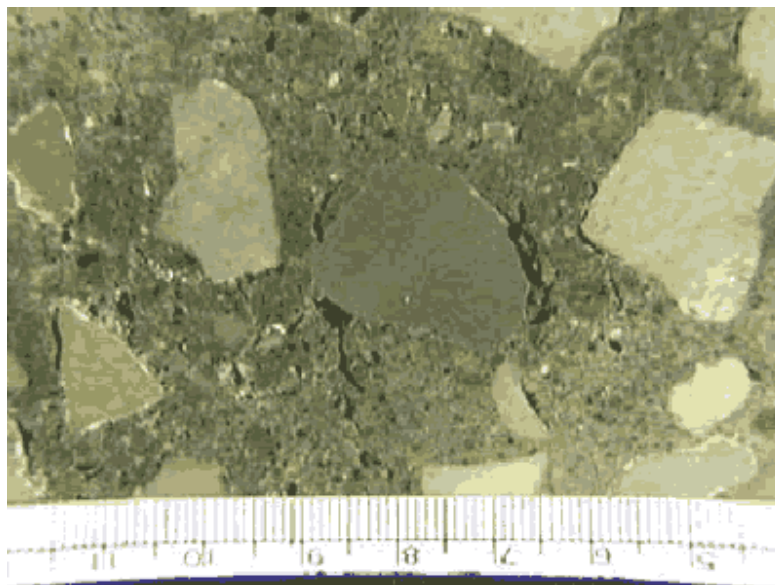
The darker line at the top surface represents the lapped, matte aggregate surface. This is an illustration of the type of flaw caused by aggregate that is fragile and recognizable by the broken aggregate surface (marked "A" flaws caused by a fragment of aggregate flaking off), and the type of flaw caused by complete or nearly complete loss of an aggregate particle that is recognizable by the shape of the cavity remaining and the texture of the paste surface within the cavity (marked "B" flaws caused by a piece of aggregate falling out). lithology exposed in the surface; however, it is generally sufficiently different from a broken surface or a natural water-worn surface of the type of aggregate for a technician to be able to distinguish a matte-lapped surface from all others. Because of the generally higher capillarity of the paste and the greater hardness of the aggregate, the matte surface on an aggregate particle is usually quite different

from the surface of a finely lapped paste. The lower the w/cm, the denser the paste becomes and the more the lapped surface on the paste becomes like the lapped surface on the aggregate. When the problem of distinguishing paste from aggregate becomes difficult, the differences in solubility in weak acid or the differences in porosity indicated by dye absorption can be used to differentiate between aggregate and paste.

The problem cannot be solved by adhering to statements such as: "The paste content calculated from the known mixture proportions is approximately 12 percent higher than the one obtained from the ASTM C 457 measurements" (Pleau, et al., 1990, p. 5). Pleau, et al. called this sort of error "an unavoidable artifact of the measurement process" (p. 6). In their work, no effort seemed to have been made to enhance the paste-aggregate boundary and lessen their error. They used the point-count method, determining paste concurrently with the analysis of the air content. They explained the difference between their mixture proportion and their point-count results by stating that there were errors made in determining the proper outlines of the aggregates when the aggregate occurred close to the surface being examined. In their specimens, the paste seemed to have been more translucent than may have normally been encountered. Reportedly, their operators frequently saw through the paste and counted an aggregate particle beneath. Also, they had occurrences of discolored portions of the paste that appeared to be aggregate particles and thus were counted as such.

Other than the dark blue&green blotchy appearance often seen in pastes containing ground granulated blast-furnace slag, the only such "discolorations" seen in the VTRC laboratory, when studied in thin section, have been determined to be lumps of cement (see figure 67) caused by either exposure of the cement to moisture during storage or an improper batching sequence. The example shown in figure 67 was found in a lump of concrete, commonly referred to as a "cement ball," found tumbling down the discharge chute of a concrete truck mixer.

Figure 67. Knot of cement exposed on finely lapped slice (rounded shape was caused by tumbling in the mixer).



A discussion of the factors that can result in this type of nonhomogeneity can be found in Gaynor and Mullarky (1975). In retempered concrete (see appendix C), some of the aggregate may have coatings of dense, partially hydrated cement. Obviously, counting a cement lump or coating as aggregate in the point-count method will decrease the ratio of paste to aggregate determined. Although Pleau, et al. (1990), found a consistent 12 percent shortage in the microscopically determined paste content in the laboratory-mixed specimens they used, they did not present any evidence that indicated that all paste contents determined microscopically should be increased by such an amount.

The percentage of paste is determined in six steps, as listed in table 16:

Table 16. Procedure for determining paste percentage.	
1.	Etch the slice if necessary.
2.	Examine the etched slice and become familiar with the way the paste and aggregates reacted to the acid.
3.	Prepare to recognize the true lapped surface of the aggregate.
4.	Survey the slice to become familiar with any features that could cause confusion.
5.	Perform the microscopical determination of the amount of aggregate in the slice.
6.	Calculate the percentage of paste.

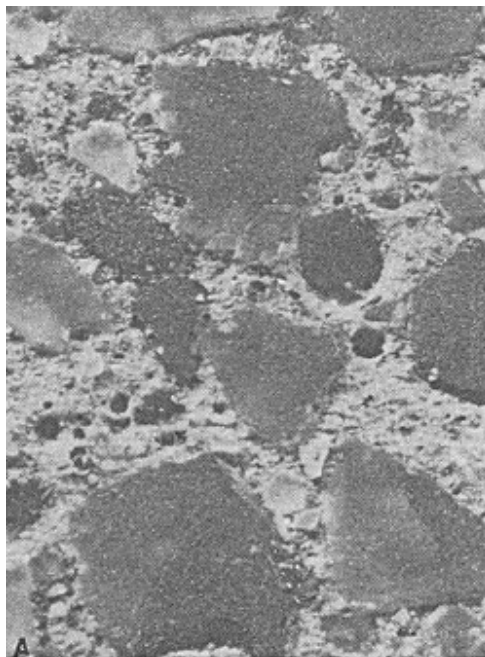
1. **Etch the slice if necessary:** Determine if etching the slice will enhance the visibility of the boundary between the aggregate and the paste. Test etchings can be performed by dropping a small quantity of acid on companion surfaces or even on the slice under examination. Most users of point-count or image analysis equipment make the paste determination concurrent with the air-void determination and forgo the greater definition of boundaries available by etching. When the color of the paste and the aggregate match and the lapped surfaces are similar, the determination of the exact boundaries between the aggregate and the paste is very difficult. If the results of the determination will have to be presented as legal evidence (and perhaps questioned by opposing expert witnesses) and sufficient specimen material is available, VTRC subjects the specimen surface to a very brief etching procedure (see section 5.2.3) so that the exact aggregate-paste boundaries can be distinguished by the different solubility of the phases in the dilute acid. Avoid etching the specimen to determine an accurate paste percentage unless sufficient slices can be obtained so that the slice etched will not have to be used for other purposes and an unetched slice will remain available for archival purposes.

CAUTION: Perform the etching procedure after the air-void determinations have been made because the acid will round off the void edges and make the voids appear larger. Therefore, if an acid etching procedure is to be used, determining the paste content must be a separate procedure from the air-void determination.

2. **Examine the slice and become familiar with the manner in which the paste and the various lithologies of aggregate reacted to the lapping and the acid:** Usually, the paste is more soluble than the aggregate and is etched down to a lower level (see figure 68). Occasionally, there may exist pieces of pure calcite in the aggregate. Calcite itself is

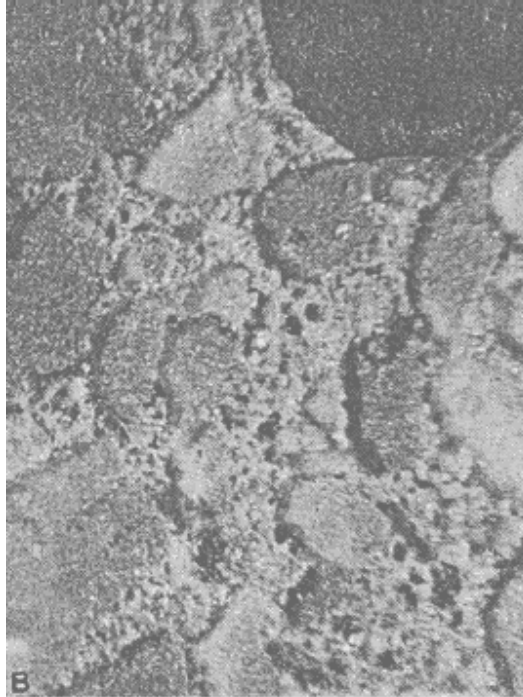
much more soluble in weak HCl than concrete paste and will be dissolved to an even greater level. Thus, there exists a solubility difference, and the boundary can be distinguished. Unless the aggregate rock used is exceptionally rich in pure calcite, this should not occur often. Impure carbonate (calcitic and dolomitic) rocks are not removed to such a great extent. The pyrites, clays, and other minerals included in the more complex carbonate rocks remain at the level to which the specimen was lapped, even if a layer of the carbonate is removed (see figure 69).

Figure 68. Etched slice: Etched surface on concrete fabricated with quartz sand fine aggregate.



Width of image is 10 mm.

Figure 69. Etched slice: Etched surface on concrete fabricated with crushed limestone fine aggregate.



Width of image is 10 mm.

3. **Prepare to recognize the true lapped surface of the aggregate as distinguished from any broken or water-worn natural gravel aggregate surfaces:** Whether the paste determination is made on a flat lapped surface or an etched surface (whether the quantity of paste is determined at the same time as the quantity of voids or not), think clearly about the fact that the matte surface on the aggregate is the portion of the aggregate that exists on the plane on which the determinations are being made. Other surfaces of the aggregate will have a natural broken or water-worn surface. Figure 66 illustrates: (1) the type of flaws caused by aggregate that is fragile and recognizable by the broken aggregate surface and (2) the type of flaws caused by the complete or nearly complete loss of an aggregate particle that are recognizable by the shape of the cavity remaining and the texture within the cavity. These flaws are not a common occurrence; however, when they are present, a mental reconstruction of the surface will usually indicate that they should be counted as aggregate. If these flaws are common and a mental reconstruction of the true surface does not indicate the proper location of the boundaries between the paste and the aggregate, the slice should be refinished or replaced with one of a better quality. For highest accuracy, the air-void determination should be made on the better prepared slice. In cases other than the flaws indicated in figure 66, refrain from recognizing as aggregate any area that is below the finely lapped surface. If a part of the aggregate that should be covered with paste is exposed, count such areas as paste. If the paste surface has been removed from over an aggregate surface (chipped off or etched off), the aggregate particle will not exhibit the finely lapped matte surface of

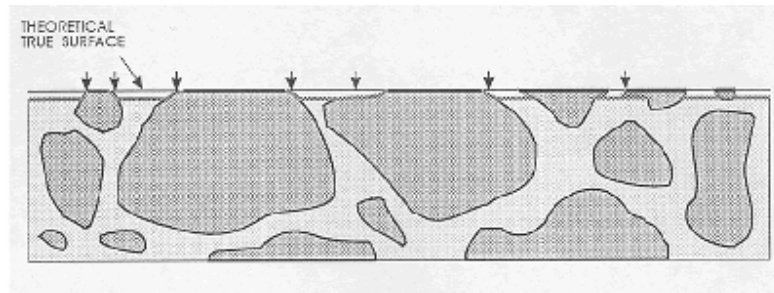
the properly exposed aggregate particle and it is likely that at a magnification of 100X (or larger) there will be a decided difference in the location of the planes of focus between the true lapped surface and any aggregate surface beneath. This difference in focus (which must be adjusted for if the surface is to be kept in focus) should alert you to the fact that you are viewing a surface that is farther from the objective lens than was the surface on which the focus was originally located.

None of these problems should cause errors if you think clearly about the view seen and mentally reconstruct the view that would have been seen if the paste area on the lapped surface accurately indicated the true proportion of the paste present. Avoid errors by allowing sufficient time for the analysis. Figure 70 illustrates some of the flawed and etched artifacts that may be observed in surfaces during the microscopical determination of the paste-aggregate ratio. These surfaces are different from the undercut surfaces discussed in section 5.2.1 (see figure 41). The undercut surfaces have a somewhat similar high relief; however, the features are rounded and there is no way a mental reconstruction of the surface will yield a good estimate of the position of the paste-aggregate boundary. Undercutting must be overcome by proper surface preparation.

4. **Survey the slice and become familiar with any portions of the paste that could be mistaken for aggregate because of coloration, carbonation, or other factors:** Paste that is dark because of concentrations of unhydrated cementitious material or paste that has been carbonated and therefore not etched as deeply as the surrounding paste will not have a lapped matte surface as the aggregate particles do. Although the calcite in carbonated areas is soluble in HCl with effervescence, these areas are seldom etched as deeply as uncarbonated paste. The calcite is completely dissolved; however, usually there remains a porous layer of material that is not soluble in the acid and is often as high as was the original lapped surface. It appears that the siliceous components of the uncarbonated paste are more soluble than the siliceous portion of the carbonated paste or that more acid is consumed dissolving the more plentiful nonsiliceous component of carbonated paste and thus attacks the siliceous component to a lesser degree than in uncarbonated paste.
5. **Perform the microscopical determination of the amount of aggregate in the surface:** With the exception of the kinds of flaws shown in figure 66, be careful to count as aggregate only those portions of the aggregate that were at the surface when the air-void determination was made (i.e., the high matte-lapped surfaces of the aggregate).
6. **Calculate the air-free percentage of paste:** The percent of paste in the concrete is determined by subtracting from 100 percent the sum of the percent of aggregate and the percent of air voids, as shown below:

$$\% \text{ Paste} = 100 \% \text{ minus } (\% \text{ aggregate plus } \% \text{ air voids})$$

Figure 70. Cross section of surface demonstrating problems of boundary distinction.



The darker line at the top surface represents the lapped, matte aggregate surface, and the shaded line just below the top represents the etched surface with possible misinterpretations at arrows. Acid-etched surface shows the need for counting as aggregate only the matte-lapped surface of the aggregate.

7.2 AGGREGATE AND OTHER COMPONENTS

The percentage of a specific type of aggregate or other substance should be determined when deemed important by the client or the petrographer. Any substance that can be recognized when seen on the surface of the slice as being composed of a particular material can be counted by the point-count method or measured by linear traverse equipment and an estimated volume percentage of the substance can be determined. The accuracy of such determinations is dependent on the frequency of the occurrence of the particles of the substance, as discussed in section 7.1.2.

Substances cannot be distinguished on the basis of size. It is possible to know only that the exposed cross section of an object indicates that the object is large enough to have the particular cross section. The object may be much larger.

Occasionally, the petrographer is requested to determine the relative amounts of coarse aggregate and fine aggregate. If there is a distinct lithologic difference between the two (e.g., a fine-grained greenstone coarse aggregate and quartz sand fine aggregate), an estimate of the percentage of each can be made using point-count or linear traverse equipment. If there is no readily recognizable lithologic difference (most often the case when crushed limestone is used for the fine as well as the coarse aggregate), it is impossible to make a percentage determination of the relative amounts of these materials by readily available optical methods (see section 12.3). The calculation of diameters from chords such as that of Lord and Willis (1951) that are dependent on the spherical shape of the item measured cannot be used for aggregate particles. The distinction cannot be made on the size of the area of the particle exposed on the lapped surface because a piece of coarse aggregate may be almost hidden, with only a tiny corner showing. At present, the available methods include removing the paste with an acid or disaggregating the concrete by freezing with liquid nitrogen and subsequent sieve analysis of the aggregate. Both methods can be confounded—the acid dissolution approach if the aggregate contains a carbonate component and the freezing approach if the aggregate contains unsound or sensitive components.

An experienced petrographer will usually be able to tell by comparison with other specimens of concrete if an unusual amount of either coarse or fine aggregate is present. The original design of the mixture should indicate the sizes intended to be used (see figures 71 and 72).

If the petrographer feels that the aggregate is not sized according to the intended grading, an investigation of the sizes of the materials in the stockpiles can be made. If the sizes in the stockpiles are within specification, the problem may be in the proportioning of the aggregates during fabrication of the concrete mixture.

Figure 71. Varying amounts of aggregate size fractions: (A) Concrete fabricated without larger sizes of coarse aggregate.

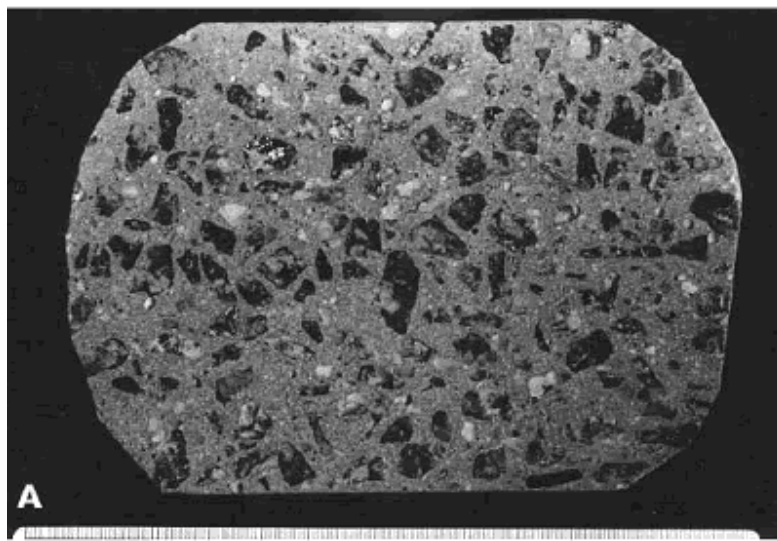
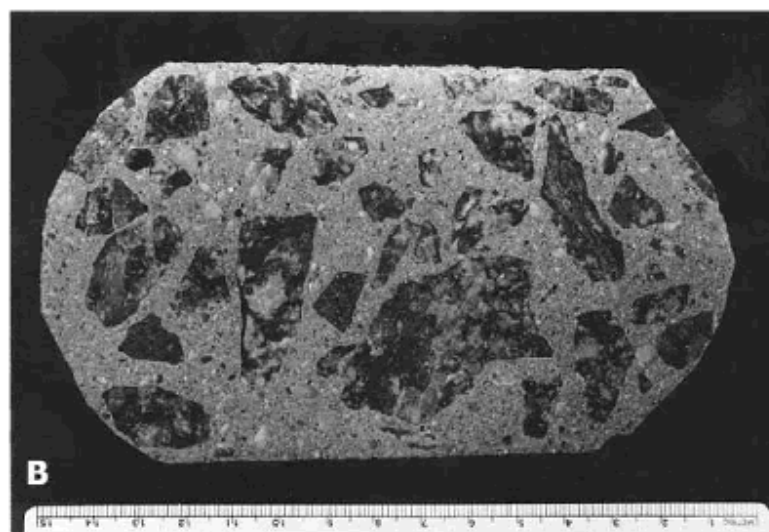


Figure 72. Varying amounts of aggregate size fractions: (B) Concrete fabricated with coarse aggregate that is larger than what is now considered to be normal for bridge deck concrete.



APPENDIX B. CAUSES AND PREVENTION OF PLASTIC SHRINKAGE CRACKING

B.1 CAUSES

Plastic shrinkage cracks occur when the rate of evaporation from the surface of the HCC exceeds the rate of bleeding (see ACI 224R). Bleeding is a process whereby the solids of the HCC, including the cement and other fine particles, settle and water rises to the top. (The process is thought to be a form of syneresis by some.) The bleed water forms a "sheen" on the top of the HCC. When the process proceeds as it should, water is evenly distributed throughout the thickness of the HCC placement. The water sheen on the surface prevents the top portion of the HCC from becoming drier than the bottom portion (i.e., the water on the surface maintains 100-percent humidity throughout the concrete). The condition of 100-percent humidity is required so that there will be sufficient water for the remainder of the hydration to take place and so that the HCC will fill the space appropriately and not shrink.

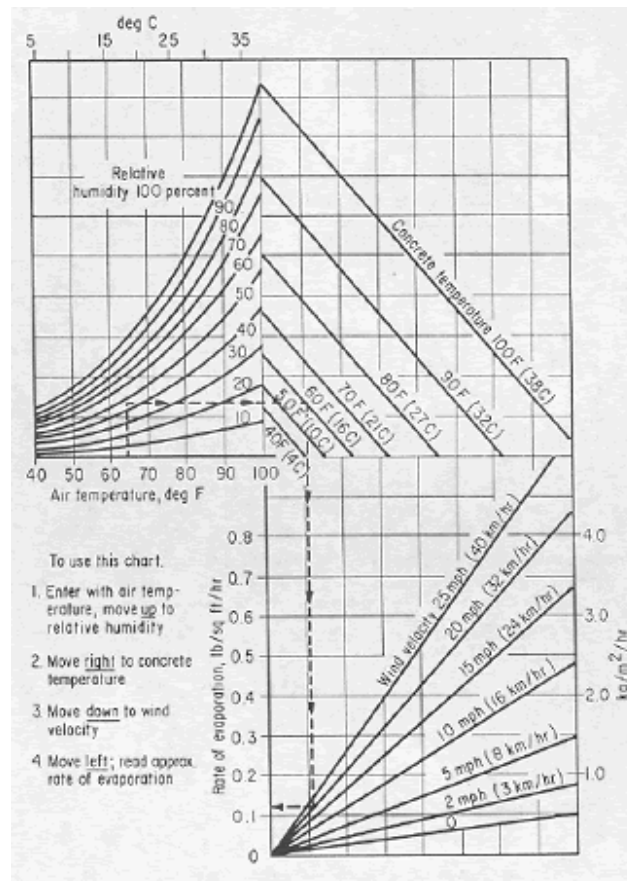
When the proper humidity is not maintained, the top portion of the HCC becomes drier than the lower portions of the HCC, and shrinkage (loss of volume) occurs within the drier portion. When HCC shrinks, it can no longer fill the space it occupies. The lower portion (where there is 100-percent humidity) does not shrink and, therefore, the entire body does not change size. The drier top (the smaller portion) cracks to accommodate the shrinkage, but remains attached to the larger bottom portion.

When plastic shrinkage cracking of any great extent is observed, careful inquiry into the inspector's records and the observations of others who were near the placement will almost always indicate that one or more of the following occurred:

1. The drying conditions were so severe (see figure 205) that the work should have been postponed until more favorable climatic conditions existed.
2. The paving train became so strung out that there was too much time for evaporation between loss of surface water and the finishing and curing operations.
3. Curing was not begun as specified.
4. Curing was not maintained as specified:
 - o Misting was not continued.
 - o The burlap dried.

- Polyethylene, burlap, or both were removed by the wind.

Figure 205. Effect of concrete temperature, air temperature, wind velocity, and relative humidity on the rate of evaporation of surface moisture from a concrete surface.



If the rate of evaporation approaches the danger point for the concrete being used, precautions against plastic shrinkage cracking are necessary (ACI Manual of Concrete Practice (updated yearly)).

B.2 PREVENTION

When finishing is completed and the sheen disappears by evaporation of the surface bleed water, curing procedures must begin promptly. At this point, there is no layer of water to protect the HCC from drying or to maintain the 100-percent humidity within the HCC. If there is a wind blowing, the humidity is low, the ambient temperature is high, or the temperature of the HCC is high, the rate of evaporation will be especially rapid. Promptness is the essence of efficient curing. Figure 204 shows how all of these conditions combine to contribute to the rate of evaporation.

For ordinary bridge deck concrete, the rate of evaporation should not exceed 0.5 kilograms per square meter per hour (kg/m²/h). For latex-modified concrete overlays and other cement

concrete with a w/cm less than 0.40, the maximum evaporation rate must not exceed 0.25 kg/m²/h (Kuhlman, 1991).

The curing procedures must be maintained properly. When climatic conditions are very unfavorable, it may be necessary to raise the humidity by misting the air over the concrete, erecting wind breaks or sunshades, or limiting the placement of HCC to cooler nighttime hours. The moisture must be maintained in the HCC throughout the curing period. It will be necessary to remoisten any curing cover (such as burlap) periodically

B.3 LEGAL INVESTIGATIONS

The client or an adversarial witness in a court proceeding may wish to inquire concerning the following:

1. Was the shrinkage cracking noticed before the finishing operations were completed?
2. Did the finishing procedures tend to hide the cracking (see figure 33)?
3. Did the inspector warn the contractor against proceeding with the placement for any reason, at any time? Why?
4. What corrections in the procedures did the inspector recommend?
5. What were the data concerning concrete temperature, air temperature, humidity, wind velocity, and direction? If the climatological data are not available from the inspector's records, they can usually be obtained from a nearby airport.

REFERENCES

American Concrete Institute. ACI 224R: Control of Cracking in Concrete Structures, *ACI Manual of Concrete Practice: Part 2, Construction Practices and Inspection*. Farmington Hills, MI.

American Concrete Institute. *ACI Manual of Concrete Practice, Volumes 1–5* (revised yearly). Farmington Hills, MI.

Kuhlman, L.A. 1991. "Cracks in LMC Overlays: How Do They Get There?, How Serious Are They?, What to Do About Them?," *Transportation Research Record No. 1301*. Transportation Research Board, Washington, DC, pp. 17–21.

APPENDIX C. RETEMPERING

C.1 OVERVIEW

Retempering is the process of changing the consistency of a concrete mixture by adding water and remixing. As it is common to send the concrete to the placement site with slightly less water than the maximum that may be used, it is expected that a specified amount of water can be added if necessary. The contractor may add the water because the mixture arrives at the site in a condition that would make placement and finishing difficult. These difficult HCCs are often

called *harsh mixtures*. They lack workability. (The only quantitative measure of workability is slump.) (See sections 6.1 and 8.4, Gaynor and Meininger, 1983; Pigeon, Saucier, and Plante, 1990.)

The usual cause of a harsh mixture is sand with a high void content (see appendix D). Sands with a high void content are usually irregular in shape with an abundance of re-entrant angles and internal fractures and voids. Iron-stained clay coatings are common. Other causes of concrete that seems too dry are improper grading (size distribution) of the aggregate and the presence of mud or mud coatings on the aggregate. In addition, a deficiency of fine aggregate or coarse aggregate that is oversized or has a very poor particle shape can create fresh concretes with a difficult texture.

Mixtures with a low w/cm (below 0.45) can be difficult to place unless an effective water reducer is used. A good air-void system or the presence of fly ash as a substitute for part of the cement can help make a mixture with a low w/cm more workable. Apparently the air acts as a fluid and the particles of fly ash are more equant than those of cement and act as ball bearings.

C.2 LIKELY RETEMPERING SCENARIO

Rims of cement on the aggregate and knots of cement in the paste (see section 8.7) suggest that the following typical scenario may have occurred. When the ready-mix truck arrived at the job site, it was quickly noted that the fresh HCC had a rough texture and looked as if it required more water. If the mixture was designed to have a low w/cm, each of the aggregate particles in the mixture was coated with this very adhesive mixture. Such HCC may be very difficult to place unless a sufficient quantity of a water-reducing admixture was used. If the coarse aggregate is oversized or has a poor shape or the sand is present in an insufficient amount, is unusually angular, contains many cracks, or has many re-entrant angles, the mixture will look stiff and difficult to place (harsh mixtures). It is common under such circumstances for water to be added to the mixture to increase the slump and workability. The additional water must not increase the total water above that designed for the mixture lest the concrete become weakened because of the higher w/cm.

C.3 EFFECT OF RETEMPERING

C.3.1 On HCC Paste

When water is added after hydration of the cement has begun and mixing is restarted, it commonly happens (especially in mixtures with a low w/cm) that the water is not distributed throughout the entire mixture, but is mixed only into the larger spaces between the aggregates. The material already adhering to the aggregates remains as a rim of darker material with a low w/cm around the aggregate particles and in the re-entrant angles. Patches of the original paste (unaltered by the additional water) may remain and can be found to be completely surrounded by the paste with a higher water content. The problems of incomplete mixing are akin to the problems encountered in particular cooking situations. With gravy or white sauce, the thickening agent (such as flour) must be completely mixed with the cool water before the flour is affected by heat and begins to hydrate. If the flour and hot water mixture becomes too coherent, it may be

impossible to add more water and create a smooth paste. The added water will mix with only a portion of the paste, and lumps of flour coated with stiff hydrated material will remain no matter how much mixing takes place.

Whenever water is added to the mixture without additional cement being added, the w/cm is raised. The higher the w/cm , the weaker the HCC. When more than the allowable amount of water for a given amount of cement is added to the mixture, the HCC will not have the designed strength. When the rims indicating incomplete mixing are present, a large portion of the cement can be concentrated in the thin bands of very rich paste around the aggregate and in the lumps of the original paste. The remainder of the paste is relatively depleted of cement and is thereby weaker than would be expected from the w/cm calculated from the originally delivered mixture plus the additional water. Thus, it can be seen that areas of HCC with a high w/cm can exist in close proximity to areas with a low w/cm .

It must be remembered that any material is only as strong as its weakest zone. Stress in HCC in service or in a testing apparatus will cause cracking. Cracks will always follow the zones of weakness. In HCCs that have paste areas with different w/cm 's, the cracks are going to develop in the areas of higher w/cm and thus the strength will be dependent on the extent and continuity of those areas.

The skeptic will mention the fact that the bond between the aggregate and the paste in many HCCs is the weakest area and say that the dark rims of high cement content eliminate this problem. Although this is true, the fact that weak bond areas are not as continuous throughout the paste as are the light-colored areas with a high w/cm (low cement content, high water content) obviates the value of rims with a high cement content as bonding agents.

C.3.2 On Air Voids

C.3.2.1 Quantity

Air-entraining agents are more active in the presence of additional water. When retempering has occurred and the mixing has not been completed, petrographic examination will show that many portions of the paste have a much higher void content than does the HCC of the rims and dark patches. Thus, the weakness of the portion with a high w/cm is compounded by the portion containing more than its proportionate share of air voids. In moderate cases, the spacing factor of the air-void system may change very little because the spacing factor is most dependent on the very small voids. Pigeon, et al. (1990), reported that there was little change in the spacing factor in the mixtures they studied if the retempering did not increase the slump by more than 100 mm.

C.3.2.2 Shape

When remixing takes place after some coalescence of the HCC has occurred, the remixing may occur after the individual integrity of some of the small air voids has formed. In such cases, many of these voids will retain their surface area, but lose their original spherical shape and become ovoid, or squashed, or develop an angular shape. Many angular voids may be seen in figure 74.

C.3.2.3 Size

Retempering can cause an increase in the size of air voids, the number of air voids, or both. The size of the voids caused by retempering as evidenced by the microscopical examination shows that the larger voids (more than 1 mm across) nearly all occur within the portion with the higher w/cm. In normal, well-proportioned HCC, the percentage of voids whose diameter expressed on the surface examined exceeds 1 mm should be less than 2 percent of the total concrete.

REFERENCES

- Gaynor, R.D., and Meininger, R.C. 1983. "Evaluating Concrete Sands," *Concrete International*, Volume 5, No. 12, pp. 53–60.
- Pigeon, M.; Saucier, F.; and Plante, P. 1990. "Air-Void Stability: Part IV, Retempering," *ACI Materials Journal*, Volume 87, No. 3, pp. 252-259.

New Automated Concrete Evaluation Will Save Time and Money

Business Issue

Knowledge of the air-void structure in hardened concrete is a valuable tool toward predicting concrete durability and performance. However, current manual methods following ASTM standard C457-90 are extremely time-consuming, tedious and require highly skilled and experienced personnel. Variability of testing results from human subjectivity and other factors also are a concern. Despite these concerns, many DOTs, including MoDOT, continue to depend upon ASTM C457 using a human operator for evaluating the air-void system in hardened concrete. This data is used to make decisions, which may have significant physical and financial impact, both short and long term. An automated system designed to provide reliable ASTM C457 results would save both time and effort while also improving the overall consistency and repeatability of the evaluation process.

Background

Since 1998, the Missouri Department of Transportation (MoDOT) has collaborated with the National Nuclear Security Administration-Kansas City Plant (NNSA-KCP), a government contractor for the U.S. Department of Energy, to develop a fully automated system capable of reliably analyzing hardened concrete in accordance with ASTM C457 using the linear traverse method. This effort was accomplished in early 2005 resulting in a prototype system specifically designed to analyze a sample of hardened concrete in accordance with ASTM C457's linear traverse method. This system, called ACE for Automated Concrete Evaluation, includes both hardware components for image acquisition and customized software for image analysis and component identification.

The ACE system (shown in Figure 1) uses a high precision, two-dimensional computer-controlled stage to move the concrete sample under a research grade microscope. The image acquisition system consists of a digital color CCD camera, a fire wire digital image acquisition interface, and a 3.2 GHz tower PC. Customized image processing and pattern recognition software has been developed to identify air voids and extract void characteristics. Currently, the system is capable of identifying air voids as small as 5 microns in size.

Extracted concrete component characteristics are used to calculate the concrete microscopical properties of interest in accordance with ASTM C457. All system components are linked via a graphical user interface, which aids the operator in the data acquisition, image analysis, and reporting processes (Figure 2).

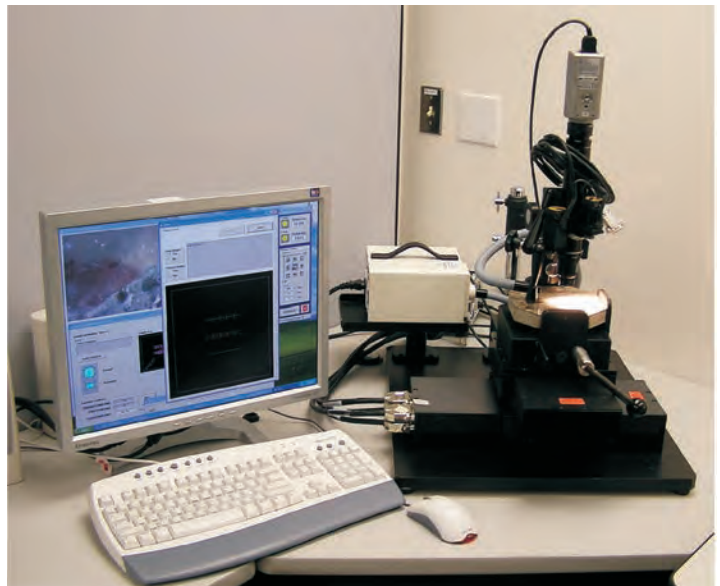


Figure 1. Prototype ACE system for concrete evaluation.

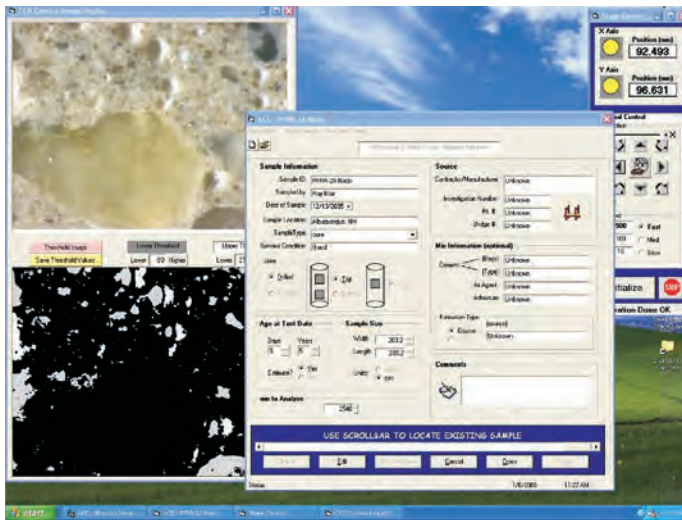


Figure 2. Graphical user interface for sample scanning and image.

The ACE system is designed to automatically scan and acquire imagery of a concrete sample. The acquired imagery is then stored on the analysis computer and may be written to a DVD. This latter option allows the acquired imagery to be transferred to another computer for automated analysis. In this way, a single computer workstation may be dedicated to the sample scanning and image acquisition process, while previously acquired imagery can be transferred to and processed on any other available computer.

Approach

The potential of the prototype system prompted MoDOT in 2002 to take the lead on a national pooled fund effort with several other states to further advance and complete the development of the ACE system with the NNSA-KCP. In addition to funds contributed by Missouri and NNSA-KCP, 12 states have contributed and participated in the pooled fund effort. These states include Arkansas, California, Colorado, Illinois, Indiana, Iowa, Minnesota, Montana, Nebraska, Ohio, Virginia, and Wisconsin. The pooled fund study not only helped secure the project financially, but also provided an opportunity to draw on the experience and knowledge of others with the ASTM C457 test method. In addition, it enabled a much broader range of concrete samples (e.g. various aggregate types, paste characteristics, air-void systems) upon which the ACE system could be improved and validated.

A key component of this pooled fund effort was the execution of a two-phase round robin study¹ among nine laboratories (ten in phase 2) to estimate the variability of the ASTM C457 linear traverse method when applied manually. Sources of known variability associated with the linear traverse include: specimen preparation effects, operator experience and ability, equipment (magnification, method of viewing, lighting), and inherent statistical variability of the method itself. Assessing the variability of the linear traverse test method would then provide a benchmark for performance of the ACE system.

The round robin testing used five concrete specimens that were obtained from different locations around the country. In each phase, the participating labs performed a total of nine linear traverse tests – one linear traverse on four of the specimens, and five linear traverses, using five different sets of traverse lines, on the fifth specimen. All tests were to be run at 100X magnification on the participating lab's equipment. For phase 1, the concrete specimens were prepared by the lab supplying the specimen, using the lab's standard equipment and procedure. For phase 2, the five concrete specimens were collected and the surfaces were prepared again but by one lab. Air void system parameters evaluated for variability in the study included air content, voids per inch, spacing factor, and specific surface.

Findings of the round robin study indicated that wide variations exist in the between-laboratory results derived from the manual application of the ASTM C457-90 standard. This result strongly supports the development of an automated image analysis system for performing ASTM C457 measurements. For the purpose of comparing the round robin results with those derived from the automated ACE results, a smaller subset of the manually derived laboratory results was identified using the results from five of the laboratories that demonstrated the most consistency in their measurements.

Assessment of ACE Performance Relative to the Round Robin Testing Results

As a way of assessing the performance of the ACE system, the Phase 2 round robin samples, PFRR-1 through PFRR-5, were analyzed by the ACE system. These results were then compared directly to the results derived from manual evaluations of these samples as part of the round robin testing. Further, sample PFRR-2 was analyzed multiple times in order to assess the repeatability of the ACE system. The results are described below.

Repeatability of the ACE System

To evaluate the repeatability of the ACE system, round robin sample PFRR-2 was analyzed five times, with the sample rotated 90 degrees between analysis runs, generating results for each of the four rotations (Sides A, B, C, and D). For the fifth analysis run, Side A was again ran, but a different set of analysis lines were selected (Side A1).

The analysis results are shown in Table 1 where the mean value of the measured parameters are shown, along with either the standard deviation or the coefficient of variation of each of the parameters across the five analysis runs. Also shown in the table are the repeatability results derived from the round robin testing. As can be seen, the repeatability of the ACE analysis results compare favorably to those derived manually.

Accuracy of the ACE System

The accuracy of the ACE system is determined through a comparison of the ACE-derived results with those derived manually in the round robin study. Given that the true air-void parameters

¹ Simon, Marcia J., (2005). An Interlab Evaluation of the Variability in the ASTM C 457 Linear Traverse Method. Report. OR6-009, Missouri Department of Transportation, Jefferson City, MO, USA

ACE Repeatability Test Results --- PFRR-2, Phase 2				
Sample PFRR-2	% Air	Voids per inch	Spacing Factor	Specific Surface
Side A	5.7	17.85	0.0036	1260
Side B	6.035	18.82	0.00344	1247.2
Side C	6.165	16.6	0.00376	1076.5
Side D	6.41	19.32	0.0033	1207
Side A1	5.74	17.8	0.0036	1238
Mean	6.01	18.08	0.0035	1205.74
SD	0.30	1.05	0.00018	74.85
CV (%)	4.95	5.81	4.96	6.21
Round Robin Repeatability Test Results --- PFRR-2, Phase 2				
Over All Labs	% Air	Voids per inch	Spacing Factor	Specific Surface
Pooled SD	0.35			
Pooled CV (%)		6.20	5.60	5.90

Table 1. Repeatability of ACE evaluation process as assessed for PFRR-2.

for each of the samples is unknown, the 95% confidence interval for each parameter, as computed from the manual round robin results, was used as a comparison metric. In order to succinctly present this comparison data, each of the measured air-void parameters (ACE and round robin) was scaled to the manually derived 95% confidence interval, resulting in a scaled value of between 0.0 (lower limit of the interval) and 1.0 (upper limit of the interval). Hence, a scaled value of 0.50 means the particular air void parameter fell in the center of the 95% confidence interval (i.e., at the mean measured for the parameter). Any value less than 0.0, or greater than 1.0, would be considered to fall outside the 95% confidence interval.

Variance Relative to the Round Robin Results (5 lab) 95% Confidence Interval

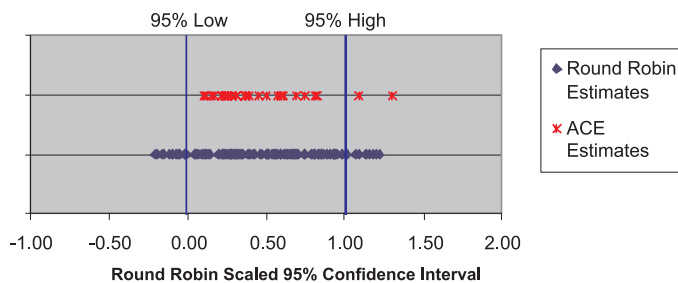


Figure 3.

This comparison is shown in Figure 3 where the ranges of the ACE derived and manually derived air-void parameters (25 per each data source) are shown relative to the 95% confidence interval. As can be seen from the figure, the manually derived results from the round robin testing do display some variability across the samples. The ACE derived results also demonstrate a similar variability, but compare favorably with the manually derived results.

Overall Agreement

The ultimate goal of any manual or automated process that implements ASTM C457-90 is to assess the overall quality of the measured sample, and to determine if the sample meets standards or does not. Overall agreement between the ACE system and manual operators is established if the overall “accept vs.

reject” decision provided by the ACE agrees with the decision provided by a manual operator. For comparison purposes, the spacing factor and specific surface parameters were used to compare automated decision to manual decisions. Industry accepted limits for these two parameters are that the spacing factor for a sample be less than .008 in. and the specific surface be greater than 600 in.⁻¹ Figures 4 and 5 show comparisons of the ACE-derived values and the manually-derived values for these two parameters. These figures show that, at least for the five round robin samples analyzed in this study, the ACE system provides measurements of these two parameters, which are in agreement with the manually derived results. Further, these figures also show that ACE, again for at least the five round robin samples used in this study, never rejects a sample that manual results indicate should be accepted (Type I testing error), nor does the ACE accept samples that manual results indicate should be rejected (Type II testing error). As such, the automated system provides “accept vs. reject” decisions which are identical to those provided by manual analysis.

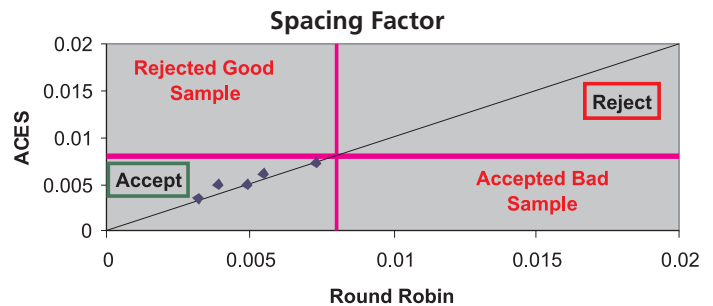


Figure 4.

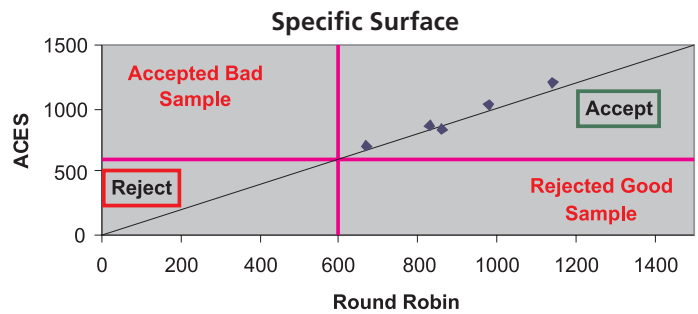


Figure 5.

Findings and Conclusions

The results of this study provide a number of findings and conclusions as detailed below:

- Given the variability, which is recognized to exist in manually derived ASTM C457 linear traverse results, the ACE-derived results fall reasonably well within this variability and are comparable to the round robin manually derived ASTM C457 results.

- The ACE image acquisition and analysis process requires 7-8 hours of computer time, but only 10 – 20 minutes for the operator to mount the sample and set all scan parameters. As such, a major savings in labor time is realized through the use of the ACE system.

- While the ACE scanning and image acquisition processes require a dedicated computer, the analysis of the archived imagery can be performed on any computer.
- Results of this study indicate that the repeatability, accuracy, and overall assessment quality of the ACE system in conducting the ASTM C457 linear traverse method are comparable to results obtained by manually (human-based) conducting ASTM C457 linear traverse method.

For More Information

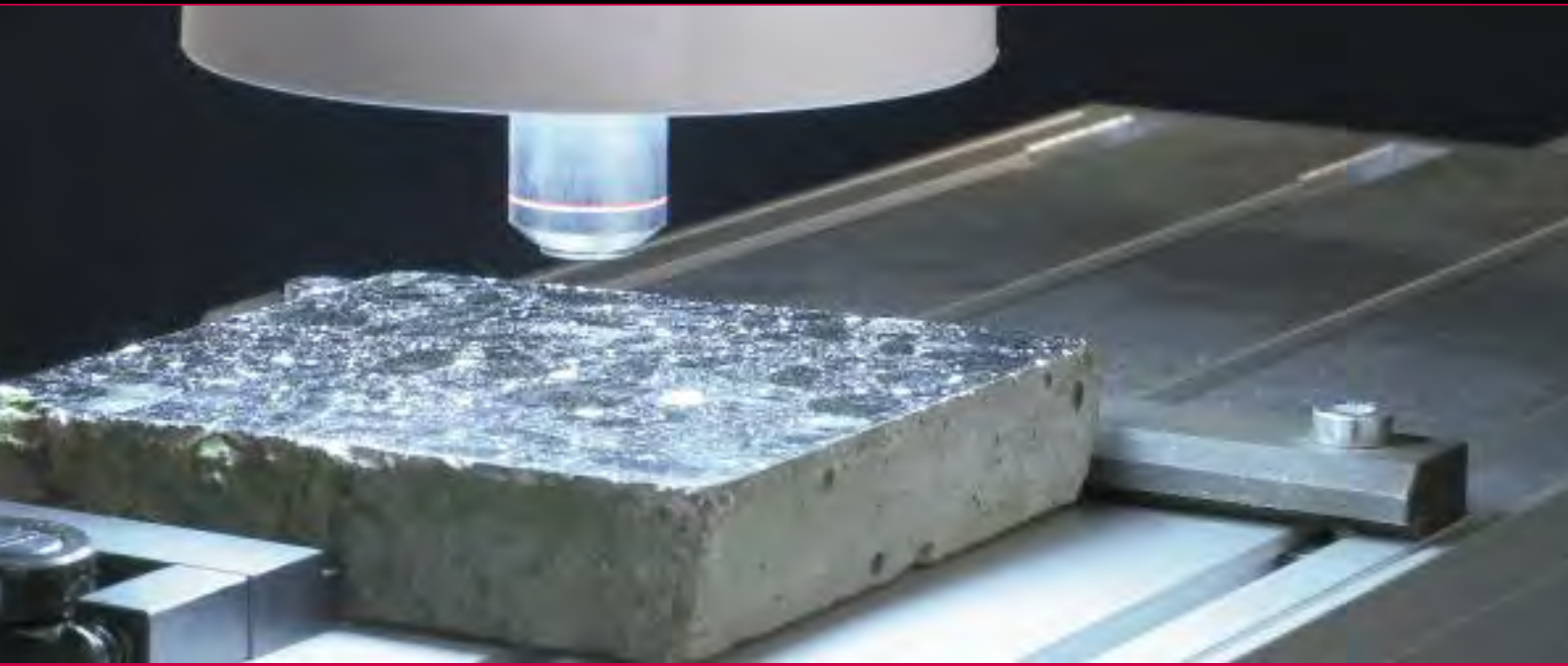
Patty Lemongelli, P.E.
Missouri Department of Transportation
(573) 526-4328
patricia.lemongelli@modot.mo.gov

Chris Baumgart, Ph.D.
National Nuclear Security Administration / Kansas City
Plant
(505) 844-2585
cbaumgart@nnsa.doe.gov



Missouri Department of Transportation
Organizational Results
P.O. Box 270
Jefferson City, MO 65102

573.751.3002
1 888 ASK MODOT
rdtcomments@modot.mo.gov
www.modot.org/services/rdt



RapidAir 457

Air void analyzer

AUTOMATIC TEST OF AIR VOID DISTRIBUTION
IN HARDENED CONCRETE IN LESS
THAN 15 MINUTES IN YOUR LABORATORY

- Increased productivity
- Operator independent
- Excellent repeatability
- Excellent reproducibility
- Good accuracy

RapidAir 457

Air void analyzer

AUTOMATIC TEST OF AIR VOID DISTRIBUTION
IN HARDENED CONCRETE IN LESS
THAN 15 MINUTES IN YOUR LABORATORY

The RapidAir 457 equipment provides an automatic system for analyzing the air content in hardened concrete. The analysis time with the RapidAir 457 system is less than 15 minutes, which should be compared to the 4-6 hours normally required for manual analysis with conventional types of equipment.

The system can replace the manual test performed as described in the ASTM designation C 457-98 "Standard Test Method for Microscopical Determination of Parameters of the Air-Void System in Hardened Concrete" or the test performed according to EN 480-11 "Determination of air void characteristics in hardened concrete". Both methods include specifications for grinding, and polishing a plane section of concrete, and for measuring the air void distribution with the use of a microscope according to the linear traverse method.

Advantages

- Increased productivity
- Operator independent
- Excellent repeatability
- Excellent reproducibility
- Good accuracy

Hardware and Software

The RapidAir 457 test equipment consists of an automatic analysis system comprising a computerized control unit (PC) with a 19" color monitor, a video camera, a microscope objective mounted on a moving stage, and a user friendly analysis software operating in a MS-Windows environment. The RapidAir 457 system has a resolution better than 2.5 microns, and is delivered pre-configured,

aligned, tested, and ready for Plug-and-play use. The user-interface comprises an "Analysis Wizard" allowing the daily operations to be handled in an easy and logical fashion that minimizes the risk of analysis or reporting errors.

Sample Preparation

Following the traditional grinding and polishing steps of ASTM C 457, a contrast enhancing technique (described in EN 480-11) is used to obtain a plane section surface where the air voids appear bright white, and the remaining surface appears black. Such a surface contrast facilitates maximum precision, and identification of all air voids present in the concrete sample. The time needed to perform a contrast enhancement is approximately 30 minutes. Since all preparation defects are addressed during the preparation procedure, the advantage of the contrast enhancement is that it eliminates the need for a "split second" human judgment, which is typically encountered during the normal manual type analysis.

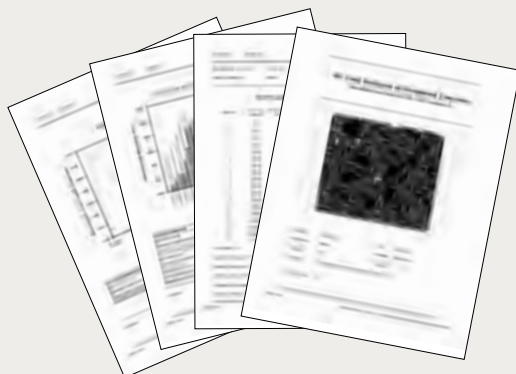
Analysis

Following contrast enhancement, the plane section is mounted onto the

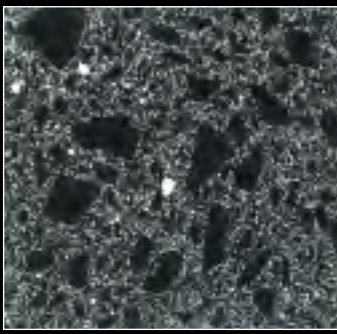
moving stage that is positioned under the video camera. The analysis control unit now automatically moves the stage, and the air void distribution is determined from a typical scan of 1364 areas throughout the plane section (1364 areas provide a 2413 mm line of traverse as is required by ASTM C 457 for concrete with a 1" maximum size aggregate).

Report Generation

After scanning the plane section, a report file (in MS-Excel format) is automatically saved. The operator can choose between compliant calculations according to ASTM C 457 and EN 480, between using SI and US units, and between letter size and A4 paper formats. In addition to the calculated air void parameters notably air content, specific surface area, and spacing factor, the report file also contains tabular as well as graphical presentations of the results of the air void analysis. The report file also contains a worksheet with the raw data in case the operator would like to perform additional user-specific calculations. At any time following the analysis, the report file can be printed or viewed from within the RapidAir software user-interface using the "Analysis Wizard".



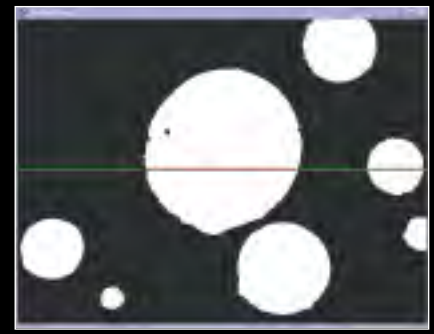
Example of the four page ASTM C457 report with a picture of the analyzed plane section (optional) on the front page.



Black and white contrast enhanced surface ready for air void analysis. In the final step of the contrast enhancement, any defects in the concrete, and any voids in the aggregate have been blackened to reduce any potential error.

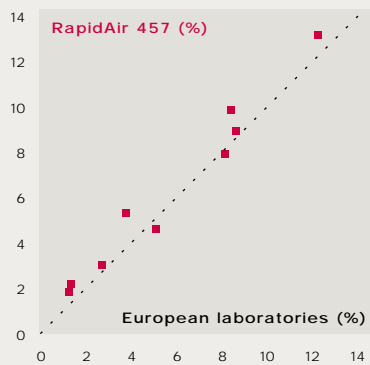


The MS-Windows based user-interface of the RapidAir 457 software with a live image, a binary image, a window (top left) for threshold setting, and for positioning of the stage, and the Analysis Wizard window (top right) for configuring the individual analysis.

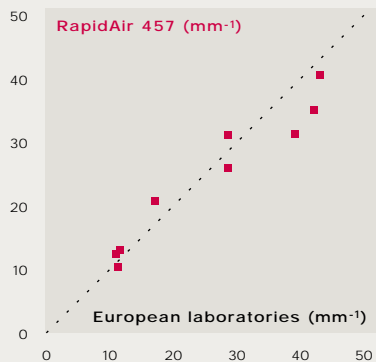


Close-up of the binary image with the analysis in progress. Where the green line of traverse intersects an air void, it turns red – here two chords are recorded. The field of view is 1.82 x 1.35 mm, i.e. with 768 x 576 pixels the resolution is better than 2.5 microns.

Air content



Specific surface area



Air content, and specific surface area of the same nine concretes were measured by RapidAir 457, and by thirteen European laboratories. The values presented from RapidAir 457 are the average of four measurements where the sample was rotated 90 degrees between the measurements, and the values of the European laboratories are the average of thirteen measurements, i.e. one from each laboratory. The values of the thirteen European laboratories were reported in the paper: "Automated air void analysis on hardened concrete: Results of a European intercomparison testing program" by Dr. Jan Elsen in Cement and Concrete Research, 31, pp. 1027-1031, 2001.

Repeatability of RapidAir 457 analysis

Sample ID	Analysis no.	Air content (%)	Specific surface area (mm ⁻¹)	Spacing factor (mm)
1	1	2.94	42.87	0.14
	2	3.34	39.29	0.14
	3	3.13	42.49	0.14
	4	2.74	45.48	0.14
2	1	5.28	37.74	0.12
	2	5.44	36.26	0.13
	3	5.22	39.77	0.12
	4	5.29	38.63	0.12
3	1	12.93	33.24	0.06
	2	13.53	34.84	0.06
	3	12.99	36.32	0.06
	4	13.25	36.05	0.06
4	1	2.20	17.18	0.40
	2	2.06	20.06	0.35
	3	2.25	18.00	0.38
	4	2.25	18.14	0.38
5	1	10.04	30.71	0.09
	2	9.81	31.26	0.09
	3	9.63	30.94	0.09
	4	10.01	30.05	0.09
6	1	5.17	33.15	0.14
	2	4.84	33.31	0.14
	3	3.93	36.74	0.14
	4	4.49	36.41	0.14
7	1	8.20	18.96	0.15
	2	7.46	21.83	0.15
	3	8.30	20.19	0.14
	4	7.63	20.98	0.15
8	1	8.79	26.06	0.11
	2	9.92	25.53	0.10
	3	8.85	28.05	0.10
	4	8.11	26.94	0.11
9	1	1.92	18.07	0.41
	2	1.82	19.21	0.39
	3	2.08	20.01	0.36
	4	1.58	22.52	0.36
Standard deviation		0.37	1.58	0.011

Air void parameters of nine different concrete samples measured by RapidAir 457, and the corresponding estimated standard deviations. Each sample was measured four times at identical settings, and between each measurement the sample was rotated 90 degrees.



RapidAir 457

Air void analyzer

Training Course

With the purchase of a RapidAir 457 system, Concrete Experts International will provide free of charge (travel and accommodation not included) a one-day training course in performing air void analysis at our facilities. For a longer course or a seminar at the client's office, arrangements can be made. Please contact Concrete Experts International for details.

**Concrete Experts
International ApS**

Annekegade 1
DK-2100 Copenhagen Ø
Denmark

Tel +45 / 3916 1660

Fax +45 / 3916 1760

info@concrete-experts.com

www.concrete-experts.com

Concrete Property Test

Air Entrainment 3-4: Air Content (Hardened Concrete)

Purpose – Why Do This Test?

Another method of determining the quality of an air-void system in concrete is microscopical analysis of hardened concrete. This method provides information on the total air content, as well as the spacing factor and other parameters.

Principle – What is the Theory?

The air-void structure of concrete can be measured and characterized by examining a section of a core with a microscope. The linear traverse method consists of measuring the air voids as a polished concrete sample travels under a microscope in regularly spaced lines. The length of travel across air voids is compared to the length of travel across paste and aggregate, and the data are used to calculate the air content, spacing factor, and specific surface of the air voids in the concrete sample.

Test Procedure – How is the Test Run?

The manual method is described in ASTM C 457. A core from the slab is sectioned and polished. The apparatus is used to move a core sample under a microscope (or vice versa) in straight lines. The total length traversed and the length traversed across air voids are recorded.

Alternate automated methods use computer hardware and software to analyze an image of a polished concrete sample. These image analysis methods produce similar results for entrained air properties of concrete.

Test Apparatus (figure 1)

- Saw for cutting a section of a core.
- Polishing tools for grinding, lapping, and preparing the core section.
- Hardware and software for measuring air voids in the core section.

Generic Automated Test Method – Refer to ASTM C 457 for Comprehensive Guidance or Manufacturer's Recommendations for Specific Image Analysis Techniques

1. Obtain a core from the pavement.
2. Cut a section of the core.
3. Grind, lap, and polish the core section until it is smooth and flat.
4. Cover the polished face of the core section with black ink from a stamp pad.
5. Heat the core to 54°C (130°F) and coat the ink-covered core section with a zinc paste.
6. Allow the core section to cool, and scrape the zinc paste off the surface. The melted zinc paste will remain in the

[continued on next page](#)

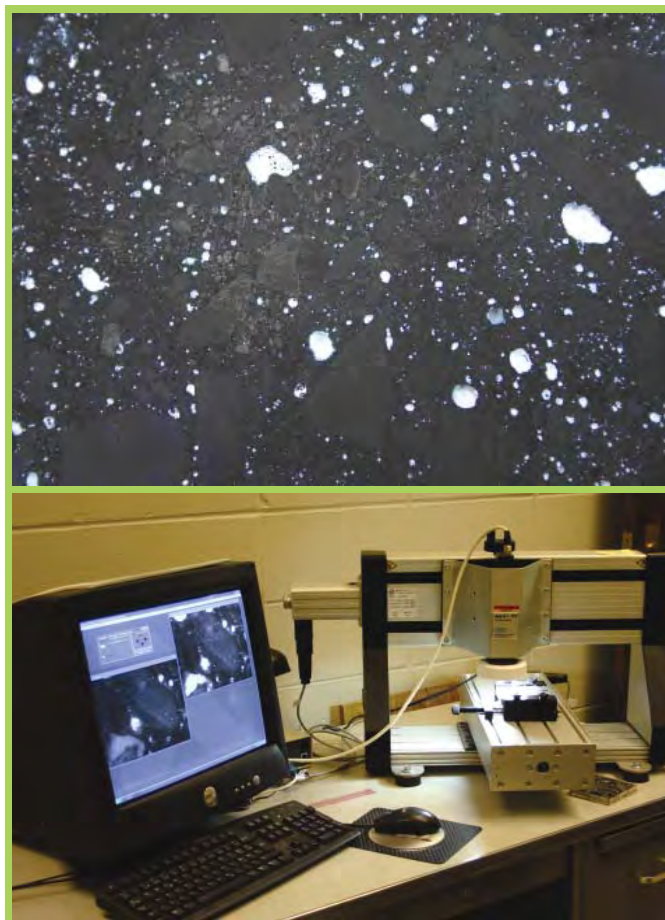


Figure 1. Close-up of a concrete core section prepared for testing and rapid-air test equipment

- air voids of the surface, providing a white contrast to the black ink surface of the core section.
- 7. Mount the prepared core section in the image analysis apparatus.
 - 8. Start the image analysis apparatus.
 - 9. The image analysis hardware and software automatically traverse the section and record the data.

Output – How Do I Interpret the Results?

The software produces a tabular report showing air content, spacing factor, and specific surface area of the air voids (table 1). A digital image of the core section can also be viewed or printed.

The air content is expressed as a percent of volume of the concrete sample.

Spacing factor is the average distance from any point to the nearest air void, or the maximum length measured from the cement paste to the edge of an air void.

Specific surface area is the surface area of the air voids divided by the air voids’ volume.

Construction Issues – What Should I Look For?

Spacing factors should be less than 0.2 mm (0.008 in.).

Air-void spacing can be impacted by many factors, ranging from cement and admixture chemistry to mixing time to aggregate grading.

Table 1. Example Hardened Air Test Results

Air-void parameter	Chords < 0.0197 inch	Chords < 0.0394 inch	All chords
Number of voids	2683	2752	2770
Percent of total number of voids	96.9	99.4	100
Length of air traversed (in.)	11.01	12.85	14.00
Percent of total length of air traversed	78.7	91.8	100
Air content (%)	11.59	13.52	14.73
Average chord length (in.)	0.0041	0.0047	0.0051
Paste to air ratio	2.07	1.77	1.63
Specific surface (in ⁻¹)	974.8	856.8	791.6
Void frequency (in ⁻¹)	28.24	28.97	29.16
Spacing factor (in.)	0.0021	0.0021	0.0021

Purpose

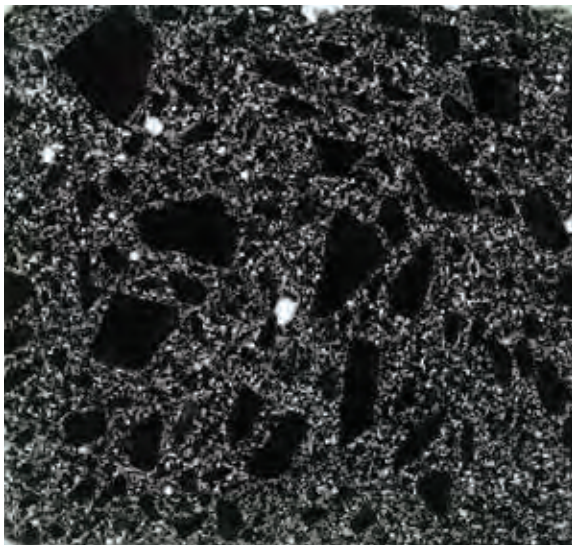
RapidAir is an image analysis system for automatic determination of the air content in hardened concrete according to the linear traverse method in ASTM C457: "Test Method for Microscopical Determination of Parameters of the Air-Void System in Hardened Concrete."

The measured parameters of the air-void structure are total air content, spacing factor, and specific surface.

Principle

A core is taken from the structure, sliced, ground, and lapped in the laboratory. The resulting surface is plane, smooth, and with sharp edges along the perimeter of air voids. Before final specimen preparation, the lapping quality is checked under a stereomicroscope.

The lapped surface is colored black with a hard stamp pad containing black ink. After heating the specimen to 55 °C, a white zinc paste is applied to the surface with a rubber spatula. The zinc paste melts on the surface and flows into the voids.



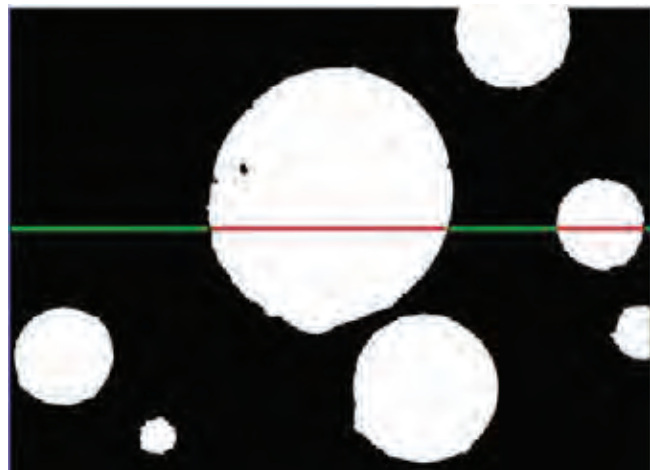
After cooling to room temperature, excess paste is removed from the surface with a straight, sharp steel blade. The quality of the black-white contrast is checked under a stereomicroscope. The voids should be totally filled with white paste and no white regions should be visible on the surface. Finally, voids in aggregates and obvious cracks are colored black under the stereomicroscope using a black marking pen. The photo on the left shows a properly prepared specimen.

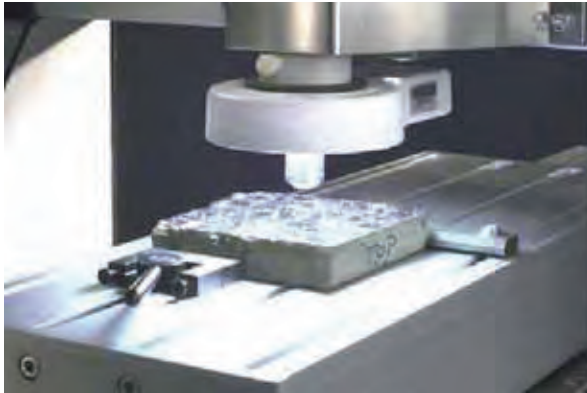
The preparation of a well-lapped specimen surface for analysis takes about 30 minutes. The **RapidAir** measurement is done automatically in less than 17 minutes. This should be compared with a time of 4 to 6 hours normally required for manual analysis using a light microscope in accordance with ASTM C457.

Following contrast enhancement, the prepared specimen is mounted on a moving X-Y-Z stage positioned below a video camera.

The **RapidAir** control unit automatically moves the stage, and the software determines the portion of the total traverse length that passes through the white air voids, as shown in the magnified view to the right. After the scan is completed, the air-void parameters are determined in accordance with ASTM C457.

The specimen scan is saved automatically in a report file documenting the air content, spacing factor, and specific surface. In addition, graphical presentation of the air-void distribution and the raw data are available.





Prepared specimen positioned on the moveable stage ready for image analysis.

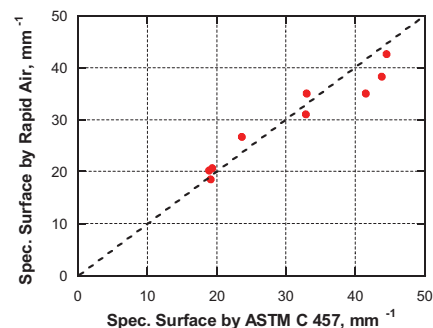
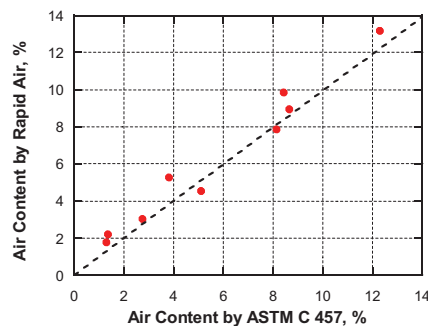


Overall view of **RapidAir** system in operation.

Correlation with ASTM C457 and Precision

As reported in Pade, C., Jakobsen, U.H. and Elsen, J., "A New Automatic Analysis System for Analyzing the Air Void System in Hardened Concrete," *International Cement Microscopy Association Conference*, San Diego, CA, USA, April 2002, very good agreement was found between the air-void system parameters measured by the **RapidAir** system and by the ASTM C 457 standard method. The study involved thirteen European laboratories. The standard deviations of the air-void parameters determined by **RapidAir** were as follows:

- Air content: 0.37 %
- Specific surface: 1.57 mm⁻¹
- Spacing factor: 0.011 mm



Comparison between **RapidAir** and ASTM C457 determinations of air content and specific surface

RapidAir Ordering Number

The **RapidAir-3000** system shown to the right comes as a complete system, ready to plug in and operate, including PC with software, control unit, and manual.

A one day course is offered separately by a **RapidAir** specialist.



GERMANN INSTRUMENTS A/S

Emdrupvej 102, DK-2400 Copenhagen, Denmark

Phone: +45 39 67 71 17, Fax +45 39 67 31 67

E-mail: germann-eu@germann.org Web site: www.germann.org



GERMANN INSTRUMENTS, Inc.

8845 Forest View Road, Evanston, Illinois 60203, USA

Phone: (847) 329-9999, Fax: (847) 329-8888

E-mail: germann@germann.org Web Site: www.germann.org



Test smart - Build right

APPENDIX C

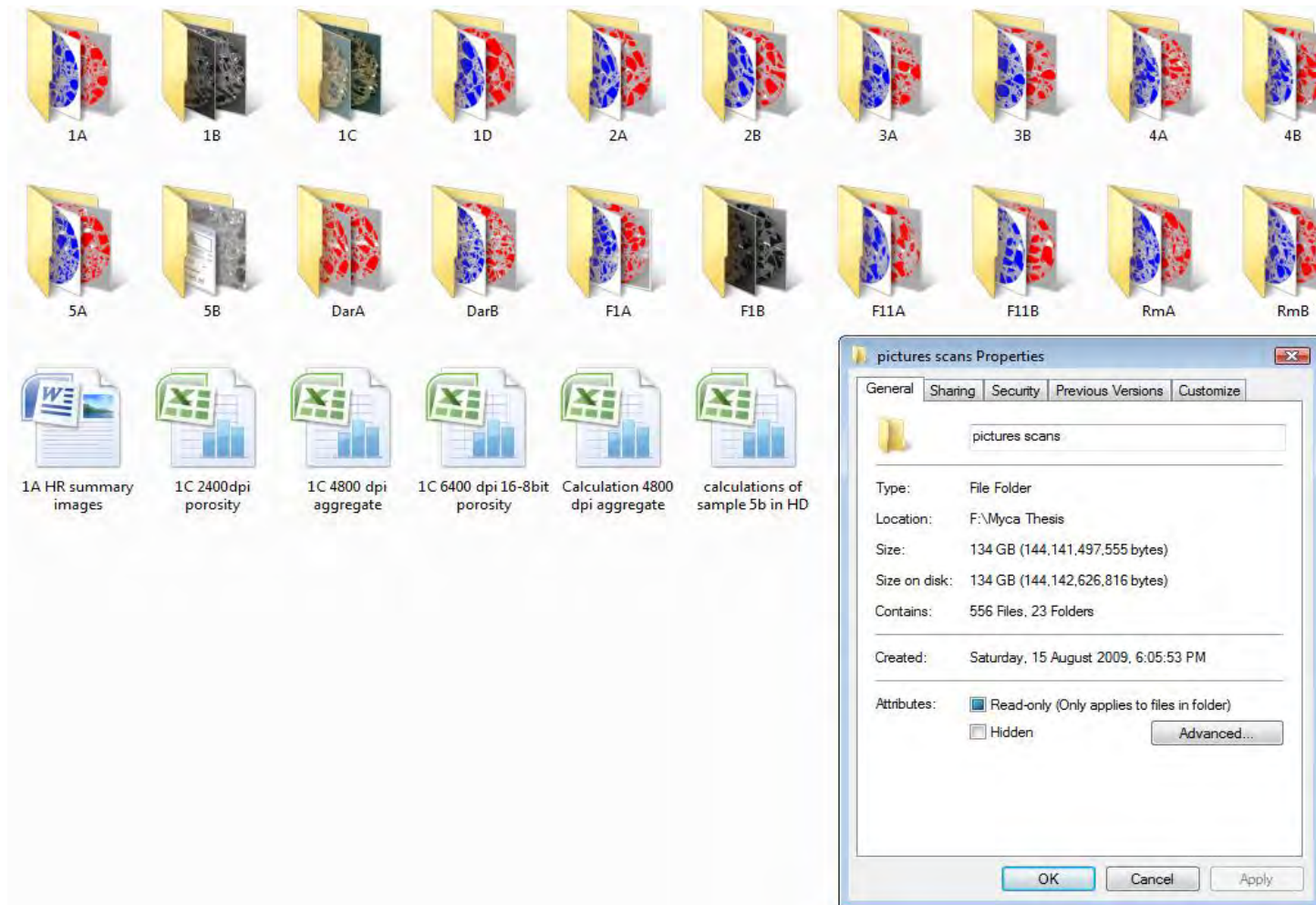
The following pages contain screen dumps of Digital Images folders on my PC.

1. 72 ppi
2. 2400 ppi
3. 4800 and 6400 ppi
4. Pages of individual folders from Sample 1A to Sample FIIB

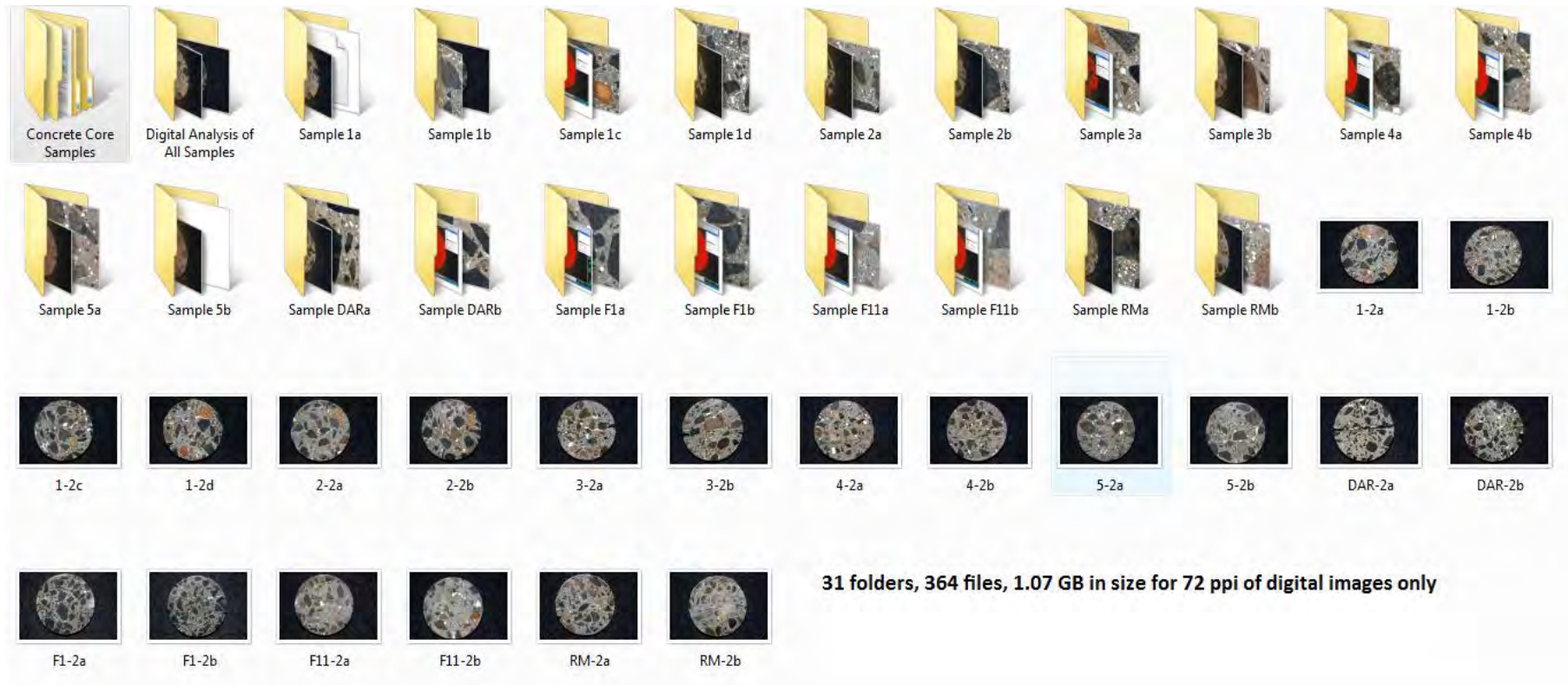
All proprietary documentation will be kept on seven (7) 25 GB Blu-ray Discs (~ 2 TB analysis and image data) in the office of Professor Chris Sorrell, School of Materials Science and Engineering of UNSW, Kensington, Sydney.

199 files, 17.3 GB in size for 2400 ppi folder of digital images only

4800 ppi and 6400 ppi Digital Images Only Folders

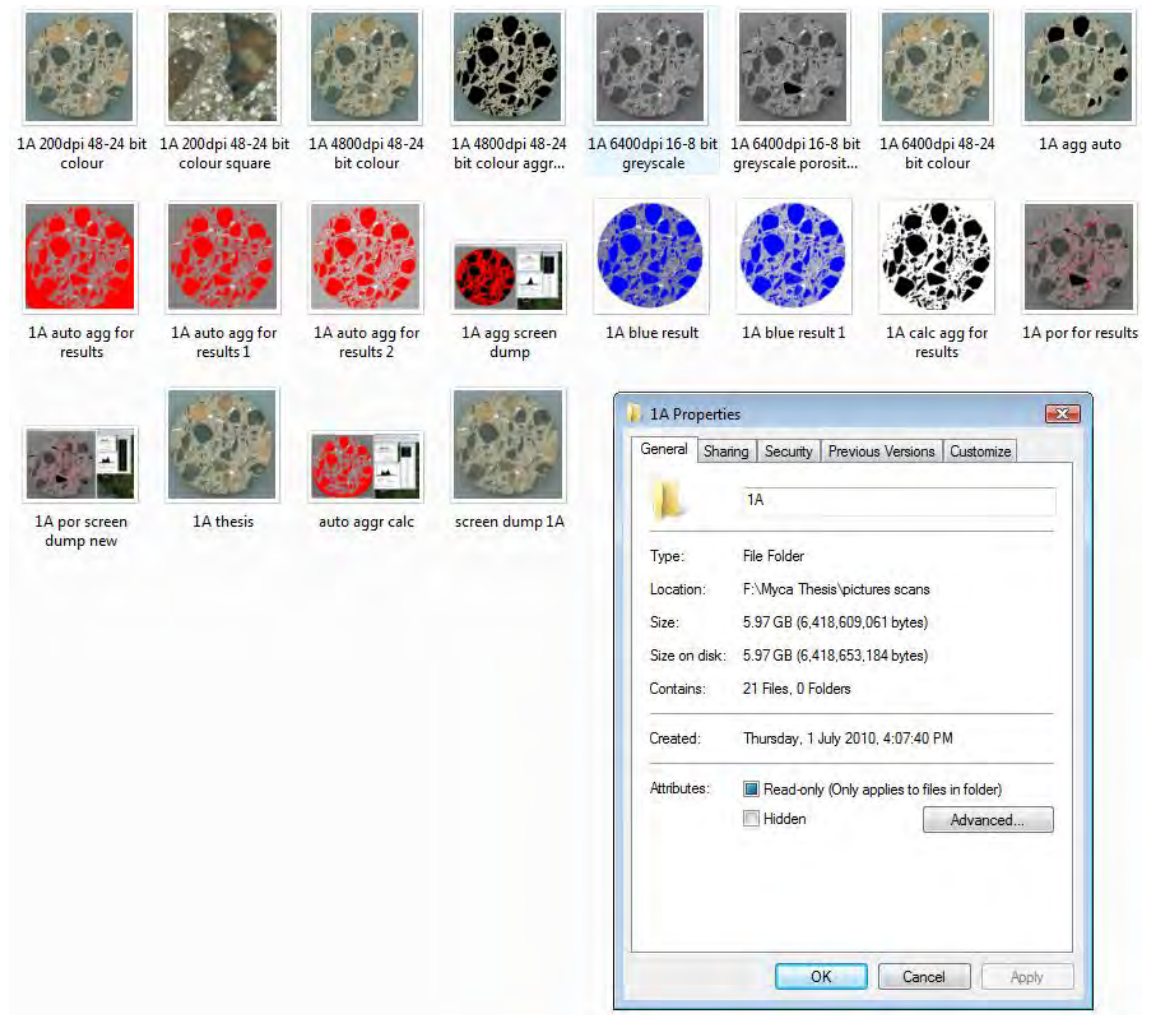


72 ppi Digital Images Only Folders

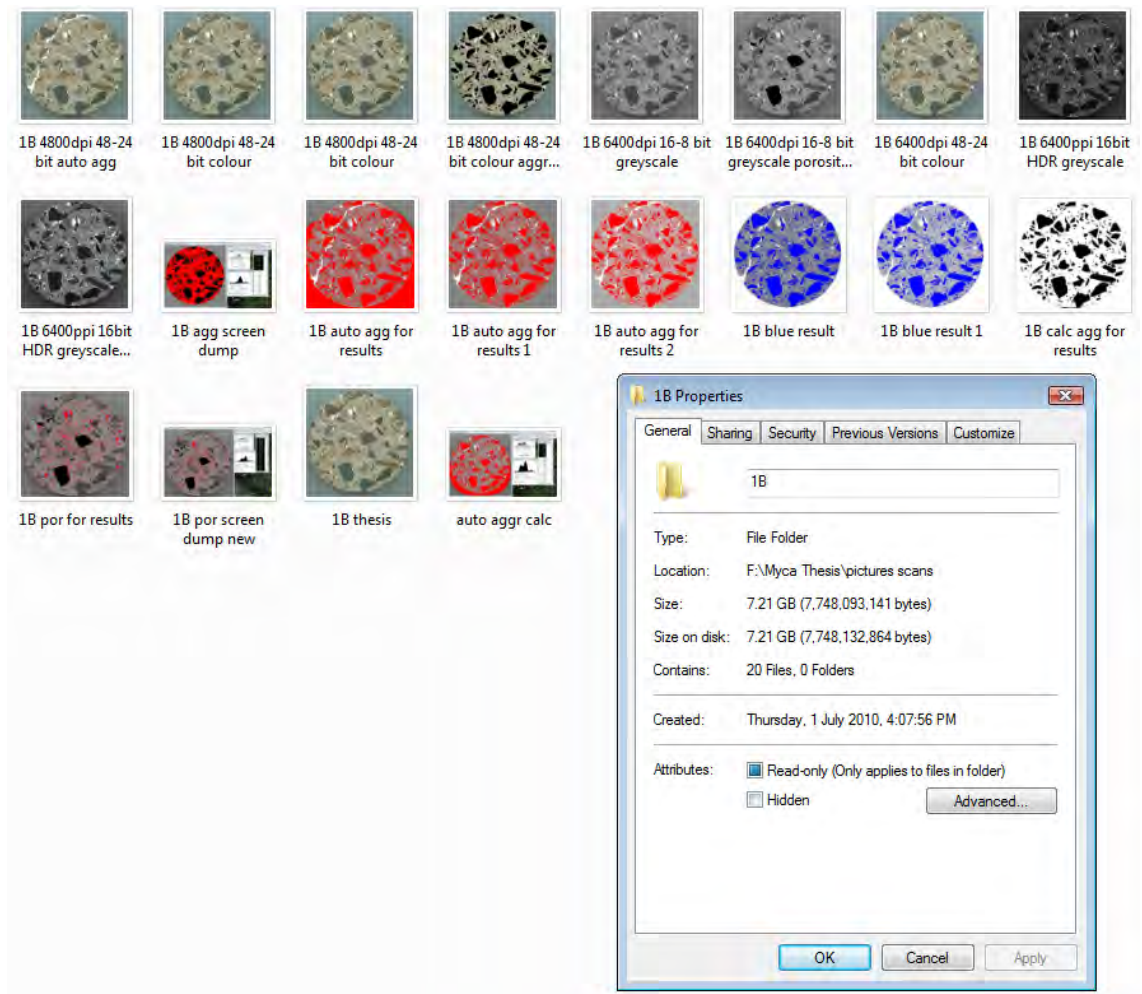


31 folders, 364 files, 1.07 GB in size for 72 ppi of digital images only

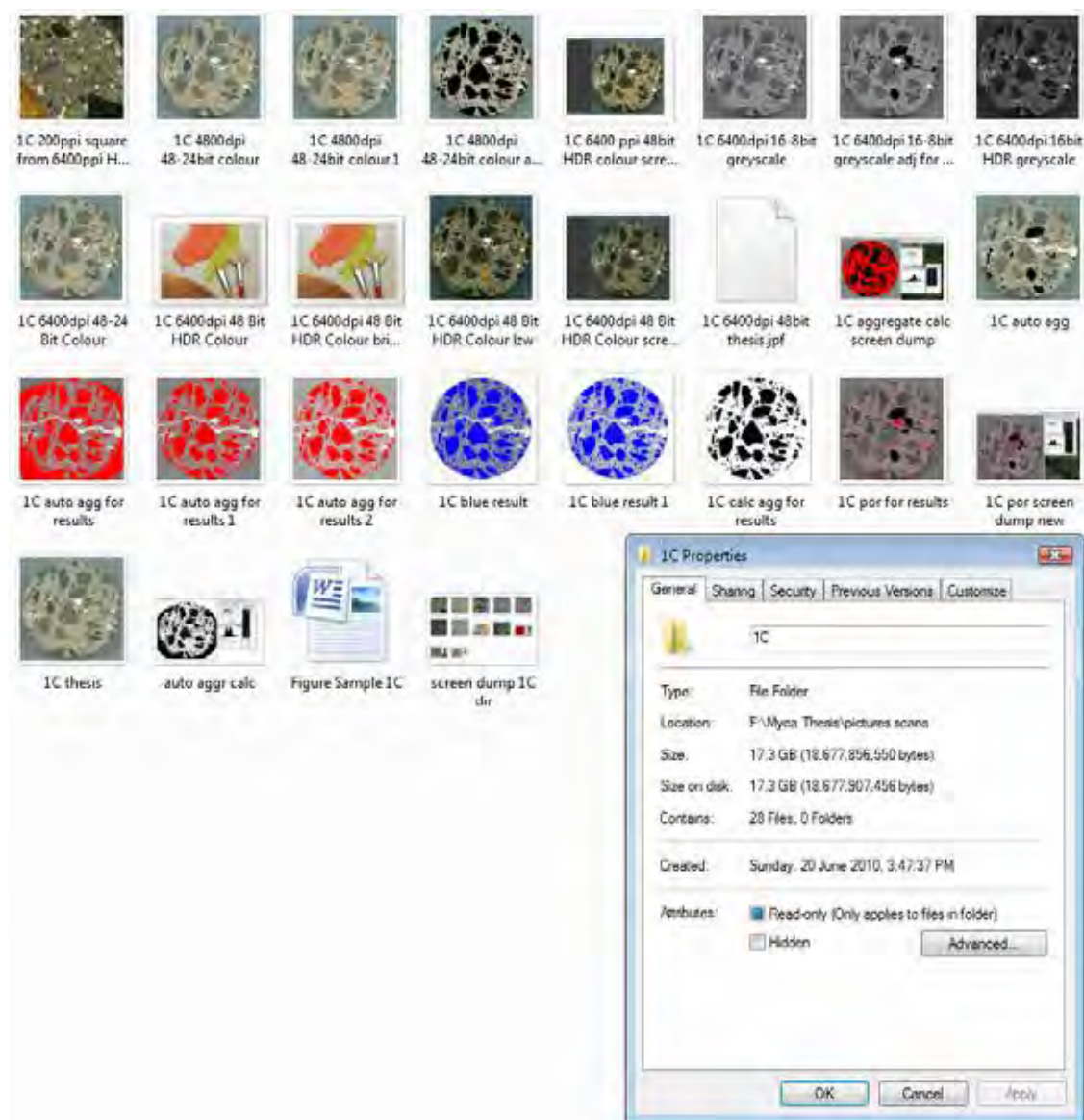
Sample 1A High Resolution Digital Image Only Folder



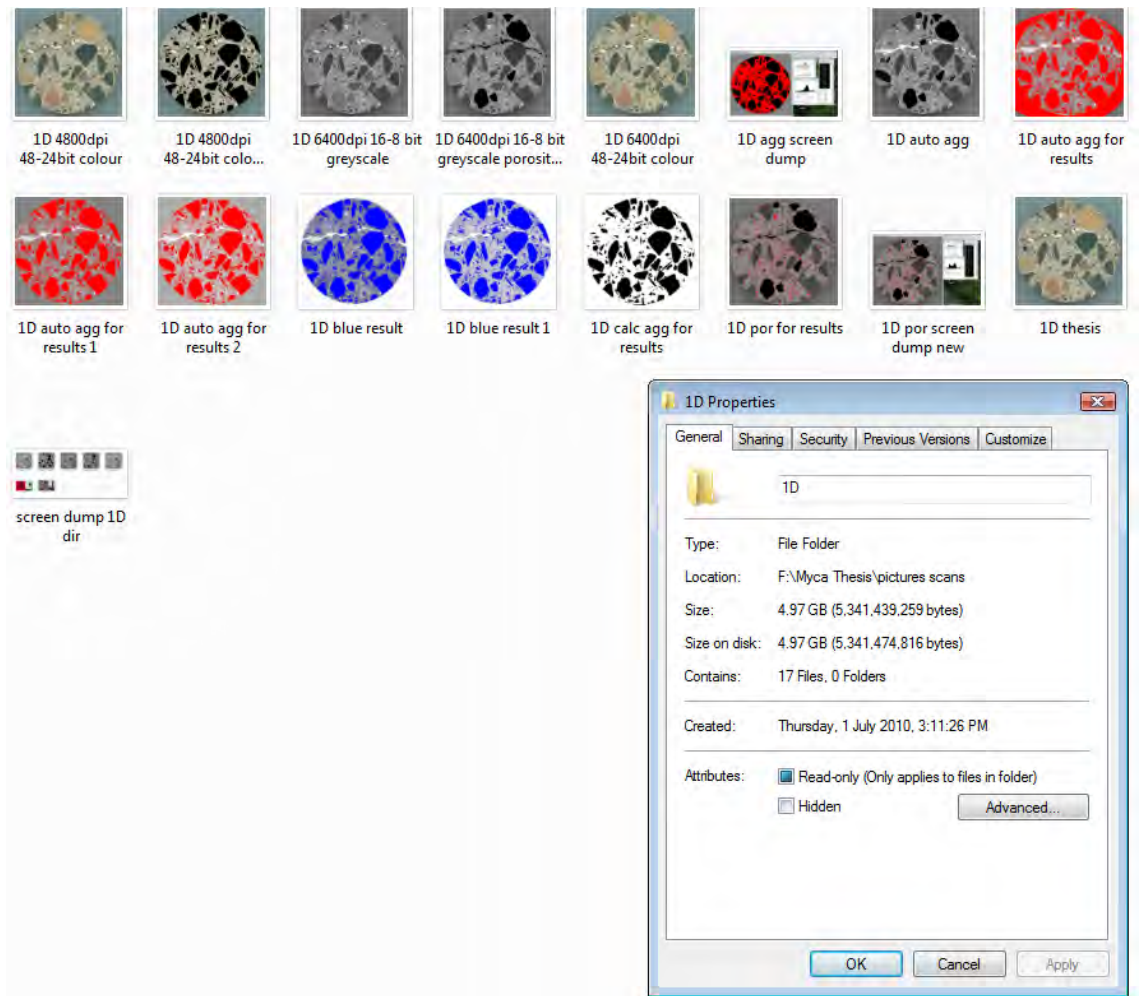
Sample 1B High Resolution Digital Image Only Folder



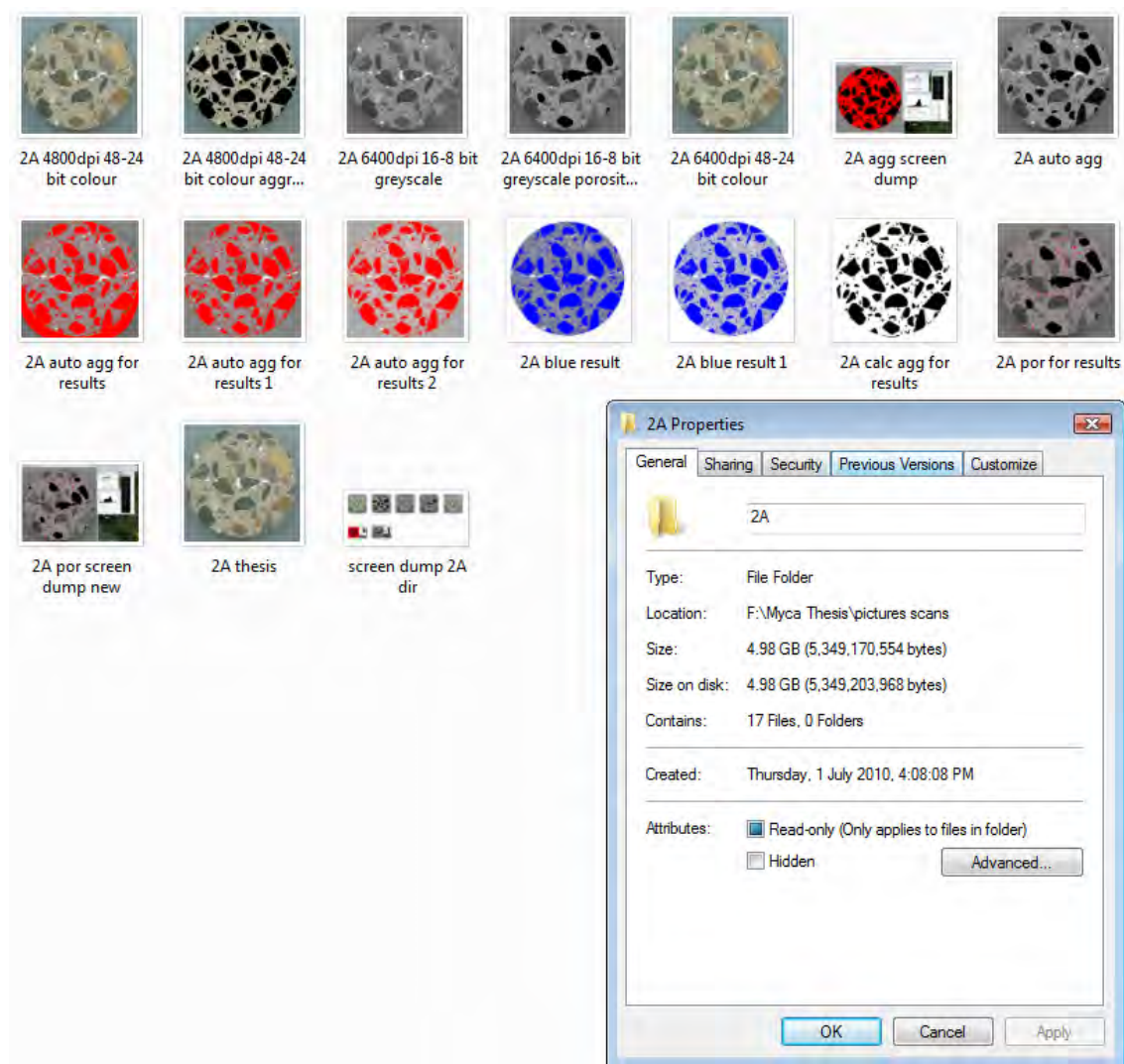
Sample 1C High Resolution Digital Image Only Folder




Sample 1D High Resolution Digital Image Only Folder




Sample 2A High Resolution Digital Image Only Folder




Sample 2B High Resolution Digital Image Only Folder




2B 4800dpi 48-24 bit colour



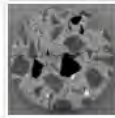
2B 4800dpi 48-24 bit colour aggr...




2B 4800dpi 48-24 bit colour auto agg




2B 6400dpi 16-8 bit greyscale



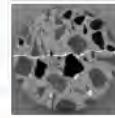
2B 6400dpi 16-8 bit greyscale porosit...



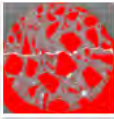
2B 6400dpi 48-24 bit colour



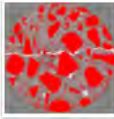
2B agg screen dump



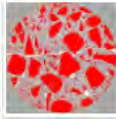
2B auto agg



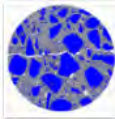
2B auto agg for results



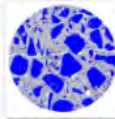
2B auto agg for results 1




2B auto agg for results 2



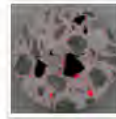
2B blue result




2B blue result 1




2B calc agg for results




2B por for results




2B por screen dump new



2B thesis



auto aggr calc



screen dump 2B dir

2B Properties

General

Sharing

Security

Previous Versions

Customize

2B

Type: File Folder

Location: F:\Myca Thesis\pictures scans

Size: 5.98 GB (6,422,193,346 bytes)

Size on disk: 5.98 GB (6,422,224,896 bytes)

Contains: 19 Files, 0 Folders

Created: Thursday, 1 July 2010, 4:08:15 PM

Attributes: ☒ Read-only (Only applies to files in folder)
☐ Hidden

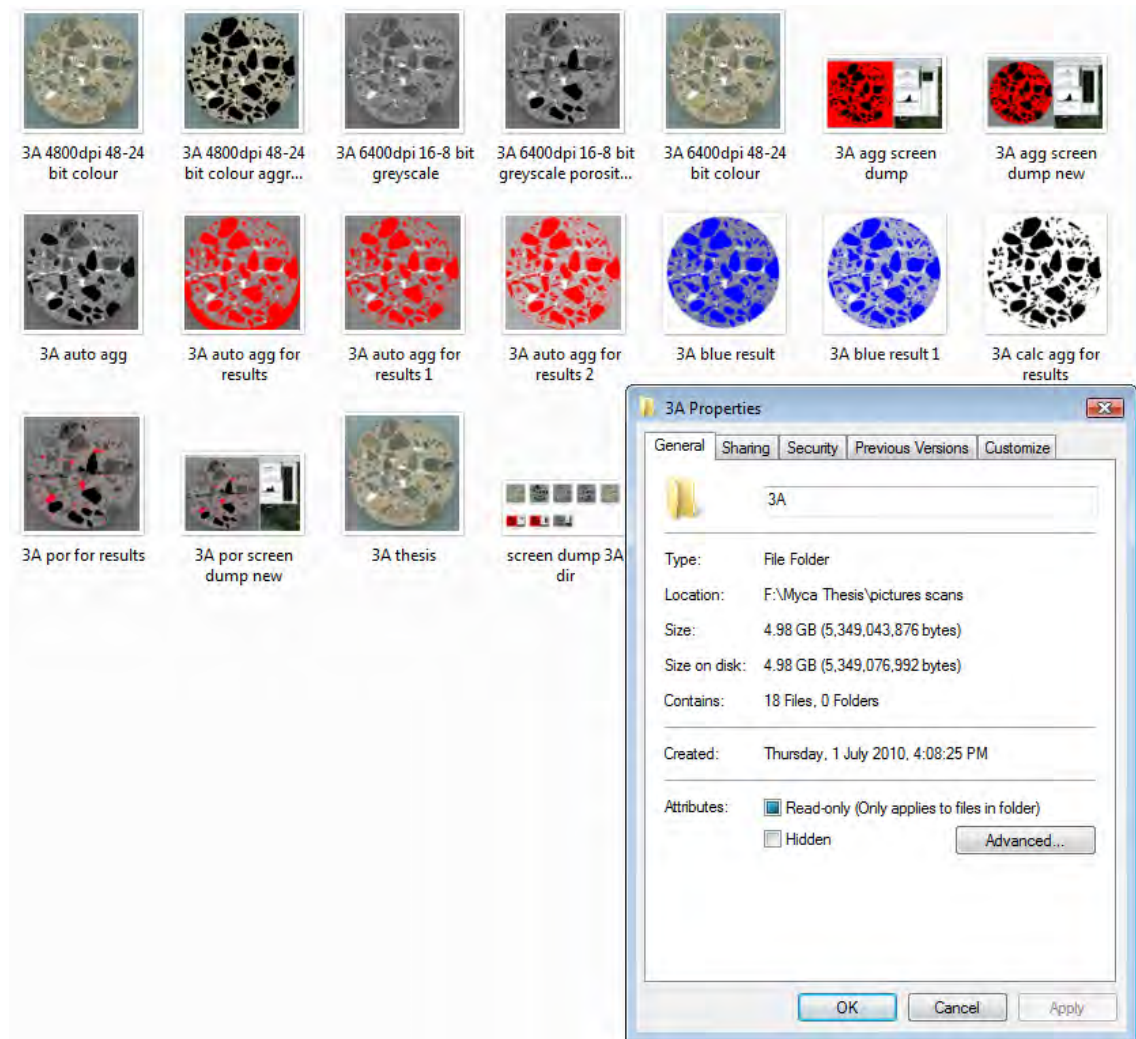
Advanced...

OK

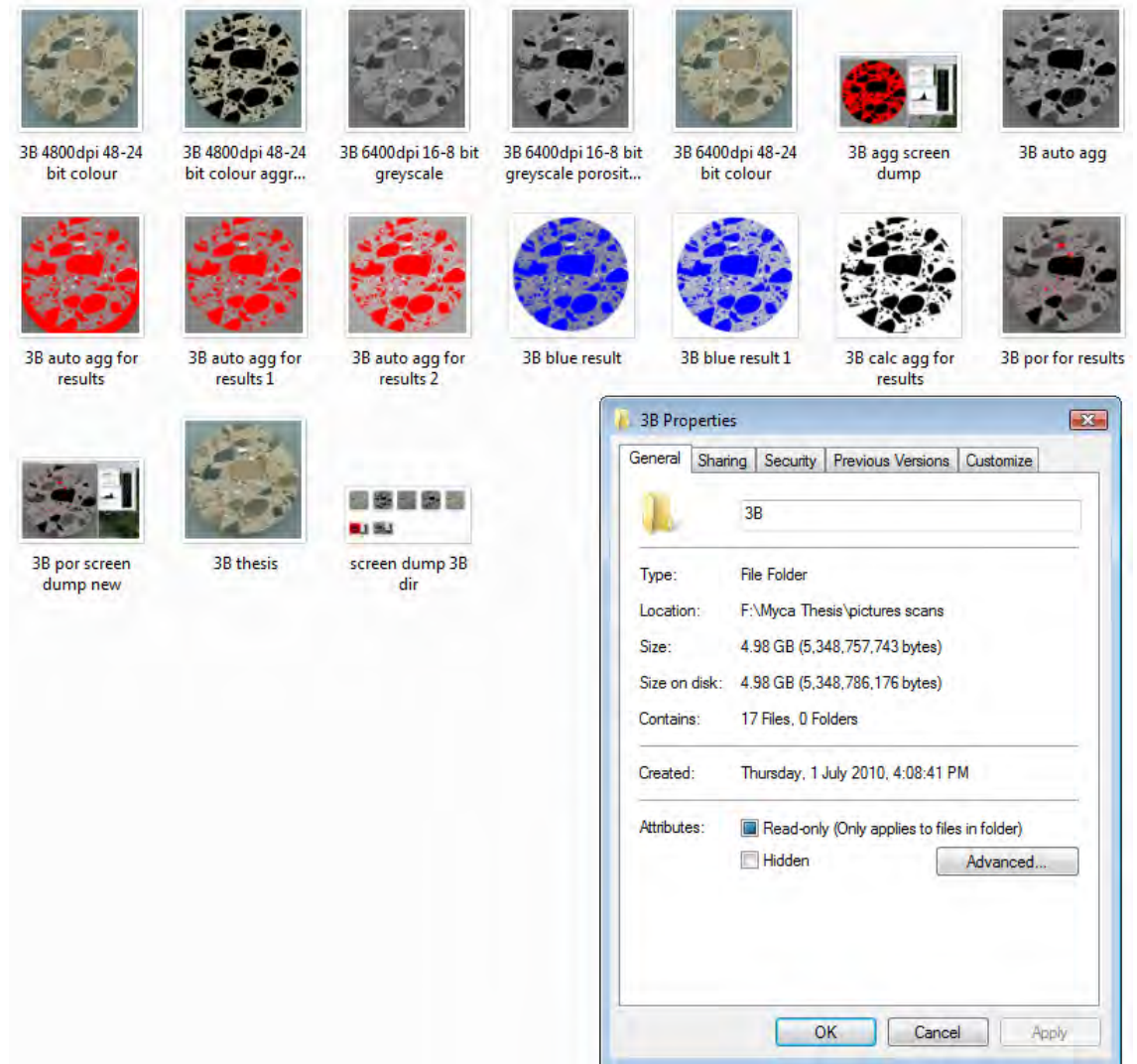
Cancel

Apply

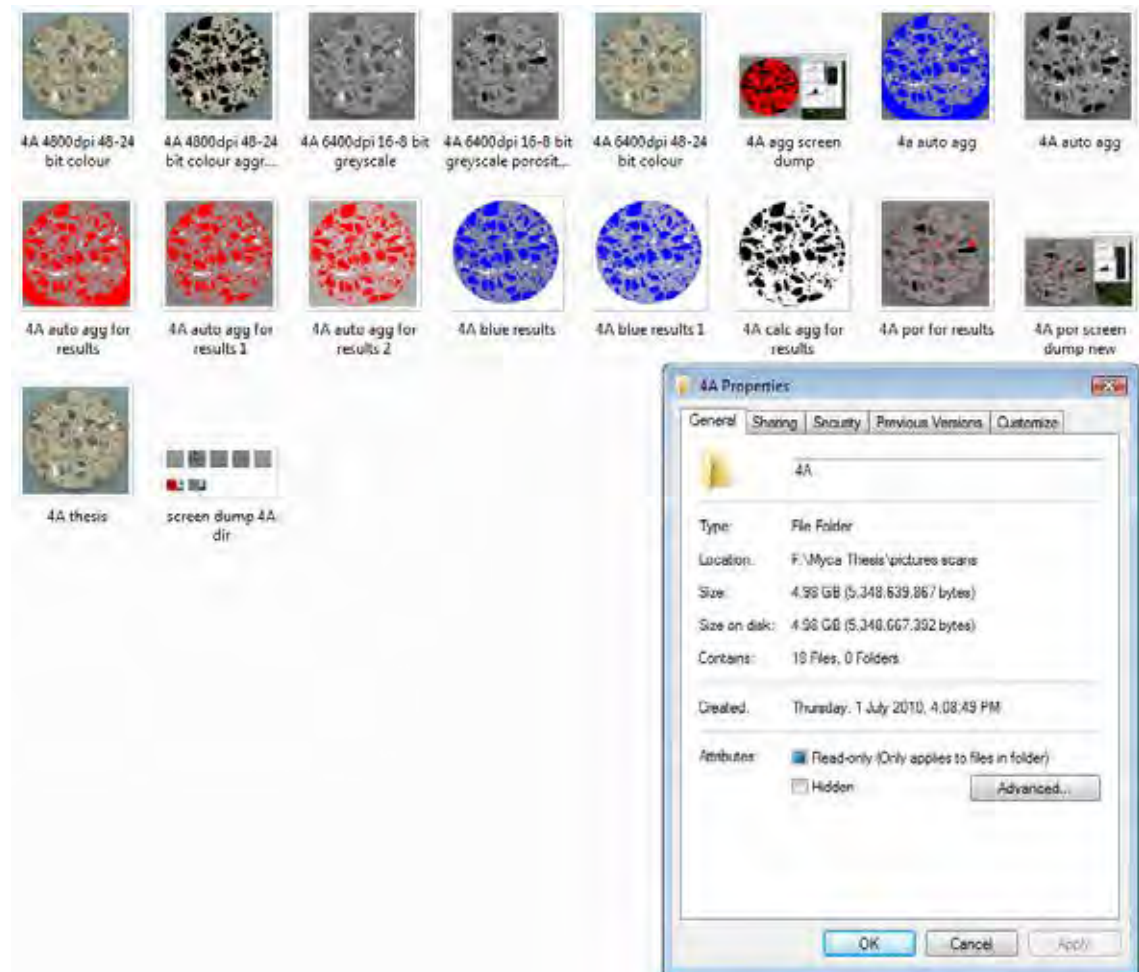
Sample 3A High Resolution Digital Image Only Folder



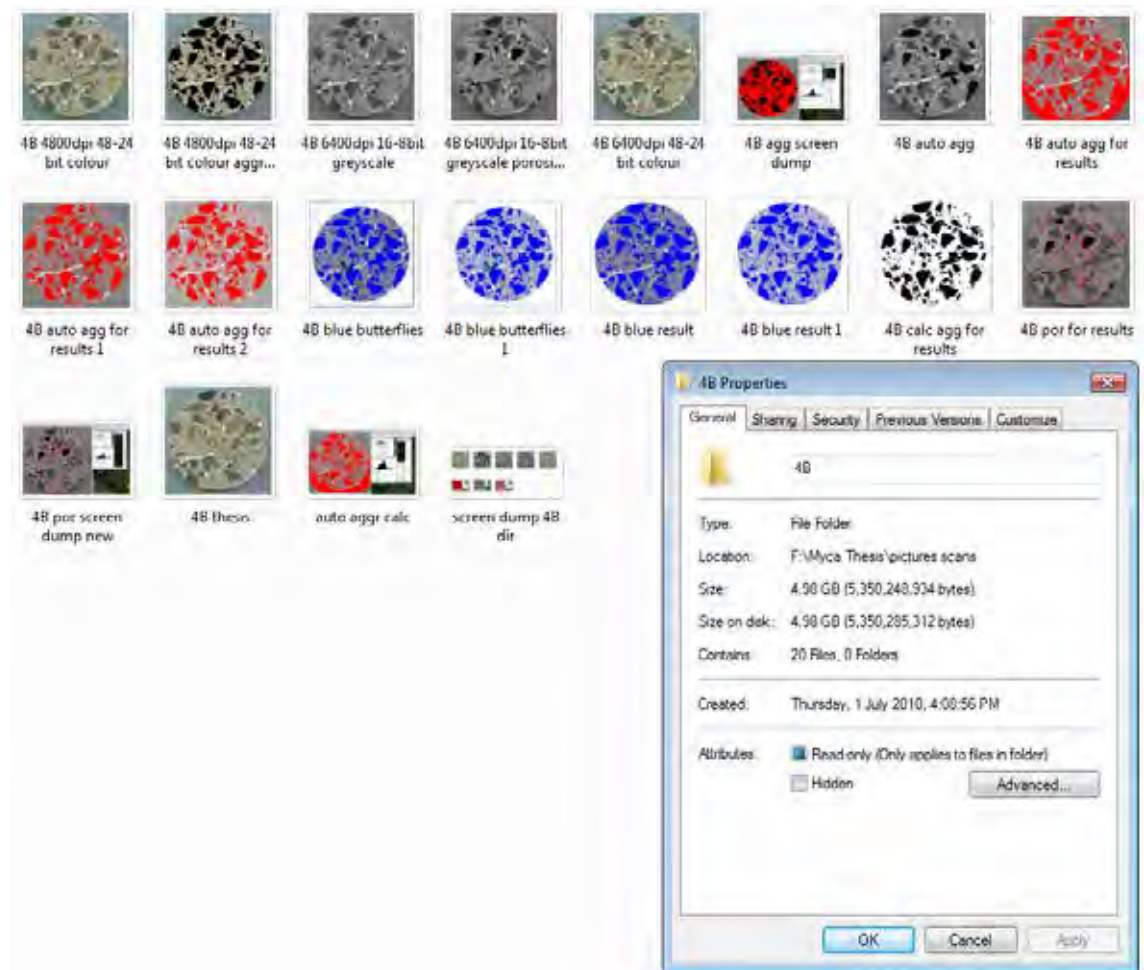
Sample 3B High Resolution Digital Image Only Folder



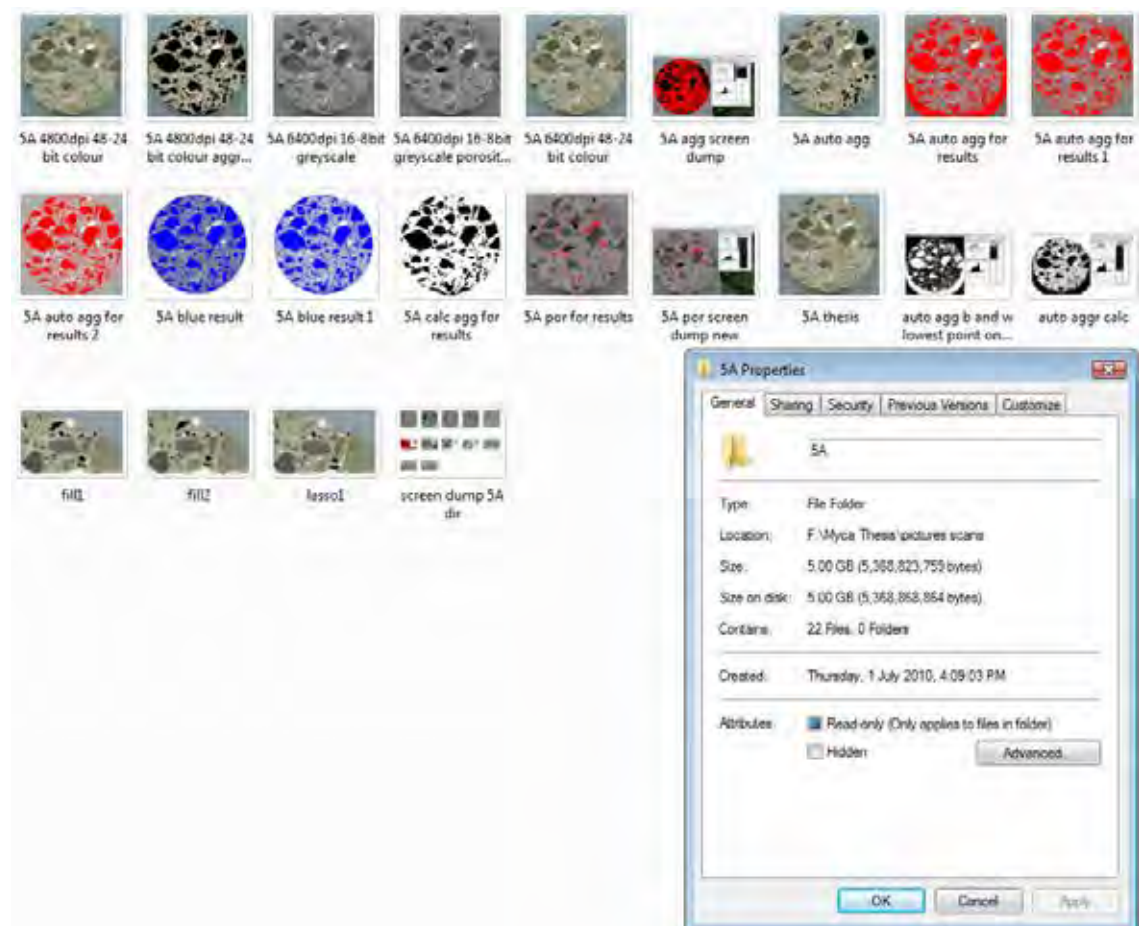
Sample 4A High Resolution Digital Image Only Folder



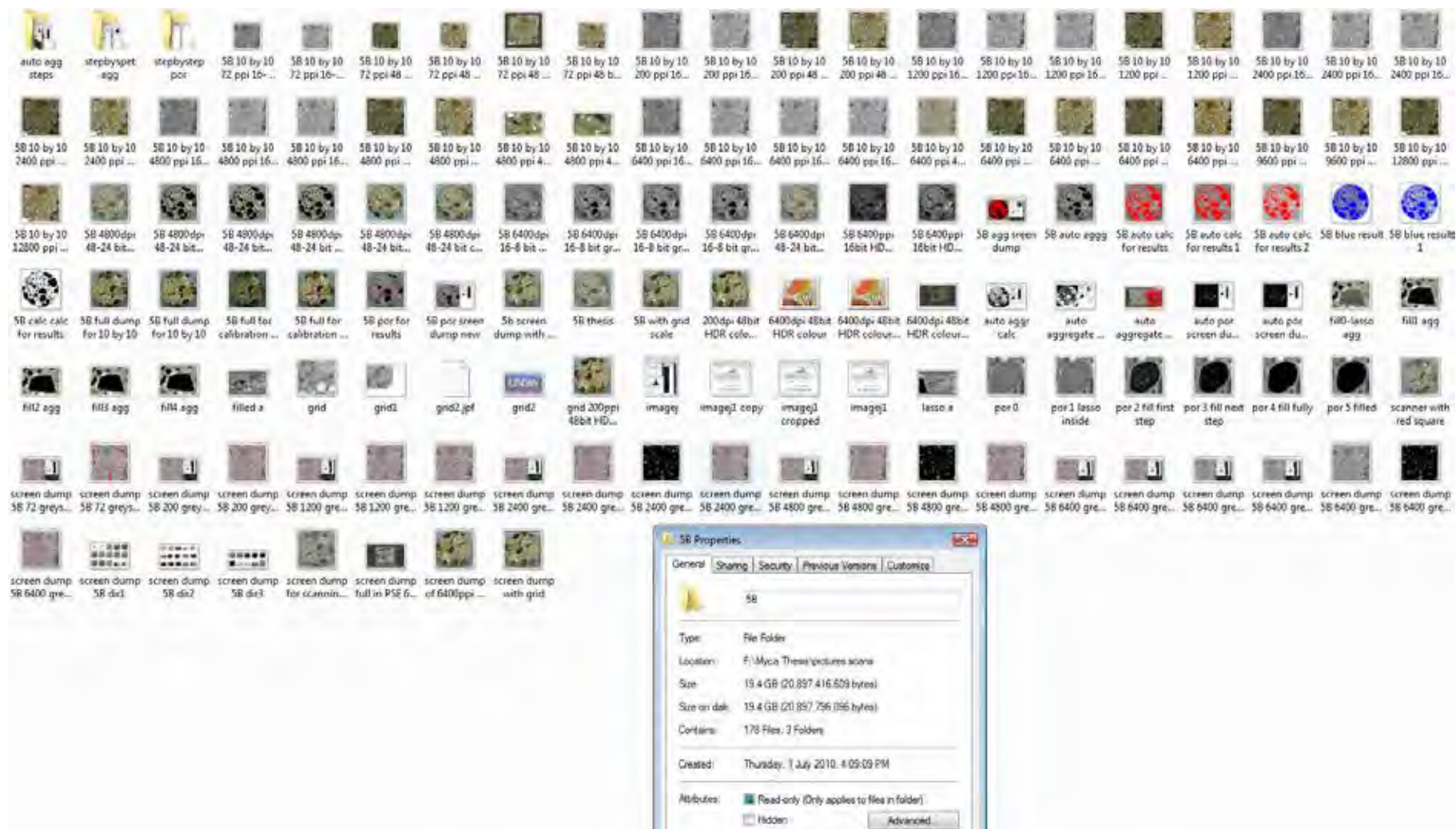
Sample 4B High Resolution Digital Image Only Folder



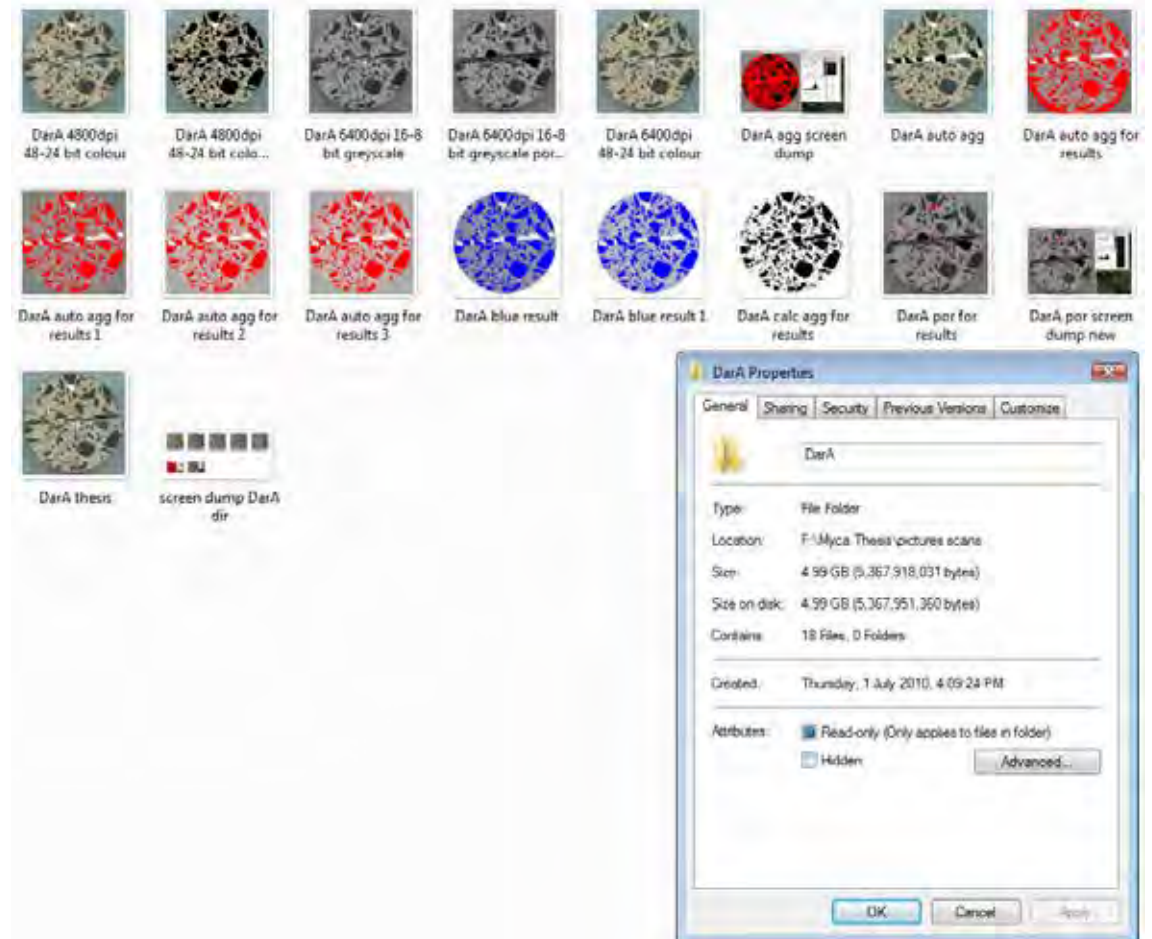
Sample 5A High Resolution Digital Image Only Folder



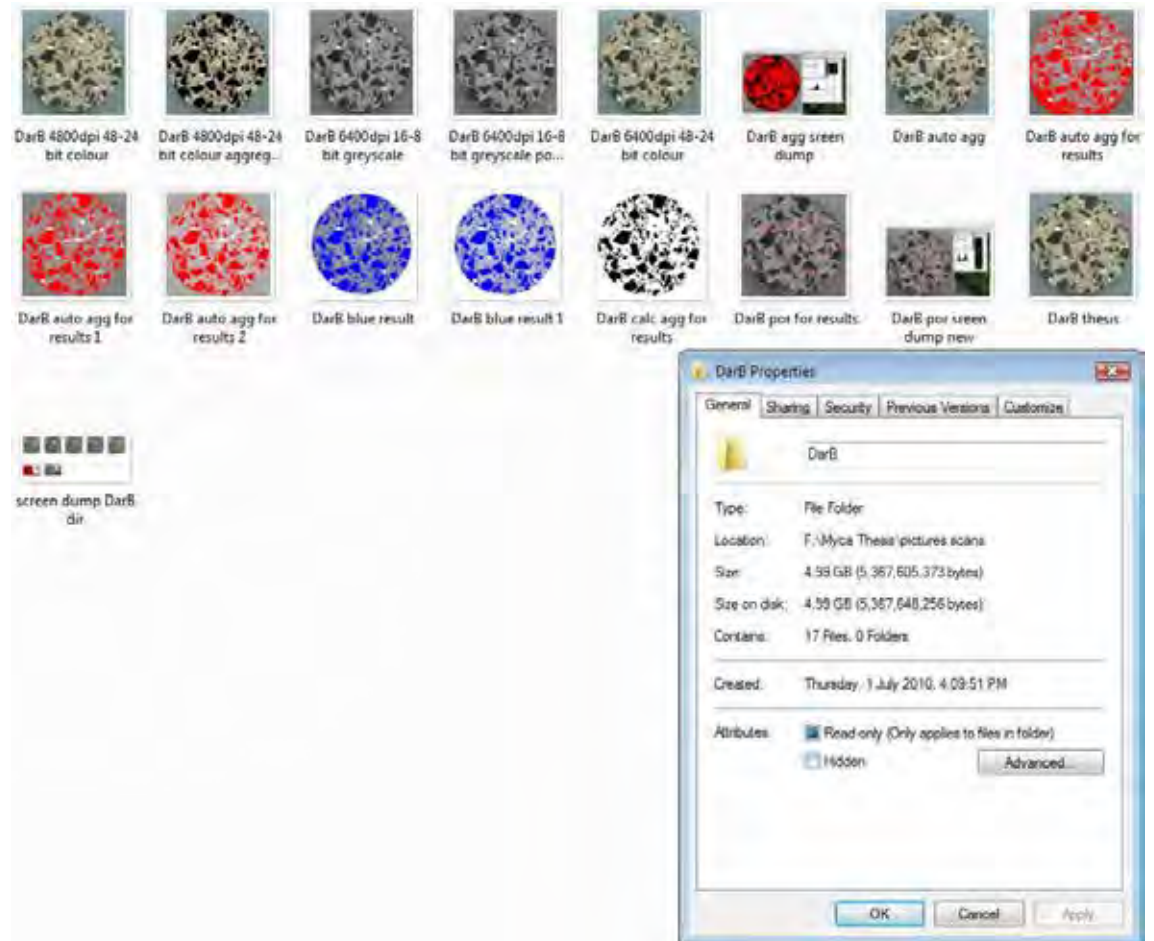
Sample 5B High Resolution Digital Image Only Folder



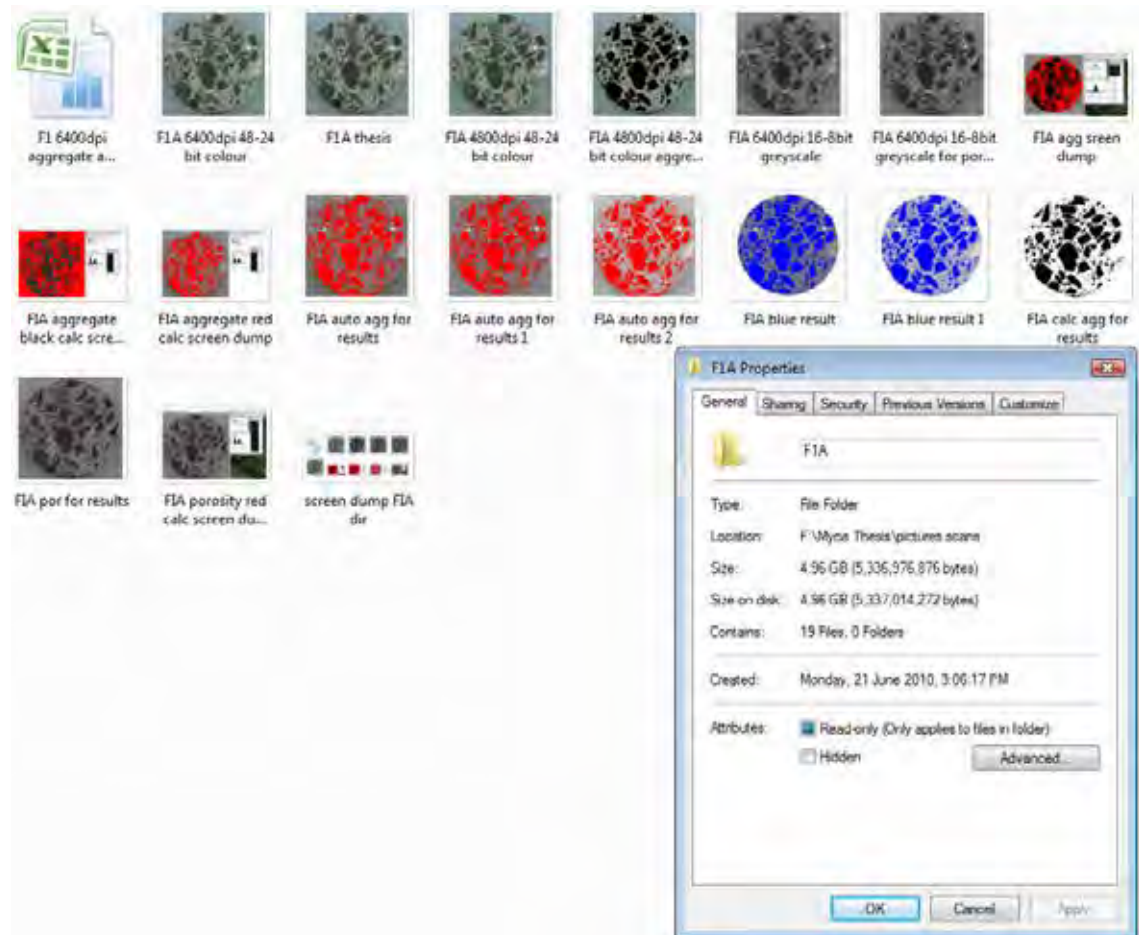
Sample DarA High Resolution Digital Image Only Folder



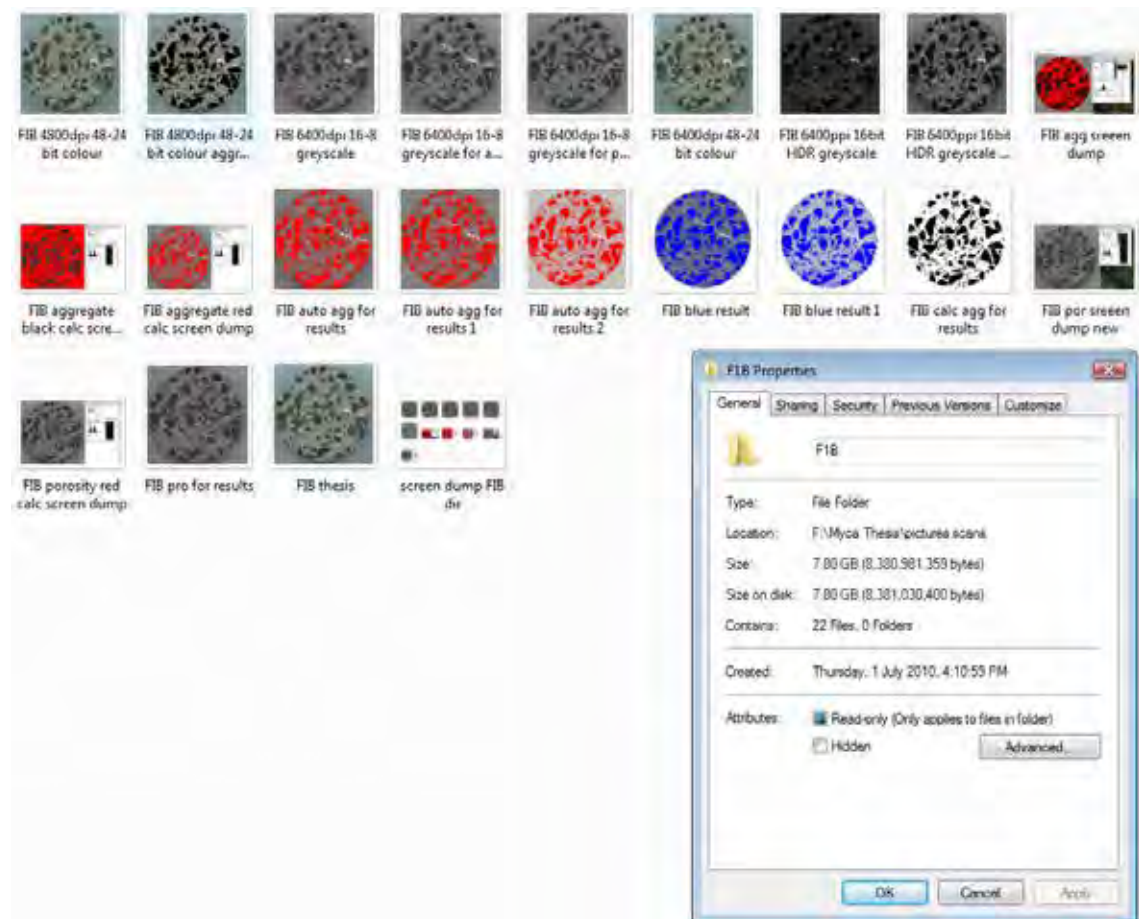
Sample DarB High Resolution Digital Image Only Folder



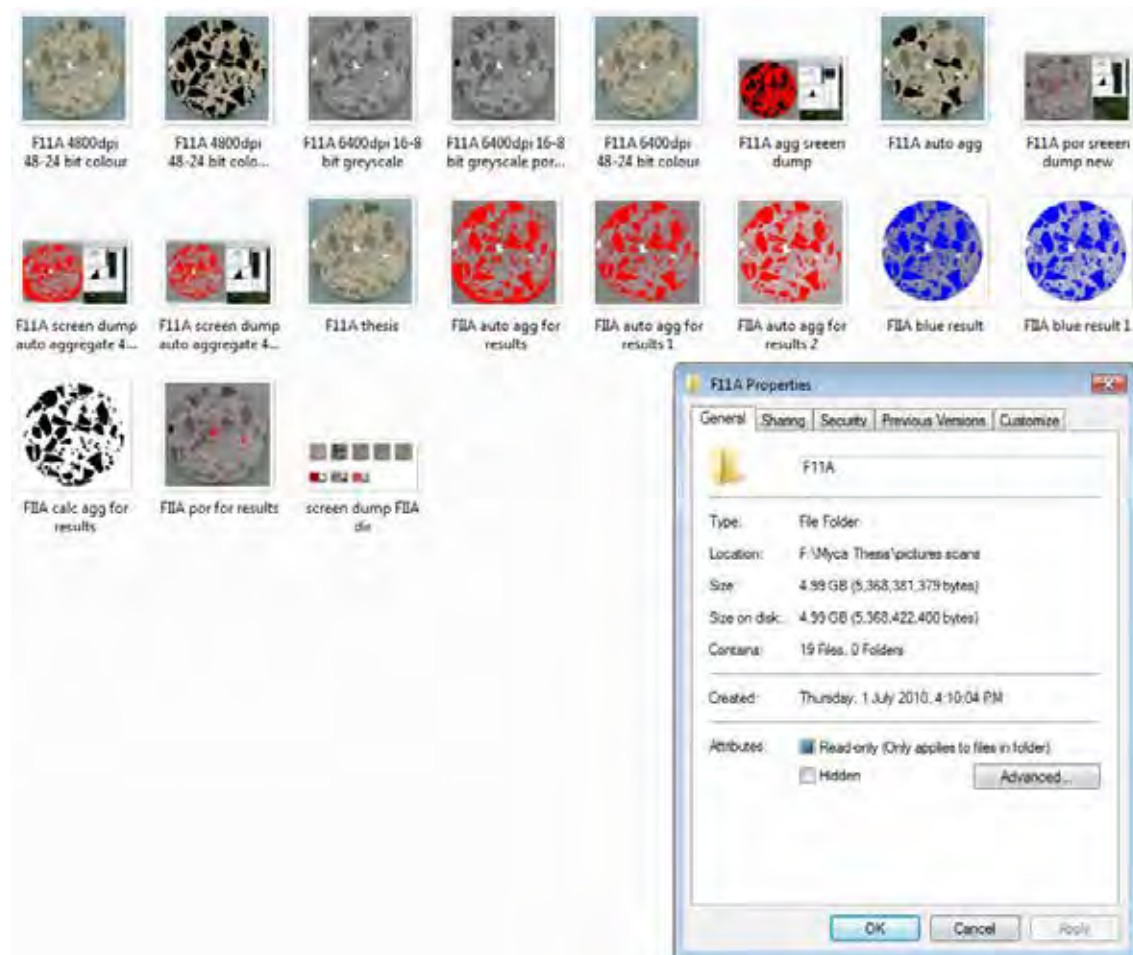
Sample FIA High Resolution Digital Image Only Folder



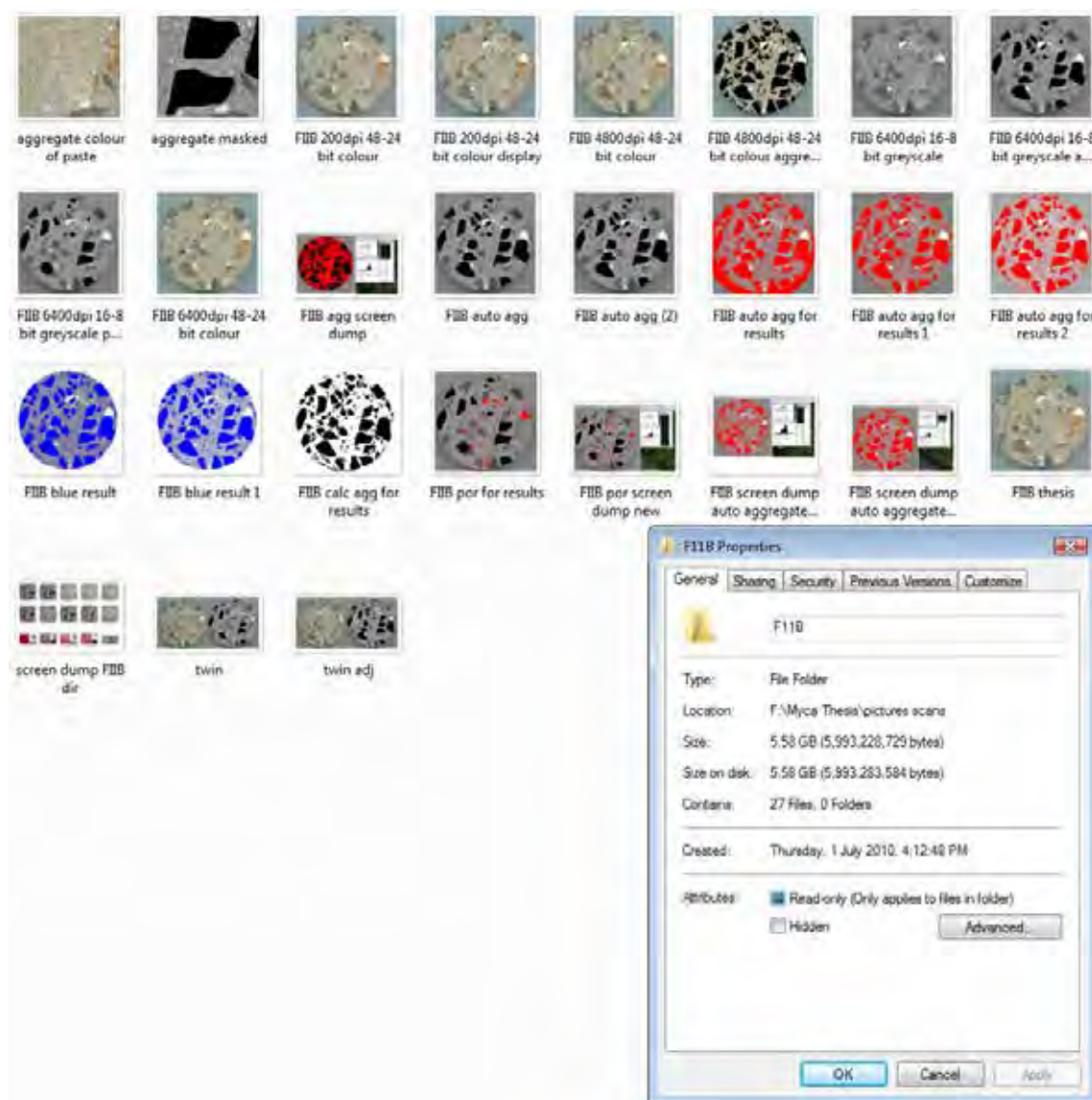
Sample FIB High Resolution Digital Image Only Folder



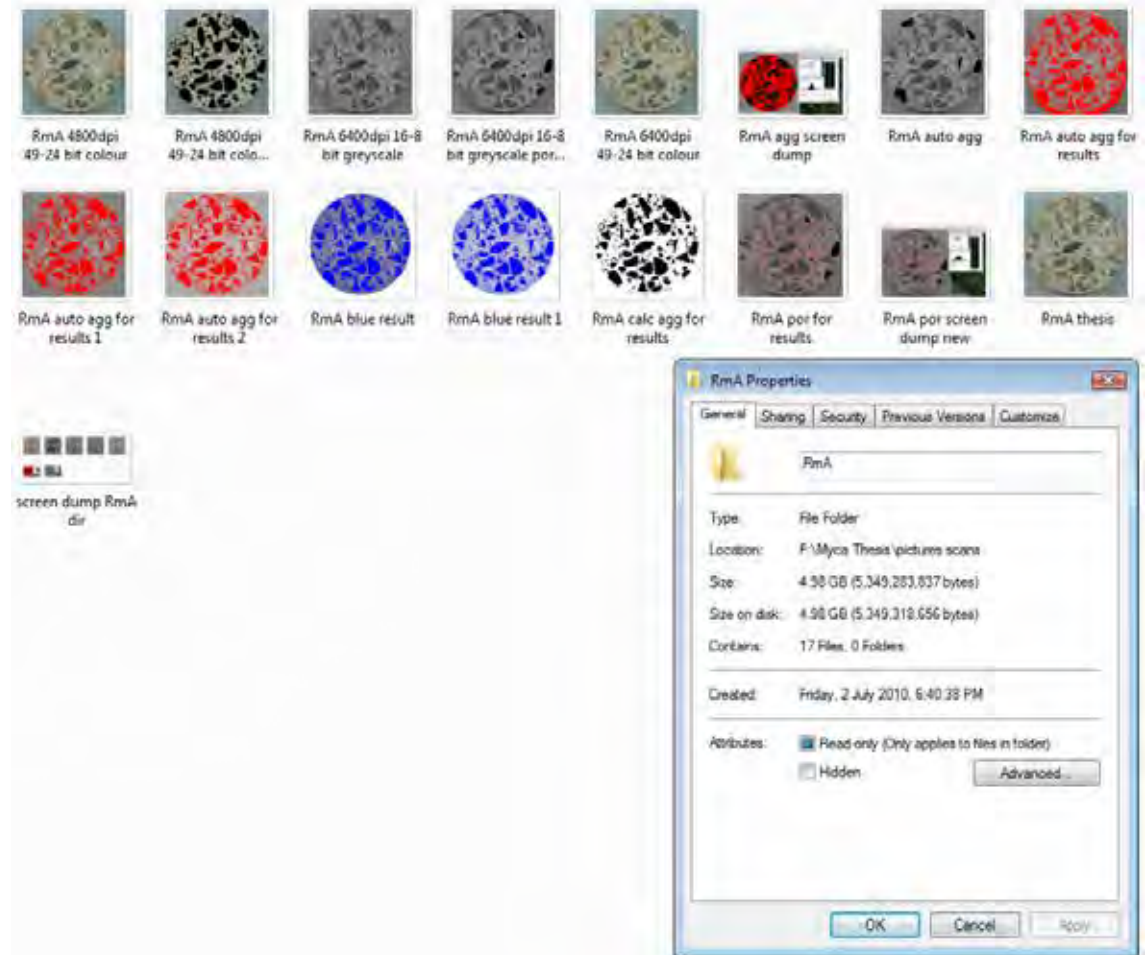
Sample F11A High Resolution Digital Image Only Folder



Sample FIIB High Resolution Digital Image Only Folder



Sample RmA High Resolution Digital Image Only Folder



Sample RmB High Resolution Digital Image Only Folder

